

Establishing the Chronostratigraphy and Miocene-Pliocene
Palaeoenvironmental History of the Fazzan Basin, Libyan
Sahara.

Thesis submitted for the degree of
Doctor of Philosophy

Submitted September 2016

by

Helena Elizabeth White

Department of Geography, University of Leicester

Abstract

Establishing the Chronostratigraphy and Miocene-Pliocene Palaeoenvironmental History of the Fazzan Basin, Libyan Sahara.

By Helena E. White

The vastness of the Sahara Desert makes it a key region for the study of global climate change. Large and important gaps remain, however, in our understanding of the palaeoenvironmental history of the Sahara due to limited terrestrial evidence. The Fazzan Basin, south-west Libya, is one of a few regions to document North Africa's palaeohydrological history in the form of lake shorelines and sedimentary deposits. The most extensive of these belongs to the Al Mahruqah Formation, recently upgraded to Group status, which is believed to have been deposited by Lake Megafazzan.

Previous dating using OSL/U-series has revealed the deposits to be of Quaternary age. However, the origin and age of the deposits are still subject to ongoing debate with the chronological and palaeoenvironmental framework of Miocene-Pliocene units severely lacking. In order to develop and extend the knowledge of the basin during the Neogene, geochemical and sedimentological analyses have been conducted on deposits from six stratigraphic sections from across the northern Fazzan Basin. Palaeomagnetic dating, which is able to date beyond the range of previous dating techniques, has also been completed.

This research provides what is believed to be the only low resolution, long-term palaeoenvironmental record of the central Sahara. Magnetostratigraphic and geochemical assessments question the previously proposed ages of the Al Mahruqah Group revealing that several humid intervals leading to several phases of lake development not only occurred in the Quaternary, but throughout the Miocene and early Pliocene. It is therefore proposed that the main drainage networks of the Fazzan basin were established in the early Miocene and hence ideas originally thought about the geomorphological history of the basin need to be redeveloped.

It is hoped this research will not only help to fill the palaeoclimatic void of this important region but also potentially contribute to the understanding of the wider Saharan palaeoclimate.

Acknowledgments

Special thanks to my primary supervisor Dr. Sue McLaren for her valuable support and guidance not only during my PhD, but also my previous years at Leicester. I'd also like to gratefully acknowledge the support both academically and financially from my external supervisors, Prof. Nick Drake and Dr. Mark Hounslow. Thanks also to Dr. Arnoud Boom and Javier for their assistance and guidance with stable isotope analysis.

I would like to acknowledge the support of the QRA who kindly awarded me a 'New Research Workers Award' in October 2014 which allowed me to complete the final palaeomagnetic measurements at Lancaster.

I am grateful to the many people, namely, Mustafa Salem, Ahmed El-Hawat, Osama Hlal, Dr. Kevin White, and Dr. Simon Armitage, who provided logistical support and assisted in data collection during the number of field seasons to Libya. Hopefully one day I will be able to visit the area I feel I know so well for myself.

Thanks must be given to all the technicians in the Department including Gemma Ollerenshaw and Colin Cunningham for their help when making my endless amounts of thin sections. Special thanks must be given to Simon Benson who I imagine never wants to make phosphoric acid again (even though he should now be an expert!). To Nick Marsh and especially to Dr. Mike Norry for assistance with XRF analysis. I must also thank the technicians, Vassil Karloukovski and Sam Harris, from the CEMP lab in Lancaster for helping prep samples and training me to use the GM400, even though it was temperamental to say the least.

A special shout out must be made to my friends, Becky, Tim, Sandor, Kirsty, Amy and Sam, to my fellow PhD students Alex and Dave and especially to my best friend and all round partner in crime and bad influence, Hannah. They have helped support me and provided so many much needed laughs during my PhD. And the least we say about our office tomfoolery the better.

Finally, and most importantly, thanks so much to my parents, Mary and Rob, and my soon to be husband, Karl, for supporting me financially and emotionally through the often difficult and somewhat stressful journey of a PhD. Without their love and support, completing this PhD would not have been possible and I will be eternally grateful to them all.

Table of Contents

Abstract.....	i
Acknowledgments	ii
Table of Contents	iii
List of Tables	vi
List of Plates and Figures	ix
Abbreviations	xx
1 Introduction	1
1.1 The Sahara Desert: A Key Region for Global Climate Studies.....	1
1.2 Importance of the Fazzan Basin.....	3
1.3 Current Physical Characteristics of the Fazzan	5
1.3.1 Climate	5
1.3.2 Geological and Geomorphological setting	6
1.4 Aim	8
1.5 Structure of Thesis	8
2 Literature Review	10
2.1 Palaeoclimatic/environmental Evolution of the Sahara: A Central Saharan Perspective	10
2.1.1 Miocene	11
2.1.2 Pliocene	19
2.2 Geological and geomorphological history of the Fazzan and neighbouring basins 22	
2.2.1 Late Miocene	23
2.2.2 Pliocene	26
2.3 The Al Mahruqah Formation: Current Lithostratigraphic understanding.....	30
2.4 Magnetostratigraphy	39
2.4.1 Secular variation	41
2.4.2 Polarity change and polarity transitions	42
2.4.3 Excursions and Tiny Wiggles.....	44
2.4.4 Miocene-Pliocene Magnetostratigraphy	45
2.4.5 Magnetic Minerals	46
2.4.6 Magnetisation Process in Deposits	51
2.4.7 Magnetic chronology studies in arid/semi-arid environments	53
2.5 Terrestrial Carbonates and the use of Stable Isotopes	55

2.5.1	Terrestrial carbonates	55
2.5.2	Palaeohydrology: The use of Oxygen and Carbon Stable Isotopes.....	63
2.6	Formulation of Research Questions.....	71
3	Study Sites.....	73
3.1	Identification of Study Sites	73
3.2	Study Site Information.....	74
4	Research Methodology.....	101
4.1	Laboratory Analyses	103
4.1.1	Thin Section Analysis.....	103
4.1.2	Stable Isotope Analysis	106
4.1.3	Palaeomagnetism	106
Sample Collection and Preparation	106	
Sample Measurements.....	107	
Sample Analysis	108	
4.1.4	Additional Methods Explored	109
5	Results: The Shabirinah and Brak Formations.....	112
5.1	Palaeoenvironmental Indicators: Petrography and Palaeohydrology	112
5.1.1	Shabirinah Formation	112
5.1.1.1	Ariel Section	112
5.1.1.2	Maharshim Member (M Mbr).....	120
5.1.1.3	Stromatolite Member (STR Mbr)	121
5.1.1.4	Tmessah Member (TM Mbr)	128
5.1.1.5	Kunayr Member (K Mbr).....	131
5.1.1.6	Brak Section.....	140
5.1.2	Brak Formation.....	142
5.2	Magnetostratigraphy: Age of the Shabirinah and Brak Formations	150
5.2.1	Scalar Magnetic Properties.....	150
5.2.2	Palaeomagnetic Results	154
5.2.3	Mean Directions and Palaeopoles.....	161
5.2.4	Magnetostratigraphic Age Model.....	163
6	Results: The Zarzur Formation	171
6.1	Palaeoenvironmental Indicators: Petrography and Palaeohydrology	171
6.1.1	Sayl Member (SL Mbr)	171

6.1.2	Sifar Member (SI Mbr).....	173
6.1.3	Bir al Zallaf Member (BZ Mbr)	192
6.2	Magnetostratigraphy: Age of the Zazur Formation	202
6.2.1	Scalar Magnetic Properties.....	202
6.2.2	Palaeomagnetic Results	207
6.2.3	Mean Directions and Palaeopoles.....	218
6.2.4	Magnetostratigraphic Age Model.....	220
7	Discussion: Palaeoenvironment of the Fazzan.....	228
7.1	Interpretation of the Early Miocene (Aquitanian-Burdigalian) deposits	228
7.1.1	Shabirinah Formation (Lower Ariel section).....	228
7.1.2	Maharshim-Tmessah Members (Temssah section).....	230
7.2	Interpretation of the Middle Miocene (Langhian-Serravallian) Deposits.....	236
7.2.1	Kunayr Member (Upper Tmessah/Ariel sections).....	236
7.2.2	Brak and the Brak Formation	239
7.3	Revised palaeoenvironmental understanding of the Miocene Fazzan Basin.....	243
7.4	Interpretation of the Late Miocene (late Tortonian-Messinian) deposits	253
7.4.1	Sayl Member	253
7.4.2	Sifar Member.....	253
7.5	Interpretation of the Late Miocene-Early Pliocene (Messinian-Zanclean) deposits 259	
7.5.1	Bir al Zallaf Member	259
7.6	Revised palaeoenvironmental understanding of the Late Miocene-Early Pliocene Fazzan Basin	261
8	Discussion: Assessing the Palaeomagnetic Age	268
8.1	Differences in age of the AMG to previous U-series dates	268
8.2	Chronological Controls.....	272
8.3	The use of Palaeomagnetism	274
9	Conclusion.....	277
9.1	Further work	279
	Appendix	281
	References	313

List of Tables

Table 2.1 Summary of key characteristics of the members of the Al Mahruqah Formation described in Thiedig et al. (2000), Geyh and Thiedig (2008). Note: Ages are detrital corrected Th/U ages documented in Geyh and Thiedig (2008).....	34
Table 2.2. Summary of the key characteristics of some of the most common magnetic minerals found in deposits. 1-Opdyke and Channell (1996), 2-Tarling and Hrouda (1993), 3-Tarling (1983), 4-Lanza and Meloni (2006), 5-Gribble and Hall (1992), 6-Butler (1992), 7-Maher (2007), 8-Maher (2011)	51
Table 2.3. Micromorphological differences of Alpha and Beta calcretes. 1-Tucker and Wright (1991, pg6), 2-Wright and Tucker (1990, pg345), 3-Alonso-Zarza (2003), 4-Klappa (1980).....	62
Table 3.1. Site details of the Ariel section. Note: The codes in the ‘site’ column correspond to the pins on the Google Earth image seen in Figure 3.6, pg82.....	75
Table 3.2 Site details of the Tmessah section. Note: The codes in the ‘site’ column correspond to the pins on the Google Earth image seen in Figure 3.7, pg83.....	76
Table 3.3 Site details of the Brak section. Please see Figure 3.8 for a Google Earth Image of the site on pg84.	77
Table 3.4 Site details of the Bir al Zallaf sections. Note: The codes in the ‘site’ column correspond to the pins on the Google Earth image seen in Figure 3.12, pg90.....	86
Table 3.5 Site details of the Al Wafa section. Note: The codes in the ‘site’ column correspond to the pins on the Google Earth image seen in Figure 3.17, pg98.....	92
Table 3.6 Site details of the Qarat al Mrar 1/2 sections. Note: The codes in the ‘site’ column correspond to the pins on the Google Earth image seen in Figure 3.18/19, pg99/100.....	94
Table 3.7 Year collected and location of additional samples collected.....	94
Table 4.1 Summary to show what palaeomagnetic measurements were conducted by the author during this project and what measurements, including heavy mineral, were conducted before the start of this PhD. Note: CEMP – Centre for Environmental Magnetism and Palaeomagnetism. CASP – geological research company formerly known as Cambridge Arctic Shelf Programme.	102
Table 5.1. Hand sample descriptions of the SHF and K Member of the AP section.	115
Table 5.2. Correlation matrix of the AP deposits. Values in bold are those discussed in the text.	117
Table 5.3. Hand sample descriptions of the deposits from the four members of the TM section..	123
Table 5.4 Hand sample descriptions of the deposits from the BC section.	143
Table 5.5 Table outlining some of the key statistics of the SHF and BKF. ‘%’ refers to the total number of specimens classified as s1-s3/t1-t3. ‘mean α_{95} ’ when listed under s-class refers to the mean α_{95} of the linear fits, when listed under t-class it refers to the mean α_{95} for the poles to the fitted planes. ‘mean excess SD’ (rho, ρ) refers to the mean excess standard deviation parameter calculated for the different classes (for s-class-calculated from the average line rho value in LINEFIND, for t-class- calculated from the average plane rho value in LINEFIND). The t-class mean excess SD could not be calculated as the plane rho values were not recorded.....	160
Table 5.6. Directional means, reversal tests and virtual geomagnetic poles for the sections of the SHF and BKF. Note: α_{95} is the Fisher 95% cone of confidence, Ntotal= total number of specimens measured, Nlines= number specimens with s-class line fit used in the mean Fisher calculation, Nplanes= number of specimens with t-class (great circle fit) and used in the mean Fisher calculation, Ra and Rb indicate a pass of the reversal test with an observed gamma of <5 and <10 respectively, R- is a failed reversal test, γ_o is the observed gamma, γ_c is the critical gamma. Dp/Dm is the semi-axes of the ellipse of confidence about the palaeomagnetic pole.	161

Table 6.1 Hand sample descriptions of the SL Mbr deposits from the QM2 section. The BZ-E section also contains one deposit related to this member, however as it is only one deposit, the hand sample characteristics are not included in this table.	171
Table 6.2 Hand sample descriptions of the SI Mbr deposits from the BZ (all), QM1/2 and M sections. The hand sample descriptions of the BZ sections are discussed as one along with the two QM sections due to the similar characteristics of the member in the sections.....	174
Table 6.3 Fossils and carbonate grains present in the deposits of the SI Member-BZ sections.....	175
Table 6.4 Average percentages of the clast size of the three main clastic units from the M section and the modern sand samples.....	188
Table 6.5 Hand sample descriptions of the Bir al Zallaf Member from the BZ-E and QM1 sections.	192
Table 6.6 Table outlining some of the key statistics of the ZF. ‘%’ refers to the total number of specimens classified as s1-s3/t1-t3. ‘mean α_{95} ’ when listed under s-class refers to the mean α_{95} of the linear fits, when listed under t-class it refers to the mean α_{95} for the poles to the fitted planes. ‘mean excess SD’ (ρ , ρ) refers to the mean excess standard deviation parameters calculated for the different classes (for s-class-calculated from the average line ρ value in LINEFIND, for t-class calculated from the average plane ρ value in LINEFIND).	213
Table 6.7 Directional means, reversal tests and virtual geomagnetic poles of the sections from the ZF. Note: α_{95} is the Fisher 95% cone of confidence, N_{total} = total number of specimens measured, N_{lines} = number specimens with s-class line fit used in the mean Fisher calculation, N_{planes} = number of specimens with t-class (great circle fit) and used in the mean Fisher calculation, R_a and R_b indicate a pass of the reversal test with an observed gamma of <5 and <10 respectively, R_- is a failed reversal test, γ_o is the observed gamma, γ_c is the critical gamma. D_p/D_m is the semi-axes of the ellipse of confidence about the palaeomagnetic pole.	219
Table 7.1 Summary of the age, deposit type and depositional environments of the deposits assigned to the SHF and BKF.....	243
Table 7.2 Summary of the age, deposit type and depositional environments of the deposits assigned to the ZF. *Although the dates do not seem to be continuous between the SI Member of the BZ sections and the overlying BZ Member in the BZ-E section they in fact are. It is impossible to know the upper age of the SI member in the BZ-W section as we do not know how much of the R polarity unit is present. Likewise, the upper age of the SI Member in the BZ-E section is actually in the BZ Member so it is hard to know the cut off age for the SI Member in this section. Equally, the lower age limit of the BZ Member in the BZ-E section can only be calculated from the base of the N polarity unit as we don’t know how much time the small R polarity unit at the base represents. **The boundary of the SI and BZ Mbrs in QM1 occur at approximately half way in the N pol unit therefore the lower age of the BZ Mbr was calculated from this half way point. The upper age of the BZ Member in QM1 is the age of the base of the uppermost R polarity unit (i.e. the minimum age) as it is impossible to know how much of this R polarity unit has been recorded.....	261
Table 7.3 Characteristics and changes in the size of hydrologically open and closed lakes based on information from Leng and Marshall (2004). $\delta^{18}O$ ranges typical for the Holocene, S=seasonality, T=temperature, δp =isotopic composition of precipitation, P/E=amount of precipitation in relation to evaporation.....	266
Table 1. Table to show site names mentioned in this thesis and the variants used in other sources	281
Table 2. Table outlining the key distinguishing criteria of lacustrine, palustrine and calcrete deposits. Note: Differences between GC (groundwater calcretes) and PC (pedogenic calcretes) are noted in Table 2.3 in section 2.5.1. 1-Flugel (2010), 2-Alonso-Zarza (2003), 3-Verrecchia (2007), 4-Freytet and Verrecchia (2002).	286

Table 3. Table of the details of the additional sections sampled at the QM site. QM3 contained deposits which overlapped with the QM2 section (Drake et al., 2011).	287
Table 4. Table to show how the polarity of each horizon was defined. When the overlying horizon is of the same polarity however, the uncertainty can be reduced i.e. a half bar of grey to a bar which is just 1/3 grey.	287
Table 5. Average stable isotope values of the samples from the Shabirinah and Brak Formations.	296
Table 6. Average stable isotope values of the samples from the Zazur Formation.....	297
Table 7. Table to show the results of the laser particle size analysis of the samples from Al Wafa and the modern sample sites.....	298
Table 8. Raw XRF data of the Ariel samples.....	300
Table 9. Raw XRF data of the Al Wafa samples.	301
Table 10. Raw XRF data of the Bir al Zallaf samples.	303
Table 11. Raw XRF data of the BZ samples with poor totals and higher than usual Na ₂ O which were not reported in the main thesis.....	304
Table 12. Explanation of statistics derived from sequence slotting and the parameters used in sequence slotting from Hounslow et al. (2017).....	310
Table 13. Weighting options of the 5 variables used in sequence slotting on the ZF composites.	310

List of Plates and Figures

Plates

- Plate 5.1. Shabirinah Formation. AP section. A-AP6, typical texture of the deposits with moderately sorted clasts in a reddened cement. Small shrinkage cracks are seen cutting through the cement and around the clasts (x5, plane polarised light (ppl)). B-AP35, quartz clasts with mineral inclusion (zircon) (x20, cross polarised light (cpl)). C-AP14, interparticle porosity infilled with iron-rich, fine-grained, muddy cement (x5, cpl). D-AP21, to the left: blackened, isotropic, organic-rich cement. Shrinkage cracks also evident cutting across the matrix (x5, cpl). Scale bar is 500µm in all photomicrographs except in B where it is 100µm..... 119
- Plate 5.2 Maharshim Member. A-TM1, bimodal sorting of quartz clasts in a floating matrix (x5, cpl). B-TM1-reddened nodular area (x5, cpl). C-TM5-spar-rich areas infilling pore spaces (x5, cpl). D-TM4-quartz clasts in floating micritic matrix (x5, cpl). E-TM4-fenestral laminoid voids (marked by arrow) infilled with secondary spar (x5, cpl). F-TM2-reddened glaebule surrounded by circumgranular cracking (x10, cpl). Scale bar is 500µm in length in all photomicrographs except for F where it is 100µm..... 125
- Plate 5.3. Stromatolite Member. A-TM3, centre of photo-‘ghost feature’ with microspar rim remaining (x10, cpl). B-TM7, vuggy porosity with void partially filled with secondary microspar cement, mold peloid also observed (arrow) (x10, cpl). C-TM7, aggregate grain of peloids in the right of the photo, fenestral type void also seen (left part of photo) (x5, cpl). D-Fragments of ostracod shells and possibly bivalves (x5, cpl). Scale bar is 100µm in A/B and 500µm in C/D... 126
- Plate 5.4 Tmessah Member. A-TM12, rounded quartz clasts with reddened rim cements (x5, ppl). B-TM15-very coarse spar cement infilling pore spaces between quartz clasts (x5, cpl). C-TM21, bimodal sorting of clasts. Large clasts have surface fracturing, meniscus cements which are locally reddened (x5, cpl). D-TM24, rim cement of bladed spar crystals (x5, cpl). E-TM24, secondary mosaic spar infilling rootlet (x5, cpl). Scale bar is 500µm in all microphotographs. 130
- Plate 5.5 Kunayr Member. TM section. A-TM63, quartz clasts in floating matrix of granular mosaic spar, bladed rim cements seen surrounding the larger quartz clast (x5, cpl). B-TM72, clustering of well sorted, sub-angular quartz (x5, cpl). C-TM66, unfilled circumgranular like cracking around corroded quartz clasts (x10, cpl). D-TM35, micritic cement surrounding a void filled with secondary drusy cement (x5, cpl). E-TM34, ovoid, structure less peloids (x5, cpl). F-TM61, wavy, elongated partially filled fractures cutting through the fabric of the deposit (x5, cpl). G-TM70, fractured brown intraclasts, spar can be seen infilling some of the fractures (x5, cpl). All scale bars are 500µm except for C which is 100µm in length. 138
- Plate 5.6 Kunayr Member-AP section. A-AP37, typical texture of AP37-42 deposits. Unfilled channel porosity evident cutting across the sediment (x5, cpl). B-AP40, vuggy porosity partially filled with secondary pore lining microspar cement (x5, cpl). C-AP48, poorly developed meniscus and rim cements. Corroded grains evident in the centre of the photo (arrow) (x10, cpl). D-AP49, NaSi infilling pore space (x5, cpl). E-AP51, boundary of carbonate-rich and clast-rich areas. Well-developed rim cements are coating the quartz clasts within the carbonate rich area (x5, cpl). Scale bar in all images is 500µm except in C where the scale bar is 100µm. 139
- Plate 5.7 Shabirinah Formation. BC Section. A-BC6, rootlet with clustering of quartz clasts (x5, cpl). B-BC1, mottled and bioturbated texture of the deposits, floating quartz clasts, vertical rootlet evident in top-left corner moving around a quartz clast (x5, cpl). C-BC7, burrow (arrowed) and rootlet. The rootlet has a dense, darker rim caused by sediment deformation with a thin fracture running through the centre (x5, ppl). D-BC7, rootlet with central fracture and quartz clasts within (x5, ppl). Scale bar is 500µm in all photomicrographs. 141

Plate 5.8 Brak Formation. BC section. A-BC11, sub-rounded quartz clasts in a floating matrix (x5, cpl). B-BC12, circular structure in the lower left corner, pore spaces infilled with sparry cement (x5, cpl). C-BC13, rounded lithoclasts separated by sparry pore filling cement (x5, ppl). D-BC17, complex fabric of a number of cementation phases observed in many of the calcrete(?) deposits, areas of dissolution and replacement can be seen (arrowed) (x5, cpl). E- BC19, complexity of the fabric, unusual wavy patterns likely where former structures have undergone replacement (x5, cpl). F-BC19, lithoclast fractured by spar cement (x10, cpl). G-BC15, clotted micrite with lithic and mold peloids, post-depositional microfracture can be seen cutting across the fabric in the top of the photomicrograph (x5, cpl). Scale bar is 500µm in all photomicrographs except F where it is 100µm. 147

Plate 6.1 Sayl Member. BZ-E and QM2 sections. A-AL12, quartz clasts in a floating matrix of micritic mud. Shrinkage cracks evident as well as red staining (cpl, x5, scale bar 500µm). B-QM51, quartz clasts with patchily developed pore-filling cement. Peloid evident in the centre of the photo (cpl, x5). C-AL12, oval peloid with microspar rim cement (cpl, x10, scale bar 100µm). D-AL12, secondary microspar filled rootlet (cpl, x10). 172

Plate 6.2 Sifar Member. BZ sections. A-BZ34, moderately sorted deposit of quartz clasts typical of the BZ-sections. A large rounded clast of quartzite can be seen in the centre of the photomicrograph (x5, cpl). B-BZ90, corroded edge of quartz clast which also contains a small mineral inclusion. Micritic pore-filling cement can be seen surrounding the clasts (x10, cpl). C-BZ84, open interparticle porosity with some pore-filling cement in the centre (x5, ppl). D-ALA2, ooid with a sub-rounded quartz clast acting as a nucleus coated by concentric micritic laminae (x10, cpl). E-ALA4, cross-sectional view through a possible charophyte stem (x20, cpl). F-BZ90, multi-chambered foram in the centre of the photomicrograph (x10, ppl). G-ALA2, complete ovate-conic shaped gastropod. Intraskelatal porosity is evident in the chambers with one mostly infilled with secondary micrite and detrital quartz (x5, cpl). H-BZ91, cluster of ostracod debris and shell fragments with open intraskelatal porosity evident in the centre of the ostracods (x5, ppl). Scale bar is 500µm in A/C/G/H and 100µm in the remaining photomicrographs..... 182

Plate 6.3 Sifar Member. QM1/2 sections. A-QM1, quartz clasts showing bimodal sorting, interparticle porosity with pores infilled with rounded micritic mud clumps (x5, cpl). B-QM2, intraclasts forming an aggregate grain cemented by a micritic outer rim (x5, cpl). C-QM8, carbonate rich deposit of QM1 section composed of microspar cement, ghost features and open pores also present (x5, cpl). D-QM61, typical bimodal sorting of the QM2 section with rounded intraclasts (x5, cpl). E-QM71, moderately-well sorted clasts many of which have the unusual fracturing (x5, cpl). F-QM63, better developed cements infilling pore spaces with microspar rim cements also evident (x10, cpl). Scale bar is 500µm in all microphotographs except for F where it is 100µm..... 191

Plate 6.4 Sifar Member. M Section. A-M7, bimodal sorting typical of the sandstones of the section, some clasts have fretted edges (x5, cpl). B- M1, well-rounded, coarse sand-sized clast with mineral inclusions (x5, cpl). C-NUS8-3, poorly developed meniscus cements (x20, cpl). D-NUS8-1, carbonate-rich sandstone with micritic pore-filling cement, thin rim cements can be seen unevenly coating some of the clasts, sparry cement infilling pore spaces (x10, cpl). Scale bar is 500µm in photomicrographs A/B, 100µm in C/D..... 191

Plate 6.5 Bir al Zallaf Member. BZ-E section. A-BZ27, parallel laminations of muddy carbonate interbedded with well-sorted quartz clasts (x5, cpl). B-BZ27, peloids joined by meniscus cements to form aggregate grains. Large fragments of carbonate mud also present. C-AL2, peloidal texture and vuggy porosity. Vugs are lined with secondary pore cements (x10, cpl). D-AL4, altered ostracod shell with intraskelatal porosity (x10, cpl). E-BZ24, high interparticle porosity with quartz clasts

showing signs of dissolution at the edges (x20, ppl). F-BZ21, rim and meniscus cements coating fretted quartz clasts (x20, cpl). G-BZ24, rounded microcrystalline chert clast (x10, cpl). H-AL1, texture of the deposit with similarities to the QM1 section (x5, cpl). Scale bar 500µm in A/H and 100µm in the remaining photomicrographs. 200

Plate 6.6 Bir al Zallaf Member. QM1 section. A-QM11, mottled matrix of micrite/microspar cement. Detrital quartz clasts seen in floating matrix. Open vugs partially filled also seen (x5, cpl). B-QM12, ghost features (arrowed) as well as a completely filled pore with drusy cement (x10, cpl). C-QM5, partially filled vug lined by secondary spar cement (x10, cpl). D-QM21, secondary mosaic spar cements completely infilling pore spaces. Possible infilled rootlet/veinlet (arrowed) (x5, cpl). Scale bar is 500µm in A/D and 100µm in B/C. 201

Figures

Figure 1.1 Schematic diagrams from Gasse (2002) of the current wind patterns/pressure in January and July/August over Africa. Note: The dotted line indicates the extent of the ITCZ. The red box shows the location of the Fazzan..... 5

Figure 1.2. Google Earth image of the Fazzan showing some of the borders of the basin as noted in the text..... 7

Figure 2.1 Summary of the timings of key climatic, tectonic and biotic events of the Cenozoic from Zachos et al. (2001). Global deep-sea oxygen and carbon isotope records based on data compiled from >40 DSDP/ODP sites are also included. The absolute ages are relative to the standard GPTS of Berggren et al. (1995) 10

Figure 2.2. Map of the stratigraphic locations described in Swezey (2009) clearly showing the lack of research on stratigraphic sections within central Libya as highlighted by the red box. Libyan sites: 9-Offshore Libya, 10-Sirt Basin, 11-Northeast Libya. Other central Saharan sites: 4-Tademait, Algeria, 7-Chotts Basin, 8-North Chad..... 14

Figure 2.3 Chart from Swezey (2009) showing the varied Cenozoic stratigraphy of the Sahara in relation to climatic changes in the Sahara, eustatic sea level, glaciation events and tectonic events around northern Africa. The red box highlights central Saharan locations. C--conglomerate, S-sandstone, SM-sandstone and mudstone, Mt-mudstone, terrestrial, Mm-mudstone, marine, G-gypsum and (or) gypsiferous mudstone, P-phosphatic mudstone and (or) phosphatic limestone, L-limestone and (or) dolomite. White/blank space-strata not present or identified..... 17

Figure 2.4. Map to show the river systems of Libya during humid periods in the Late Miocene before the blocking of Wadi ash Shati, Wadi al Hayah and Wadi Nashu by the AHAS (Drake et al, 2008a). JH=Jebal al Hasawinah, JS= Jebal as Sawda. 25

Figure 2.5 . Map to show the river and lake systems during the Messinian once the Nashu River had been blocked by the development of the AHAS (Drake et al., 2008a). JH=Jebal al Hasawinah, JS= Jebal as Sawda, AHAS=Al Haruj as Aswad. 25

Figure 2.6 Map to show the river systems during the Lower Pliocene after the refilling of the Mediterranean. Lake Megafazzan has increased in size due to the blocking of Wadi Barjuj. Initiation of the AHAB can be seen (Drake et al., 2008a). JH=Jebal al Hasawinah, JS= Jebal as Sawda, AHAS= Al Haruj as Aswad, AHAB=Al Haruj as Abyad 28

Figure 2.7. Map to show the extent of the Al Mahruqah Group. Modified from Hounslow et al. (2017). Note: Awbari is an alternative spelling of Ubari – please see Table 1 in the Appendix (pg281) for a list of alternative spellings of localities in the Fazzan..... 35

Figure 2.8 Left: New lithostratigraphy of the Al Mahruqah Group from Hounslow et al. (2017). Note: major erosion/deflation events are indicated in blue which sub-divide the new formations.	
Right: Original lithostratigraphy of the Al Mahruqah Formation from Geyh and Thiedig (2008)..	37
Figure 2.9. Diagrams to show declination (D) and inclination (I) at a specific earth location (Based on the diagrams from Archaeomagnetism-Bradford University).....	40
Figure 2.10. Schematic diagrams of the geomagnetic field of a geocentric axial dipole during normal and reversed polarity (Langereis et al., 2010).....	40
Figure 2.11. Reversal excursions in Brunhes Chron. Globally, well-dated excursions are in bold. Uncertain excursions and those only identified in restricted regions are in small text (Langereis et al., 1997). Note: Black = normal polarity, White = reversed polarity.....	45
Figure 2.12. Diagrams showing different forms of magnetisation (Tarling and Hrouda, 1993, p3). Left-hand diagrams in the pairs illustrated (a-e): Solid arrow indicates the direction of the applied magnetic field. Hollow arrow indicates the magnetisation a substance acquires when in an applied field. Right-hand diagrams: magnetisation present after the applied field has been removed.	48
Figure 2.13 Sketch of the depositional environments (some) terrestrial carbonates can form in. Modified from Alonso-Zarza (2003).....	55
Figure 2.14. Classification of calcretes based by hydrological setting (Wright and Tucker, 1991, pg5)	61
Figure 2.15. Main controls on TDIC and $\delta^{13}\text{C}$ of lacustrine carbonates. Adapted from Leng and Marshall (2004).	66
Figure 2.16 Main controls on the $\delta^{18}\text{O}$ of lacustrine carbonates. Adapted from Leng and Marshall (2004).	67
Figure 3.1 Digital Elevation Model (DEM) of the Fazzan. The box in the lower right corner of the figure shows the outline of Libya and the location of the research area as seen in the main DEM. Study sites can be identified as black symbols on the map where M-Al Wafa, TM-Tmessah, BZ-Bir al Zallaf, QM2-Qarat al Mrar 2, QM1-Qarat al Mrar 1, BC-Brak, AP-Ariel. Key town and geomorphological features are also identified: 1-Wadi ash Shati, 2-Wadi al Hayat, 3-Wadi al Ajal, 4-Wadi Tanezzuft, 5-Jebal al Hasawinah (volcano), 6-Jebal as Sawda (volcano), 7-Al Haruj al Aswad (volcano), 8-Al Hamadah al Hamra Plateau , 9-Messak Settafet, 10-Akakus Mountains ...	74
Figure 3.2 Stratigraphic log of the Ariel section. This section corresponds to the Shabirinah Formation with the Kunayr Mbr identified from AP37 upwards. Please refer to Figure 3.5 (pg81) for the log key.	78
Figure 3.3 Stratigraphic log of the Tmessah section. This section relates to the Shabirinah Formation with the members associated with this formation identified on the section (Maharshim Mbr-TM5-2, Stromatolite Mbr-TM3-9, Tmessah Mbr-TM12-24, Kunayr Mbr-TM28-69). Please refer to Figure 3.5 (pg81) for the log key.....	79
Figure 3.4 Stratigraphic log of the Brak section. This section corresponds to both the Shabirinah Formation (BC1-7) and the Brak Formation (BC8-25). Please refer to Figure 3.5 (pg81) for the log key.	80
Figure 3.5. Legend for all section logs.....	81
Figure 3.6 Google Earth images of the Ariel section and sub-sections. T=section top, B=section bottom. Please refer back to Figure 3.1 (pg74) to see where the site locality is within the Fazzan Basin.....	82
Figure 3.7 Google Earth images of the Tmessah section and sub-sections. T=section top, B=section bottom. Please refer back to Figure 3.1 (pg74) to see where the site locality is within the Fazzan Basin.....	83
Figure 3.8 Google Earth images of the Brak section. Please refer back to Figure 3.1 (pg74) to see where the site locality is within the Fazzan Basin.....	84

Figure 3.9 Stratigraphic log of the Bir al Zallaf-East section. This section corresponds to the Zazur Formation and contains deposits which relate to the Sayl Mbr (AL12), Sifar Mbr (AL11-AL6) and the Bir al Zallaf Mbr (BZ28-AL1). Please refer back to Figure 3.5 (pg81) for the log key.	87
Figure 3.10 Stratigraphic log of the Bir al Zallaf-West Section. This section corresponds to the Sifar Mbr of the Zazur Formation. Please refer back to Figure 3.5 (pg81) for the log key.	88
Figure 3.11 Stratigraphic log of the Bir al Zallaf-Twin Hills section. This section corresponds to the Sifar Mbr of the Zazur Formation. Please refer back to Figure 3.5 (pg81) for the log key.	89
Figure 3.12 Google Earth images of the Bir al Zallaf sections. Please refer back to Figure 3.1 (pg74) to see where the site locality is within the Fazzan Basin.....	90
Figure 3.13 Possible lithostratigraphic correlations between the sections of Bir al Zallaf. Distance (km) between the sections is also noted. Please refer back to Figure 3.5 (pg81) for the log key. ...	91
Figure 3.14 Stratigraphic log of the Al Wafa section. This section is composed of deposits which relate to the Sifar Mbr of the Zazur Formation. Please refer back to Figure 3.5 (pg81) for the log key.	95
Figure 3.15 Stratigraphic log of the Qarat al Mrar-1 section. This section relates to the Zazur Formation. Geologic members which are part of this formation are marked on the log (Sifar Mbr QM1-8, Bir al Zallaf Mbr QM5-23). Please refer back to Figure 3.5 (pg81) for the log key.	96
Figure 3.16 Stratigraphic log of the Qarat al Mrar-2 section. This section is composed of deposits which relate to the Sayl Mbr (QM50-54) and Sifar Mbr (QM55-77) which are part of the Zazur Formation. Please refer back to Figure 3.5 (pg81) for the log key.	97
Figure 3.17 Google Earth images of the Al Wafa section and sub-sections. T=section top, B=section bottom. Please refer back to Figure 3.1 (pg74) to see where the site locality is within the Fazzan Basin.	98
Figure 3.18 Google Earth images of the Qarat al Mrar-1 section and sub-sections. Please refer back to Figure 3.1 (pg74) to see where the site locality is within the Fazzan Basin.	99
Figure 3.19 Google Earth image of the Qarat al Mrar-2 section. The black line marks the bowl of the hill where the deposits were sampled. Sampling was conducted from east (base of the section) to the west (top of the section). Please refer back to Figure 3.1 (pg74) to see where the site locality is within the Fazzan Basin.....	100
Figure 5.1. Legend for all sediment logs.....	113
Figure 5.2. Key characteristics of the thin sections from the AP section. Note: the clast size refers to grains of sand-sized material. Please refer back to Figure 5.1 (pg113) for the log key.	114
Figure 5.3. Aluminium normalised Si-K diagram.....	118
Figure 5.4. Key characteristics of the thin sections from the TM section. Note: thin sections of TM6, 14 and 19 were not produced. The clast size refers to grains of sand-sized material. Please refer back to Figure 5.1 (pg113) for the log key.	124
Figure 5.5. Graph to show the stable isotope values of members assigned to the Shabirinah Formation from the TM section. Carbonates of the STR Member are circled. For raw isotopic data please see Table 5 – Appendix, pg297.....	127
Figure 5.6. Isotopic values vs stratigraphic height of the TM section. The black, white and grey bars to the left of the log refer to the polarity of each of the deposits analysed where black = normal polarity, white = reversed and grey = unsure. Dashed box indicates the deposits which have good covariance between $\delta^{18}\text{O}/\delta^{13}\text{C}$. Please refer back to Figure 5.1 (pg113) for the log key.	133
Figure 5.7 Graph to show all isotopic data of the Shabirinah Formation including the K Member data from both the TM and AP sections. Black circles indicate the grouping of values observed in the K Member from the TM section.....	136
Figure 5.8 Key characteristics of the thin sections from the BC section. Note: the clast size refers to grains of sand-sized material. Please refer back to Figure 5.1 (pg113) for the log key.	144

Figure 5.9 Isotopic value vs stratigraphic height for the Brak Formation. The black, white and grey bars to the left of the log refer to the polarity of each of the deposits analysed where black = normal polarity, white = reversed and grey = unsure. Dashed box indicates the deposits which have good covariance between $\delta^{18}\text{O}/\delta^{13}\text{C}$ as discussed in the text. Please refer back to Figure 5.1 (pg113) for the log key.	148
Figure 5.10. Graph to show the comparison of the isotopic values of the Shabirinah and Brak Formations.....	149
Figure 5.11 NRM intensity and magnetic susceptibility of all specimens from the Shabirinah and Brak Formations. Samples beneath the dotted line are diamagnetic. Note: magnetic susceptibility values have +2 added to them to overcome the problems of plotting negative values on a log scale.	152
Figure 5.12 Changes in NRM intensity and magnetic susceptibility with demagnetisation temperatures for select specimens from the Shabirinah and Brak Formations. Note: B13, 22 TM33 MS values have +2 added to them due to some negative values.	153
Figure 5.13 Components extracted from demagnetisation data of the BC, TM and AP sections and their statistical evaluation. ChRM statistics can be found in Table 5.6, pg161.	156
Figure 5.14 Representative demagnetisation data from the Shabirinah Formation. 1-3=Ariel section, 4/5=Tmessah section. 1) AP2A-normal polarity (N, s2 behaviour), ChRM from 400-570°C. 2) AP25A-reverse polarity (R?, t3 behaviour), erratic trend to R polarity evident from 570°C, intermediate stability component is northerly directed-overprint of present day field? 3) AP46C-reverse polarity (R, behaviour t2), showing component 'A' from NRM to 350°C, above which an erratic trend towards reverse polarity, with reverse polarity evident from 500°C. 4) TM1A-reverse polarity (R? t3 behaviour) showing a strong A component from 100-460°C, the steps at 520-550°C recovers a reverse component. A GC plane fitted from 490°C to origin. 5) TM71-reverse polarity (R,s2 behaviour), showing a ChRM from 510°C to the origin.	157
Figure 5.15 Representative demagnetisation data for the Brak Formation (specimens from the Brak section). 1) BC18A-normal polarity (N?, t2 behaviour), component 'A' from NRM to 400°C. A GC is fitted from 490°C to the origin. 2) BC22-reverse polarity (R?, t1 behaviour), component 'A' from NRM to 300°C with a GC plane fitted from 300°C to the origin.	158
Figure 5.16 Magnetostratigraphic data summary of the i) AP, ii) TM and iii) and BC sections. A- Natural Remnant Magnetisation. B-Demagnetization behaviour categorised into good (s1) and poor (s3) characteristic remanent magnetisation (ChRM) line fits, great-circle (GC) fit quality range from good (t1) to poor (t3). C-Interpreted specimen polarity quality. No interpreted polarity data in column headed X. D-The virtual geomagnetic pole (VGP) latitude, red triangles representing s-class ChRM, black diamonds t-class GC behaviour specimens. To the right of the figure is the interpreted magnetic polarity stratigraphy, white -reversed polarity, black - normal, grey - uncertain.	160
Figure 5.17 Miocene to recent North African palaeopoles, with 95% confidence cones shown for the Shabirinah and Brak Fm. Green triangle-Ariel section, Red triangle-Tmessah section, blue triangle-Brak section. Pink triangles from Jebel as Sawda (JSV1/2). Black triangles are poles (age in Ma), listed in Torsvik et al. (2012). FV=Famara Volcanics, Canary Islands (CI); BS= Basalt Series II, CI; MV= Miocene Volcanics, CI; MC=Basalt Series I, CI; MERr= Main Ethiopian Rift Basalts; HB= Hadar Basin, Ethiopia; SH= South Holhol-Djibouti; BCF= Blue Clay Fm, Malta; FB=Flood Basalts, Ethiopia. Grey triangles are the Gondwana apparent polar wander path (APWP) from Torsvik et al (2012; Table 7), labelled in 10Ma increments.....	162
Figure 5.18 Palaeomagnetic correlations and composite options of the SHF sections as discussed in the text. Scale of the composites are in the metre scale of the AP section. Sb codes relate to the	

assigned magnetozones of the composite. Note: black = normal polarity, white = reversed, grey = uncertain. For additional illustrative information please see the key in Figure 5.19.	165
Figure 5.19 Sequence slotting model output for Composite-B showing data for the three most likely correlation models. a) the statistical summary of the correlation models. b) The H-matrix plot, where the brighter blue bands correspond to alternative correlation models. The mostly likely model (ending in Serravallian) is shown as the white boxes across the plot, with y-axis height corresponding to GPTS chron duration. The band corresponding to the Tortonian/Oligocene model are arrowed. The x-axis on this plot is the magnetozone number. c) and d) The input data to the slotting model, plotted against chron age for the two correlation options. e) Depth-age models for the two polarity composites A and B, and the Tortonian and Serravallian age models. The age-depth relationships for the two age models are similar for composite A and B apart from the upper part of the composite sections.	169
Figure 5.20 Composite-B magnetic polarity stratigraphy with the final age model on the right. Chron correlation lines (green) to the GPTS (Ogg, 2012) derived from sequence slotting. Please refer to the key within the figure for illustrative information.	170
Figure 6.1. Legend for all sediment logs.	176
Figure 6.2 Key characteristics of the thin sections from the BZ-T section. Note: the clast size refers to grains of sand-sized material. Please refer back to Figure 6.1 (pg176) for the log key.	177
Figure 6.3 Key characteristics of the thin sections from the BZ-W section. Note: the clast size refers to grains of sand-sized material. Please refer back to Figure 6.1 (pg176) for the log key. ...	178
Figure 6.4 Aluminium normalised Mg-Ca diagram of the BZ sections.	179
Figure 6.5 Key characteristics of the thin sections from the QM2 section. Only limited thin sections were produced from this section due to the friable nature of the deposits hence the lack of detail from QM73 up. Note: the clast size refers to grains of sand-sized material. Please refer back to Figure 6.1 (pg176) for the log key.	185
Figure 6.6 Stable isotope values of the SI Member deposits analysed from the QM1, BZ-E/T and M sections.	188
Figure 6.7 Key characteristics of the thin sections from the M section. Note: the clast size refers to grains of sand-sized material. Please refer back to Figure 6.1 (pg176) for the log key.	189
Figure 6.8 Key characteristics of the thin sections from the BZ-E section. Note: the clast size refers to grains of sand-sized material. Please refer back to Figure 6.1 (pg176) for the log key.	194
Figure 6.9 Stable isotope values of the Bir al Zallaf (BZ) Member from the QM1 and BZ-E sections.	195
Figure 6.10 Key characteristics of the thin sections from the QM1 section. Note: the clast size refers to grains of sand-sized material. Please refer back to Figure 6.1 (pg176) for the log key. ...	197
Figure 6.11 QM1 isotopic data vs stratigraphic height. The black, white and grey bars to the left of the log refer to the polarity of each of the deposits analysed where black=normal polarity, white=reversed and grey=unsure. Dashed box indicates the deposits which have good covariance between $\delta^{18}\text{O}$ / $\delta^{13}\text{C}$. Please refer back to Figure 6.1 (pg176) for the log key.	198
Figure 6.12 NRM intensity and magnetic susceptibility of i) specimens from the members of the QM1/2 and M sections (Zazur Formation), ii) specimens from the members of the BZ sections. Note: magnetic susceptibility values have +2 added to them to overcome the problems of plotting negative values on a log scale.	203
Figure 6.13 Changes in intensity and magnetic susceptibility with demagnetisation temperature of specimens from the QM2 section and the BZ-E sections. Note: The MS values of BZ26 have +2 added to them due to some negative numbers.	205
Figure 6.14 Changes in intensity and magnetic susceptibility with demagnetisation temperature of specimens from the BZ-W and BZ-T sections.	206

Figure 6.15 Components extracted from demagnetisation data of the QM1, QM2 and M sections and their statistical evaluation. ChRM statistics can be found in Table 6.7, pg219..... 210

Figure 6.16 Components extracted from demagnetisation data of the BZ-E, BZ-W and BZ-T sections and their statistical evaluation. ChRM statistics can be found in Table 6.7, pg219..... 211

Figure 6.17 Representative demagnetisation data from the Zazur Formation. 1-3=Qarat al Mrar 1 section, 4/5=Qarat al Mrar 2 section. 1) QM5A-normal polarity (N, s1 behaviour), showing component 'A' from 100-350°C, ChRM from 375°C to the origin. 2) QM18B-reverse polarity (R,t1 behaviour), ChRM from 15-25mt.3) QM21A-?Polarity, t3 behaviour, strong component from 0-45mt, unclear polarity possibly due to the influence of lightning strikes. 4) QM64-normal polarity (N??, t3 behaviour), component 'A' from NRM to 300oC, normal polarity evident from 550°C. 5) QM70-reverse polarity (R?, s3 behaviour), component 'A' from NRM to 200°C, ChRM evident from 400-460°C, last few points likely due to a viscous component from the GM400. 212

Figure 6.18 Representative demagnetisation data of the Al Wafa section from the Zazur Formation. 1) M5-6-normal polarity (N?, t1 behaviour), component 'A' from 100-400°C. 2) M22-2-reverse polarity (R?, t3 behaviour), component 'A' from 100-300°C. 213

Figure 6.19 Representative demagnetisation data from the Zazur Formation. 1-2 Bir al Zallaf East section. 3-4 Bir al Zallaf West section. 5-6 Bir al Zallaf Twin Hills section. 1) AL4-1-normal polarity (N?, S2 behaviour), component 'A' from NRM to 230°C, ChRM evident from 320-530°C. 2) BZ20-reverse polarity (R, t2 behaviour), component 'A' from NRM-430°C. 3) BZ41-normal polarity (N?, t3 behaviour), component 'A' from NRM-430°C, a strong component also shown from 430-520°C. 4) BZ61-reverse polarity (R, s2 behaviour), component 'A' from NRM-300°C, ChRM evident from 300-430°C. 5) BZ86A-reverse polarity (R??, t2 behaviour), component 'A' from NRM-430°C,a GC plane fitted from 460°C to the origin. 6) BZ93A-normal polarity (N?, S2 behaviour), component 'A' from NRM-430°C, ChRM evident from 520-580°C..... 214

Figure 6.20 Magnetostratigraphic data summary of the i) QM1, ii) QM2, iii) M, iv) BZ-E, v) BZ-W, vi) BZ-T sections. A-Natural Remnant Magnetisation. B-Demagnetization behaviour categorised into good (s1) and poor (s3) characteristic remanent magnetisation (ChRM) line fits, great-circle (GC) fit quality range from good (t1) to poor (t3). C-Interpreted specimen polarity quality. Poor quality data in column headed X. D-The virtual geomagnetic pole (VGP) latitude, red triangles representing s-class ChRM, black diamonds t-class GC behaviour specimens. To the right is the interpreted magnetic polarity stratigraphy, white-reversed polarity, black-normal, grey-uncertain. *BZ46 is equivalent to BZ60, therefore this part of the section would have N polarity. BZ47 is equal to BZ61 and would thus be part of the overlying R polarity section. 217

Figure 6.21 Miocene to recent North African palaeopoles, with 95% confidence cones shown for the Zazur Fm. Blue triangle-Bir al Zallaf-East, red triangle-Bir al Zallaf-Twin, Green triangle-Bir al Zallaf-West, Purple triangle-Qarat al Marar1, Orange triangle-Al Wafa, Pink triangle-Qarat al Mrar2. Pink triangles (with purple confidence cones) from Jebel as Sawda (JSV1/2). Black triangles are poles (age in Ma), listed in Torsvik et al (2012). FV=Famara Volcanics, Canary Islands (CI); BS= Basalt Series II, CI; MV= Miocene Volcanics, CI; MC=Basalt Series I, CI; MERr= Main Ethiopian Rift Basalts; HB= Hadar Basin, Ethiopia; SH= South Holhol-Djibouti; BCF= Blue Clay Fm, Malta; FB=Flood Basalts, Ethiopia. Grey triangles is the Gondwana apparent polar wander path (APWP) from Torsvik et al (2012; Table 7), labelled in 10Ma increments. 219

Figure 6.22. Palaeomagnetic correlations and composite-A option of the ZF sections as discussed in the text. Scale of the composite is in the metre scale of the BZ-E section. ZA codes relate to the assigned magnetozones of the composite. Note: black = normal polarity, white = reversed, grey = uncertain. For additional illustrative information please see refer back to the key in Figure 5.19. 222

Figure 6.23 Palaeomagnetic correlations and composite-B option of the ZF sections as discussed in the text. Scale of the composite is in the metre scale of the BZ-E section. ZA codes relate to the

assigned magnetozones of the composite. Note: black = normal polarity, white = reversed, grey = uncertain. For additional illustrative information please see refer back to the key in Figure 5.19. 223

Figure 6.24 Sequence slotting model output for composites-A/B showing data for each Messinian-Zanclean correlation model. a) The statistical summary of the correlation models. b) The H-matrix, plot of Composite-A, where the brighter blue bands correspond to alternative correlation models. The Composite-A model is shown as the white boxes across the plot, with y-axis height corresponding to GPTS chron duration. The x-axis on this plot is the magnetozone number. c) and d) The input data to the slotting model, plotted against chron age for the two correlation options. e) Depth-age models for the two polarity composites A and B. The age-depth relationships for the two age models are similar for composite A and B apart from the upper part of the composite with sequence slotting placing the start of composite-B at ~1Ma younger than composite-A. 226

Figure 6.25 Composite-A (Messinian-Zanclean model) magnetic polarity stratigraphy with the final age model on the right. Chron correlation lines (purple) to the GPTS (Ogg, 2012) derived from sequence slotting. Note the * next to the composite represents the magnetozones (Za5r.an/Za5r.ar) not included in the sequence slotting model. Note: black = normal polarity, white = reversed, grey = uncertain. For additional illustrative information please see refer back to the key in Figure 5.19. 227

Figure 7.1 Extensive rootleting in the lower Ariel section..... 228

Figure 7.2 Stromatolite bed showing where deposit TM3 was sampled..... 233

Figure 7.3. The model of progressive vadose diagenesis included cement types from Gardner and McLaren (1993). 234

Figure 7.4 Diagram from Tandon and Andrews (2001) to illustrate the possible stable isotope variations in palustrine limestones based on Cretaceous to Tertiary calcitic data from numerous papers. 241

Figure 7.5 Summary of the Miocene-Pliocene palaeoenvironmental change and volcanism of the central Sahara based on the current understanding (i.e. based on the information in the literature review, section 2.1.) and the findings of this study, namely the age of the members and their depositional environment. Central Saharan Climate: Blue=humid phase, yellow=arid phase, orange=fluctuating arid/humid climate resulting in desert-lake patterns, white=no data. SHF/BKF: Dark blue=lacustrine, light blue=palustrine, green=fluvial, brown=palaeosol, white=no data. In the SHF column, the results of the AP section are to the left and the TM to the right. 246

Figure 7.6 DEM of the Fazzan with the probable river systems (late Miocene) mapped by Drake et al. (2008) overlaid. Symbols of the study sites are the same as in Figure 3.1 (page 74) where the diamond = Brak, Star = Ariel and Pentagon = Tmessah. 247

Figure 7.7 Top of the Stromatolite bed visible as white patches in the wadi bottom (and a stromatolite 'dome' - on the left). In the distance, two limestone beds of the Kunayr Member are seen. Photo taken looking NW from the hill on which the upper-most logged sandstone was sampled at the Tmessah section 26°30'48.00"N 16°29'59.77"E. 249

Figure 7.8 DEM of the current topography of the Fazzan Basin with mapped outcrops of the AMG. Positions of the AP and TM sections are noted to show their position in relation to the AHAS. K Member at Ariel (top photo) and TM section shown. Black line=Fazzan catchment..... 252

Figure 7.9 Aeolian cross-bedding in upper part of the QM2 section. 257

Figure 7.10 Summary of the palaeoenvironmental change and volcanism of the central Sahara throughout the Miocene-Pliocene based on the information in the literature review (section 2.1) and the findings of this study, namely the age of the members and their depositional environment. Central Saharan Climate: Blue=humid phase, yellow=arid phase, orange=fluctuating arid/humid climate resulting in desert-lake patterns, white=no data. SHF/BKF/ZF: Dark blue=lacustrine, light blue=palustrine, green=fluvial, brown=palaeosol, white=no data. In the SHF column, the results of

the AP section are to the left and the TM to the right. In the ZF column, the results of the M section are to the left, QM in the middle and BZ to the right.....	263
Figure 7.11 Cross-section of the basin from the M to BZ sections. The dashed line on the Google Earth image above shows the transect followed between the two sections. The larger rectangle in both the Google Earth image and the graph show the increase in elevation of the Gargaf uplift and the smaller rectangle the decrease in elevation as the transect passes through the Wadi ash Shati depression.....	264
Figure 7.12 Cross-section of the basin from the M to BZ sections. The dashed line on the above Google Earth image shows the transect followed between the two sections	265
Figure 8.1 Photomicrograph of TM6 low in silicate detritus. Field fo view approximately 2.5 cm wide	270
Figure 8.2 The detrital corrected $^{230}\text{Th}/^{238}\text{U}$ vs $^{234}\text{U}/^{238}\text{U}$ data. The series of sloping lines represent age contours (50 to 500 ka). Data points to the right of the 500 ka contour plot in a ‘forbidden zone’ where the observed isotope compositions cannot be generated by normal U decay to Th (Hounslow et al., 2017).....	271
Figure 1. Key areas highlighted where the AMG outcrops and was sampled by Hounslow et al. (2017). Imagery of these sites are in the figures below.....	282
Figure 2. Box ‘A’ in figure 1 highlighting the route of the Wadi ash Shabirinah, the STR Mbr and the location of the TM site.	282
Figure 3. Box ‘B’ in figure 1 outlining the Washkat Zazur region, the town of Brak, Wadi Kunayr and outcrops of the SHF to the east (AP site location).	283
Figure 4. Box ‘C’ in figure 1 marking the locations of key wadis in the northern Ubari region and outcrops of the Zarzatine Formation. The location of Wadi Sifar (arrowed) is near to the location of the QM sites.	283
Figure 5. Shabirinah Formation. Left: AP3-rootlets. Right: AP10- mottled, bioturbated deposit.	289
Figure 6. Shabirinah Formation. AP14-black, vein-like organics.....	289
Figure 7. Maharshim Member. Hand sample of TM4 with fenestral laminoid voids.....	290
Figure 8. Tmessah Member. Left: Reddened outer surface of TM15. Right: Cut surface of TM 15.	290
Figure 9. Tmessah Member. TM24-honey-comb texture and rhizoliths.....	291
Figure 10. Kunayr Member. AP42-fine grained white limestone.....	291
Figure 11. Kunayr Member. AP51-mottled sandstone.....	292
Figure 12. Kunayr Member. TM25-pitted outer surface of the sample caused by dissolution.	292
Figure 13. Brak Formation. Left: BC12-dense carbonate band separating more sandy intervals. Right: BC21-white lithoclasts in a carbonate matrix	293
Figure 14. Brak Formation. BC15-textural differences of the deposit forming areas of zoning....	293
Figure 15. Bir al Zallaf Member. BZ27 parallel laminated carbonate interbedded with fine-grained green muddy layers.	294
Figure 16. Bir al Zallaf Member. QM15-vugs partially filled with secondary cements.	294
Figure 17. Section logs of AP and TM with the polarity of each horizon noted.....	305
Figure 18. Section log of BC with the polarity of each horizon noted and the Key for each of the logs.	306
Figure 19. Logs of the QM1, QM2 and M sections with the polarity of each horizon noted.	307
Figure 20. Logs of the BZ-E, BZ-W and BZ-T sections with the polarity of each horizon noted.	308
Figure 21. Composite-A (SHF/BKF) sequence slotting output. a) the statistical summary of the Tortonian and Serravallian correlation models. b) The H-matrix plot, where the brighter blue bands correspond to alternative correlation models. The mostly likely model (ending in Serravallian) is shown as the white boxes across the plot, with y-axis height corresponding to GPTS chron	

duration. The band corresponding to the Tortonian model is arrowed. The x-axis on this plot is the magnetozone number. c) and d) The input data to the slotting model, plotted against chron age for the two correlation options. 311

Figure 22. Composite-B (Messinian-Zanclean model) magnetic polarity stratigraphy with the final age model on the right. Chron correlation lines (purple) to the GPTS (Ogg, 2012) derived from sequence slotting. Note the * next to the composite represents the magnetozones (Za4r.an/Za4r.ar) not included in the sequence slotting model. 312

Abbreviations

Climatology

ASM-African Summer Monsoon
DSDP – Deep Sea Drilling Project
EAIS-East Antarctic Ice Sheet
ITCZ-Intertropical Convergence Zone
MMCC-Mid Miocene Climatic Cooling
MMCO-Mid-Miocene Climatic Optimum
MSC-Messinian Salinity Crisis
ZWP-Zeit Wet Phase

Geochemistry

NaSi-Sodium Silicate (solution)
TDIC-Total Dissolved Inorganic Carbon
XRF-X-ray Florescence

Petrology

CPL-Cross Polarised Light
PPL-Plane Polarised Light
TS – Thin Section

Magnetostratigraphy

AF-Alternating Field Demagnetisation
ARM-Anhysteretic Remanent Magnetisation
ChRM-Characteristic Remanent Magnetisation
CRM-Chemical Remanent Magnetisation
D-Declination
DRM-Detrital Remanent Magnetisation
GC Plane-Great Circle Plane
GPTS-Geomagnetic Polarity Timescale
I-Inclination
IRM-Isothermal Remanent Magnetisation
MS-Magnetic Susceptibility
NRM-Natural Remanent Magnetisation
SV-Secular Variation
TD-Thermal Demagnetisation
TVRM-Thermal Viscous Remanent Magnetisation
VGP – Virtual Geomagnetic Pole

Volcanoes

AHAS-Al Haruj al Aswad
AHAB-Al Haruj al Abyad
JH-Jebal al Hasawinah
JS-Jebal as Sawda

Study Sites

AP-Ariel
BC-Brak
BZ-Bir al Zallaf
M-Al Wafa
QM-Qarat al Mrar
TM-Tmessah

Geologic Groups

AMG-Al Mahruqah Group

Geologic Formations

AMF-Al Mahruqah Formation
BKF-Brak Formation
SHF-Shabirinah Formation
SIF-Shati Formation
ZF-Zarzur Formation

Geologic Members

BZ Mbr-Bir al Zallaf Member
K Mbr-Kunayr Member
M Mbr-Maharshim Member
SL Mbr-Sayl Member
SI Mbr-Sifar Member
STR Mbr-Stromatolite Member
TM Mbr-Tmessah Member

1 Introduction

1.1 The Sahara Desert: A Key Region for Global Climate Studies

The Sahara Desert, covering 9,500,000 km², is the most extensive arid region on Earth (Guo et al., 2000). It is increasingly clear however that the aridity experienced today has not always been present (Drake et al., 2013). The late Cenozoic, for example, was a time of many significant changes in climate which were felt globally, such as during the mid-Miocene climatic optimum (17-15 Ma) and the mid-Pliocene warm period (3.29-2.97 Ma) (John et al., 2003). These periods were characterised by increased CO₂ levels compared to today as well as an increase in temperature and precipitation levels (Zachos et al., 2001; Kurschner et al., 2008; Salzmann et al., 2008; Feakins and deMenocal, 2010). One region particularly affected by these dramatic changes was the Sahara and wider North African region which, as a result of these perturbations, often experienced an increase in humidity (Senut et al., 2009).

Humidity brought about many changes to the Sahara, having profound influences on the evolution of habitats and biota (van Zinderen Bakker and Mercer, 1986). Increased surface water occurred with the development of large fluvial systems such as the As Sahabi River and the expansion of lakes including Lake Chad (Griffin, 1999; 2002; Novello et al., 2015). It is thought that during humid periods, basins such as the Chad and Sirt (Libya) could have been linked (Drake et al., 2008b; Otero et al., 2009). Changes in vegetation and vegetation patterns also occurred with flora ranging from xerophytic shrubland and grasslands to tropical forest trees (Pound et al., 2011; 2012). The increase in water and vegetation allowed the subsequent expansion north of many species of fauna including hippos, crocodiles and several species of freshwater fish (Pickford, 2000; Boisserie et al., 2003; Otero et al., 2009). The expansion of C4 grasses throughout Africa in particular is thought to have triggered hominid speciation (~3-2.5 Ma) and bipedalism (deMenocal, 1995; Novello et al., 2015). Although primarily documented from sites in eastern Africa, the Sahara, in particular areas in Chad such as Toros Menalla, also document a significant hominid record (Schuster et al., 2006; Novello et al., 2015). As well as in evolution, the Sahara has also played key roles in human migration, providing humid corridors across the region thanks to fluvial and lake expansion and also to the development of agriculture (Brooks et al., 2003; Osbourne et al., 2008; Drake et al., 2010).

The cause of the palaeoclimatic changes experienced in the Sahara throughout the late Cenozoic was complex and influenced by an interplay of factors. Redevelopment of major ice sheets such as those on the East Antarctic, and tectonic impacts, including the opening/closure of ocean gateways, resulted in changes in ocean circulation and sea level, for example (Flower and Kennet, 1994; Kender et al., 2009). The overriding control responsible for bringing increased moisture to the Sahara however appears to be the strength and position of the African monsoon which oscillated with the orbital cycles, especially the precessional cycle (deMenocal, 1995; Griffin, 2002; Zhang et al., 2014). Local factors including magmatism also impacted on the Saharan landscape, especially during the Pliocene with the blocking and re-directing of many key rivers (Drake et al., 2008b) resulting in spatial variability.

Much of the evidence of the changing Saharan climate comes from marine sequences, eastern Sahara sites surrounding the Nile and coastal sites along the North African margin (Swezey, 2009). Climate models are also a key component for enhancing our understanding of the Neogene climate of the region (e.g. Salzmann et al., 2008; Zhang et al., 2014). Terrestrial evidence in comparison is severely lacking due to depositional hiatuses (Otero et al., 2009; Zan et al., 2015). This is especially true for the central Saharan region with research further hampered by the limited accessibility. The timing of climatic changes in the Sahara and also their extent and consequences (Drake et al., 2013) cannot be fully understood until all regions of the Sahara have been subject to in-depth investigative studies. Along with untangling the causal factors and timing of more humid phases, debate still surrounds the question of when aridification leading to full desert conditions first occurred in the Sahara. Sandstone outcrops in Chad dated to 7 Ma are believed to provide the earliest record for aridity in the Sahara (Schuster et al., 2006), however many researchers (e.g. Swezey, 2006; Kropelin, 2006) dispute these claims preferring evidence suggesting a late Pliocene age. It is important to know the exact timing of initiation as modelling has shown that the introduction of the Sahara Desert leads to aridification and cooling in Africa (Micheels et al., 2009). The development of the Sahara also has more far-reaching effects contributing to cooling in central Asia, North America and the northern high latitudes (Micheels et al., 2009).

1.2 Importance of the Fazzan Basin

The Sahara is subject to very little international investigation and many areas are lacking palaeoenvironmental research (Brooks et al., 2005). The climate history of the central Sahara is much less well studied than the surrounding climate zones, resulting in a scarcity of reliable palaeoenvironmental information (White et al., 2000). One such neglected area is the Fazzan Basin. Although one of the harshest and most inaccessible places on Earth (White and Mattingly, 2006), the Fazzan Basin in SW Libya contains a wealth of evidence which alludes to times of greater humidity in the past. Relict landforms and discontinuous but widespread deposits of lacustrine origin have been discovered (White et al., 2000; Drake et al., 2011). The lacustrine record within the Fazzan is believed to be the most extensive in the central Sahara and has provided new opportunities for developing a palaeoenvironmental chronology (Mattingly et al., 2007; White et al., 2013).

Studies of these deposits date as far back as the 1930/40s (e.g. Bellair, 1944), but it was not until studies in the 1980s (e.g. Petite-Maire et al., 1980b, Gaven et al., 1981) and more recently in the 2000s (e.g. Thiedig et al., 2000; Armitage et al., 2007; Geyh and Thiedig, 2008) that a reliable chronology and palaeoenvironmental understanding of the region began to develop. Much of the current understanding of the Fazzan has been gained thanks to research expeditions as part of the Desert Migration Project (Drake et al., 2009). Originally set up to investigate the archaeological history of the Fazzan, the project has in turn led to increased research on the palaeoclimatic and hydrological change of the region, particularly during the Quaternary (Mattingly et al., 2007).

The lacustrine deposits, dated to the Pleistocene, have been assigned to the Al Mahruqah Formation, recently upgraded to Group status by Hounslow et al. (2017). Lithostratigraphic investigations on the lacustrine deposits and their spatial extent has led researchers such as Armitage et al. (2007) to suggest they were deposited by a megalake known as Lake Megafazzan which, at its maximum size, covered 135,000 km² (Drake et al., 2008a). Studies of the deposits (Geyh and Thiedig, 2008) show the scale of the megalake was dependent on the intensity of the humid phases and also connection of drainage channels to the NE towards the Sirt Basin. Knowledge of the palaeodrainage of the Fazzan is limited, though Drake et al. (2008a) attempted to describe the palaeohydrology of the basin since the late Miocene, with details before this time unknown. This poor knowledge stems from a lack of information about preserved deposits of pre-Quaternary age within the basin. The chronological framework and understanding of the regional relationships of pre-Quaternary deposits is therefore limited, even though

lacustrine and fluvial units thought to be older have been mapped (e.g. Parizek et al., 1984; Seidl and Rohlich, 1984). The Pleistocene deposits, dated by U-series (Thiedig and Geyh, 2004; Geyh and Thiedig, 2008), are from carbonate intervals in the uppermost part of the Al Mahruqah Group (AMG). Uncertainty however surrounds the ages of the Pleistocene units of the Al Mahruqah Group. Saturated OSL signals of the deposits previously dated using U-series, for example, question the reliability of some of the ages (Armitage et al., 2007).

During recent fieldwork to the basin, extensive sedimentary sequences exposed beneath the Pleistocene deposits were documented. These sequences, which contain clastic as well carbonate intervals, could potentially help fill the chronological gap and provide more detail regarding the palaeodrainage. A re-investigation of the AMG, which includes these new sedimentary sequences, is thus needed. Further investigation of the deposits would not only provide a more detailed palaeoenvironmental history of the basin but also help to fill the palaeoclimatic void of the central Sahara, in particular by providing terrestrial evidence.

1.3 Current Physical Characteristics of the Fazzan

1.3.1 Climate

The Fazzan, Libya's south-western desert province, lies in the centre of the Sahara Desert, covering up to 640,000 km² (Mattingly et al., 2003; White and Mattingly, 2006). At present, the region is hyper-arid and receives very little rainfall, even in higher elevation regions (Mattingly et al., 2003). The meteorological station in the city of Murzuq shows the mean annual rainfall to be between 0-10 mm (Perego et al., 2011) with the average rainfall for the whole region documented by a number of sources (e.g. White et al., 2006; Armitage et al., 2007) to be <20 mm per annum. The climate exhibits high interannual variability resulting from the seasonal migration of the Intertropical Convergence Zone (ITCZ, Figure 1.1) which is due to changes in the location of maximum solar heating (Brooks et al., 2003; Perego et al., 2011). This monsoonal climate results in summer rains and winter drought (Perego et al., 2011). Atlantic storms also affect the region (Geyh and Thiedig, 2008). Mean annual temperature is between 22-25°C, which in summer can rise to over 50°C (Perego et al., 2011; Mattingly et al., 2003). During 1945-2009 an increase in the mean annual minimum temperature has been recognised in Libya, accelerating at a rate of 0.032°C per year. This increase is much quicker than the global mean temperature increase (0.74±0.18°C over the last 100 years) with the most rapid warming occurring in summer and autumn (Ageena et al., 2012). Mean annual relative humidity ranges between 30-40% while the potential evaporation rate is about 2000mm a⁻¹ (Geyh and Thiedig, 2008). The central location of the basin in the Sahara means it is located in a transitional zone between two dominate wind directions (northwestern/northeastern trade winds) which shift seasonally (Abdullah, 2010).

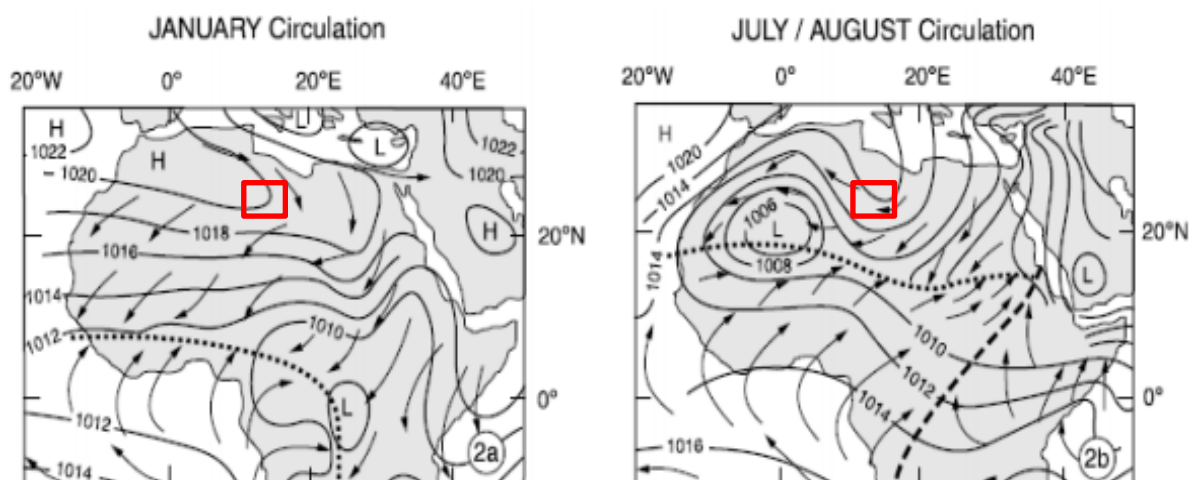


Figure 1.1 Schematic diagrams from Gasse (2002) of the current wind patterns/pressure in January and July/August over Africa. Note: The dotted line indicates the extent of the ITCZ. The red box shows the location of the Fazzan.

1.3.2 Geological and Geomorphological setting

The Fazzan basin, also known as the Murzuq (e.g. Thiedig et al, 2000), is one of several intracratonic basins in North Africa and an important feature of the central Sahara (Aziz, 2000; Abdullah, 2010). The roughly triangular shape of the basin extending from 22-28°N and 10-16°E, reflects a Variscan and Mesozoic overprint on an older structural relief (Geyh and Thiedig, 2008; Davidson et al., 2000; Klitzsch, 2000). At the end of the Tertiary (late Miocene) the basin became endhoreic (Busche, 1980) and now covers an area of ca. 450,000 km², composed of a wide variety of physiographic features (Armitage et al., 2007; Cremaschi and di Lernia, 1999). The present borders of the basin are defined by tectonic uplifts, namely the Akakus Mountains to the west, the Al Haruj al Aswad shield volcano to the east, the Hamada Mangueni to the south and the Al Hamada al Hamra plateau to the north (Davidson et al., 2000; Armitage et al., 2007, Figure 1.2). It is divided into northern and southern sub-basins separated by the Messak Sattafat, a Nubian sandstone escarpment with a mean elevation of 700 m asl (Armitage et al., 2007; Geyh and Thiedig, 2008; White et al., 2006; Cremaschi and Trombino, 1998, Figure 1.2). These sub-basins currently house two large sand seas, the Edeyen of Ubari to the north composed predominantly of linear dunes and the Edeyen of Murzuq to the south covering 20,000 km² (McLaren et al., 2006; Perego et al., 2011). Both of these sand seas were regarded by Davidson et al. (2000) to be temporary ponded sub-basins which are unlikely to be preserved in future geological records due to erosion once sediment transport pathways become re-established. Although now predominantly covered by sand seas, except at the margins, the basin contains a sedimentary fill which has a maximum thickness of 4000 m in the basin centre (Domaci et al., 1991; Davidson et al., 2000). From the basement upwards Precambrian, Palaeozoic, Mesozoic and Cenozoic units are present of both marine and continental origin (Grubic et al., 1991; Thiedig et al., 2000; Woller and Fediuk, 1980). Strata on the flanks of the basin form a concentric pattern which gently dips towards the centre of the basin exposing all rock units (Thiedig et al., 2000). The evolutionary history of the basin is discussed in detail in section 2.2.

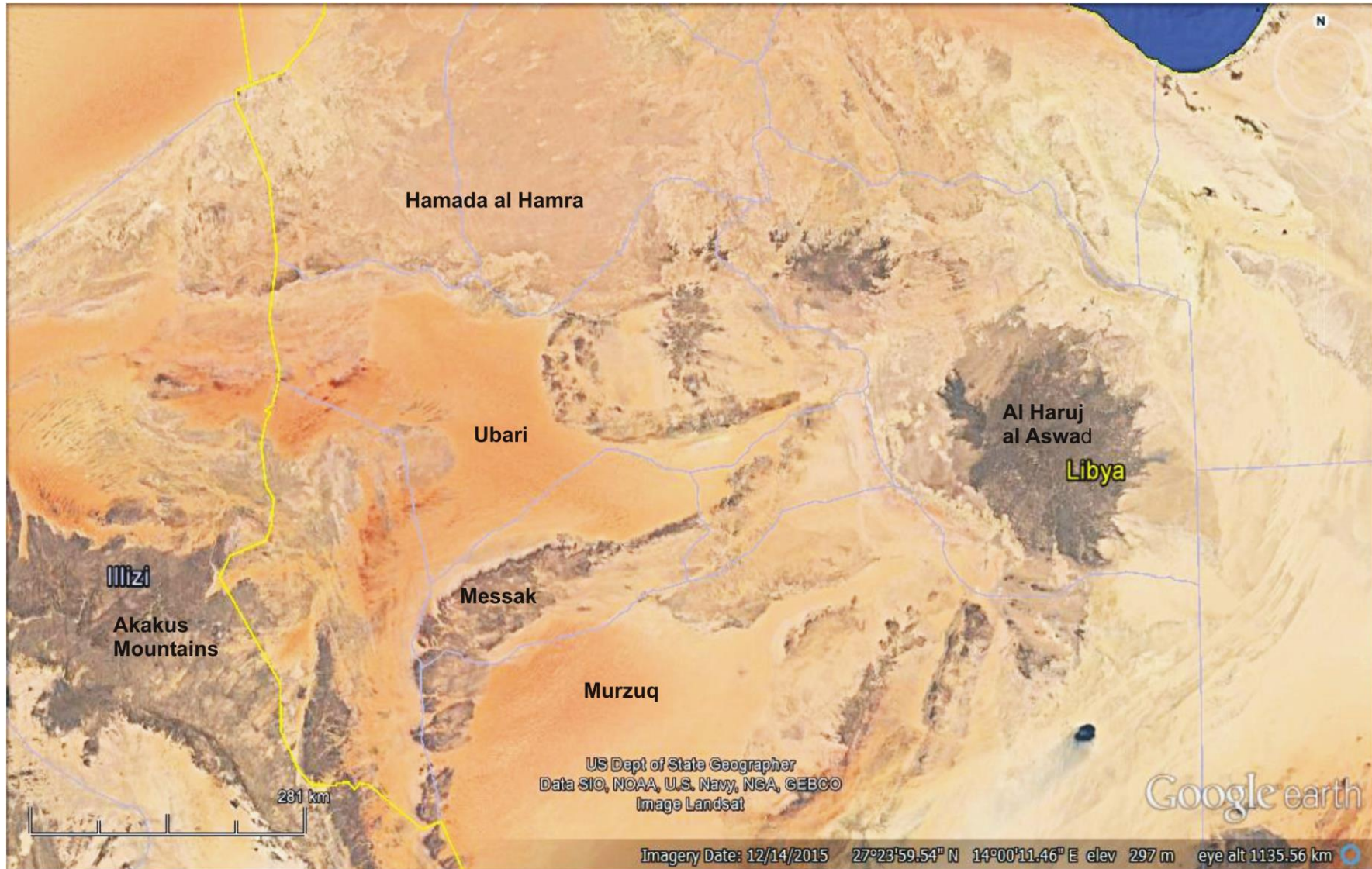


Figure 1.2. Google Earth image of the Fazzan showing some of the borders of the basin as noted in the text.

1.4 Aim

The principal aim of this research is to establish the chronostratigraphy and palaeoenvironmental history of sedimentary successions identified as part of the Al Mahruqah Group, in the Fazzan Basin, southwest Libya. This research further aims to provide a detailed chronology of newly collected sedimentary rocks from previously researched stratigraphic sections along with strata from newly discovered successions using palaeomagnetic dating. This technique has not been applied to the deposits of the Al Mahruqah Group in the past and is able to date beyond the range of previously employed dating methods. The deposits will be examined petrographically to help define their key characteristics and depositional environment. Geochemical analyses, in particular stable isotope analysis, will also be completed to provide information regarding the palaeohydrology of the region.

1.5 Structure of Thesis

Chapter 1-As previously read, the first chapter outlines the importance of the Sahara, and in particular the Fazzan Basin, as an archive for palaeoclimatic/environmental studies. It also includes a brief overview of the current physical characteristics of the Fazzan. Lastly, the overall aim of this project is stated.

Chapter 2-This chapter is a detailed review of the literature. The first sub-section includes a detailed overview of the Saharan palaeoclimate from the Miocene onwards from a central Saharan perspective. It then goes on to discuss the current understanding of the geological and geomorphological evolution of the Fazzan followed by the lithostratigraphy of the basin, in particular, the Al Mahruqah Formation. This is followed by two sub-sections providing important information regarding the dating tool used in this study, magnetostratigraphy and then details on terrestrial carbonates as palaeoclimatic archives and the use of stable isotopes when analysing these strata. The final sub-section summarises the main points derived from the literature and states the four research questions to be answered by the project.

Chapter 3/4-Within this chapter identification of the study sites is discussed. This is followed by information on the study sites as well as stratigraphic logs of the sections from each of the sites. The methodology for each of the analyses is discussed in detail.

Chapter 5/6-The results are examined in two chapters. The first focuses on the Shabirinah and Brak Formations which are represented by the Ariel, Tmessah and Brak sections. The second includes results of the Zazur Formation and its respective sections sections. In each chapter, the petrographic and geochemical results are first examined. Palaeomagnetic results then follow and finally there is assessment of the palaeomagnetic age of the successions investigated.

Chapter 7-This discussion chapter contains two parts. The first discusses the petrographic and geochemical data providing interpretations regarding the depositional environments of the deposits. Based on these interpretations, the palaeoenvironmental history of the basin is re-examined for the Miocene and Pliocene. The second part focuses on assessment of the palaeomagnetic age of sections and chronological controls which help support the dates achieved. The limitations of magnetostratigraphy are also included.

Chapter 8-The final chapter of the thesis ends with the main conclusions drawn from the project and further work which could be carried out to enhance future investigations of the Fazzan.

2 Literature Review

2.1 Palaeoclimatic/environmental Evolution of the Sahara: A Central Saharan Perspective

The Cenozoic Era is defined by an overall trend of global cooling, yet it is also a time of significant changes in climate (Flower and Kennet, 1994; John et al., 2003). The timings of these key changes, as well as tectonic and biotic events, are summarised in Figure 2.1. Several factors which could have contributed to long-term changes in moisture over Africa took place from the Miocene onwards including, for example, the slow closure of the Tethys seaway until the mid-Miocene, the uplift of the Atlas Mountains during and since the early Miocene and the cooling and glaciation of Antarctica (Ruddiman et al., 1989). The effect of climatic change on the Sahara Desert during the Miocene-Pliocene will be examined, in particular whether the region was in a humid, arid or transitional state. Where possible, evidence of the central Saharan palaeoclimate/environment will be discussed yet, as Ruddiman et al. (1989) outlines, most records of the late Cenozoic come from east Africa, not from modern desert regions.

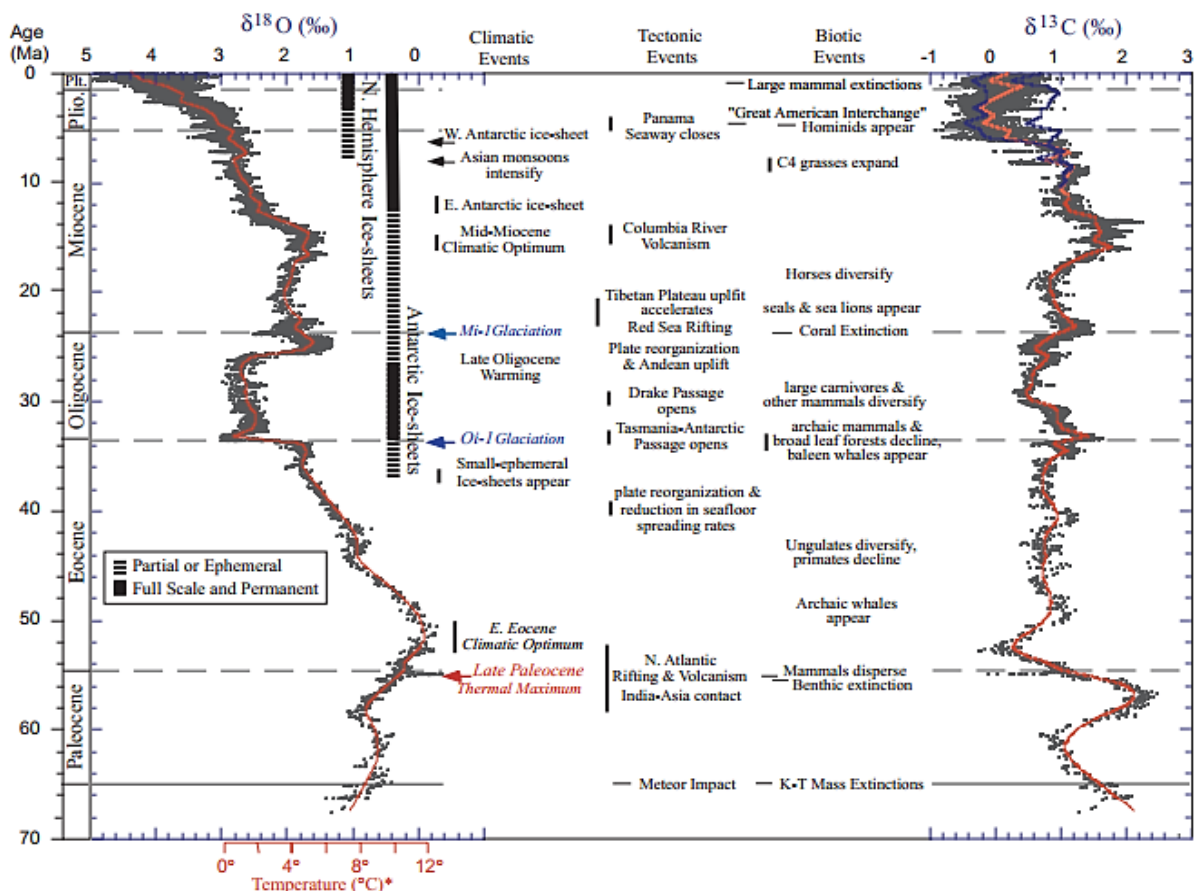


Figure 2.1 Summary of the timings of key climatic, tectonic and biotic events of the Cenozoic from Zachos et al. (2001). Global deep-sea oxygen and carbon isotope records based on data compiled from >40 DSDP/ODP sites are also included. The absolute ages are relative to the standard GPTS of Berggren et al. (1995)

2.1.1 Miocene

Early-Mid Miocene

The Miocene, which belongs to the late phase of Cenozoic cooling, is characterised by a series of extreme climatic optima (Micheels et al., 2009; 2011; Kurschner et al., 2008). In general, the Miocene was warmer and more humid than the present climate, however understanding of global climate cooling from the Miocene to today remains incomplete (Micheels et al., 2009). This is particularly true for the early-mid Miocene with limited studies conducted over this time, especially in North Africa. Around 22 Ma a change of the African plate motion occurred with Africa beginning to move north-eastwards (Guiraud et al., 2005). Acceleration in the uplift of the Tibetan Plateau (Figure 2.1) occurred during the early Miocene yet climatic simulations focusing on North Africa show that this event had no significant effect on the climate (Zhang et al., 2014). CO₂ levels based on stomatal counts from fossil leaves show a drastic decline during the Oligocene-Miocene transition from 600 to 340 ppmv remaining low until the mid early Miocene (Kurschner et al., 2008). These values differ dramatically from *p*CO₂ estimates of 260-190 ppmv derived from isotopic compositions of individual organic compounds of haptophyte algae and carbonates from surface-dwelling foraminifera (Pagani et al., 1999). The mid early Miocene is characterised by a warm phase which peaked around 17-15 Ma known as the Mid Miocene Climatic Optimum (MMCO) (Figure 2.1, Zachos et al., 2001). This event is mostly recognised from deep sea deposits with scarce terrestrial sequences available due to depositional hiatuses (Zan et al., 2015). The MMCO is distinguished by deep-water and high-latitude surface water temperatures 6°C warmer than today (Pagani et al., 1999). The mechanisms causing this climatic variation have proved difficult to understand (Kender et al., 2009). As noted in Figure 2.1, low mean-ocean $\delta^{18}\text{O}$ values, which represent the warmest temperatures of the Neogene, occur at the same time as abnormally high mean-ocean $\delta^{13}\text{C}$ values (Zachos et al., 2001; Kender et al., 2009). These values were originally thought to be due to the result of enhanced ocean productivity and burial of ¹²C (Kender et al., 2009). Pagani et al. (1999) stated there was ‘no evidence for high *p*CO₂ during the late early Miocene climatic optimum’ questioning the link between CO₂ levels and Miocene climate. More recent studies however, such as by Kurschner et al. (2008), reveal CO₂ levels at 20 Ma increase to a maximum of 400-500 ppmv by the MMCO suggesting elevated CO₂ levels contributed to the MMCO.

Terrestrial evidence of the climatic changes experienced in the Sahara during the early Miocene are limited, especially for the Aquitanian. Swezey (2009) describes a

change in terrestrial ‘preservation space’ in the Miocene Sahara coincident with a rise in sea level and a progressively warmer and more humid climate allowing preservation of terrestrial strata via a rise in the water table and increased vegetation. The Gebel Zeltan locality in the Sirt Basin (Cyrenaica) houses numerous fossil remains of crocodiles of lower Miocene (Burdigalian) age (Llinas Agrasar, 2004). These remains indicate the presence of a tropical, warm and humid climate (Llinas Agrasar, 2004). From the same site, coincident with the MMCO (17.5 Ma), fossil bracket fungus has been documented along with tropical forest trees (Senut et al., 2009).

The termination of the MMCO was dramatic (Pagani et al., 1999). CO₂ levels again decreased to 280 ppmv (Kurschner et al., 2008), however as for the MMCO, Pagani et al. (1999) documented no decrease in CO₂. This period, known as the Mid Miocene Climatic Cooling (MMCC), experienced a global temperature drop of more than 5°C (Flower and Kennett, 1994). Flower and Kennett (1994) note two stages of transition in the MMCC. During the early stage (16-14.8 Ma) there were major short-term variations in global climate, sea level, deep ocean circulation and the re-establishment of the East Antarctic Ice Sheet (EAIS) (Flower and Kennett, 1994). The later stage (14.8-12.9 Ma) was a time of major growth of the EAIS (Flower and Kennet, 1994). Associated with this Antarctic cooling the eustatic sea level dropped by 100 m (John et al., 2003); there was initial widespread deep sea erosion and changes in the pattern of deep sea sedimentation (Potter and Szatmari, 2009); a permanent shift in $\delta^{18}\text{O}$ of +1‰ occurred, interpreted to reflect deep water cooling including the increased production of Southern Component Water (Pagani et al., 1999, Flower and Kennet, 1994; Zachos et al., 2001); and also a distinct increase in the meridional temperature gradient (Flower and Kennet, 1994). The understanding of the mechanisms causing the MMCC are debated, however, it is accepted that climatic changes occurred when one or more of the parameters exceeded threshold levels (John et al., 2003; Kender et al., 2009). According to John et al. (2003) discussion is focussed on two major controls. The first is alteration of ocean circulation due to widening/closing of ocean gateways (John et al., 2003). Kender et al. (2009) for example discussed the closure of the Tethys Ocean ~18 Ma and a brief re-opening ~16-15 Ma which was thought to have increased poleward heat and moisture transport thus causing increased precipitation and aiding ice accumulation. This theory however cannot explain the high benthic $\delta^{18}\text{O}$ values and $p\text{CO}_2$ between 16-15 Ma (Kender et al., 2009). The second cause is $p\text{CO}_2$ variability involving CO₂ sequestering and subsequent cooling (John et al., 2003).

The presence of ice at the poles which often follow 40 or 100 kyr orbital cycles can influence the strength of the African Summer Monsoon (ASM) (Zhang et al., 2014). North African aridity varies with the strength of the monsoon which is also influenced by the 20 kyr precession cycle (Zhang et al., 2014). Before the Quaternary, aridity in North Africa was mainly controlled by the position of the monsoon which oscillated with the orbital cycles (Zhang et al., 2014). After the development of the EAIS, Flower and Kennet (1994) explain that the meridional temperature gradient increased and the climatic boundary zones strengthened resulting in increased aridification of Africa in the mid-latitudes. This however is contradictory to the findings of John et al. (2003) who studied continental weathering rates and terrigenous fluxes on the North African margin (Malta). They propose that a major consequence of the EAIS was that northward winds from the southern hemisphere were stronger than those from the northern hemisphere, therefore pushing atmospheric fronts, such as the ITCZ, further north than today (John et al., 2003). This consequently allowed water vapour from the tropical belt to be carried farther northwards resulting in increased regional precipitation on the North African continent (John et al., 2003).

Unfortunately, proxy evidence of climatic conditions in the central Sahara are severely lacking for the mid Miocene. In the eastern Sahara an unconformity is present at the transition from Lower Miocene strata to Middle Miocene which Swezey (2009) suggested may be of regional extent. Its origin may be due to a fall in eustatic sea level and hence a drop in the water table (Swezey, 2009), conditions which are not conducive to preservation as outlined by Stokes and Bray (2005). Vertebrate fossils of *Hipparion* of late mid Miocene (Serravallian) age were found within the Beglia Formation, Tunisia (Swezey, 2009). This formation was deposited by a fluvial system which flowed north to the Mediterranean Sea (Swezey, 2009). Fossil crocodiles from central Tunisia are also documented in late Serravallian (12 Ma) strata which indicate the former presence of large and deep rivers flowing northwards (Senut et al., 2009). The record of Neogene environments is sporadic with most data regarding the African continent from eastern Africa (Otero et al., 2011). During the mid Miocene in Libya, Swezey (2009) states that marine strata (e.g. parts of the Marada Formation- Gammudi and Keen (1993)) rather than fluvial, accumulated in the Sahara in response to a eustatic rise in sea level. The most comprehensive records of Libyan climate, as Swezey (2009) highlighted (Figure 2.2), are found from three locations: offshore northwestern Libya, the coastal region of central Libya and northeast Libya and the Sahabi Channel region. Understanding of the climatic

evolution of central Libya, such as in the Fazzan, is all but absent for the early-mid Miocene due to the limited amount of stratigraphic sections in the basin and lack of research on any exposed sections.

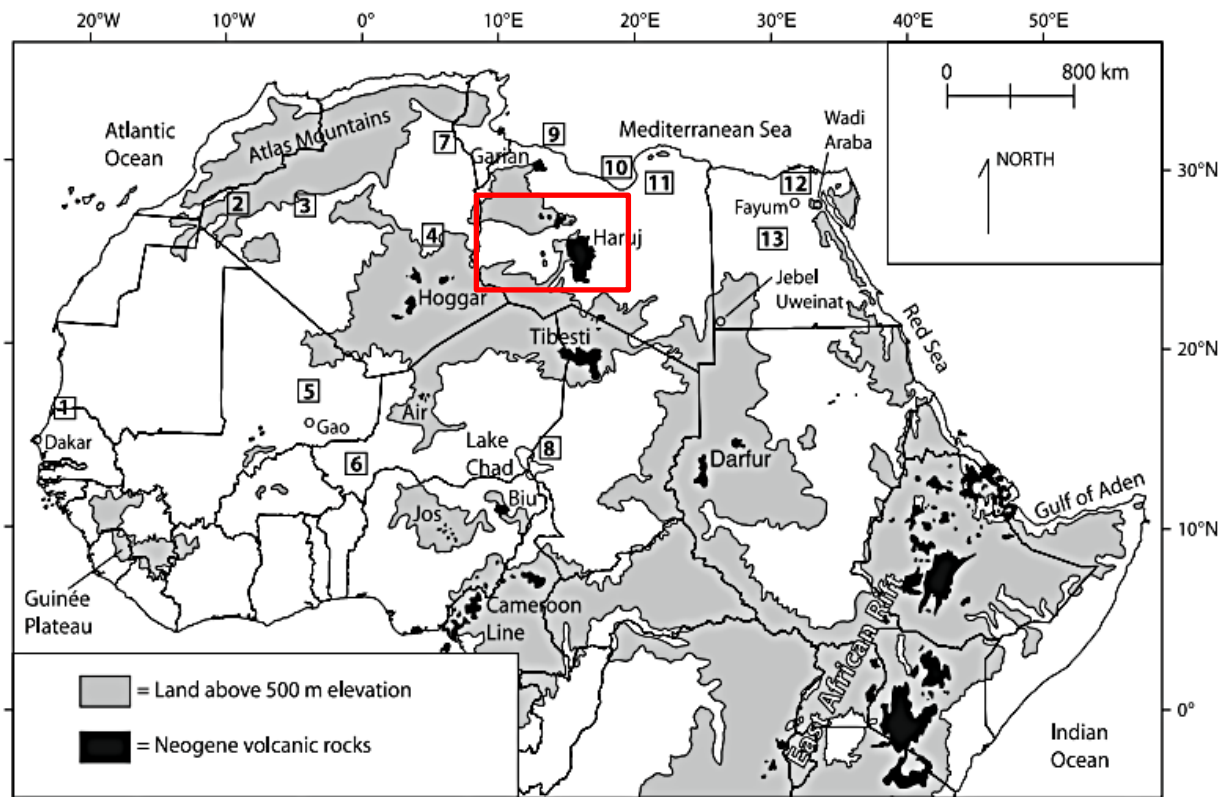


Figure 2.2. Map of the stratigraphic locations described in Swezey (2009) clearly showing the lack of research on stratigraphic sections within central Libya as highlighted by the red box. Libyan sites: 9-Offshore Libya, 10-Sirt Basin, 11-Northeast Libya. Other central Saharan sites: 4-Tademait, Algeria, 7-Chotts Basin, 8-North Chad

Late Miocene

In comparison to the early/mid Miocene, the late Miocene climatic evolution is documented fairly well in the Sahara from proxy records and also via climate model simulations. Many studies focus on this period of African history due to the search of fossil hominoids, particularly in the eastern part of the continent (Otero et al., 2011). Otero et al. (2011) noted however that the comparative lack of records of the Neogene terrestrial environment elsewhere in Africa limits palaeoenvironmental comparisons at a continental scale. During the Tortonian the African plate motion altered, becoming directed to the northwest (Guiraud et al., 2005). The late Miocene, although globally warmer and wetter (Marzocchi et al., 2016), was a time of many climatic perturbations. CO₂ levels again began to rise with Pagani et al. (1999) documenting levels between 260-300 ppmv and Kurschner et al. (2008) up to 340 ppmv. Simulations of the Saharan climate during the

Tortonian have been conducted by several researchers. A Tortonian vegetation reconstruction by Pound et al. (2011) using the HadAM3 model found only a small Sahara with desert areas restricted to the north and northeast of the modern Saharan area. The model instead predicts the expansion of tropical savanna, tropical grassland, tropical xerophytic shrubland and temperate sclerophyll woodland and shrubland across the Sahara (Pound et al., 2011; 2012). Micheels et al. (2011) found similar results when running COSMOS model simulations for the Tortonian with the Sahara replaced by grassland/savannah. Micheels et al. (2011) explain the presence of this type of vegetation due to the open Central American Isthmus which leads to a decrease in northward ocean heat transport but an increase in atmospheric heat transport. In the northern mid-latitudes transient eddies increase compared to today and in the Tortonian model run correlates to intensified storm tracks (Micheels et al., 2011). Terrestrial evidence of a humid Sahara during this time is also documented. Fossil crocodiles from deposits in central Tunisia which were identified at 12 Ma are still preserved at 10 Ma (Senut et al., 2009). Pickford (2000) also reported the occurrence of crocodiles in the Beglia Formation (fluvial deposits) at 10 Ma. The Monte Gibliscemi section, Sicily, contains an archive to trace the late Miocene (9.7-7 Ma) conditions of North Africa (Kohler et al., 2010). Geochemical proxy records of the lower part of the section (9.5-8.4 Ma) show little variation suggesting a stable climate and also a high sedimentation rate with low CaCO₃ content indicating high terrigenous input originating from North Africa (Kohler et al., 2010). Contrasting these models and field evidence is the Tortonian model simulation using NorESM run by Zhang et al. (2014). This model shows the Tortonian to be a key period for triggering aridity in North Africa and creating the Sahara. They demonstrate that the ASM was substantially weakened by the shrinkage of the Tethys Sea as the Afro-Arabian and Eurasian plates collided causing a reorganisation of atmospheric moisture transport thus allowing arid conditions to expand over North Africa (Zhang et al., 2014). Griffin (2002) also notes the occurrence of a Tortonian Dry Phase over North Africa, a time of extreme conditions when the monsoon was at its most southern latitude, a situation similar to today. It appears this hypothesis is based on the presence of evaporites (halite) in the South Gharib Formation (Red Sea) in eastern Africa (Griffin 1999; 2002). Further terrestrial evidence for aridity during the Tortonian is however lacking at present.

The late Tortonian-early Messinian was notably a time of change. Expansion of C4 plants took place during this time. Cerling et al. (1993) shows a well-defined change in the isotopic composition of palaeosol carbonate in Pakistan beginning ~7.4 to 5 Ma. In a later

paper by Cerling et al. (1997) the authors suggest an increase in biomass of C₄ photosynthesising plants between 8-6 Ma based on the study of fossil tooth enamel from a number of continents, including Africa. They showed however that the C₄ endmember diet was not reached until 5 Ma (Cerling et al., 1997). The cause of the expansion according to Cerling et al. (1993; 1997) may have been the result of low CO₂ as the C₄ pathway is favoured in low CO₂ concentrations. Intense debate however surrounds this as *p*CO₂ reconstructions, such as those mentioned earlier, show CO₂ levels were increasing (Feakins and deMenocal, 2010). An alternative hypothesis stems from the uplift of the Himalayas. Uplift caused an intensification in the Indian Monsoon altering the seasonality of precipitation in the region with increased aridity resulting in a shift to C₄ vegetation in Pakistan and mixed C₃/C₄ vegetation in east Africa (Feakins and deMenocal, 2010). More recent research of plant leaf wax isotopic compositions identified two C₄ expansions, one much earlier than previously documented by Cerling et al. (1993; 1997) occurring at 11-9 Ma and another 6-5 Ma (Feakins et al., 2013).

The late Miocene climate is also responsible for the first appearance of the Sahara Desert (Micheels et al., 2009). Schuster et al. (2006) recorded sandstone outcrops in the Djurab Sand Sea (Chad) dated to 7 Ma which the authors believe provide the earliest in situ record for an arid climate and aeolian sand accumulation in the Sahara. At this time, desert conditions were also initiated in the Taklimakan Desert with Sun et al. (2009) documenting the first in situ aeolian sands. The timing of the first appearance of the Sahara however has been questioned, for instance by Swezey (2006), with evidence showing that humidity, in particular in the form of fluvial deposition (Swezey, 2009; Pound et al., 2012), was also a feature of the late Miocene in the central Sahara. Vegetation patterns of the Tortonian as outlined by Pound et al. (2011; 2012) continued and repeated aeolian-lacustrine sequences have been recorded in the Chad basin from 7 Ma (Schuster et al., 2006; 2009). Lebatard et al. (2010) documented at least three major Lake Chad episodes, one at 6.5-6.2 Ma, one covering the Miocene-Pliocene boundary at 5.9-4.8 Ma and a final one in the late Pliocene-Quaternary (4.2-1.1 Ma). This desert-lake pattern implies that repetitive arid-humid cycles occurred rather than continuous periods of humidity as experienced in the Quaternary (e.g. deMenocal et al., 2000; Drake and Bristow, 2006; Schuster et al., 2009). Lebatard et al. (2010) noted the difficulty in defining the exact number of lake phases due to the rapid change in lateral facies from the basin margin to the centre. Swezey (2009) also noted the great variety in lithology of the late Miocene Saharan strata which include sandstones, evaporites and palaeosols as shown in Figure 2.3.

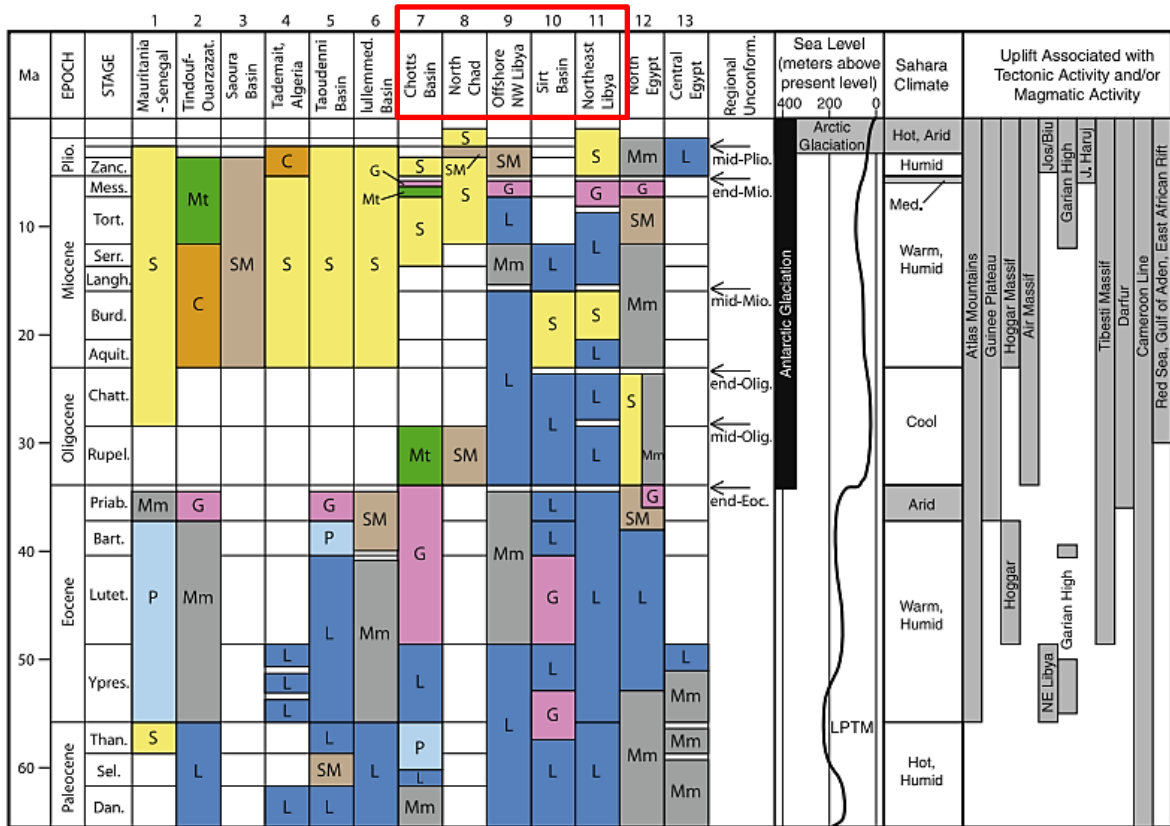


Figure 2.3 Chart from Swezey (2009) showing the varied Cenozoic stratigraphy of the Sahara in relation to climatic changes in the Sahara, eustatic sea level, glaciation events and tectonic events around northern Africa. The red box highlights central Saharan locations. C--conglomerate, S-sandstone, SM-sandstone and mudstone, Mt-mudstone, terrestrial, Mm-mudstone, marine, G-gypsum and (or) gypsiferous mudstone, P-phosphatic mudstone and (or) phosphatic limestone, L-limestone and (or) dolomite. White/blank space-strata not present or identified.

The expanded Lake Chad coincided with the Zeit Wet Phase (ZWP) (~7.5-4.6 Ma), the most prolonged period of humidity during the last 12 Ma (Feakins and deMenocal, 2010; Griffin, 2002). This period, named by Griffin (1999), was a time of high rainfall and sediment yield rates. Griffin (1999) provided stratigraphic evidence from the Gulf of Suez/Red Sea of a humid northeastern Africa during the Messinian. It is thought the central Sahara also became humid at this time, not only documented by Lake Chad but also by the development of the Sahabi River in Libya providing evidence for this interpretation (see section 2.2 for more details) (Griffin, 2002). Other proxy evidence that the Sahara experienced humidity during this time is documented from fossils of freshwater fish in Chadian outcrops (Otero et al., 2009; 2011). Low terrigenous fluxes, up to 2x lower than in the Quaternary, have been recorded by Colin et al. (2014) between 6.2-4.9 Ma implying more humid conditions. Ruddiman et al. (1989) also documented low and, in some cases, declining terrigenous fluxes from several DSDP sites off the west coast of North Africa. The development of the ZWP is thought to be due to the initiation and early evolution of

the Asian (SW) monsoon and African (SE) monsoon and also modification of the drawdown of the Mediterranean (Griffin, 1999; 2002). Griffin (2002) discussed how the physical aspects of the Tibetan Plateau; its degree of uplift, size and latitude allowed the 21 ka cyclical nature of insolation to cause differences in the monsoons. During times of high insolation the SW monsoon was emphasised and vice versa for the SE monsoon (Griffin, 2002). It was the SE monsoon which was responsible for bringing increased moisture to northern Africa on a cyclical basis (Griffin, 2002).

The occurrence of a wet phase in the central Sahara during the Messinian is surprising given at this time the Mediterranean underwent a period of aridity. This idea of aridity stems from the discovery of the Messinian Salinity Crisis (MSC) (Hsu et al., 1973; 1977). The MSC, dated to 5.97-5.33 Ma, represents the most dramatic examples of ocean change and base-level fluctuations in the geological record (Butler et al., 1999; Krijgsman et al., 1999; Christeleit et al., 2015). However, whereas in North Africa the climate was primarily controlled by the monsoon, an interplay of factors were associated with the MSC allowing aridity/humidity to occur in close proximity (Griffin, 2002). The cause of evaporation of the Mediterranean and deposition of thick (~1500 m) evaporite deposits during the MSC is still debated with several models proposed (see Rouchy and Caruso, 2006). It is generally accepted that the cyclic deposition during the MSC was related to circum-Med climate changes driven by change in Earth's precession and also to non-orbitally induced glacio-eustatic sea level changes (Krijgsman et al., 1999). Many (e.g. Krijgsman et al., 1999; Butler et al., 1999; Ochoa et al., 2015) favour a tectonic origin for the MSC with the closure of the Betic and Rifian gateways which previously connected the Atlantic and Mediterranean thus reducing sea water exchange leading to precipitation of evaporites (Krijgsman et al., 1999; Ochoa et al., 2015). Flecker et al. (2015) mentions however that the large volume of salt preserved in the Mediterranean suggests that one or more of the marine connections remained open. The MSC ended with the 'Lago Mare' event and associated deposits which occurred during the re-flooding of the Mediterranean giving rise to brackish conditions (Do Couto et al., 2014). The effect of the MSC impacted the North African region, in particular river systems. A major period of downcutting occurred during this time as discussed in more detail in section 2.2.

2.1.2 Pliocene

By the end of the Miocene much of the African landscape would have been recognisable today (Potter and Szatmari, 2009). Unlike the late Miocene which showed a gentle rise in $\delta^{18}\text{O}$ values (due to cooling), the early Pliocene is marked by a subtle warming trend (Zachos et al., 2001). The early Pliocene in the central Sahara was still characterised by more humid conditions with fossil hippo remains recovered from the Djurab Desert, Chad, which are aged between 5-3 Ma (Boisserie et al., 2003). Several changes in climate occurred during the Pliocene (Ruddiman et al., 1989). The mid Pliocene (4.5-3 Ma) for example is characterised by globally warmer conditions, in particular during the mid-Pliocene Warm Period (3.29-2.97 Ma) (Haywood and Valdes, 2006; Feakins and deMenocal, 2010). This period is one of the most intensively studied intervals in the Cenozoic, primarily due to it being an analog for today's climate, but it is also one of the most scientifically controversial according to Haywood and Valdes (2006). Temperatures increased by 3°C with CO_2 levels at 360-400 ppmv (Salzmann et al., 2008; Feakins and deMenocal, 2010). Sea levels were also 15-25 m above modern levels and there was reduced Antarctic ice (Feakins and deMenocal, 2010). The causes of the mid Pliocene warmth are only partially known and are thought to be related to a number of changes in orography, atmospheric gas concentrations, ocean circulation and more (Salzmann et al., 2008). Feedback mechanisms, such as through reduced land ice cover and surface albedo, may have also been important (Salzmann et al., 2008). Climate models such as PRISM suggest North Africa was 5°C warmer and also wetter with precipitation levels between 400-1000 mm annually (Feakins and deMenocal, 2010). Other models such as the HadAM3 used by Haywood and Valdes (2006) used to investigate vegetation distribution also note decreases in bare soils indicative of less extensive arid deserts. Salzmann et al. (2008) also showed a smaller desert zone with semi-desert xerophytic shrubland and grasslands in North Africa, although tropical savanna is still recorded in the Chad region. The presence of tropical savanna vegetation in Chad was believed by Novello et al. (2015) to be due to the presence of the recurring large Lake Chad which triggered vegetation changes at a local scale. The effect of these lake phases, which are believed to be comparable in size to the Megalake Chad events of the Quaternary, have been studied by Contoux et al. (2013). They found that precipitation was drastically reduced above the lake surface as deep convection was inhibited by the overlying cooler air while at the same time convective activity was increased around the lake, transporting colder and moister air towards the eastern shore of the lake (Contoux et al., 2013). In spite of this, they conclude

that the effect of the lake on precipitation and temperature is not enough to widely impact vegetation patterns (Contoux et al., 2013).

Proxy evidence, such as marine pollen from ODP site 658 (Cape Blanc), shows tropical forest occurred at this latitude (21°N) and also suggests a palaeoriver flowed continuously until 3.35 Ma (Leroy and Dupont, 1994). Marine records also indicate that Pliocene African climate was controlled by precessional frequency, hence variations in the strength of monsoonal precipitation (deMenocal, 1995; Feakins and deMenocal, 2010). Unlike marine records however, terrestrial records are often too low resolution to identify the Pliocene variability (Feakins and deMenocal, 2010). A 200 m long borehole drilled in the Bol Archipelago (Lake Chad) contains diatom assemblages which indicate freshwater lacustrine conditions at Bol since at least 4.7 ± 0.1 Ma (Novello et al., 2015). Deposits in the Sahabi area of Libya also provide evidence of a humid central Sahara. The deposits, belonging to the Sahabi Formation (early-mid Pliocene) are well known as an important palaeontological site and record of the palaeoenvironmental evolution over North Africa (De Heinzelin et al., 1987; El-Shawaihdi et al., 2014). The 120 m thick formation contains sands and clays which record sedimentation of a variety of depositional environments from shallow marine transgressions which pass through littoral and lagoonal facies and ends with deltaic, fluvial and palaeosols (Griffin, 2002). The formation contains 23 plant taxa and a wealth of fossil evidence including vertebrate fauna of 22 families of mammals, six families of bird and nine families of fish, whose recent species live in freshwater (Griffin, 2002). As well as climatic effects influencing the palaeoenvironmental evolution of North Africa, the Pliocene was also a time of tectonic and magmatic activity in the Sahara (Swezey, 2009). This is especially apparent in Libya and the central Sahara with the development of a number of volcanoes blocking and redirecting the flow of many rivers as discussed in more detail in section 2.2.

The late Pliocene sees a shift towards more arid conditions in North Africa. In the Bol Archipelago from 3.6 ± 0.1 Ma onwards there is a quasi-absence of diatoms implying episodic or reduced lacustrine conditions (Novello et al., 2015). Leroy and Dupont (1994) noted that wind transport of pollen grains via trade winds rather than fluvial transport increased between 3.3 and 2.5 Ma. Aridification around this time is thought to have influenced the evolution of hominoids, especially in eastern Africa (Cane and Molnar, 2001). The closure of the Isthmus of Panama is thought to have contributed to aridity by changing North Atlantic ocean circulation, although an alternative hypothesis concerning the closure of the Indonesian Seaway 3-4 Ma was proposed by Cane and Molnar (2001).

They believe this led to the decrease of sea surface temperatures in the Indian Ocean leading to reduced rainfall over eastern Africa (Cane and Molnar, 2001). Significant Northern Hemisphere glaciation also began and intensified between 3.2-2.6 Ma due to orbitally induced insolation changes with obliquity paced glacial cycles commencing (Lisiecki and Raymo, 2005; Feakins and deMenocal, 2010). This is likely the main trigger of aridity in the Sahara due to shift to cold North Atlantic sea surface temperatures (deMenocal, 1995). Persistent and widespread aeolian deposits appeared in the Sahara at this time (Swezey, 2006; 2009). For this reason, some researchers (Kropelin, 2006; Swezey, 2006; 2009) still prefer to associate the late Pliocene, not the late Miocene, as the time of the first onset of desert conditions in the Sahara.

It is apparent that the global climate of the Miocene-Pliocene was a time of change which had dramatic implications for the palaeoclimatic evolution of North Africa and the central Sahara. The orbitally controlled monsoon appears to be the main driver of humidity/aridity in the region. However, it is also clear that the palaeoclimate was not just influenced by this control but a complex interplay of factors such as tectonics and ice development which resulted in the many changes and spatial variability in the region. Unfortunately evidence of change is limited in the central Sahara, especially for the early-mid Miocene. It is evident that more research is needed in this region to help fill the palaeoclimatic gap which remains and also to possibly help settle some of the ongoing debates, including the time of the first onset of aridity in the Sahara.

2.2 Geological and geomorphological history of the Fazzan and neighbouring basins

Expeditions to investigate the geology of the Fazzan have a long history dating back to the 1850s (Grubic et al., 1991). Many of the more recent investigations (e.g. Parizek et al., 1984; Aziz, 2000) have been conducted during the search for oil in the region (Grubic et al., 1991). These expeditions have allowed the evolutionary history of the basin to become increasingly well understood. This section will summarise the geological/geomorphological evolution of the basin since the Palaeozoic followed by a more detailed discussion of events since the late Miocene.

The 600 km wide Fazzan Basin is one of the major basins in northern Africa (Thiedig et al., 2000). The basin, according to Davidson et al. (2000), should be thought of as an erosional remnant of a larger Palaeozoic-Mesozoic basin that originally extended over much of Africa. Throughout the Palaeozoic-Mesozoic, the basin was shaped by a number of tectonic events including the Hercynian orogeny (Aziz, 2000; Peregi et al., 2003). A consequence of this event was the overprinting of the early Palaeozoic structural relief by E-W structural elements (Klitzsch, 2000). The NE part of the basin was also incorporated into the present-day basin as the collision formed the Gargaf uplift (Klitzsch, 2000). The main periods of uplift of this large, broad anticlinal structure took place during the mid-Cretaceous and early Tertiary (Binsariti and Saeed, 2000; Davidson et al., 2000). Throughout the Palaeozoic the basin was also influenced by a number of marine transgressions (Thiedig et al., 2000). Tectonic events, such as the Gargaf uplift, however prevented later transgressions into the basin (Seidl and Rohlich, 1984). Subsequently sedimentation in the basin slowed and stopped during the early Cretaceous with continental conditions interrupted only by the Maastrichtian transgression (Klitzsch, 2000; Thiedig et al., 2000). Since the late Cretaceous the deposits of the basin have been progressively deflated, only filled intermittently during the Quaternary by the development of large lakes (Thiedig et al., 2000).

While the central Sahara is now arid/hyper-arid, extensive palaeodrainage systems used to exist in the region (Paillou et al., 2012). The palaeohydrology and the sequence of geological events which led to the formation of river systems and closed basin lakes is poorly understood in Libya, particularly in the Fazzan Basin (Drake et al., 2008a). Drake et al. (2008a) tried to address these issues by focussing on the geological and geomorphological events that took place in the Fazzan since the late Miocene, a critical time for assessing the palaeoclimate of the region (Drake et al., 2012). Prior to this time, the palaeohydrology of the region was poorly understood (Drake et al., 2012).

2.2.1 Late Miocene

The hydrological system at this time led to the development of two large river systems: the As Sahabi and Nashu rivers (Drake et al., 2008a; 2012). The As Sahabi drained eastern and central Libya (Drake et al., 2008a). It is believed the NNW-SSE trending structural axis of the Ajdabaya trough at the centre of the neighbouring Sirt basin had a crucial influence over the hydrology of eastern and central Libya (Drake et al., 2008a; 2012). The As Sahabi River was at the centre of this depression (Drake et al., 2008a). It is not clear when the As Sahabi first originated, but Griffin (2006) suggested an age close to the Messinian. Remote sensing suggests the As Sahabi drained into the Mediterranean at the Gulf of Sirt (Griffin, 2002; 2006) and was fed by headwaters originating in the Tibesti Mountains, the Al Kufrah basin to the south and also the outflow of Megalake Chad (Griffin, 2002; 2006; Drake et al., 2008a). The main channel can be traced for 200 km, is ~1-5 km in width widening as it nears the present day coastline and >396 m deep cutting into middle Miocene limestones (Barr and Walker, 1973; Benfield and Wright, 1980; Nicolai., 2008). In comparison to the As Sahabi, little is known about the Nashu River. It drained much of western Libya originating in the mountains surrounding the Fazzan and terminating on the north-eastern margin of the Gulf of Sirt (Drake et al., 2012). Along with these main river systems, four large west-east flowing channels also existed in the Fazzan: Wadi al Hayah, Wadi ash Shati, Wadi Nashu and Wadi Barjuj (Drake et al., 2008a; 2012-Figure 2.4.).

It is clear from the literature (e.g. Griffin, 2002; 2006, Drake et al., 2008a/b; 2012; El-Hawat, 2008) that there was an important interplay of fluvial activity and volcanism in the region. Volcanism had already started in the region before the late Miocene with the establishment of the volcanic centre of Jebal al Hasawinah during 24.9-15.7 Ma (Busrewil and Oun, (1991). Jebal as Sawda, covering 6,000 km², was dated using K/Ar and palaeomagnetism to 12.3-10.5 Ma by Ade-Hall et al. (1975). Busrewil and Esson (1991) using K/Ar found that volcanic activity began 16 Ma and lasted to 8 Ma occurring in several distinguishable phases. To the east of Jebal as Sawda lies the Al Haruj as Aswad (AHAS) basalt province, the largest volcanic area in north Africa covering 45,000 km² (Ade-Hall et al., 1974; Abdel-Karim et al., 2013). The oldest lavas were dated using K/Ar and palaeomagnetism by Ade-Hall et al. (1974) to 6-0.4 Ma, with most dated flows younger than 2.2 Ma. More recent dating of the lavas has been conducted such as by Drake et al., (2008a) who conducted K/Ar dating to work out the timing of growth and merger of the Al Haruj as Aswad and its sister volcano, Al Haruj as Abyad (AHAB). They found that

the coalescing took place sometime between 5 and 2 Ma, dates which are in good agreement with those of Peregi et al. (2003). Cvetkovic et al. (2010) K/Ar dated 26 lava flow samples of the eastern AHAS and found that 22 ranged in age between 5.4-0.4 Ma, a similar age range to that of Ade-Hall et al. (1974). The most recent dating has been completed by Bardintzeff et al. (2012) who dated, using K/Ar, a basaltic lava flow 'probably belonging to the Al Haruj field'. Dates of 5.1 and 8.1 Ma were found thus extending the ages previously reported for the Al Haruj lavas (Bardintzeff et al., 2012). It was noted by Woller and Fediuk (1980) that the ages of the Libyan basalts decreased in age from NNW to SSE. This decrease however is poorly constrained with researchers such as Bardintzeff et al. (2012) indicating that the volcanic fields exhibit more complex ages than originally thought. Many studies (e.g. Radivojevic et al., 2015; Cvetkovic et al., 2010), although trying to increase knowledge of the volcanism of Libya, acknowledge that the ages of magmatism and also the composition of the lavas are poorly known.

As volcanic activity took place on the eastern margin of the Fazzan (Figure 2.5), in particular the growth of Al Haruj as Aswad towards Jebal as Sawda, blocking of Wadi Nashu, Wadi al Hayah and Wadi ash Shati occurred allowing the subsequent development of a closed basin in the northern half of the Fazzan (Drake et al., 2008b). It is thought that after this closure and the change in palaeohydrology, a palaeolake would have formed in the basin (Drake et al., 2012-Figure 2.5). Climatic changes during the Messinian (see previous section) brought about many changes to the region. Via seismic investigations Barr and Walker (1973) postulated that the As Sahabi drainage system experienced a substantial period of downcutting and extension due to the drop of the Mediterranean sea level of ~400 m. This has since been supported by Griffin (2002; 2006) who also suggests that the now extended As Sahabi had a connection to Megalake Chad. Otero et al. (2009) further substantiates the existence of a connected drainage system via the presence of fossil Aride fish found in both the Chadian and Libyan basins. The river systems would have had open waters with permanent flow based on the habitat preference of the fossil fish (Otero et al., 2009). The link to the Chadian basin resulted in the doubling of the As Sahabi River's catchment (Drake et al., 2008b). The tributaries of the As Sahabi also extended into the southern Fazzan (Drake et al., 2012). Drake et al. (2008a) notes that this extension would have been particularly effective at the catchment boundary with Wadi Nashu as this river could not benefit from the fall in base level due to the development of the Al Haruj as Aswad. Whilst this wadi, along with Wadi ash Shati and Wadi al Hayah, escaped

downcutting, Wadi Barjuj grew in size capturing much of the headwaters of the Wadi Nashu catchment (Drake et al., 2008a/b; 2012, Figure 2.5).

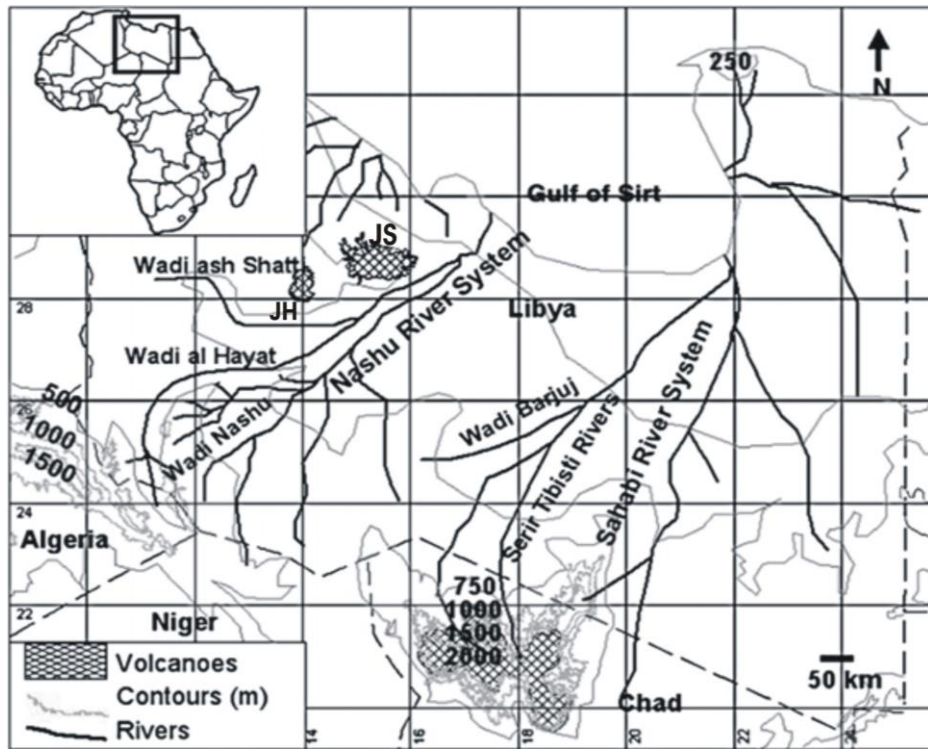


Figure 2.4. Map to show the river systems of Libya during humid periods in the Late Miocene before the blocking of Wadi ash Shati, Wadi al Hayah and Wadi Nashu by the AHAS (Drake et al, 2008a). JH=Jebal al Hasawinah, JS= Jebal as Sawda.

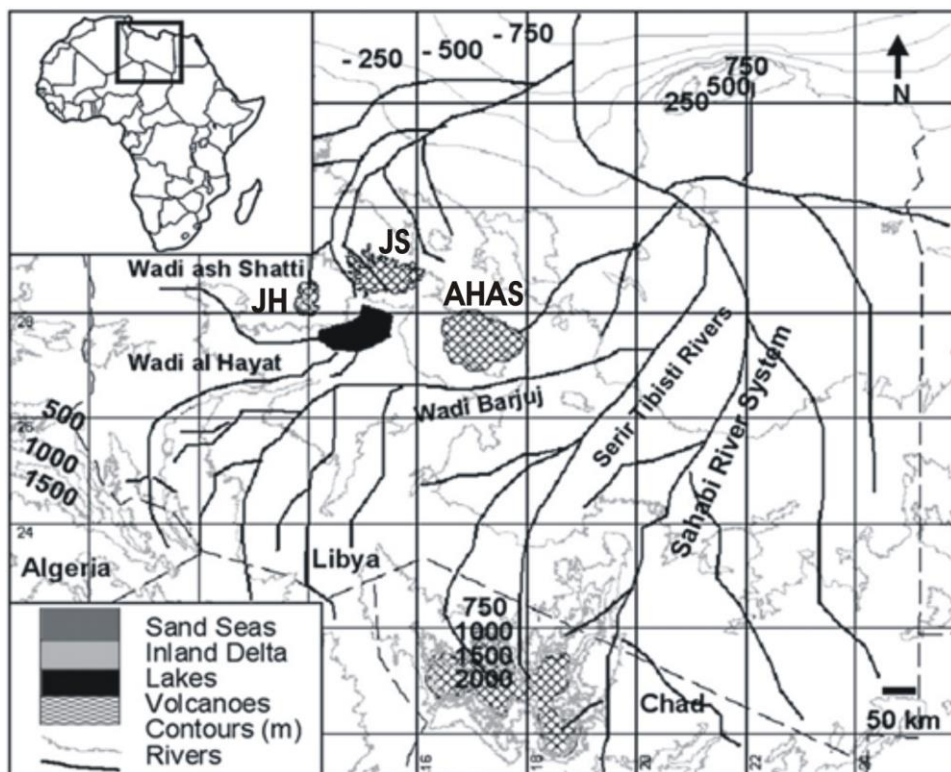


Figure 2.5 . Map to show the river and lake systems during the Messinian once the Nashu River had been blocked by the development of the AHAS (Drake et al., 2008a). JH=Jebal al Hasawinah, JS= Jebal as Sawda, AHAS=Al Haruj as Aswad.

2.2.2 Pliocene

The start of the Pliocene was the beginning of the end of the As Sahabi River (Drake et al., 2008b). The transgression of the Mediterranean following the MSC resulted in a marine incursion into the Sirt basin causing flooding of the river and for it to gradually silt up (Drake et al., 2008a). At the same time, volcanism in the Tibesti (Deniel et al., 2015) affected the headwaters of the river and cut off the outflow from Megalake Chad causing a drastic reduction in size of the river system (Drake et al., 2008b). During this time, subsidence took place in the Al Kufrah basin (SE of the Fazzan) and allowed a rejuvenation of the Al Kufrah River system which expanded southwards (Drake et al., 2008a). Differences in topographic characteristics shows this affected the As Sahabi catchment with little of the main As Sahabi channel remaining at the end of the Pliocene (Drake et al., 2008b). Expansion of the Al Kufrah led to the development of a broad alluvial fan, thought to be an inland delta (Di Cesare et al., 1963) near the northern end of the river system covering 15,000 km² (Drake et al., 2008a; Paillou et al., 2009). Humid periods and subsequent subsidence allowed further growth of the delta with a lake of up to 6000 km² in size periodically developing at the base (Drake et al., 2008a). Drake et al. (2008a) note that the deposits of this lake described by Di Cesare et al. (1963) (the Garet Uedda Formation) are very similar to those of the Pleistocene deposits of Lake Megafazzan.

The Kufrah River was a 900 km-long palaeodrainage system in eastern Libya (Paillou et al., 2009; 2012). The precise age of the origin of the Kufrah River system is unknown but Paillou et al. (2009) believe it could have originated in line with the uplift of the Tibesti in the midMiocene, with it more than likely in place at the end of the Miocene. Mapping and thus reconstruction in this region is difficult due to the presence of vast sand dune systems such as the Calansico Sand Sea (Paillou et al., 2009). In spite of this, SRTM topographic data has revealed local depressions and a 300 km-long link which allowed the Kufrah River to be connected to the Mediterranean via the As Sahabi palaeochannel (Paillou et al., 2009; 2012). This data also suggests there was no connection between the Kufrah Basin and Lake Chad due to the elevation of the Erdi region (Paillou et al., 2009; Griffin, 2002). More recently seven palaeochannels belonging to the Kufrah drainage system have been mapped by Paillou et al. (2012). Four of these channels, which range in length from 110-190 km, appear to start on the borders of the Al Haruj (Paillou et al., 2012). Paillou et al. (2012) do not provide an age of these palaeochannels but believe their formation is related to the continued volcanic activity in the Pliocene of the Al Haruj

(Drake et al., 2012). The merger of the Al Haruj as Aswad and the Al Haruj al Abyad, between 5-2 Ma also influenced western Libya (Drake et al., 2008a/b). Wadi Barjuj was blocked as a result of the growth leading to the doubling in size of the closed Fazzan basin (Drake et al., 2008a/b, Figure 2.6). The effect of the blocking of Wadi Barjuj on the As Sahabi is uncertain but it is thought it would have led to the start of lake development in the western side of the Al Haruj al Aswad which, during humid intervals, could have merged with the lake within Wadi ash Shati (Drake et al., 2008a/b). This is thus an important time in the development of Lake Megafazzan which would have increased in size due to the newly available accommodation space.

Drake et al. (2008a) pose an important question regarding Lake Megafazzan—could the lake have ever become so large that overspill flowed out of its catchment and, if so, in which direction? The authors show two low points to the north and south of Al Haruj al Aswad which contain river gravels where overspill may have occurred. Overspill from the south may have linked to the As Sahabi (Drake et al., 2008b). Drake et al. (2008a) K/Ar dated two lavas overlying fluvial gravels to 4.68 ± 1.52 and 3.43 ± 0.32 Ma. The gravels lack sedimentary structures (e.g. bedforms) and, given that the basin originated from fluvial and volcanic activity, the presence of gravels could be explained by thermal uplift of previously existing channels (Drake et al., 2008a/b). Drake et al., (2008a/b) therefore acknowledge that it is not possible to say for certain if the deposits were formed by overspill and thus linked to the As Sahabi. Conclusive evidence in the form of a channel with braided bars and meanders was found however to the north of Al Haruj al Aswad where two other overspill points occurred (Drake et al., 2012).

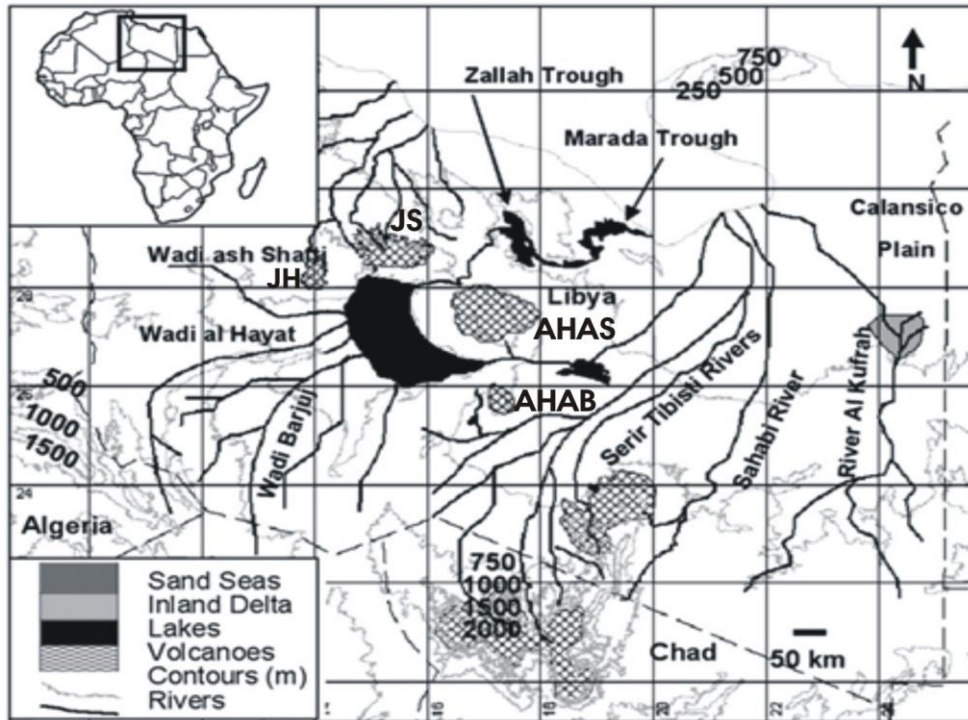


Figure 2.6 Map to show the river systems during the Lower Pliocene after the refilling of the Mediterranean. Lake Megafazzan has increased in size due to the blocking of Wadi Barjuj. Initiation of the AHAB can be seen (Drake et al., 2008a). JH=Jebel al Hasawinah, JS= Jebel as Sawda, AHAS= Al Haruj as Aswad, AHAB=Al Haruj as Abyad

Quaternary

Little change took place to the As Sahabi during the Late Pleistocene and Holocene, although it is likely that based on the climatic conditions (increased aridity at times), there would have been a reduction in fluvial activity (Drake et al, 2008b). Subsidence of the Al Kufrah basin continued as did the development of fluvio-lacustrine features (Drake et al., 2008a). The Al Haruj al Aswad/Abyad continued to expand allowing a larger and deeper closed basin to develop in the Fazzan (Drake et al., 2008a; 2012). The Quaternary is a key period of time for the sedimentation of Lake Megafazzan as discussed in section 2.3.

It is clear from what limited literature there is regarding the geological/geomorphological history of the region that it resulted from a complex interplay of factors, in particular fluvial activity and volcanism. The evolution of the Fazzan basin cannot however be considered alone. To fully understand its history it is paramount that the activities of neighbouring basins which have exerted an important influence on the palaeohydrology of central Libya are also taken into consideration. Although research of the area has increased in recent years, in particular for the Quaternary, there is still a lack

of detailed studies on the palaeodrainage prior to the Late Miocene. It is also clear that further studies are needed to better constrain the timing of volcanic activity and also the geochemistry of the lavas. An already difficult region to access, the current unrest is hampering any further research of the basin. It is hoped however that the deposits collected for this study will aid in contributing to the understanding of this important region of the Sahara.

2.3 The Al Mahruqah Formation: Current Lithostratigraphic understanding

The Al Mahruqah formation (AMF), preserved as erosional remnants, is the youngest rock unit to exist in the Fazzan Basin (Geyh and Thiedig, 2008; Drake et al., 2008a; Parizek et al., 1984). Predominantly found in Wadi ash Shati and along the NE rim of the Ubari, it unconformably overlies Palaeozoic and Mesozoic Formations (Geyh and Thiedig, 2008; Domaci et al., 1991). The name of the formation, along with the age and origin, have been debated since the 1930s. Thiedig et al. (2000) and Geyh and Thiedig (2008) provide a detailed history of the formation. Before the name 'Al Mahruqah' became widely used, other names such as 'Murzuq Limestone' (Desio, 1936; cited in Gundobin, 1985) or simply 'continental deposits' were employed. Desio (1936 cited in Thiedig et al., 2000) believed the Murzuq Limestone to be of marine origin and Miocene in age. Later researchers however argued for different ages and provenance such as Pagni (1938, cited in Geyh and Thiedig, 2008) who suggested Jurassic and lacustrine based on gastropods and freshwater algae in the deposits, Bellair (1944) who suggested a Quaternary-Pliocene age and lacustrine origin, and Collomb (1962) who identified the unit as Miocene and lacustrine. Petit-Maire et al. (1980) and Gaven et al. (1981) were the first to publish radiometric ages of the limestone deposits from Wadi ash Shati. Th/U dating of *Cardium* shells revealed lacustrine periods occurring during the late Pleistocene such as during 22.5-26.5ka BP (Petit-Maire et al., 1980), 130ka BP (Gaven et al., 1981) and a less extensive phase around 90ka BP (Petit-Maire et al., 1980).

The Al Mahruqah Formation, named after the village of Al Mahruqah (Parizek et al., 1984), was first applied by Seidl and Rohlich (1984) to a carbonate unit on the north side of Wadi ash Shati of continental origin which originated in a probably brackish to saline lacustrine environment of unknown Tertiary or Quaternary age (Parizek et al., 1984; Thiedig et al., 2000). This name has subsequently been used by other researchers such as Domaci et al. (1991) and El Ebaidi and Abdulsamad (2005) who state that 'in general, the lithology of the Al Mahruqah Formation consists of whitish to yellowish limestones with some clay and chalky-limestones in the middle part of the sequence'. Thiedig et al. (2000) finally went on to provide a new definition of the AMF applying it to all Quaternary carbonate rock units. This re-defined formation comprised three separate limestone bearing members with a fourth defined by Geyh and Thiedig et al. (2008, Table 2.1). It is believed these carbonate units were deposited by a vast lake that existed in the region during times of greater humidity known as Lake Megafazzan (Armitage et al., 2007). Th/U dates obtained from these limestone units indicate there to be a correlation between times of

limestone accumulation and the 100,000 year eccentricity cycle of orbital forcing during the last 500,000 yr (Thiedig and Geyh, 2004; Geyh and Thiedig, 2008).

The uncertainty surrounding the age and origin of the Al Mahruqah Formation can be attributed to the lack of facies information (Abdullah, 2010) and lack of/inconsistent dating. Although it has become increasingly researched (e.g. Geyh and Thiedig, 2008; Armitage et al., 2007), a number of discrepancies in the lithostratigraphy still exist. Drake et al. (2008a) do not recognise the members of the Formation described by Geyh and Thiedig (2008). Instead, Drake et al. (2008a; 2009) show that the Al Mahruqah Formation has a complex stratigraphy with the formation at numerous locations consisting of beds of lacustrine limestones separated by aeolian sands/silts. A wide variety of units covering a large geographic range were examined by Hounslow et al. (2017). They also believe that none of the existing assigned members can be adequately applied to their investigated sections. There are also differing views on the spatial distribution of the Formation. Errors are apparent in the reported locations of palaeolake deposits of the Bir al Zallaf Member (Drake et al., 2012). Observations of the Formation, such as by Drake et al. (2012; 2011), show that the altitude of the Al Mahruqah Formation is variable, however a map produced by Thiedig and Geyh (2004) suggests the spatial distribution of the members can be assumed based on four distinct altitudes at which they were found. The age of the Formation is also still uncertain with much of the dating only conducted on deposits at/or near to the top of the formation (Drake et al., 2008a). Armitage et al. (2007) dated some of the members of the Formation reported by Thiedig and Geyh (2004) using OSL dating. For the Brak Member, Armitage et al. (2007) confirmed it to be extremely old, and likely older than the reported age of 380ka (Th/U), however how much older was not known due to the saturated OSL signal. OSL dating of the Bir al Zallaf Member also showed saturated signals except for one, with a single unsaturated date of 420 ± 37 ka (Armitage et al., 2007). Armitage et al. (2007) note however that a meaningful comparison cannot be made to Thiedig et al. (2000) as it was unclear which limestone from the site was dated. The most recent dating to be completed using Th/U has been conducted by Abdullah (2010) on both the Brak and Bir al Zallaf Members. The Th/U age determinations show large age discrepancies for the calcretes of the Brak Member with dates of the micritic matrix ranging from 334 ± 10 ka to 349 ± 14 ka (Abdullah, 2010). Abdullah (2010) believes these ages to be unreliable stating that Th/U dating has significantly underestimated the age of the member reported in his research as well as dates reported by Geyh and Thiedig (2008).

Abdullah (2010) postulates that the Brak Member could be as old as the Cretaceous and the Bir al Zallaf of middle Miocene age.

	Type Locality (TL) & Distribution	Lithology & Depositional Environment	Previously Reported Th/U Age	Other Important Features
Aqar Member	<p>TL-outcrop 10km E of Quttach and 0.6km S of main road. Also found 1km SW of Al Mahruqah village. 27°31'26"N; and 14°06'08"E</p> <p>Isolated outcrops with small <i>Cardium</i> shells widespread over an area of 80km by 15km between Wanzarik and Brak</p>	<p>3-5m thick</p> <p>Carbonate packstone consisting of mainly shells of <i>Cardium glaucum</i>, gastropods and ostracods cemented together</p> <p>Brackish palaeolake</p>	<p>138-128ka, large part coincides with MIS5e</p> <p>Youngest Member</p>	<p>Originally covered an area of 1400km²</p>
Bir al Zallaf Member	<p>TL-18km SE of town of Brak (27°26'N; 14°23'E)</p> <p>Mainly preserved as inselbergs in dune field S of Wadi ash Shati due to limestone cover. Occurs over a distance of 150km</p>	<p>Max thickness 25m</p> <p>Consists of two 2-3m units of thinly bedded dolomitic sandy wackestone separated by poorly cemented pale green sandstone. In several locations, beds of pale brown-creamy white gypsum and clay are intercalated. Carbonate skeletal grains are rounded and embedded in a micritic matrix and a number of fossils are also present including ostracods and small fish bones.</p> <p>Lacustrine deposit suggesting non-perennial lake</p>	<p>285-205ka during MIS8 and MIS7</p>	<p>Originally covered an area of 5400km²</p> <p>Until Thiedig et al. (2000) this unit had been included in the term 'continental deposit'</p>
Brak Member	<p>TL-Quarry on an inselberg 20km W of town of Brak and 5km E of Al Mahruqah village (27°30.5'N; 14°04'E)</p>	<p>5-12m thick</p> <p>Consists of 2 parts.</p>	<p>380-290ka</p> <p>Many ages correlate with MIS9</p>	<p>Member originally covered maximum area of 52,000km²</p>

	Widely developed through N part of Murzuq basin	<p>Lower- of conglomerate containing clasts of Palaeozoic rock. Poorly halite-cemented sandstone is locally intercalated</p> <p>Upper- massive, highly brecciated and partly dolomitic sandy packstone, carbonate mudstone and wackestone with irregularly distributed chert nodules. Fossils and fine organic detritus are not common</p> <p>Freshwater lacustrine</p>		<p>Asymmetric distribution-occurs mainly on the N margin of both sand seas</p> <p>Rests on weathered Palaeozoic rock</p>
Antalka-hata Member	<p>TL-situated at 26°43' N and 12°12' E (1:250 000 Geological Map of Libya, Sheet Awbári NG 33-5)</p> <p>Scarce remnants-max extent uncertain</p>	<p>1m thick consisting of lower and upper parts.</p> <p>Lower-0.7m thick is composed of poorly laminated mudstone which contains spores, pollen and gastropods of Pliocene-Quaternary age. Upper-30cm thick, contains laminated pale pink packstone and wackestone with isolated quartz grains</p> <p>Fossil content indicates freshwater lacustrine setting</p>	<p>>420ka</p> <p>MIS11 and 13</p> <p>Oldest Member</p>	

Table 2.1 Summary of key characteristics of the members of the Al Mahruqah Formation described in Thiedig et al. (2000), Geyh and Thiedig (2008). Note: Ages are detrital corrected Th/U ages documented in Geyh and Thiedig (2008).

Based on these unresolved problems, the lithostratigraphy of the Al Mahruqah Formation was revised by Hounslow et al. (2017). The proposed framework by Hounslow et al. (2017) upgrades the Formation to Group status. This includes not just the carbonate units, but all intervening clastics. The Al Mahruqah Group (AMG) includes two major unconformities which bound different sediment packages. The expansion to group status thus allows a more detailed lithostratigraphic designation of the units. Hounslow et al. (2017) applies the revised lithostratigraphy to the edge of the Ubari sand sea and east towards the western edges of the outcrops of Palaeogene and Eocene age in the southwestern fringes of the Sirt Basin in Sarir al Qattusah and finally south towards Tmassah turning east along Wadi ash Shabirinah (Figure 2.7).

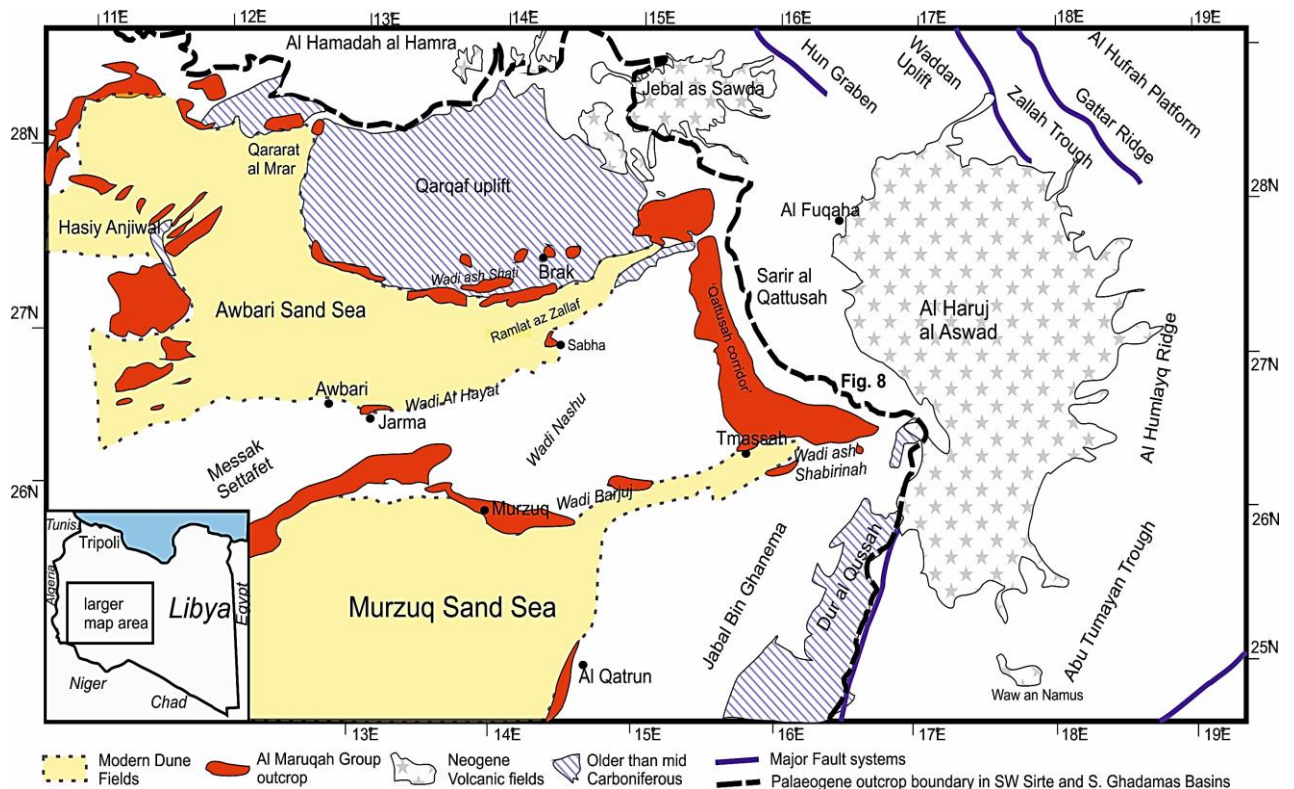


Figure 2.7. Map to show the extent of the Al Mahruqah Group. Modified from Hounslow et al. (2017). Note: Awbari is an alternative spelling of Ubari – please see Table 1 in the Appendix (pg281) for a list of alternative spellings of localities in the Fazzan.

Within the Group, three new formations are proposed, namely the Shati, the Zarzur and the Shabirinah. Additionally, the Brak Member previously assigned by Thiedig et al (2000) and Geyh and Thiedig (2008), is upgraded to the Brak Formation. The units associated with the group all unconformably overlie strata of Palaeozoic and Mesozoic age. A thorough account of the newly proposed lithostratigraphy (Figure 2.8) including

type sections, naming decisions and brief lithologic descriptions is given in Hounslow et al. (2017) with key details outlined below. It should be stressed that the results of this research are built upon the revised lithostratigraphy of Hounslow et al. (2017).

Shati Formation (SIF)-Named after Wadi ash Shati, this is the youngest formation of the Group. The base of formation is defined by an erosional unconformity seen throughout the Fazzan and in Wadi ash Shati (Figure 3-Appendix, pg283), this unconformity cuts down into the underlying Zazur Formation. It includes the newly named fossil-rich mudstones and siltstones of the Bir al Hasy Member and the Aqar Member. The Aqar Member is already in use in the literature (Geyh and Thiedig, 2008) commonly dated to ~250ka to the Holocene (Petit-Maire et al., 1980; Geyh and Thiedig, 2008). None of the sections investigated in this project belong to the Shati Formation.

Zazur Formation (ZF)-This formation is named after the Washkat Zazur region (Figure 3-Appendix, pg283) with the base marked by an erosional unconformity. It is older than the overlying SIF as indicated by unconformable relationships with this formation and the inverted stratigraphic elevation in Wadi ash Shati. Saturated OSL dates measured by Armitage et al. (2007) also suggest an older age. In Wadi ash Shati, and in the Qarat al Mrar area of the northern Ubari, it cuts down into the Palaeozoic basement below. Within this Formation are 4 Members; the Bir al Zallaf (BZ Mbr), Sifar (SI Mbr), Nahiyah and Sayl (SL Mbr). The youngest member (BZ Mbr) is retained from Geyh and Thiedig (2008) as their description of this unit relates to the 2/3 limestone beds at the top of this Formation. Geyh and Thiedig (2008) used elevations of units to infer relative ages. It is clear however from the differing elevations of the younger units in this formation such as in the Qarat al Mrar area (400m) and in Wadi ash Shati (~378m) that relative ages cannot be determined this way.

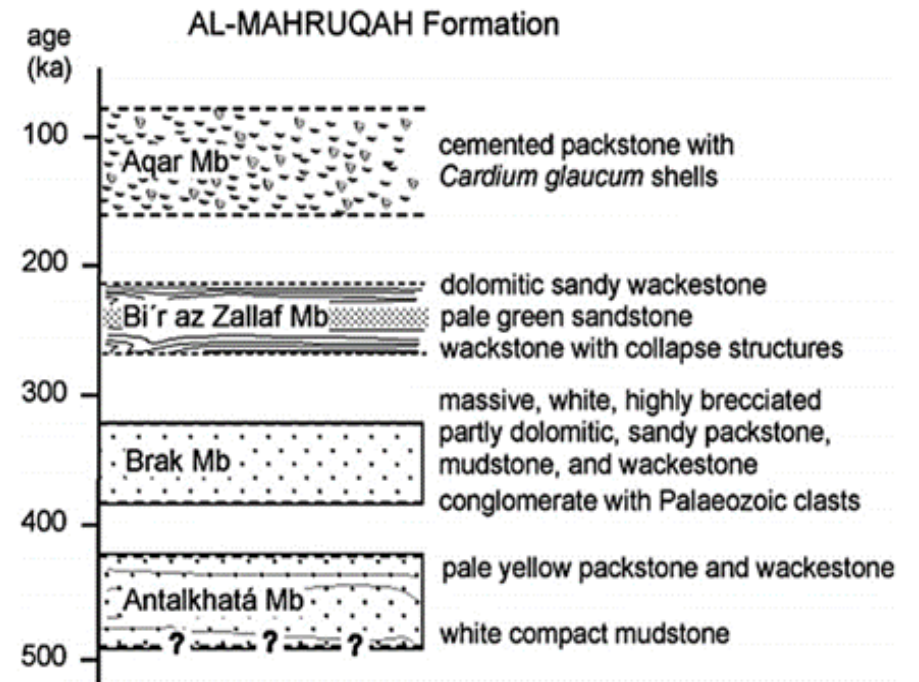
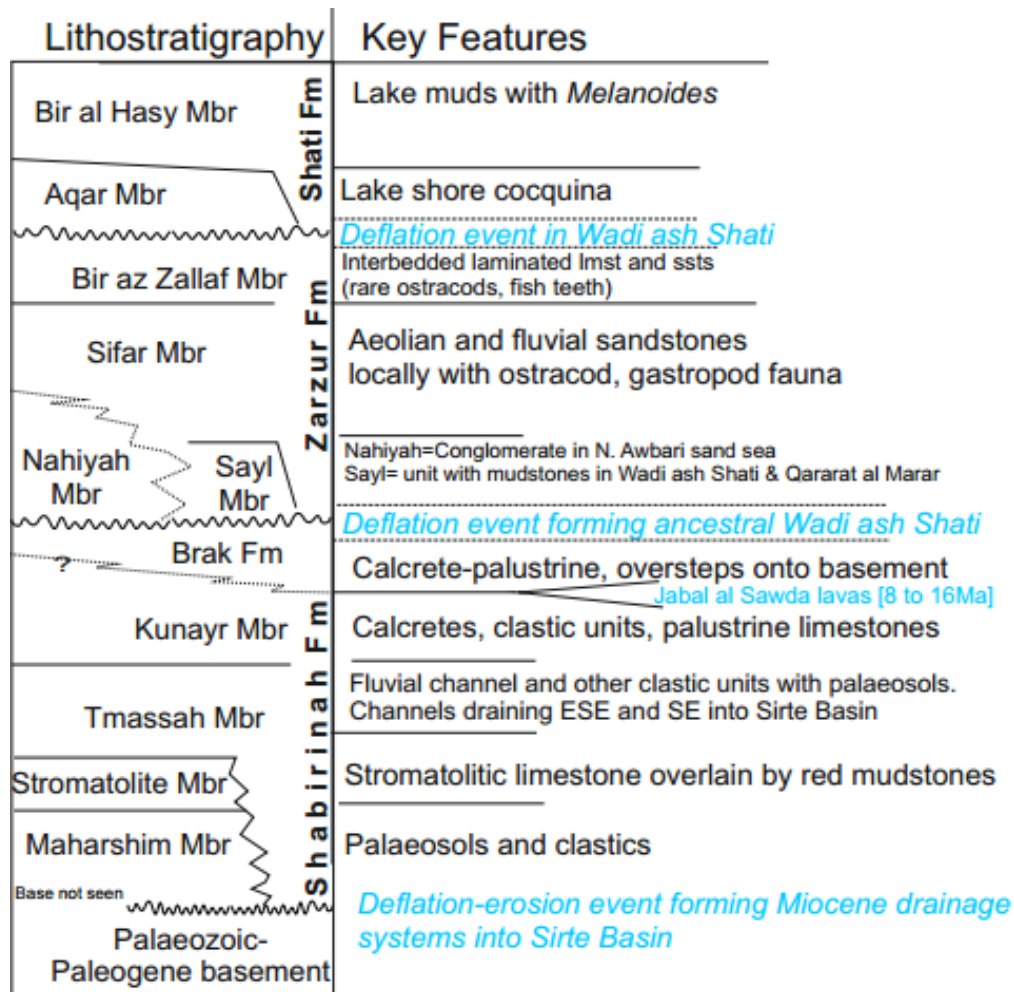


Figure 2.8 Left: New lithostratigraphy of the Al Mahruqah Group from Hounslow et al. (2017). Note: major erosion/deflation events are indicated in blue which sub-divide the new formations. Right: Original lithostratigraphy of the Al Mahruqah Formation from Geyh and Thiedig (2008).

Brak Formation (BKF)-The type section of this formation is at the location of the Brak Member noted by Geyh and Thiedig (2008) and Thiedig et al. (2000). It has previously been defined as the 'Murzuq Limestone' by Desio (1936, cited in Domaci et al., 1991) and also the 'Al Mahruqah Formation' by Seidl and Rohlich (1984). It is seen in Wadi ash Shati with elevations ranging from 390m at the BC section location (see section 3.2) to 438m on the southern flanks of the Jebal al Hasawinah. In the field an E-W difference in elevation was noted likely due to tilting or faulting after deposition. Like Geyh and Thiedig (2008), it is thought this formation is an older unit based on the inverted elevation stratigraphy seen in Wadi ash Shati implying a major period of erosion of the Brak Formation. Nowhere in the field has the Zazur Formation been seen resting on the Brak. The top of the formation is a major unconformity surface while the base has been defined by well cemented, pure limestone with brecciated texture.

Shabirinah Formation (SHF)-This is the oldest formation in the revised lithostratigraphy named after Wadi ash Shabirinah, an E-W orientated wadi east of Tmassah (Figure 2-Appendix, pg282). It underlies the Brak Formation with the base of the formation resting on Mesozoic or Palaeozoic basement. The transition between the lower Brak and upper Shabirinah Formation was not documented in the field however it is inferred that the Brak terminates the upwards increase in calcretisation seen in the Shabirinah Formation. Four members are associated with this formation; Maharshim (M Mbr), Stromatolite (STR Mbr), Tmassah (TM Mbr) and Kunayr (K Mbr). The bipartite-facies association (fluvial siliclastics below calcretised clastics) of this formation can be recognised throughout the Fazzan, including at basin margins. It is thought the Stromatolite bed noted by Thiedig et al. (2000) which was assigned to their Bir al Zallaf Member is the same stromatolite bed now assigned to the Shabirinah Formation. This bed could be traced westwards along the north side of Wadi ash Shabirinah towards Tmassah. In Wadi ash Shabirinah the Stromatolite Member passes eastwards into clastic-rich units which are indistinguishable from the overlying Tmassah Member. In the base of the Kunayr Member at the northern side of Wadi ash Shabirinah, lacustrine limestones pass laterally into calcretes/palustrine limestones.

2.4 Magnetostratigraphy

Palaeomagnetic studies assisted in the renewal of the continental drift hypothesis and the formation of the plate tectonics hypothesis, and have thus had profound effects on the development of the Earth Sciences (Opdyke and Channell, 1996, p1; Cox et al., 1964). In the Earth Sciences, dating and time control are of high importance and the study of palaeomagnetism has allowed a type of stratigraphy to be developed based on the aperiodic reversal of polarity of the geomagnetic field, known as magnetostratigraphy (Langereis et al., 2010; Opdyke and Channell, 1996, p1).

The polarity of the Earth's magnetic field has repeatedly reversed in the geological past (King and Peck, 2001). Due to the dipole nature of the magnetic field, polarity reversals are globally nearly isochronous and thus magnetostratigraphy has shown to be a powerful tool for providing timeframes for sedimentary sequences from a variety of depositional environments (Opdyke and Channell, 1996, p2; Lovlie and Leroy, 1995). The cause of field reversals is still debated, however it has been suggested that changes in heat flow at the core-mantle boundary could be important for controlling the reversal rates (Jackson et al., 2000; Langereis et al., 2010). The Earth's magnetic field is a vector which varies in field strength and direction with location on the Earth's surface (King and Peck, 2001; Lowe and Walker, 1997, p275). At any point in time and space the magnetic field can be characterised by three components (see Figure 2.9):

- 1) *Declination*-the horizontal angle between the magnetic field and geographic north (Lowe and Walker, 1997, p275).
- 2) *Inclination*- the dip of the magnetic vector below the horizontal plane (King and Peck, 2001). The inclination value varies from +90° at the magnetic north pole to 0° at the magnetic equator, to -90° at the south magnetic pole (Lowe and Walker, 1997, p275).
- 3) *Intensity*- the strength of the magnetic field (~0.08 mT).

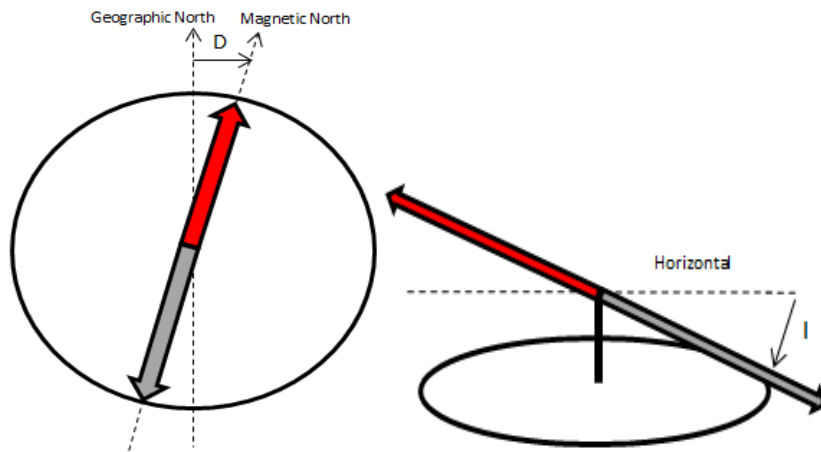


Figure 2.9. Diagrams to show declination (D) and inclination (I) at a specific earth location (Based on the diagrams from Archaeomagnetism-Bradford University).

The magnetic field varies in differing types of periodicity from milliseconds to tens of millions of years (Lowe and Walker, 1997). The longer events result from internal factors related to the geodynamo while the short-lived events are atmospheric and ionospheric in origin which include, for example, interactions between the solar wind and magnetosphere (Finlay et al., 2010; Opdyke and Channell, 1996, p14) On the Earth's surface the field produced can be approximated to a geocentric axial dipole field (Figure 2.10, Langereis et al., 2010).

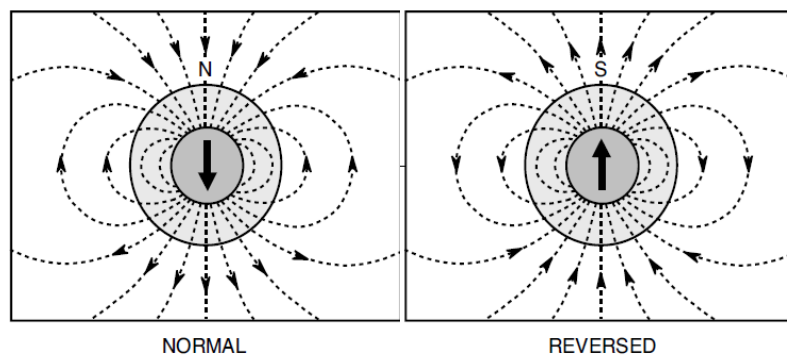


Figure 2.10. Schematic diagrams of the geomagnetic field of a geocentric axial dipole during normal and reversed polarity (Langereis et al., 2010).

During periods of normal (positive inclination in N. hemisphere) polarity the averaged magnetic north pole is at the geographic north pole (Langereis et al., 2010). Although physically a south pole, the north pole can be defined as the pole which attracts the north seeking needle of a compass (Langereis et al., 2010). During periods of reversed polarity the opposite happens, i.e. the compass needle points south and inclination is negative in the northern hemisphere and positive in the southern hemisphere (Langereis et al., 2010).

2.4.1 Secular variation

The Earth's magnetic field is spatially complex exhibiting a wide range of time-dependent variation (Love, 2000). About 90% of the observed field at the surface approximates a dipole field which constantly fluctuates/drifts by a few tens of degrees about the Earth's rotational axis (Ogg, 2012; Takatsugi and Hyodo, 1995; Deenen et al., 2011) on a timescale of 100-1000's of years. Changes in direction and magnitude of the surface geomagnetic field over periods of 1000's years is known as geomagnetic secular variation (SV) (Butler, 1992, pg7; Ogg, 2012). The changes in field direction that occur during SV are too small to be mistaken for complete (180°) reversal (Ogg, 2012). The modern SV field has been documented from historical records for the last 150 years and appears to show a decay in the dipole strength which some have interpreted as signalling an imminent reversal (Love, 2000; Donadini et al., 2010).

SV in the magnetic field studied over millennia determined from archaeomagnetic and palaeomagnetic sedimentary records appear to show a dominant westward drift that still has no causal mechanism (Donadini et al., 2010; Finlay et al., 2010). The fast cooling time of archaeomagnetic artifacts is important in the averaging of SV (Donadini et al., 2010), whereas lavas can take 10-100's of years to cool (Donadini et al., 2010). Although these materials are generally preferred due to their acquired thermoremanent magnetisation, deposits, in particular of lacustrine origin, can record the spatial and temporal variation in SV due to their often continuous sequences (Barton and McElhinny, 1981; King and Peck, 2001). Barton and McElhinny (1981) identify weaknesses in using lacustrine SV, in particular 'the absence of proof that the result is consistent both between cores from a given lake and between lakes in a given region'. Barton and McElhinny (1981) plus others (e.g. Liddicoat and Coe, 1997; Rolph et al., 2004; Frank, 2007) have tried to overcome this. The SV record in sediment from three crater lakes in SE Australia (Barton and McElhinny, 1981) found good inter-core agreement providing the first long continuous SV curve for the S. Hemisphere. Within the cores, low intensity values were found to coincide with high directional scatter linked to poor magnetic stability (Barton and McElhinny, 1981). This has been documented elsewhere with an increase in the scatter of virtual geomagnetic poles (VGPs - a pole calculated from a single observation of the direction of the geomagnetic field, Butler, 1992, pg124) with latitude (Deenan et al., 2011). The study by Frank (2007) of two long cores from Errlongwan Maar lake, NE China reflected variation in the magnetic field over the last 37 kyr, showing that inclination and declination values correlate well to palaeoSV records published for NE Asia.

2.4.2 Polarity change and polarity transitions

The palaeomagnetic record preserved in rocks allows us to obtain the most direct information on the long-term behaviour of the Earth's magnetic field (Hoffman, 1992). A continuous accumulation of sediment uninterrupted through time would provide ideal conditions for recording geomagnetic polarity (Opdyke and Channell, 1996, p88). Marine deposits (especially deep sea) can be excellent at fossilising geomagnetic field behaviour (e.g. Kent and Schneider, 1995; Backman et al., 1990) and thus tend to produce the longest and most continuous records (Lanza and Meloni, 2006, p218). However, terrestrial deposits are rarely homogenous in lithology and have variable sedimentation rates, hence magnetic studies on land are often integrated with other studies providing radiometric or biostratigraphic dates (Opdyke and Channell, 1996, p88).

Transitions between normal and reversed states of the geomagnetic field, geological speaking, occur rapidly, lasting ~5kyr (Cox et al., 1964; Merrill and McFadden, 1994; Ogg, 2012). Considering this rapidity, Ogg (2012) states that 'palaeomagnetic correlation is the most precise method available for global correlation in virtually all stratified rocks of all ages, but only directly at the recorded reversal boundary'. Polarity transition records are the only source of information about what happens to the field as it reverses (Clement, 2000). However, due to their brief nature, records of polarity transitions are difficult to obtain and reliability can be uncertain as subtle biases can influence the relatively weak magnetisations that characterise polarity transitions (Kent and Schneider, 1995).

Palaeomagnetic reversals are irregular and their frequency varies significantly (Amit et al., 2010). Nevertheless, as reversals are potentially recorded simultaneously in rocks worldwide, magnetostratigraphic divisions, compared to lithostratigraphic for example, are not time-transgressive (Ogg, 2012). The pattern of reversals can be determined by measuring the magnetisation of samples from a stratigraphic section (Tauxe et al., 2016). The 'bar-code' pattern allows correlation of rock strata from a range of depositional environments (Ogg, 2012). Analysis of polarity changes recorded in the Oceanic crust has led to the development of the Geomagnetic Polarity Timescale (GPTS) from the late Jurassic (Langereis et al., 2010). The main application of the GPTS is as a dating tool for stratigraphic sequences (Tauxe et al., 2016). A precise temporal framework of volcanic or sedimentary successions can be achieved if the polarity zones can be clearly correlated to the GPTS (Tauxe et al., 2016).

Since the first pioneering timescale by Heirtzler et al. (1968, cited in Lowrie and Kent, 2004), further development of the GPTS has involved adjustment of the relative spacing of some magnetochrons and better calibration of the polarity with time (Cande and Kent, 1992). Cande and Kent (1992) constructed a magnetic polarity timescale (the CK92) for the late Cretaceous and Cenozoic improving resolution of the magnetochron durations by using marine magnetic anomaly profiles throughout the world's ocean basins. Some uncertainties are associated with this timescale, in particular for the late Cretaceous and early Cenozoic as these time intervals correspond to a time of rapid change in the spreading rate in the south Atlantic and thus have the most potential for error (Cande and Kent, 1992). Cande and Kent (1995) later revised the GPTS (CK95) of Cande and Kent (1992) which moved the K/P boundary from 66Ma to 65Ma and gave an age of 5.23Ma for the older boundary of sub-chron C3n.4n. Since the CK95 GPTS, other timescales have been produced such as by Berggren et al. (1995) and Ogg (2012). The modern GPTS is an integrated magnetobiochronologic timescale with correlated biostratigraphic, chemostratigraphic and cyclostratigraphic events (Berggren et al., 1995; Ogg 2012). It is this 2012 timescale that will be referred to within this thesis.

In order for the GPTS to be successfully employed, a stable nomenclature for the succession of magnetochrons must be established, this however is difficult, especially when including short duration events (Ogg, 2012). The four youngest chrons spanning the last 6 Ma are named after leading geomagnetists; Brunhes (0-0.781 Ma), Matuyama (0.781-2.581 Ma), Gauss (2.581-3.596 Ma) and Gilbert (3.596-5.235 Ma) (Ogg, 2012). The standard chron-naming nomenclature in use today was developed by Cande and Kent (1992; 1995) and involves numbering of polarity intervals backwards in time in the order in which they occur. Numbering in this way however is problematic and a system is needed that doesn't change dramatically with the addition of a newly discovered polarity interval (Ogg, 2012). The nomenclature system of the GPTS is discussed in the Appendix (pg284).

The duration of a collection of polarity intervals has been described by a number of different statistical models, based on stochastic, exponential or gamma distributions (Lowrie and Kent, 1983). Lowrie and Kent (2004) divided the C-sequence into two linear segments that intersect near chron C12r as this chron is an order of magnitude longer than the average subsequent chrons. Based on this division, the younger segment has a mean chron duration of 0.248 Ma compared to the older half which has a mean chron duration of 0.749 Ma (Lowrie and Kent, 2004). Lowrie and Kent (1983) noted the dramatic effect on

mean chron duration when short events were added to the timescale. When included, the recomputed mean interval length of the younger segment is reduced to 0.219 Ma suggesting that short events have a strong influence on the statistical properties of the timescale (Lowrie and Kent, 1983; Lowrie and Kent, 2004).

2.4.3 Excursions and Tiny Wiggles

Along with SV and reversals, other departures from the dipole field can occur. Cande and Kent (1992) identified short wavelength anomalies known as ‘tiny wiggles’. These ‘tiny wiggles’ were interpreted to be short sub-chrons with a duration of <30kyr which include, for example, the Reunion sub-chron. In total ten sub-chrons have been identified occurring in the Matuyama, Gauss and Gilbert Chrons. However, no sub-chrons have been documented for the Brunhes Chron but a number of excursions have been identified (Merrill and McFadden, 1994; Langereis, 1999). An ‘excursion’ is commonly used to describe intervals with a VGP deviation $>90^\circ$ (Merrill and McFadden, 1994). Low intensities of the Earth’s dipole seem to favour the occurrence of excursions (Langereis, 1999). It has been suggested, such as by Hoffman (1981; 1992), that excursions are aborted reversals, an idea that remains unresolved (Merrill and McFadden, 1994). Excursions have been documented from both volcanic and sedimentary deposits such as Pleistocene lake deposits (Liddicoat, 1990) and in loess (Zhu et al., 1999), however global correlation of these events is difficult as they are too short to be detected in marine magnetic anomalies (Gubbins, 1999; Langereis et al., 2010). Although common in the Brunhes Chron, problems occur in identifying them in the reverse Matuyama Chron as it is difficult to demonstrate that excursions are not overprinting from the modern field (Langereis, 1999). A sedimentation rate of >10 cm/kyr is required to successfully document excursions (Roberts and Winklhofer, 2004). The influence of post-depositional remanent magnetisation is thought to also contribute to the lack of globally documented excursions (Roberts and Winklhofer, 2004). Langereis et al. (1997) discusses in detail six globally accepted excursions and another five that, at present, are not globally correlated as seen in Figure 2.11. For an excursion to be confirmed as a real geomagnetic phenomenon, the same excursion field must be identified using at least two sites a great distance apart (Takatsugi and Hyodo, 1995).



Figure 2.11. Reversal excursions in Brunhes Chron. Globally, well-dated excursions are in bold. Uncertain excursions and those only identified in restricted regions are in small text (Langereis et al., 1997). Note: Black = normal polarity, White = reversed polarity.

Excursions, sub-chrons and secular variations indicate that the geomagnetic field displays a complex range of behaviours (Channell and Opdyke, 1996, p99). Although the GPTS is continuing to improve in accuracy and resolution, polarity patterns can be difficult to correlate to the GPTS, especially if only short sections are investigated with small numbers of polarity zones (Channell and Opdyke, 1996, p91). Hiatuses are also problematic as chrons or sub-chrons may be missing (Channell and Opdyke, 1996, p91).

2.4.4 Miocene-Pliocene Magnetostratigraphy

The GPTS from the middle Jurassic to present is largely based on ocean-floor magnetic anomalies from oceanic crust produced during sea-floor spreading (Ogg, 2012; Langereis et al., 2010). These anomalies serve as a template for polarity reversals in sections and cores from the deep-sea or land (Ogg, 2012; Hilgen et al., 2012). Pelagic deep-sea cores have provided many of the most detailed magnetostratigraphic records prior to 5 Ma (Channell and Opdyke, 1996, pg101; Butler, 1992, pg162). Shallow water platform carbonates have also proved crucial for gaining palaeomagnetic information for the Pliocene (Channell and Opdyke, 1996, pg101). For the early-mid Miocene, cores of calcareous deposits retrieved from the north Atlantic during expeditions with the DSDP provide some of the best palaeomagnetic results (Channell and Opdyke, 1996, pg130). Clement and Robinson (1986) for example obtained a nearly continuous polarity record from the Brunhes to the mid-upper Oligocene during Leg 94. The records from these high-

accumulation rate cores also identified two short normal sub-chronozones within the Matuyama which were correlated with the Cobb Mountain and Reunion subchrons (Clement and Robinson, 1986). The existence of the four youngest polarity chrons has also been established on land, particularly via dating of lava flows (Ogg, 2012). Other continental records of the Pliocene (and Pleistocene) have been obtained from lacustrine and loess sequences (e.g. Heller and Tung-Sheng, 1982; Channell and Opdyke, 1996, pg145). Obtaining these records has largely been motivated by enhancing chronology of the Pliocene-Pleistocene glaciations (Channell and Opdyke, 1996, pg145).

In Cenozoic terrestrial sequences mammals have been useful organisms for dating deposits (Hilgen et al., 2012). Many well-dated sequences occur in East Africa, led by the search for hominins, and has resulted in an over-representation of Neogene faunas (Hilgen et al., 2012). A few studies are documented from North Africa such as Benammi et al. (1996) who carried out a magnetostratigraphic study on middle-Miocene to upper-Pliocene lacustrine deposits in Morocco which contained micromammal faunas. The dating of this sequence was also in agreement with Ar/Ar dates from volcanic ash layers (Benammi et al., 1996). A problem with using fossils to help date palaeomagnetic sequences is that there is often difficulty in correlating marine fossils with their continental time-equivalents (Langereis et al., 2010). Recent development in age control of the GPTS are the identification of astronomical signals with cyclostratigraphic methods, leading to the development of astrochronology and construction of the Astronomical Time Scale (Langereis et al., 2010; Hinnov and Hilgen, 2012). Increasingly, studies (e.g. Hilgen et al., 1995; 2000; Abdul Aziz et al., 2008) are using an integration of magnetostratigraphic, biostratigraphic and radioisotopic results of marine and terrestrial deposits to help refine the validity and accuracy of the GPTS (Langereis et al., 2010, Backman et al., 1990).

2.4.5 Magnetic Minerals

Due to the effects of the magnetic field on electron motions in atoms, all matter responds in some way to an applied field, although the response varies and is often weak for most materials (Opdyke and Channell, 1996, p26). Domains in ferrimagnetic minerals align with the Earth's magnetic field and hence are the palaeomagnetic recorders of that field (Maher et al., 1999, p1; Langereis et al., 2010). Variation in the composition, domain state and abundance of magnetic grains can also serve as sensitive magnetic recorders of palaeoclimatic/environmental change (Maher et al., 1999, p1). Loess-palaeosol sequences, for example have been investigated extensively using magnetic minerals providing

information on palaeorainfall (Maher and Thompson, 1995), the timing of pedogenesis in interglacial periods (Heller et al., 1991; Dearing et al., 2001) and stratigraphic definition (Maher, 1998). Magnetic minerals have also been used as a proxy to investigate other climatic features such as reddening of dune sands in the Namib Desert (Walden and White, 1997).

Materials can behave in one of five ways when a magnetic field is applied:

Diamagnetic:-When all electron shells are complete in a substance the electron spins precess around the magnetic field (Tarling and Hrouda, 1993, p2). Although weak, this produces an induced magnetisation which is opposite in direction to the applied field (Figure 2.12, Tarling and Hrouda, 1993, p2; Opdyke and Channell, 1996, p26). On removal of the applied field no induced magnetisation remains (Butler, 1992; pg 17; Opdyke and Channell, 1996, p26). The susceptibility of diamagnetic minerals (such as in calcite, quartz and halite) is small and negative and independent of temperature (Opdyke and Channell, 1996, p26; Butler, 1992, pg17).

Paramagnetic:-Paramagnetic substances have incomplete electron shells (Tarling and Hrouda, 1993, p2). Their electron spins precess in an applied field resulting in an induced magnetic moment (unlike diamagnetic materials), in the same direction as the applied field (Tarling and Hrouda, 1993, p3). Like diamagnetic materials, the alignment (and magnetisation) is lost when the applied field is removed as the weak alignment of spin moments is randomised by thermal vibrations (Opdyke and Channell, 1996, p26; Tarling and Hrouda, 1993, p3). The susceptibility of paramagnetic minerals is positive and small, but often greater than diamagnetic minerals (Maher, 2007). Examples of paramagnetic minerals include many Fe and Mn-containing silicates, carbonates and clay minerals (Maher, 2007; Opdyke and Channell, 1996, p26).

Ferromagnetic:-Unlike dia/paramagnetic materials, when an applied field acts on the substance the electron spins become spontaneously coupled and results in alignment of the individual spins magnetisations (Figure 2.12, Tarling and Hrouda, 1993, p4). This alignment remains even in the absence of an applied field and hence ferromagnetic materials have much larger positive susceptibility than paramagnetic materials and can also carry a strong remanent magnetisation (Tarling and Hrouda, 1993, p4; Opdyke and Channell, 1996, p27). The susceptibility of ferromagnetic materials varies with the strength of the applied field (Opdyke and Channell, 1996, p27). Ferromagnets show steep increases

in induced and remanent magnetisation with applied field (Maher, 2007). Once saturation is reached they display hysteresis where induced magnetisation lags the applied field and is irreversible (Maher, 2007). The characteristic temperature at which the remanence in ferromagnetic materials is destroyed is the Curie or Néel temperature (Opdyke and Channell, 1996, p28). At or above this temperature the material becomes effectively paramagnetic (Butler, 1992, pg18). Natural iron is perhaps the most common example of a ferromagnetic mineral.

Ferrimagnetic and Antiferromagnetic: -In ferrimagnetic materials adjacent spin moments are antiparallel, however due to their unequal magnitude a net moment still remains resulting in the mineral grain having a net remanence (Figure 2.12, Tarling and Hrouda, 1993, p4; Opdyke and Channell, 1996, p28). Ferrimagnetic materials have high susceptibilities, high magnetisation intensities and low coercivities (Opdyke and Channell, 1996, p29). Magnetite is an example of a ferrimagnetic mineral. In pure antiferromagnetic materials the opposite occurs as adjacent spins are antiparallel and of the same magnitude resulting in no net magnetisation (Tarling and Hrouda, 1993, p4; Opdyke and Channell, 1996, p28-29). However due to small structural differences or impurities antiferromagnetic minerals often have a small permanent remanence. Haematite and goethite are common antiferromagnetic minerals.

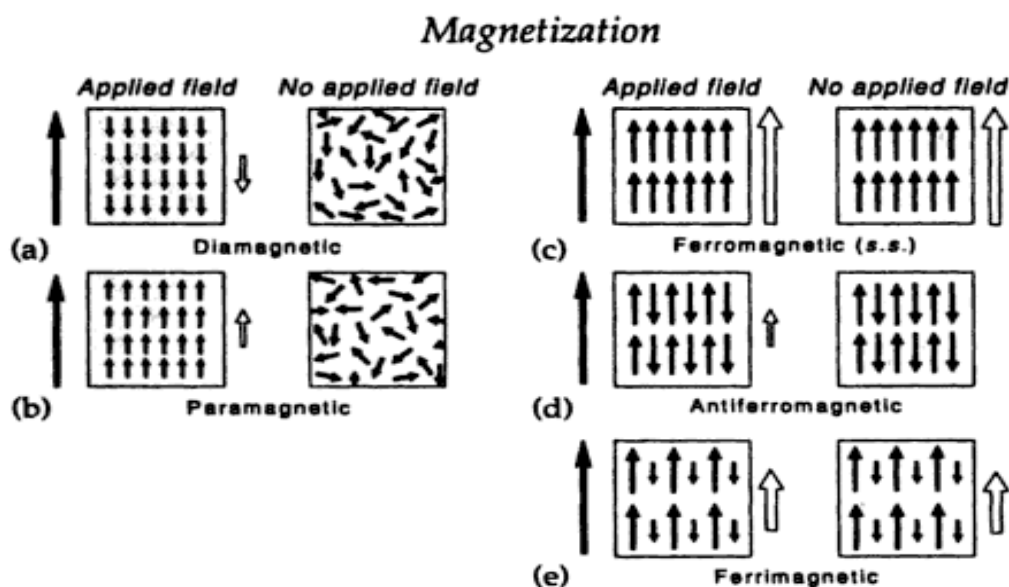


Figure 2.12. Diagrams showing different forms of magnetisation (Tarling and Hrouda, 1993, p3). Left-hand diagrams in the pairs illustrated (a-e): Solid arrow indicates the direction of the applied magnetic field. Hollow arrow indicates the magnetisation a substance acquires when in an applied field. Right-hand diagrams: magnetisation present after the applied field has been removed.

Identification of the mineral(s) carrying remanent magnetisation (see Table 2.2) is important when conducting palaeomagnetic studies, allowing key information to be obtained including possibly inferring the age of the magnetisation, the mechanism of how remanence was acquired and helping to define geological conditions (Tarling, 1983, p42).

<u>Mineral</u>	<u>Shape</u>	<u>Curie/Néel Temp/°C</u>	<u>Magnetic Properties</u>
Magnetite	Cubic with inverse spinel structure ¹	580 ⁶	<ul style="list-style-type: none"> -Ferrimagnetic^{2,7} -Most common magnetic mineral on Earth¹ -Coercivity dependent on grain size, max coercivity of 0.2 T occurring for single-domain sized grains³ -Metastable with respect to haematite in the presence of oxygen⁷ -Low temperature oxidation e.g. during sub-aerial weathering, often produces maghemite³
Maghemite	Spinel structure (with composition of haematite) ²	640 ¹	<ul style="list-style-type: none"> -Magnetic properties similar to magnetite with slightly lower saturation magnetisation and comparable coercivity¹ -Natural maghaematite converts to haematite at 300-350°C²
Titanomagnetite	Cubic ⁴	Curie temperature decreases as Ti content increases ⁴	<ul style="list-style-type: none"> -Ferrimagnetic¹ -Common in igneous and metamorphic rocks and are prominent detrital component in some deposits¹ -Saturation magnetization and Curie temperature decrease with increasing amounts of Ti¹
Haematite	Rhombohedral symmetry and corundum structure ^{1, 7}	680 ⁶	<ul style="list-style-type: none"> -Canted antiferromagnetic⁷ -Common in red beds and sometimes important in soils^{6,7,8}

			- Saturation magnetisation much lower than magnetite and remanent coercivity higher ¹
Titanohaematite	Rhombohedral with corundum structure ⁴	Curie temperature decreases as Ti content increases ⁴	-Saturation magnetisation 2 order smaller than magnetite, very high coercivity ⁴ -A some Ti contents ferrimagnetic (high saturation magnetisation ¹), otherwise antiferromagnetic -Associated with metamorphic rocks ¹
Goethite	Orthorhombic ⁵	120 ¹	-Impure antiferromagnetic behaving like weak ferrimagnet ² -Weak saturation magnetisation and very high coercivity ¹ -Dehydrates to haematite at 300°C and changes directly to magnetite above 380°C ^{1,2} -Similar characteristics to haematite ⁷ -Important iron oxides in soils- released from primary Fe-bearing minerals by weathering ⁷ -Results from alteration of pyrite ⁶
Pyrrhotite	Monoclinic ¹	320 ^{1,6}	-Ferrimagnetic ⁷ -Uncommon in weathered igneous and metamorphic rocks ⁶ -Saturation magnetisation is 10x that of haematite and half of magnetite. Coercivity is greater than magnetite ¹ -Sometimes forms in exceptionally reducing (anaerobic) environments e.g. estuarine muds ⁷

Greigite	-	320 ¹	-Ferrimagnetic ¹ -Coercivities similar to magnetite ¹ -Forms in some reducing (anaerobic) environments e.g. estuarine muds ⁷ -Carries stable magnetisation in some lake and marine deposits ¹
----------	---	------------------	--

Table 2.2. Summary of the key characteristics of some of the most common magnetic minerals found in deposits. 1-Opdyke and Channell (1996), 2-Tarling and Hrouda (1993), 3-Tarling (1983), 4-Lanza and Meloni (2006), 5-Gribble and Hall (1992), 6-Butler (1992), 7-Maher (2007), 8-Maher (2011)

2.4.6 Magnetisation Process in Deposits

Rocks and deposits which contain magnetic minerals are magnetised during formation and subsequently ‘lock-in’ the palaeomagnetic signal (Lowe and Walker, 1997, p275; Langereis et al., 2010). This is known as the natural remanent magnetisation (NRM) and the direction is dependent on the geomagnetic field and later geological processes since formation (Butler, 1992, pg42). In most cases the NRM of rocks and deposits is due to more than one magnetic component, which may be acquired at different times in the history of the rock (Opdyke and Channell, 1996, p50). Secondary NRM is acquired after the rocks formation and can obscure the primary NRM complicating palaeomagnetic studies (Butler, 1992, pg 42; Lowe and Walker, 1997, pg275). This magnetic overprinting may result from chemical changes affecting the magnetic minerals, lightning strikes, long-term exposure to the geomagnetic field since formation (i.e. viscous remanent magnetisation-VRM), weathering reactions or thermochemical reactions associated with burial or tectonic processes (Butler, 1992, pg43; Langereis et al., 2010). In order to remove the overprinting the sample is subjected to ‘magnetic cleaning’ techniques which include thermal demagnetisation or alternating field demagnetisation (see section 4.1.3) (Langereis et al., 2010).

The reliability of magnetostratigraphy depends on the validity of the assumption that the polarity of the record was acquired at or near to the time of deposition (Sagnotti et al., 2005). There are three main types of primary NRM acquisition which occur depending on the mechanism of palaeomagnetic signal acquisition (Langereis et al., 2010).

Thermoremanent magnetisation (TRM) is acquired by a grain during cooling through its blocking (Curie) temperature in the presence of a magnetic field (Langereis et al., 2010; Opdyke and Channell, 1996, p34; Butler, 1992, pg43), which aligns the magnetic domains with the magnetic field. TRM is acquired by cooling in igneous rocks and the resulting remanence may be stable for billions of years (Langereis et al., 2010; Opdyke and Channell, 1996, p35).

Chemical remanent magnetisation (CRM) is most commonly acquired in sedimentary rocks (Butler, 1992, pg48). Langereis et al. (2010) define CRM as ‘the magnetisation acquired when a magnetic mineral grows through a critical ‘blocking volume’ (i.e. grain size) at which the field is locked in and the remanence acquired may again be stable for billions of years’. CRM occurs via diagenesis leading to growth of new magnetic oxides (Lovlie and Leroy, 1995; Lowe and Walker, 1997, p275). An example of natural CRM would be the post-depositional formation of haematite (from goethite) which primarily occurs in red deposits (Butler, 1992, pg49). CRM is classed as a primary magnetisation when haematite is produced soon after deposition and thus the field direction is essentially contemporaneous (Butler, 1992, pg50). Red deposits are a good source of palaeomagnetic data and thus the magnetisation processes that occur in these deposits are important, however the mode and timing of acquisition of remanent magnetisation has been debated as ‘the red bed controversy’ (Butler, 1992, pg50; Tarling, 1999).

In most deposits the primary remanence is acquired by alignment of magnetic grains in the magnetic field during deposition and initial compaction (Goddu et al., 2007; Lovlie and Leroy, 1995; Butler, 1992, pg50), a remanence called *detrital remanent magnetisation* (DRM) (Lovlie and Leroy, 1995). Detrital grains align with the magnetic field usually in the upper 10-20 cm of soft water-saturated sediment as well as during settling in the water column (Opdyke and Channell, 1996, p35; Langereis et al., 2010; Butler, 1992, pg50). Remanence acquired shortly after deposition but before consolidation is referred to as post-depositional remanent magnetisation (pDRM) (Lovlie and Leroy, 1995; Butler, 1992, pg 50). Unsurprisingly this is important in unconsolidated deposits as small magnetite grains, which often carry the remanence, can be free to rotate in pore spaces after deposition and will have delayed remanence acquisition (Pisarevsky, 1999; Katari et al., 2000; Dinares-Turell and Dekkers, 1999). Post-depositional processes such as bioturbation can also improve or enhance the magnetisation and hence the accuracy of palaeomagnetic records

from sedimentary rocks has been questioned (Butler, 1992, pg50). McCabe et al. (1983) state that in many apparently reliable studies of carbonates the remanence may be of post-depositional origin. However, Katari et al. (2000) found that there is little convincing evidence that pDRM is a dominant mechanism by which deposits become magnetised. They also found that bioturbation only enhanced remagnetisation through resuspension of deposits and not the remoulding of deposits below the surface. The lock-in time of DRM can range up to 10^3 yrs (dependent on deposition rates) yet the recording of DRM is particularly efficient in calm depositional environments which contain fine-grained deposits (Goddu et al., 2007).

2.4.7 Magnetic chronology studies in arid/semi-arid environments

Lake deposits are sensitive recorders of regional and global climate change and of the geomagnetic field (Goddu et al., 2007; Katari et al., 2010). Magnetostratigraphic studies on palaeolake deposits are scarce, since most such studies have been on Bruhnes-age lake deposits, however, extensive studies using this technique have been conducted on palaeo megalake Bungunna, South Australia with the oldest lake deposits dated to 2.4 Ma (McLaren et al., 2009). Magnetostratigraphic methods have helped confirm the timing of the onset of aridity in south Australia (McLaren and Wallace, 2010). These have been used to estimate the timing of a shift from perennial to ephemeral conditions in SE Australia (investigated beds corresponds to the Brunhes-Matuyama chrons) with the transition from fluvial-lacustrine to saline arid conditions occurring 400-700 ka (Fujioka and Chappell, 2010).

Lacustrine palaeomagnetic studies from North Africa, in particular the Sahara, are limited, although rare, palaeomagnetic studies have been conducted in the region. Coster et al. (2012) refined the chronostratigraphy of the Algerian Eocene continental formations of the El Kohol (containing lacustrine limestone member) and Glib Zegdou using palaeomagnetic and biochronological data. Benammi et al. (1996) and Benammi and Jaeger (2001) carried out a magnetic study on middle Miocene to upper Pliocene lacustrine sedimentary deposits from the Ait Kandoula Basin, southern High Atlas, Morocco with the aim of dating the faunal exchange between North Africa and Western Europe. The deposits provided a polarity sequence with a duration of 5.18 Myr covering ten polarity zones from Chron C5n.2n to the beginning of C3n.4n (Benammi et al., 1996). Benammi and Jaeger (2001) found that in North Africa there is no radiometric dating available for mid-Miocene continental formations and also no previous studies analysing the magnetostratigraphy of

the Miocene in the Maghreb, indicating palaeomagnetic studies in this continental region are of increased future importance. There is also a lack of direct correlations between continental and marine formations (Benammi and Jaeger, 2001). Although only a few palaeomagnetic studies using lacustrine deposits have been completed in the Sahara, a number of studies, mostly from the Eastern Sahara and Eastern Africa (Lean et al., 1998; Abdeldayem, 1996), suggest palaeomagnetic dating of continental deposits should be more widely used. Dupont-Nivet et al. (2008) used this technique to date and characterise the depositional environment of the Hominin-bearing Hadar Formation in Ethiopia.

While palaeomagnetic studies on lake deposits are increasingly common, a number of limitations can arise. Along with diagenetic affects, which alter the primary magnetic signal and therefore distort the geomagnetic signal, the main problems are the differing rates of deposition, hiatus level and possible slumps (Frank, 2007; Tarling, 1983, p174). Beyer and Lundschein (2000) state that due to the continental nature of many formations in the Murzuq Basin (Libyan Sahara) and the relatively limited burial depth, many units from this area, which are Palaeozoic in age, could be suitable for magnetostratigraphy. A recent study by Drake et al. (2011) presenting initial magnetostratigraphic results from Qarat al-Mrar (N Ubari sand sea), Murzuq Basin indicates how this technique is suitable for deposits much younger than the Palaeozoic dating probably to the mid-Pliocene. This study aims to build on the previous palaeomagnetic data collected from the Fazzan by Drake et al. (2011).

2.5 Terrestrial Carbonates and the use of Stable Isotopes

2.5.1 Terrestrial carbonates

When compared to their marine counterparts, terrestrial carbonates unfortunately receive little attention (Wright et al., 1997). These deposits, which accumulate in continental environments, reflect a complex interplay of factors including sediment availability, chemical activity, hydrologic conditions and biotic activity with the overriding controls of climate and tectonics influencing these (Tanner, 2010). Terrestrial carbonates can therefore provide crucial data that aids in the interpretation of sedimentary records and information regarding the evolution of terrestrial palaeoclimates/environments (Alonso-Zarza, 2003; Marshall, 1992; Tucker and Wright, 1990).

Terrestrial carbonates can form under a variety of conditions in a range of depositional environments, some of which are seen in Figure 2.13.

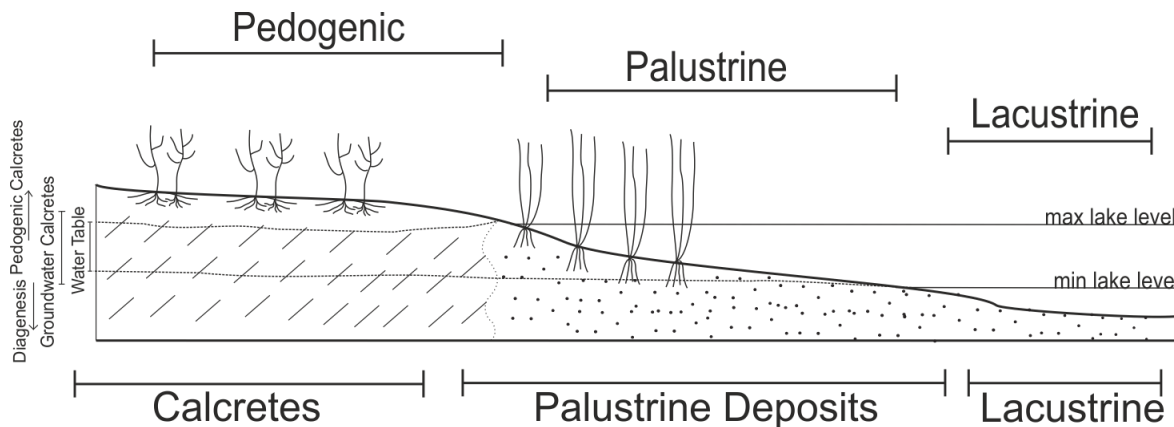


Figure 2.13 Sketch of the depositional environments (some) terrestrial carbonates can form in. Modified from Alonso-Zarza (2003).

According to Flügel (2010, pg11), carbonates can be classified under one of two groups:

- 1) *Carbonates formed in terrestrial sub-aerially exposed settings*: pedogenic carbonates, palaeosols, calcretes, palustrine carbonates, cave/karst carbonates and aeolian carbonates.
- 2) *Carbonates formed in terrestrial aquatic settings*: freshwater carbonates such as travertines and tufas, lacustrine carbonates and fluvial carbonates.

Three of these carbonates, lacustrine, palustrine and calcretes, are discussed in more detail below.

Lacustrine

Lakes are sensitive recorders of climatic and environmental change belonging to the most important continental archives and potentially providing some of the most continuous and high resolution records (Burrough and Thomas, 2009; Froehlich et al., 2005; Schleser et al., 1999; Verschuren, 2002). A key objective of palaeolimnology is to develop continental palaeorecords of global environmental change which are comparable to ice/ocean cores (Schnurrenberger et al., 2003). Although lacustrine studies are increasing, there is limited data from arid and semi-arid regions, especially when compared to the humid tropics (Burrough and Thomas, 2009). Terrestrial carbonates are vulnerable rocks in the geologic record, especially beyond the Quaternary, rarely surviving erosion and dissolution processes which are particularly prevalent in arid/semi-arid regions (Gandin and Capezzuoli, 2008).

The development of a lake results from the convergence of climate and tectonics causing the confinement of the water body, often in topographic lows (Tanner, 2010; Nichols, 2009, pg151). Alonso-Zarza et al. (2012) found that in the Teruel Graben, NE Spain, as well as climate, tectonism and rates of movement of faults created accommodation space allowing water body development. Lakes can have a variety of origins, however large lake systems are commonly tectonic in origin (Tucker and Wright, 1990). One such example is the intracratonic sag basin in central North Africa which houses the endorheic Lake Chad (Schuster et al., 2009). As noted by de Wet et al. (2015) when investigating the Miocene-Pliocene Opache Formation in the Atacama Desert, in order for terrigenous limestones to form in appreciable amounts there must however be limited active tectonism to avoid inundation with siliclastic material. Rainfall must also be limited reducing weathering and transport of this material into the productive carbonate environment, though sufficient water is needed to create conditions optimal for carbonate development (de Wet et al., 2015). Deposition of carbonate in lacustrine settings is therefore often associated with a semi-arid climate (de Wet et al., 2015; Tanner, 2010). The effects of climate can also influence the timing of carbonate precipitation due to changes in temperature and rainfall patterns (Gierlowski-Kordesch, 2010). For example, high evaporation rates which exceed inflow are often important in many saline lakes and can trigger the precipitation of carbonate (Tucker, 2001, pg 152; Boggs, 2009, pg 375). Yet, the presence of lacustrine deposits alone are not an indicator of climate as local controls operating on individual lakes as well as the source and mechanisms of carbonate

precipitation can be independent of climate (Tanner, 2010; Gierlowski-Kordesch, 2010; Baioumy et al., 2010; Alonso-Zarza et al., 2012).

Carbonate minerals which enter a lake can be classified based on their source (Verrecchia, 2007). These are:

Allogenic-minerals are derived from outside of the lake and thus would include erosion from the catchment. They are generally associated with stream or riverine input (Leng and Marshall, 2004) but can also be derived from shore erosion and atmospheric fallout (Verrecchia, 2007).

Endogenic-endogenic minerals are linked with biogeochemical processes within the lake itself (Verrecchia, 2007).

Authigenic-minerals of this source form inside the lake deposits and/or during diagenesis (Verrecchia, 2007).

The formation of lacustrine carbonates are related to four main processes, namely biogenic precipitation, clastic/detrital input, primary inorganic precipitation and post-depositional alteration (Baioumy et al., 2010; Tucker and Wright, 1990, pg 168) as discussed below.

Biogenic Precipitation-Non-marine invertebrates, such as ostracods and gastropods, are common in many lakes (Boggs, 2009, pg375). They live in/on the substrate and also in the water column deriving calcium carbonate ions from the water which binds to the protein matrix of the organism to build their shells (Gierlowski-Kordesch, 2010). Shell deposits however often only make up a small proportion of the overall carbonate sediment within a lake (Boggs, 2009, pg 375). One of the most important processes leading to biogenically precipitated calcium carbonate is the removal of CO₂ via photosynthesis (Tucker and Wright, 1990, pg167). Cyanobacteria for example can become encrusted by carbonate as a result of this process (Tucker and Wright, 1990, pg173). Microbial and algal filaments can also trap and bind sedimentary particles both within and outside an organism allowing the development of finely laminated organosedimentary structures such as stromatolites (Tucker and Wright, 1990, pg 173; Arenas et al., 2007). These structures are found in quiet, shallow ponded areas with water depths of 10 m or less (Arenas et al., 2007; Nichols, 2009, pg 156). The biological induction of calcium carbonate can also be caused

by organisms utilising bicarbonate for photosynthesis (Tucker and Wright, 1990, pg 168). Charophytes, via the process of intracellular assimilation and extracellular adsorption of CaCO_3 , fix a large amount of calcium from the water (Soulie-Marsche et al., 2010). Charophytes are found in fresh and brackish waters and can be indicative of the palaeobathymetry of lakes, such as the Trou au Natron, Tibesti, Chad indicating water cover of 4-6 m during the Late Pleistocene (Soulie-Marsche, 2008; 2010).

Clastic/Detrital Input- CaCO_3 can accumulate as a result of river input and/or erosion of the shoreline (Tucker and Wright, 1990, pg 167). For example, in the Teruel Graben, NE Spain alluvial channels entering the lake allowed the transport and re-deposition of fragments of brecciated limestone (Alonso-Zarza et al., 2012). Carbonate minerals can also be derived via an aeolian supply. For example, aeolianites which occur adjacent to shorelines composed of bioclastic carbonate can contribute to the carbonate content entering the lake (Boggs, 2009, pg380; Nielsen et al., 2004).

Inorganic Precipitation-Temperature and CO_2 pressure are important for carbonate precipitation, in particular a raised temperature or lowering pressure (Tucker and Wright, 1990, pg 168). Under increasing evaporation, other forms of carbonate such as dolomite and aragonite are precipitated (Leng and Marshall, 2004). The occurrence of these minerals is dependent on the Mg/Ca ratio (Tucker and Wright, 1990, pg 169).

Post-depositional Alteration-Diagenesis can cause geochemical and mineralogical changes (McLaren, 1993). For example, aragonite is thermodynamically unstable and hence can convert to low-Mg calcite (Leng and Marshall, 2004; McLaren, 1993). Groundwater and pore water chemistries can lead to the precipitation of secondary carbonates often via the process of replacement (Gierlowski-Kordesch, 2010). Additional diagenetic processes include recrystallisation, cementation in pore spaces and compaction.

Lakes are dynamic systems composed of deposits with complex facies patterns due to the often unstable environment in which they are precipitated (Tucker and Wright, 1990, pg 177). Because of this, Tucker and Wright (1990, pg 177) state that ‘there is no single set of reliable criteria for recognising lacustrine deposits’. Freytet and Verrecchia (2002) have provided a synthesis of the facies and microfacies of lacustrine deposits. These include the

occurrence of lacustrine chalk and marl, varves, turbidites, micritic-laminated and-layered limestones, algae/stromatolite deposits and biologic remains. Indeed, if present, biota are one of the most reliable indicators of a lacustrine setting (Tucker and Wright, 1990, pg177).

Palustrine

In the geological record, palustrine limestones assist in recognising seasonal wetland environments (Flugel, 2010, pg742). Low-energy carbonate lacustrine environments, which are prone to lake-level fluctuations, results in the frequent exposure of marginal lacustrine areas during low stands (Platt, 1989; Armenteros and Daley, 1998; Djamali et al., 2006). This can be caused due to climatic changes (Dunagan and Driese, 1999) or tectonism such as subsidence due to tilting of the basin floor (Alonso-Zarza, 2003). This intermittent flooding allows the sub-aerially exposed lacustrine carbonates to undergo pedogenic modification resulting in the formation of palustrine limestones (Khalaf and Gaber, 2008; Alonso-Zarza et al., 2012). Short lived, isolated ponds characterised by abundant hydrophytic vegetation within the distal area of alluvial flood plains can also result in the formation of these deposits (Alonso-Zarza, 2003). Wright and Platt (1995) note that a large number of studies of palustrine limestones have been documented from Europe and North America in Carboniferous to Neogene sequences. In New York for example, well-developed palustrine features are present in Upper Devonian terrestrial carbonates from the Catskill Magnafacies (Dunagan and Driese, 1999), Eocene palustrine deposits have been documented on the Isle of Wight (Armenteros and Daley, 1998) and extensive Miocene deposits (up to 25 m) have been documented in NE Spain such as in the Madrid Basin (Bustillo and Alonso-Zarza, 2007; Alonso-Zarza et al., 2012). Limited studies have been conducted on palustrine deposits from North Africa with studies such as those conducted in Egypt by Khalaf and Gaber (2008) trying to rectify this.

Identifying palustrine facies can often cause confusion as they are characterised by both sub-aerial and freshwater criteria (Verrecchia, 2007; Flugel, 2010, pg 11). Many studies, for example by Freytet and Verrecchia (2002), have been conducted to help distinguish between lacustrine and palustrine facies. Diagnostic features of palustrine carbonate superimposed on the sedimentary fabric due to pedogenic activity include desiccation cracks and brecciation, nodualisation, root traces, burrows and mottling (Freytet, 1973; Verrecchia, 2007; Freytet and Verrecchia, 2002).

Calcretes

Calcretes are important archives containing information which can aid in interpreting ancient ecosystems, their palaeogeography and the tectonic, climatic and sedimentary regimes in which they formed (Alonso-Zarza, 2003). Wright and Tucker (1991, pg1) describe calcretes as ‘a near-surface, terrestrial accumulation of predominantly calcium carbonate, which occurs in a variety of forms from powdery to nodular to highly indurated’ and state that ‘it results from the cementation and displacive and replacive introduction of calcium carbonate into soil profiles, bedrock and deposits in areas where vadose and shallow phreatic groundwaters become saturated with respect to calcium carbonate’. The development of calcretes is controlled by three main factors, namely climate, the availability of carbonate-rich solution and the host sediment (Khalaf, 2007). Calcretes can be used as an indicator for climatic conditions, forming in areas with arid-to semi-arid climates which previously underwent a more humid period (Khalaf, 2007). Along with a warm climate, low seasonal rainfall (100-500mm) is also required (Wright, 2007). A net moisture deficit is thus clearly needed for formation, however McLaren et al (2012) noted that it was not just the rainfall amount that was necessary for calcrete formation, but the relationship between annual rainfall and evaporation.

The sources of carbonate in calcretes are varied (Wright, 2007). The local lithology, surface runoff, bioclasts, vegetation, sea spray, dust and rainfall all act as sources, with the latter two often being the primary source in pedogenic calcretes in semi-arid/arid environments (Wright, 2007; Wright and Tucker, 1991, pg8). Calcretes typically contain low-Mg calcite but dolomitic forms are common e.g. Khalaf (2007) (Wright and Tucker, 1990, pg345). Two main types of calcrete occur, pedogenic and groundwater. Pedogenic calcretes occupy surficial settings above the groundwater table (Alonso-Zarza, 2003) and develop as a result of carbonates moving through deposits in solution, both laterally and vertically which, with time, become concentrated (Nash and McLaren, 2003). In soil profiles, illuviation moves CaCO_3 from the upper soil layers to the lower levels (Wright, 2007, pg26). Groundwater calcretes are formed in the phreatic zone and around the capillary fringe due to the interplay of processes such as cementation and replacement (Alonso-Zarza, 2003). Evaporation, evapotranspiration, CO_2 degassing and the common ion effect are all important mechanisms in the formation of these calcretes (Alonso-Zarza, 2003). The influence of phreatophytic plants is also important (Alonso-Zarza, 2003). Calcretes form over long periods of time, in the order of several tens to thousands of years (Tucker, 2001, pg152). In particular, mature pedogenic calcretes need lengthy residence times and thus are found at stable surfaces (Wright, 2007, pg 26).

Identifying the origin of a calcrete is of the utmost importance if its palaeoenvironmental significance is to be correctly evaluated (Nash and McLaren, 2003). Yet, identifying and distinguishing between different types of calcretes is difficult. Problems often occur, for example, when trying to separate the influence of groundwater or pedogenic processes (Nash and Smith, 2003). Nash and Smith (2003) note that this is particularly challenging in areas where groundwater fluctuations occur close to the zone of near-surface pedogenesis resulting in a fused profile e.g. Nash and Smith (1998). To help overcome such problems, a number of attempts have been made to classify calcretes, however classification is complex as several different criteria may be used (Alonso-Zarza, 2003). Calcretes can be classified based on their hydrological setting as seen in Figure 2.14, the stages seen in the development of calcretes in profiles, their morphology and their microstructure (Wright and Tucker, 1991, pg3-6).

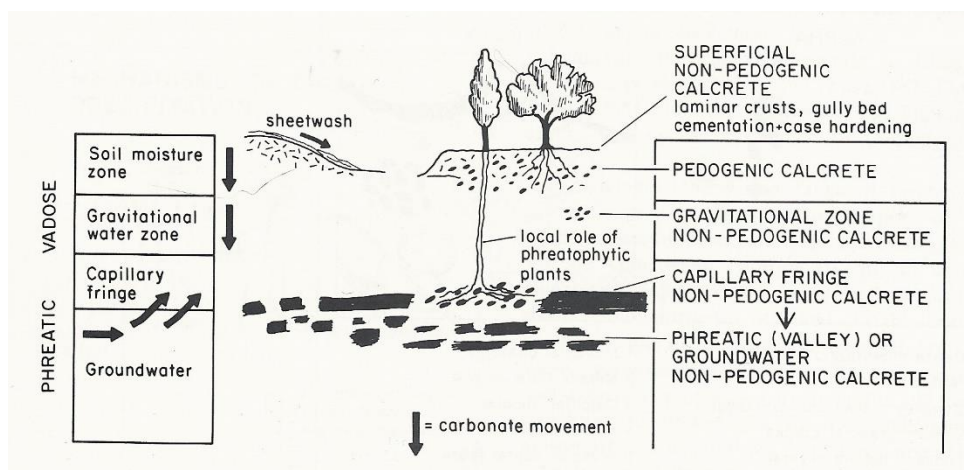


Figure 2.14. Classification of calcretes based by hydrological setting (Wright and Tucker, 1991, pg5)

Calcretes are secondary carbonates and although they are not included in any soil classifications, they are typically found in aridisols, vertisols, mollisols and alfisols (Tucker and Wright, 1990, pg344). The stages of calcrete development in soil profiles is noted in a number of sources e.g. Wright and Tucker (1991, pg4-5), Tucker and Wright (1990, pg345). Classifying calcretes in this way is problematic. These profiles are often complex with similar horizons found at different positions or horizons absent in the profile due to truncations (Alonso-Zarza, 2003). The microscopic features of calcretes are varied, yet two end members are recognised: alpha and beta. The main difference between these calcretes is the lack of biological evidence in alpha calcretes compared to beta (Tucker and Wright, 1990, pg345). Alpha fabrics can occur in all types of calcrete whereas beta

calcretes are commonly found on carbonate substrates within the soil or deeper where phreatophytes are present (Tucker and Wright, 1990, pg345). Further criteria of these end members are noted in Table 2.3.

Alpha Calcretes	Beta Calcretes
Dense microfabric ¹	Microbial coatings-often irregular micritic envelopes ^{1,3}
Nodules ^{1,3}	Needle fibre calcite up to 10µm wide and 50µm in length ^{1,2}
Complex cracks, fine fractures and crystallaria ^{1,2}	Calcified filaments and tubules ^{1,3}
Circum-granular cracks ¹	Rhizoliths ^{3,4}
Rhombic calcite crystals ¹	Calcified pellets ¹
Fine crystal size ²	Alveolar septal fabric ^{1,3}
Embayed grains and floating textures (usually silicates) ^{1,2,3}	<i>Microcodium</i> ^{1,3}

Table 2.3. Micromorphological differences of Alpha and Beta calcretes. 1-Tucker and Wright (1991, pg6), 2-Wright and Tucker (1990, pg345), 3-Alonso-Zarza (2003), 4-Klappa (1980)

It is clear that groundwater calcretes are still poorly understood compared to pedogenic. For example, in the literature it is often only the formation stages of pedogenic calcretes which are discussed, and where groundwater calcretes are discussed they are often generalistic descriptions (Nash and McLaren, 2003). Nash and McLaren (2003) suggest this may be due to the assorted types of groundwater calcretes forming under different geomorphological settings. It has become increasingly important to increase our understanding of individual varieties of non-pedogenic calcretes (Nash and Smith, 2003). Nash and Smith (2003) have attempted this by conducting an in-depth study on channel calcretes in the Tabernas Basin, Spain. Further in-depth studies on groundwater calcretes could also provide more significant palaeoenvironmental data in comparison to their pedogenic equivalents. McLaren et al. (2012) questioned the usefulness of pedogenic calcretes in palaeoreconstructions due to their polygenetic nature and influence of diagenesis throughout their evolution. Studies of monogenetic, groundwater calcretes such as those from Wadi Dana, Jordan (McLaren et al., 2012) may provide more reliable data.

2.5.2 Palaeohydrology: The use of Oxygen and Carbon Stable Isotopes

Primary (i.e. not diagenetic origin) authigenic carbonates have great potential for providing information regarding the terrestrial palaeoclimate and are now a widely used proxy as they can provide an integrated climate signal for the whole rock sample (Baïoumy et al., 2010; Marshall, 2002). Authigenic carbonates form via evapotranspiration at an emergent water table and can be used to infer changes in the isotopic composition of the lake water and changes in temperature via stable isotope investigation (Zuppi and Sachi, 2004; Leng and Marshall, 2004). Stable isotopes of oxygen and carbon have advantages over other palaeoclimatic proxies as the factors which affect these stable isotope ratios are relatively few and also well known (Gasse et al., 1987; Gasse, 2005; Zuppi and Sachi, 2004). However, as the stable isotope ratios can be influenced by a wide range of interlinked environmental processes (discussed later in the section), environmental reconstruction can be difficult (Leng et al., 2005). As such, most records are qualitative, as a quantitative interpretation requires a number of factors to be well known including a detailed understanding of the current and past hydrology of the lake (Gasse, 2005; Leng et al., 2005).

Carbonates are assumed to precipitate in isotopic equilibrium with the lake water (Leng and Marshall, 2004; Leng et al., 2005). Isotopic equilibrium is predictable by thermodynamics whereby the oxygen isotopic composition of the mineral is determined by temperature and the isotopic composition of the lake water (Leng et al., 2005). Disequilibrium effects may also occur causing the mineral precipitate to have an isotopic composition different to that predicated by thermodynamics, i.e. different to the lake water (Leng et al., 2005; Leng and Marshall, 2004). Disequilibrium effects include micro-environment induced changes and a variety of rate effects (e.g. pH) (Leng et al., 2005; Leng and Marshall, 2004). Carbonates investigated using stable isotopes of carbon ($\delta^{13}\text{C}$) and oxygen ($\delta^{18}\text{O}$) can provide key information regarding hydrological changes in palaeoclimate studies. For example, Gasse et al. (1987) states that fluctuations in ^{13}C content can provide information about water mixing, residence times and the importance of biological effects on total dissolved inorganic carbon (TDIC). When investigating the $\delta^{13}\text{C}$ content of carbonates it is important to understand the environmental processes which can influence and thus control $\delta^{13}\text{C}$ content (Leng and Marshall, 2004). During carbon cycle transitions, carbon isotopes become fractionated and integrated within authigenic and biogenic carbonates (Leng and Marshall, 2004). When carbonates precipitate, a small temperature effect occurs along with a small carbon isotope fractionation between the

TDIC and the mineral phase (Leng and Marshall, 2004). The $\delta^{13}\text{C}$ of the mineral phase can therefore provide information regarding the past $\delta^{13}\text{C}$ of the TDIC from within the lake (Leng and Marshall, 2004). Leng and Marshall (2004) state that, on the whole, three predominant processes control the inorganic carbon isotope composition of TDIC (Figure 2.15).

1) Isotopic composition of inflowing water.

Much of the carbon input into lakes is derived from plant respiration and CO_2 production in the soils (Leng and Marshall, 2004). This input, via soil water and shallow groundwater, often results in depleted $\delta^{13}\text{C}$ values as isotopically light CO_2 is released during decay of terrestrial organic matter (Leng and Marshall, 2004). Lezine et al. (1990) attributed the decrease in $\delta^{13}\text{C}$ (approx. -6‰) in the Chemchane Sebkha, Mauritania, to this cause.

2) Photosynthesis/Respiration in lake water.

Biological activity, in particular by photosynthesising aquatic plants, can alter the lake TDIC (Leng and Marshall, 2004; Lamb et al., 2000). Aquatic plants selectively remove ^{12}C from lake TDIC thus causing enriched $\delta^{13}\text{C}$ content of precipitating carbonates (Leng and Marshall, 2004; Lamb et al., 2000).

3) CO_2 exchange between atmosphere and water TDIC.

This process results in carbonates enriched in $\delta^{13}\text{C}$ (Leng and Marshall, 2004; Lamb et al., 2000). The enriched values result from the different degrees of equilibration of the TDIC with atmospheric CO_2 (Leng and Marshall, 2004). This is often accompanied by enriched $\delta^{18}\text{O}$ and can lead to isotopic equilibrium (Leng and Marshall, 2004). Under such conditions, atmospheric CO_2 , which has a value of ca. 8‰, will result in lake water $\delta^{13}\text{C}$ to be between 1-3‰ (Leng and Marshall, 2004). This process becomes more important as residence time increases indicating that residence time has a central role in the production of high $\delta^{13}\text{C}$ in lakewaters via exchange and also high $\delta^{18}\text{O}$ due to evaporation (Lamb et al., 2000). $\delta^{13}\text{C}$ content related to isotopic equilibrium and changes to residence time can be observed, for example, in the palaeolakes of the Great Western Erg, Algeria (Gasse et al., 1987) and Lake Tilo, Ethiopia (Lamb et al., 2000).

In modern lake and palaeolake environments it cannot be assumed that the $\delta^{18}\text{O}$ of lakewater is solely a reflection of mean annual precipitation (Leng and Marshall, 2004).

The residence time and modification of water composition via lake and catchment processes are important factors to consider (Leng and Marshall, 2004). For example, changes in temperature and the amount of precipitation/evaporation are important (Figure 2.16.) (Leng et al., 2005). When investigating lacustrine environments it is also extremely important to have an understanding of the lake hydrology, in particular whether the lake is hydrologically open or closed (Leng et al., 2005). Hydrologically open lakes are often permanent water outlets characteristic of exohoreic regions having some degree of throughflow (Tucker and Wright, 1990, pg165; Leng and Marshall, 2004). Inflow to the lake from the surrounding drainage basin and precipitation is balanced by evaporation and outflow thus resulting in a stable shoreline and lake chemistry (Tucker and Wright, 1990, pg165). The $\delta^{18}\text{O}$ isotopic composition is a reflection of the precipitation received by the lake (Rozanski and Gonfiantini, 1990). 'Amount effects' are common in open lakes and are influenced by temperature changes (Rozanski and Gonfiantini, 1990; Leng et al., 2005). As such, depositional carbonate reflects cold/mild climate characterised by minima/maxima values of $\delta^{18}\text{O}$ respectively (Rozanski and Gonfiantini, 1990). Typically $\delta^{18}\text{O}$ will vary by no more than a few ‰ as evaporation has minimal influence on open lakes (Leng and Marshall, 2004). Closed basin lakes differ to open lakes as they have no regular outlet (Tucker and Wright, 1990). As such, when compared to open lakes, lake level and chemistry are more variable and complex (Rozanski and Gonfiantini, 1990). The isotopic composition of the water is controlled by inflow, precipitation, exchange with atmospheric moisture and evaporation which is a particularly important control in arid regions (Tucker and Wright, 1990, pg165; Rozanski and Gonfiantini, 1990; Leng and Marshall, 2004). Evaporation in turn is controlled by a number of factors including humidity, temperature and wind speed (Leng et al., 2005). Climatic changes results in closed lakes having waters with variable oxygen isotope compositions (Leng et al., 2005). Carbonates precipitated in closed lakes also contain variable $\delta^{18}\text{O}$ values but they are generally high and more positive than regional rainfall due to effects of evaporation which preferentially remove ^{16}O (Rozanski and Gonfiantini, 1990; Leng and Marshall, 2004; Leng et al., 2005).

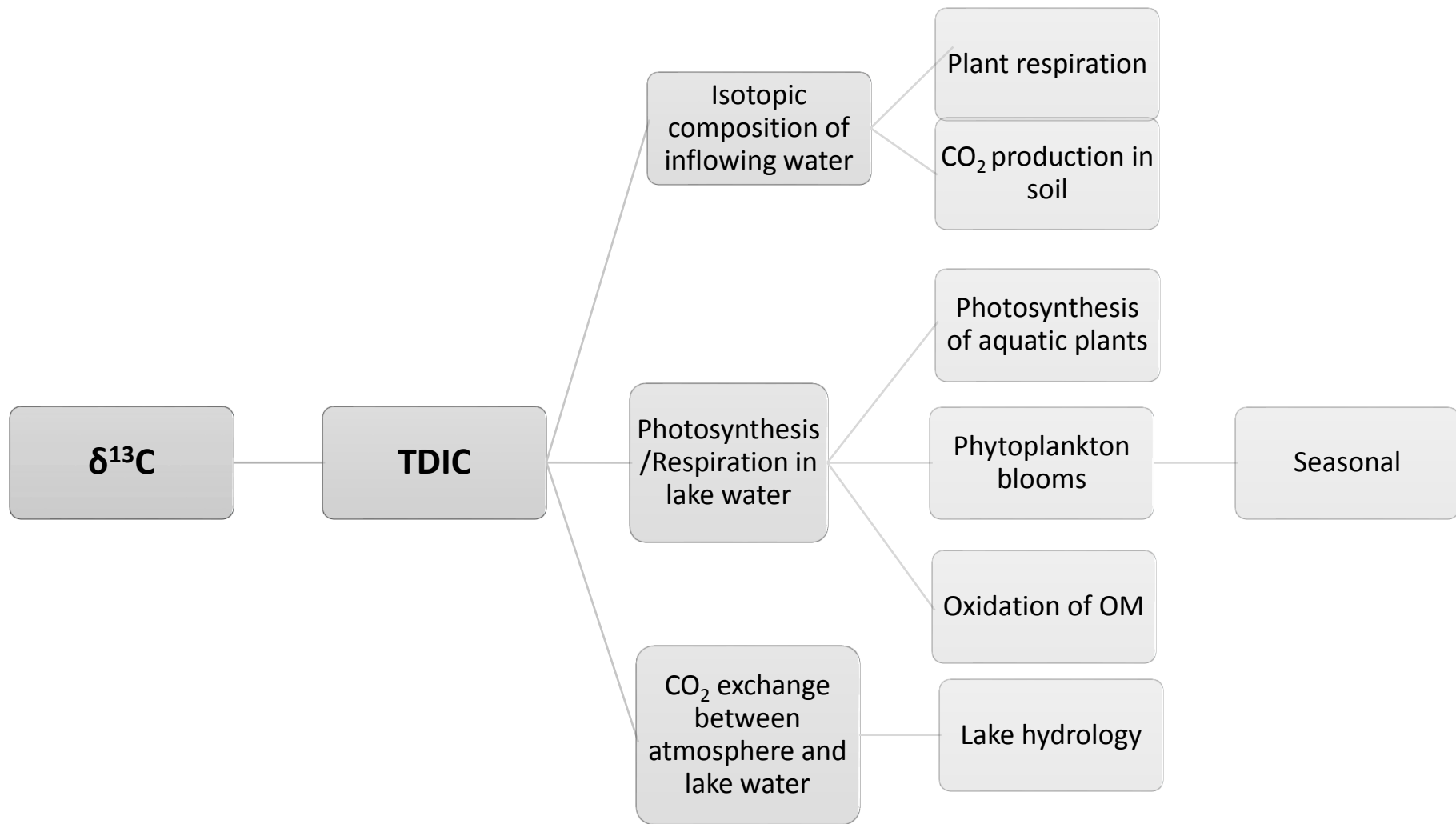


Figure 2.15. Main controls on TDIC and $\delta^{13}\text{C}$ of lacustrine carbonates. Adapted from Leng and Marshall (2004).

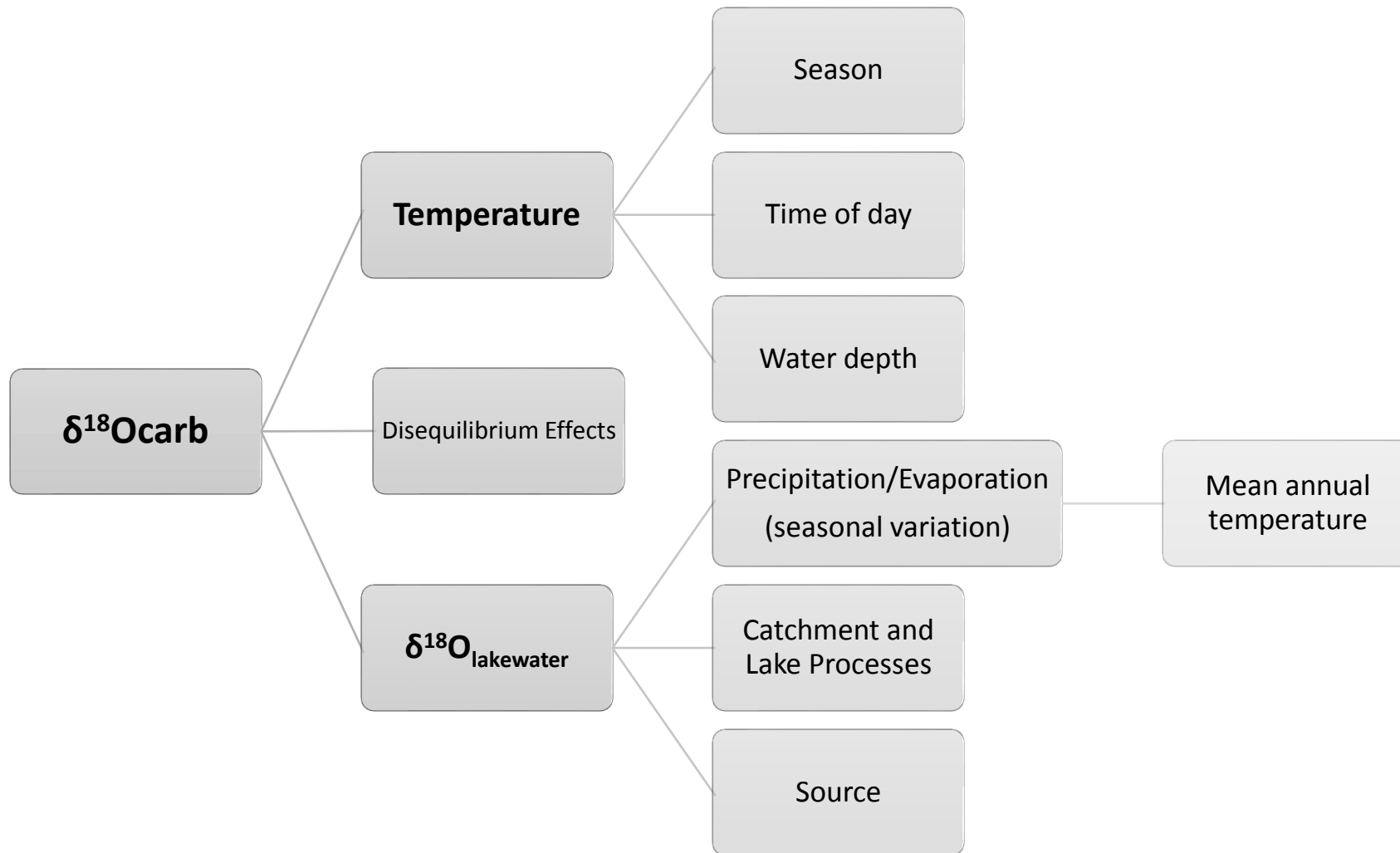


Figure 2.16 Main controls on the $\delta^{18}\text{O}$ of lacustrine carbonates. Adapted from Leng and Marshall (2004).

In closed basins, the relationship between $\delta^{18}\text{O}$ - $\delta^{13}\text{C}$ is a function of vapour exchange, hydrological change, lake productivity and total CO_2 concentration (Li and Ku, 1997). Changes in lake volume of closed lakes will be reflected in $\delta^{18}\text{O}$ - $\delta^{13}\text{C}$ (Li and Ku, 1997). If lake volume declines, both the $\delta^{18}\text{O}$ and $\delta^{13}\text{C}$ values will increase leading to strong covariance (Li and Ku, 1997). Many closed basins in arid regions show covariance (Leng and Marshall, 2004). Covariance is often observed in lake deposits which have experienced hydrological closure for $>5,000$ yr however, Li and Ku (1997) state that on shorter timescales certain subtleties in the use of $\delta^{18}\text{O}$ - $\delta^{13}\text{C}$ covariance as an indicator of hydrology must be recognised. Talbot (1990) found that, although the isotopic composition of individual closed lakes can be variable, the isotopic composition behaves in a systematic and predictable way which is constrained by climatic setting and the lakes hydrology. Typically the correlation of $\delta^{18}\text{O}$ - $\delta^{13}\text{C}$ in carbonates precipitated in closed lakes have high correlation with $r \geq 0.7$ and thus can be used as an indicator of lake hydrology (Talbot, 1990). Talbot (1990) not only concluded that covariance can be an indicator for hydrological closure, but can also indicate the following:

- Long-term stability in the inflow composition and hydrological characteristics.
- Provide information on basin morphology, palaeogeography, climatic settings, evaporative history and isotopic composition of inflow to the lake.
- A potential tool for basin analysis, for example confirming hydrological closure between basins.

Stable isotope studies on lacustrine carbonates from the central Sahara/North African region are limited with many available studies focussing on Quaternary carbonates. The Quaternary is focussed on lacustrine studies in this region due to the increased preservation of these deposits and also due to the climatic perturbations that occurred during this period resulting in variations in the isotopic composition of precipitation (Zuppi and Sachi, 2004). Water recharged during the African Humid Period (Late Pleistocene-Early Holocene) for example was depleted in ^{18}O compared to modern precipitation. This suggested that during recharge the temperature was lower causing changes in air saturation leading to an increase in precipitation and/or high summer rainfall resulting in surface water dilution (Zuppi and Sachi, 2004; Lamb et al., 2007). Depleted $\delta^{18}\text{O}$ values have been recorded in the eastern Sahara from the West Nubian Palaeolake (-8 to -4‰) and from Palaeolake Gureinat, Sudan (Abell and Hoelzmann, 2000; Hoelzmann et al., 2000; 2010). Hoelzmann et al. (2010)

attributed the low $\delta^{18}\text{O}$ values in Palaeolake Gureinat to either reduced influence of evaporation as a result of increasing water depths and hence decreased surface/volume ratio, or to lower water temperatures from increased seepage caused by a rising groundwater table resulting from increased monsoonal rainfall. Enriched $\delta^{18}\text{O}$ values have also been recorded in both modern and ancient lakes across the Sahara. During the period 1975-2001 Lake Hayq, Ethiopia, recorded $\delta^{18}\text{O}$ values ranging from +7.1‰ to +9.1‰ indicating evaporative enrichment (Lamb et al., 2007). Deposits from the Chemchane Sebkhah, Mauritania dating to the Late Pleistocene and mid Holocene also show a rise in $\delta^{18}\text{O}$ responding to stronger evaporation which induced more CaCO_3 precipitation (Lezine et al., 1990).

Palustrine and Calcretes

In comparison to lacustrine carbonates, the parameters that influence the geochemical signatures of palustrine carbonates and calcretes are more complex (Alonso-Zarza, 2003). Soil processes and diagenesis, either vadose or phreatic, act on the sediment resulting in modification of isotopic values (Alonso-Zarza, 2003). Vegetation cover is also more important (Alonso-Zarza, 2003). Palustrine carbonates often show isotopic heterogeneity when compared to open lacustrine carbonates (Platt, 1989) along with lower $\delta^{13}\text{C}$ and $\delta^{18}\text{O}$ isotopic values. For example, palustrine limestones from the Cameros Basin, Spain, reveal more negative isotopic values in comparison to lacustrine deposits, as a result of pedogenic input of light meteoric oxygen and carbon isotopes (Platt, 1989).

Calcretes, especially mature calcretes, may reflect numerous and often different geochemical/palaeoenvironmental regimes (Wright and Tucker, 1991, pg21). As a result, interpretations of ancient calcrete isotopic values are particularly difficult (Wright and Tucker, 1991, pg21). This interpretation, as for palustrine carbonates, is further hampered by problems of overprinting and diagenetic alteration, such as recrystallisation, which have acted on the sediment (Wright, 2007; Wright and Tucker, 1991, pg 21). Cerling (1984) refers to overprinting as 'the imposition of later climatic information on previous information' and states that the variation in isotopic values, especially for calcretes, is due to this problem. Mature calcretes tend to have highly varied isotopic compositions with bulk sampling yielding values which are time-averaged (Wright and Tucker, 1991, pg 21; Wright, 2007). This limits the temporal resolution and hence only material with limited isotopic heterogeneity should be used to make isotopic interpretations (Wright, 2007).

In a global study of more than 300 measurements of stable isotopic values on calcretes, Talma and Netterberg (1983) found that the $\delta^{13}\text{C}$ and $\delta^{18}\text{O}$ values range between -12 to +4‰ PDB and -9 to +3‰ PDB respectively. However, in the arid zone (annual rainfall <250mm) Talma and Netterberg (1983) noted that $\delta^{13}\text{C}$ values <-6‰ were rare and $\delta^{18}\text{O}$ <-5‰ were not recorded. In areas receiving <350mm of annual rainfall, all samples had $\delta^{18}\text{O}$ values > -2‰ (Talma and Netterberg, 1983). In general, the isotopic composition of calcretes is a reflection of the source material, temperature and mechanisms involved in the formation and post-formation (Talma and Netterberg, 1983). The main controls on the $\delta^{13}\text{C}$ values of calcretes is the $\delta^{13}\text{C}$ content of the dominant plants in the region (Talma and Netterberg, 1983). The density of vegetation cover also contributes to the isotopic value (Alonso-Zarza, 2003). $\delta^{18}\text{O}$ values are directly related to the composition of meteoric water from which they formed (Alonso-Zarza, 2003; Wright and Tucker, 1991, pg 21). Selective infiltration, small temperature effects and evaporation also cause changes (Alonso-Zarza, 2003). Evaporation, often due to increasing aridity, can sometimes lead to positive covariance between $\delta^{13}\text{C}$ / $\delta^{18}\text{O}$ (Alonso-Zarza, 2003; Talma and Netterberg, 1983). This was observed for example in Miocene calcretes, and in particular palustrine deposits, of the Duero Basin, Spain (Huerta and Armenteros, 2005).

Of particular interest in studies of calcretes is determining their origin: pedogenic or groundwater. The use of geochemical signatures of pedogenic calcretes is still limited by relatively poor understanding of the real nature of calcrete development (Wright, 2007). Geochemical studies of these deposits are however still important in palaeoenvironmental reconstructions (Alonso-Zarza, 2003). From the same area, pedogenic and groundwater calcretes can show similar isotopic signals (Alonso-Zarza, 2003). Talma and Netterberg (1983) noted that groundwater calcretes typically have more isotopically consistent values. These calcretes also have lower $\delta^{13}\text{C}$ and $\delta^{18}\text{O}$ values than pedogenic carbonates from the same region, typically occurring at the low end of the range (Talma and Netterberg, 1983). This is not surprising as groundwater is influenced by deep roots (low $\delta^{13}\text{C}$) in comparison to shallow soils and heavier rainfall events with lower $\delta^{18}\text{O}$ leading to recharged aquifers (Talma and Netterberg, 1983).

2.6 Formulation of Research Questions

It is clear from the above review of the literature that a number of gaps remain in our understanding of the geochronology and palaeoenvironmental history of the Fazzan Basin. This is especially true for the important sedimentary succession known as the Al Mahruqah Group and also the wider central Saharan region. To try and address some of these gaps in knowledge, four research questions have been formulated.

Evidence for the origin of the Al Mahruqah Group as a predominantly lacustrine succession is increasing. Yet is it apparent from previous studies (e.g. Armitage et al., 2007; Abdullah, 2010), especially Drake et al. (2008a), that the age of this succession remains unresolved as only the uppermost sections of the Al Mahruqah Group stratigraphy have been studied and previous dating techniques applied to the group were possibly not suitable for a reliable date to be generated. With this in mind, the first question is as follows:

- 1. Is the chronology of the Al Mahruqah Group, as suggested by previous research, valid?**

Little is known about the geology of the Fazzan prior to 7 Ma (Drake et al., 2008a).

However since the late Miocene, several geological events have taken place in the Fazzan, in particular volcanism, such as the growth of the Al Haruj al Aswad. Growth of volcanoes resulted in the Fazzan becoming a closed basin, by blocking the flow of many wadis. Throughout this time, the central Sahara also experienced numerous climatic perturbations such as the MSC and the mid-Pliocene warm period. The second research question is therefore:

- 2. What geological controls, in particular volcanism, and palaeoclimatic changes have influenced the sedimentary successions of the Al Mahruqah Group and the overall palaeoenvironment of the Fazzan basin?**

Evidence of a lacustrine palaeoenvironment in the form of carbonates and scattered shelly fossiliferous beds, in particular from Wadi ash Shati, have been documented by numerous studies (e.g. Petit-Maire et al., 1980; Gaven et al., 1981; Armitage et al., 2007). Thiedig et al. (2000) documented the occurrence of lacustrine deposits at three distinct levels and proposed the idea that a large ‘megalake’ existed in the Fazzan during more humid

intervals, later named Lake Megafazzan (Armitage et al., 2007). The deposits of the Al Mahruqah Group are believed to have been deposited by this lake and hence:

3. What petrographic and geochemical evidence from the Al Mahruqah Group indicates the presence of a large lake, namely Lake Megafazzan?

It is apparent from the literature that data concerning the Miocene-Pliocene palaeoclimate of North Africa is sparse. This is especially true for proxy evidence with much of the known information, such as vegetation patterns, generated from climate model simulations (e.g. Salzmann et al., 2008; Pound et al., 2011; 2012). This lack of information is particularly prevalent in Libya in the central Sahara with limited studies focussed on the inland desert regions in comparison to studies along the North African margin and the Mediterranean and also neighbouring Chad to the south. For this reason, the final research question is:

4. How can the information gained from this research help to fill the palaeoclimatic void of the central Sahara, in particular that of Miocene-Pliocene climate?

3 Study Sites

3.1 Identification of Study Sites

Visited field sites were selected by examination of the following:

Geological maps of the region. In particular, geological maps of 1:250,000 scale compiled between 1983-1985 on behalf of the Industrial Research Centre, Tripoli and their associated explanatory booklets (e.g. Roncevic, 1984; Gundobin, 1985).

Satellite imagery and digital elevation models (DEMs). Previous studies of the Fazzan (e.g. Drake et al., 2008a, 2011) have documented in detail the use of satellite imagery in identifying potential field sites. A range of remotely sensed imagery has been employed when mapping the Fazzan catchment which can subsequently be used as a guide in the field. For example, Landsat Thematic Mapper (TM) false colour composite imagery has shown to be useful in identifying and mapping outcrops of lake deposits, such as limestone, as they can be discriminated from other materials (Drake et al., 2008a). Regions of interest can be investigated using higher spatial resolution imagery such as ASTER (visible and near-infrared) along with SPOT (Drake et al., 2011). Radarsat imagery has also proven to be useful in distinguishing areas of active sand and older, more consolidated sandstone in the Ubari as the older deposits have rougher surfaces that enhance radar backscatter relative to the surrounding sands (Drake et al., 2011). Guided by DEM height differences, suitable outcrops for continuous palaeomagnetic dating could be identified.

Knowledge and information gained from previous field visits. The region was visited almost annually between 1998 and 2011 by a team as part of the Fazzan Project sponsored by the Society for Libyan Studies. This allowed a detailed knowledge of the basin to be developed. The knowledge of team members Mustafa Salem and Ahmed el Hawat were particularly important during field visits.

Study sites referred to in the literature. Important sites visited by other research teams working in the area, such as Geyh and Thiedig (2008), Thiedig et al. (2000).

3.2 Study Site Information

In total, 295 samples were collected from exposures from six main study sites: Ariel, Tmessah, Brak, Bir al Zallaf, Al Wafa and Qarat al Mrar. The sites roughly follow a west to east transect across the northern part of the Fazzan Basin as seen in Figure 3.1. The samples were collected by several teams over four field seasons during January 2007, 2008, 2009 and 2011, however the author was not present for any of the data collection. At each site the stratigraphy of exposed sections was logged and samples collected for analyses. Details of each study site are discussed below.

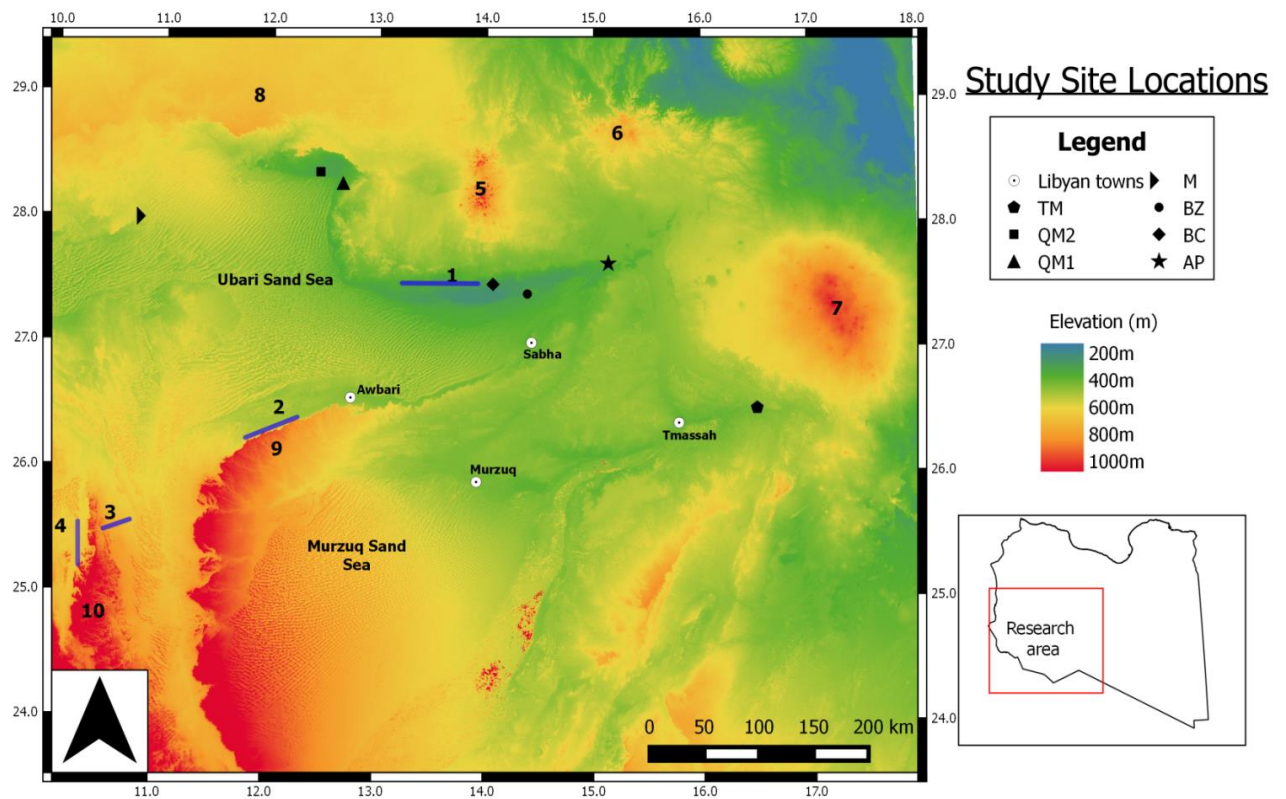


Figure 3.1 Digital Elevation Model (DEM) of the Fazzan. The box in the lower right corner of the figure shows the outline of Libya and the location of the research area as seen in the main DEM. Study sites can be identified as black symbols on the map where M-Al Wafa, TM-Tmessah, BZ-Bir al Zallaf, QM2-Qarat al Mrar 2, QM1-Qarat al Mrar 1, BC-Brak, AP-Ariel. Key town and geomorphological features are also identified: 1-Wadi ash Shati, 2-Wadi al Hayat, 3-Wadi al Ajal, 4-Wadi Tanezzuft, 5-Jebal al Hasawinah (volcano), 6-Jebal as Sawda (volcano), 7-Al Haruj al Aswad (volcano), 8-Al Hamadah al Hamra Plateau , 9-Messak Settafet, 10-Akakus Mountains

Ariel (AP)

This site is named after the proximity to the Ariel Agricultural Project in the north-eastern corner of the Ubari Sand Sea. It is composed of four sub-sections (Figure 3.6) tied together by lithostratigraphic and height correlation in the field by Ahmed El Hawat. The sub-sections were exposed along a trackway down a SW facing bluff from the Agricultural Project on the plateau top into Wadi Kunayr. This section corresponds to the Shabirinah Formation and includes the Kunayr Member as seen in the section log (Figure 3.2) further site details are noted in Table 3.1.

The base of the section is locally reddened and consists of a unit of sandstones and a few mudstones. The redness of the deposits is typically 5Y/R 4/6 and 10YR 6/4 on the Munsell Colour Chart. The lower part of the section is composed of sandstones and mottled mudstones with some palaeosols. These deposits are overlain by black to maroon silty palaeosols capping fining-up channel sandstones. The channels are well exposed 3.7 km to the east of the section where they are orientated towards 135° and at their widest are up to 150-200 m. The upper part comprises mottled and rootleted sandstones. Local nodular calcrete development in the Kunayr Member and some clear palaeosol horizons are also present. The section ends before the plateau top as a result of complex down-cutting relationships. This made identifying stratigraphic relationships unclear in regards to the units occupying the plateau top.

<u>Field Season</u>	<u>Site</u>	<u>Sample ID</u>	<u>Total No. of Samples</u>	<u>Total Section Thickness/m</u>	<u>GE location</u>
Jan 2009	AP1	AP1-30	59	39.21	27°40'29.98"N 15° 8'8.67"E
	AP2	AP31-35			27°40'33.15"N 15° 8'11.44"E
	AP3	AP36-44			27°40'34.56"N 15° 8'10.70"E
	AP4	AP45-59			27°40'33.62"N 15° 8'12.35"E

Table 3.1. Site details of the Ariel section. Note: The codes in the 'site' column correspond to the pins on the Google Earth image seen in Figure 3.6, pg82.

Tmessah (TM)

Tmessah is the most southerly and easterly site to be sampled (Table 3.2 and Figure 3.7). The name Tmessah was given due to its proximity to the town of Tmassah which is located approximately 70 km to the south-west. The section is composed of five sub-sections which are tied together via lithostratigraphic correlation. It is part of the Shabirinah Formation and contains all the members associated with this formation: the K Mbr, TM Mbr, STR Mbr and M Mbr. The samples which relate to these members are noted on the section log in Figure 3.3.

The lowest part of the section contains locally red, mottled sandstones and siltstones (the Maharshim Member) overlain by stromatolitic limestones of the Stromatolite Member. Red mudstones are present in the upper part of the Stromatolite Member. Mudstones of this member were found to thicken considerably to the south and west of the study site. This indicates the overlying Temessah Member is probably an incised channel (hiatus observed at the base) which has cut into the mudstones. The Temessah Member, forming the mid part of the section, is composed of fine-coarse grained sandstone. The sandstone is occasionally red/green with some mottling. Rootleting and minor calcareous nodules are also evident. The upper part of the section (K Mbr) consists of well-developed white and pink (typically 7.5YR 7/3) limestone beds capped by a well-cemented sandstone unit. Extensive modification (e.g. rootleting) is observed in some of the limestone rich units, likely of pedogenic origin.

<u>Field Season</u>	<u>Site</u>	<u>Sample ID</u>	<u>Total No. of samples</u>	<u>Total Section Thickness/m</u>	<u>GE location</u>
Jan 2009	TM1	TM5-10, 14-17	48	19.85	26°30'52.57"N 16°30'11.74"E
	TM1b	TM9-13			26°30'50.65"N 16°30'10.26"E
	TM2	TM18-26, 29-35			26°30'53.74"N 16°30'1.33"E
	TM3	TM60-69			26°30'48.00"N 16°29'59.77"E
	TM4	TM70-72			26°30'46.88"N 16°30'9.08"E

Table 3.2 Site details of the Tmessah section. Note: The codes in the 'site' column correspond to the pins on the Google Earth image seen in Figure 3.7, pg83.

Brak (BC)

As for the Tmessah section, the name Brak is derived due to the proximity to the town of Brak, 15 km to the ENE. The section contains deposits of the Shabirinah Formation (the lowest 4.5 m of the section) and the overlying Brak Formation as seen in Figure 3.4. This section is the type section of the AMF of Seidl and Rohlich (1984). The deposits were sampled from a modern working quarry in central Wadi ash Shati (Figure 3.8).

The lower part of the section is composed of light brown-red mudstone with some green mottling, typically 7.5YR or 5YR 6/4 on the Munsell colour chart. This transitions into calcareous sandstone-sandy limestone, which in turn grades up into the main white limestone (calcrete?) rich part of the Brak Formation. Unfortunately in the field the detail of the transition between the Brak and the top of the Shabirinah Formation was not documented. It has been inferred that the Brak is the termination of the upwards increase in calcretisation within the Shabirinah Formation. Additional details of this section are noted in Table 3.3.

<u>Field Season</u>	<u>Site</u>	<u>Sample ID</u>	<u>Total No. of samples</u>	<u>Total Section Thickness/m</u>	<u>GE location</u>
Jan 2009	BC1	BC1-11	25	19.51	27°30'20.10"N 14° 4'5.00"E
	BC2	BC12-25			

Table 3.3 Site details of the Brak section. Please see Figure 3.8 for a Google Earth Image of the site on pg84.

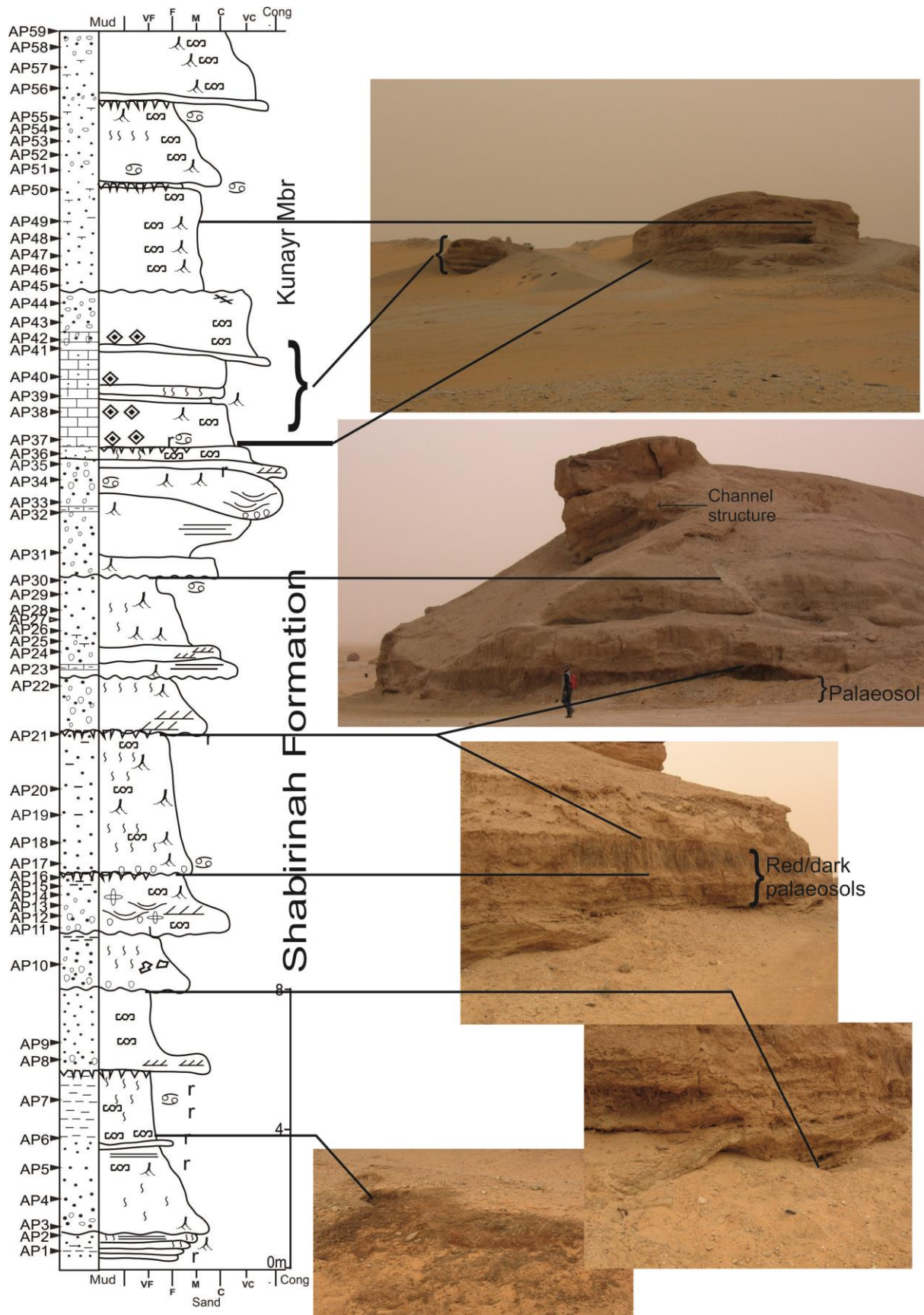


Figure 3.2 Stratigraphic log of the Ariel section. This section corresponds to the Shabirinah Formation with the Kunayr Mbr identified from AP37 upwards. Please refer to Figure 3.5 (pg81) for the log key.

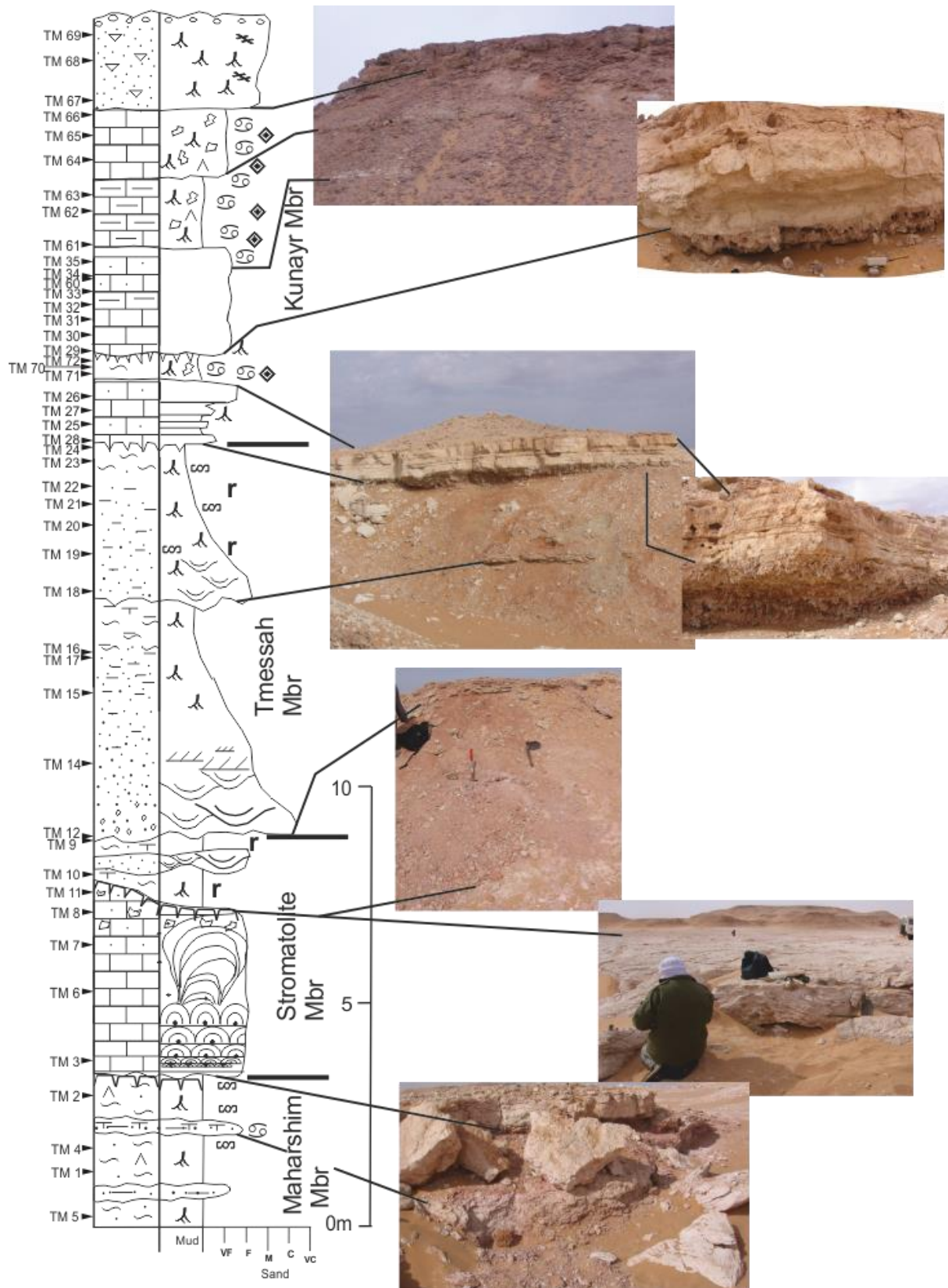


Figure 3.3 Stratigraphic log of the Tmessah section. This section relates to the Shabirinah Formation with the members associated with this formation identified on the section (Maharshim Mbr-TM5-2, Stromatolite Mbr-TM3-9, Tmessah Mbr-TM12-24, Kunayr Mbr-TM28-69). Please refer to Figure 3.5 (pg81) for the log key.

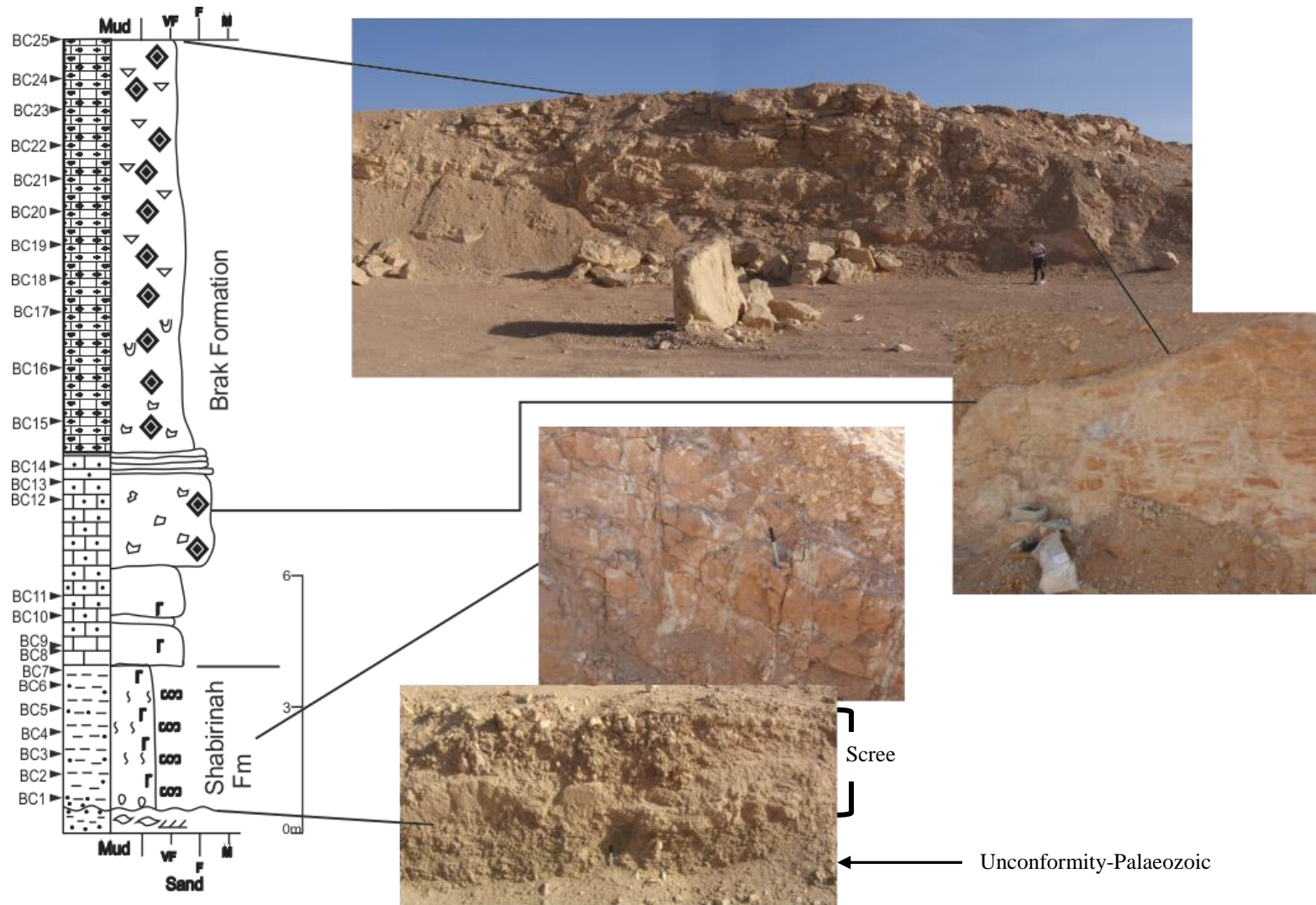


Figure 3.4 Stratigraphic log of the Brak section. This section corresponds to both the Shabirinah Formation (BC1-7) and the Brak Formation (BC8-25). Please refer to Figure 3.5 (pg81) for the log key.

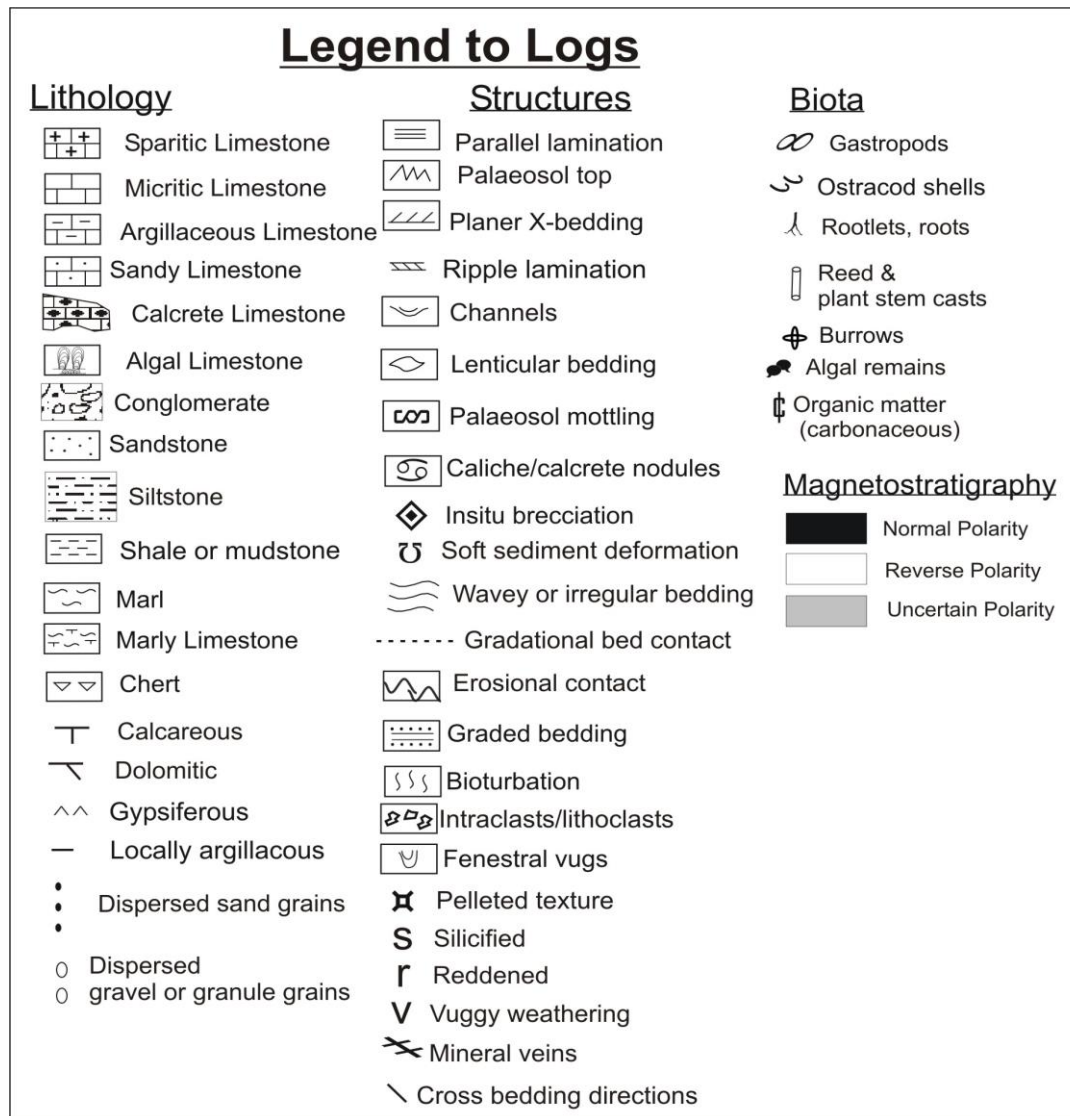


Figure 3.5. Legend for all section logs.

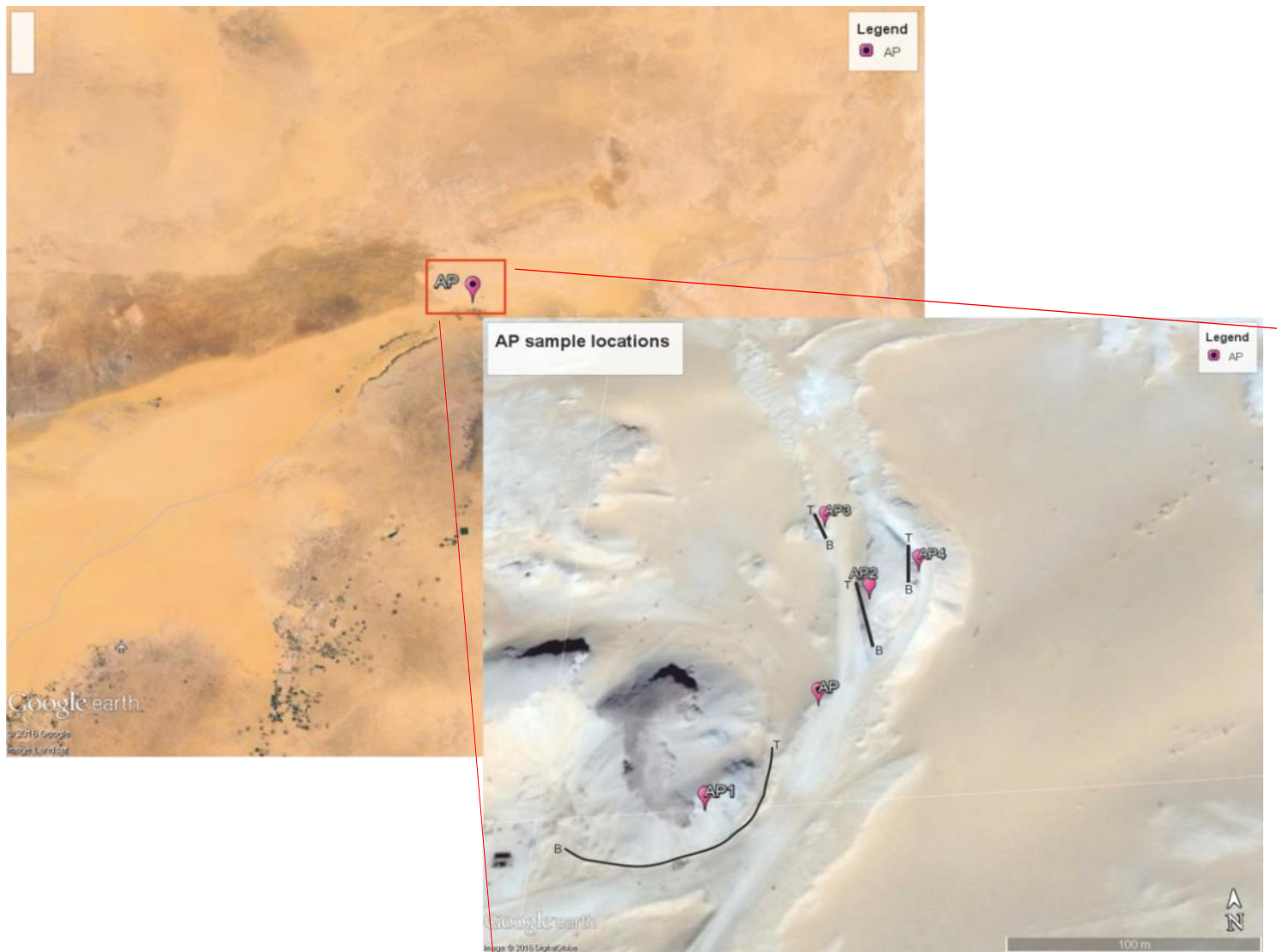


Figure 3.6 Google Earth images of the Ariel section and sub-sections. T=section top, B=section bottom. Please refer back to Figure 3.1 (pg74) to see where the site locality is within the Fazzan Basin.

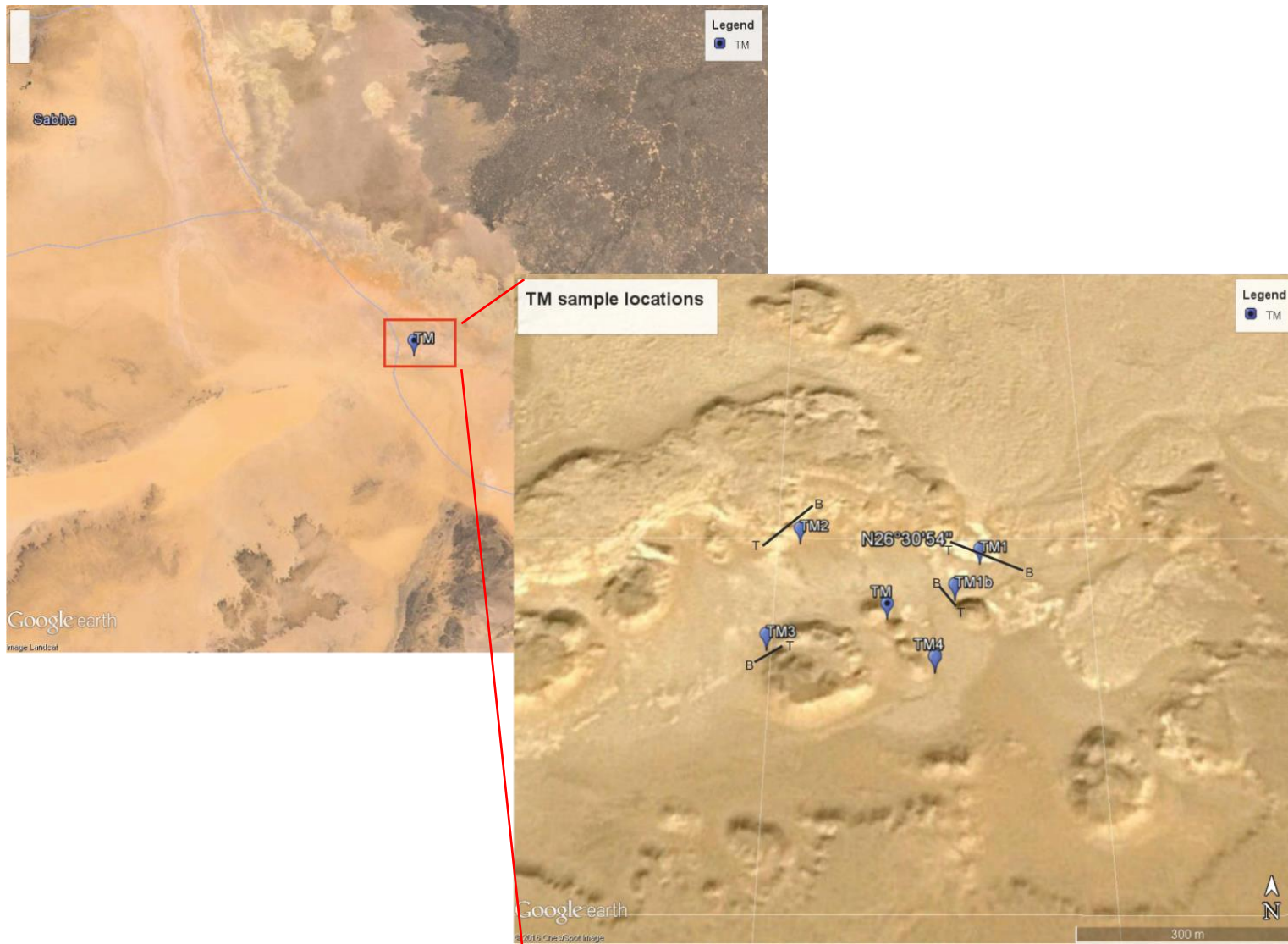


Figure 3.7 Google Earth images of the Tmessah section and sub-sections. T=section top, B=section bottom. Please refer back to Figure 3.1 (pg74) to see where the site locality is within the Fazzan Basin.



Figure 3.8 Google Earth images of the Brak section. Please refer back to Figure 3.1 (pg74) to see where the site locality is within the Fazzan Basin.

Bir al Zallaf (BZ)

This study site is named after the Ramlat az Zallaf sand sea and the inselbergs within it which are south of Wadi ash Shati. The site was first visited in 2007 and again in 2011. The main reason for revisiting the site was to conduct additional sampling to enhance the magnetostratigraphic survey due to gaps in the original section as a result of coverage by colluvium (Drake et al., 2011). The BZ site comprises three composite sections-Bir al Zallaf East, West and Twin Hills as seen in Table 3.4 and Figure 3.12. All the BZ sections are part of the Zazur Formation. The correlations between the three BZ sections based on lithological ties are summarised in Figure 3.13.

BZ-E

BZ-E contains deposits of the Sifar Member and Bir al Zallaf Member and also one deposit (AL12) which relates to the Sayl Member as seen in Figure 3.9. The lower and mid parts of the section are lithologically fairly homogenous, made up of pale brown, fine-medium grained sandstone. Some areas are rootleted and contain calcareous patches and gypsum. A large sampling gap of 7.2 m is seen between the lower Sifar Member and the Bir al Zallaf Member due to poor exposure of the deposits at this outcrop. This hiatus can be correlated to the deposits of the NE sub-section in the BZ-W section. The upper part of the section contains two laminated limestone units interbedded with pale-yellow (Munsell No. 5Y 7/3) to olive (Munsell No. 5Y 6/4) coloured, often poorly consolidated, sandstone.

BZ-W

This section is made up of two sub-sections, the Knoll section and the NE sub-section and contains deposits of the Sifar Member (Figure 3.10). The lower Knoll sub-section contains light greenish grey and pale yellow (Munsell No. 5Y 8/2) sandstones. The majority of these sandstones are coarse grained, locally pebbly and also rootleted. The mid part of the sub-section also contains local calcareous nodular development. The NE sub-section is lithologically fairly similar throughout. It is predominantly composed of light grey (Munsell No. 5Y 7/2), medium grained sandstones with calcareous nodules. It is also heavily rootleted in the mid-part of the section.

BZ-T

Like the BZ-W section, this section is part of the Sifar Member (Figure 3.11). The lower and mid parts of the section are lithologically similar, composed of friable pale-yellowish

brown and pale olive sandstone. The sandstones are typically coarse grained with some locally calcareous. Towards the top of the mid part of the section, two fossiliferous beds are evident containing mostly shell fragments of gastropods. The upper part of the section is also composed of coarse grained, pale brown sandstone, however these units are heavily rootleted with weak, incipient calcrete nodules also apparent.

<u>Field Season</u>	<u>Site</u>	<u>Sample ID</u>	<u>Total No. of samples</u>	<u>Total Section thickness/m</u>	<u>GE location</u>
Jan 2007	<u>East Hill (BZ-East)</u> Main Bir al Zallaf section	AL1-12	23	20.02	27°26'0.80"N 14°23'31.70"E
Jan 2011	Bir al Zallaf- additional samples	BZ20-28			
Jan 2011	<u>West Hill (BZ West)</u> Knoll section NE sub-section	BZ30-47 BZ60-69	28	8.34	27°25'47.50"N 14°23'12.20"E
Jan 2007	<u>Twin Hills (BZ-Twin)</u> Twin Hills near Bir al Zallaf	ALA1-6	21	18.72	27°24'38.20"N 14°21'58.10"E
Jan 2011	Twin Hills in-fill sampling	BZ80-94			

Table 3.4 Site details of the Bir al Zallaf sections. Note: The codes in the 'site' column correspond to the pins on the Google Earth image seen in Figure 3.12, pg90.

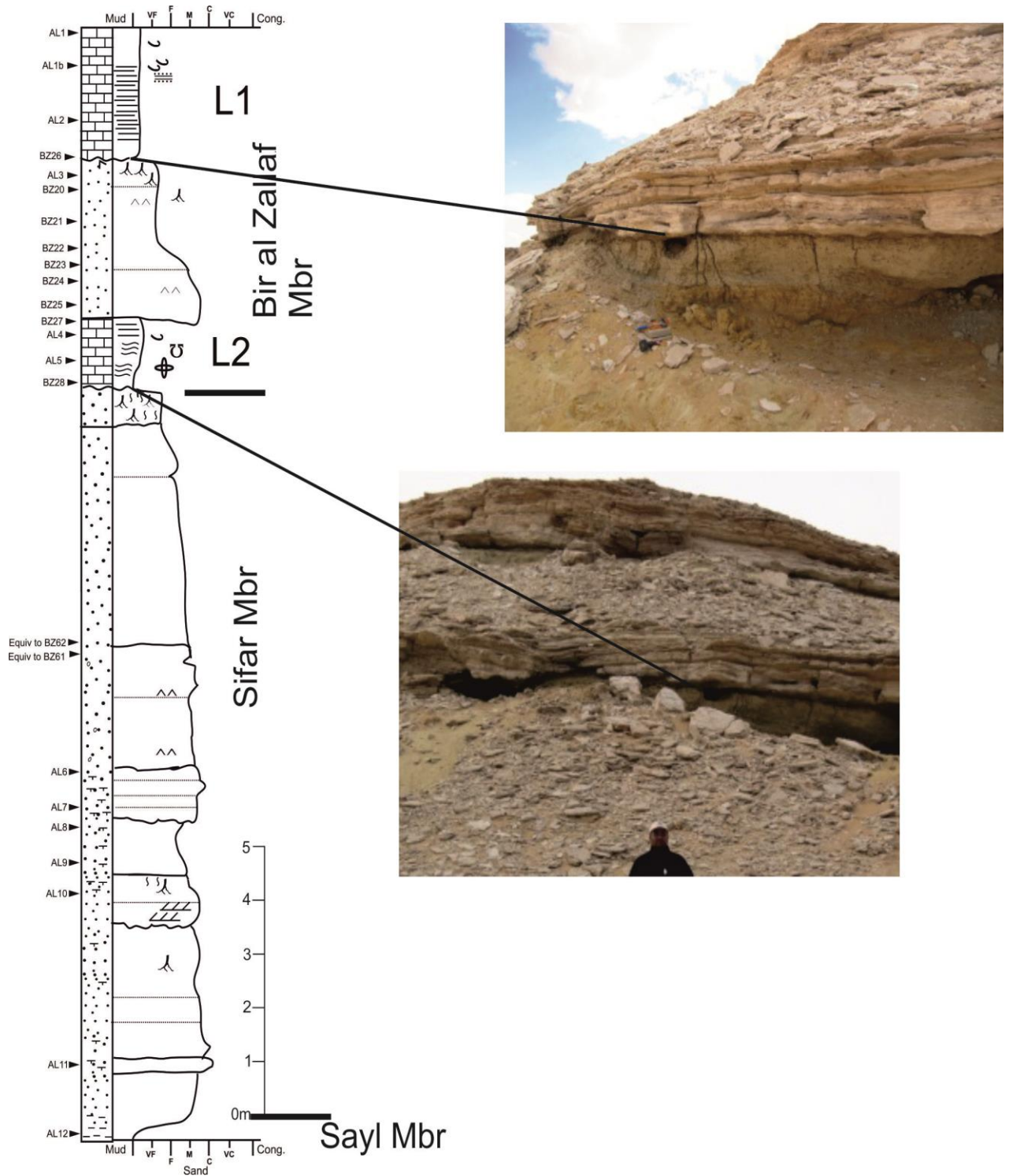


Figure 3.9 Stratigraphic log of the Bir al Zallaf-East section. This section corresponds to the Zazur Formation and contains deposits which relate to the Sayl Mbr (AL12), Sifar Mbr (AL11-AL6) and the Bir al Zallaf Mbr (BZ28-AL1). Please refer back to Figure 3.5 (pg81) for the log key.

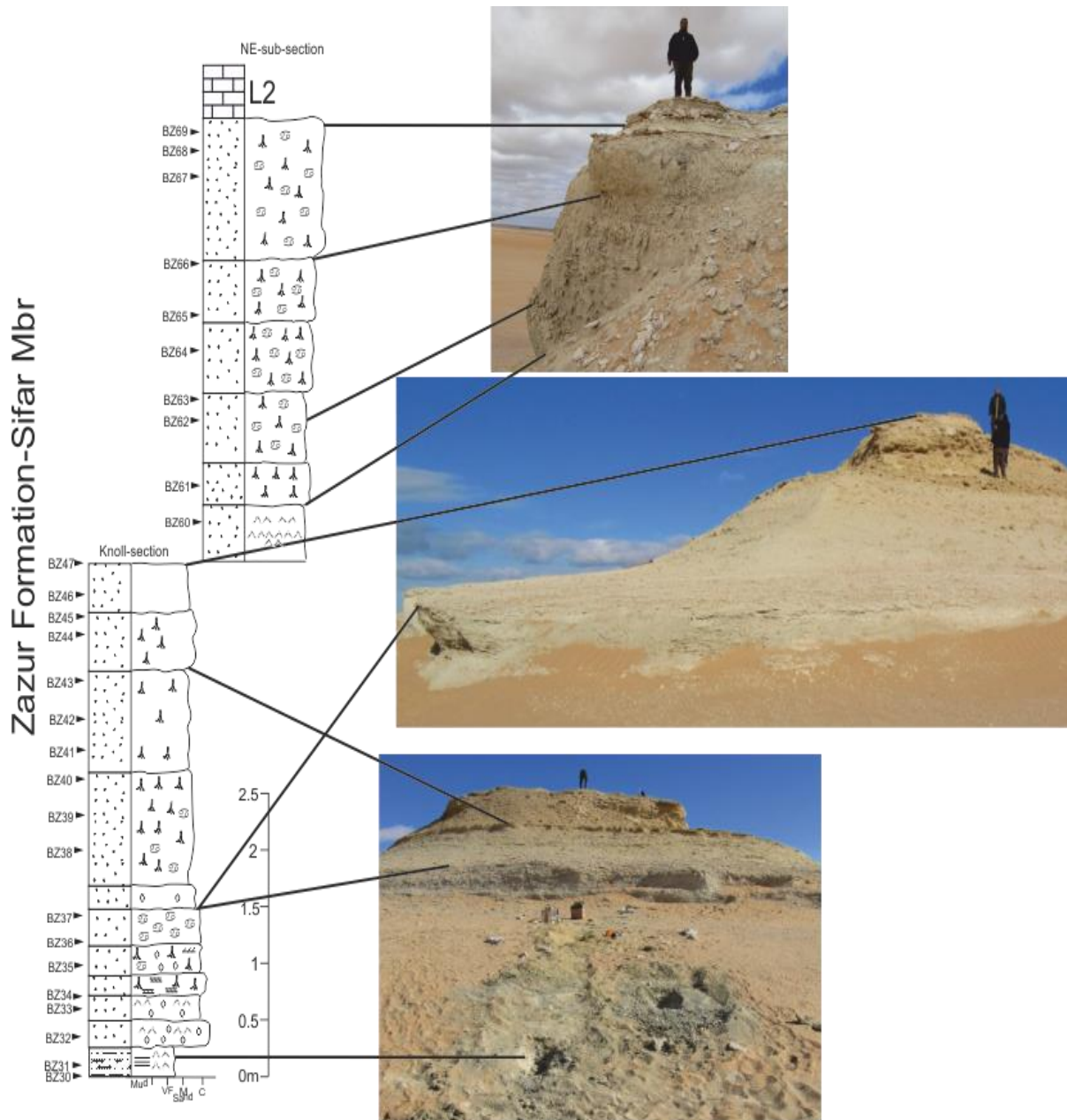


Figure 3.10 Stratigraphic log of the Bir al Zallaf-West Section. This section corresponds to the Sifar Mbr of the Zazur Formation. Please refer back to Figure 3.5 (pg81) for the log key.

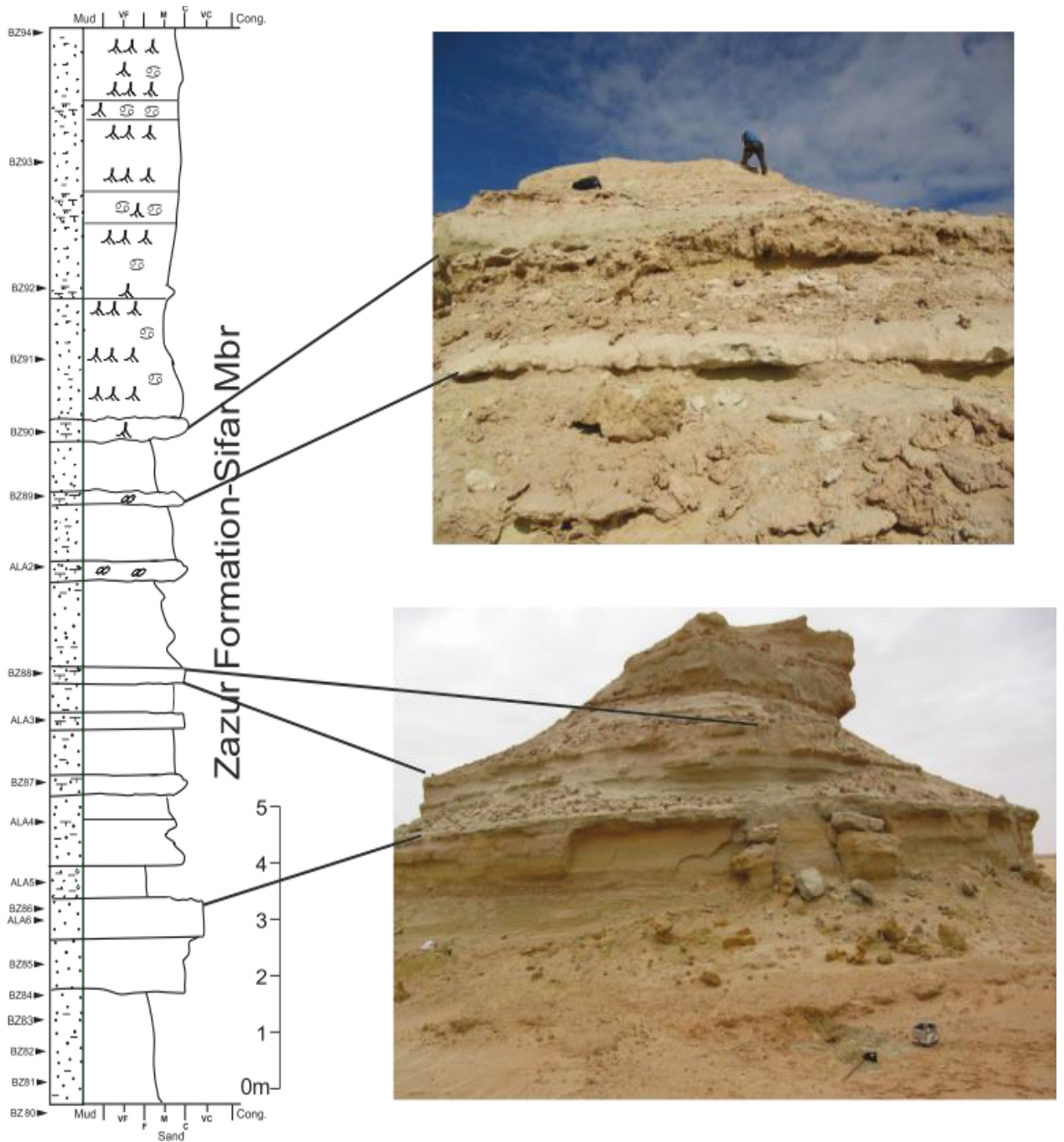


Figure 3.11 Stratigraphic log of the Bir al Zallaf-Twin Hills section. This section corresponds to the Sifar Mbr of the Zazur Formation. Please refer back to Figure 3.5 (pg81) for the log key.

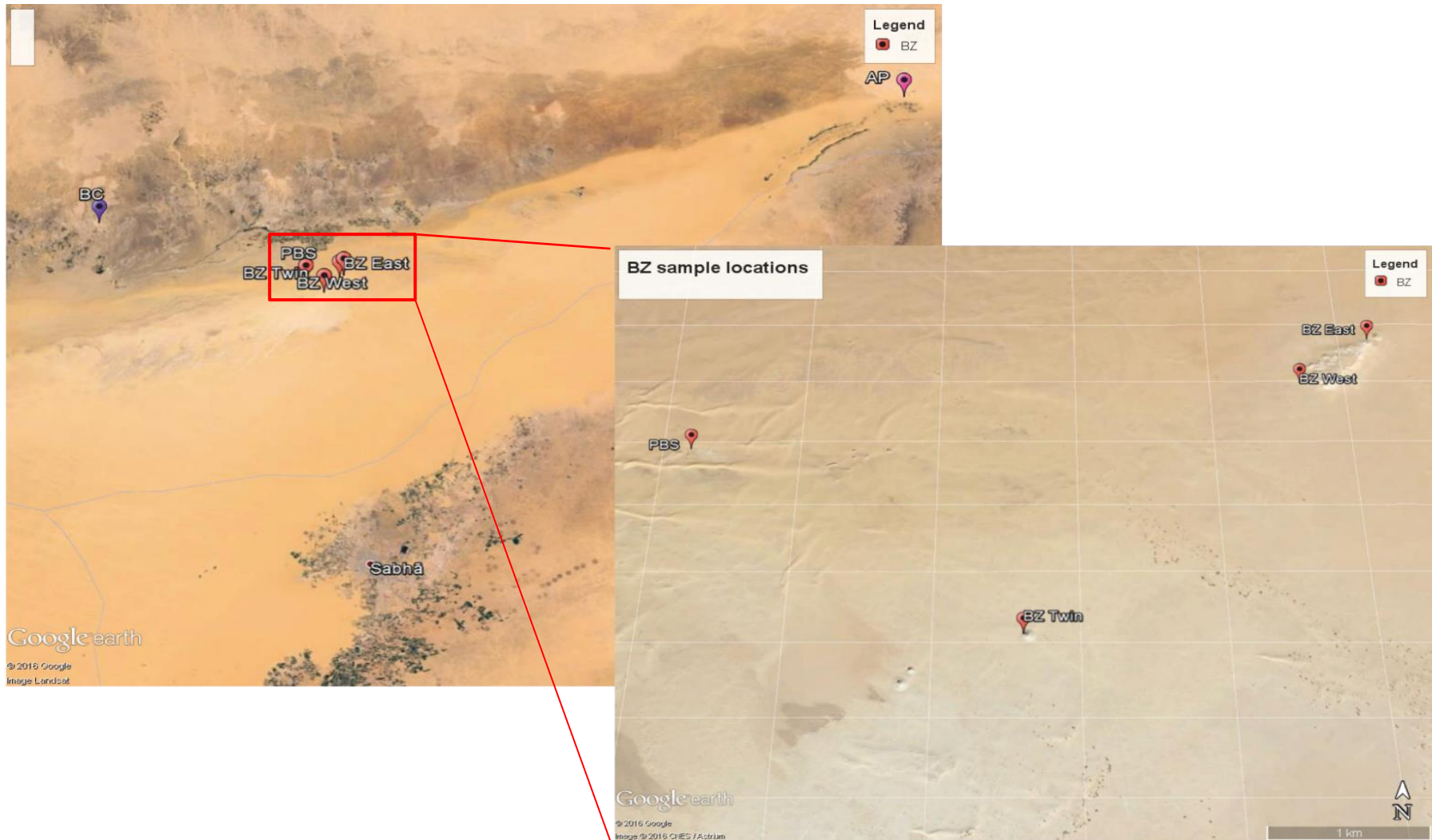


Figure 3.12 Google Earth images of the Bir al Zallaf sections. Please refer back to Figure 3.1 (pg74) to see where the site locality is within the Fazzan Basin.

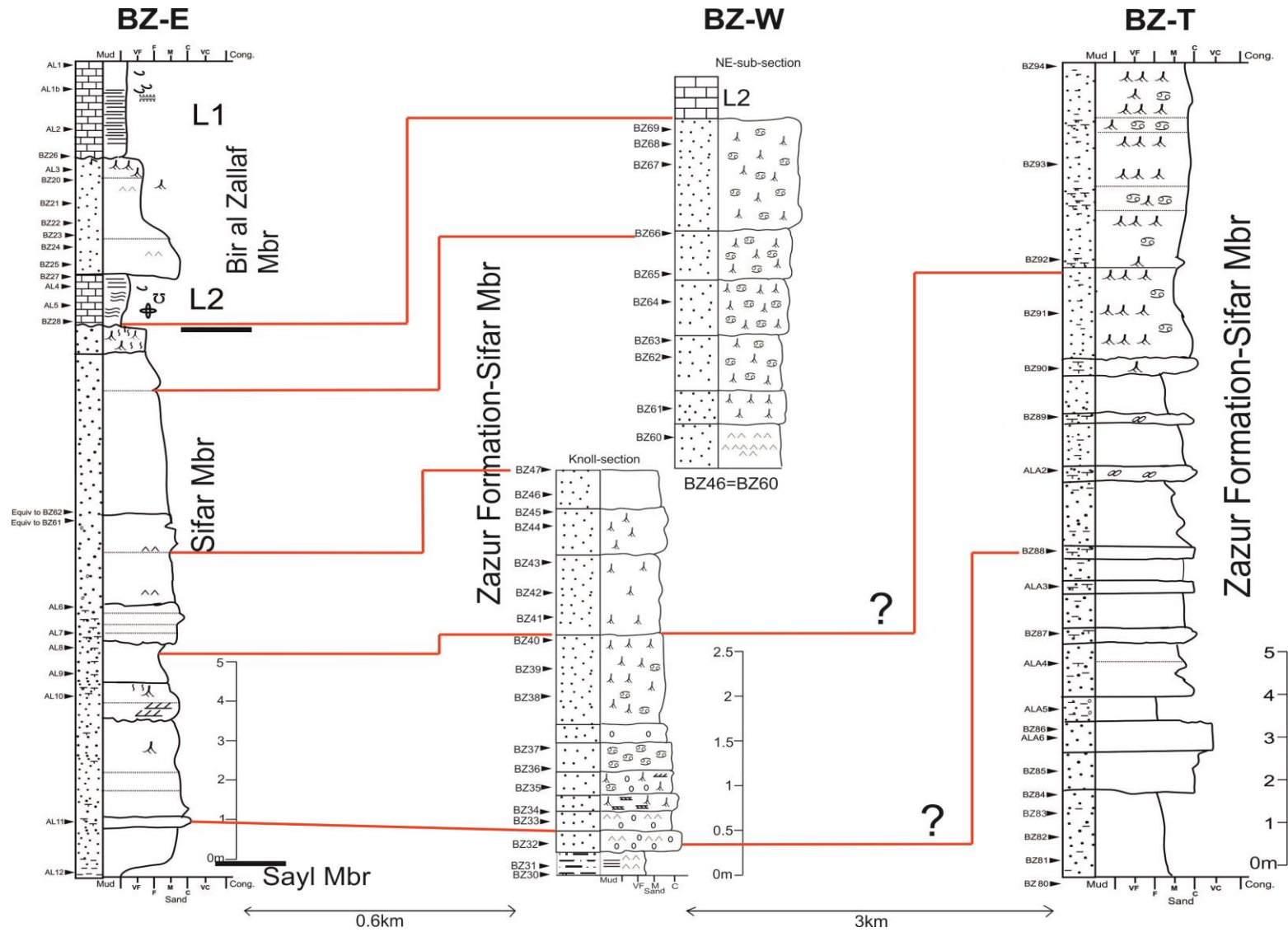


Figure 3.13 Possible lithostratigraphic correlations between the sections of Bir al Zallaf. Distance (km) between the sections is also noted. Please refer back to Figure 3.5 (pg81) for the log key.

Al Wafa (M)

Al Wafa, named after the oil field of the same name, is the most westerly site located on the edge of the Ubari Sand Sea (Figure 3.17). Deposits from the section relate to the Sifar Member of the Zazur Formation (Figure 3.14). Along with rock samples, 22 sand samples were also collected from this site (Table 3.5). The section unconformably overlies Triassic deposits of the Zarzaitine Formation (Aziz, 2000; Davidson et al., 2000). The lower part (6 m) of the section is composed of pale-brown to very-pale brown, medium grained sandstone interbedded with three well developed, sandy limestone (chalky-calcrete) units. The mid part of the section contains parallel laminated sandstones with some rootletting. Above this unit, sandstones with large scale aeolian cross-bedding are evident. This unit is then capped by a light-reddish brown (Munsell No.5YR 6/4) sandy limestone with some wavy/irregular bedding observed.

<u>Field Season</u>	<u>Site</u>	<u>Sample ID</u>	<u>Total No. of samples</u>	<u>Total Section Thickness/m</u>	<u>GE Location</u>
Jan 2008	M1	M1-4, NUS8-11-NUS8-10	34	13.13	27°59'47.49"N 10°50'16.24"E
	M2	M13-15			27°59'48.90"N 10°50'16.95"E
	M3	M19-26			27°59'50.41"N 10°50'19.02"E
	M4	NUS8-4-NUS8-1			27°59'49.22"N 10°50'19.68"E
Jan 2008	Al Wafa	M (sand samples)	22	-	28°, 00', 54.4"N 10°, 47', 53.6"E

Table 3.5 Site details of the Al Wafa section. Note: The codes in the 'site' column correspond to the pins on the Google Earth image seen in Figure 3.17, pg98.

Qarat al Mrar (QM)

This site is named after the area named by Gundobin (1985) in an exploratory booklet on the region. In total, five sections were sampled at this site but due to lack of time, sections QM3-5 were not analysed. Information on these sections can be found in Table 3 in the Appendix (pg287). The analysed sections of QM1-2 are located on opposite sides of a prominent bend in the northern Ubari Sand Sea approx. 23km apart (Figure 3.18). The site details of QM1 and QM2 are noted in Table 3.6. Both of these sections relate to the Zazur Formation with the QM1 section containing the Sifar Member and Bir al Zallaf Member and QM2 containing the Sifar Member and Sayl Member (Figures 3.15 and 3.16).

QM1

The QM1 section is made up of three sub-sections and sits on the Palaeozoic basement. It is thought this section represents the basin margin (SI Mbr). The lowest 5 m of the section is composed of predominantly pale and greyish brown siltstones with some units richer in chalky calcrete. Evidence of bioturbation is apparent in this part of the section, in particular in the limestone rich units. Rootlets, burrows and also a layer of reed casts are present. The upper part of the siltstone is laminated (parallel) and marks the transition into the overlying limestone unit. As in the limestones below, rootletting is evident. A sampling gap of 2.7 m occurs in the Bir al Zallaf Member of this section. This is due to Holocene lacustrine deposits which infill a valley cut into the older Bir al Zallaf Member deposits below (Drake et al., 2011). The uppermost part of the section continues in limestone with some rootletting and mottling seen. The deposits are also more reddened in comparison to the limestones below the Holocene infill, resulting in pinkish white (5YR 8/2) coloured deposits.

QM2

In comparison to QM1, QM2 is located more towards the basin centre at a lower elevation (~381 m today compared to QM1 at ~403 m). It is one continuous section which follows the bowl of a hill from east to west (Figure 3.19). The lowest ~2 m of the section which relate to the Sayl Member consists of fine-grained sandstones interbedded with siltstones. Some of these deposits are reddened, resulting in the deposits being assigned the colour of pale brown on the Munsell colour chart. In the lowest part of the Sifar Member fine-grained sandstones continue however, rootlets and some calcareous nodules are present. Overlying these deposits is a coarser grained, fossiliferous unit containing gastropods. The

mid part of the section is dominated by parallel-and ripple-laminated, rootleted sandstones which transition into predominantly cross-bedded sandstones. The upper most part of the section consists of sandstones interbedded with four horizons of layered and nodular calcrete rich deposits. Calcrete nodules are also locally developed in this part of the section.

<u>Field Season</u>	<u>Site</u>	<u>Sample ID</u>	<u>Total No. of samples</u>	<u>Total Section Thickness/m</u>	<u>GE location</u>
Jan 2008	<u>Qarat-al Mrar 1 (QM1)</u> 1	QM1-8	23	12.60	28°18'11.76"N 12°39'58.51"E
	2	QM9-15			28°18'10.24"N 12°40'0.67"E
	3	QM16-23			28°18'9.76"N 12°39'58.79"E
Jan 2011	<u>Qarat-al Mrar 2 (QM2)</u>	QM50-77	27	23.94	28°23'22.10"N 12°27'19.50"E

Table 3.6 Site details of the Qarat al Mrar 1/2 sections. Note: The codes in the 'site' column correspond to the pins on the Google Earth image seen in Figure 3.18/19, pg99/100.

As well as the six main sites, a number of 'modern' sand samples were also collected from additional sites (Table 3.7).

Additional Sites

<u>Year Collected</u>	<u>Sample</u>	<u>Location</u>
2011	SUS 2-5 Dune crest sediment ('Modern')	26°39'35.23"N 12° 9'24.14"E
2011	SUS 2-5 Inactive sand-dune flank ('Modern')	26°39'31.67"N 12° 9'32.73"E
2011	SUS 2-4 Sand F210-135	-
2011	Ziber Interdune ('Modern')	26°42'26.06"N 12°33'40.85"E
2011	Ziber Crest ('Modern')	26°42'26.06"N 12°33'40.85"E

Table 3.7 Year collected and location of additional samples collected.

Zazur Formation-Sifar Member

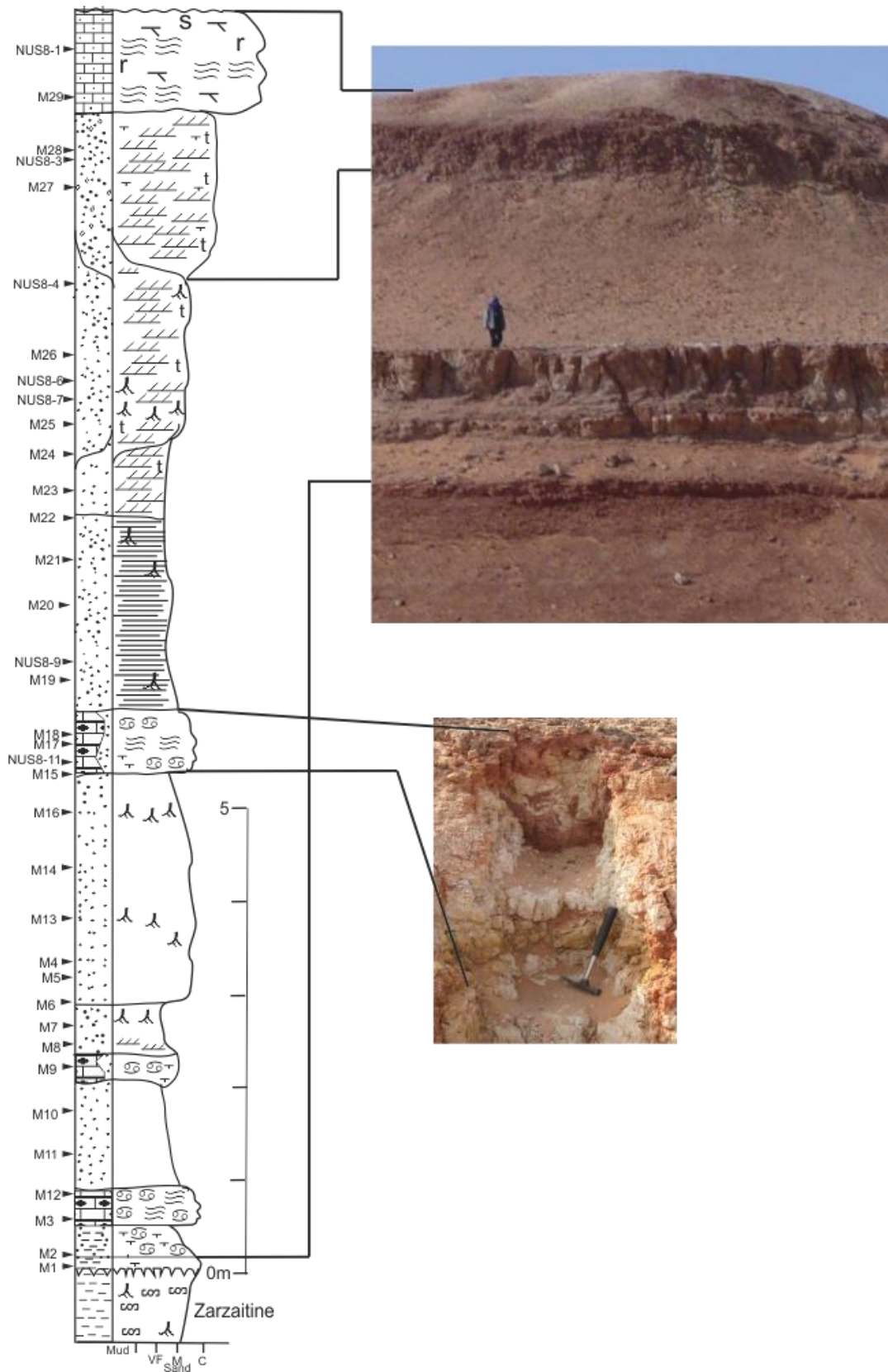


Figure 3.14 Stratigraphic log of the Al Wafa section. This section is composed of deposits which relate to the Sifar Mbr of the Zazur Formation. Please refer back to Figure 3.5 (pg81) for the log key.

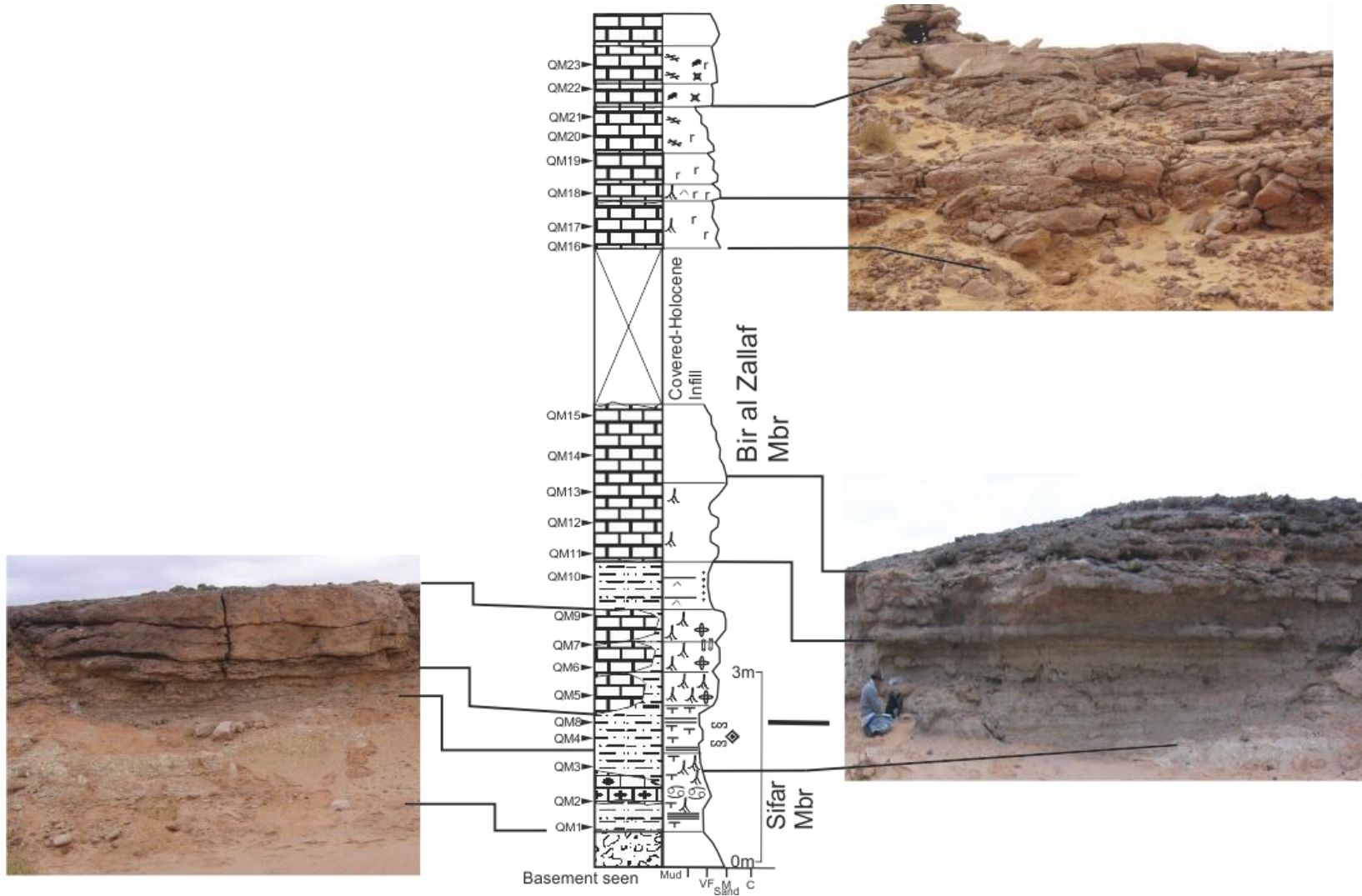


Figure 3.15 Stratigraphic log of the Qarat al Mrar-1 section. This section relates to the Zazur Formation. Geologic members which are part of this formation are marked on the log (Sifar Mbr QM1-8, Bir al Zallaf Mbr QM5-23). Please refer back to Figure 3.5 (pg81) for the log key.

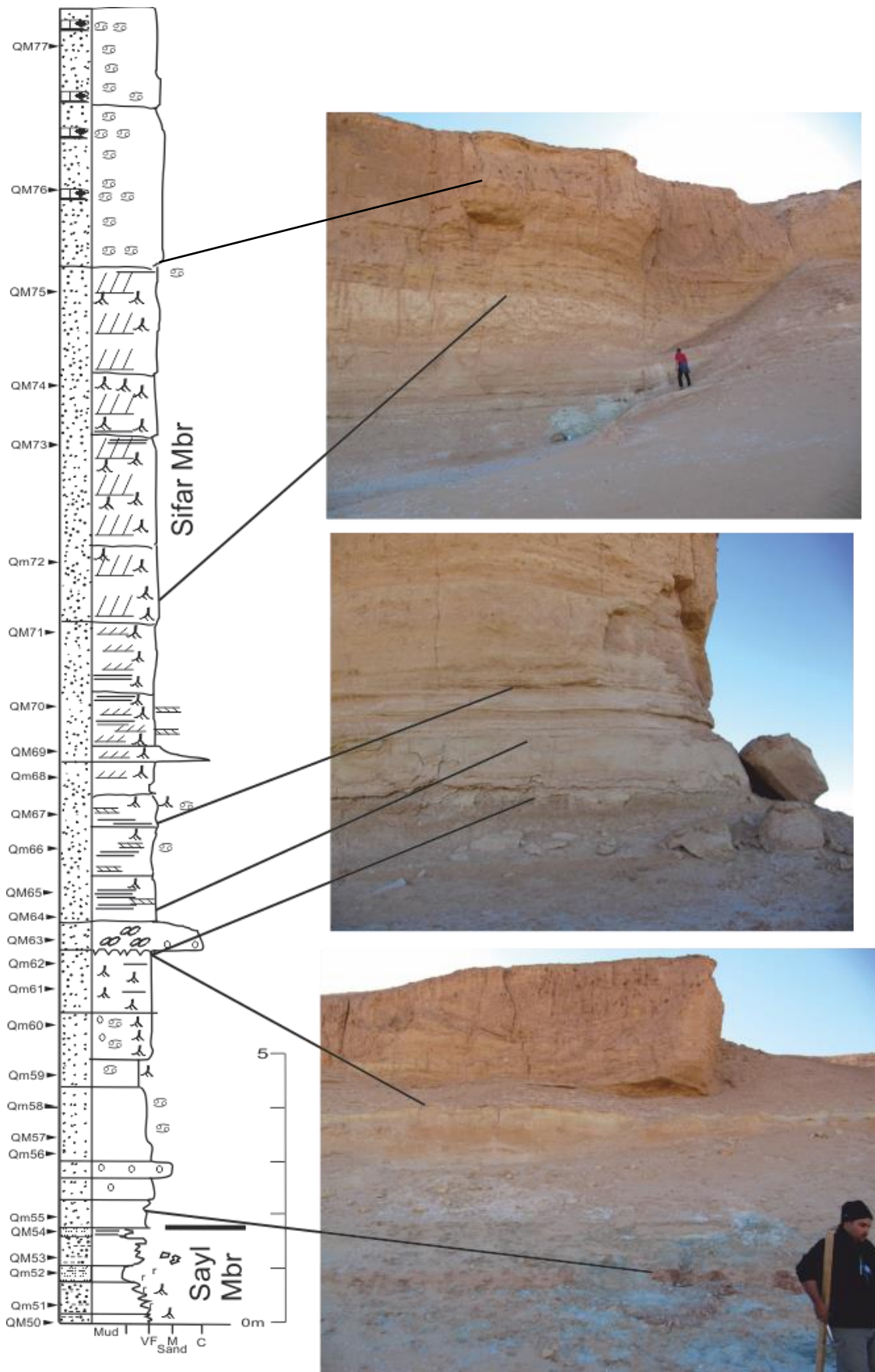


Figure 3.16 Stratigraphic log of the Qarat al Mrar-2 section. This section is composed of deposits which relate to the Sayl Mbr (QM50-54) and Sifar Mbr (QM55-77) which are part of the Zazur Formation. Please refer back to Figure 3.5 (pg81) for the log key.

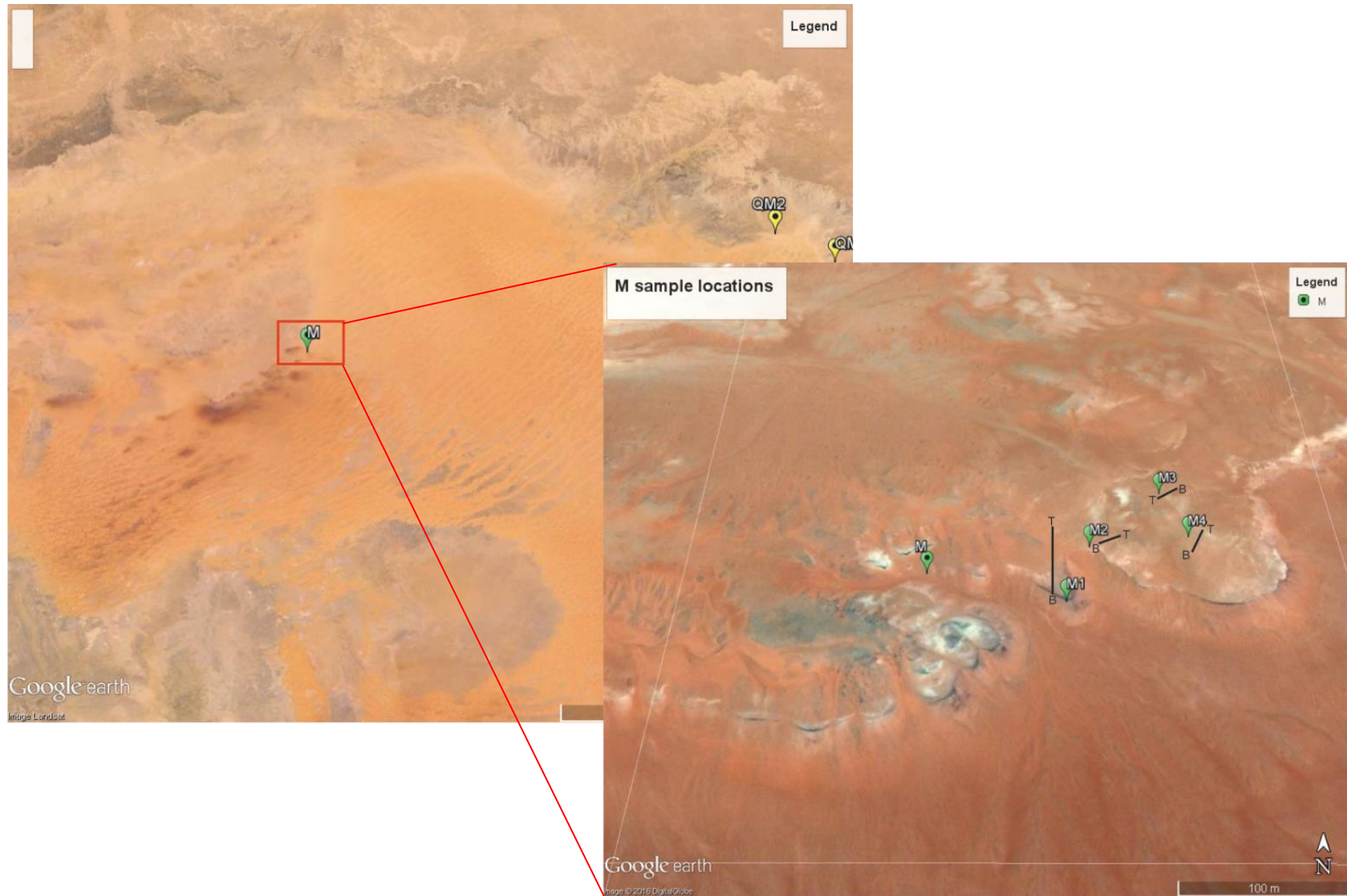


Figure 3.17 Google Earth images of the Al Wafa section and sub-sections. T=section top, B=section bottom. Please refer back to Figure 3.1 (pg74) to see where the site locality is within the Fazzan Basin.

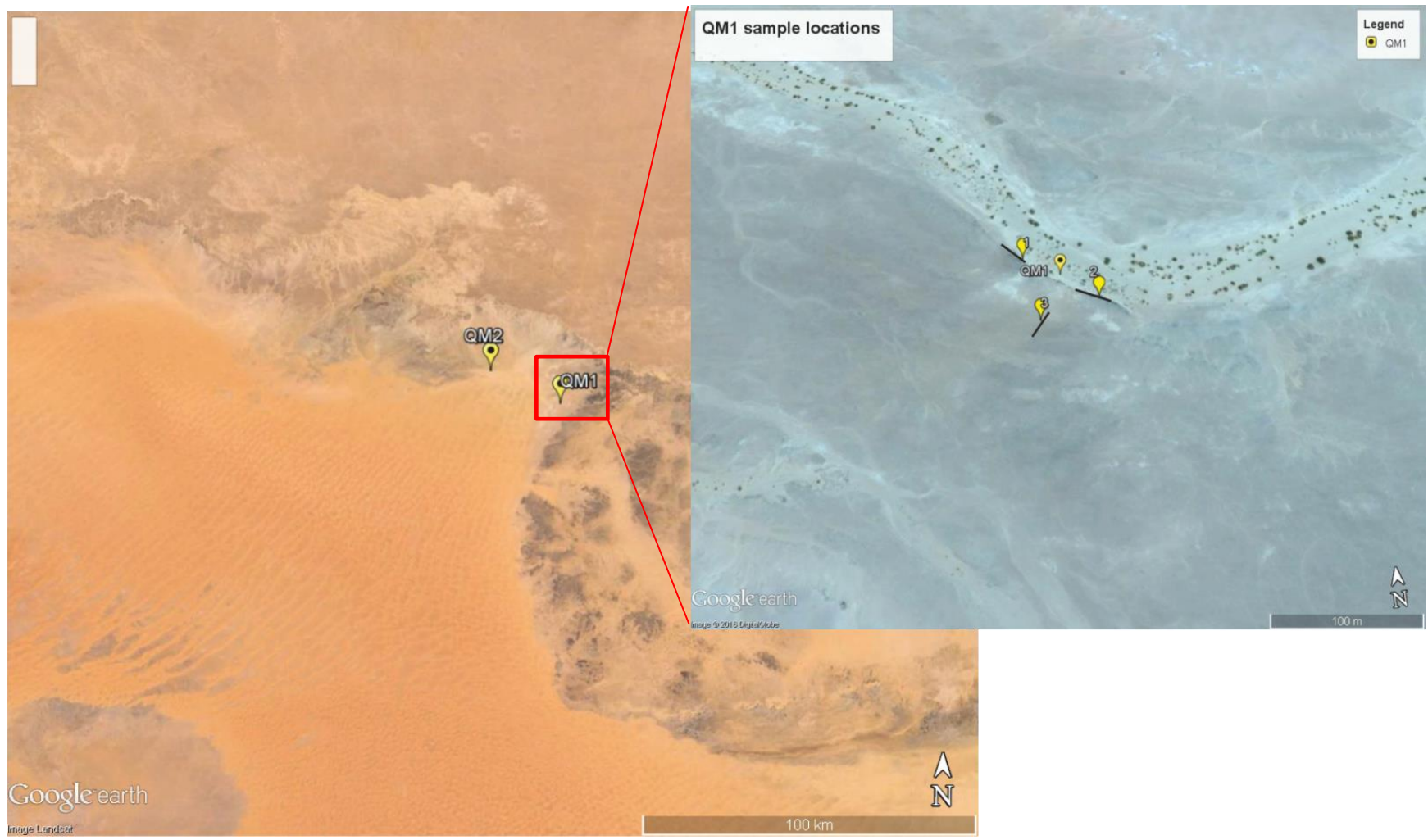


Figure 3.18 Google Earth images of the Qarat al Mrar-1 section and sub-sections. Please refer back to Figure 3.1 (pg74) to see where the site locality is within the Fazzan Basin.



Figure 3.19 Google Earth image of the Qarat al Mrar-2 section. The black line marks the bowl of the hill where the deposits were sampled. Sampling was conducted from east (base of the section) to the west (top of the section). Please refer back to Figure 3.1 (pg74) to see where the site locality is within the Fazzan Basin.

4 Research Methodology

It should be noted that most of the samples collected in the field were originally only going to be used for palaeomagnetic dating. During sample collection, many loosely consolidated deposits were coated with diluted sodium silicate solution ($\text{Na}_2\text{SiO}_3 \cdot n\text{H}_2\text{O}$) in order to help consolidate and harden the samples for transport. Unfortunately, no ‘clean’ samples were also taken and thus the presence of sodium silicate (NaSi) solution in some of the samples has limited the analyses that can be conducted on the deposits, in particular, stable isotope analysis due to the addition of oxygen.

As data collection took place over a number of field seasons, and due to the amount of time between field seasons and the commencement of this project, some palaeomagnetic measurements were conducted before the author began work on this PhD. To clarify what palaeomagnetic measurements and additional analyses were completed before this PhD project began and by whom, Table 4.1 is included below.

Laboratory Activity	Location	Person/company who conducted the activity	Conducted before PhD began (Y/N)
Palaeomagnetic measuring – samples from Ariel section	CEMP, Lancaster University, UK	M. Riding from Lancaster University	Y
Palaeomagnetic measuring – samples from Al Wafa section	CEMP, Lancaster University, UK	M. Riding from Lancaster University	Y
Palaeomagnetic measuring – samples from Qarat al Mrar 1 section	CEMP, Lancaster University, UK	M. Riding from Lancaster University	Y
Palaeomagnetic measuring – samples from Bir al Zallaf (AL/ALA coded samples)	CEMP, Lancaster University, UK	M. Riding from Lancaster University	Y
Palaeomagnetic measuring – samples from Brak section	CEMP, Lancaster University, UK	H. White	N
Palaeomagnetic measuring – samples from Tmessah section	CEMP, Lancaster University, UK	H. White	N
Palaeomagnetic measuring – samples from Qarat al Mrar 2 section	CEMP, Lancaster University, UK	H. White	N
Palaeomagnetic measuring – samples from Bir al Zallaf (BZ coded samples)	CEMP, Lancaster University, UK	H. White	N
Heavy Mineral measurements and analysis	CASP, Cambridge, UK	A. Morton	Y

Table 4.1 Summary to show what palaeomagnetic measurements were conducted by the author during this project and what measurements, including heavy mineral, were conducted before the start of this PhD. Note: CEMP – Centre for Environmental Magnetism and Palaeomagnetism. CASP – geological research company formerly known as Cambridge Arctic Shelf Programme.

4.1 Laboratory Analyses

4.1.1 Thin Section Analysis

Thin sections were produced following the Department of Geography's (University of Leicester) Laboratory Protocol. During thin section production, new thin sectioning equipment was installed and thin sections were produced following a new Laboratory Protocol. Both the original and new Laboratory Protocols are outlined below. All thin sections were produced by the author however, due to the amount of thin sections to be made, it was decided that 54 samples from the Bir al Zallaf sections would be made professionally by Wagner Petrographic, USA. Nine samples from the Brak section were also made professionally by Petrolab UK.

Sample Descriptions

Before samples were prepared for thin section analysis, the hand samples were first described visually and photographed. Each hand sample was also compared to the Munsell Soil Colour Chart.

Impregnation of samples

Samples were prepared for impregnation by first cutting the samples into a small enough piece to impregnate and then thoroughly cleaned and dried. Araldite glue was prepared using 100g of Araldite DBF resin to 33g of araldite XD716 hardener. Araldite DW blue colouring paste was added to the glue in order to highlight pore spaces when viewing the thin section under the microscope. Up to 3% by weight of colour paste could be added to the glue without significantly changing the properties of the material. The glue was poured over the samples which were then placed in a vacuum (-20 in Hg.) for ~15 minutes. The samples were then removed from the vacuum and left to dry.

Slide Preparation (Frosting)-Original Method

The slide was polished on a glass sheet with a paste of black silicon carbide 600 grit and water until a flat surface was achieved. The sediment sample was also ground down to a smooth, flat surface using a Metaserv 2000 grinder and then as above using the grit.

Slide Preparation (Frosting)-New method

Glass slides were frosted using a Logitech LP50 Precision Lapping & Polishing System. Four slides were placed on a PLJ2 lapping jig and held in place by a vacuum

chuck. The slides were then ground on a cast iron lapping plate with Silicon Carbide 1000 abrasive grit for ~20minutes. In total, three PLJ2 lapping jigs were used with a total of 12 slides frosted at one time.

Mounting the sample (Original and New)

The sample was mounted onto the slide using Araldite 2020 adhesive. Once mounted, the sample was placed on a bonding jig in order to firmly hold the sample on the frosted slide until the adhesive dried. Following the new method, before the sample was mounted onto the slide, the slide thickness was measured using a Mitutoyo Micrometer.

NOTE: It was noticed that, during stages of the thin section process that involved wetting the sample, a white precipitate was being produced when the samples were drying. This is likely to be gypsum or another salt or possibly NaSi. The precipitate produced caused problems when gluing the sample to the slide. To try and overcome this problem, after impregnation with Araldite glue, some of the samples were soaked in water for ~10 minutes so the NaSi could be drawn out of the sample before continuing with the thin section process. This approach appeared to be successful

Sample Cutting and Thinning (Original and New)

Once dried, any excess rock on the slide needed to be trimmed off using a PetroThin saw. The slide was positioned onto a vacuum chuck and when the vacuum pressure gauge reached between 12-15 inches of mercury the sample was cut off and ground down using the diamond wheel until a uniform thickness of 30 μ m was achieved. If the sample was still slightly too thick after using the PetroThin, the sample was ground by hand on a glass sheet with a paste of black silicon carbide 600 grit.

Following the new method, the sample was thinned down on the PetroThin to ~250 μ m. Once this thickness was achieved the slides were ground to 30 μ m thickness using a Logitech LP50 Precision Lapping & Polishing System as described below.

Firstly 250ml of Silicon Carbide 1000 abrasive grit to 2 litres of deionised water was measured into the autofeed cylinder. The cast iron lapping plate was ground to a uniform thickness of 0 μ m using the abrasive to allow for removal of any rust development. The precision jig was first zeroed on the granite master block. Once zeroed, the precision jig was placed onto the PLJ2 lapping jigs and set to the correct height. This height was calculated by adding the slide thickness, the end sample thickness (30 μ m) and the

thickness of the abrasive, which was calculated to be 16µm. Slides of the same thickness and preferably a similar lithology were placed onto the lapping jigs held in place by the vacuum chuck. The lapping jigs were then placed on the lapping plate and the slides ground to 30µm. The time the samples were left on the jigs to grind down to the desired thickness was dependent on the lithology of the sample, e.g. for softer limestones ~15minutes was needed, whereas for harder sandstones composed predominantly of quartz >1 hour was required.

All finished thin sections were examined using a Nikon Eclipse LV100ND microscope fitted with a Nikon Digital Sight DS-Fi2 camera. NIS Elements software package was also used to aid petrographic analysis.

Staining

It has been noted in previous studies of the Al Mahruqah Formation e.g. Abdullah (2010), that deposits from the Brak and Bir al Zallaf sites contain a high percentage of dolomite. In order to test for the presence of dolomite, samples BC15a,19,23 and BZ samples which also were analysed using XRF, were stained with alkaline Alizarin red S following the method in Tucker (1988, pg99). Dolomitic areas are stained purple while calcite remains unstained.

4.1.2 Stable Isotope Analysis

For samples thought to contain little or no NaSi, a small sub-sample was broken off from each of the sediment samples to be analysed. The sub-samples were powdered using a pestle and mortar in order to extract carbonate. Typically <80µm lacustrine carbonate material is used for analysis as it is comprised of mostly calcites with clays (Gasse et al, 1987; Anderson and Leng, 2004). The ground sample was wet sieved with deionised water through a 75µm sieve to remove unwanted particles that may ‘contaminate’ the sample. After each sample had been sieved the sieve was placed in an ultrasonic bath with deionised water in order to ensure the sieve was thoroughly cleaned. The <75µm material was filtered and oven dried for 4 hours at 65°C. After drying, samples were placed in a Mini Lyotrap Freeze Drier for a minimum of 24 hours to ensure the samples were completely dry. Once dry, the <75µm material was powdered in a ball mixer mill. Triplicate samples were analysed using a SERCON Hydra 20-20 continuous flow isotope ratio mass spectrometer. CO₂ gas from the acidified samples was also obtained using a Gilson autosampler system. The total sub-sample weight used in analysis was approx. 2mg, however for samples which were analysed and produced a low signal, samples were re-run with a greater sample amount. The increased sample amount used was dependent on the signal value. Exetainers containing the 2mg of sample were flushed with He to remove air. The samples were then acidified with ~0.2ml of 100% phosphoric acid prepared following McCrea (1950). Samples were then left at 50°C for three hours in order to equilibrate before measurement. Calibration was via IAEA calcite standard CO8. The precision of carbonate analysis is 0.08‰ for δ¹⁸O and 0.04‰ for δ¹³C. Isotope values are reported per mil (‰) vs VPDB.

4.1.3 Palaeomagnetism

Sample Collection and Preparation

In the field, hand samples were collected from outcrops using a hammer and chisel. On each sample, a suitable flat surface was orientated using a magnetic compass and a specially designed orientation staff. The dip of the reference surface was determined to an accuracy of ±0.5°. The horizontal reference (right) direction (the strike), using a magnetic compass, was determined with respect to magnetic north

Sample preparation and magnetic measuring was conducted at Lancaster University’s Centre for Environmental Magnetism and Palaeomagnetism (CEMP). In the laboratory, hand samples were re-orientated in dental plaster using an orientation device.

Once set, a diamond saw was used to cut the samples into 2.2 x 2.2 x 2.2 cm cubic palaeomagnetic specimens. The majority of samples were cut wet. Some samples however, were not strong enough to withstand wetting and so were cut dry. Before cutting, some fragile samples, mostly with sandy, mudstone composition were impregnated with NaSi solution which was hardened by heating at 40°C (Hounslow and McIntosh, 2003). Once hardened, the samples were cut into slices and NaSi solution reapplied to the cut sides in order to consolidate the material. Once dry, the slices were cut into cubic palaeomagnetic specimens using a diamond saw. The use of NaSi solution as a hardener, although capable of causing changes in magnetic susceptibility, the remanent magnetisation is not influenced significantly (Kostadinova et al., 2004). No bedding correction was applied as all the beds were horizontal. The magnetic deviation of each sample (the strike) was however corrected using the International Geomagnetic Reference Field Model (IGRF) in order to correct for the magnetic deviation of the compass.

Sample Measurements

202 specimens from the QM1, M, some of the AP and the AL/ALA coded samples of the BZ-E and BZ-T sections were measured before this PhD was undertaken by M. Riding and V. Karloukovski. These specimens were demagnetised using alternating field (AF) demagnetisation along with thermal demagnetisation (TD). Specimens were first subjected to TD up to between 230-400°C. After this, demagnetisation was continued using a Molspin Alternating Field Demagnetiser (tumbling method). This technique can be used to erase NRM carried by grains that have coercivities less than the peak demagnetising field (Butler, 1992, pg82). Progressively larger peak fields were applied ranging from 5-70mT in increments of 5-10mT. After each demagnetisation step the remnant magnetisation was measured along with the specimen's susceptibility. On the whole, this method proved ineffective for many of the specimens likely due to the presence of high coercivity haematite or possibly greigite (Butler, 1992, pg83).

Samples not subjected to AF were demagnetised using TD alone. The natural remanent magnetisation (NRM) of each specimen was measured using a CCL GM400 3-axis cryogenic magnetometer (noise level ca.0.002mA/m) using multiple sample positions. Specimens from each horizon were subjected to TD using a Magnetic Measurements Ltd. Thermal Demagnetiser caged in Helmholtz coils. On the whole 2-3 specimens from each horizon were measured depending on whether a clear polarity could be identified along with the characteristic remanent magnetisation (ChRM). Heating stages conducted during

TD was dependent on how the intensity of the sample reacted to heating. In general, TD was conducted in 100°C increments from 0°C to 300-400°C and then in 30-50°C increments up to 580/630°C or until the sample was demagnetised and/or the measured intensity dropped below the noise level. The magnetic susceptibility was measured after each heating stage to allow monitoring of mineralogical changes (Hounslow and McIntosh, 2003). This low field magnetic susceptibility (K_{lf}) was measured using a Bartington MS2 susceptibility meter.

Sample Analysis

Demagnetisation data was analysed visually using stereographic and Zijderveld orthogonal plots. The demagnetisation plots were inspected and a decision made as to whether the ChRM was reversed (R) or normal (N) with the following sub-categories used based on the uncertainty of the specimen: R?, R??. ?, N?, N??. The demagnetisation results were analysed and secondary remanent magnetisation components and ChRM directions isolated using principal component analysis in LINEFIND (Kent et al., 1983, MS Dos version by M. Hounslow, 1991, version 3.0). This program 'utilises the variance of the magnetisation measurement, available from the repeated magnetisation measurements on each specimen axis' (Hounslow and McIntosh, 2003). Both linear trajectory fits and great circle data has been used to define palaeomagnetic behaviour.

Classes were assigned to the specimens based on the behaviour of the specimen during demagnetisation. The specimens were classified into either s or t-class, with specimens classed as s-class having a ChRM line fit, while all t-class had a great circle (GC) plane, which ideally, passed near the expected ChRM direction. S-class specimens are ones that had suitable linear trajectory line fits and were split into three classes (s1-s3) based on the quality of the data, s1 being the best quality (Hounslow et al., 2008). T-class behaviour was classified based on the scatter and the visual length of the demagnetisation points about the GC (Hounslow et al., 2008). As for s-class, one of three classes could be assigned (t1-t3), with t1 indicating the best quality data.

Once all specimens had an assigned line class, the mean directions were computed using PMAGTOOLS Version 4.2a (Hounslow, 2006). A combined mean direction was calculated using Fisher statistics (Fisher et al., 1987). This is calculated using both the fitted-lines from s-class specimens (ChRM) and the GC plane information from t-class specimens. A stability test, known as a Reversal Test, was conducted on the data. This test was run on the data as it is important to establish that the palaeomagnetic directions

analysed are antimodal and not contaminated by other components (McFadden and McElhinny, 1990). No fold test could be completed as the zero dip of the sections prevents this. The VGP pole of the newly computed mean was also determined. The VGP pole should ideally be near to poles of a similar age and thus can be used as a test of directional reliability.

The final stage of palaeomagnetic analysis was to determine the virtual geomagnetic pole (VGP) latitude which 'represents the latitude of individual VGP in coordinates of the overall palaeomagnetic pole' (Opdyke and Channell, 1996, pg91). This was calculated separately for s-class and t-class specimens. For s-class specimens, it was calculated by converting the ChRM directions into VGP latitude with respect to the combined mean direction of the section (Hounslow and McIntosh, 2003). This was also done for t-class, but was calculated using the point on each specimen's GC plane that was used in the calculation of the combined mean (Hounslow and McIntosh, 2003).

4.1.4 Additional Methods Explored

Along with the methods described above, additional laboratory methods were explored with the aim of improving correlation between the sections.

X-ray fluorescence (XRF)

Samples that were quartz-rich and contained little carbonate were chosen for XRF analysis. In total, XRF analysis was conducted on 26 samples from the Ariel (seven samples), Al Wafa (six samples) and Bir al Zallaf (13 samples) sections. Each of the samples were first crushed using a flypress to a grain size of no greater than 2-3mm. Approximately 60ml of sample was placed into agate cased sample pots and four agate balls placed in each. The material was then ground to a fine powder in a Retsch Planetary Mill.

Following grinding, pressed powder pellets were produced so that trace element concentrations could be measured. Approximately 7g of powder was combined with Moviol 88 solution in order to bind the powder into small lumps. The mixture was then placed into a 32mm diameter die and a plunger added. The complete die was placed inside a hydraulic press and 10 tons per square inch of pressure applied in order to compact the powder into pellet form. The pellet was removed from the die and left to dry for 3-4 hours.

Along with pellets, fusion beads were also made as these are the best way of determining major element concentrations in rocks, providing a homogenous medium and

removing mineralogical effects. Firstly 4-5g of powder was placed in a 10ml glass vial and dried overnight at 110°C to remove low-temperature absorbed volatiles. Loss on ignition (LOI) was then performed on the samples. The weight of the fused Al₂O₃ ceramic crucible was recorded along with the crucible plus sample before and after ignition for 1.5 hours in a muffle furnace at 950°C. Once LOI had been determined, samples could be prepared for the final stage of the process. 3g of dried lithium tetraborate flux, plus a previously determined weight loss of the flux (due to the hygroscopic nature of the flux), in this case 0.0147g, was accurately weighed into a Pt/Au crucible. 0.6g of ignited powder was then weighed on top of the flux and mixed together. The crucible was placed onto a Spartan gas burner and heated. During heating the crucible was agitated to remove powder from the sides and bubbles from the liquid. Once fully homogenised, a casting plate burner was ignited and a Pt/Au casting dish heated until it reached operational temperature. The contents of the crucible, using titanium tongs, was poured into the casting dish. Forced air cooling was then switched on for 3-4 minutes until the fusion bead was seen to part from the casting dish. Finished samples were run on a PANalytical Axios Advanced XRF spectrometer.

As previously discussed, NaSi solution was applied to a number of samples in the field. Although every effort was made to use ‘clean’ samples, it is probable that some of the samples used in XRF analysis may contain this contaminate. In order to see how the presence of NaSi in the samples may affect the XRF results, a sample of the NaSi solution was run on an ICAP-Qc quadrupole ICP mass spectrometer to determine its geochemical composition. The results of the analysed sodium silicate sample show a very interesting and complex chemistry. Because of this, difficulties may arise when unpicking the chemistry of possibly contaminated samples, especially as no ‘clean’ samples are available for comparison

Laser Particle Size Analysis

The laser sizing technique has been noted for its efficiency (Konert and Vandenberghe, 1997; Di Stefano et al., 2010) and thus was the chosen particle size technique in this study. Unfortunately, truly unconsolidated material was only available from the Al Wafa section as many samples were consolidated either naturally or by NaSi solution and any attempt at disaggregating the sample may produce false grain sizes. Analysis was completed on the set of 25 sand samples from Al Wafa and five ‘modern’

sand samples (Table 3.7). The 'modern' samples are known to be aeolian in origin and hence can be used as a control when analysing the data.

The samples were dry sieved through a 2 mm sieve to isolate the <2 mm fraction. A sub-sample of the <2 mm grains were taken from each sample and placed in a beaker with 5% Calgon solution (sodium hexametaphosphate) in order to disperse the grains and create a suspension. The sample was then placed into the reservoir of the Coulter LS32 Particle Size Analyser and measured. The results produced were analysed using GRADISTAT Version 8.0 (Blott, 2010).

Pollen

Pollen can act as an excellent biomarker in sedimentary rocks and hence the presence of pollen grains in the sections was explored. Six samples, three from Tmessah (TM7, 18, 26), two from Qarat al Mrar (QM6, 11) and one from Ariel (AP6) were sent to Prof. Ulrich Salzmann at the Department of Geography, Northumbria University to see whether any pollen could be extracted. Unfortunately, no identifiable pollen grains or spores were found as the samples were too corroded and weathered. The poor preservation could be due to in-situ weathering or may have occurred due to post-depositional processes.

Heavy Mineral Analysis

Except for at a few well exposed sections, magnetostratigraphic dating conducted in this research project is unlikely to be able to fully resolve the dating of the outcrops in the basin. Because of this, an alternate means of reliable correlation is needed. Changes in provenance of the sand may enable stratigraphic distinction of packages of aeolian sand and provide a way of regional stratigraphic correlation. This can be achieved by investigating heavy mineral and magnetic mineral inclusions. A set of 25 sand samples collected from the Al Wafa section were sent to Andy Morton at HM Research Associates for analysis.

5 Results: The Shabirinah and Brak Formations

5.1 Palaeoenvironmental Indicators: Petrography and Palaeohydrology

The focus of this chapter is the results obtained from the AP, TM and BC sections which correspond to the Shabirinah and Brak Formations. The petrographic results and, where available, geochemical results of the Formations and their associated members are examined below in chronological order.

5.1.1 Shabirinah Formation

5.1.1.1 Ariel Section

The lower Ariel section is not assigned to a certain member within the Shabirinah Formation as seen in Figure 5.10. In thin section (TS) the deposits are composed of quartz clasts which range in size from coarse silt to granules with the majority of deposits containing clasts of fine-to-medium sand-sized. The clasts are predominantly moderately sorted and are sub-angular to sub-rounded (Plate 5.1-A). Some of the clasts are corroded at the edge as a result of dissolution (Hogg et al., 1992), with clasts occasionally containing mineral inclusions of muscovite (e.g. AP22, Plate 5.1-B) and zircon. Many of the clasts have an unusual surface fracture pattern. The cause of this is unknown but a possible explanation is discussed in the ‘results’ section of the Appendix (pg 288). In the lower part of the section some of the deposits are almost completely clast supported. Matrix supported deposits are more prevalent from ~AP14 upwards as shown in Figure 5.2. The deposits are partially infilled with an often Fe-oxide rich, patchily developed muddy cement (Plate 5.1-C). The cement of the deposits near to the top of this half of the AP section are less reddened than the underlying deposits and more carbonate-rich with poorly developed micritic rim and pore-filling cements. Some structureless, blackened isotropic cement areas (Plate 5.1-D) occur in the deposits believed to be organic in origin. Further study using techniques such as fluorescence microscopy and vitrinite reflectance (Potter et al., 2005, pg 270) are needed to help identify the origin of this organic matter. Small, wavy cracks <20µm in width and of various lengths are observed in some of the reddened deposits near the base (Plate 5.1-A). These cracks are unfilled, often cutting through the cement and around the outside of clasts suggesting they developed after deposition. Based on the deposit type (clay-rich mudstones/sandstones) and the size of the cracks they are assumed to be shrinkage/synaeresis cracks caused by drying of the deposit or compaction (Plummer and Gostin, 1981). However, they may also relate to shrinkage caused by NaSi treatment.

Although evidence of bioturbation, in particular rootletting, is apparent in the hand samples as described in Table 5.1, little evidence is seen in the TS.

Due to the limited amount of carbonate within the deposits, and in particular the presence of NaSi, isotope analysis was not performed. XRF analysis was however conducted on six of the samples from the AP section (and one from the upper K Mbr). One line of evidence investigated when researching aridity of the Sahara is the presence and geochemical composition of dust, as Saharan dust has an identifiable composition (Stuut et al., 2009; Ehrmann et al., 2013). The samples chosen for XRF from this section and from the BZ/M sections of the Zazur Formation were predominantly sandy in nature. Sandy horizons can often be indicative of more arid conditions, although they can also form via fluvial deposition. To investigate whether elements typical of Saharan dust were present in the sandy horizons XRF was employed; unfortunately the results failed to yield this information with low concentrations of typical dust elements (e.g. Ti, Fe). Despite this, useful data was still obtained from the XRF analysis. It should be noted that the values of Na are viewed with caution due to the possibility of NaSi contamination.

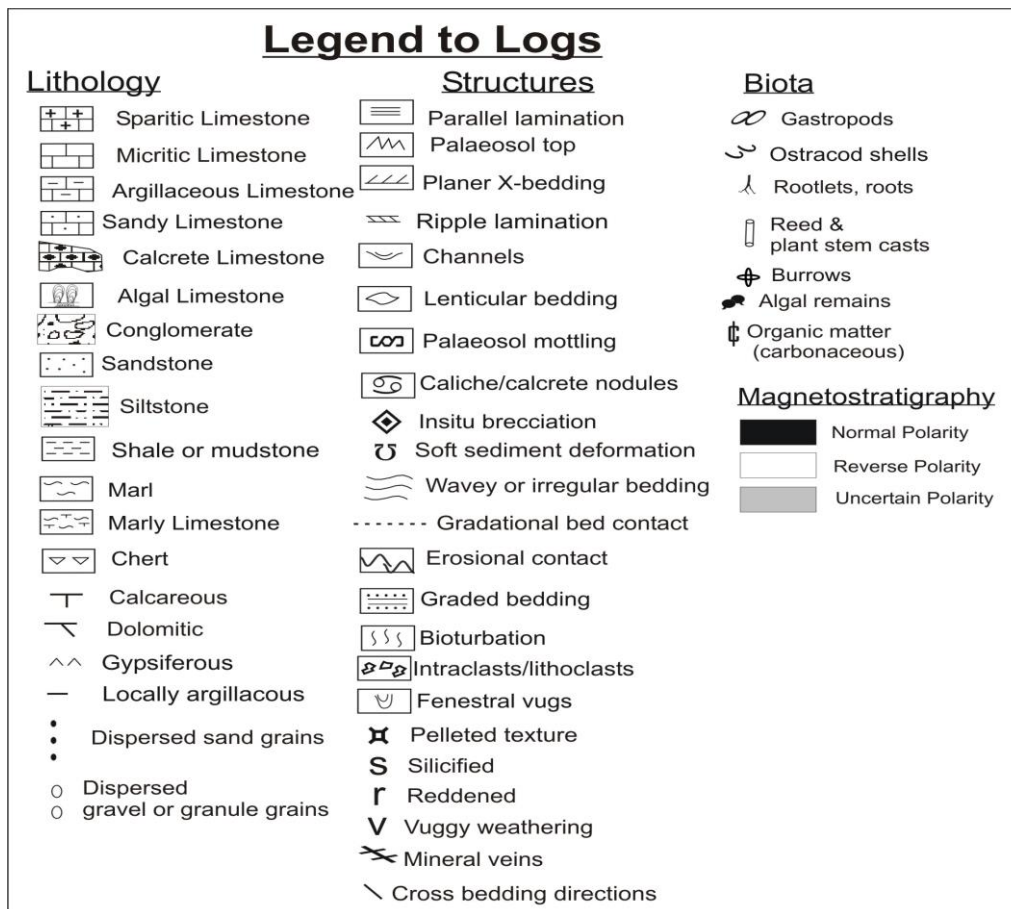


Figure 5.1. Legend for all sediment logs.

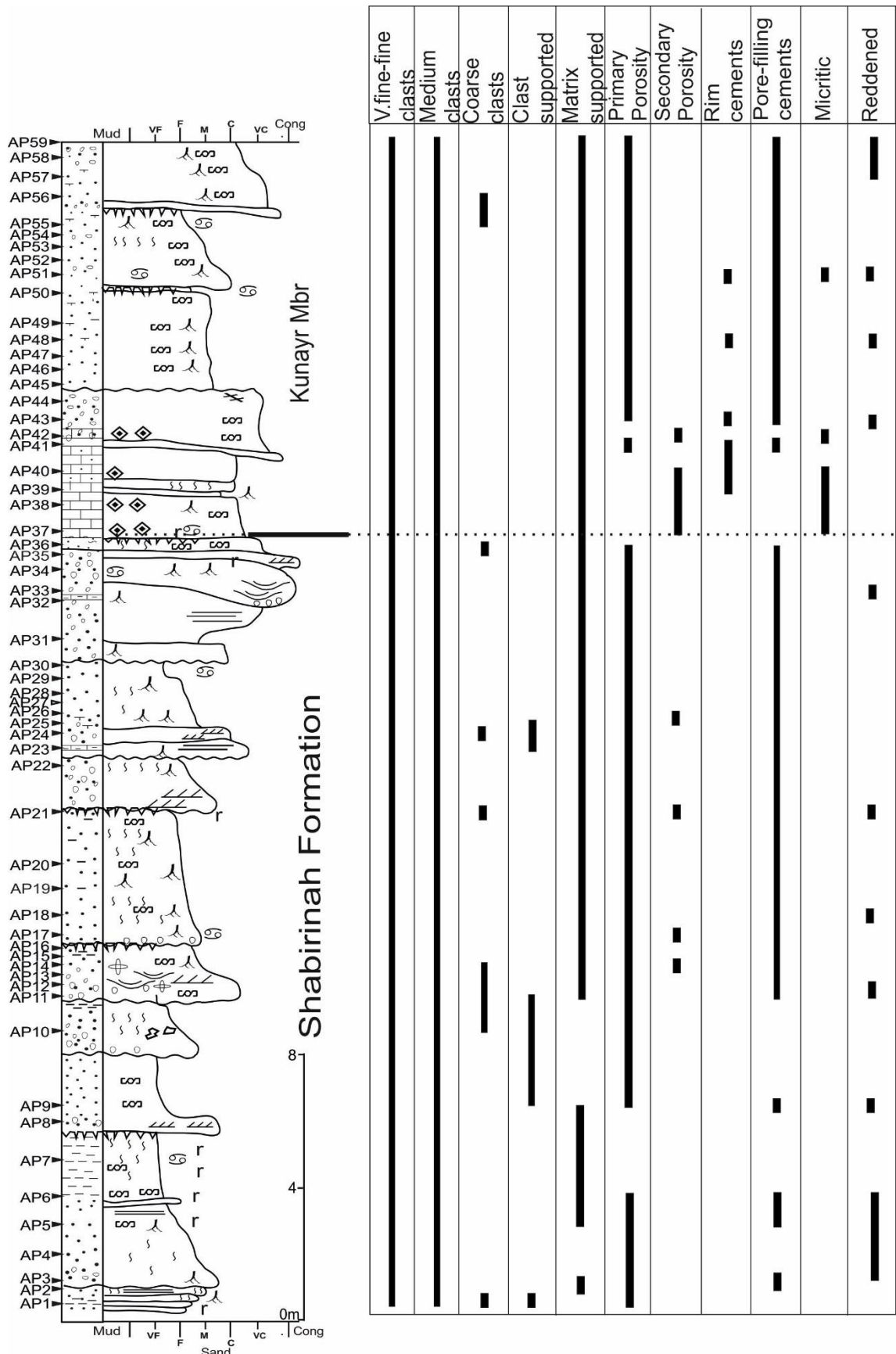


Figure 5.2. Key characteristics of the thin sections from the AP section. Note: the clast size refers to grains of sand-sized material. Please refer back to Figure 5.1 (pg113) for the log key.

<u>Shabirinah Formtion (AP1- 36)</u>	
Colour	Reddening of the samples prevalent near the base and decreases up the section with deposits predominantly light gray (5Y 7/2) or pale/light brown (2.5Y 7/4)
Texture	Clastic-sandstones, mudstones (near the base), mottled
Grain size/sorting	Typical medium sand-sized. Granule/pebble clasts in some beds. Also muddy units. Clasts predominantly sub-rounded and moderately to well-sorted
Composition	Quartz-rich
Structures	Parallel laminations-sporadic, likely lost due to bioturbation
Key Features	Bioturbation-rootlets and rhizoliths (Fig 5-Appendix, pg289). Black (organic?) patches/veins in some deposits (Fig 6-Appendix, pg289).
NaSi coating	Present on nearly all of the deposits
<u>Kunayr Member (AP37-59)</u>	
Colour	Typically white (WHITE 2.5Y) or pinkish gray (5YR 7/2)
Texture	Clastic-sandstone, microclastic limestone, some brecciation, some mottling
Grain size/sorting	AP37-42- fine-medium sand-sized, some coarse-granule, well sorted. AP43-59-coarser grained, more moderately sorted
Composition	AP37-42-carbonate-rich, AP43-59-quartz-rich, some calcite cement and carbonate nodules, some clays
Key Features	Bioturbation in AP43-59
NaSi coating	Evident on some of the more loosely consolidated samples

Table 5.1. Hand sample descriptions of the SHF and K Member of the AP section.

XRF results reveal the deposits to have a large percentage (>83%) of Si (quartz). The problem with sediment chemistry is that a large increase in one component causes a diluting effect on the others (Rollinson, 1993, pg141; Norry et al., 1994). This can be overcome by dividing the dataset by Al (Norry et al., 1994). Two interesting points regarding the Ariel samples are evident from the XRF results. The first is the relatively large abundance of the elements Nb and Nd (see Table 8- Appendix, pg300). The values are particularly high in AP3 and AP27, 29, 31 with the latter three samples spanning 2.15 m of the section. A correlation matrix (see Table 5.2) used to identify the most highly correlated element pairs was produced for the samples. A positive relationship was observed between Nb/Nd and the other rare earth element La with the elements Ti, Al and Fe. The second point of interest is the relatively high amount of Al in the samples with the higher values occurring in the deposits with greater amounts of Nb/Nd such as AP3/31 as shown by the strong positive relationship in Table 5.2. Al also correlates well with K whereas Si has a strongly negative (-0.96) relationship with Al. Figure 5.2 shows K/Al vs Si/Al. While a small range of values between 0.06-0.15 are observed for K/Al a much

larger spread is seen for Si/Al. The three highest values are from AP8, 10 and 44 with the two lowest from AP3 and 31.

	SiO ₂	TiO ₂	Al ₂ O ₃	Fe ₂ O ₃	MgO	K ₂ O	CaO	Ba	Cr	La	Nb	Nd	Sr	V	Zn	Zr
SiO ₂	1.00															
TiO ₂	-0.92	1.00														
Al ₂ O ₃	-0.96	0.97	1.00													
Fe ₂ O ₃	-0.88	0.89	0.85	1.00												
MgO	0.19	-0.23	-0.14	-0.38	1.00											
K ₂ O	-0.82	0.66	0.81	0.49	0.14	1.00										
CaO	0.11	-0.27	-0.17	-0.47	0.73	0.18	1.00									
Ba	0.05	-0.13	-0.16	-0.27	-0.35	-0.02	0.33	1.00								
Cr	0.09	-0.11	-0.16	0.21	-0.82	-0.33	-0.81	-0.05	1.00							
La	-0.76	0.66	0.73	0.66	-0.57	0.71	-0.43	0.09	0.38	1.00						
Nb	-0.91	0.90	0.97	0.72	-0.05	0.90	-0.11	-0.15	-0.23	0.76	1.00					
Nd	-0.84	0.76	0.81	0.76	-0.55	0.73	-0.45	0.06	0.31	0.97	0.81	1.00				
Sr	-0.51	0.43	0.40	0.62	-0.73	0.09	-0.39	0.23	0.56	0.58	0.24	0.54	1.00			
V	-0.52	0.68	0.55	0.74	0.01	0.08	-0.27	-0.43	-0.12	0.01	0.38	0.19	0.22	1.00		
Zn	-0.92	0.95	0.97	0.89	-0.34	0.71	-0.40	-0.20	0.08	0.82	0.92	0.87	0.52	0.53	1.00	
Zr	-0.74	0.94	0.85	0.83	-0.26	0.40	-0.43	-0.24	-0.04	0.47	0.75	0.59	0.37	0.79	0.87	1.00

Table 5.2. Correlation matrix of the AP deposits. Values in bold are those discussed in the text.

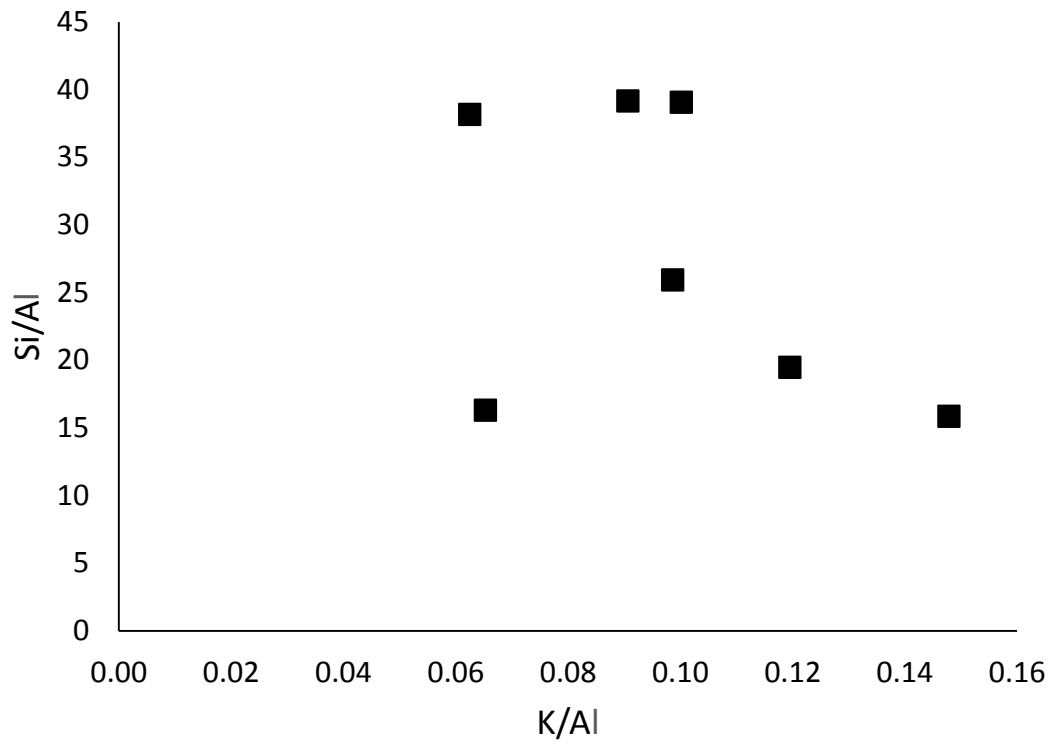


Figure 5.3. Aluminium normalised Si-K diagram.

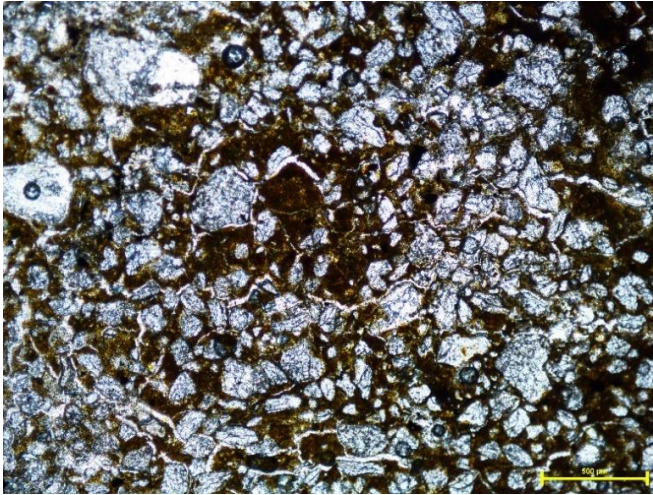
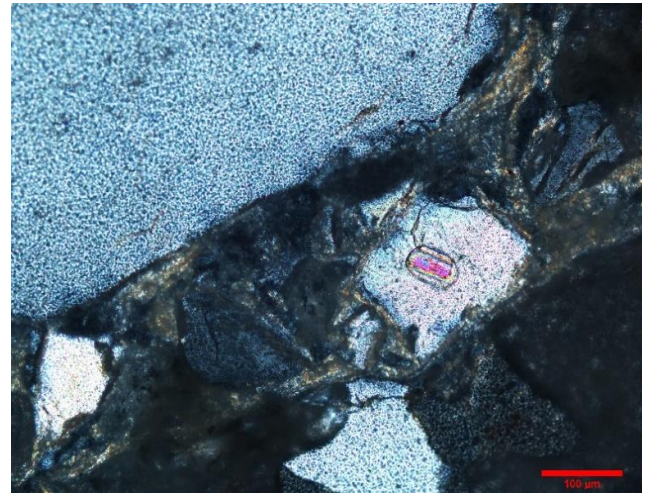
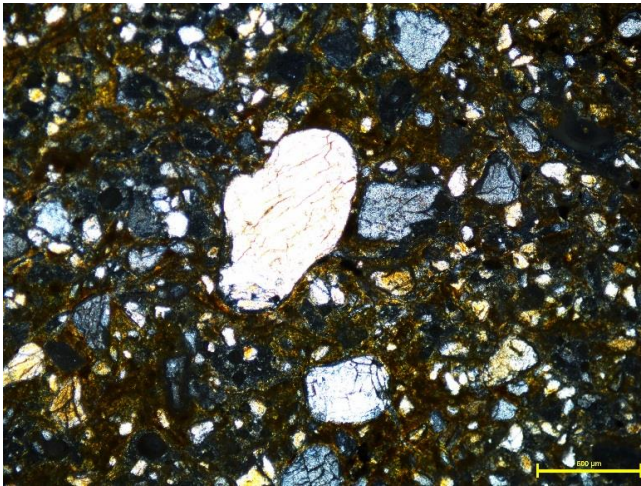
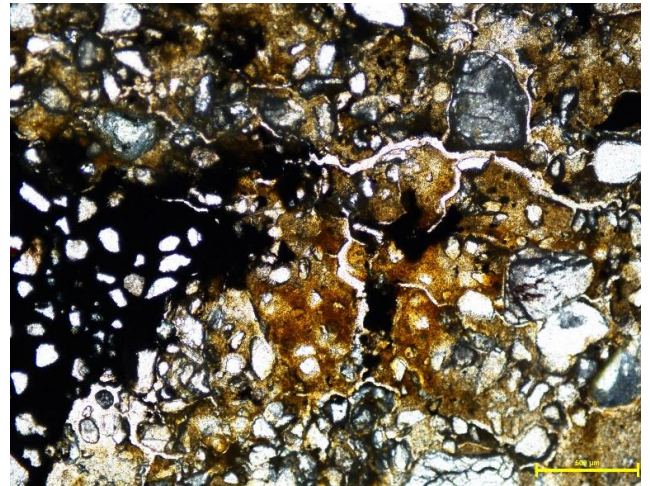
A**B****C****D**

Plate 5.1. Shabirinah Formation. AP section. A-AP6, typical texture of the deposits with moderately sorted clasts in a reddened cement. Small shrinkage cracks are seen cutting through the cement and around the clasts (x5, plane polarised light (ppl)). B-AP35, quartz clasts with mineral inclusion (zircon) (x20, cross polarised light (cpl)). C-AP14, interparticle porosity infilled with iron-rich, fine-grained, muddy cement (x5, cpl). D-AP21, to the left: blackened, isotropic, organic-rich cement. Shrinkage cracks also evident cutting across the matrix (x5, cpl). Scale bar is 500 μ m in all photomicrographs except in B where it is 100 μ m.

5.1.1.2 Maharshim Member (M Mbr)

Just four deposits from the Tmessah section make up this member, however differences between the lower two and upper two deposits are apparent in TS. Within the lower two deposits (TM5/1) quartz clasts are in a floating matrix and have bimodal sorting, especially in TM1 (Plate 5.2-A). Coarse-silt-to-very fine sand-sized clasts are sub-angular-to-sub-rounded while larger clasts ($\geq 500\mu\text{m}$) are sub-rounded to rounded. The porosity of these two deposits appears to be primary with some pore spaces unfilled. The cement is composed of micrite which is better developed in TM1 and in places is reddened, likely due to the presence of haematite or clays. Nodular reddened areas are also present (Plate 5.2-B). Within TM5, areas of granular spar are also seen (Plate 5.2-C), often increasing in size towards the centre of the pore where more space is available for growth (McLaren, 1993). The overlying deposits of TM4/2 contain fewer clasts than lower two deposits and are more carbonate-rich. The clasts are unimodal, composed of sub-angular to sub-rounded quartz (Plate 5.2-D). The clasts are in a floating matrix of homogenous micrite which is reddened in patches. Secondary cements are also evident in these samples with spar crystals infilling the majority of laminoid fenestral voids (Plate 5.2-E). Reddened nodular or 'glaebule' areas are also present which are surrounded by unfilled circumgranular cracks (Plate 5.2-F).

Successful stable isotope analysis was performed on all deposits from the TM section and hence values are available for all the associated members of this section (see Table 5-Appendix, pg297). The deposits of this member have isotopic values differing by 1.5‰ for $\delta^{13}\text{C}$ and 5.4‰ for $\delta^{18}\text{O}$. The base deposit records the most depleted $\delta^{18}\text{O}$ value but the most enriched $\delta^{13}\text{C}$ equalling -8.8‰ and -4.8‰ respectively. A large jump in isotopic value, especially in $\delta^{18}\text{O}$ which becomes enriched by 4.6‰, occurs between the base deposit and its neighbouring deposit. Little variation occurs in the $\delta^{13}\text{C}$ and $\delta^{18}\text{O}$ in overlying deposits as seen in Figure 5.5/5.6, especially between TM1-TM2 with $\delta^{18}\text{O}$ values differing by 0.8‰ and just 0.4‰ for $\delta^{13}\text{C}$.

5.1.1.3 Stromatolite Member (STR Mbr)

The three uppermost deposits of this member were extremely friable and had begun to fracture with NaSi loosely consolidating the samples. Thin sections were attempted to be produced from these deposits but due to their fragility proved unsuccessful. The thin section descriptions below therefore only refer to limestone deposits of this member.

Analysis of the thin sections show the deposits to be almost entirely composed of dense micrite. Voids and ‘ghost features’ (Plate 5.3-A), caused by dissolution (Flugel, 2010, pg280) are present giving the deposits a vuggy porosity. Some of these voids have open porosity but most are partially filled by secondary microspar pore-filling cements lining the voids (Plate 5.3-B). Some irregular, partially filled fenestral voids are also present. Rounded peloids of various shapes are present, especially in TM7/8. The peloids are 250µm or less in size and lack internal structure. In some areas the peloids result in a clotted fabric. Based on these characteristics it is likely the peloids are ‘lithic peloids’ caused by reworking or ‘microbial peloids’ with precipitation triggered by microbes (Flugel, 2010, pg112-113). It is difficult however to fully establish the origin of the peloids as they display a number of characteristics belonging to a variety of peloid types (see Flugel, 2010, pg 112). Clusters of peloids are evident in TM7 cemented together by meniscus cements forming an aggregate grain (Plate 5.3-C). Pore spaces are evident in between some of the peloids. Fragments of ostracods, and possibly some bivalve, are present in all of the analysed thin sections (Plate 5.3-D). The centre of the ostracods have been replaced by micrite and the shells have also been partially replaced by secondary microspar cement. Shells that have only undergone dissolution and not replacement has led to the formation of ‘mold peloids’ (Plate 5.3-B). Laminations typically observed in thin sections of stromatolites (Casanova and Hillaire-Mercel, 1993; Brook et al., 2011) are not apparent in any analysed.

Isotopic analysis was conducted on all deposits from this member, including TM11-9 which were noted to have been coated by NaSi in the field. The values obtained from these deposits seem reliable, especially when compared to the untreated carbonates of the member. It is likely the lack of porosity of these clay-rich mudstones resulted in the NaSi having minimal effect on the deposits. Little variation (1.3‰) in both $\delta^{13}\text{C}$ and $\delta^{18}\text{O}$ occurs throughout this member despite the lithological changes (see Table 5 in the Appendix, pg297 for raw isotopic data). More variation occurs in the $\delta^{18}\text{O}$ values of the carbonate deposits differing by 0.9‰ compared to a difference of 0.4‰ in $\delta^{13}\text{C}$. More variation is also apparent in the $\delta^{18}\text{O}$ values of the mudstones in comparison to the $\delta^{13}\text{C}$

values differing by 1.2 and 0.6‰ respectively. The $\delta^{13}\text{C}$ values of the mudstones are slightly enriched in $\delta^{13}\text{C}$ compared to the underlying carbonates with an 0.6‰ increase occurring between the uppermost carbonate (TM8) and the basal mudstone (TM11). Regression analysis was completed on the deposits of this member, however the correlation coefficient (r^2) equalled 0.27 indicating very poor covariance between $\delta^{18}\text{O}$ and $\delta^{13}\text{C}$.

<u>Maharshim Member</u>	
Colour	Pinkish white (5YR 8/2). TM5 light reddish brown (2.5YR 6/4)
Texture	Clastic/microclastic. Some crystalline areas. Marly limestone and siltstone. Mottled
Grain size/sorting	Fine grained. Well sorted
Composition	Carbonate-rich, some quartz clasts
Key Features	Deposits become more indurated up the member. Laterally elongated fractures filled with secondary calcite cement (Fig 7-Appendix, pg290)
<u>Stromatolite Member</u>	
Colour	Lower half (TM3-8) of member-white (WHITE 10YR), upper half (TM11-9) of member-light red (2.5YR 6/6), mottled
Texture	TM3-8-non-clastic limestone, TM11-9-clastic/microclastic mudstones
Grain size/sorting	Clasts not evident by eye. Very well sorted
Composition	TM3-8 carbonate-rich, TM9-11-clay-rich, some quartz
Structures	N/A
Key Features	TM3-8-borings, up to 10cm in length, open space structures-prevalent on cut surfaces, also pitted. Some of the voids filled with large (seen by eye) calcite
NaSi coating	NaSi loosely consolidating TM11-9
<u>Tmessah Member</u>	
Colour	Range of colours, predominantly pale to very pale brown (10YR 8/2) and pale yellow (5Y 8/2). Weathered outer surfaces are heavily reddened compared to freshly cut surfaces (Fig 8-Appendix, pg290)
Texture	Clastic-sandstones, siltstones, some brecciation (TM18) and mottling
Grain size/sorting	Range of grain sizes and sorting. TM12-15, 16-coarse sand and granule sized clasts, moderately sorted with the clast size decreasing up to TM16. TM17-particularly fine grained clasts, well sorted. TM18-24-fine sand-sized clasts, some granule/pebble sizes, moderately-well sorted. TM22/23-clay-rich
Composition	Quartz, carbonate matrix in some deposits, some locally argillaceous, evaporite nodules on surface of TM16/17. TM18 more carbonate-rich
Key Features	Evidence of bioturbation. TM17-rootletted which are infilled with reddened sand. TM22/23 blackened organic areas. TM24-more indurated with honey comb texture resulting from calcite cemented rhizoliths (Fig 9-Appendix, pg291)
<u>Kunayr Member</u>	

Colour	White (WHITE 2.5Y) becoming pink to pinkish white/gray (7.5YR 7/2) from TM63 upwards
Texture	Three distinct units within the member. Homogenous micritic and crystalline limestone (TM28-35), marly (greener) limestones (TM71-72) overlying the micritic limestones, clastic-sandstone and sandy limestones (TM61-69), some brecciation (e.g. TM31) and mottling (red/green)
Grain size/sorting	Three main units to the member. TM28-35-grain size not visible. TM71-72-fine-coarse sand-sized clasts, well-moderately sorted. TM61-69-grain size not visible except for fine-medium sand-sized clasts in the deposits capping the member
Composition	Carbonate, quartz clasts in a calcite matrix, some locally argillaceous deposits. TM61-69 less well cemented than underlying deposits
Key Features	More carbonate-rich than equivalent member in the AP section. Open-space structures (possible borings) on the cut surfaces of TM28-35 sometimes filled with coarse calcite cement. The outer surfaces are weathered resulting in a pitted surface but also smooth/rounded areas (Fig 12-Appendix, pg292) due to dissolution/wind erosion. Black organic specks 250-500µm in size. Lateral, wavy, open fractures cut through some of the deposits of TM61-69.

Table 5.3. Hand sample descriptions of the deposits from the four members of the TM section.

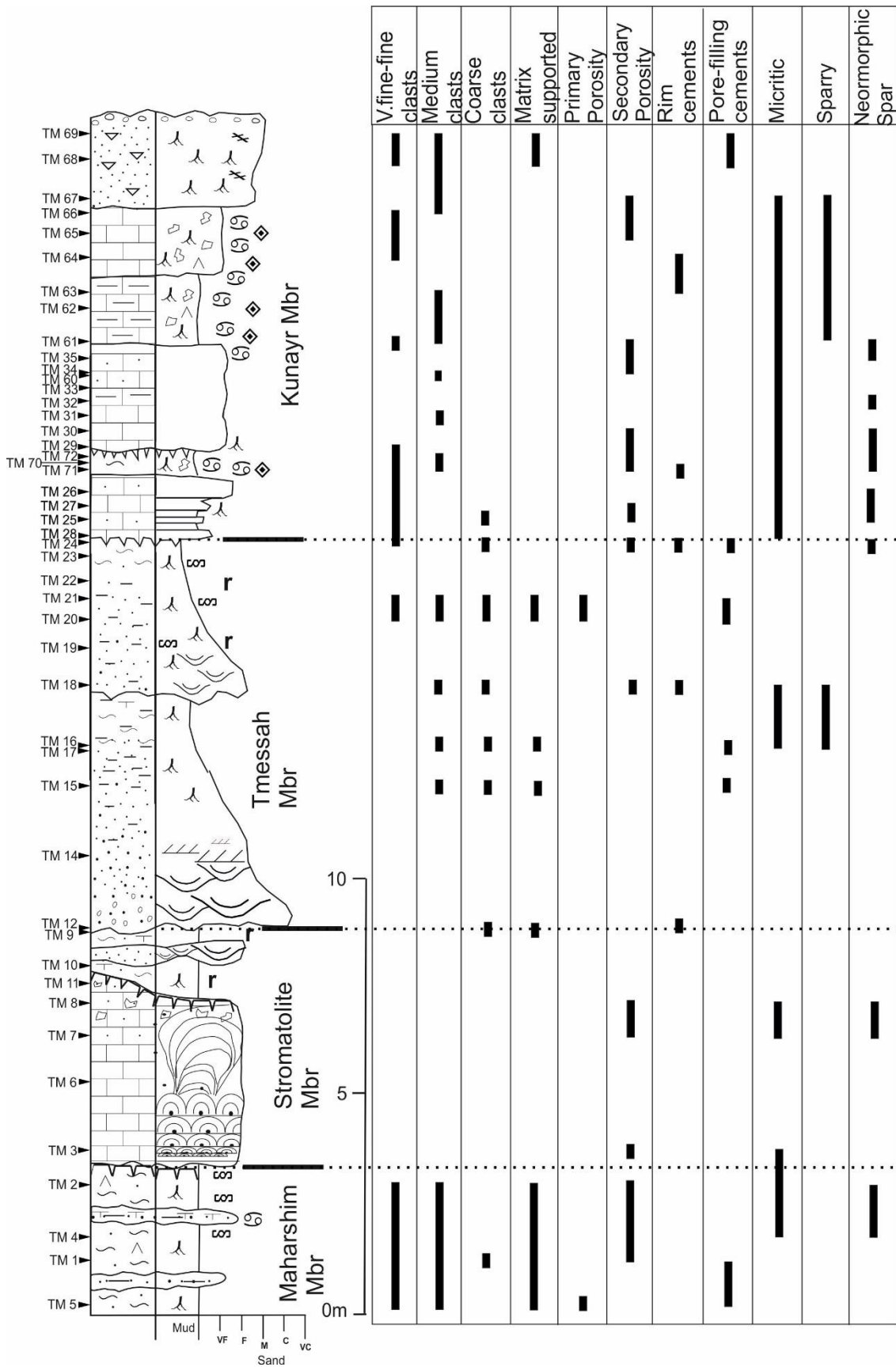


Figure 5.4. Key characteristics of the thin sections from the TM section. Note: thin sections of TM6, 14 and 19 were not produced. The clast size refers to grains of sand-sized material. Please refer back to Figure 5.1 (pg113) for the log key.

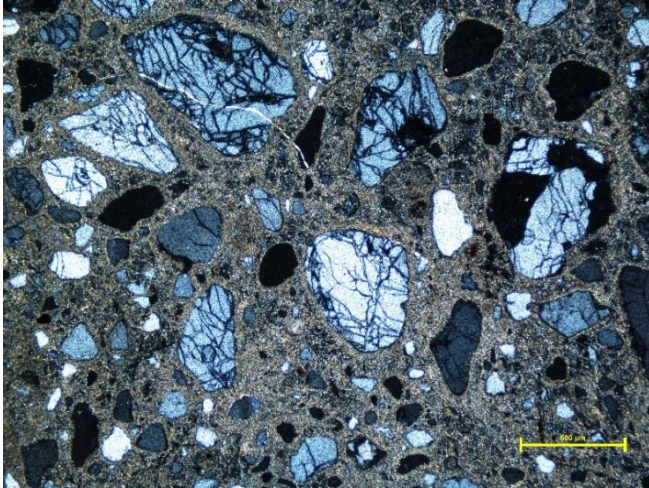
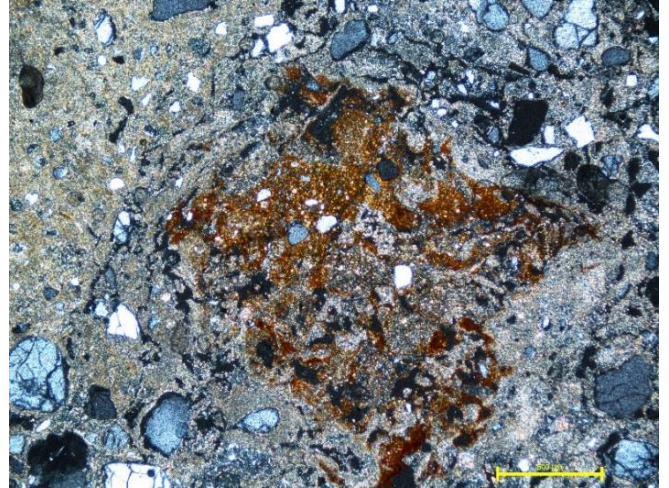
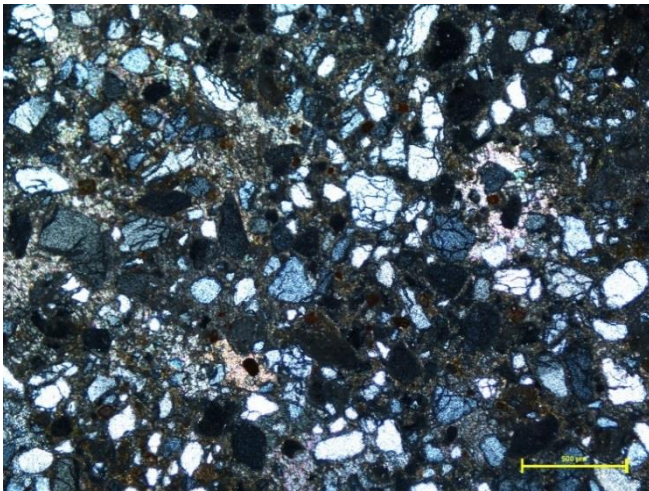
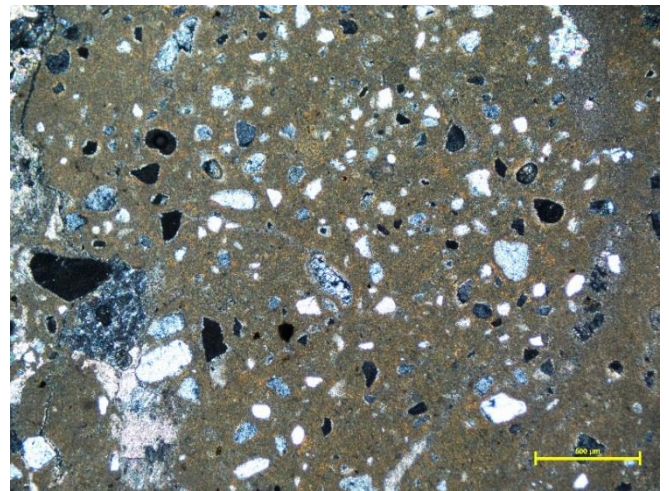
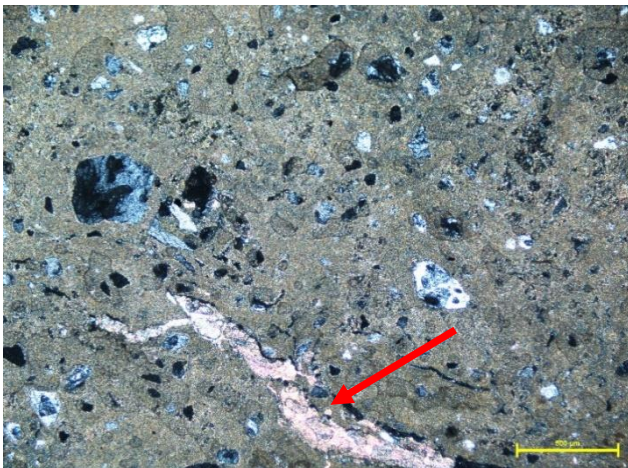
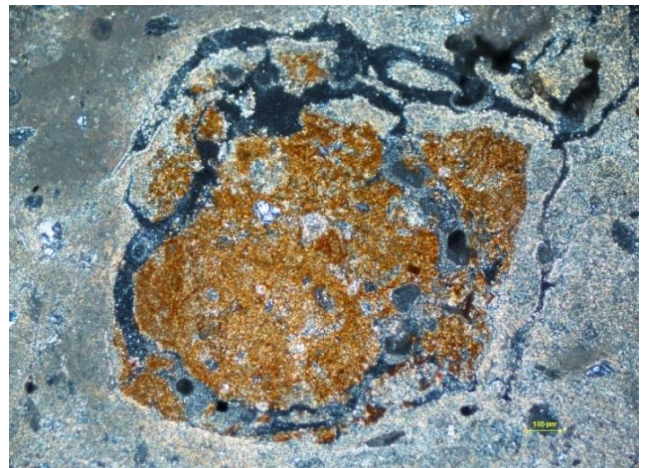
A**B****C****D****E****F**

Plate 5.2 Maharshim Member. A-TM1, bimodal sorting of quartz clasts in a floating matrix (x5, cpl). B-TM1-reddened nodular area (x5, cpl). C-TM5-spar-rich areas infilling pore spaces (x5, cpl). D-TM4-quartz clasts in floating micritic matrix (x5, cpl). E-TM4-fenestral laminoid voids (marked by arrow) infilled with secondary spar (x5, cpl). F-TM2-reddened glaebule surrounded by circumgranular cracking (x10, cpl). Scale bar is 500 μ m in length in all photomicrographs except for F where it is 100 μ m.

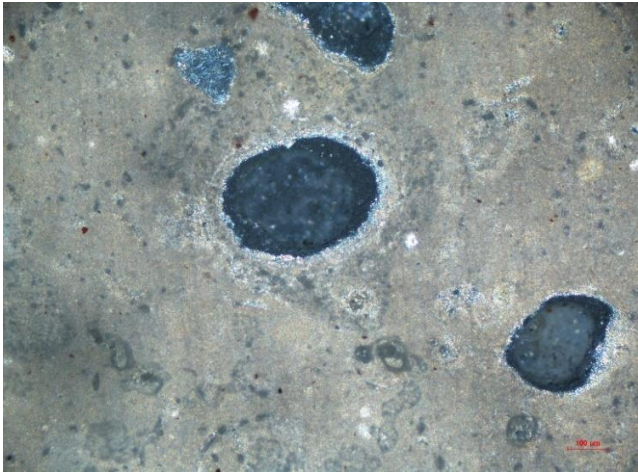
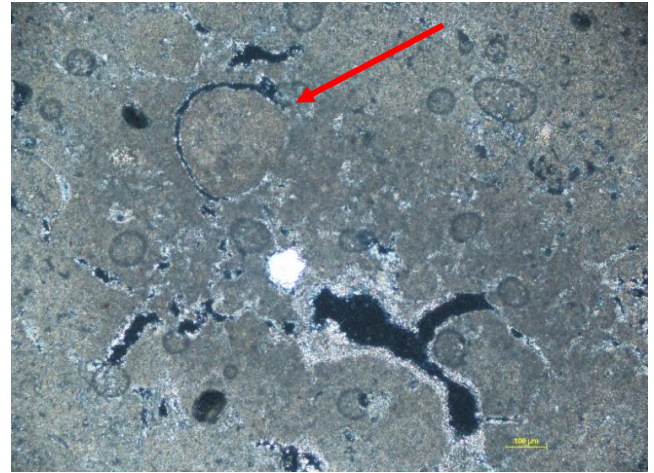
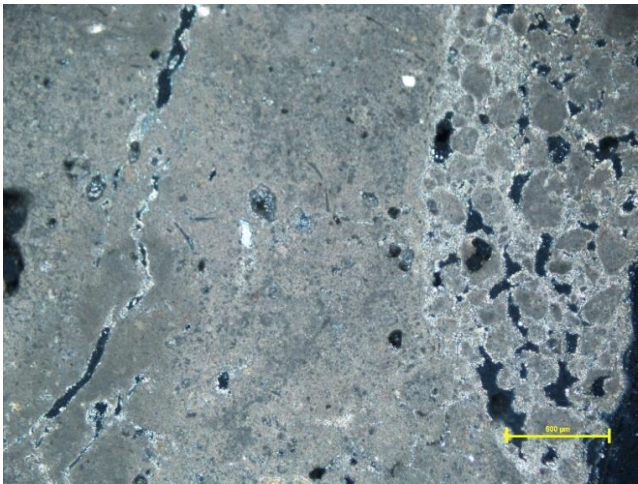
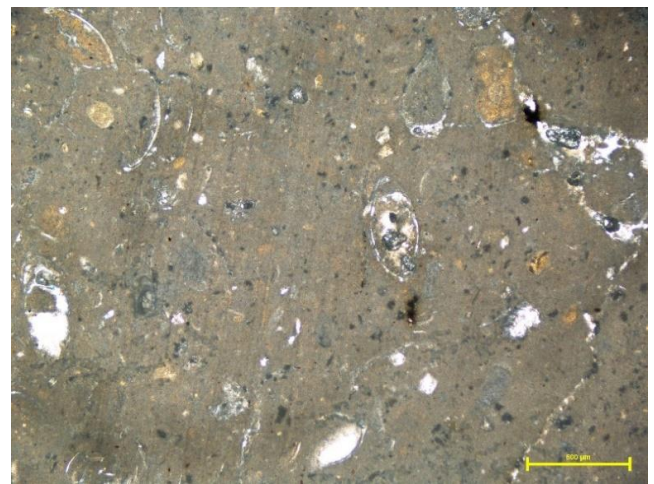
A**B****C****D**

Plate 5.3. Stromatolite Member. A-TM3, centre of photo-‘ghost feature’ with microspar rim remaining (x10, cpl). B-TM7, vuggy porosity with void partially filled with secondary microspar cement, mold peloid also observed (arrow) (x10, cpl). C-TM7, aggregate grain of peloids in the right of the photo, fenestral type void also seen (left part of photo) (x5, cpl). D-Fragments of ostracod shells and possibly bivalves (x5, cpl). Scale bar is 100μm in A/B and 500μm in C/D.

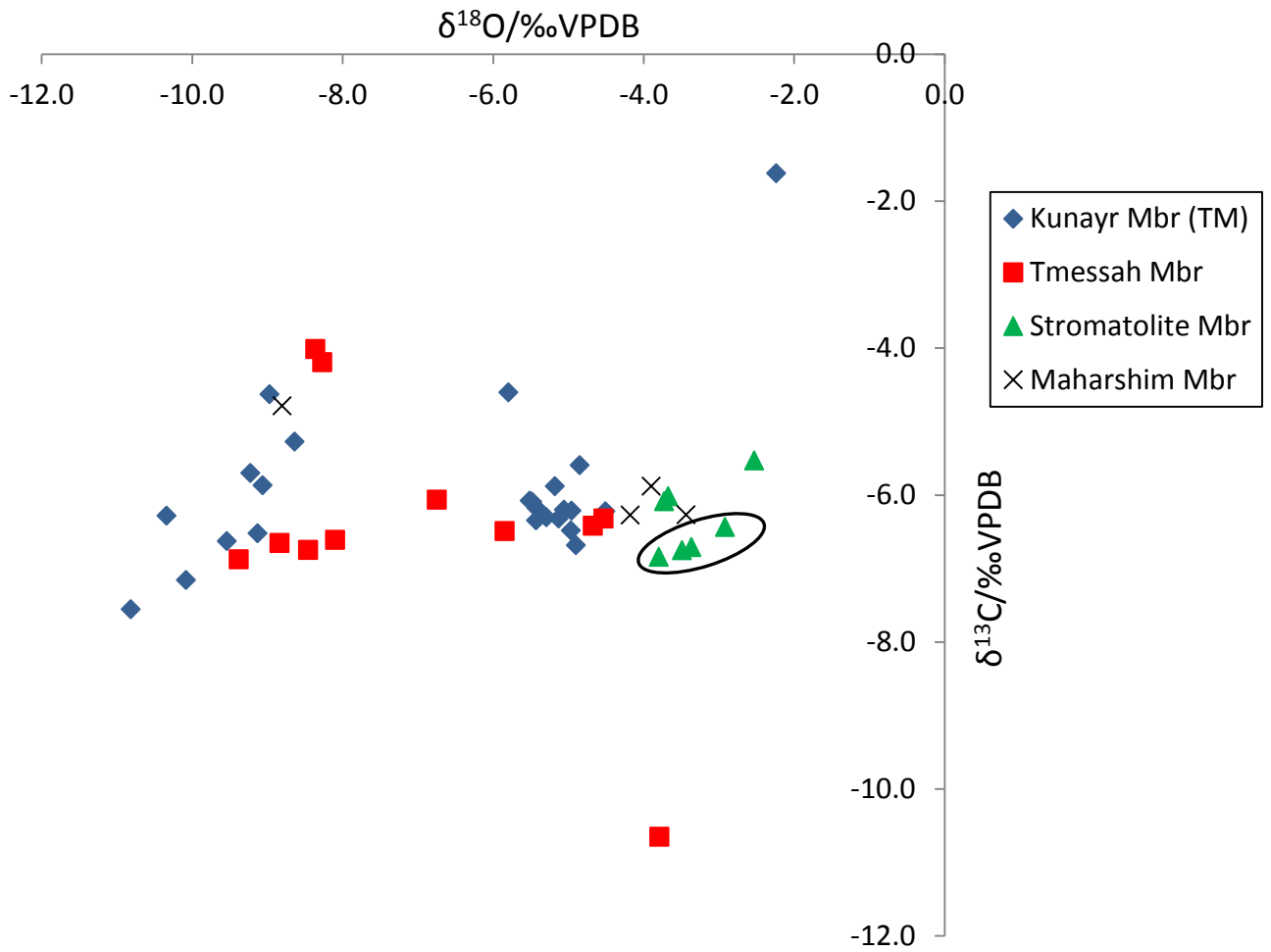


Figure 5.5. Graph to show the stable isotope values of members assigned to the Shabirinah Formation from the TM section. Carbonates of the STR Member are circled. For raw isotopic data please see Table 5 – Appendix, pg297

5.1.1.4 Tmessah Member (TM Mbr)

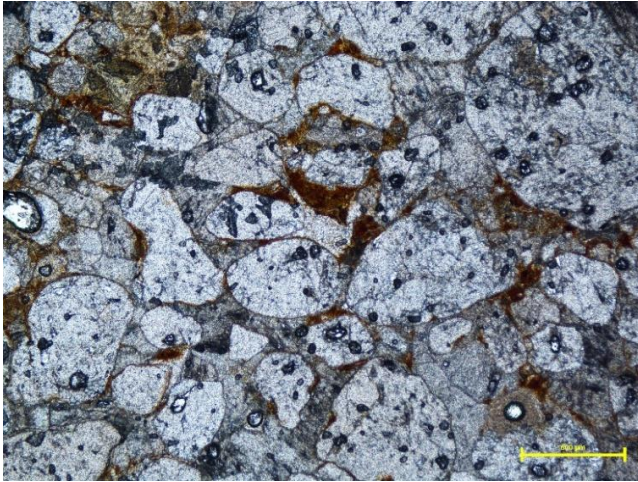
In thin section, differences are apparent in the deposits of this member as shown in Figure 5.4. The lower half of this member (to TM16) is quartz-rich, containing clasts which are sub-rounded to rounded. The clasts are moderately-to-well sorted with grain sizes of medium-to-coarse sand and some granules. Some of the clasts of TM12 have reddened rim cements caused by an Fe-oxide coating (Plate 5.4-A). Some clasts also show dissolution of the clast edges due to the formation of carbonate cement. The deposits have infilling primary sparry cement (Plate 5.4-B). The crystals are coarse, some $>500\mu\text{m}$, and are equant in shape suggesting precipitation over a long period of time. Within TM16, as well as coarse spar cements, finer microspar patches are also seen, in particular in areas with few quartz clasts.

The clasts of the upper half of the member (TM18 up) have bimodal sorting. The larger clasts, typically medium-coarse sand-sized are rounded while the smaller clasts (coarse silt to fine sand-sized) are angular to sub-angular (see Figure 5.4). Some of the clasts, especially in TM20, have fretted edges caused by dissolution. Many of the larger clasts within TM21 (Plate 5.4-C) also have the unusual thin section fracturing observed on many of the clasts from the Shabirinah Formation -AP section. Within the more carbonate-rich deposits of TM18/24 rim cements of coarse ($100\text{-}250\mu\text{m}$), bladed spar is seen coating some of the larger clasts (Plate 5.4-D). The rim cements are anisopachous coating the entire of the clast but varying in thickness. It is likely that these cements are first generation or co-generational. Surrounding the rim cements are second generation pore-filling cements of micrite and spar. Secondary granular mosaic spar crystals are also seen infilling rootlet spaces in TM24 (Plate 5.4-E). The cements of the remaining deposits within the upper half of the member are composed of pore-filling cements which are occasionally poorly developed with areas of open porosity evident (Plate 5.4-C). Some areas of cement are also locally reddened.

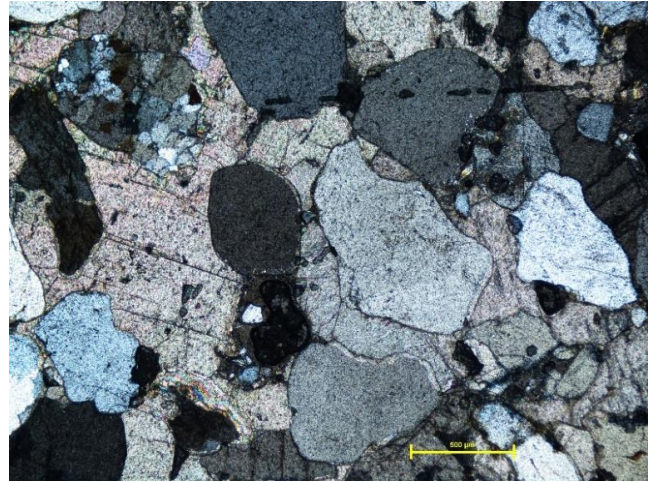
Despite there being distinct characteristics in thin section of the lower and upper halves of this member, this on the whole is not reflected isotopically. Large and abrupt changes do however occur in the isotopic values throughout this member (Table 5-Appendix, pg297). The $\delta^{13}\text{C}$ values vary overall by 2.9‰ ranging between -6.9 and -4.0‰. The largest $\delta^{13}\text{C}$ differences of 2.7‰ are observed between the basal deposit and overlying TM14. This same difference is also observed between the top (TM16) and basal (TM18) deposits of the upper and lower halves of the member. The $\delta^{18}\text{O}$ values of the lower member are fairly stable differing by just 0.5‰. Much larger variations occur in the upper

deposit values with $\delta^{18}\text{O}$ ranging between -9.4‰ (TM18) to -4.5‰ (TM23), a difference of 4.9‰. When large jumps in values of $\delta^{18}\text{O}$ occur between neighbouring samples, such as a 3.6‰ difference between TM23/24, little variation (0.3‰) occurs in the values of $\delta^{13}\text{C}$. Overall the $\delta^{18}\text{O}$ values are however slightly more enriched in the upper half of the member. The calculated correlation coefficient of the lower and upper halves of the member equal 0.26 and 0.40 respectively. The carbonate-poor sandstone of TM17 produced anomalous values, in particular of the $\delta^{13}\text{C}$ value. The original run of this sample revealed a poor signal indicating there was not enough carbonate present for an accurate value. The sample was re-run with x10 the sample amount but the signal remained poor. It is also likely the sample was exposed to NaSi in the field voiding the values of this sample

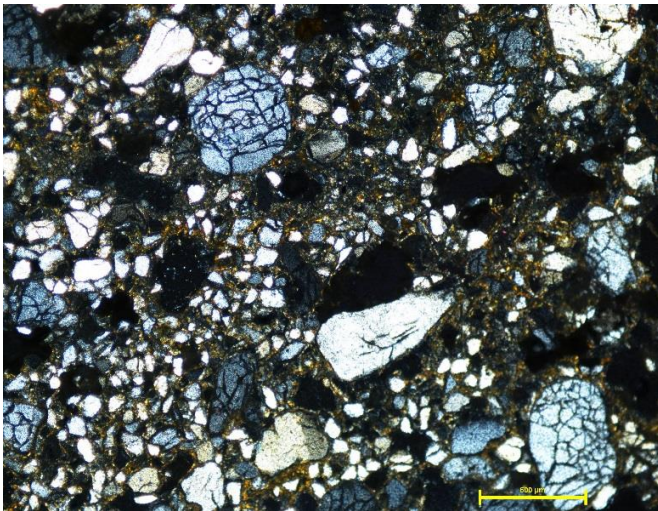
A



B



C



D



E

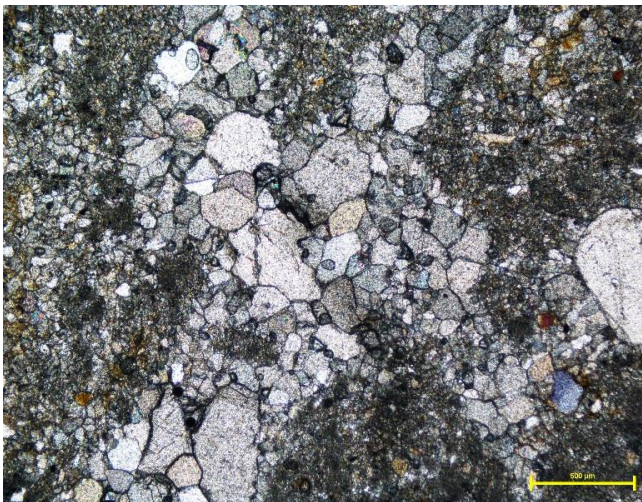


Plate 5.4 Tmessah Member. A-TM12, rounded quartz clasts with reddened rim cements (x5, ppl). B-TM15-very coarse spar cement infilling pore spaces between quartz clasts (x5, cpl). C-TM21, bimodal sorting of clasts. Large clasts have surface fracturing, meniscus cements which are locally reddened (x5, cpl). D-TM24, rim cement of bladed spar crystals (x5, cpl). E-TM24, secondary mosaic spar infilling rootlet (x5, cpl). Scale bar is 500μm in all microphotographs.

5.1.1.5 Kunayr Member (K Mbr)

This member contains 24 and 22 deposits from the TM and AP sections respectively.

TM section

The thin sections show the deposits in general to be largely clast poor, even in the 'sandy' unit capping the member (refer back to Figure 5.4). Clasts typically either occur in a floating matrix or in clusters (Plate 5.5-A). Those within a floating matrix range in size but are often silt-to-fine sand-sized and are sub-angular-to-rounded compared to the well sorted, silt sized clasts which occur in clusters (Plate 5.5-B). Some of the matrix supported clasts have corroded edges caused by dissolution. Partial, circumgranular-like cracking (Plate 5.5-C) is observed around some of the clasts which also cuts through the matrix. These cracks are usually unfilled and are likely caused by drying of the deposit resulting in shrinkage. The cement is composed of a mix of primary micritic and microspar cement in the lower carbonate deposits of the member (TM28-26, 29-35). Secondary drusy mosaic spar is seen infilling voids (Plate 5.5-D) characterised by pore-filling cements increasing in size towards the centre of the pore (Flugel, 2010, pg294)

The upper limestones (TM61-66) are more typically composed of coarser (>50µm) granular mosaic spar cement. The length of time of the wetting phase affects the carbonate precipitation and thus the crystal size (McLaren et al., 2012) therefore suggesting the upper carbonates experienced slower precipitation over a longer period of time. Uneven bladed and equant rim cements (Plate 5.5-A), likely first generation, are seen coating some of the quartz clasts which are then surrounded by micritic cement. Burrows are apparent in the limestones as are rootlets which can be differentiated from the burrows by their distinctive branching. The voids produced by burrowing and rootletting are often filled with secondary blocky spar. Within the cement, rounded, ovoid peloids occur usually <500µm in size and lacking internal structure (Plate 5.5-E). As in the Stromatolite Member, it is thought these are lithic peloids caused by reworking, although they are not as well defined. As burrows are present in the deposits it is possible they could be of faecal origin with the peloids having some of the diagnostic criteria such as their size, homogenous nature and their lack of internal structures (Flugel, 2010, pg111/112). Lateral, open fractures observed in the hand samples of the upper limestones can also be seen in thin section. These elongated, wavy fractures cut across the fabric of the deposit causing fracture porosity (Plate 5.5-F). Some of the voids are partially filled by secondary cements but the majority remain unfilled. Textural differences occur in the deposits of TM71-72 which interrupt this

predominantly limestone member. Although still mostly composed of sparry cement, the deposits contain a greater amount of clasts which are well sorted and also dark brown, angular intraclasts (Plate 5.5-G). Fractures, which are usually unfilled, cut through the intraclasts resulting in brecciation. The pattern of fracturing is similar to that of mud cracks caused by desiccation.

As in the Tmessah Member, large and abrupt swings in the isotope data occurs in the K member data, especially for $\delta^{18}\text{O}$. These variations are however more extreme with the most enriched and depleted $\delta^{18}\text{O}$ values equalling -4.5‰ (TM33) and -10.8‰ (TM64) respectively, a difference of 6.3‰ as seen in Figure 5.5 and Table 5-Appendix, pg296. This calculated difference does not include the possibly anomalously enriched (in both $\delta^{18}\text{O}/\delta^{13}\text{C}$) value of TM35. The largest change occurs between deposits TM72 and TM29 where an enrichment of 4.1‰ occurs (refer to Table 5-Appendix, pg296). The $\delta^{13}\text{C}$ values are similar to those of the Tmessah Member. The $\delta^{13}\text{C}$ values have a much narrower range compared to $\delta^{18}\text{O}$ differing by 3‰ throughout the member with the largest change of 2‰ occurring between TM61/62. When plotted, the values form two distinct groups as seen in Figure 5.5. One group clusters having on the whole a narrow range of $\delta^{18}\text{O}$ and $\delta^{13}\text{C}$ while the other has more variation, especially in $\delta^{13}\text{C}$. The correlation coefficient was calculated for this member but showed poor covariance ($r^2=0.17$). The correlation coefficient was also calculated for the whole of the TM section and showed an extremely poor covariance. This is not surprising given the disparity between $\delta^{18}\text{O}$ and $\delta^{13}\text{C}$ values when plotted against stratigraphic height (Figure 5.6). From figure 5.6 a good correlation was clear however from TM29-35 and an excellent covariance occurs with $r^2=0.91$. The correlation also looked relatively good from TM29-67, yet the r^2 value was relatively poor equalling 0.38.

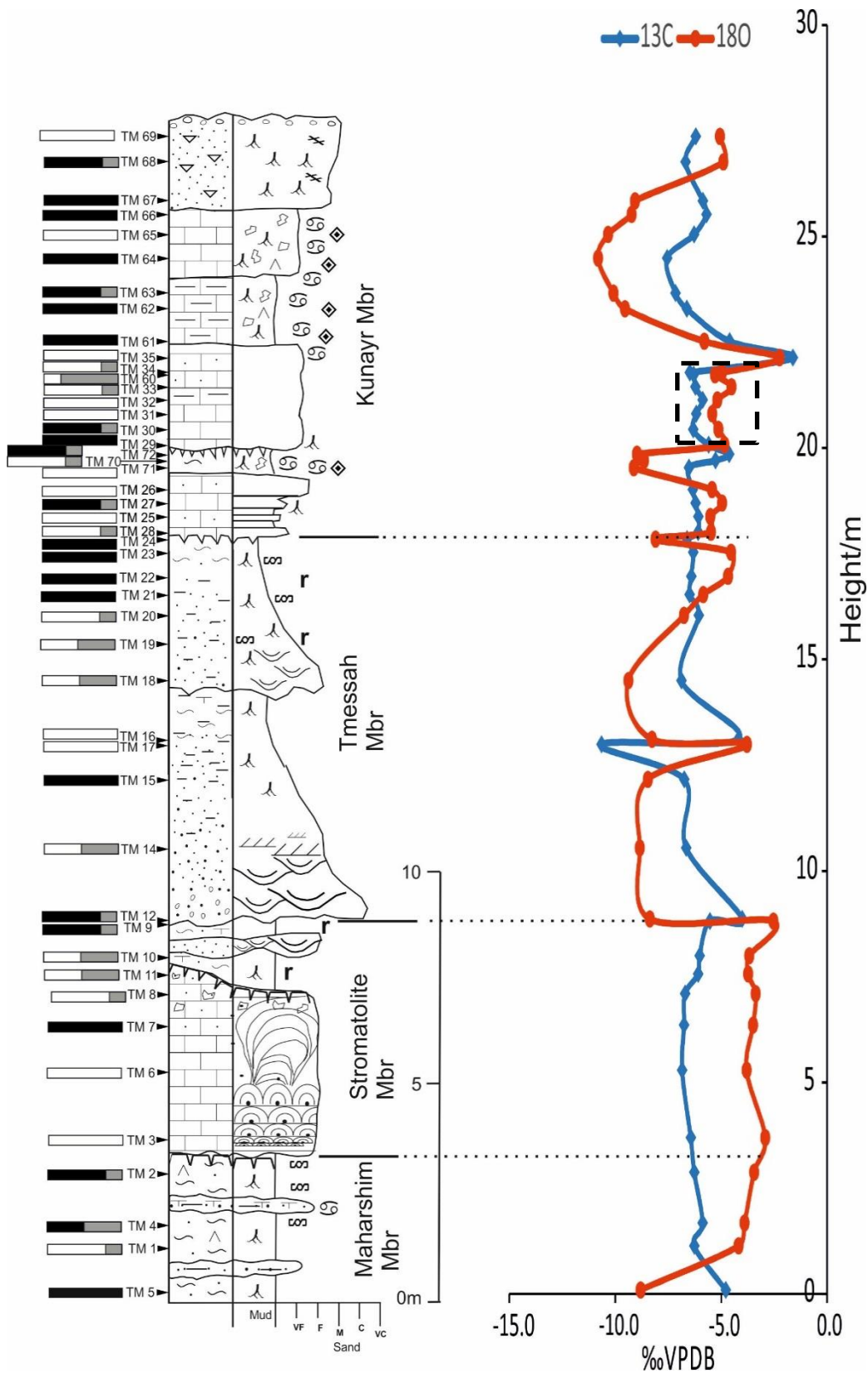


Figure 5.6. Isotopic values vs stratigraphic height of the TM section. The black, white and grey bars to the left of the log refer to the polarity of each of the deposits analysed where black = normal polarity, white = reversed and grey = unsure. Dashed box indicates the deposits which have good covariance between $\delta^{18}\text{O}$ / $\delta^{13}\text{C}$. Please refer back to Figure 5.1 (pg113) for the log key.

Ariel Section

The samples of AP37-42 are different in lithology to the other samples of this member and also the Ariel section as a whole. The thin sections of AP37-42 reflect the characteristics observed in the hand sample (refer back to Table 5.1, pg115). The clasts in these deposits show bimodal sorting. The larger size fraction ($>500\mu\text{m}$) are sub-angular to rounded while the smaller fraction, many of which are $<125\mu\text{m}$, are more angular (Plate 5.6-A). Micro clasts are also evident. The clasts are comprised of quartz, however some minerals such as muscovite and olivine occur sporadically in the samples (e.g. AP41) but in very small quantities. The clasts are in a floating matrix (pore-filling cement) of homogenous micrite and microspar. Some of the clasts are coated by uneven, first generation, rim cements. The deposits generally lack porosity however, vuggy porosity occurs in some of the deposits, especially AP37-40. This type of porosity, which is independent of the depositional fabric, is caused by solution enlargement of pores (Flügel, 2010, pg281/286). The vugs are partially lined with secondary spar cements (Plate 5.6-B). Unfilled wavy, elongated fractures of a similar width also occur resulting in channel porosity in some of the deposits. It is thought that the fractures may have been produced by rootletting or are the result of cycles of wetting and drying.

The deposits overlying AP42 are clast-rich and carbonate-poor. The clasts are predominantly sub-angular-to-rounded quartz and are moderately sorted. Some of the clasts have fretted edges due to dissolution and also the unusual surface fracturing observed in other members. The deposits have interparticle porosity. Poorly developed rim cements and meniscus cements of micrite and microspar occur as well as patchy pore filling cements (Plate 5.6-C). Some areas of the cement are heavily reddened, likely due to the presence of Fe-oxides or clays. In some of the deposits with high porosity, what is presumed to be NaSi can be seen infilling pore spaces (e.g. AP45/49, Plate 5.6-D). The NaSi is acicular in shape and occasionally forms a lattice type structure. In crossed-polars the NaSi is birefringent typically having first order interference colours. From AP50 upwards carbonate contents begins to increase. The deposits are not as carbonate-rich as AP39-42 and differ texturally with areas of well-developed patches of carbonate surrounded by more clast-rich areas (Plate 5.6-E). The cement is micritic with some patchy areas of microspar resulting in a mottled appearance. Bladed ($<100\mu\text{m}$) rim cements are seen coating some of the quartz clasts within the micritic cement. The quartz clasts are similar in size and sorting to those of the underlying deposits of AP43-49. Within the quartz-rich areas, the cements are more poorly developed and occasionally reddened.

Reddening can be caused by the mobilisation of Fe^{2+} during wetting and the formation of Fe^{3+} via oxidation when water levels are low (Verrecchia, 2007).

All of the deposits from the AP section assigned to the Kunayr Member had stable isotope analysis performed on them. Only six of the samples returned reliable values, even after re-running the samples with x10 the sample amount. Values were obtained from five samples from the limestone unit (see Table 5-Appendix, pg296) at the base of the member and also from AP55, in the more carbonate-rich unit near to the top of the member. Unlike the equivalent member in the TM section, abrupt changes in $\delta^{18}\text{O}$ do not occur between the deposits with the values relatively stable for the main limestone unit. The $\delta^{18}\text{O}$ values of this unit vary by 0.6‰ with the most enriched equalling -5.3‰. The $\delta^{13}\text{C}$ of these deposits also differ by only 1‰ as shown in Figure 5.7. Regression completed on the limestone unit reveals the deposits to have an r^2 value of 0.91 indicating excellent covariance between $\delta^{13}\text{C}$ and $\delta^{18}\text{O}$. The $\delta^{13}\text{C}$ value of AP55 is more enriched than the underlying limestone unit, as is the $\delta^{18}\text{O}$ equalling -4.9 and -3.6‰ respectively. When compared to the K member of the TM section, the $\delta^{18}\text{O}$ values plot in a similar region to the narrow cluster of values of this member as seen in Figure 5.7. The $\delta^{13}\text{C}$ of AP39/40 are slightly more depleted than the majority of $\delta^{13}\text{C}$ values from the deposits of this member from both the AP and TM section.

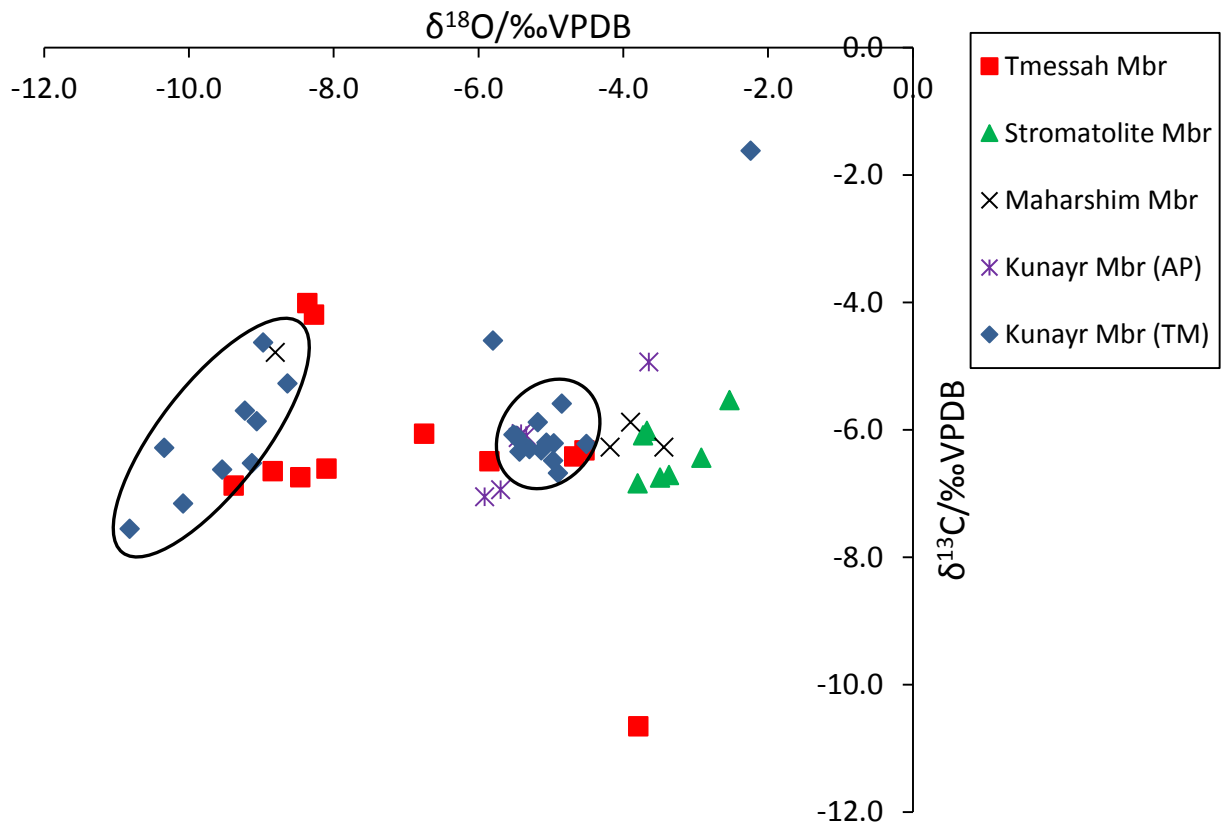
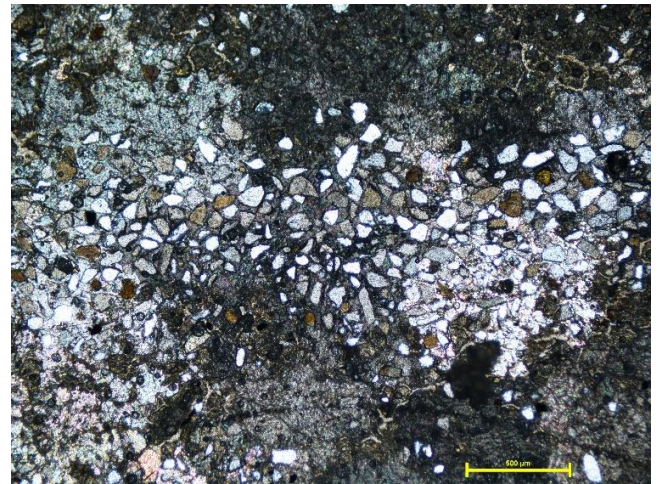


Figure 5.7 Graph to show all isotopic data of the Shabirinah Formation including the K Member data from both the TM and AP sections. Black circles indicate the grouping of values observed in the K Member from the TM section.

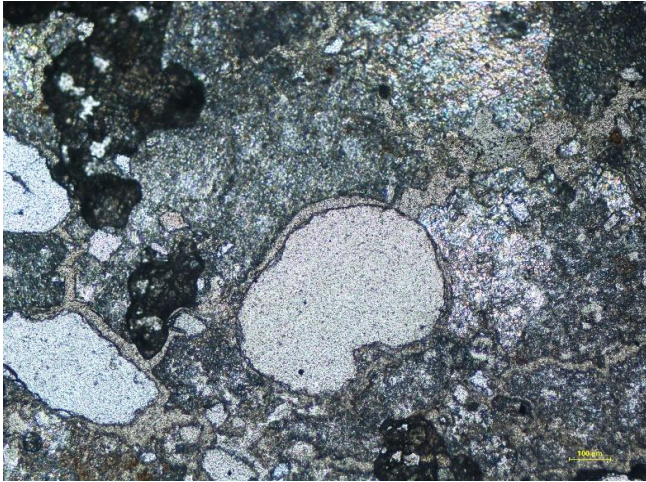
A



B



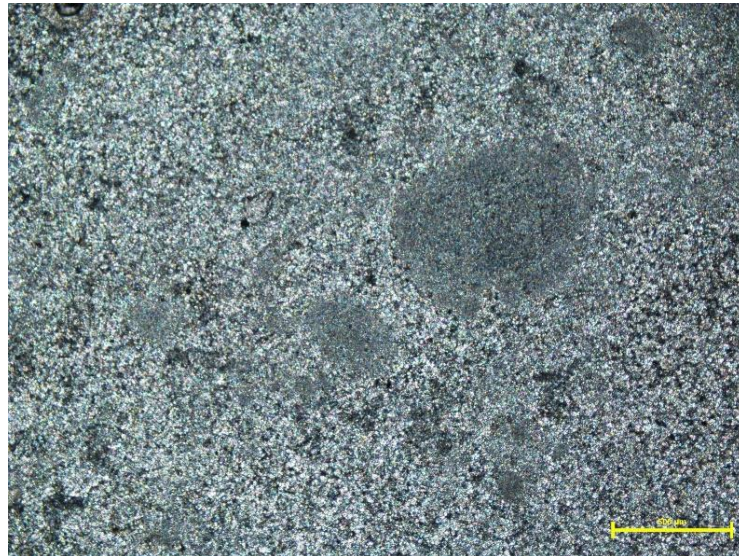
C



D



E



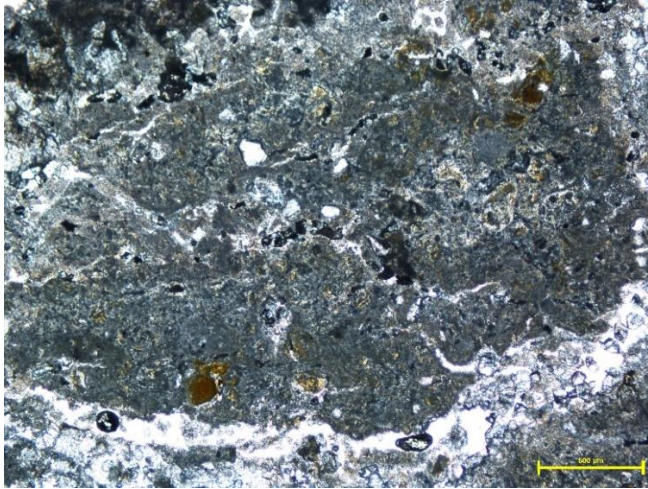
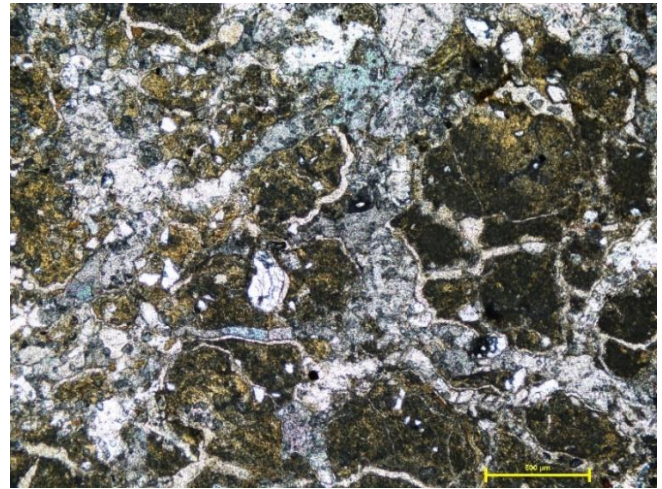
F**G**

Plate 5.5 Kunayr Member. TM section. A-TM63, quartz clasts in floating matrix of granular mosaic spar, bladed rim cements seen surrounding the larger quartz clast (x5, cpl). B-TM72, clustering of well sorted, sub-angular quartz (x5, cpl). C-TM66, unfilled circumgranular like cracking around corroded quartz clasts (x10, cpl). D-TM35, micritic cement surrounding a void filled with secondary drusy cement (x5, cpl). E-TM34, ovoid, structure less peloids (x5, cpl). F-TM61, wavy, elongated partially filled fractures cutting through the fabric of the deposit (x5, cpl). G-TM70, fractured brown intraclasts, spar can be seen infilling some of the fractures (x5, cpl). All scale bars are 500 μ m except for C which is 100 μ m in length.

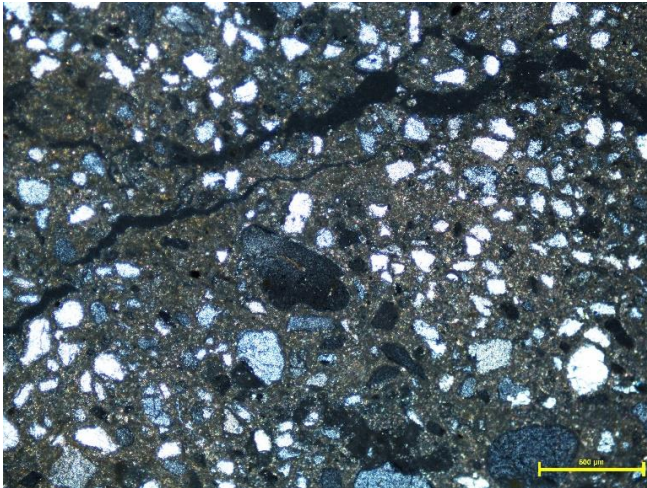
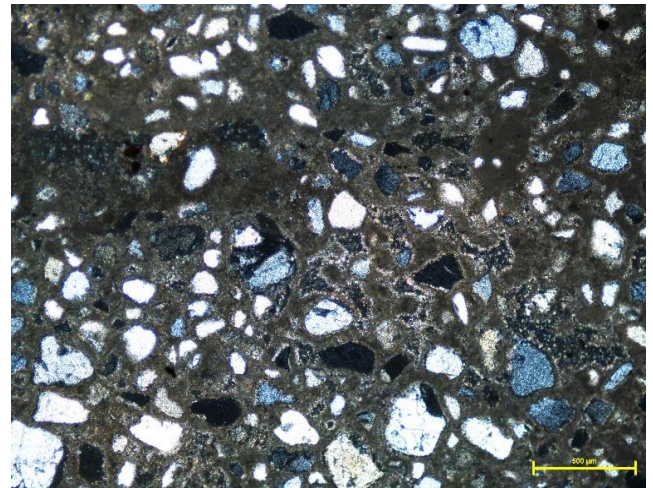
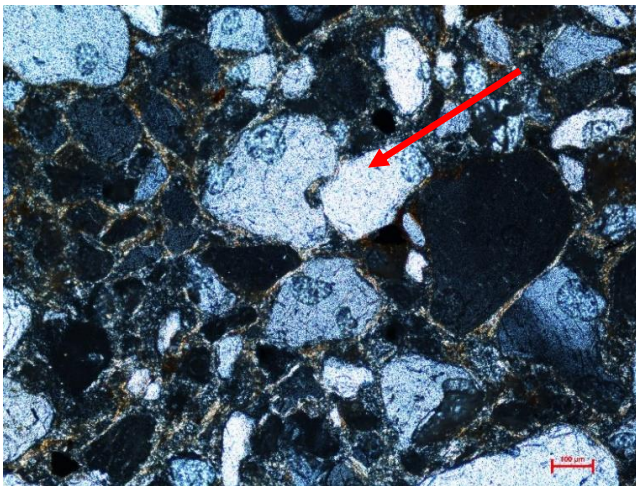
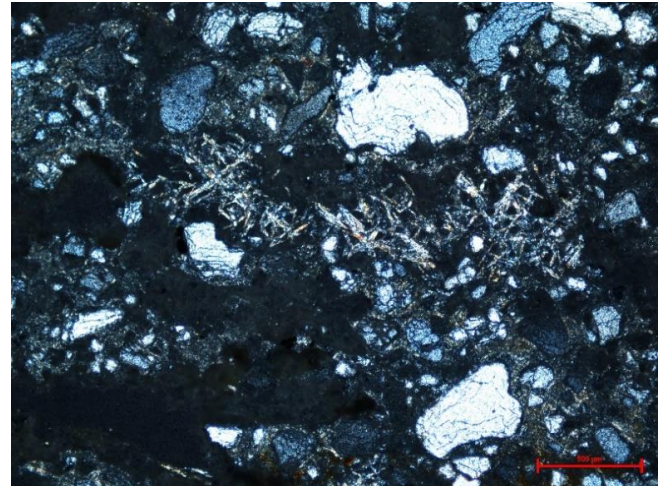
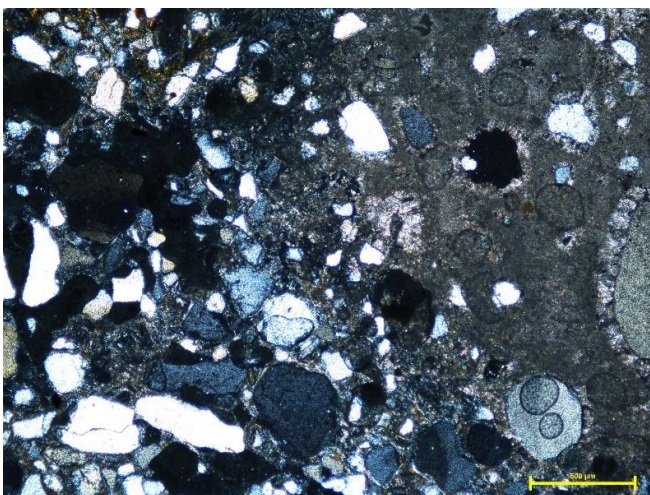
A**B****C****D****E**

Plate 5.6 Kunayr Member-AP section. A-AP37, typical texture of AP37-42 deposits. Unfilled channel porosity evident cutting across the sediment (x5, cpl). B-AP40, vuggy porosity partially filled with secondary pore lining microspar cement (x5, cpl). C-AP48, poorly developed meniscus and rim cements. Corroded grains evident in the centre of the photo (arrow) (x10, cpl). D-AP49, NaSi infilling pore space (x5, cpl). E-AP51, boundary of carbonate-rich and clast-rich areas. Well-developed rim cements are coating the quartz clasts within the carbonate rich area (x5, cpl). Scale bar in all images is 500 μ m except in C where the scale bar is 100 μ m.

5.1.1.6 Brak Section

Only petrographic results are available for this part of the BC section (BC1-8) due to NaSi coating the samples. Photomicrographs of the deposits show clasts within the deposits to be composed of detrital quartz with some opaques present. Two size fractions occur, one typically ranging in size from ~250-25 μ m and the other <25 μ m. The larger clasts are sub-angular to sub-rounded while the finer fractions are more angular. Some of the clasts are fractured, and reddened rim cements are evident in the more clast-rich sample of BC8. The clasts occur in a floating matrix but some clustering is observed, such as in BC6 (Plate 5.7-A). The deposits lack porosity composed of a dense reddish-brown, clay-rich, muddy matrix. The matrix is inhomogeneous and mottled with some black organic particles present (Plate 5.7-B). The mottled appearance is due to bioturbation causing sediment deformation. Burrows are evident as well as rootlets (Plate 5.7-C). Rootlets can be differentiated from burrows as they display branching, tapered ends (Flugel, 2010, pg185) and are seen to move around clasts. In some rootlet traces, quartz clasts occur suggesting deposition after the formation of the rootlet (Plate 5.7-D). It is likely that bioturbation led to the clustering of clasts apparent in some of the deposits. The texture of BC8 differs to the underlying deposits having not only a muddy texture, but also carbonate-rich areas. Coarse (up to 1.5mm), blocky spar crystals occur in this sample suggesting precipitation over a long period of time as the amount of time in the wetting phase will affect crystal size (McLaren, 1993). BC8 is also rootleted which have later become infilled with secondary spar. For a summary of the thin section characteristics see Figure 5.8.

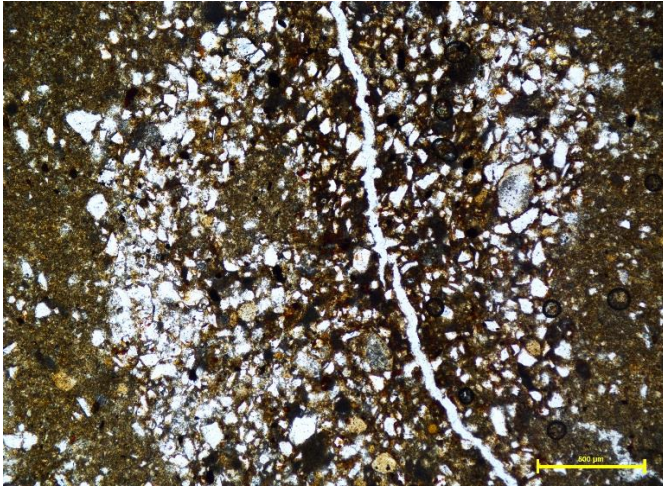
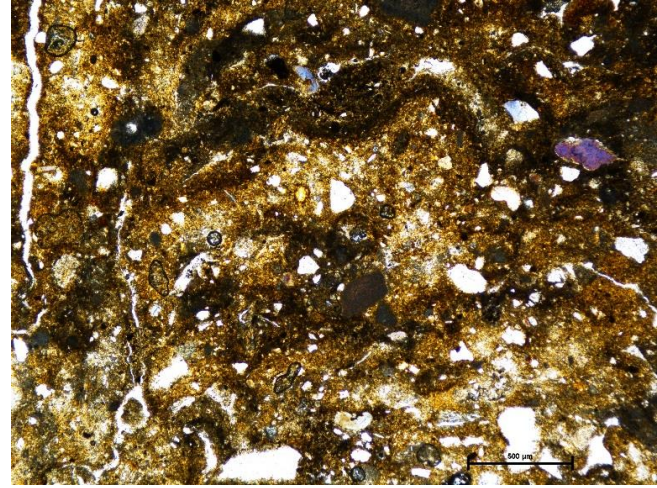
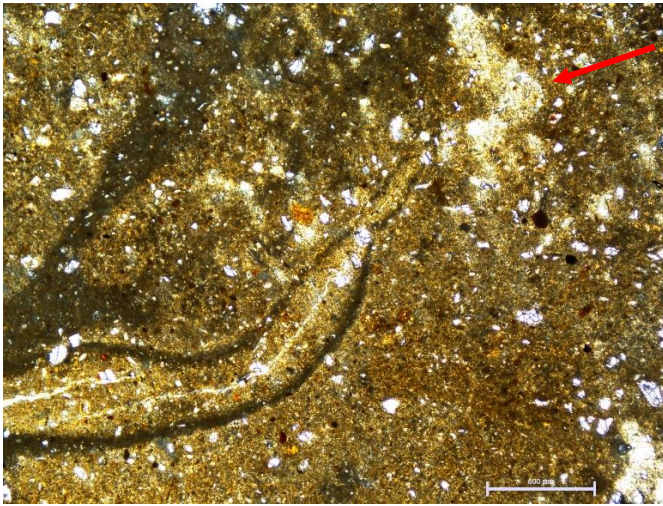
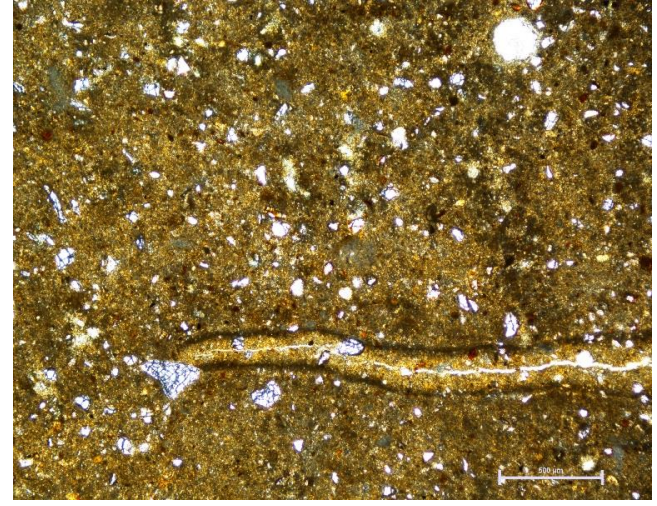
A**B****C****D**

Plate 5.7 Shabirinah Formation. BC Section. A-BC6, rootlet with clustering of quartz clasts (x5, cpl). B-BC1, mottled and bioturbated texture of the deposits, floating quartz clasts, vertical rootlet evident in top-left corner moving around a quartz clast (x5, cpl). C-BC7, burrow (arrowed) and rootlet. The rootlet has a dense, darker rim caused by sediment deformation with a thin fracture running through the centre (x5, ppl). D-BC7, rootlet with central fracture and quartz clasts within (x5, ppl). Scale bar is 500 μ m in all photomicrographs.

5.1.2 Brak Formation

The hand sample descriptions of this formation and the underlying Brak deposits assigned to the Shabirinah Formation are noted in Table 5.4, pg143. Due to the similarities between the deposits at the base of the Brak Formation and the underlying deposits assigned to the Shabirinah Formation (see Figure 5.8, pg144), the thin sections of these samples will not be discussed. The basal deposits of the Brak Formation are transitional deposits composed of sandy limestones. These deposits, in particular BC11, contain clasts which are fine-medium sand-sized, moderately sorted and sub-angular-to-sub-rounded (Plate 5.8-A). The clasts, which occur in a floating matrix, are mostly composed of quartz, but clasts of feldspar (plagioclase) occur in BC14. The matrix of the deposits is highly complex, composed of a number of different phases of cementation. The cement is mainly micritic/microspar and often mottled. Within the cement are areas which have more structure, such as circular areas of cement surrounded by faint concentric coatings as seen in Plate 5.8-B. These features possibly indicate the former presence of a structure, such as shell or a soil glaebule, which has undergone dissolution and replacement. Lithoclasts occur throughout the deposits. They are often darker than the main matrix, sub-angular to rounded with some etching of the edges, a range of sizes and generally lacking internal structure. Surrounding and separating the lithoclasts are rim and pore filling cements. The rim cements are likely first generation. Pore-filling cements are typically composed of drusy mosaic spar. It is thought the fabric observed in TS was formed by the following process. It is likely the deposits were originally composed of mud as demonstrated in the underlying Shabirinah Formation deposits. Overtime the muddy matrix has undergone dissolution and replacement by calcite resulting in areas of sparry cement and muddy lithoclasts (Plate 5.8-C). The micritic mud may also have been forced apart by the development of spar.

The overlying calcrete(?) samples are generally clast poor. There are however areas within some of the deposits which are more clast-rich, often present in lithoclasts and nodular areas. As in the underlying deposits, the clasts are typically sub-rounded and cemented within a floating matrix. Surrounding some of the clasts are rim cements. These first generation cements are often uneven and poorly developed however better developed rim cements of bladed spar are seen in BC17/23. Many similarities can be made between the fabric of these deposits and the underlying transitional deposits yet the complexity of their formation, in particular their cementation phases, has increased (Plate 5.8-D/E). Many lithoclasts are present resulting in mottling and brecciation. These carbonate grains vary in

size and shape often surrounded by pore filling cements of spar which in some cases has fragmented the lithoclast as seen in Plate 5.8-F. It is thought these grains have formed in the same way to those in the underlying deposits. The sparry areas of the deposits vary in crystal size however it is often drusy. As in the underlying deposits, possible former structures which have undergone replacement are present. These are often circular/wavy and in some cases the centre of the former structure has undergone dissolution and replacement leaving only a dark, dense micritic rim (Plate 5.8-D). Within BC15/16 areas clotted and peloidal micrite occur. These grains are a range of shapes but often rounded, some etching has occurred at the grain edge and they range in size between 100-250µm. They generally lack internal structure but in some, denser/lighter micritic areas occur with some having a fine micritic rim (Plate 5.8-G). These grains could be classed as lithic and mold peloids. Lithic peloids are formed from the reworking of carbonate mud while mold peloids occur due to dissolution of thin-shelled organisms leaving the central mold of the organism (Flügel, 2010, pg 113,116). Post-depositional microfractures cut across the fabric of the deposits as do possible rootlets. Both of these features are filled with secondary spar.

<u>Shabirinah Formation (BC1-8)</u>	
Colour	Heavily reddened. Light brown (7.5YR 6/4) to light reddish brown (5YR 6/3)
Texture	Clastic-mudstones/siltstones. Mottling
Grain size/sorting	Muddy, clay-rich matrix. Some medium-coarse clasts present. Very well sorted. Upper most sample (BC8) is coarser grained.
Composition	Clay-rich, some calcareous nodules. BC8 is more carbonate-rich
Key Features	Palaeosol mottling and bioturbation (burrows). Carbonate cement infilling rootlet trace in BC8
NaSi coating	Present on all deposits
<u>Brak Formation (BC9-25)</u>	
Colour	White (WHITE 2.5Y 8.5/1 or 10YR 8/1)
Texture	Clastic-sandy limestones. Crystalline/micritic limestone, brecciated
Grain Size and sorting	BC11-14-medium-coarse sand-sized clasts, some granules, well sorted with areas of moderate sorting. BC15-25-clast size not visible.
Composition	Carbonate-rich, some detrital quartz. Distinct changes in lithology. Lowest two deposits very similar to underlying SHF with the deposits become more indurated up the section. BC11-14 transitional deposits between the underlying mudstones and overlying calcretes(?). BC24 more similar to transitional deposits.
Key Features	White angular intraclasts which decrease from BC19 up. Reddened intraclasts in BC11-due to reworking from underlying mudstones. Mineral veins up to 1cm diameter. Fractures cut across the deposits infilled by calcite cement-caused by rootletting or shrinkage? Areas of vuggy porosity caused by dissolution. Distinct textural changes occur in some of the calcretes(?) as seen in Fig 12/14-Appendix, pg292/293.
NaSi coating	Possible NaSi coating on lower most deposits of this formation

Table 5.4 Hand sample descriptions of the deposits from the BC section.

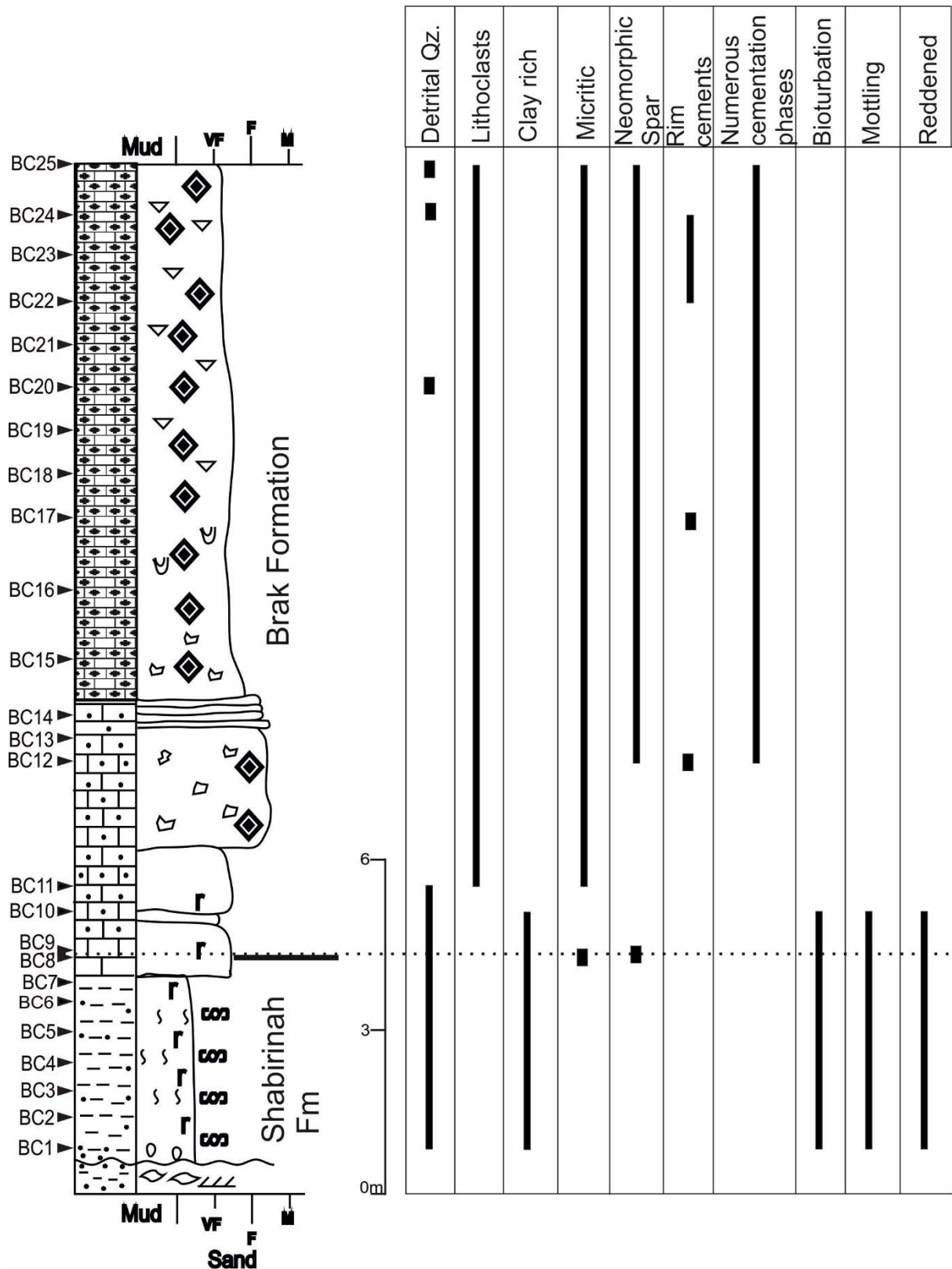
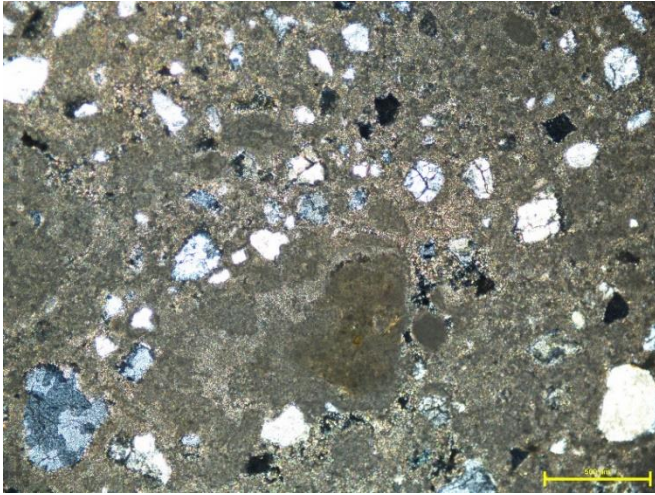


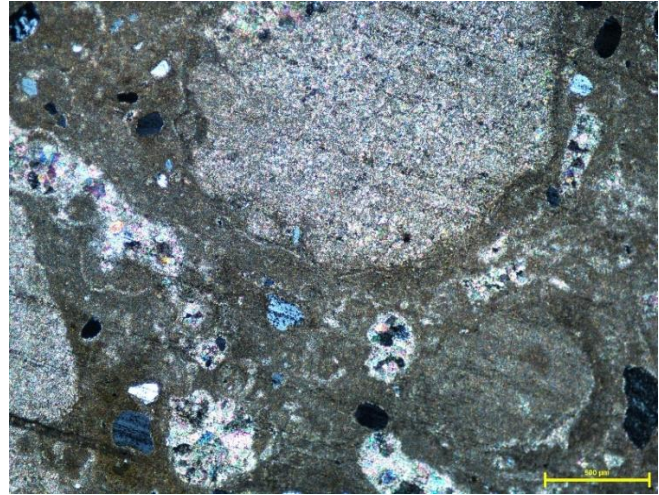
Figure 5.8 Key characteristics of the thin sections from the BC section. Note: the clast size refers to grains of sand-sized material. Please refer back to Figure 5.1 (pg113) for the log key.

Stable isotope values were obtained from 14 samples from BC11 upwards. The values of this formation range from -6.6‰ to -9.1‰ for $\delta^{18}\text{O}$. Despite the slight difference in lithology between the transitional deposits and the calcretes(?), little isotopic difference occurs. The calcretes(?) are however on the whole slightly more depleted in $\delta^{18}\text{O}$ than the underlying deposits with the most enriched $\delta^{18}\text{O}$ value from BC11. Not taking this value into account, the $\delta^{18}\text{O}$ value of the formation differs by only 1.4‰ with an average of -8.3‰. Similarly the $\delta^{13}\text{C}$ of the deposits, including BC11, differs by 1.1‰ ranging from -6.7‰ to -7.8‰. These small variations in the formation are more apparent when plotting the isotopic values against stratigraphic height as shown in Figure 5.9. Based on the similar trends observed in Figure 5.9 between $\delta^{18}\text{O}/\delta^{13}\text{C}$, regression analysis was conducted to establish whether the values of $\delta^{18}\text{O}/\delta^{13}\text{C}$ covaried. When conducted on all deposits the r^2 value was moderate equalling 0.50. If run on the calcretes(?) only (i.e. from BC15 up), the r^2 value increases to 0.77 indicating good covariance between $\delta^{18}\text{O}/\delta^{13}\text{C}$. The isotopic results of this formation were also compared to the Shabirinah. The Brak Formation values for both $\delta^{18}\text{O}/\delta^{13}\text{C}$ are distinctive having a much narrower range than the Shabirinah Formation as seen in Figure 5.10. Apart from a few deposits, the Brak Formation is also typically more depleted in $\delta^{13}\text{C}$ than the Shabirinah.

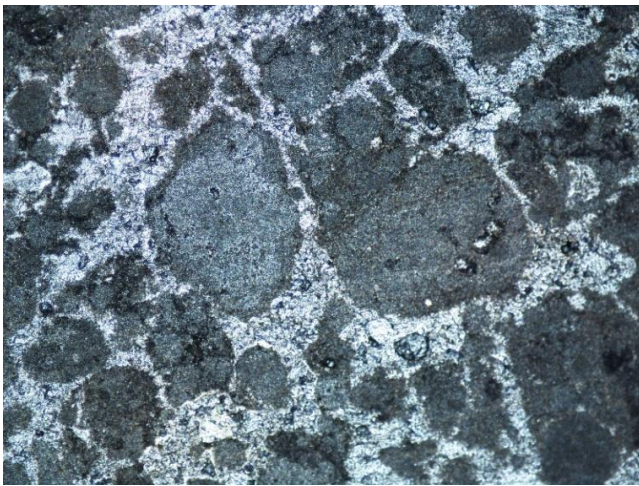
A



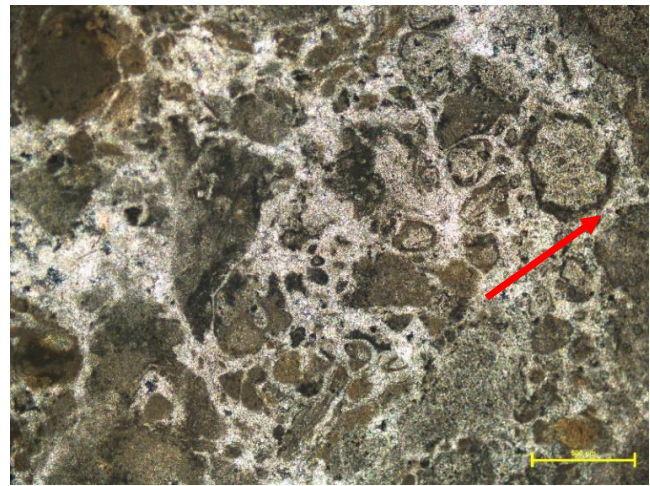
B



C



D



E



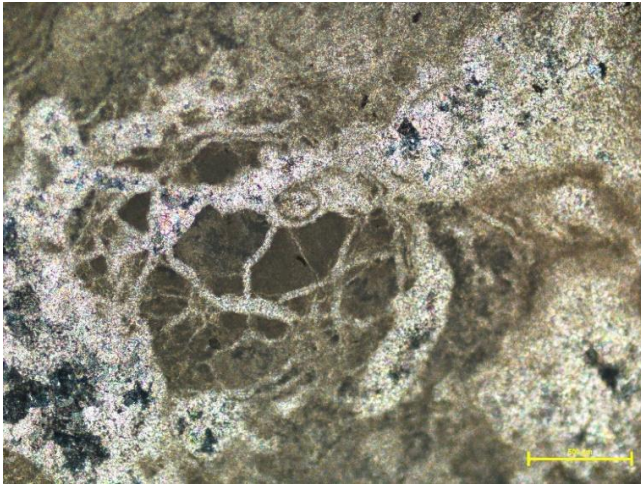
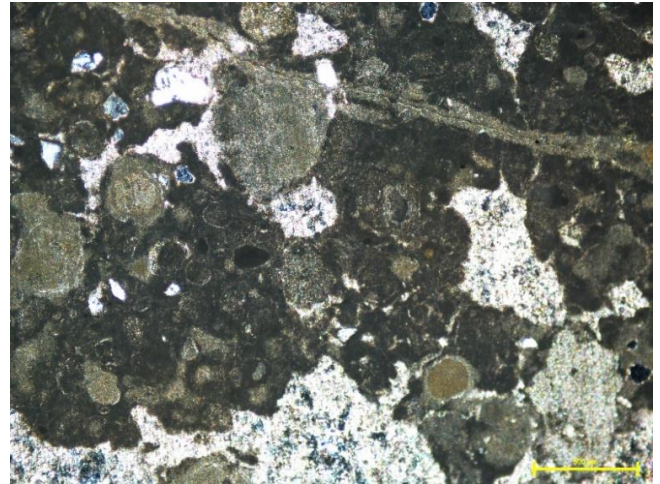
F**G**

Plate 5.8 Brak Formation. BC section. A-BC11, sub-rounded quartz clasts in a floating matrix (x5, cpl). B-BC12, circular structure in the lower left corner, pore spaces infilled with sparry cement (x5, cpl). C-BC13, rounded lithoclasts separated by sparry pore filling cement (x5, ppl). D-BC17, complex fabric of a number of cementation phases observed in many of the calcrete(?) deposits, areas of dissolution and replacement can be seen (arrowed) (x5, cpl). E- BC19, complexity of the fabric, unusual wavy patterns likely where former structures have undergone replacement (x5, cpl). F-BC19, lithoclast fractured by spar cement (x10, cpl). G-BC15, clotted micrite with lithic and mold peloids, post-depositional microfracture can be seen cutting across the fabric in the top of the photomicrograph (x5, cpl). Scale bar is 500 μ m in all photomicrographs except F where it is 100 μ m.

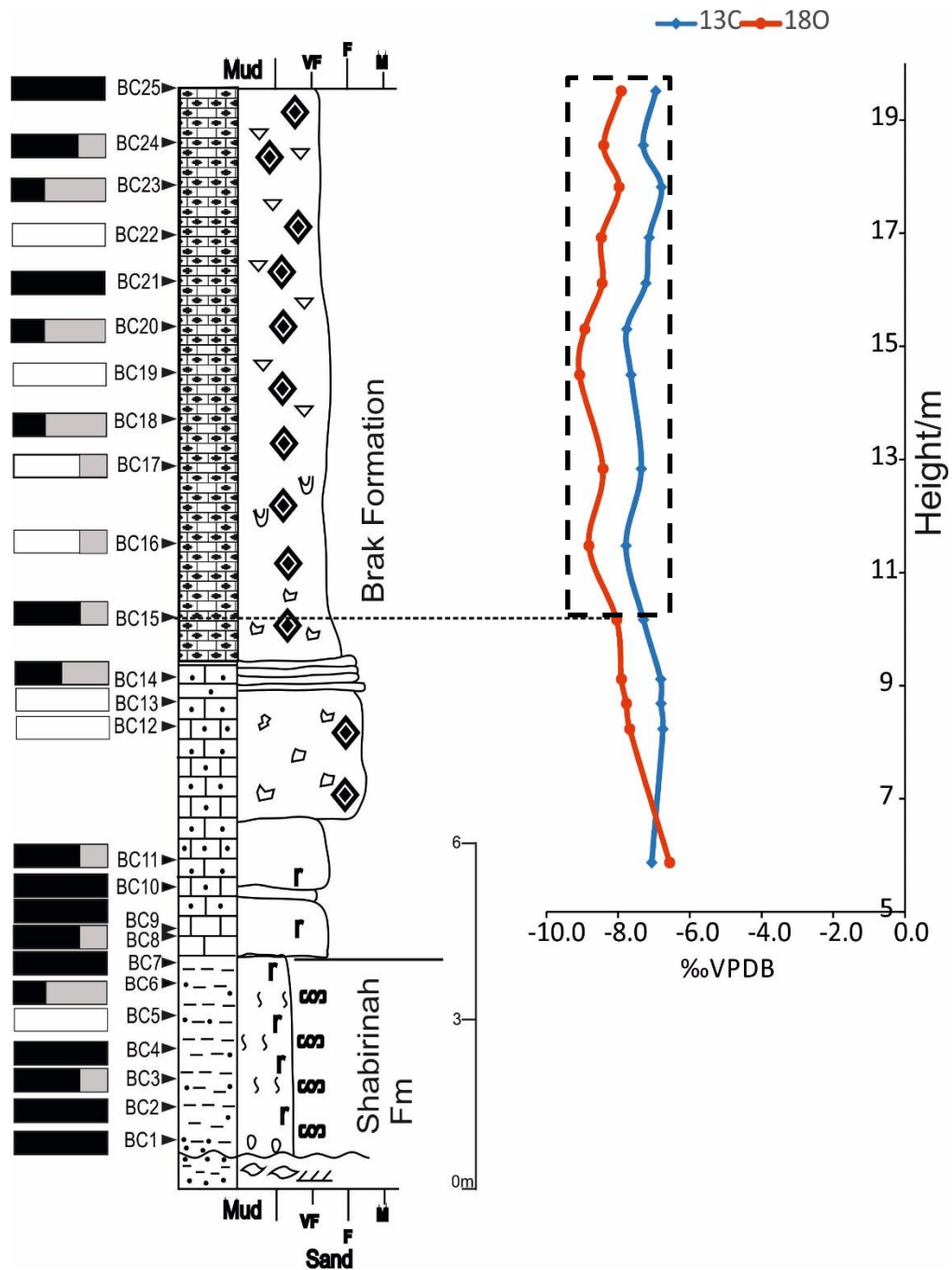


Figure 5.9 Isotopic value vs stratigraphic height for the Brak Formation. The black, white and grey bars to the left of the log refer to the polarity of each of the deposits analysed where black = normal polarity, white = reversed and grey = unsure. Dashed box indicates the deposits which have good covariance between $\delta^{18}\text{O}$ / $\delta^{13}\text{C}$ as discussed in the text. Please refer back to Figure 5.1 (pg113) for the log key.

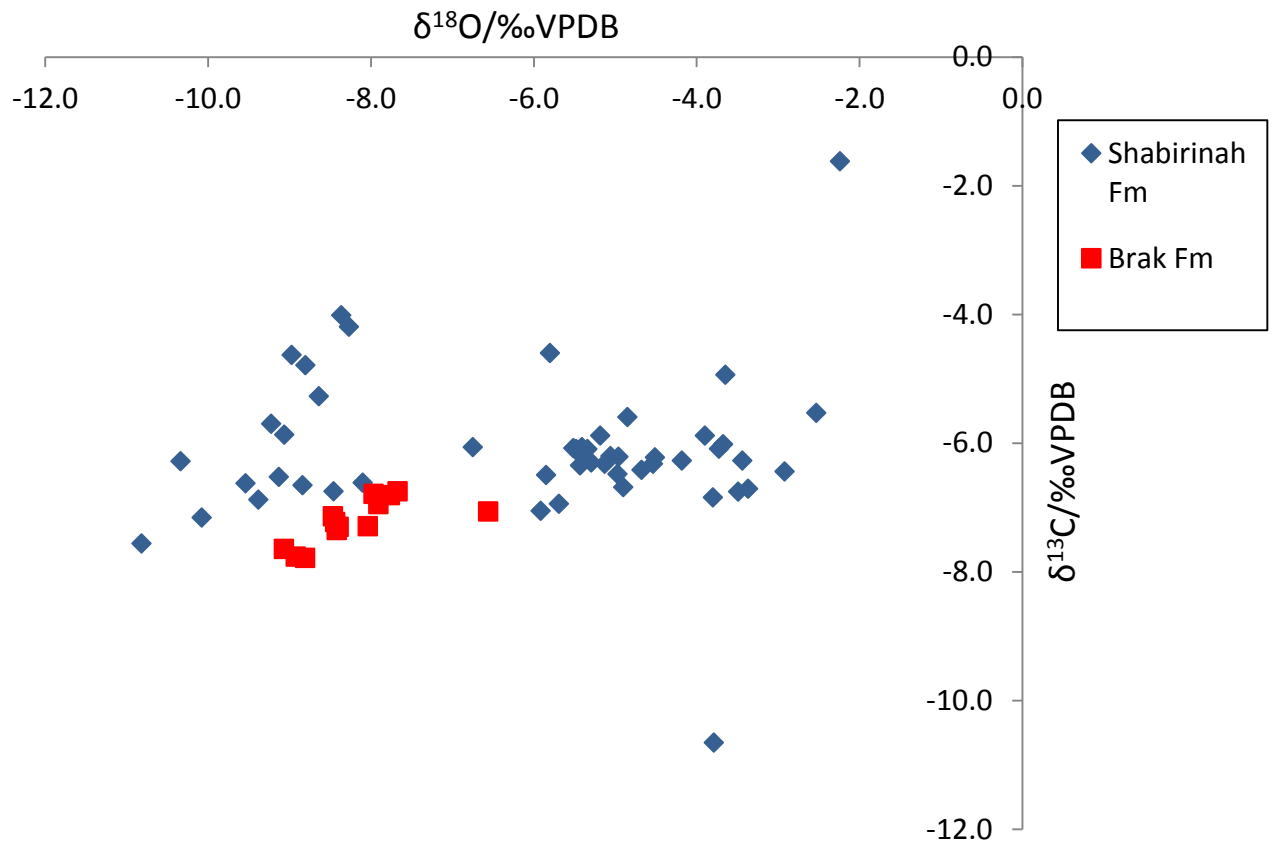


Figure 5.10. Graph to show the comparison of the isotopic values of the Shabirinah and Brak Formations.

5.2 Magnetostratigraphy: Age of the Shabirinah and Brak Formations

5.2.1 Scalar Magnetic Properties

The NRM magnetic susceptibility (MS) and intensity of specimens belonging to the Shabirinah and Brak Formations, and also those specifically from the Kunayr Member, were plotted (Figure 5.11). Overall, a clear trend of increasing NRM intensity with increasing MS can be observed. Distinct divisions are also apparent between the high susceptibility and NRM intensity values of the Shabirinah Formation, the intermediate values of the Kunayr Member and low values of the BC- Brak Formation. This trend can be explained by the lithology of the samples with carbonate-rich samples (Krijgsman et al., 1995) of the TM-Kunayr Member and especially the BC-Brak Formation having weak, sometimes diamagnetic susceptibilities (below line in Figure 5.11) compared to the higher susceptibility clastic specimens of the AP- Shabirinah Formation and BC- Shabirinah Formation for example. High NRM susceptibilities are particularly prevalent in samples which are reddened and which contain pedogenic features/palaeosols (Nielsen et al., 2004), where the susceptibility values can be up to 25x greater compared to carbonates. This difference becomes particularly noticeable when NRM intensity is plotted against the section height (Figure 5.16 i, A).

The changes in MS and NRM intensity with each heating stage were investigated to detect mineralogical alteration. On the whole, the MS of the specimens belonging to the Shabirinah and Brak formations remain relatively stable until 490-510°C suggesting little alteration. The NRM intensity of the samples however do not remain stable up to these temperatures. The severity of changes in intensity differs for many of the samples with the largest changes (a large drop in intensity) typically occurring between 300-430°C. Differences are apparent in specimens of different lithology. In reddened mudstones/siltstones, such as those from the lower BC (e.g. BC3) and AP sections (SHF), the susceptibility tends to remain fairly stable with alteration only taking place at high temperature stages (>600°C) indicating the presence of a high coercivity mineral such as haematite (Butler, 1992,pg83; Lowrie, 1990). The NRM intensity of reddened specimens drops dramatically after the first heating step as shown in Figure 5.12 where BC3 and AP11 decrease from 7.45 to 3.29 and from 2.70 to 1.55 respectively which is possibly suggestive of goethite partly carrying the NRM (Marton et al., 1980). In clastic deposits which have little-to-no reddening, the trend in intensity with temperature is variable. The NRM intensity typically drops suddenly between 400-500°C and can sometimes continue in a downwards trend such as in AP23. More often though, slight increases in intensity

occur in the latter temperature stages (e.g. AP42). Changes in MS (a slight increase) also occur at these temperatures indicative of mineralogical alteration. Haematite (or pyrite) can be converted to magnetite via reduction when heated to 400-450°C often accompanied by an increase in susceptibility (Butler, 1992). Alteration could also occur due to thermally induced mineralogical changes of clay minerals within the deposit (Henry et al., 2005). Carbonate-rich deposits (e.g. TM33, BC13, BC22) show larger changes in NRM intensity at similar temperature stages to the clastic deposits, typically around 400-430°C. These deposits show greater variability in intensity and especially susceptibility in lower temperature stages compared to reddened deposits (from 430°C onwards). This could be due to the breakdown of metastable minerals such as maghaematite (Lowrie and Heller, 1982; Butler, 1992, pg29). In some specimens, such as BC22 and other limestone-rich deposits, there is evidence of magnetic alteration in the higher temperature stages. Above 500°C, pronounced changes in the magnetic mineralogy of limestones (marine) can occur due to the growth of new magnetite (Lowrie and Heller, 1982). This alteration can occasionally obscure the recovery of the remanence at higher demagnetisation temperatures. Hounslow et al. (2017) conducted IRM on deposits of the Shabirinah/ Brak Formations. The results confirm that substantial amounts of haematite are present in many of the samples, especially the reddened deposits such as those from the BC section (Hounslow et al., 2017). The presence of high coercivity haematite can cause difficulties when demagnetising using AF (Butler, 1992, pg83; Borradaile, 1999) which agrees with the ineffective use of this method on the AP samples. The IRM results also indicate the presence of a more dominant, low coercivity phase in the non-reddened deposits of the BC/TM sections indicative of magnetite or Ti-magnetite (Hounslow et al., 2017).

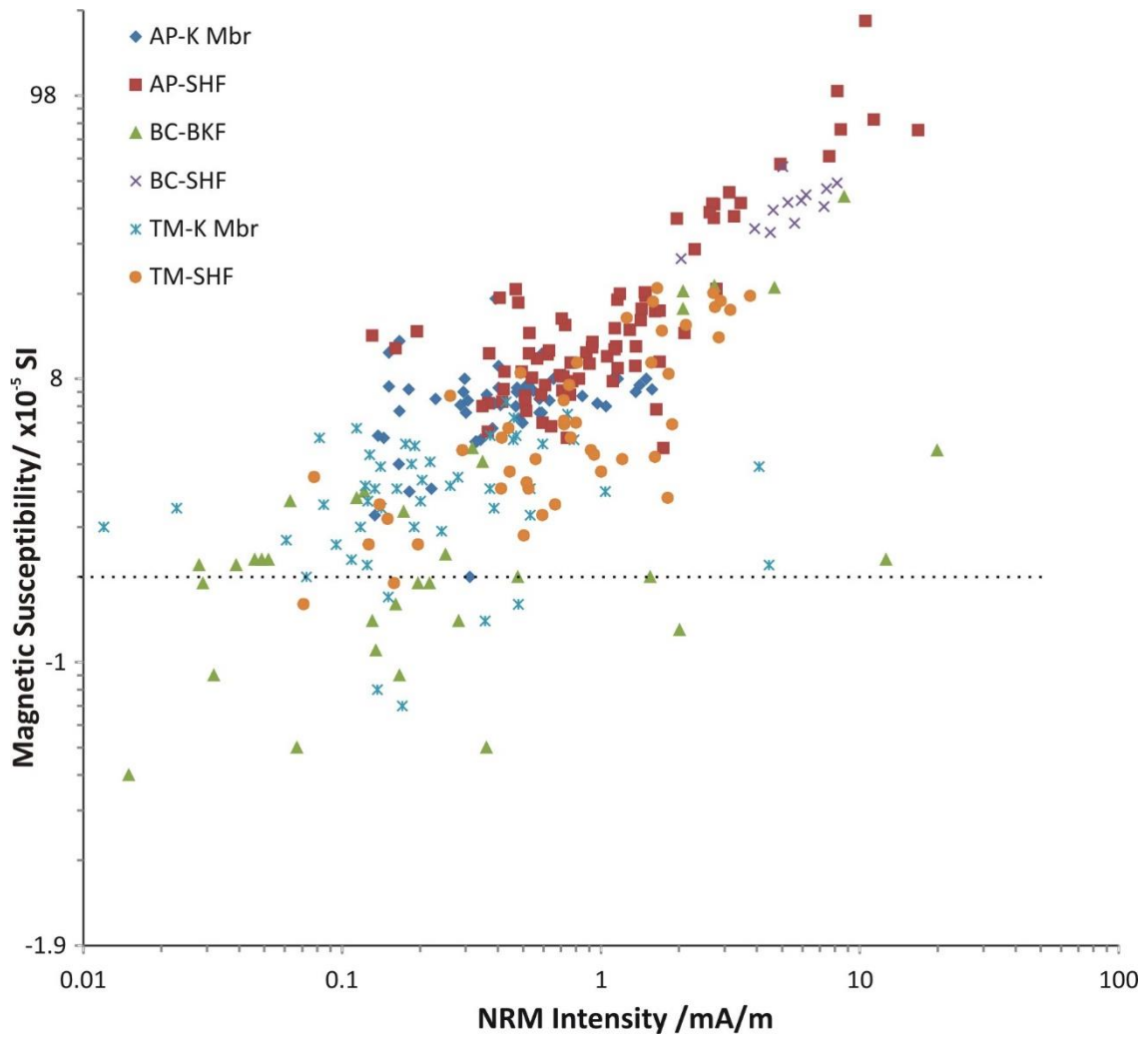


Figure 5.11 NRM intensity and magnetic susceptibility of all specimens from the Shabirinah and Brak Formations. Samples beneath the dotted line are diamagnetic. Note: magnetic susceptibility values have +2 added to them to overcome the problems of plotting negative values on a log scale.

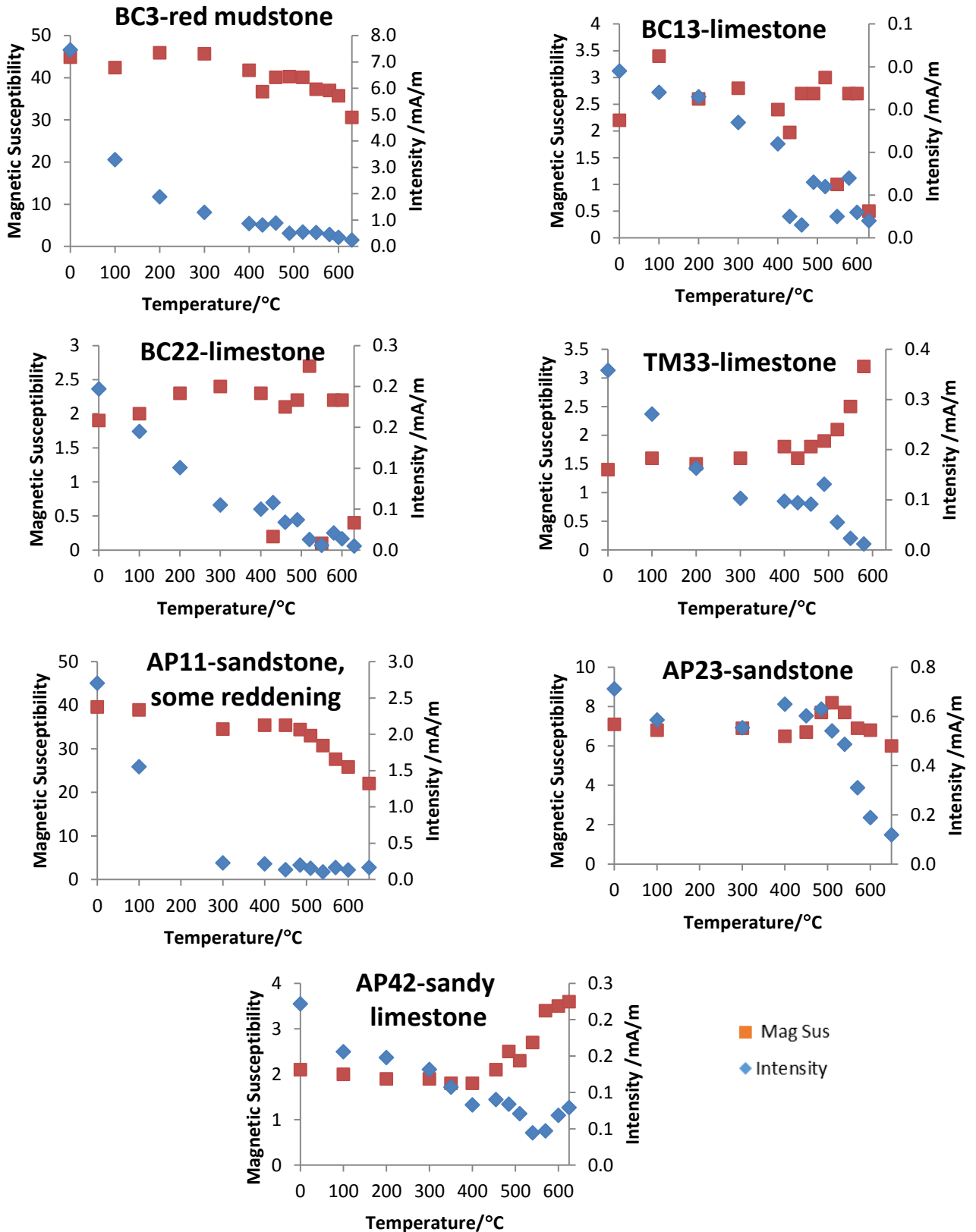


Figure 5.12 Changes in NRM intensity and magnetic susceptibility with demagnetisation temperatures for select specimens from the Shabirinah and Brak Formations. Note: B13, 22 TM33 MS values have +2 added to them due to some negative values.

5.2.2 Palaeomagnetic Results **Shabirinah Formation**

In total, 275 specimens were measured from the AP, TM and BC sections. Of these, 243 specimens relate to the Shabirinah Formation. A low stability component ('A') was present in 83% of the specimens from this formation. The A component was typically identified between room temperature and up to between 300-450°C in the AP and TM sections. In the BC section, the A component was often present at demagnetisation temperatures starting at room temperature/100°C to between 200-430°C. In the three sections, the component is generally northerly directed with positive inclination (Figure 5.13). A low stability component (southerly directed, positive inclination) is also identified, particularly in the AP section. It is thought the low stability component is a modern Brunhes overprint as the expected geocentric axial dipole (GAD) is similar to that of the ChRM direction (000/45) and possibly a combination of another primary component.

Intermediate stability components are identified in 26% of the TM specimens, 74% of the AP and 50% of the BC. It typically occurs at demagnetisation temperatures from ~300-400°C to 460-580°C. This component Figure 5.13, has a lot of directional scatter with no identifiable clusters.

The ChRM (s-class), or high stability components, were difficult to isolate from the specimens of the Shabirinah Formation with only 26% providing suitable line-fits to the demagnetisation data (Figure 5.13). However, of the 14 specimens from the BC section which correspond to this formation, a ChRM was isolated from 43% of the specimens. This success rate is a reflection of the clay-rich, reddened lithology of the samples which often display the best palaeomagnetic behaviour (Butler, 1992, pg150; Nielsen et al., 2004). Reddened deposits are less common in the AP section, and especially the TM section. The ChRM was often extracted at demagnetisation temperatures from 300-400°C to 570-600°C (Figure 5.14). Some ChRM directions were also present at >600°C but the majority of samples fully demagnetised around 600°C indicating the remanence is probably largely carried by magnetite as magnetite's Curie temperature is 580°C in comparison to haematite which has a Curie temperature of 680°C (Butler, 1992, pg18). In some of the samples such as AP23/42 remanence was still evident beyond 630°C suggesting haematite as the remanence carrier.

The ChRM data was assigned a class based on quality, in particular the noisiness of the principal component fits. The best quality data, s1, was assigned to just 2% of all the

measured specimens compared to s3, which was assigned to 12% (Figure 5.16 i-iii B). 50% of the total specimens displayed GC trends towards interpreted normal or reverse polarity reflecting the difficulty in isolating the ChRM from the low and intermediate components. As for the s-class, t-class data was classified into three classes based on qualitative visual assessment of the noisiness and length of the GC path (t1 best quality- Figure 5.16 i-iii B). The mean α_{95} for the poles to the fitted planes show little variation between the data (s) classes equalling 21.0°, 22.7° and 22.1° respectively. Of this data, GC fits (t-class) which included the origin were obtained from just 16% of the specimens (Table 5.5). 24% of the specimens were not able to provide reliable evidence of a primary magnetisation, largely as a result of directional scatter. This moderate success rate is likely a reflection of the predominantly sandy, clay-poor and calcrete-rich deposits in these sections.

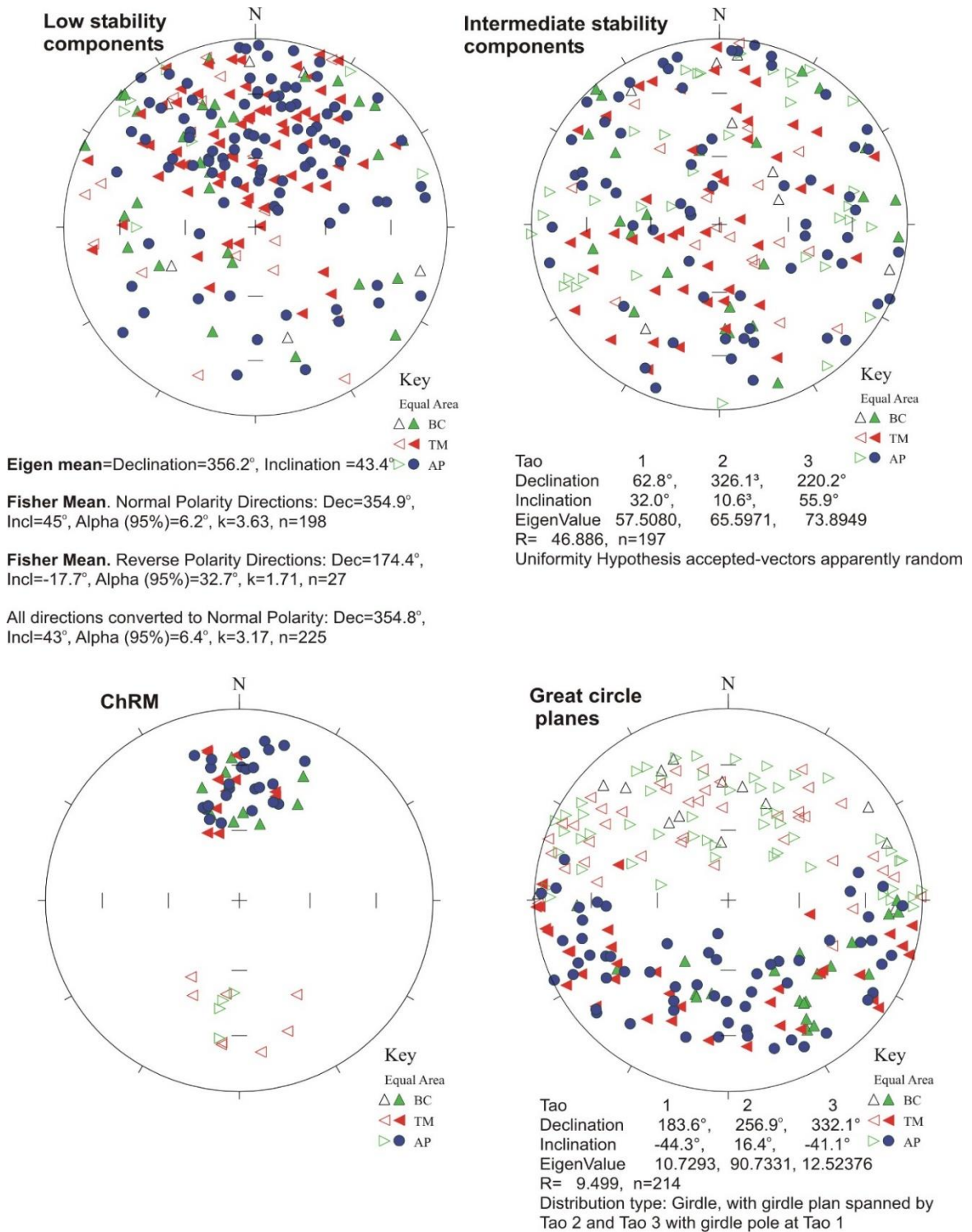


Figure 5.13 Components extracted from demagnetisation data of the BC, TM and AP sections and their statistical evaluation. ChRM statistics can be found in Table 5.6, pg161.

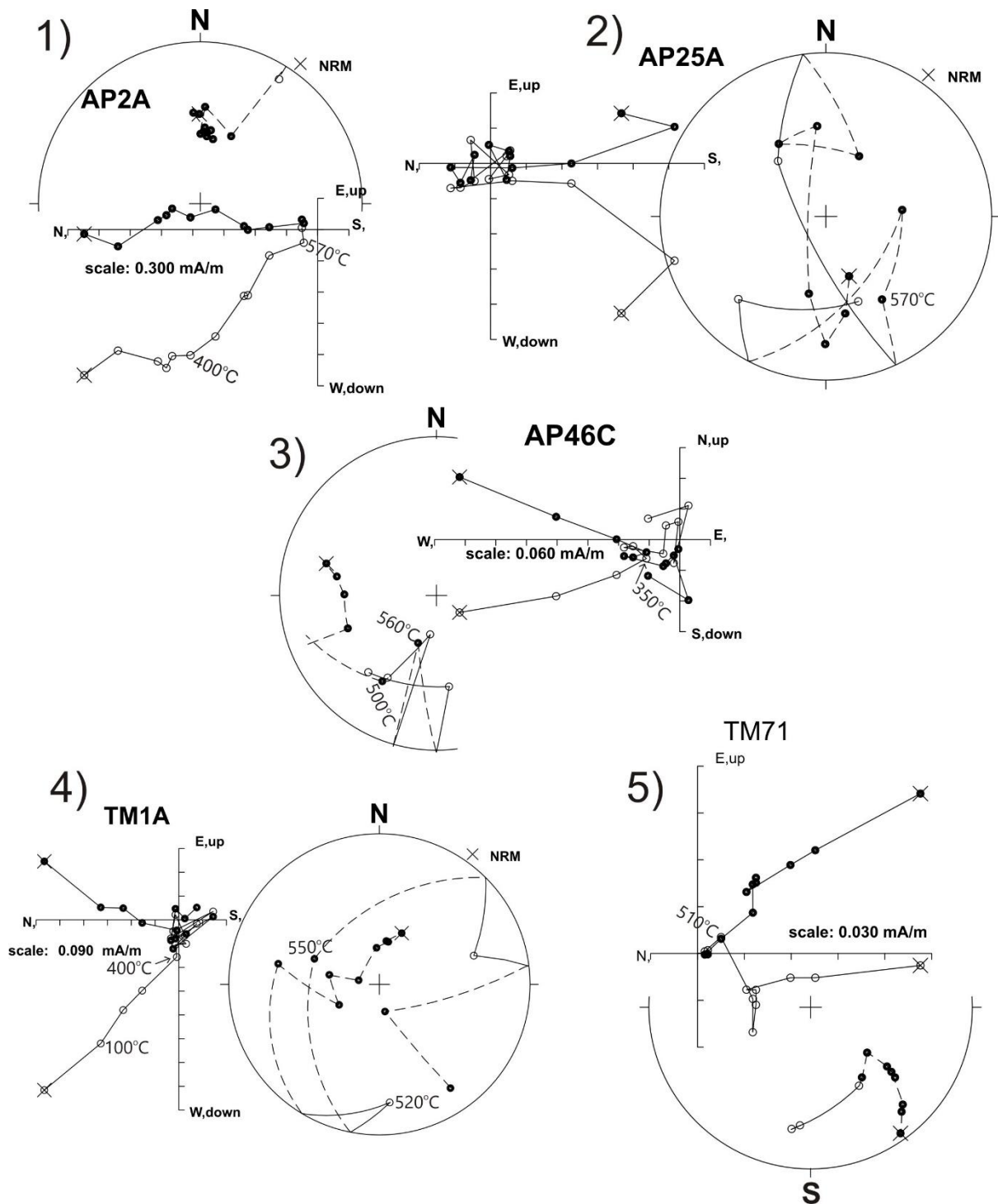


Figure 5.14 Representative demagnetisation data from the Shabirinah Formation. 1-3=Ariel section, 4/5=Tmessah section. 1) AP2A-normal polarity (N, s2 behaviour), ChRM from 400-570°C. 2) AP25A-reverse polarity (R?, t3 behaviour), erratic trend to R polarity evident from 570°C, intermediate stability component is northerly directed-overprint of present day field? 3) AP46C-reverse polarity (R, behaviour t2), showing component 'A' from NRM to 350°C, above which an erratic trend towards reverse polarity, with reverse polarity evident from 500°C. 4) TM1A-reverse polarity (R??, t3 behaviour) showing a strong A component from 100-460°C, the steps at 520-550°C recovers a reverse component. A GC plane fitted from 490°C to origin. 5) TM71-reverse polarity (R,s2 behaviour), showing a ChRM from 510°C to the origin.

Brak Formation

Representative demagnetisation data of the Brak Formation can be seen in Figure 5.15. The low and intermediate components of the Brak Formation are observed at similar demagnetisation temperatures to the Shabirinah Formation, generally from room temperature to 300-400°C and up to 500-580°C. The directions of the low stability components are predominantly northerly directed with positive inclination and southerly directed with positive inclination. The intermediate components show scatter with a mix of directions evident. Of the 32 specimens which relate to the Brak Formation, a ChRM (s-class) was isolated from just 9% of the samples, with 3% assigned an s1 classification and 6% an s3 (Figure 5.16 iii B). The ChRM was usually isolated between 430-630°C with the majority of specimens that have a ChRM, lacking an intermediate component. 72% of the total specimens from this formation displayed GC trends towards interpreted normal or reverse polarity. Nearly three times as many (47%) specimens had GC planes which intersected the origin compared to the Shabirinah Formation. From this formation, 19% of the specimens were not able to provide reliable evidence of primary magnetisation. The difference in the amount of ChRM's isolated from the Brak Formation compared to the Shabirinah Formation can be explained by the lithology, as calcretes can be poor palaeomagnetic recorders often due to low concentrations of magnetic minerals, labile magnetic minerals or a tendency towards viscous magnetic behaviour (Nielsen et al., 2004; Lowrie and Heller, 1982). Furthermore, the Brak Formation samples have a long and complex formation history which could explain the mix of directions in the intermediate components due to partial overprinting such as during late diagenetic growth (Lowrie and Heller, 1982), and the rather poor preservation of primary magnetisation observed in these

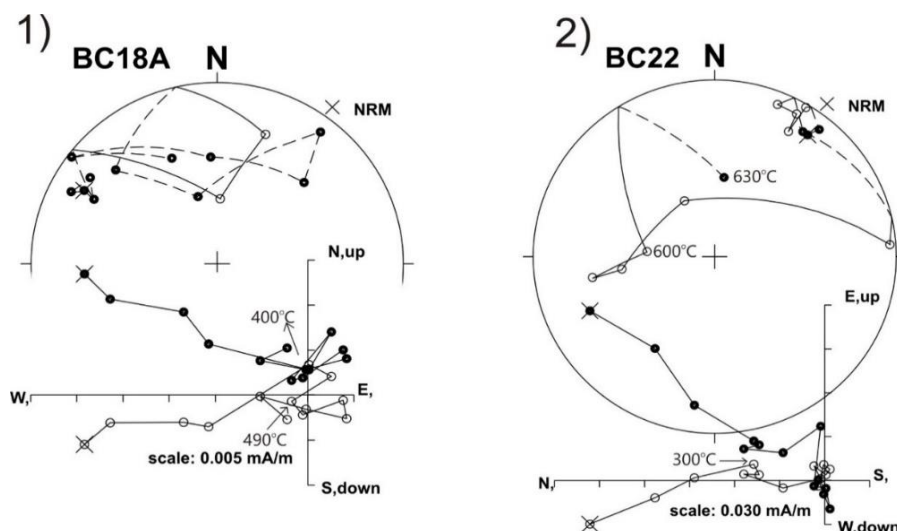
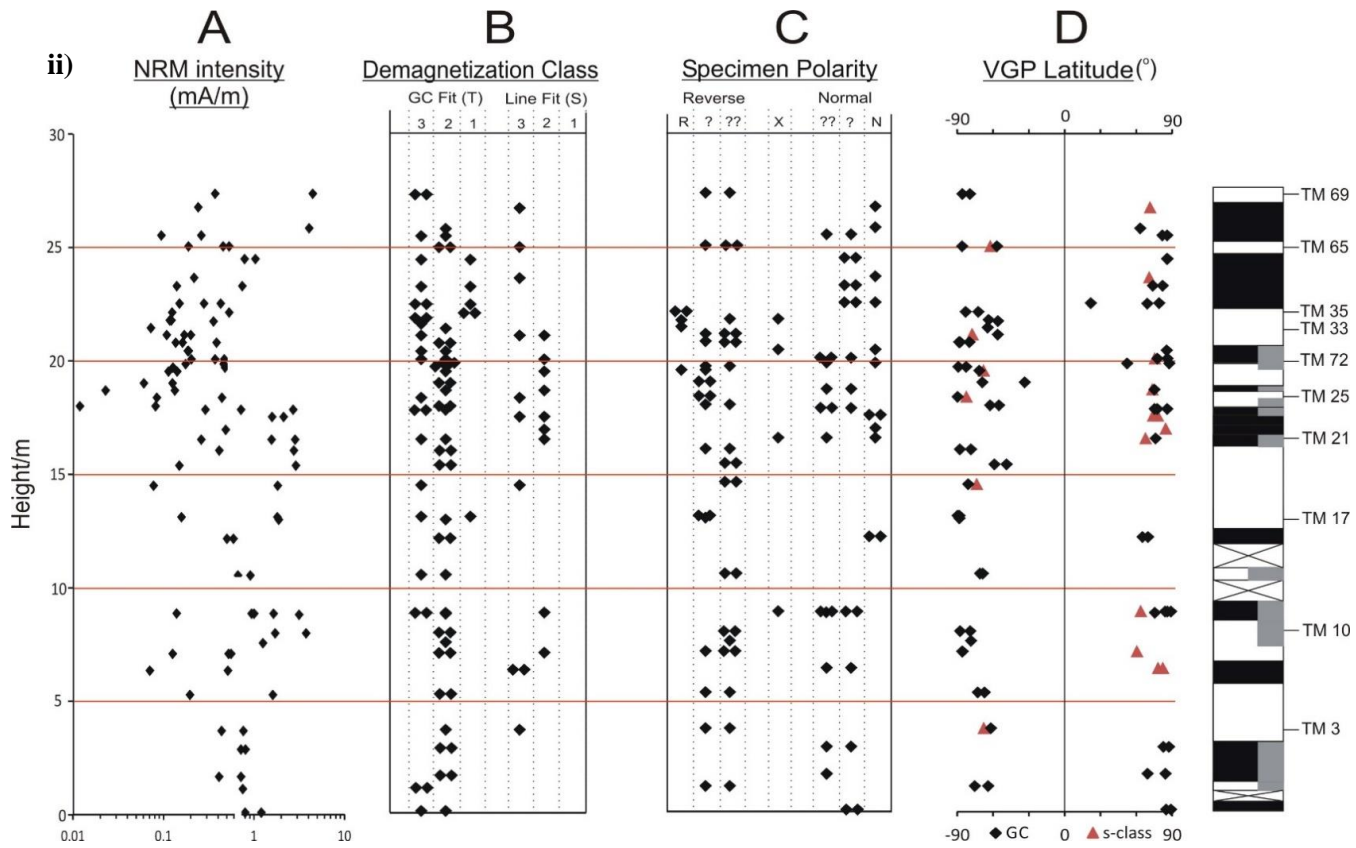
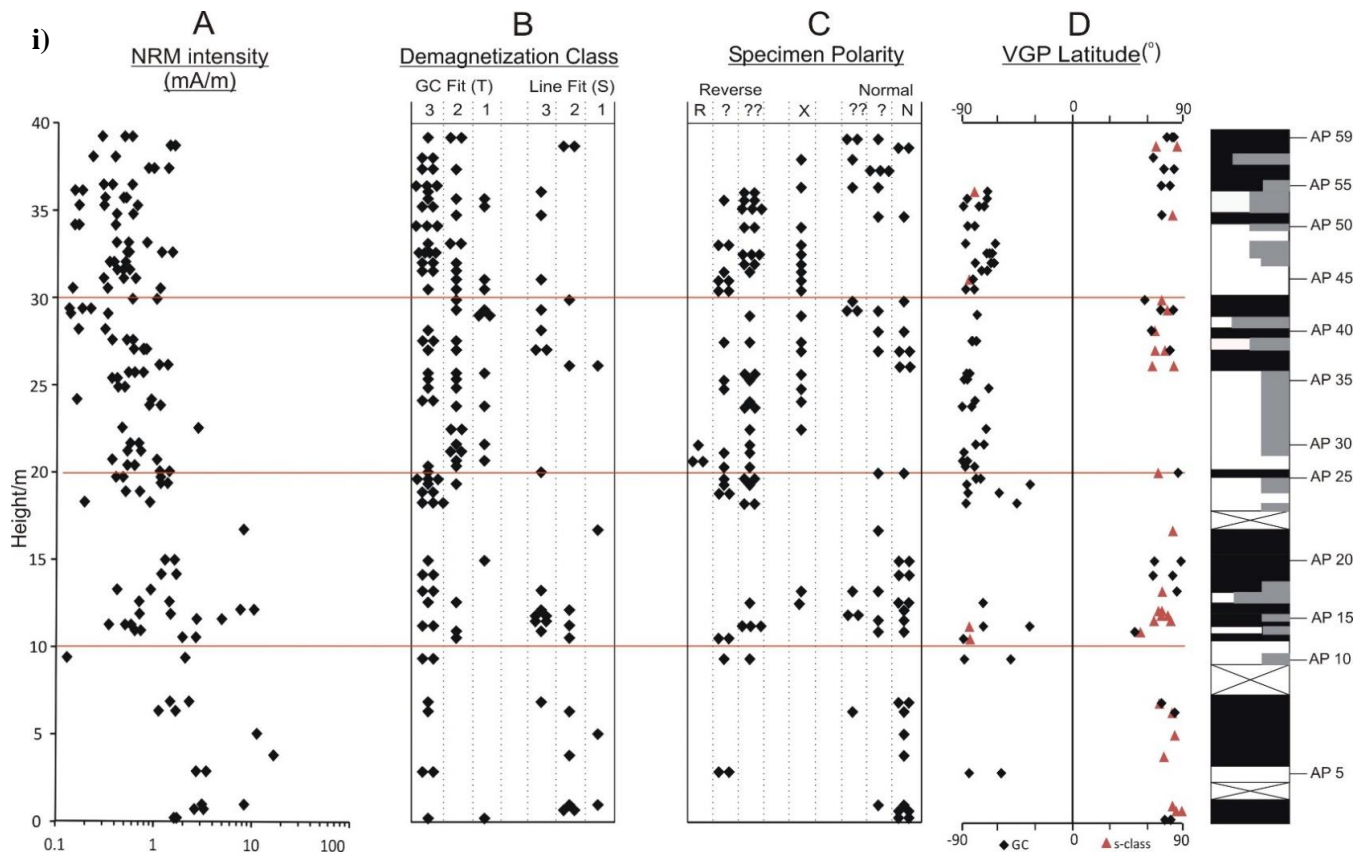


Figure 5.15 Representative demagnetisation data for the Brak Formation (specimens from the Brak section). 1) BC18A-normal polarity (N?, t2 behaviour), component 'A' from NRM to 400°C. A GC is fitted from 490°C to the origin. 2) BC22-reverse polarity (R?, t1 behaviour), component 'A' from NRM to 300°C with a GC plane fitted from 300°C to the origin. specimens.



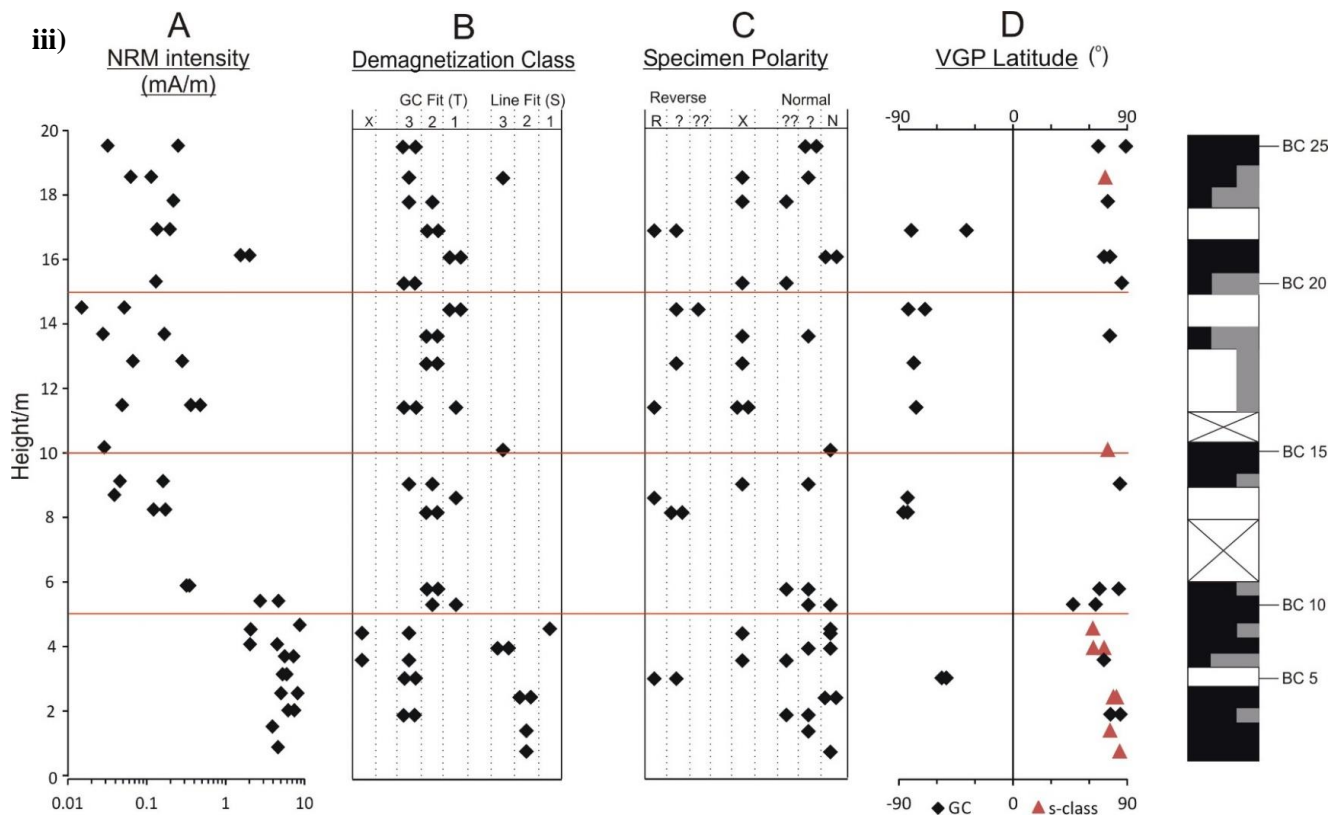


Figure 5.16 Magnetostratigraphic data summary of the i) AP, ii) TM and iii) and BC sections. A-Natural Remnant Magnetisation. B-Demagnetization behaviour categorised into good (s1) and poor (s3) characteristic remanent magnetisation (ChRM) line fits, great-circle (GC) fit quality range from good (t1) to poor (t3). C-Interpreted specimen polarity quality. No interpreted polarity data in column headed X. D-The virtual geomagnetic pole (VGP) latitude, red triangles representing s-class ChRM, black diamonds t-class GC behaviour specimens. To the right of the figure is the interpreted magnetic polarity stratigraphy, white - reversed polarity, black - normal, grey - uncertain.

	GC planes with interpreted polarity (%)	Origin intersecting GC planes (%)	S1 %/ mean α_{95} (°)/ mean excess SD (ρ)	S2 %/ mean α_{95} (°)/ mean excess SD (ρ)	S3 %/ mean α_{95} (°)/ mean excess SD (ρ)	T1 %/ mean α_{95} (°)/ mean excess SD (ρ)	T2 %/ mean α_{95} (°)/ mean excess SD (ρ)	T3 %/ mean α_{95} (°)/ mean excess SD (ρ)
SHF	50	16	2/3.8/1.8	10/10.2/2.1	12/14.5/2.9	7/21/-	22/22.7/-	27/22.1/-
BKF	66	44	3/8/12	0/-/-	6/12.5/2.1	13/28.3/-	34/19.9/-	28/23.4/-

Table 5.5 Table outlining some of the key statistics of the SHF and BKF. ‘%’ refers to the total number of specimens classified as s1-s3/t1-t3. ‘mean α_{95} ’ when listed under s-class refers to the mean α_{95} of the linear fits, when listed under t-class it refers to the mean α_{95} for the poles to the fitted planes. ‘mean excess SD’ (ρ) refers to the mean excess standard deviation parameter calculated for the different classes (for s-class-calculated from the average line ρ value in LINEFIND, for t-class- calculated from the average plane ρ value in LINEFIND). The t-class mean excess SD could not be calculated as the plane ρ values were not recorded.

5.2.3 Mean Directions and Palaeopoles

It is possible in palaeomagnetic studies to determine the mean directions for the majority of horizons using multiple successfully measured specimens per horizon known as ‘horizon means’ (Hounslow et al., 2008). However, defining a horizon by only two or three specimens cannot adequately represent the true secular variation (Hounslow et al., 2008), and as such, ‘specimen based’ means were used to determine the mean directions from the sections. Specimen based means use specimens with GC paths combined with those that had a line-fit ChRM (s-class) to produce a combined Fisher mean using the method of McFadden and McElhinney (1988). This method uses maximum likelihood analyses and calculates a mean by including the ‘fixed point’ ChRM directions and points on the projected GCs which maximise the resultant length (i.e. the calculated points on the GC which are nearest to the combined mean direction). The mean directions of the three sections are shown in Table 5.6 along with the VGP pole. The VGP pole positions of the three sections and the mean inclinations are similar, although the BC section inclination is slightly steeper. A reversal test (a form of stability test) was also conducted. A reversal test is passed if the mean direction produced from normal polarity sites is statistically equivalent to the antipodal mean direction of reverse polarity sites (Butler, 1992). The TM and BC sections pass this test but the AP narrowly fails. It is not uncommon for palaeomagnetic data to display data that is not quite antipodal (Scott and Hotes, 1996; Pares and Van der Voo, 2013) and in the case of the AP section it is likely due to unsuccessful removal of secondary ‘contaminating’ components (Butler, 1992, pg99) possibly caused by near-surface alteration (weathering) (Scott and Hotes, 1996).

Site	Mean Direction Dec/Inc/ α_{95} (°)	NTotal	NLines	NPlanes	Reversal Test [γ_o ; γ_c]	VGP Pole Lat/Long (°) (Dp/Dm) Palaeolat
Ariel (AP)	3.4/42.1/3.1	134	32	72	R-[7.67; 6.53]	85.9/145.5 (2.3/3.80) 24.31
Tmessah (TM)	1.1/42.9/3.8	95	19	58	Ra [1.59; 7.64]	88.5/153.1 (2.91/4.70) 24.92
Brak (BC)	1.2/45.2/5.7	46	9	20	Rb [9.03; 12.66]	88.9/118.1 (4.50/7.22) 25.54

Table 5.6. Directional means, reversal tests and virtual geomagnetic poles for the sections of the SHF and BKF. Note: α_{95} is the Fisher 95% cone of confidence, Ntotal= total number of specimens measured, Nlines= number specimens with s-class line fit used in the mean Fisher calculation, Nplanes= number of specimens with t-class (great circle fit) and used in the mean Fisher calculation, Ra and Rb indicate a pass of the reversal test with an observed gamma of <5 and <10 respectively, R- is a failed reversal test, γ_o is the observed gamma, γ_c is the critical gamma. Dp/Dm is the semi-axes of the ellipse of confidence about the palaeomagnetic pole.

As a test of reliability of true directions, the VGP poles of the three sections were compared with palaeopoles of a similar age from Africa. The VGP map projection (Figure 5.17) includes the limited number of palaeopole data of Pliocene and Miocene age from North Africa in Torsvik et al. (2012). The poles of the Jebel as Sawda volcanic rocks (JSV1/2) from Libya are also included (Ade-Hall et al., 1975; Shultz and Soffel, 1973). Poles from Torsvik et al. (2012) are south poles, so the poles of the sections had to be inverted in order to compare them (i.e. $\pm 180^\circ$). The poles of the sections in this study, especially the TM/BC, are located fairly near to each other and to the east of the Gondwana apparent polar wander path (APWP). The confidence intervals of the palaeopoles of the three sections overlap with the APWP for the 0-30Ma intervals and thus show reliability of the mean directions. Generally, the poles are displaced to the east of the APWP while the JSV1/2 poles are much lower in latitude as a result of shallower mean inclinations compared to the poles of the sections and the APWP.

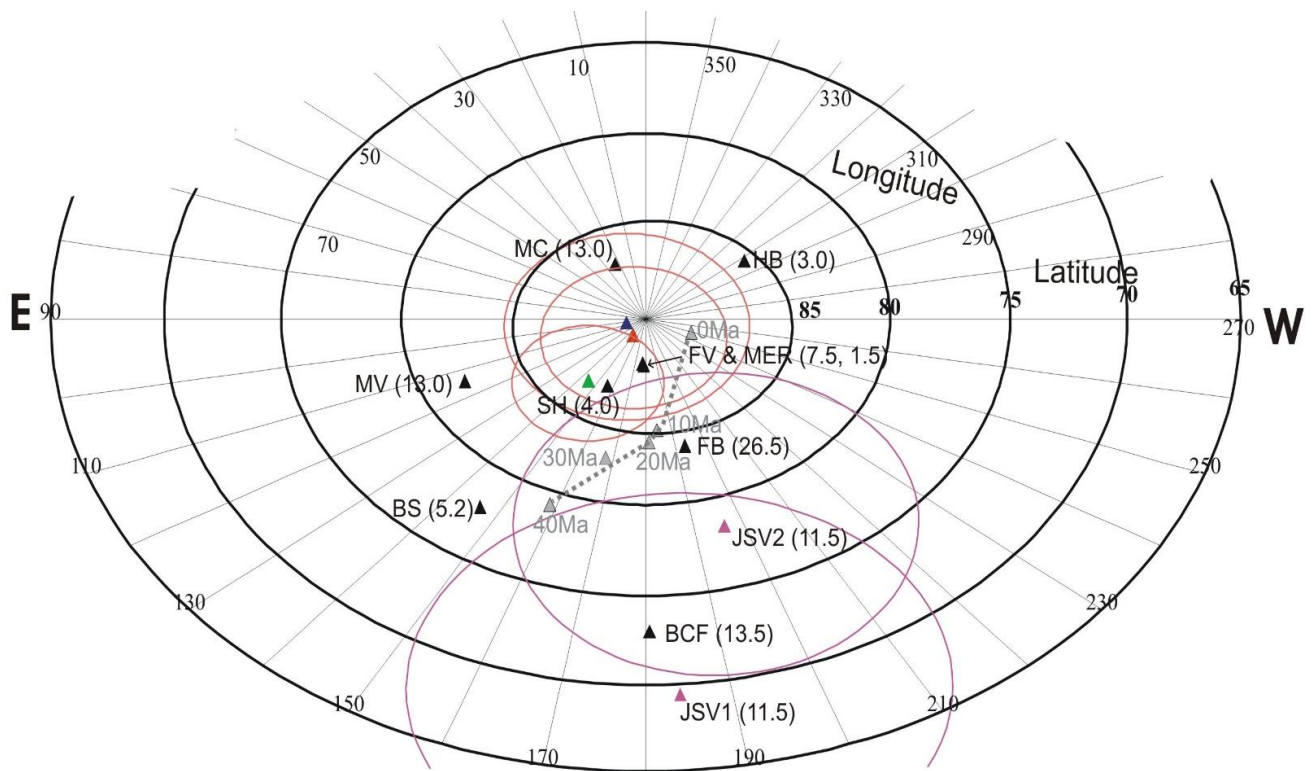


Figure 5.17 Miocene to recent North African palaeopoles, with 95% confidence cones shown for the Shabirinah and Brak Fm. Green triangle-Ariel section, Red triangle-Tmessah section, blue triangle-Brak section. Pink triangles from Jebel as Sawda (JSV1/2). Black triangles are poles (age in Ma), listed in Torsvik et al. (2012). FV=Famara Volcanics, Canary Islands (CI); BS= Basalt Series II, CI; MV= Miocene Volcanics, CI; MC=Basalt Series I, CI; MERr= Main Ethiopian Rift Basalts; HB= Hadar Basin, Ethiopia; SH= South Holhol-Djibouti; BCF= Blue Clay Fm, Malta; FB=Flood Basalts, Ethiopia. Grey triangles are the Gondwana apparent polar wander path (APWP) from Torsvik et al (2012; Table 7), labelled in 10Ma increments.

5.2.4 Magnetostratigraphic Age Model

Line-fit ChRM (s-class) directions from the three sections were converted to VGP latitude using the VGP pole in Table 5.6. For specimens with no line-fit (t-class), the point on their GC nearest this mean was used for VGP latitude calculation (Figure 5.16 i-iii D). Based on the VGP latitude and behavioural class, each specimen was assigned a polarity quality (R, R?, R??, ?, N??, N?, N). For 13 horizons, 10 from the Shabirinah Formation and three from the Brak Formation, a single specimen with good quality palaeomagnetic data (s1/2, t1/2) was enough to define the horizon polarity. The majority of the horizons needed two specimens, with many from the AP requiring three specimens to confidently determine the horizon polarity. Details of how the horizon polarity quality was defined is noted Table 4-Appendix, pg287. Overall, 11% of the total specimens were assigned an uncertain ('?') polarity (Figure 5.16 i-iii C). When comparing the Shabirinah and Brak Formations however, the Shabirinah Formation contains 9% of specimens with a '?' polarity compared to 25% in the Brak Formation reflecting the difficulty in extracting magnetic data from this formation. None of the horizons (i.e. at least one specimen from each horizon was assigned polarity) however failed to yield specimens which could be reliably used to determine magnetic polarity. No horizons contained specimens of opposite polarity.

Section correlations and composite development

Once polarity was assigned to each horizon (Figures 17/18 – Appendix, pg305/306), the sections could be correlated to one another and a polarity composite developed. The TM/AP sections can be correlated to one another using the base of the Kunayr Member which overlies a thick unit of reverse polarity (Figure 5.18). Based on additional section logs recorded in the field (see Hounslow et al. 2017), it appears ~3 m of red mudstones are missing from the upper part of the Stromatolite Member in the TM section. This is due to down cutting of the channel sandstone at the base of the overlying Tmessah Member. Because of this, it was decided that the TM section should be sub-divided (Figure 5.18). The youngest normal polarity unit in the Tmessah Member was correlated with the base of the normal polarity unit in the AP section with its lower boundary at 11.4 m. This correlation links the palaeosols of the AP section to the fluvial (lower) part of the Tmessah Member in the TM section. The youngest parts of the Shabirinah Formation in all three sections can be correlated to one another due to the dominant normal polarity. This allows a composite magnetostratigraphy to be developed which incorporates all the sections.

There is however some uncertainty in how to correlate the lower part of the BC section to the upper part of the AP/TM sections. Because of this, two composite polarity options were derived (composite A/B Figure 5.18), one where the top normal polarity unit of the TM section relates to the lowest normal polarity unit of the BC section and one where it relates to the second lowest normal polarity unit. It is thought that composite B may be the better option as it correlates the sandstone bed at the top of the TM section to the reddened clastics at the base of the BC section. Magnetozone codes were assigned to each of the composites (32 to composite-A, 34 to composite-B) but the normal polarity magnetozone, Sb6r.1n, was not detected in the TM section. This may suggest a potentially missing part of the TM section due to some degree of uncertainty when correlating (lithostratigraphically) the sub-sections of TM at this level in the field. The composites were generated using the numerical optimisation technique outlined in Hounslow (Submitted) which minimises the sum of the squared residual offset for each chron boundary. For each section the polarity boundary heights were scaled to a new composite height (Hounslow, Submitted), in this case, the metre scale of the AP section whose data remained unscaled. The technique however allowed the BC section to be shifted without a change in scale, whereas for the TM section both a shift and a scale change took place. A constant sedimentation rate is assumed for all the sections and so a linear rate function was applied (Hounslow, Submitted). The measure of the overall chron misfit was performed using the Solver function in Microsoft Excel (Hounslow, Submitted).

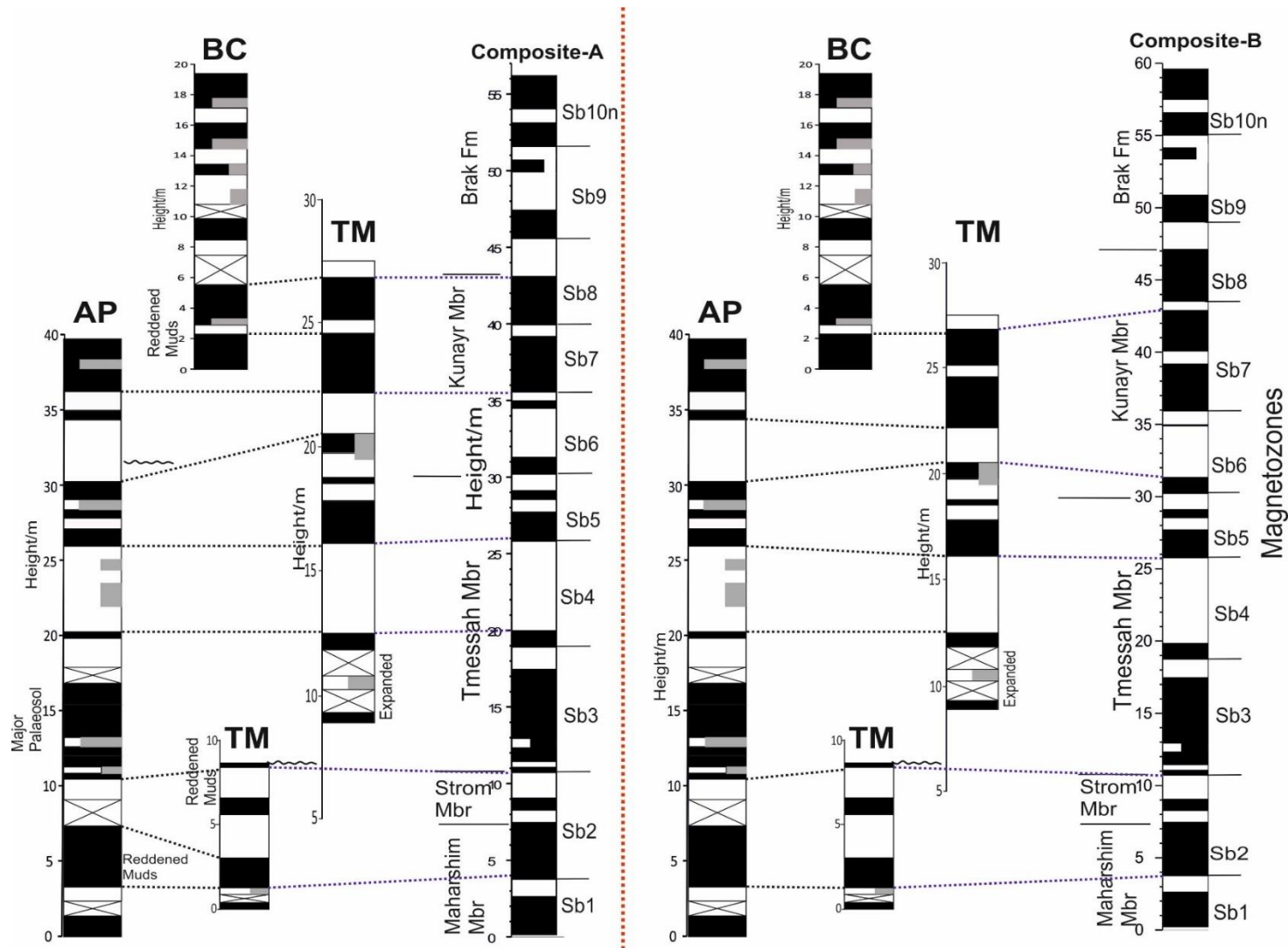


Figure 5.18 Palaeomagnetic correlations and composite options of the SHF sections as discussed in the text. Scale of the composites are in the metre scale of the AP section. Sb codes relate to the assigned magnetozones of the composite. Note: black = normal polarity, white = reversed, grey = uncertain. For additional illustrative information please see the key in Figure 5.19.

Confirming the Palaeomagnetic Age

Unfortunately, as biostratigraphic or radiometric evidence is not present in the sections, no firm age tie points can be applied to the sections. As a result, a quantitative method of correlation to the GPTS was needed to successfully date the successions. A number of statistical methods were explored which included a cross-correlation method using the \log_e of the ratio (r_i) of the lengths of the underlying magnetozones (i.e. $r_i = L_i/L_{i-1}$ where L = magnetozone lengths in metres or Ma duration for the GPTS; Man, 2008). A maximum-likelihood based method was also considered where the sediment deposition (and erosion) of a section is regarded as a stochastic process ‘whose discrete time increments are independent and normally distributed’ (Man, 2011). Both of these methods are however limited by the need for all polarity chrons to be recorded in the sections. The method of Man (2011) is also limited by the ability of the program to only be able to identify 14 geomagnetic polarity reversals at most as a result of complying with a single stochastic sedimentation model. A final method investigated was that of Maron et al. (2015) which correlates the thickness of magnetozones between the sections and a ‘standard’ (i.e. the GPTS) assuming that thickness is a linear proxy of time. This was conducted by means of a Student t -test however, this method does not automatically include information about the relative duration of adjacent magnetozones.

The overriding problem in all of the explored methods is that they only employ one characteristic of the polarity pattern (duration of r_i). The nature of the GPTS may be better expressed when multiple characteristics are taken into consideration including polarity bias around the chron and the relative duration of more than two adjacent chrons (Olson et al., 2014). The use of characteristics from adjacent magnetozones allows some smoothing of the response function which limits the uncertainty of magnetozone height (Hounslow et al., 2017). It was decided that the best approach for quantitatively correlating the composites to the GPTS was the sequence slotting method (Clark, 1985; Thompson and Clark, 1989; Thompson et al., 2012) implemented in the CPLSLOT programme. Sequence slotting is a quantitative correlation method which optimally ‘slots’ two ordered datasets by minimising the dissimilarity between the two. This method has many advantages over the methods previously described. It can deal with multivariate datasets with different weightings between variables applied to downgrade/upgrade impact. Analysis is not restricted to a limited number of polarity reversals. It differs to cross correlation methods as well as those of Man (2008; 2011) as it is not constrained to sequential matching of data points and hence can deal with missing chrons within the composite and variable sedimentation rates.

Five variables were used to parameterise each magnetozone: polarity, -1 (R magnetozone) +1 (N magnetozone); duration (in Ma); $\text{Log}_e(\text{ri})$; the polarity bias which includes the two adjacent chrons and the Sherman's ω_2 statistic which using the two adjacent chrons, measures the deviation of the magnetozone length as a proportion of the average length (see Table 12-Appendix, pg310) (Olson et al., 2014). For each of the variables a different weighting (i.e. a value) was applied to see which variable impacted on the model the most. In all options it was clear a higher weighting for the polarity and duration produced better models. For each run a Euclidean distance metric (similarity/dissimilarity) (Gary et al., 2005) and a blocking constraint of two (Thompson and Clark, 1989), which limits missing chrons in the GPTS to one chron/subchron, were used. The duration of the magnetozones for both composite options were estimated using section durations based on reversal rates of 0.259Ma^{-1} . This is the median rate for the last 29 Ma from the GPTS of Ogg (2012) if chrons <40kyr are excluded.

The success of the sequence slotting can be measured in two ways; by evaluating the 'short' and 'long-range' success. Short-range success can be evaluated using conventional slotting parameters, especially the Δ (see Table 12-Appendix, pg310) which indicates how well sequences are matched together (values >0 to 1 where ~ 0.5 indicating very good similarity). The use of the Δ alone can be misleading as it can be strongly impacted by data variability nearby to the levels considered and so different correlation options can result in a similar value. Matrix association coefficients (R_c , RV_2 and standardised RV) evaluate the long-range success by comparing the similarity of the whole configuration of variables between the two datasets (Smilde et al., 2009). Compared to the Δ parameter these coefficients are less impacted by local noise, responding better to visual similarity when data are plotted next to one another. Solutions can best be imaged by the H-matrix (Figure 5.19) (Gordon et al., 1988), a visual representation of the matching similarity of the two datasets as they are slid past each other.

Sequence slotting solutions for both tested composites indicate there are two likely match solutions, a Tortonian model and a Serravallian model. A less likely Oligocene model was also identified from the solutions of composite-B but was dismissed as a possible solution based on poorer values of the matrix coefficients along with a poorer association probability and the greater amount of missing chrons ('a' Figure 5.19). For the composite-A Tortonian model, sequence slotting relates Sb10n.2n to C3Br.2n (section top) and Sb1r to C5Cn.2r (section base) while the Serravallian model is placed so Sb10n.2n=C5An.1n and Sb1r=C6Br. For both of these models the slotting parameter Δ is

similar while larger matrix coefficients are given for the Serravallian model. The Tortonian solution of composite-B is placed so $Sb10n.2n=C3Br.2n$ and $Sb1r=C5Cn.2r$ compared to the Serravallian which matches $Sb10n.2n$ to $C5An.1n$ and $Sb1r$ to $C6Br$. As for composite-A, the Serravallian model has the larger matrix coefficients, with Δ parameter similar for both models. When comparing the Serravallian models of composites-A and B, composite-B has a smaller Δ and larger matrix coefficients. The association probability is also 10% greater for composite-B and has fewer missing chrons. Based on these results, the composite-B Serravallian model is the preferred age model option (Figure 5.20). When carrying out sequence slotting it became clear that to achieve the best visual match the weightings of the variables of duration, polarity bias and polarity were of particular importance. For the composite-B Serravallian model these variables were therefore set to a higher impact value (2, 2 and 5 respectively) than the remaining variables (set to 1).

Overall, composite-B ranges in age from 22.564-12.174Ma. The carbonate-rich units of the composite, indicative of a more humid conditions, are found within the Stromatolite Member, the lower Kunayr Member and the Brak Formation. These occur during the late Aquitanian (~21.8-21.2Ma), the latest Burdigalian to Langhian (~16.5-14.6) and the Serravallian (13.4-12.2Ma) respectively. The accumulation rates of the Tmessah Member and Brak Formation are broadly similar however a decline is apparent in the Stromatolite Member. As the composite polarity does not capture the dominant reverse polarity well through chrons C6Ar and C6AA, it suggests there may be a regional hiatus at the base of the Tmessah Member. It may also be due to a shut down in coarse clastic supply in the Stromatolite Member as it is predominantly composed of micritic carbonate and mudstone.

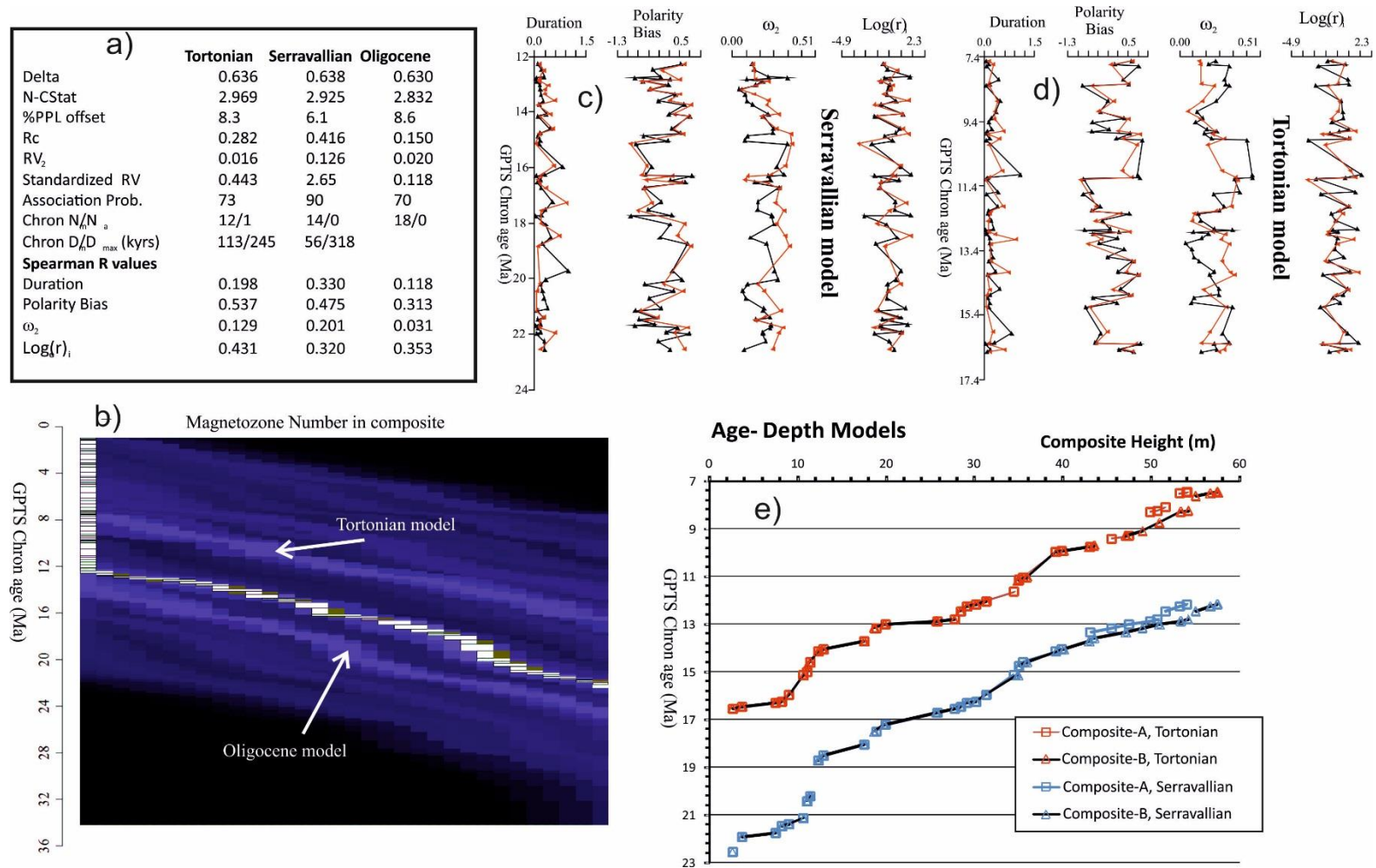


Figure 5.19 Sequence slotting model output for Composite-B showing data for the three most likely correlation models. a) the statistical summary of the correlation models. b) The H-matrix plot, where the brighter blue bands correspond to alternative correlation models. The mostly likely model (ending in Serravallian) is shown as the white boxes across the plot, with y-axis height corresponding to GPTS chron duration. The band corresponding to the Tortonian/Oligocene model are arrowed. The x-axis on this plot is the magnetozone number. c) and d) The input data to the slotting model, plotted against chron age for the two correlation options. e) Depth-age models for the two polarity composites A and B, and the Tortonian and Serravallian age models. The age-depth relationships for the two age models are similar for composite A and B apart from the upper part of the composite sections.

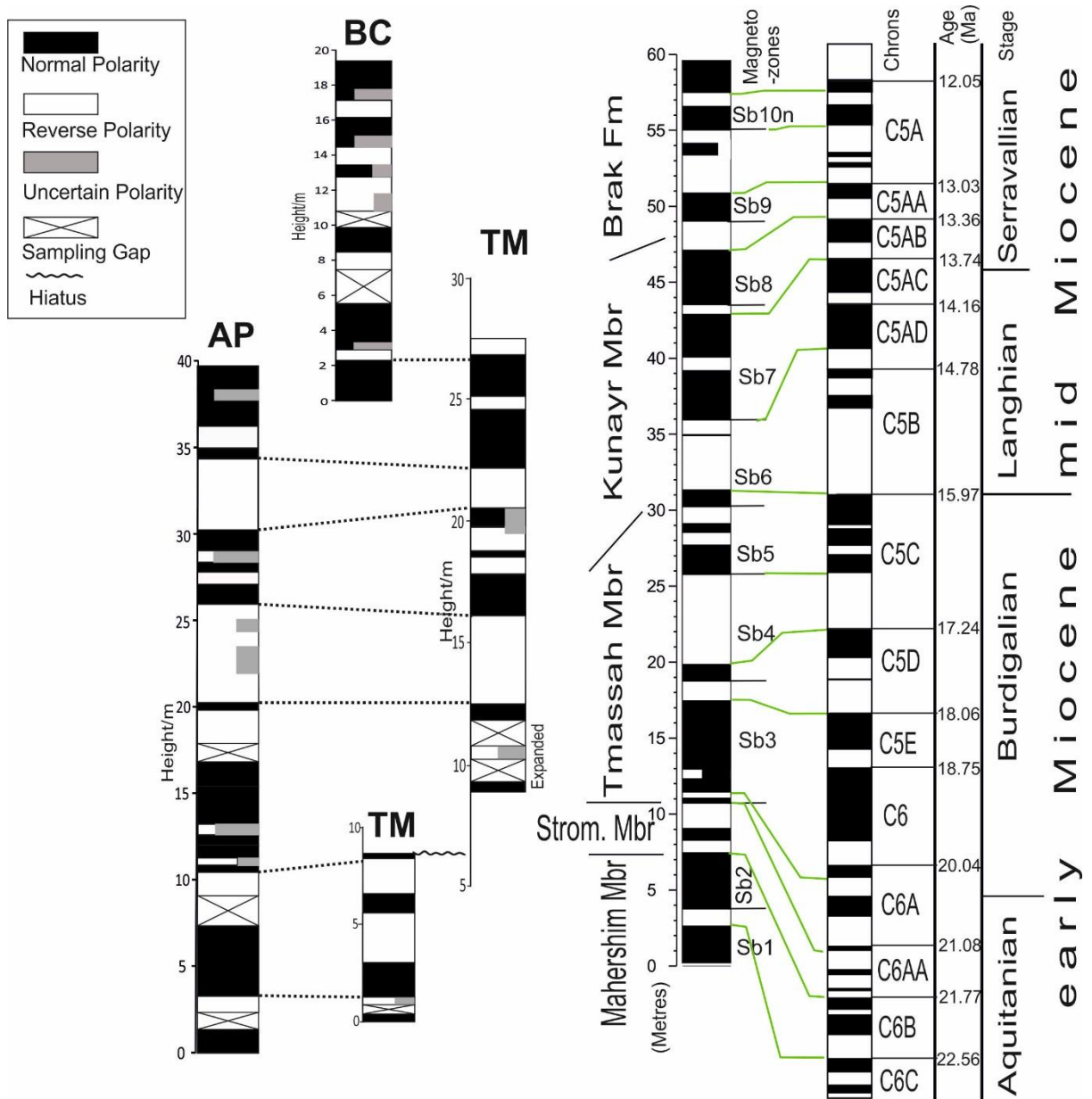


Figure 5.20 Composite-B magnetic polarity stratigraphy with the final age model on the right. Chron correlation lines (green) to the GPTS (Ogg, 2012) derived from sequence slotting. Please refer to the key within the figure for illustrative information.

6 Results: The Zarzur Formation

The focus of this chapter is on the sections that relate to the Zazur Formation, namely the QM1 and QM2 sections, the M section and the three BZ sections.

6.1 Palaeoenvironmental Indicators: Petrography and Palaeohydrology

6.1.1 Sayl Member (SL Mbr)

Only petrographic data is available for this member as summarised in Figures 6.5/6.8. Five deposits from the base of the QM2 section and one from the base deposit of the BZ-E section are assigned to this member. The hand specimen descriptions of the QM2 deposits are noted in Table 6.1. On the whole the clasts in the TS are sub-angular to sub-rounded, fairly uniform in size (often <125µm) and composed of quartz. Clasts are in a floating muddy matrix, especially in AL12 (Plate 6.1-A). Clasts are more abundant in the deposits of QM2 and can be seen in contact with one another in places. Patchily developed pore-filling cements can be seen in the QM2 sections with these deposits having open primary porosity (Plate 6.1-B). AL12 is composed of micrite which in areas is dense and likely clay-rich. The cement is green in colour: possibly indicative of reducing environmental conditions (Maher and Thompson, 1995). Micritic peloidal type grains (Plate 6.1-C) are present and cemented by a micritic rim. They are scarce, generally oval in shape and lacking internal structure and likely formed due to reworking of the mud (Flugel, 2010, pg114). Secondary porosity in the form of long, occasionally sinuous, shrinkage cracks occur in AL12, possibly due to desiccation. The cracks pass around the clasts suggesting they developed later in the deposits evolution. Some of these cracks are filled by secondary microspar cement which is also seen occupying rootlet traces (Plate 6.1-D). Red staining is also observed in the TS suggestive of more oxidising conditions.

<u>Sayl Member</u>	
Colour	Pale brown (2.5Y 8/2) to yellowish red (5YR 5/6)
Texture	Clastic-sandstones/siltstones, some mottling
Grain size/sorting	Very-fine to fine sand-sized, some coarse-granule sized clasts. Well sorted.
Composition	Quartz-rich, some clays
Key Features	Very friable, some horizontal fractures
NaSi coating	Evident on all deposits

Table 6.1 Hand sample descriptions of the SL Mbr deposits from the QM2 section. The BZ-E section also contains one deposit related to this member, however as it is only one deposit, the hand sample characteristics are not included in this table.

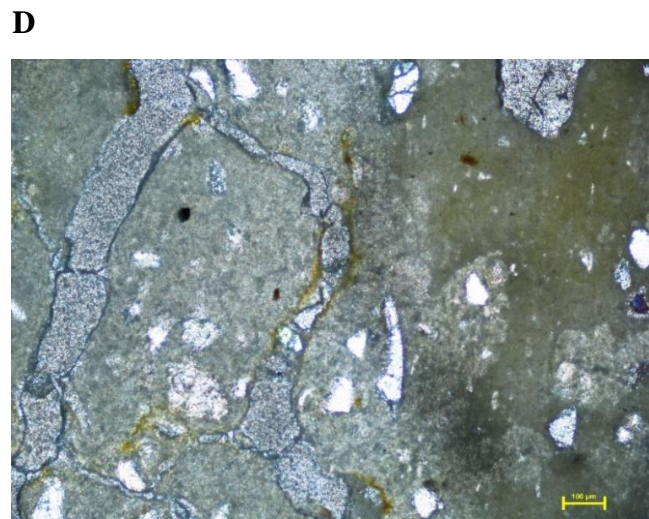
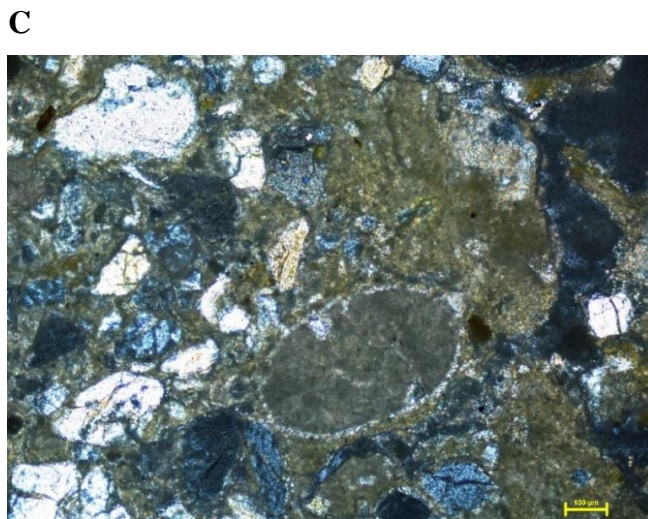
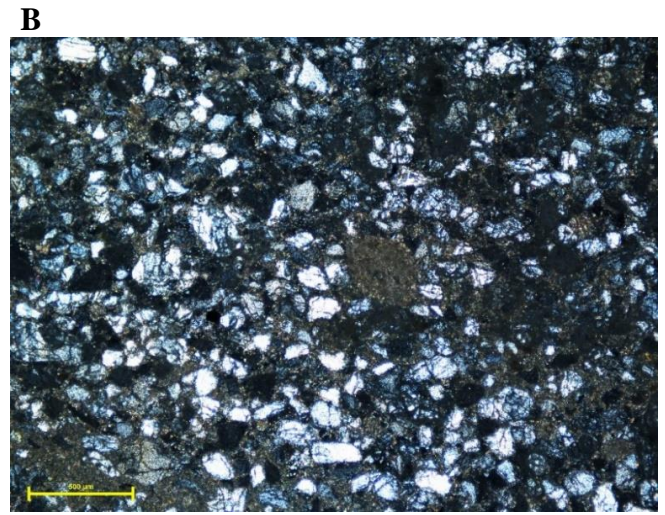
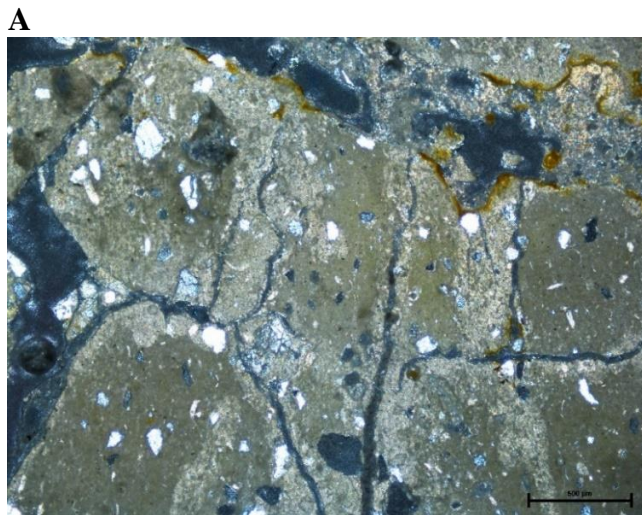


Plate 6.1 Sayl Member. BZ-E and QM2 sections. A-AL12, quartz clasts in a floating matrix of micritic mud. Shrinkage cracks evident as well as red staining (cpl, x5, scale bar 500 μ m). B-QM51, quartz clasts with patchily developed pore-filling cement. Peloid evident in the centre of the photo (cpl, x5). C-AL12, oval peloid with microspar rim cement (cpl, x10, scale bar 100 μ m).D-AL12, secondary microspar filled rootlet (cpl, x10).

6.1.2 Sifar Member (SI Mbr)

Six sections have deposits assigned to this member. Due to the large number of samples, the results will be discussed based on the section site (i.e. the sections of BZ as one, the sections of QM as another and M alone). Where appropriate, comparisons will be noted between the sections from the same site and also between sites. The hand specimen characteristics of the member from each site are described in Table 6.2 below.

<u>Sifar Member (BZ)</u>	
Colour	Predominantly pale yellow (5Y 7/3) and pale brown (2.5Y 7/3). More variation in colour observed in NE sub-section of BZ-W and in BZ-T. Pale olive-olive coloured deposits at the base of BZ-W
Texture	Clastic-sandstone, siltstone and mudstones. More variation in BZ-W, especially the lower half of the knoll section, some mottling also occurs. BZ91 and up (in BZ-T) more crystalline and indurated
Grain size/sorting	Fine-medium sand-sized clasts but often containing coarse-granule sized clasts resulting in well to moderate sorting. Better sorting from BZ91 in BZ-T as lacks coarse clasts
Composition	Quartz-rich, calcite matrix, calcareous nodules
Key Features	Fractures cut through many of the deposits-filled/partially filled with calcite
NaSi coating	Many of the deposits, especially from BZ-W have NaSi coating. Difficult in some deposits to tell which have had a NaSi coating
<u>Sifar Member (QM1/2)</u>	
Colour	QM1/2-Very pale brown (10YR 8/2), QM1 also has pale brown deposits (2.5Y 8/2)
Texture	Similar in both sections. Clastic-sandstones, more siltstones in QM1
Grain size/sorting	Very fine to fine sand-sized clasts. Occasional coarse clasts. Well sorted.
Composition	Quartz-rich, some calcite cements and calcareous nodules
Structures	Faint parallel laminations in QM2 deposits. In some deposits the coarse clasts form distinct bedding
Key Features	Fractures up to 5 mm wide cut through some of the samples-caused by rootletting
NaSi coating	Loosely cemented/friable deposits especially near the base of the member in QM2-NaSi coating evident
<u>Sifar Member (M)</u>	
Colour	Predominantly pale brown (2.5Y 7/3) and very pale brown (10YR 7/4), deposits near the top of the section are more reddened
Texture	Clastic-sandstone, four units of more carbonate-rich sandstones. Deposits become more indurated from NUS8-4
Grain size/sorting	Base of the section medium-coarse sand-sized clasts with occasional small pebbles, moderately sorted. Most of section is fine sand sized

	with some medium-coarse clasts resulting in well to moderate sorting.
Composition	Quartz-rich, patchy calcite matrix, some calcareous nodules
Structures	Parallel laminations-some of which are not noted on the log. Wavy bedding observed in carbonate unit containing deposits M15-18
Key Features	Fractured and heavily rootleted which are >1 cm in diameter
NaSi coating	Evident on loosely consolidated sandstones

Table 6.2 Hand sample descriptions of the SI Mbr deposits from the BZ (all), QM1/2 and M sections. The hand sample descriptions of the BZ sections are discussed as one along with the two QM sections due to the similar characteristics of the member in the sections.

Bir al Zallaf

When studying the deposits in TS and hand specimen it was clear that the deposits from all the BZ-sections show similar characteristics (Figures 6.2/6.3/6.8) and therefore will be described as one. The clasts of the deposits are moderately sorted with bimodal size fractions. Coarse sand-sized clasts comprise the larger size fraction and are rounded-to-well-rounded while the smaller medium-to-very fine sand-sized fraction is often sub-angular to sub-rounded. The majority of clasts are composed of quartz with feldspars (microcline), rounded quartzite clasts (e.g. in BZ34/81-Plate 6.2-A) and also some opaques present. Some of the larger clasts also contain mineral inclusions. Occasionally, larger clasts are fractured due to the growth of micrite exploiting weakness within the clast. Fretted edges caused by dissolution are also evident on the clasts from all three sections (Plate 6.2-B). The deposits are cemented by a micritic/microspar and occasionally drusy spar pore-filling cement, however the development and crystal size of the cement varies in the deposits but is often patchily developed with areas of open interparticle porosity remaining (Plate 6.2-C). Some deposits, in particular those with less well developed areas of pore cement, meniscus cements can be seen between the clasts such as in BZ39/85/87. Often surrounding the larger clasts micritic rim cements occur. These are unevenly developed and are too thin to clearly see the crystal structure however denser and thicker rim cements occasionally occur. Within the deposits of BZ-E, rounded homogenous micritic clumps occur caused by reworking. Fossils are not found in this section but are present in some of the deposits of BZ-W and especially BZ-T. Fossils are more common in deposits which have better developed pore-filling cements. Table 6.3 indicates in what deposits fossils and carbonate grains occur.

Fossil/Carbonate Grain	Sample
Gastropod	ALA2, BZ91
Ostracod	ALA2, ALA4, ALA5, BZ88, BZ90, BZ91, BZ34
Foram	ALA2, BZ90
Shell Fragments	ALA2, ALA4, ALA5, BZ80, BZ88, BZ89, BZ90, BZ91, BZ92, BZ93, BZ34, BZ35
Charophyte	ALA2, ALA4
Ooid	ALA2, ALA4, ALA5, BZ91

Table 6.3 Fossils and carbonate grains present in the deposits of the SI Member-BZ sections.

Ooids up to 400 μ m are common in the BZ-T section (Plate 6.2-D). Sub-rounded, fine sand-sized quartz clasts act as a nucleus surrounded by concentric micritic laminae. Within this section possible gyrogonites (calcified part of female oogonia) of charophytes (Flügel et al., 2010, pg448) are found. They occur in cross-sectional view (Plate 6.2-E) having undergone replacement. They are typically 400 μ m wide, rounded and have a concentric outer laminae and radial internal structure. Multi-chambered forams are clearly identified based on their morphology (Plate 6.2-F). They are often found in clusters and are ~250 μ m in width. As they are found in clusters and all have similar morphology it is likely they are the same species. Due to alteration, the species of the forams and the charophytes cannot be identified. This is also the case for the gastropods and ostracods which are found. A complete gastropod nearly 2mm in length with ovate-conic shape is present in ALA2 (Plate 6.2-G). A whorl of a gastropod is also present in BZ91 but mostly only shell fragments remain in the deposits. Ostracods occur sporadically in the deposits of BZ-T/W, but in some, dense clusters of ostracod debris are found (e.g. BZ91). The ostracods range in size from 300 μ m to 1.1mm clearly identified by their ovoid shape. They typically have a thick micritic/microspar rim with the centre unfilled resulting in intraskeletal porosity (Plate 6.2-H). Intraskeletal porosity also occurs in the chambers of the gastropods and to a lesser extent in the forams. Some intraskeletal pores are partially filled with secondary pore-lining and pore-filling cements as well as occasional detrital quartz.



Figure 6.1. Legend for all sediment logs.

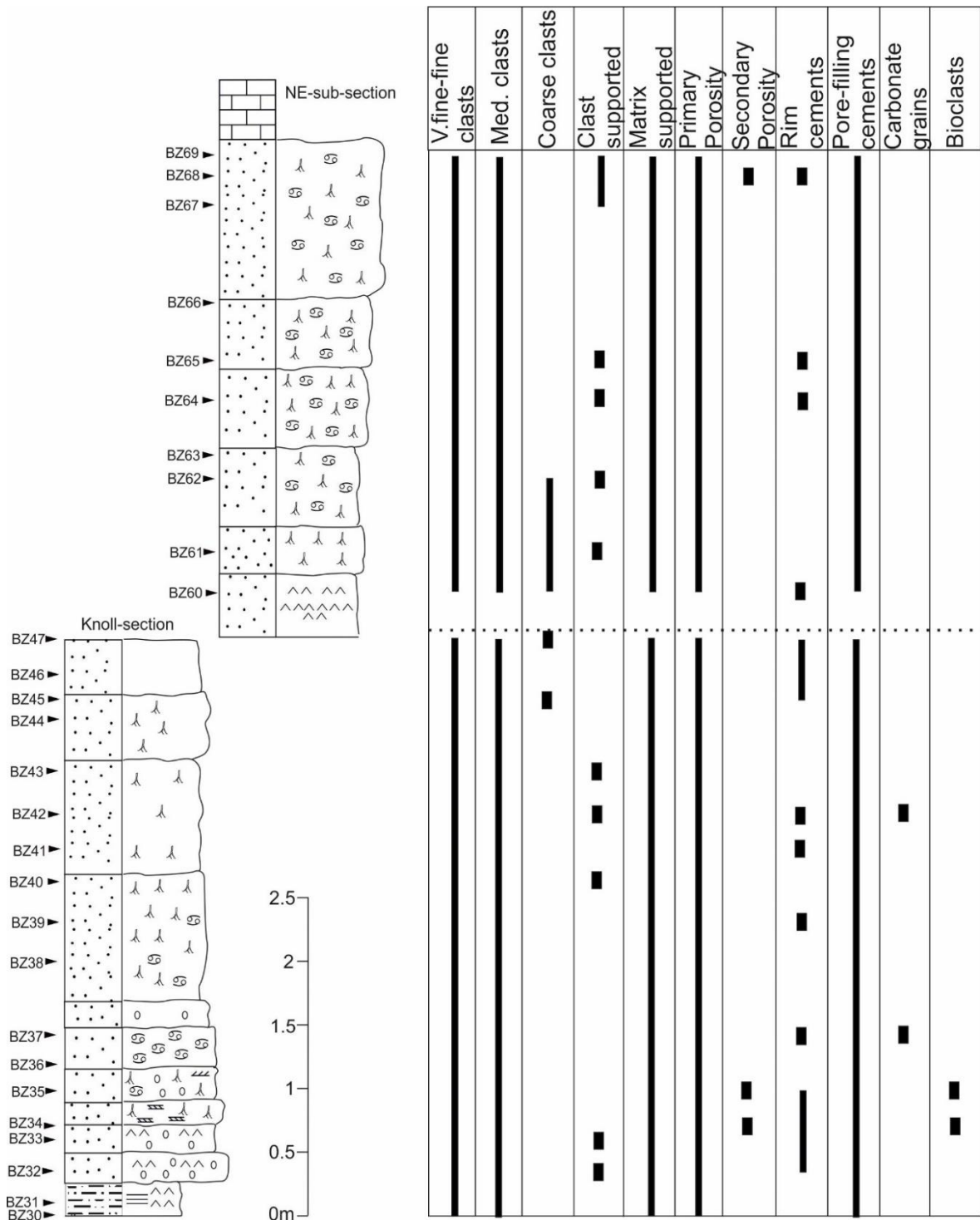


Figure 6.3 Key characteristics of the thin sections from the BZ-W section. Note: the clast size refers to grains of sand-sized material. Please refer back to Figure 6.1 (pg176) for the log key.

Limited XRF and isotopic data is also available. XRF analysis was conducted on three deposits from the Sifar Member of the BZ-T section and five deposits from the BZ-W (also two from the Bir al Zallaf Member of BZ-E). These deposits, out of all samples analysed, contain the lowest raw abundance of Si ranging between 82.44-54.78% (see Table 10-Appendix, pg303). The deposits of BZ-T/W instead contain a relatively large amount of MgO and CaO, with the CaO content in BZ91 equalling 24.15%. Calcite is the obvious mineral to contain CaO with high-Mg calcite or dolomite thought to be responsible for the high MgO values. The relationship between MgO and CaO is best demonstrated in Figure 6.4 with the deposits high in CaO having low MgO and vice versa. Large differences in the MgO/CaO content of the deposits are especially apparent in the deposits from BZ-T. In addition to the standard elements run during XRF analysis, these deposits were also run for Cl. Some deposits, such as BZ37, record extremely high Cl values thought to indicate the presence of salt. The values themselves however are not meaningful as the water-based mixture used to bind the pellet together, when dried, has caused movement of Cl to the surface resulting in erroneous values.

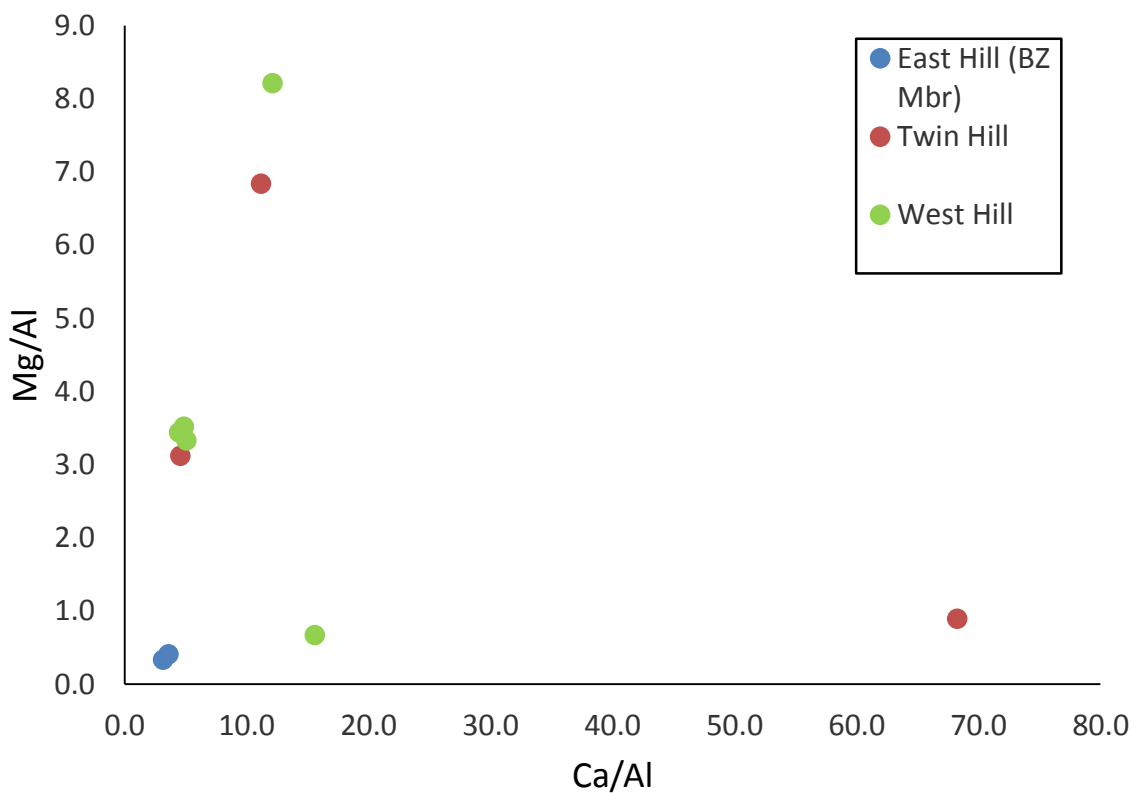
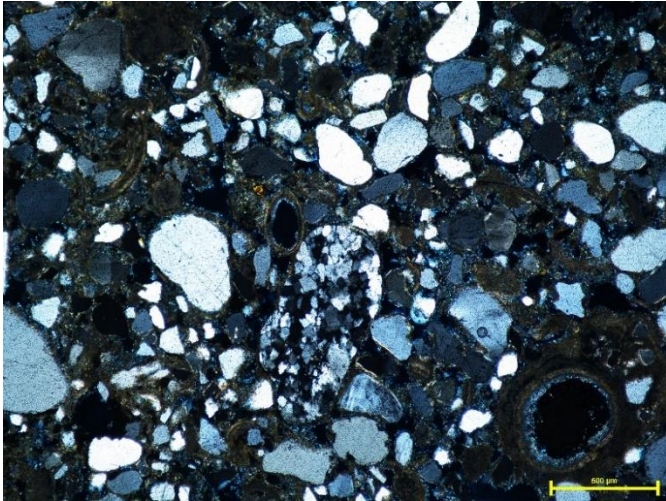


Figure 6.4 Aluminium normalised Mg-Ca diagram of the BZ sections.

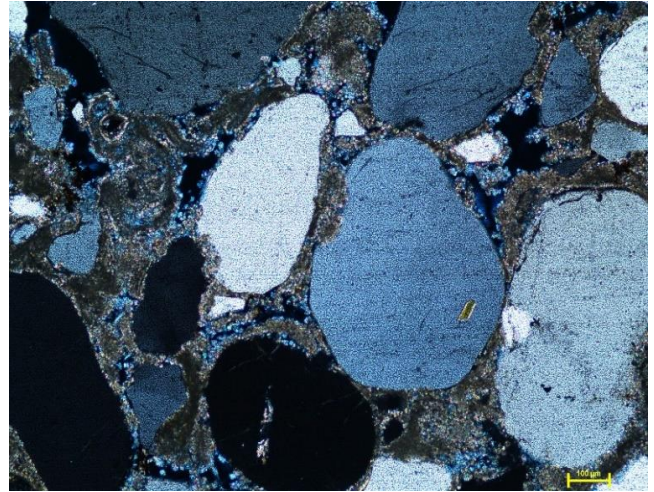
Stable isotope analysis was conducted on the AL/ALA coded deposits of the BZ-E/T sections. BZ coded samples were not analysed as many appeared to have been treated with NaSi. Six deposits from both sections were analysed. The majority of deposits from BZ-E have $\delta^{18}\text{O}$ values between -6.9 and -9.9‰ as seen in Table 6-Appendix (pg297) and Figure 6.6. AL11 however, near the base of the section, is enriched equalling +0.8‰. An extremely large depletion of 10.7‰ occurs between this deposit and the overlying deposit of AL10. It should be noted that a 3.17 m sampling gap does occur between these samples. The majority $\delta^{13}\text{C}$ values only differ by 1.1‰. The most enriched value, as for the $\delta^{18}\text{O}$, occurs in AL11 equalling -1.8‰. A depletion does occur between AL11 and AL10 however this decrease is not as extreme as the $\delta^{18}\text{O}$ equalling only 1.5‰. The calculated correlation coefficient (r^2) equals 0.58 suggesting only moderate covariance occurs between $\delta^{18}\text{O}/\delta^{13}\text{C}$.

Values of the BZ-T section are similar to those of the BZ-E section for both $\delta^{13}\text{C}$ and $\delta^{18}\text{O}$, however the $\delta^{18}\text{O}$ values are not quite as extreme as those from BZ-E as shown in Figure 6.6. Four of the deposits differ in $\delta^{18}\text{O}$ by only 0.8‰ ranging between -8.4 to -7.6‰. Two of the samples, ALA6 and ALA3, are much more enriched equalling -0.6 and -0.8‰ respectively. As in the BZ-E section, very large changes occur in the $\delta^{18}\text{O}$ values of neighbouring deposits such as between ALA6/5 where a 9‰ difference occurs. Very little variation occurs in the $\delta^{13}\text{C}$ values of the deposits, even in deposits where large fluctuations occur in the $\delta^{18}\text{O}$. Overall the $\delta^{13}\text{C}$ differs by 1.1‰ ranging between -2.7 to -1.6‰. The r^2 value of these deposits is much poorer than for the BZ-E section at 0.18.

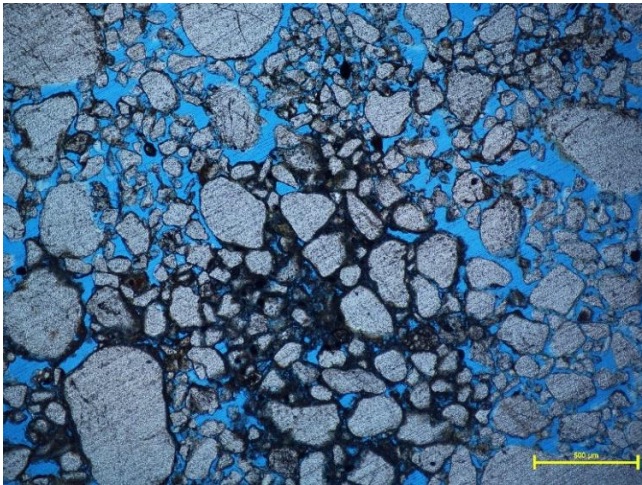
A



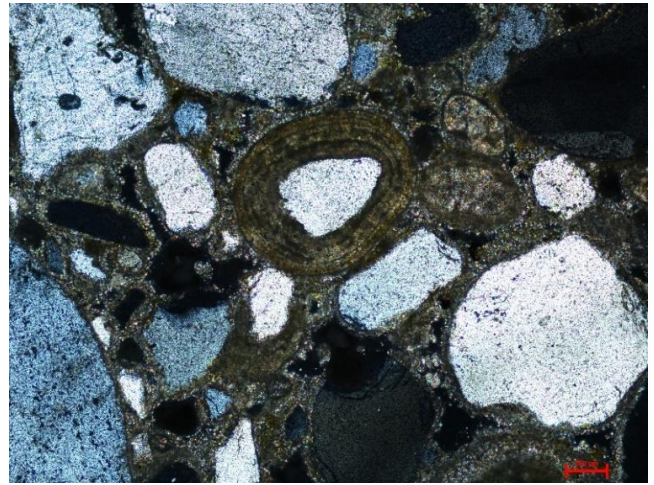
B



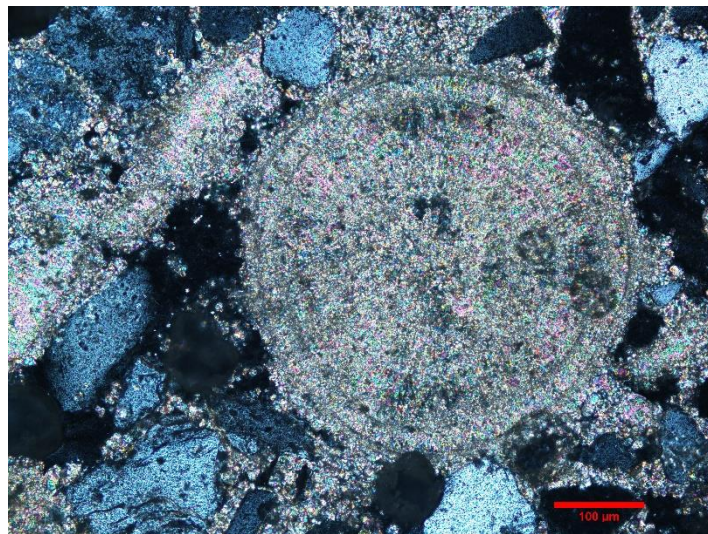
C



D



E



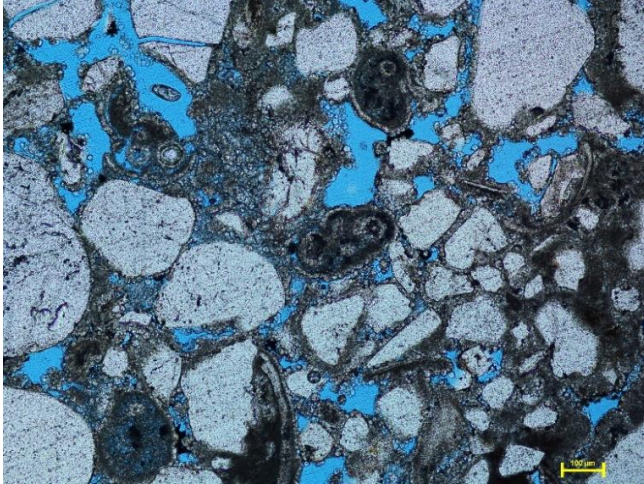
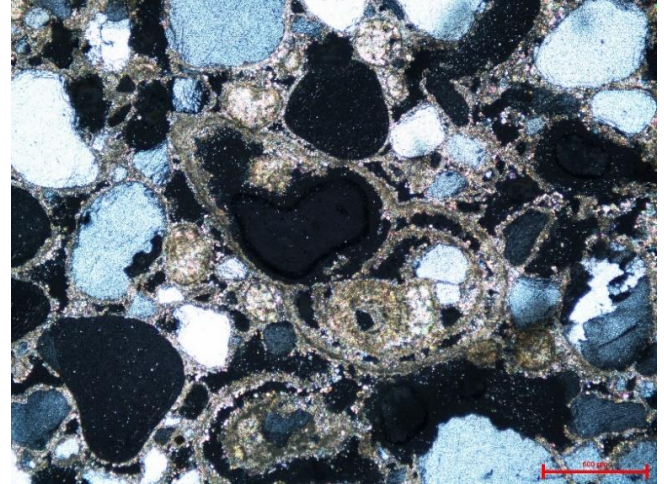
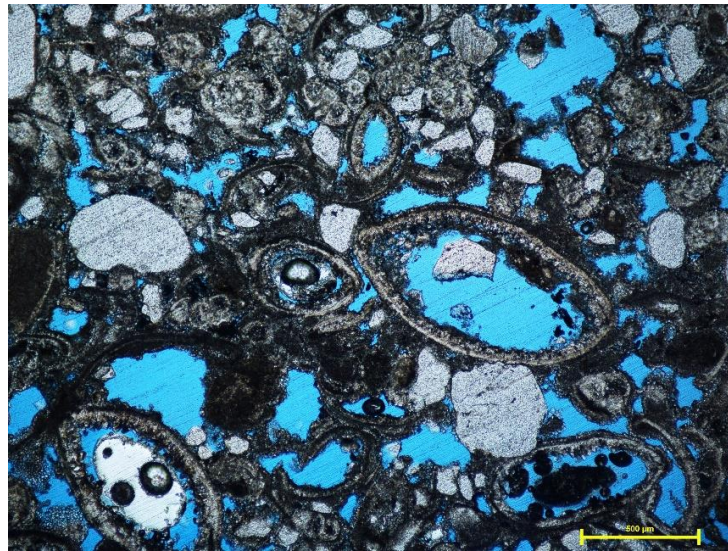
F**G****H**

Plate 6.2 Sifar Member. BZ sections. A-BZ34, moderately sorted deposit of quartz clasts typical of the BZ-sections. A large rounded clast of quartzite can be seen in the centre of the photomicrograph (x5, cpl). B-BZ90, corroded edge of quartz clast which also contains a small mineral inclusion. Micritic pore-filling cement can be seen surrounding the clasts (x10, cpl). C-BZ84, open interparticle porosity with some pore-filling cement in the centre (x5, ppl). D-ALA2, ooid with a sub-rounded quartz clast acting as a nucleus coated by concentric micritic laminae (x10, cpl). E-ALA4, cross-sectional view through a possible charophyte stem (x20, cpl). F-BZ90, multi-chambered foram in the centre of the photomicrograph (x10, ppl). G-ALA2, complete ovate-conic shaped gastropod. Intraskeletal porosity is evident in the chambers with one mostly infilled with secondary micrite and detrital quartz (x5, cpl). H-BZ91, cluster of ostracod debris and shell fragments with open intraskeletal porosity evident in the centre of the ostracods (x5, ppl). Scale bar is 500 μ m in A/C/G/H and 100 μ m in the remaining photomicrographs.

Qarat al Mrar

Just five deposits from the QM1 section are assigned to this member compared to the whole of the QM2 section. Although similar in hand specimen (see Table 6.2, pg173), distinctions can be made between the TS of the QM1 and QM2 sections. Despite being defined as siltstones, some of the deposits of QM1 are carbonate-rich, increasing in carbonate content up the member. Clasts are more abundant near the base of the member (QM1-3) generally having bimodal sorting (Plate 6.3-A). Larger clasts of 250 μ m or more (often >500 μ m) are sub-rounded while the smaller size fraction, often below 125 μ m, are more angular. The clasts are predominantly composed of quartz but occasional feldspars (plagioclase) also occur. Some of the larger clasts have fretted edges, especially ones within a floating matrix. In the carbonate poor deposits the samples have interparticle porosity infilled in places by patchily developed meniscus cements. The cement is micritic which in areas can be dense with rounded, reworked micritic clumps present between some of the clasts. Rounded intraclasts are also present which occasionally have coalesced to form larger aggregate grains (Plate 6.3-B). Unfilled fenestrae are also seen in the QM2 sample along with filled microfractures caused by rootletting. The cements of the more carbonate-rich samples (QM4/8) are composed of mottled areas of micrite and microspar. Although better developed, areas of open porosity remain caused by the presence of 'ghost features' and vuggy areas as a result of dissolution (Plate 6.3-C). Within QM4 a shell fragment was present which had undergone replacement. No other fossils were found in the QM1 deposits.

Due to the friable nature of many of the QM2 section deposits, limited TS were produced (see Figure 6.5). The TS that were produced show similarities with the TS of the lower deposits of the QM1 section including bimodal sorting, interparticle porosity, poorly developed cements including meniscus cements and rounded intraclasts (Plate 6.3-D). Unlike QM1 however, many of the clasts, large or small, have the unusual surface fracturing seen on clasts in many of the other members. The clast size becomes more unimodal from QM71 upwards with the deposits having better sorting (Plate 6.3-E). Pore filling and rim cements are better developed in QM63 with many of the quartz clasts having thin, uneven microspar rims (Plate 6.3-F). The log indicates the majority of deposits to be rootleted with distinctive bedding observed. A fossiliferous bed also occurs at QM63, however none of these features are seen in the TS.

Isotopic data is available for the Sifar Member deposits from the QM1 section only due to the use of NaSi when in the field on the QM2 samples. The more cemented deposits of QM2 which were less likely to have NaSi were tested for carbonate with 10% HCl. Many had little or no reaction suggesting limited carbonate content (subsequently confirmed in TS) hence it was decided isotope analysis should not be conducted. The $\delta^{18}\text{O}$ of the five analysed samples differ by 2.3‰ from -8.2 to -5.9‰. The deposits become gradually more depleted up the member. Very little $\delta^{18}\text{O}$ variation occurs between the lower three deposits of the member differing by 0.3‰. The largest change of 1.3‰ occurs between QM3 and QM5. Values of $\delta^{13}\text{C}$ vary by 1.9‰ from -4.8 to -2.9‰. The most $\delta^{13}\text{C}$ enriched deposit at the top of the member is the most depleted in $\delta^{18}\text{O}$. The calculated r^2 value for these deposits is 0.46 suggesting moderate covariance between $\delta^{18}\text{O}/\delta^{13}\text{C}$. When compared to the equivalent deposits of the BZ sections the QM values show much less variation in $\delta^{18}\text{O}$ as seen in Figure 6.6, with no large changes between neighbouring deposits. The $\delta^{13}\text{C}$ values are on the whole more depleted with the most depleted deposit of QM1 1.5‰ lower than the equivalent BZ value.

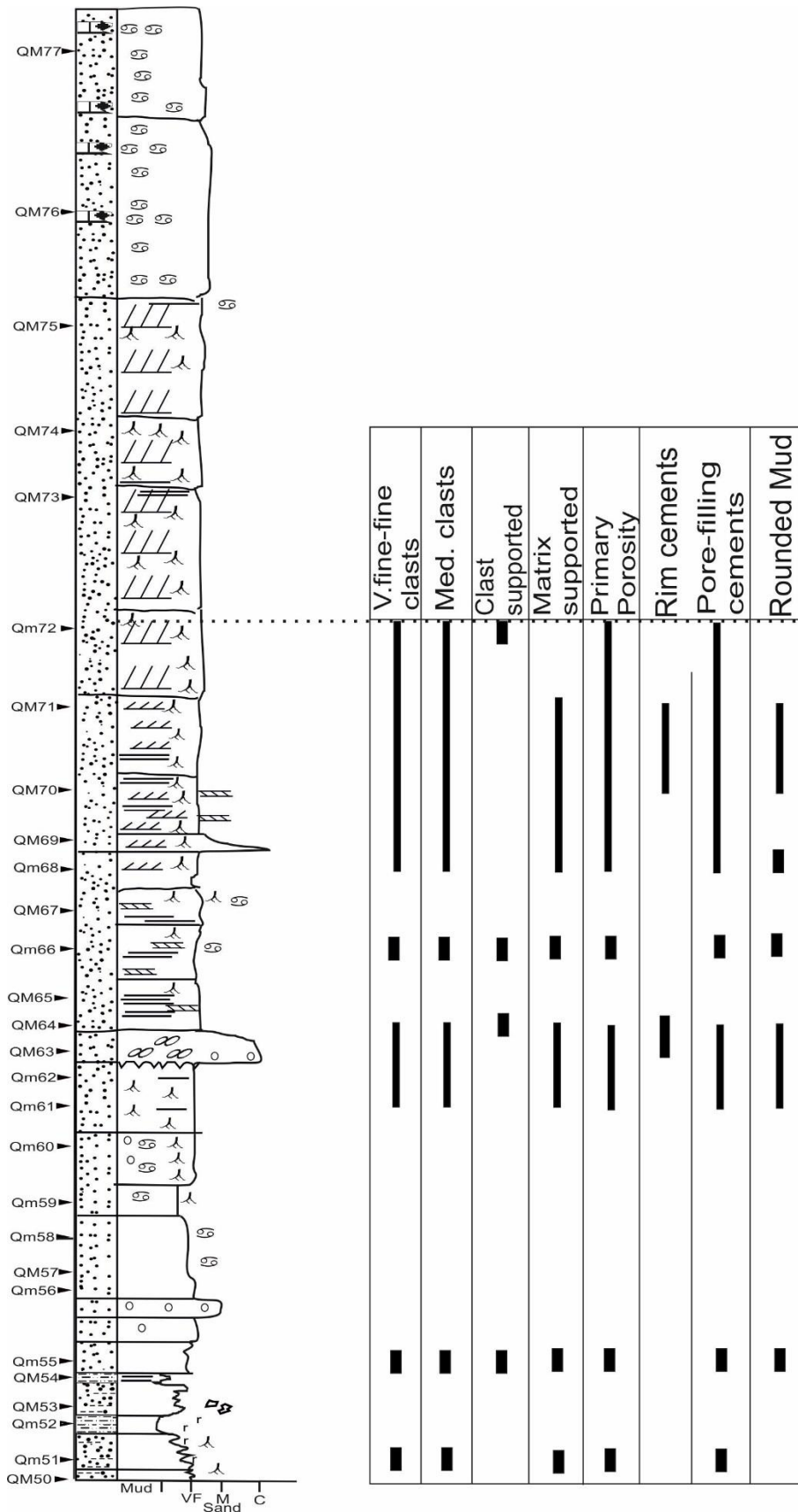


Figure 6.5 Key characteristics of the thin sections from the QM2 section. Only limited thin sections were produced from this section due to the friable nature of the deposits hence the lack of detail from QM73 up. Note: the clast size refers to grains of sand-sized material. Please refer back to Figure 6.1 (pg176) for the log key.

Al Wafa

The characteristics of the TS of the M section reflect those of the hand specimens as described in Table 6.2 (pg173/174). Not only are there similarities between the sandstone intervals, but also between the sandstone intervals and more carbonate-rich units (Figure 6.7). Based on this, the TS characteristics of the section will be discussed generally with specific references made to certain deposits/units where necessary.

The clasts are predominantly composed of quartz with some rare clasts of feldspar (plagioclase) also present. Clasts are typically moderately-to-poorly sorted often composed of two size fractions (Plate 6.4-A), which also occurs in the TS of the QM sections. The larger clasts, >400 μm , are rounded while the smaller clasts, typically <250 μm , are sub-rounded. Rounded clasts up to 1.5mm also occur in the deposits from the base of the section (M1/2, Plate 6.4-B). Some of the larger clasts contain mineral inclusions. Despite fine laminations being evident in the hand samples, they are not observed in the TS. Many of the clasts, although less so in the more carbonate-rich deposits, display the unusual surface fracturing. Some of the deposits are clast supported with interparticle porosity evident in the majority of the sandstones. In some samples, large areas of NaSi can be seen infilling the pore spaces. Very poorly developed and uneven rim cements are seen coating clasts when viewed at a relatively high magnification (x20). Corroded grains with fretted edges are also observed. Poorly developed meniscus cements are evident in some of the deposits, in particular in the sandstone interval from M25 up (Plate 6.4-C). Within the more carbonate-rich sandstones, better developed rim cements and pore-filling cements occur resulting in the clasts to be in a floating matrix (Plate 6.4-D). The cement is homogenous composed of micrite. Pore spaces formed via dissolution occur in these deposits, often infilled or partially infilled by secondary sparry cement. Areas of the cement are heavily reddened in the upper carbonate unit, especially in sample NUS8-1 indicating the presence of Fe-oxides likely due to the occurrence of clays.

Isotope values are also available for some of the deposits from the M section. It was unclear, except in a few samples, if NaSi had been applied in the field. All of the M coded deposits were therefore analysed but only seven deposits returned reliable values (see Table 6-Appendix, pg297). The useable values are sporadic; covering ~9 m of the section from M2 at the base to M25. $\delta^{18}\text{O}$ values range from -6.1 to -9.7‰. The neighbouring deposits of M2/3 and M17/18 only differ however by 0.2 and 0.1‰ respectively. The $\delta^{13}\text{C}$, unlike in the BZ and QM sections, are particularly varied. M12 is the most enriched sample at -0.9‰ compared to M25 which equals -13.7‰. This value is the most depleted

out of all the deposits analysed in both the Zazur Formation and Shabirinah/Brak Formations and hence the question must be asked if the value can actually be believed. As for the $\delta^{18}\text{O}$, minimal variation occurs in the neighbouring deposits of M2/3 yet a 4.3‰ difference occurs between M17/18 despite being sampled only 10 cm apart. When compared to the Sifar Member deposits of the BZ/QM sections, the $\delta^{18}\text{O}$ values are very similar as demonstrated in Figure 6.6. The $\delta^{13}\text{C}$ however show much more variation recording the most enriched and depleted deposits out of all Sifar Member deposits analysed.

Along with petrographic and the small amount of isotopic data, the deposits of the M section have also been analysed using XRF, heavy mineral (HM) and laser particle size analysis. As in the TS, XRF results show the six deposits analysed to be composed almost entirely of quartz with raw Si abundances typically >95.5% (see Table 9 –Appendix, pg301). On the whole, little information was gained from XRF analysis with many elements occurring in low abundances throughout the section as shown in Table 9-Appendix (pg301). The Zr was however relatively high, especially for M6. HM analysis also showed little variation within the sampled dataset. When comparing the ‘modern samples’ to those from the M section, the samples have a slightly greater HM diversity containing more unstable minerals suggesting there was input from other lithologies, likely less weathered sources.

Particle size analysis (PSA) was conducted on the majority of M samples in order to try and differentiate between an aeolian or fluvial (or combination) origin of the sandstones. Analysis in GRADISTAT indicates all the deposits to be bimodal or trimodal (M23 is unimodal), moderately or poorly sorted with very coarse clasts being the dominant clast size. Comparing the data of the different intervals of the M section (raw data- Table 7-Appendix, pg298) indicates there to be limited variability throughout the section and between the different clastic units as recorded in Table 6.4.

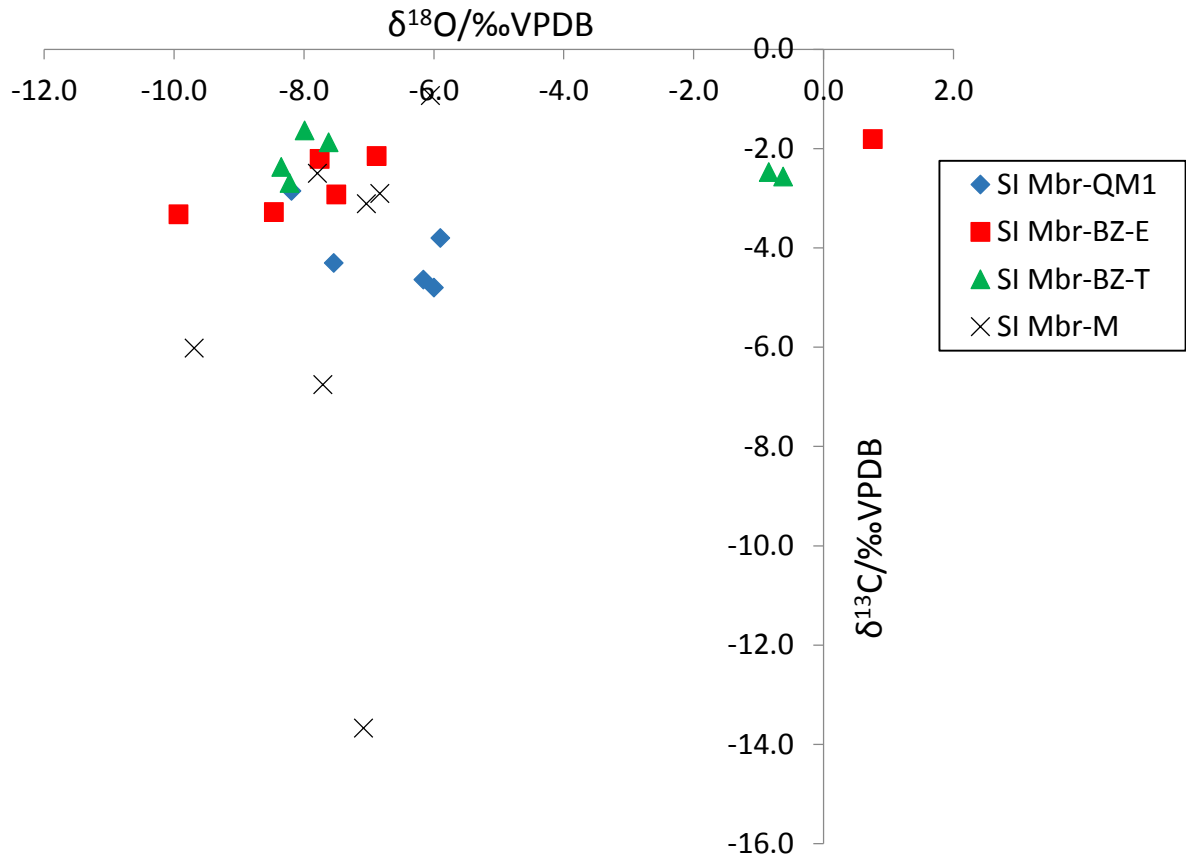


Figure 6.6 Stable isotope values of the SI Member deposits analysed from the QM1, BZ-E/T and M sections.

Unit	V.Coarse sand/%	Coarse sand/%	Medium sand/%	Fine sand/%	V.Fine sand/%	Silts & Clays/%
Base unit-no bedding (M11-15)	41.6	31.0	17.8	6.5	1.3	1.8
Parallel laminated (M19-22)	43.0	31.5	17.7	5.0	1.3	1.7
Cross-bedded (M23-28)	44.7	31.4	15.8	5.2	1.4	1.6
Modern samples	45.2	29.9	16.7	7.6	0.9	-

Table 6.4 Average percentages of the clast size of the three main clastic units from the M section and the modern sand samples.

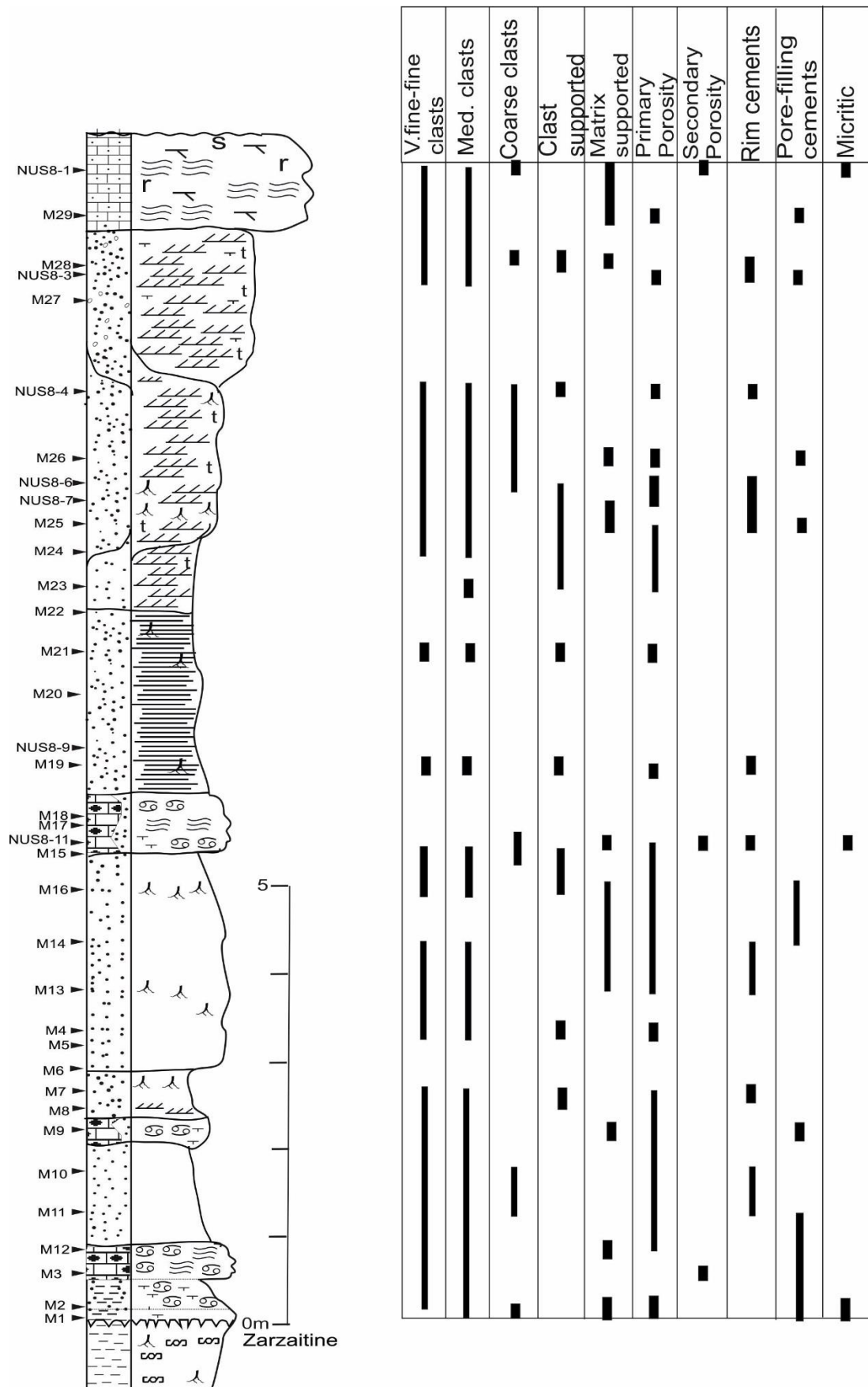
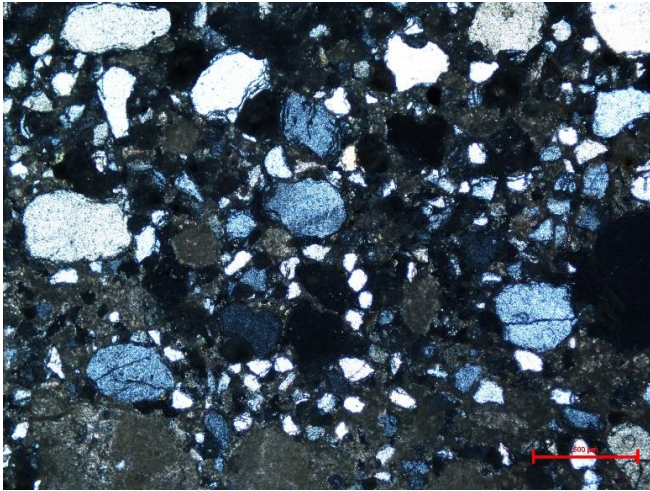
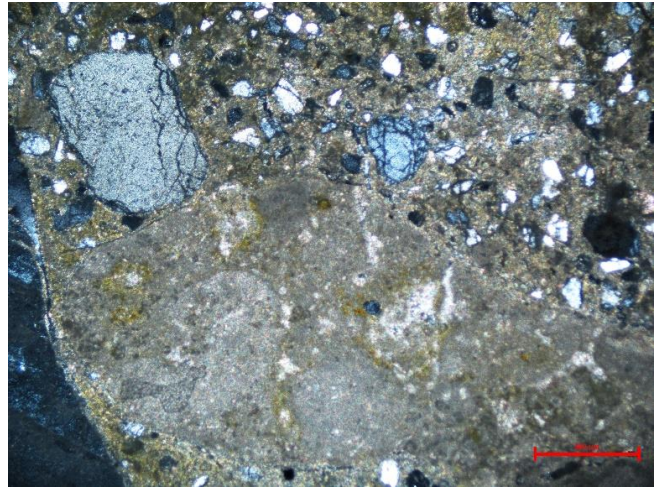


Figure 6.7 Key characteristics of the thin sections from the M section. Note: the clast size refers to grains of sand-sized material. Please refer back to Figure 6.1 (pg176) for the log key.

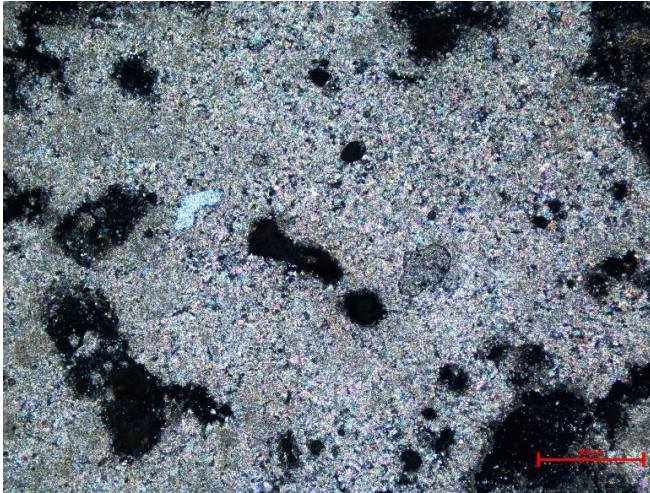
A



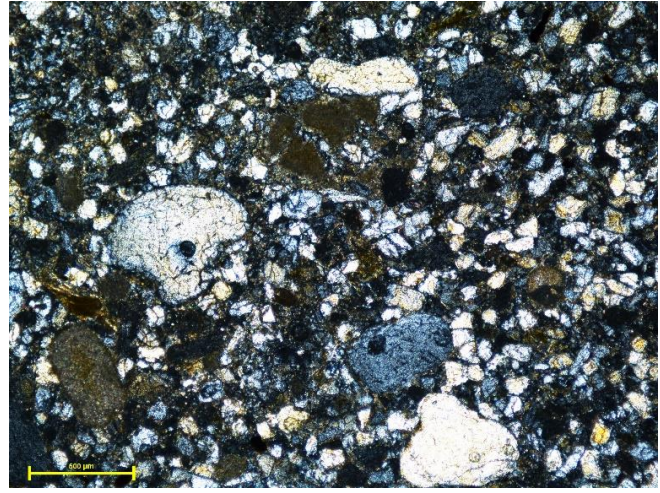
B



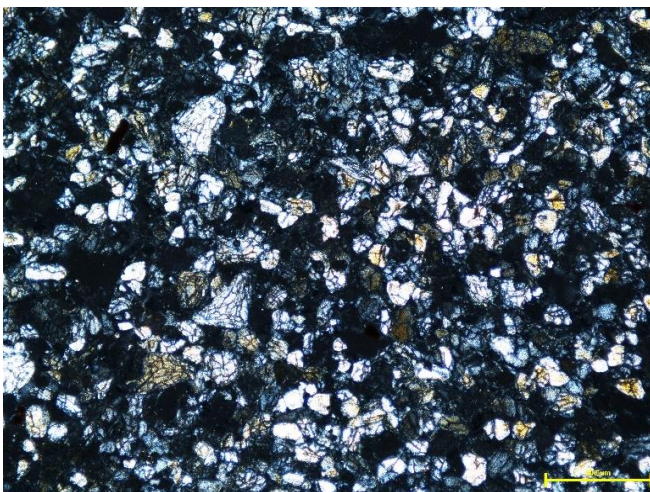
C



D



E



F

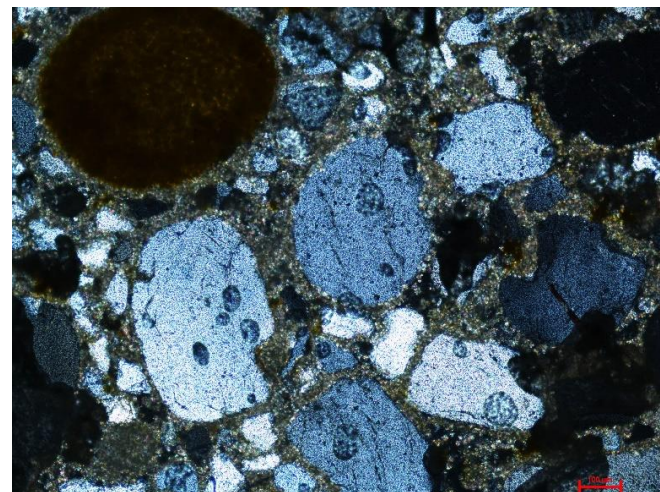


Plate 6.3 Sifar Member. QM1/2 sections. A-QM1, quartz clasts showing bimodal sorting, interparticle porosity with pores infilled with rounded micritic mud clumps (x5, cpl). B-QM2, intraclasts forming an aggregate grain cemented by a micritic outer rim (x5, cpl). C-QM8, carbonate rich deposit of QM1 section composed of microspar cement, ghost features and open pores also present (x5, cpl). D-QM61, typical bimodal sorting of the QM2 section with rounded intraclasts (x5, cpl). E-QM71, moderately-well sorted clasts many of which have the unusual fracturing (x5, cpl). F-QM63, better developed cements infilling pore spaces with microspar rim cements also evident (x10, cpl). Scale bar is 500µm in all microphotographs except for F where it is 100µm.

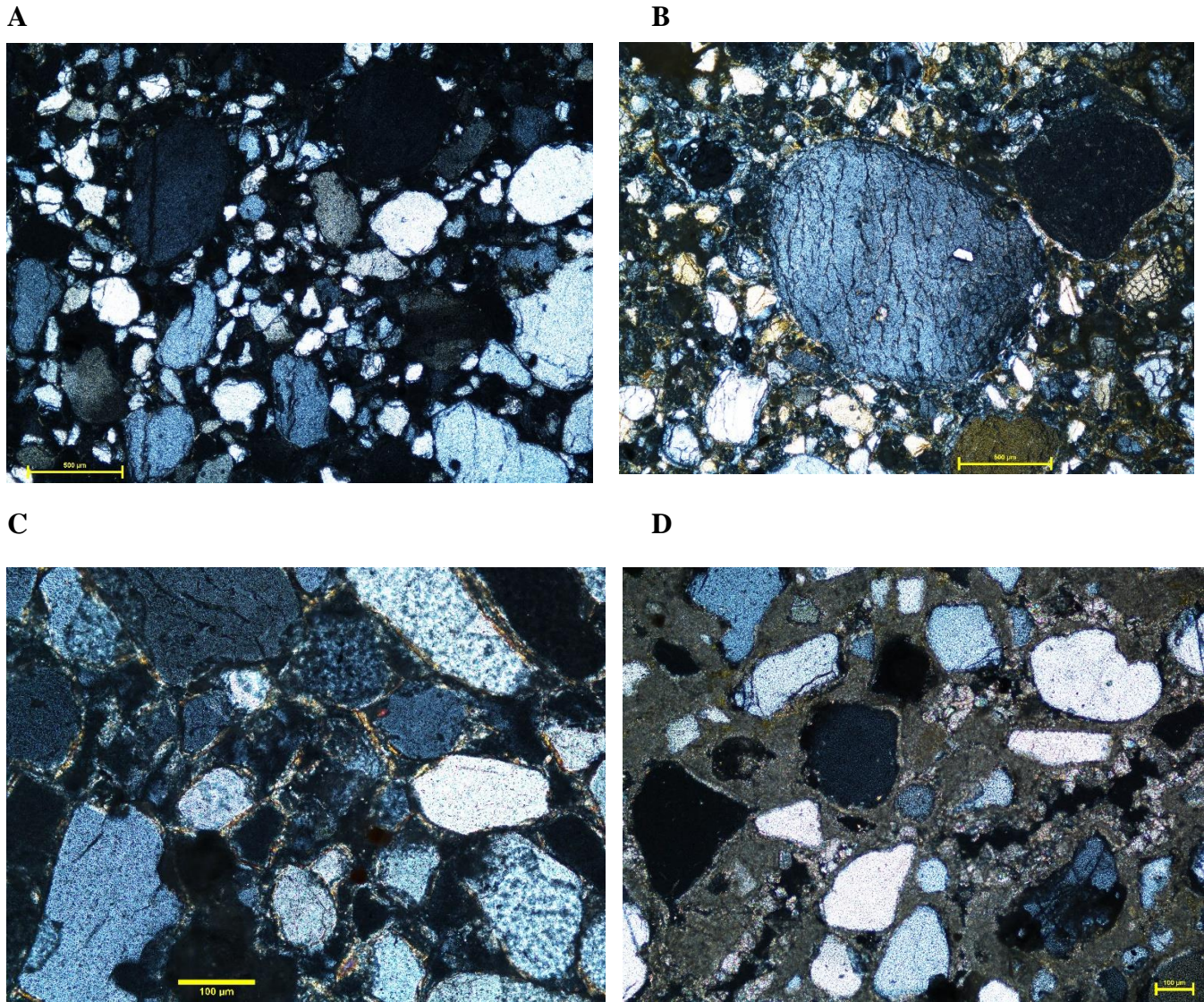


Plate 6.4 Sifar Member. M Section. A-M7, bimodal sorting typical of the sandstones of the section, some clasts have fretted edges (x5, cpl). B- M1, well-rounded, coarse sand-sized clast with mineral inclusions (x5, cpl). C-NUS8-3, poorly developed meniscus cements (x20, cpl). D-NUS8-1, carbonate-rich sandstone with micritic pore-filling cement, thin rim cements can be seen unevenly coating some of the clasts, sparry cement infilling pore spaces (x10, cpl). Scale bar is 500µm in photomicrographs A/B, 100µm in C/D.

6.1.3 Bir al Zallaf Member (BZ Mbr)

This member contains deposits from the upper BZ-E and QM1 sections. Each section will be discussed separately but comparisons between the deposits of the sections will be made where appropriate. The hand sample descriptions from both sections are noted in Table 6.5 below.

<u>Bir al Zallaf Member (BZ-E)</u>	
Colour	Predominantly white (2.5Y 8/1) and pale yellow (5Y 7/3), some pale olive
Texture	Two limestone units separated by a clastic sandstone unit. Some mottling
Grain Size and sorting	Limestone units-grains not see by eye-micritic. Sandstones-fine-medium sand-sized clasts, well sorted
Composition	Limestone units are similar in composition-carbonate-rich. Sandstone interval quartz-rich with calcite matrix, similar lithology throughout this interval however BZ27 differs sharing more similarities with underlying L2 limestone unit. BZ27 is composed of white laminated and fragmented carbonate interbedded with fine, green mudstone layers (Fig 15-Appendix, pg294).
Structures	Well defined parallel laminations in BZ27, faint laminations in AL5
Key Features	Black specks covering surfaces of the limestones-assumed to be microbial in origin. Outer surfaces of the limestones smooth and rounded as a result of dissolution and/or wind erosion
NaSi coating	Some of the deposits from the sandstone interval have an NaSi coating
<u>Bir al Zallaf Member (QM1)</u>	
Colour	Lower part of member predominantly gray (7.5YR 6/1) while the upper part is white to pinkish white (5YR 8/2)
Texture	Micritic limestone, small clastic interval-sandstone, some mottling
Grain size/sorting	Grain size only seen in sandstone unit-fine sand-sized clasts, well sorted
Composition	More carbonate-rich than underlying SI Mbr deposits. Micritic carbonate, some detrital quartz
Key Features	Majority of limestones have vuggy porosity. The voids are 1-5 mm in diameter with some coalescing to form vugs 2 cm in diameter. Most vugs unfilled, in the upper limestone unit (above hiatus) vugs are partially filled with pore lining cements (Fig 16-Appendix, pg294) or completed filled with coarse secondary calcite cement. Mineral veinlets and intraclasts are also common. Thin, black wavy lines occur in the upper limestones-algal origin or Mn-oxide coating. Altered shell fragment in QM14

Table 6.5 Hand sample descriptions of the Bir al Zallaf Member from the BZ-E and QM1 sections.

Bir al Zallaf-East section

This member is composed of two limestone units separated by a clastic interval. Both limestone units are texturally similar in TS. On the whole they are clast-poor containing only a small amount of fine sand-sized detrital quartz in a floating micritic matrix. The clast concentration is higher in BZ27. In this deposit well-sorted, sub-rounded, coarse-silt-to-very fine sand sized clasts form distinct parallel laminations interbedded with

clotted micritic mud (Plate 6.5-A). Although much of the cement in the other deposits from the limestone units are composed of dense, often mottled micrite, patches of cement are also clotted. This clotted texture results from the occurrence of peloids which range in size and shape and lack internal structure (Plate 6.5-B). Based on these characteristics the peloids can be classified as lithic peloids resulting from reworking of lithified carbonate mud (Flügel, 2010, pg 113). In places the peloids form aggregate grains joined together by thin meniscus cements (Plate 6.5-C). Isotropic black/slightly reddened specks of various shapes up to 250µm in diameter can be seen randomly covering areas of the cement. It is thought that these features developed after deposition and are microbial in origin. Within the thin sections of AL4 and BZ26 poorly preserved fragments of shell and ostracods which have undergone replacement are present. In places where the ostracods are found, intraskeletal porosity is present (Plate 6.5-D). Some of the open pores are partially filled with secondary micritic/microspar cement. Shells/ostracods are not seen in AL1 but trace fossils occur filled with secondary microspar. Within this deposit, areas of coarse granular mosaic spar crystals also occur, not seen in any of the other deposits of the L1/L2 limestones. In BZ27 open fractures are common, likely due to shrinkage during wetting/drying cycles and have resulted in areas of carbonate mud to become fragmented. Fracture porosity is also evident in the other limestones (e.g. BZ26) along with vuggy porosity. Some of these open space structures are partially lined with secondary calcite cements often with a larger crystal size than the primary cement.

The sandstone interval separating the limestones, as expected, is more clast-rich. The clast size and sorting of BZ25 is similar to that of the underlying deposit of BZ27. The size and sorting of the remaining deposits from this interval are more moderately sorted with bimodal sorting (very-fine sand sized and medium-sand sized). High primary interparticle porosity is preserved in the deposits, especially in BZ24 (Plate 6.5-E). Many of the clasts display fretted edges as a result of overgrowths of poorly developed calcite rim cements (Plate 6.5-F). As well as quartz clasts, detrital chert clasts also occur. The rounded clasts up to 500µm in size can be identified based on their microcrystalline appearance (Plate 6.5-G) (Scholle, 1979).

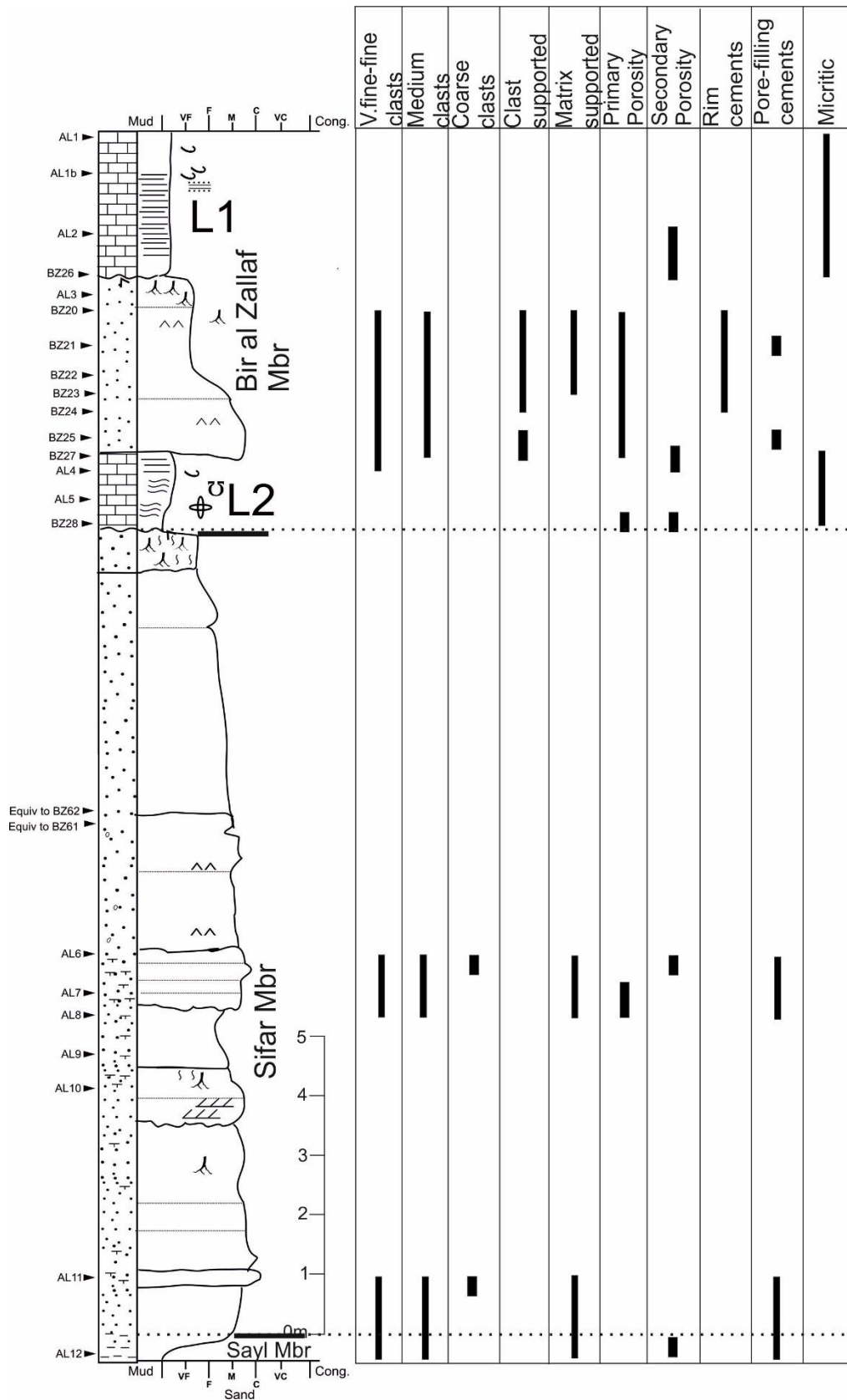


Figure 6.8 Key characteristics of the thin sections from the BZ-E section. Note: the clast size refers to grains of sand-sized material. Please refer back to Figure 6.1 (pg176) for the log key.

Stable isotope analysis was conducted on AL coded deposits of this member as these deposits correspond to the L1/L2 limestone units and lacked NaSi compared to the BZ coded deposits. The $\delta^{18}\text{O}$ values vary overall from -8 to +2.6‰ while the $\delta^{13}\text{C}$ show much less variation ranging between -1.7 to +1‰ (see Figure 6.9 and Table 6-Appendix, pg297). Both deposits from the L2 unit are enriched in $\delta^{18}\text{O}$ differing by 1.1‰ while a difference of 0.7‰ occurs in $\delta^{13}\text{C}$. As in the underlying Sifar Member, large changes in $\delta^{18}\text{O}$ occur in the L1 unit. This unit ranges between -8‰ near the base (AL3) to +1.7‰ at AL2 before decreasing again to -4.4‰ in the uppermost deposit of the member. Much less variation occurs in the $\delta^{13}\text{C}$ of this unit differing by 1.7‰. The most enriched/depleted values of the unit are recorded in the same deposits of this unit. The correlation coefficient was calculated for all the deposits of the member yet poor covariance existed between $\delta^{18}\text{O}/\delta^{13}\text{C}$ values with $r^2=0.37$. Regression could not be carried out on the L2 unit values as too few values are available. Even though only three values were analysed from the L1 unit the correlation coefficient revealed excellent covariance with $r^2=0.98$.

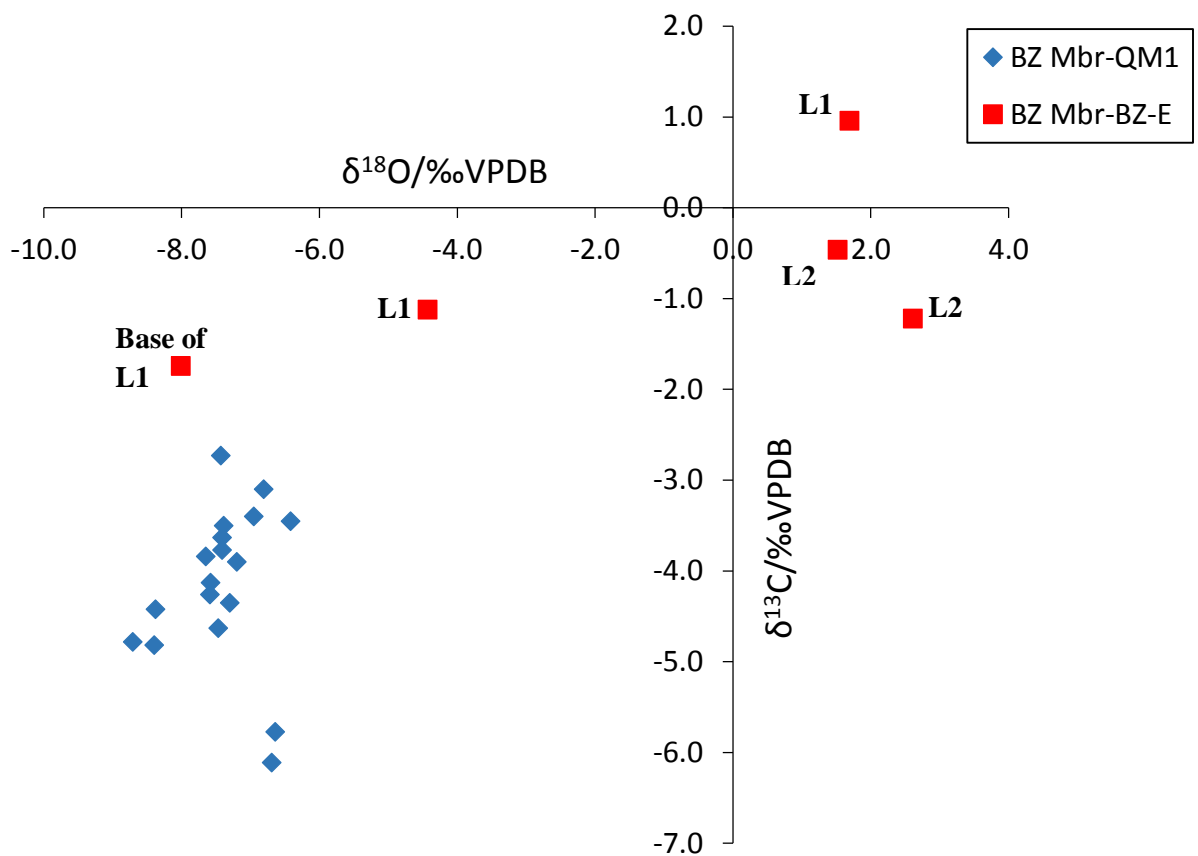


Figure 6.9 Stable isotope values of the Bir al Zallaf (BZ) Member from the QM1 and BZ-E sections.

Qarat al Mrar-1 section

In TS, a good reflection of what is observed in the hand specimen is clear (see Table 6.5, pg192). Few clasts are seen in the deposits except for a few detrital quartz clasts which often have fretted edges. The concentration of clasts increases in QM10. Clasts are in a floating matrix or occasionally bound together by meniscus cements. The deposits are largely composed of primary micritic and microspar cements. The cement is often mottled (Plate 6.6-A) and occasionally clotted with faint peloids present. Secondary porosity is evident in the deposits due to the presence of 'ghost features' and vugs (Plate 6.6-B/C). The 'ghost features' and vugs are likely caused by dissolution and/or rootletting. The TS of the limestones below the hiatus, as in the hand specimens, typically have open vugs with some partially lined by secondary spar pore filling cements (Plate 6.6-C). The amount of open pores decreases up the section with many pores completely filled with coarse granular mosaic or drusy spar cements (Plate 6.6-D). Trace fossils occur in the TS of QM11/19 with possible rootlets present in QM21. Thin post-depositional fractures also occur in some of the deposits. Parallels can be drawn between the TS characteristics of the uppermost deposit of the Bir al Zallaf Member in the BZ-E section (AL1) and those of the QM1 section (see Plate 6.5-H and Plate 6.6-A/D). The texture/fabric are similar, in particular the mottled micritic matrix, the occurrence of coarse secondary spar and the presence of traces.

Isotope results are available for all the Bir al Zallaf Member deposits of the QM1 section. Overall the $\delta^{18}\text{O}$ differs by 2.3‰ from -8.7 to -6.4‰. The $\delta^{18}\text{O}$ values of the deposits above the hiatus are marginally more depleted than those below averaging -7.8 and -7.1‰ respectively. A larger variation in values occurs in the $\delta^{13}\text{C}$ ranging between -6.1 to -2.7, a difference of 3.4‰. The two most $\delta^{13}\text{C}$ depleted values occur in the neighbouring deposits of QM14/15. When averaging the $\delta^{13}\text{C}$ of the deposits above and below the hiatus only a 0.3‰ difference occurs. Regression indicates there to be particularly poor covariance between the $\delta^{13}\text{C}/\delta^{18}\text{O}$ values of this member ($r^2=0.006$). Figure 6.11 shows better correlation of $\delta^{13}\text{C}/\delta^{18}\text{O}$ from QM16 upwards and although the r^2 value increases to 0.64, this value is not great enough to suggest good covariance. The results of the QM1 section differ compared to the BZ-E section. Overall the QM1 deposits are more depleted in $\delta^{13}\text{C}$ and more varied compared to the equivalent member in the BZ-E section. The $\delta^{18}\text{O}$ values have a much narrower range and are on the whole more depleted than the BZ-E section deposits with only AL3 similar to the $\delta^{18}\text{O}$ values of the QM1 deposits.

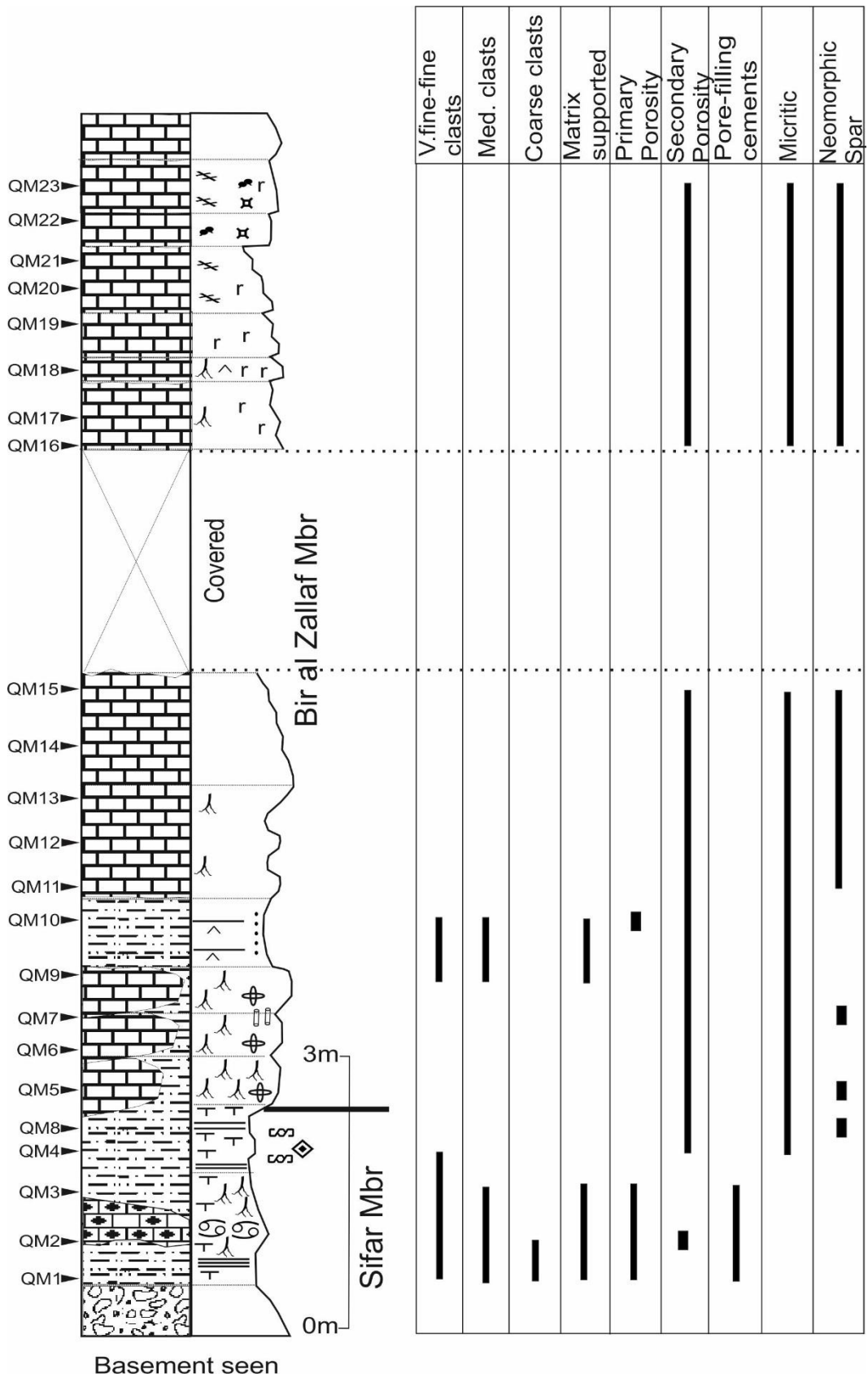


Figure 6.10 Key characteristics of the thin sections from the QM1 section. Note: the clast size refers to grains of sand-sized material. Please refer back to Figure 6.1 (pg176) for the log key.

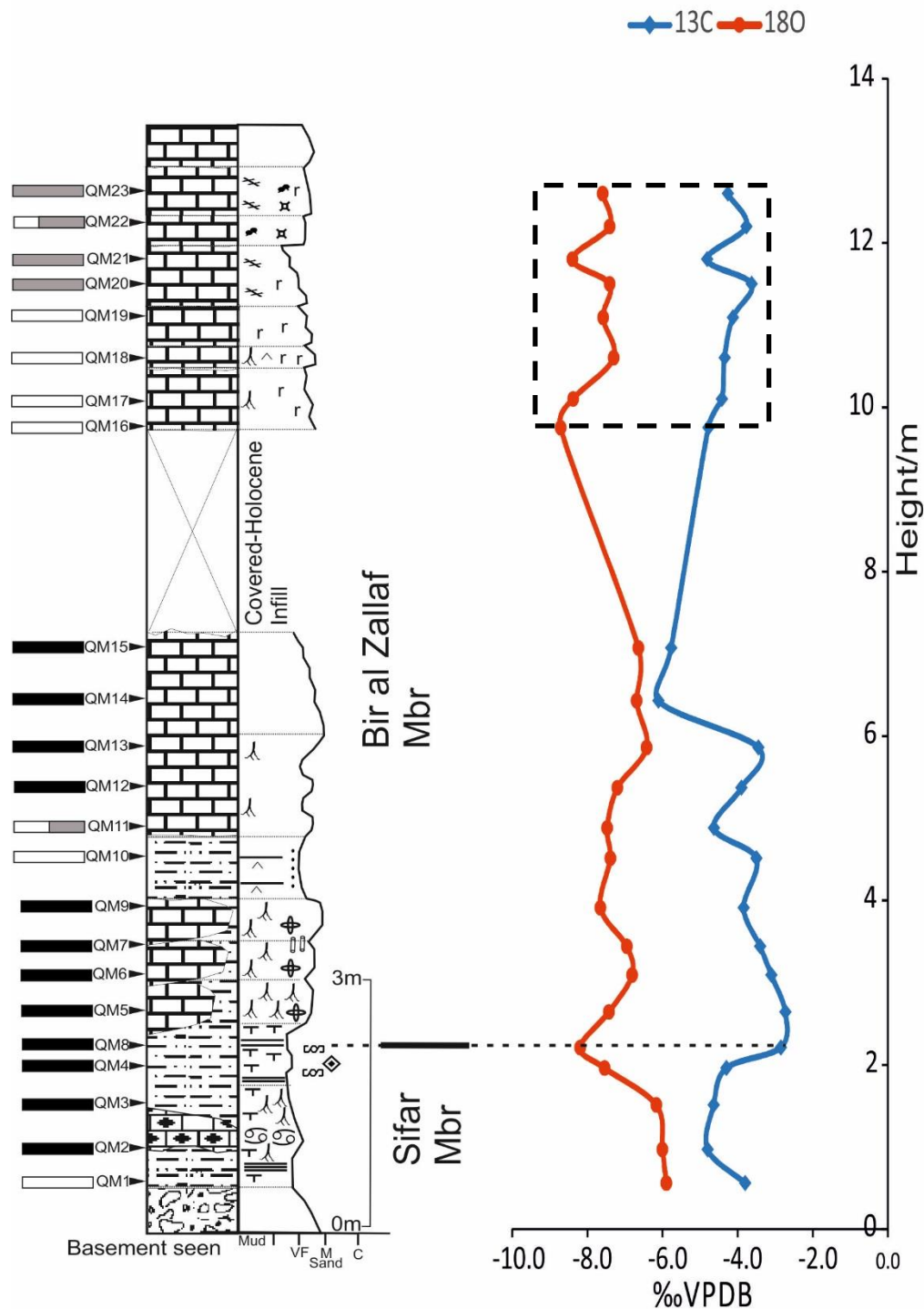
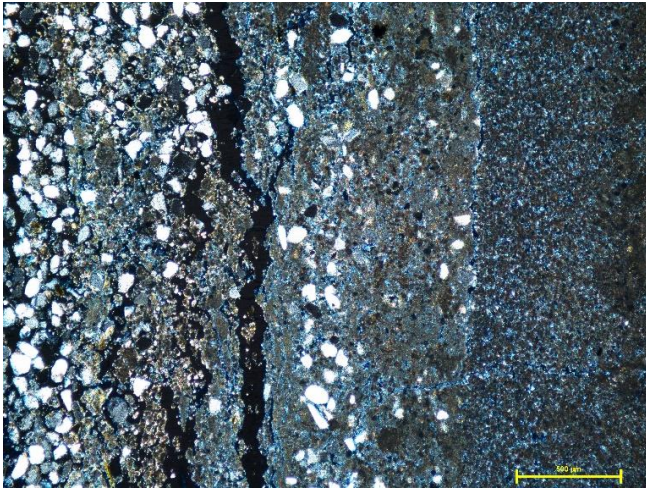
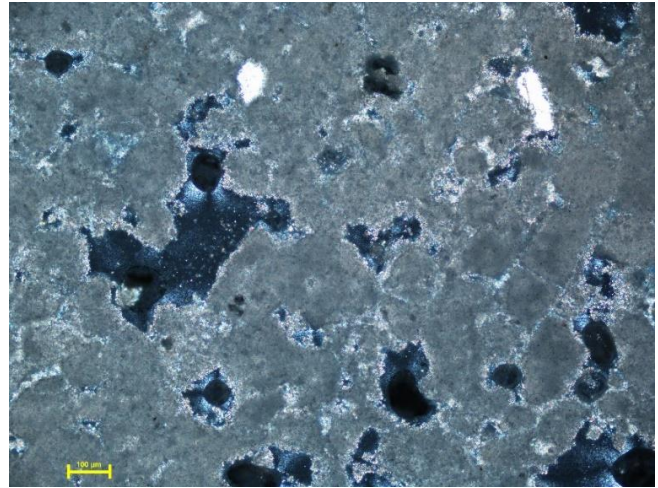


Figure 6.11 QM1 isotopic data vs stratigraphic height. The black, white and grey bars to the left of the log refer to the polarity of each of the deposits analysed where black=normal polarity, white=reversed and grey=unsure. Dashed box indicates the deposits which have good covariance between $\delta^{18}\text{O}/\delta^{13}\text{C}$. Please refer back to Figure 6.1 (pg176) for the log key.

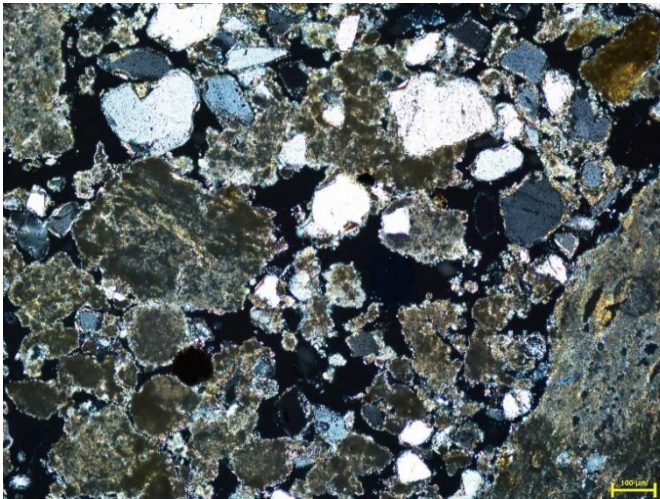
A



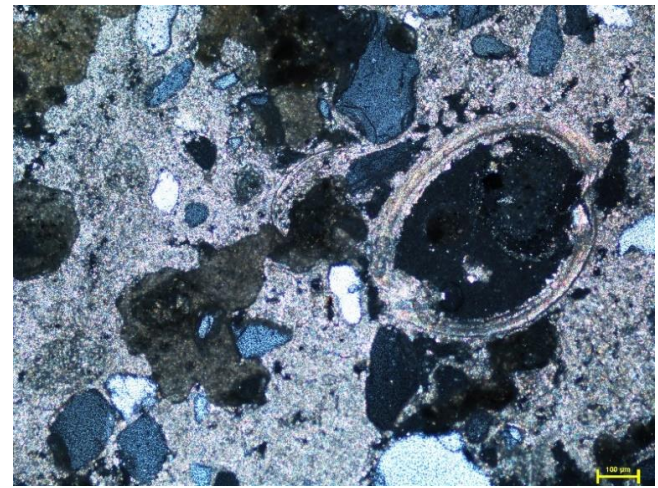
B



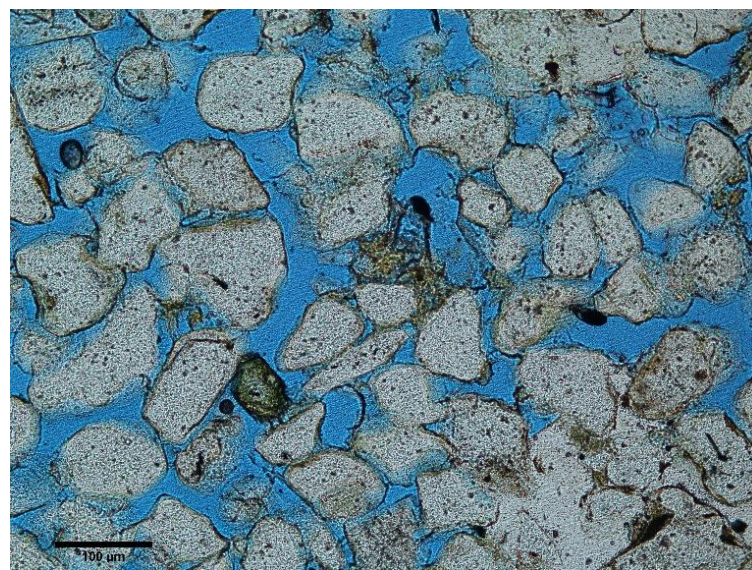
C



D



E



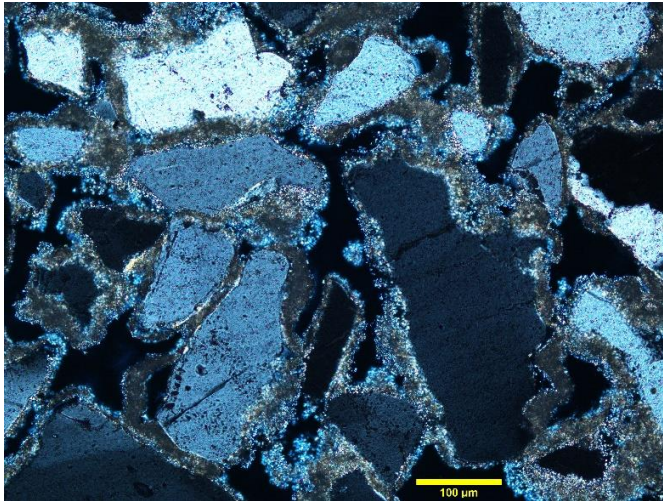
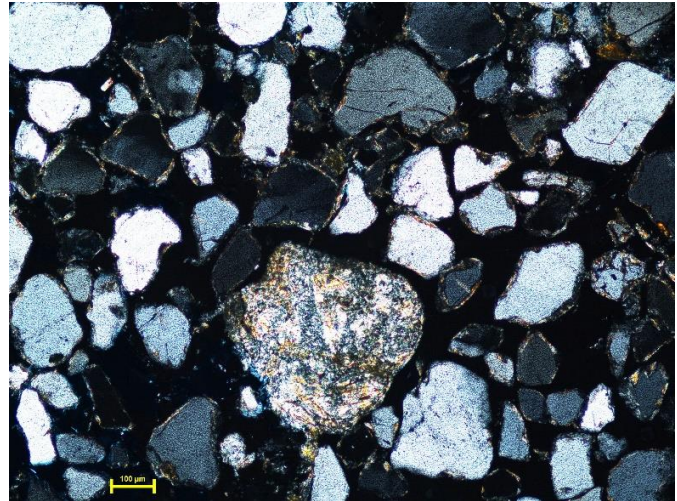
F**G****H**

Plate 6.5 Bir al Zallaf Member. BZ-E section. A-BZ27, parallel laminations of muddy carbonate interbedded with well-sorted quartz clasts (x5, cpl). B-BZ27, peloids joined by meniscus cements to form aggregate grains. Large fragments of carbonate mud also present. C-AL2, peloidal texture and vuggy porosity. Vugs are lined with secondary pore cements (x10, cpl). D-AL4, altered ostracod shell with intraskeletal porosity (x10, cpl). E-BZ24, high interparticle porosity with quartz clasts showing signs of dissolution at the edges (x20, ppl). F-BZ21, rim and meniscus cements coating fretted quartz clasts (x20, cpl). G-BZ24, rounded microcrystalline chert clast (x10, cpl). H-AL1, texture of the deposit with similarities to the QM1 section (x5, cpl). Scale bar 500 μ m in A/H and 100 μ m in the remaining photomicrographs.

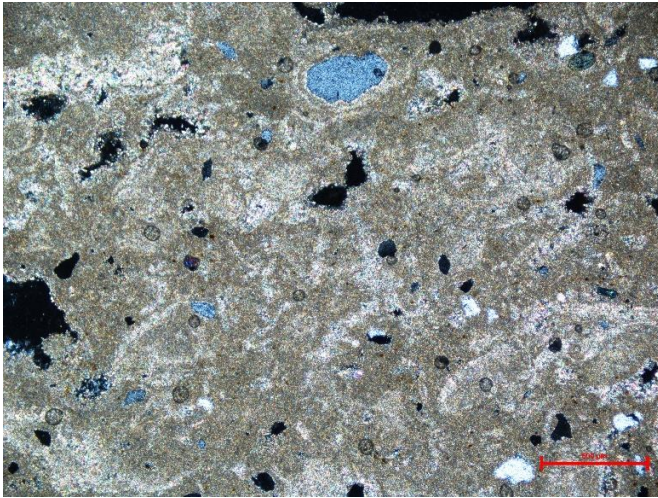
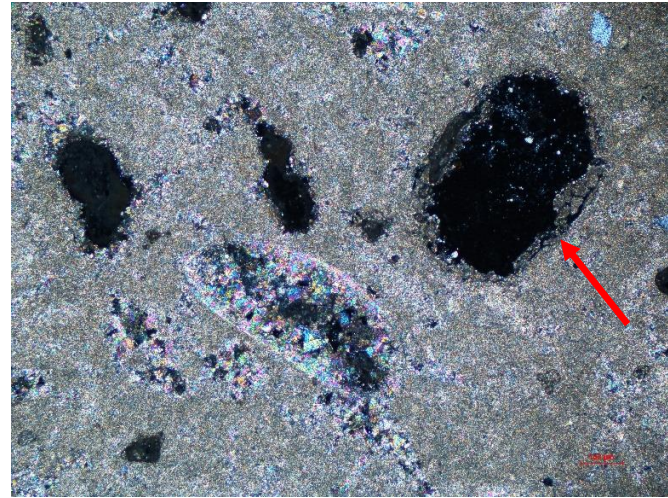
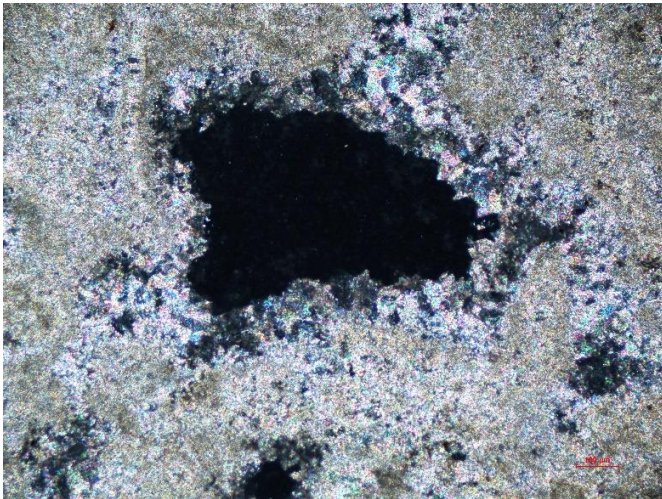
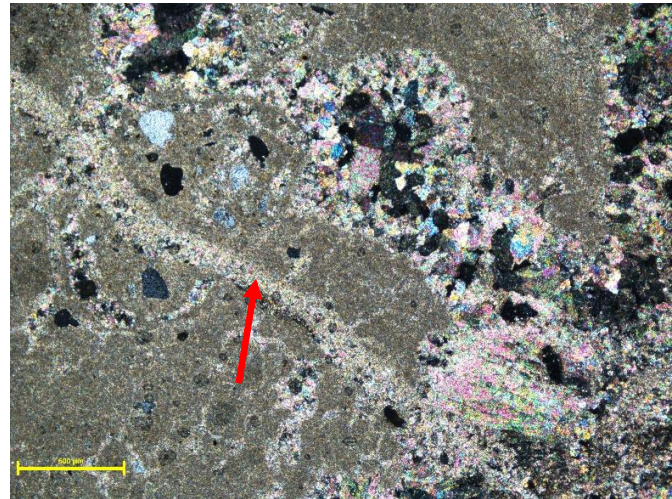
A**B****C****D**

Plate 6.6 Bir al Zallaf Member. QM1 section. A-QM11, mottled matrix of micrite/microspar cement. Detrital quartz clasts seen in floating matrix. Open vugs partially filled also seen (x5, cpl). B-QM12, ghost features (arrowed) as well as a completely filled pore with drusy cement (x10, cpl). C-QM5, partially filled vug lined by secondary spar cement (x10, cpl). D-QM21, secondary mosaic spar cements completely infilling pore spaces. Possible infilled rootlet/veinlet (arrowed) (x5, cpl). Scale bar is 500μm in A/D and 100μm in B/C.

6.2 Magnetostratigraphy: Age of the Zazur Formation

6.2.1 Scalar Magnetic Properties

The NRM intensity and MS were plotted for the members of the Zazur Formation. Two figures (Figure 6.12 i/ii) were produced, one with the members of the QM1/2 and M sections and the other with the members of the three BZ sections. Unlike the equivalent plots of the Shabirinah and Brak Formation, the relationship between the two variables in both plots is less apparent, probably due to the similar lithology of the sections of the Zazur Formation. This is also revealed when comparing the NRM intensity with their respective section height, which on the whole, show small variations (Figure 6.20, i-vi A). In Figure 6.12 (i), there is generally a fairly narrow range of intensity values. More variation is seen in the QM1-Bir al Zallaf Member specimens with two particularly high values. This is likely caused by contamination from the saw when cutting the specimens. The MS also has a fairly narrow range with specimens of the Sifar Member having similar values between the different sections. The larger susceptibility values are from the QM2-Sayl Member specimens owing to the slightly reddened colour of the samples and presence of some pedogenic features. The lowest MS values reflect the carbonate deposits of the QM1-Bir al Zallaf Member. Low values are also seen in aeolian specimens of the M-Sifar Member. Aeolian deposits often have a lower concentration of magnetic minerals and hence a lower susceptibility (Maher and Thompson, 1995; Nielsen et al., 2004). The Sifar Member of the three BZ sections (Figure 6.12 ii) show similar values to the equivalent member in Figure 6.12 (i). The deposits of the Sifar Member in the BZ sections are very similar with subtle differences in sedimentology, colour and grain size causing the small variations in values observed between the sections (Maher, 2011). The BZ-E Bir al Zallaf Member specimens have a slightly narrower range in intensity and higher MS values compared to the equivalent QM1 section member even though carbonate deposits occur in this member in both sections. The difference may be explained by the grain size of the deposits and differences in concentration of magnetic minerals dispersed throughout the carbonate matrix (Lowrie and Heller, 1982)

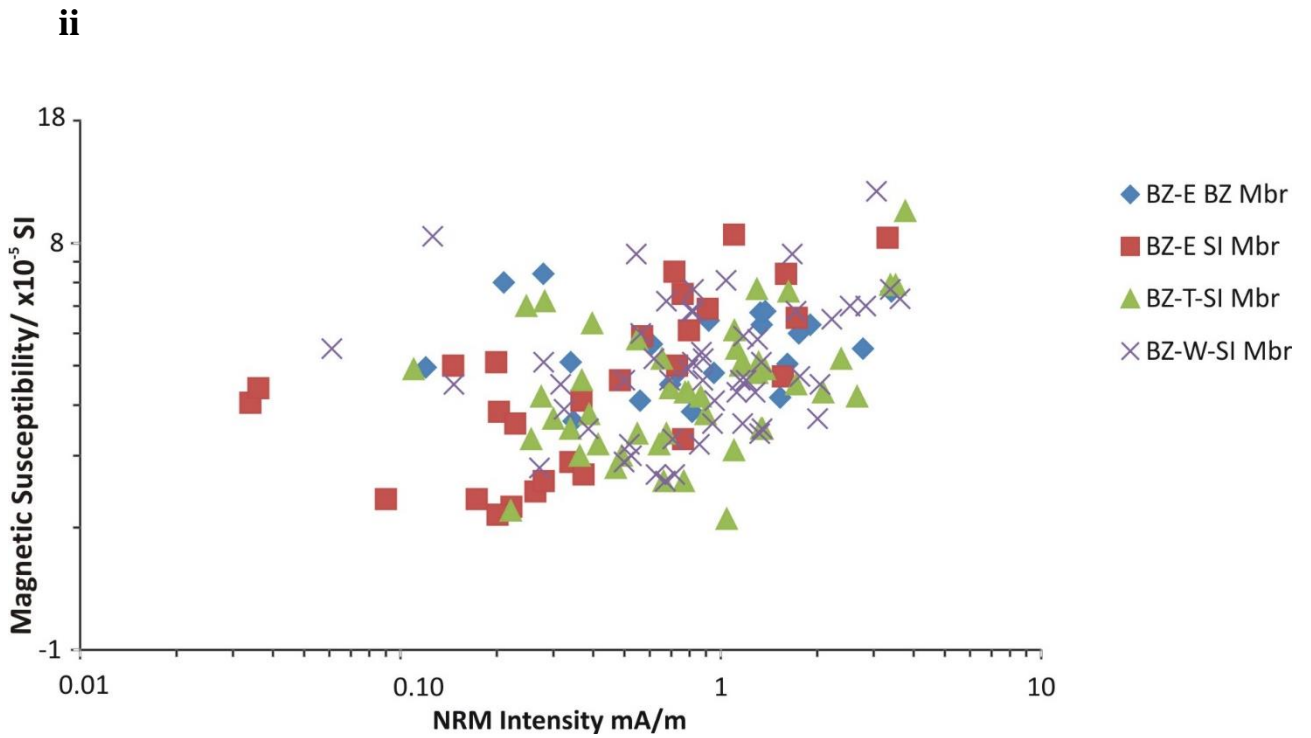
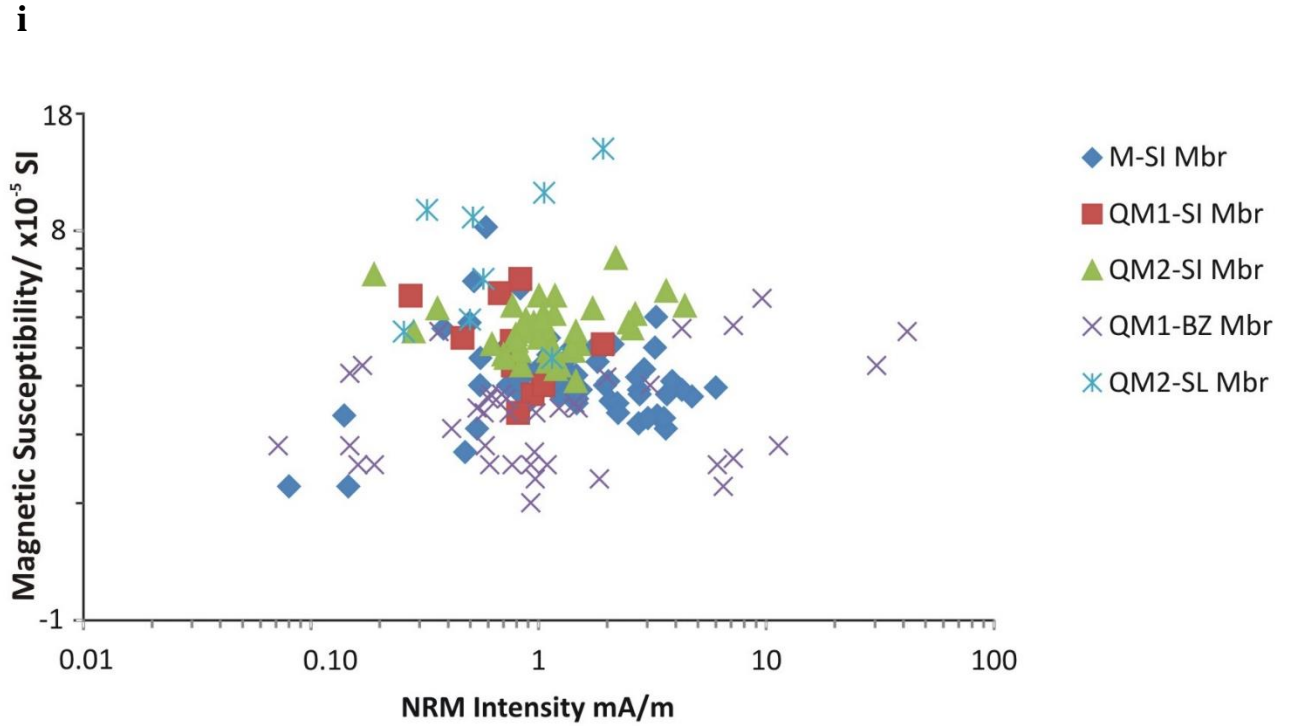


Figure 6.12 NRM intensity and magnetic susceptibility of i) specimens from the members of the QM1/2 and M sections (Zazur Formation), ii) specimens from the members of the BZ sections. Note: magnetic susceptibility values have +2 added to them to overcome the problems of plotting negative values on a log scale.

Changes in MS and intensity with temperature were compared between the sections of the Zazur Formation. Unfortunately, as the QM1, M and ALA/AL coded specimens of the BZ sections were partially demagnetised using AF, these changes could not be explored as MS values were not recorded. There are clear differences between the QM2 and BZ sections and also distinct differences between the BZ sections themselves. For the specimens of the QM2 section, the values of intensity show a clear decrease with temperature. Only very small variations are apparent in the higher demagnetisation steps such as in QM54 (Figure 6.13). MS values usually remain either fairly stable with temperature until the higher temperature stages (e.g. QM77, with the exception at 100°C). The changes in intensity and in particular susceptibility from 520°C (e.g. QM54/65) onwards indicates mineralogical alteration either due to the disappearance or formation of one ferrimagnetic phase or the formation of one ferrimagnetic phase and the simultaneous disappearance of another ferrimagnetic phase with a different coercivity (Henry et al., 2005). In this case it is likely that the mineralogical changes have resulted in the formation of magnetite possibly from destruction of clay minerals (Henry et al., 2005).

As for the QM2 section, NRM intensity values of the specimens from the BZ sections decrease with increasing temperature. Small changes are apparent in these values usually from 520-550°C. Marked differences occur in the MS of the specimens from the individual BZ sections. In the BZ-E section, some specimens such as BZ26 and BZ28 show large increases (of ~8) between the MS value at the NRM and 100°C. MS values continue to vary with increasing temperature, with variations more apparent from 400-460°C onwards. These samples are carbonate-rich with TD likely causing the breakdown of metastable minerals in the samples such as goethite/maghemite to haematite (Lowrie and Heller, 1982). Beyond 550°C the alteration is likely due to the production of new magnetite (Butler, 1992, pg147).

The knoll sub-section of the BZ-W section shows slight variations in MS until 430°C (e.g. BZ37 Figure 6.14), after which more alteration occurs probably due to the transformation of clays to magnetite (Henry et al., 2005) BZ32 (Figure 6.14) shows a similar trend to the specimens from the BZ-E section where a large increase occurs in the MS at the NRM and 100°C. Unlike the other specimens from this section, the MS of BZ32 generally decreases with each heating stage suggesting the oxidation of ferromagnetic minerals, such as titanomagnetite, to haematite (Krijgsman et al., 1995; Henry et al., 2005). The NE sub-section (BZ-W) has slightly lower MS values than the knoll sub-section. Small variations are observed in MS in this sub-section up to 460-490°C when the MS

increases with each heating stage as in the BZ-E section (e.g. BZ60, 69 Figure 6.14). The BZ-T section shows MS values that are fairly constant until 550-580°C when the values increase with temperature (e.g. BZ94, 91, 87 Figure 6.14). This is also accompanied by a slight increase in intensity suggesting the formation of magnetite as seen in the QM2 section. Overall the BZ-T section has similar lithology throughout and thus is reflected in the MS values.

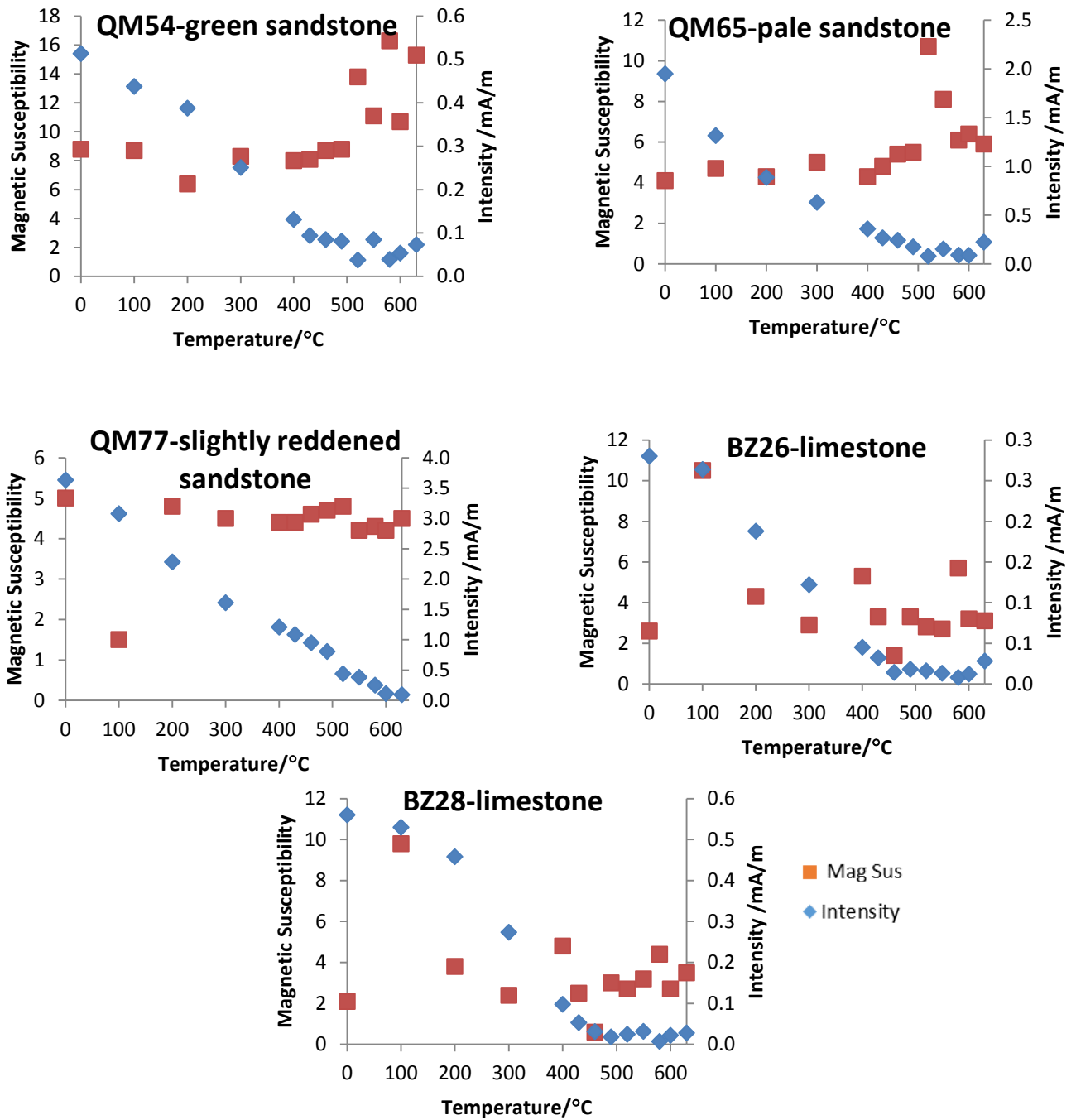


Figure 6.13 Changes in intensity and magnetic susceptibility with demagnetisation temperature of specimens from the QM2 section and the BZ-E sections. Note: The MS values of BZ26 have +2 added to them due to some negative numbers.

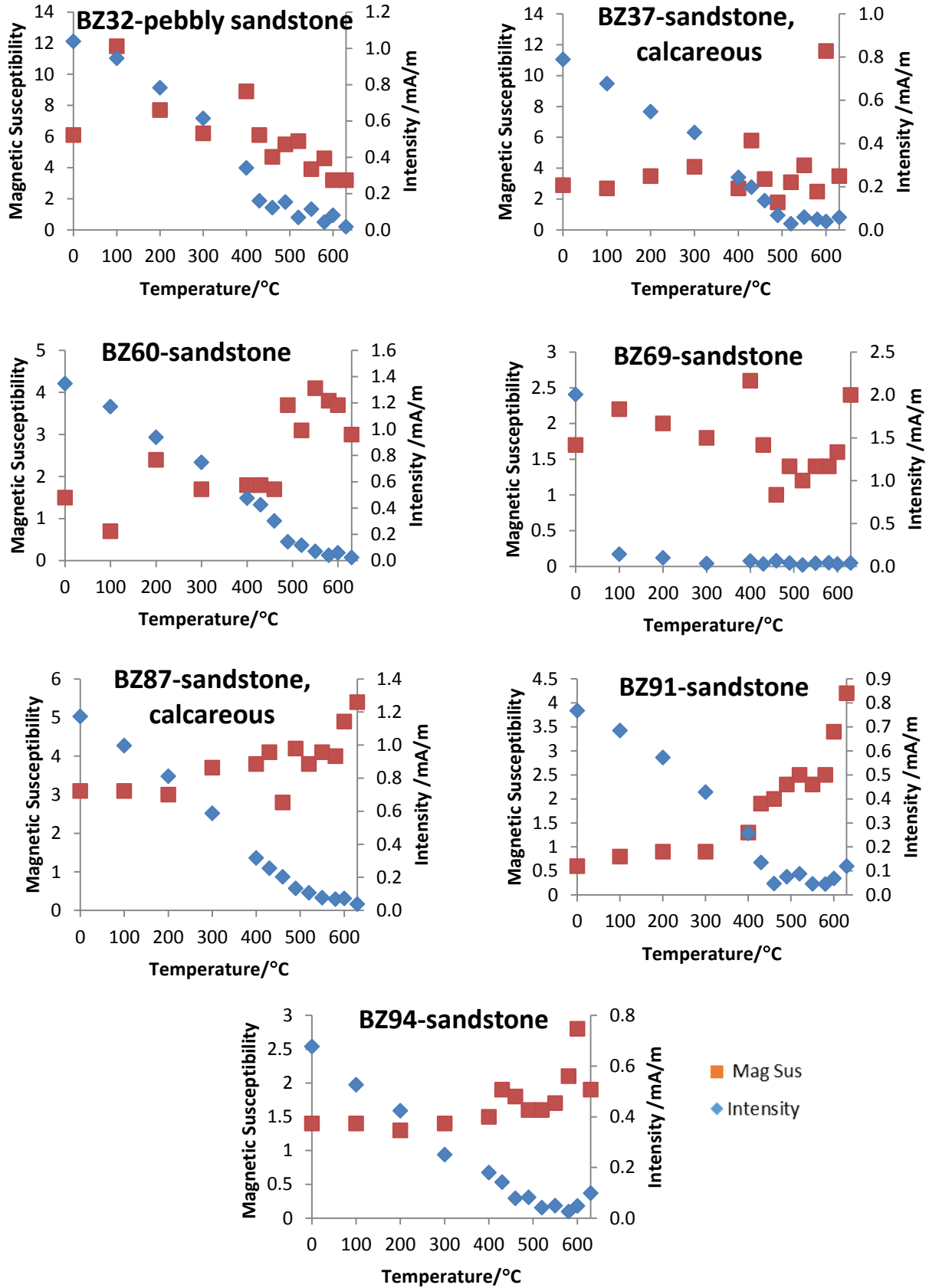


Figure 6.14 Changes in intensity and magnetic susceptibility with demagnetisation temperature of specimens from the BZ-W and BZ-T sections.

6.2.2 Palaeomagnetic Results

The palaeomagnetic results of the sections relating to Zazur Formation will be discussed in two parts: one will examine data from the QM1/2 and M sections and the other the three BZ sections. The data will be discussed in this manner due to the correlations between the QM/M sections and the three BZ sections. It also allows a more detailed investigation of the results when looking at a large number of specimen data (319 specimens).

Of the QM1/2 and M sections, 165 specimens were measured in total. When looking at the data of the QM1 section, six of the specimens from the horizons of QM23, 22 and 21, showed anomalously high NRM intensities (one or two orders of magnitude higher) when compared to the remainder of the section. These samples are from the top part of the section and represent a palaeohill that was exposed in Holocene sediment accumulation. As such, the anomalous values were interpreted to be the result of lightning strikes which remagnetised the rocks. As the intensities of the specimens from QM21 were particularly high, the data from this horizon was not included in the overall analysis of the section.

A low stability component was isolated in 81% of the specimens from the QM/M sections. In the QM2 section, 98% of specimens contained this component. Typically, the component occurred between demagnetisation temperatures of room temperature/100°C to around 200-400°C (Figure 6.17). A mix of directions are apparent from this component interpreted to be a composite. Three main directions are apparent (Figure 6.15). In the QM1 section, it is northerly directed with positive inclination. This is similar to the ChRM direction but is likely a modern Brunhes overprint. This is also seen to some extent in the QM2/M sections, with these sections also having a southerly directed positive inclination component and the QM2 a south easterly directed negative inclination component. These reverse components are 'contaminated' with a Brunhes overprint. As in the Shabirinah/Brak Formations, directional scatter is observed in the intermediate stability component (Figure 6.15). However, reverse components south-easterly and south-westerly directed with negative inclination are observed which plot either side of the interpreted ChRM. A southerly directed positive inclination component is also apparent, in particular in the M section. These directions are similar to those of the low stability component. 67%, 81% and 90% of the specimens from the QM1/2 and M sections contain the interpreted component respectively. It is isolated at a range of demagnetisation temperatures but

typically occurs between 350-460°C to 425-500°C and occasionally to higher temperatures up to 600°C.

A ChRM (s-class) direction was isolated from 28% of the specimen data with the QM2 section proving particularly difficult to isolate suitable line-fits (10% ChRM). QM1 however was much more successful, with ChRM directions extracted from 53% of the specimens. A large branch of reverse-like directions are seen for the QM2 section in the low stability component, however these directions are too shallow and hence explains the disparity in success between the two sections. Of the ChRMs isolated, the most commonly assigned class was s2 at 12% (Table 6.6; Figure 6.20 i-iii B). The ChRM was often present between demagnetisation temperatures starting at 200-400°C to between 500°C and complete demagnetisation. This suggests remanence is largely carried by magnetite based on its maximum unblocking temperature (Butler, 1992, pg18). In all, 43% of the specimens showed motion along GC paths towards interpreted normal or reverse polarity with just 16% of these GC fits including the origin. The lack of origin intersection planes is due to mineralogical alteration (increase in the MS occurred from 520°C in the QM2 section) and also viscous magnetisation acquisition at higher temperatures (due to alteration). The mean α_{95} of the assigned t-classes were similar ranging between 22.5° (t3) and 25° (t2) with the mean excess standard deviation parameters (ρ) both equalling 2.3. 29% of measured specimens failed to yield reliable evidence of primary magnetisation either via a ChRM or GC trend.

154 specimens were measured from the three BZ-sections. A low stability component was isolated between 0 and 200-430°C in 88% of the specimens (Figure 6.19). Unlike the QM/M section data, no clear clustering is apparent from this component but on average the specimens have a steep positive inclination (Figure 6.16). As in the previously analysed sections, a mix of directions is also apparent in the intermediate stability component. The mix of directions for these components could be due to a mix of components including random viscous components. The scatter observed in the intermediate component directions is reflected in the range of demagnetisation temperatures it is isolated at. Isolation occurs at a slightly lower temperature than the equivalent component of the QM/M section starting between 200-490°C up to between 450°C and complete demagnetisation. The BZ sections are the poorest recorders of palaeomagnetic behaviour with the ChRM isolated in only 14% of the specimens, half the amount of the equivalent QM/M sections. A slightly higher amount of specimens (49%) however showed motion along GC paths towards interpreted normal/reverse polarity. A

similar amount of s-class ChRM directions were isolated from each of the BZ sections (13-15%, Figure 6.20 iv-vi B) typically between 300°C up to 490-600°C. These temperatures are similar to those of the QM/M sections and similarly suggest the presence of magnetite. In the BZ-W section, only two ChRM directions were isolated from the NE sub-section compared to five from the knoll section (Figure 6.20). Of the t-class assigned specimens, 22% had fits which intersected the origin. The mean α_{95} of the assigned t-classes were similar to those of the QM/M sections. There is a slight difference in this mean between the classes with the smallest mean value calculated for t1 specimens (20° , $\rho=2.7$) and the largest for t3 (21.3° , $\rho=2.0$). This is not surprising as the poorest quality data would be expected to have a larger associated error.

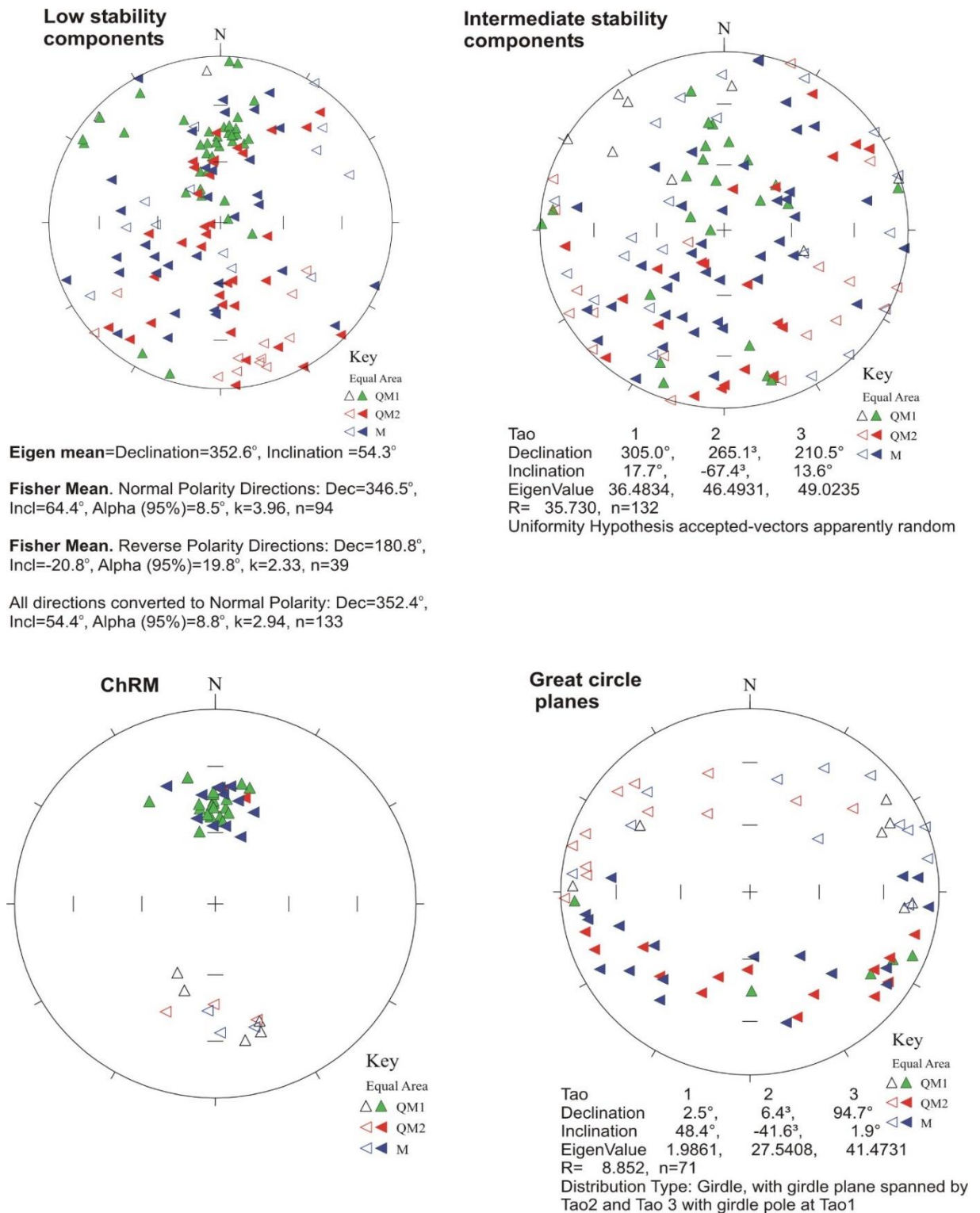


Figure 6.15 Components extracted from demagnetisation data of the QM1, QM2 and M sections and their statistical evaluation. ChRM statistics can be found in Table 6.7, pg219.

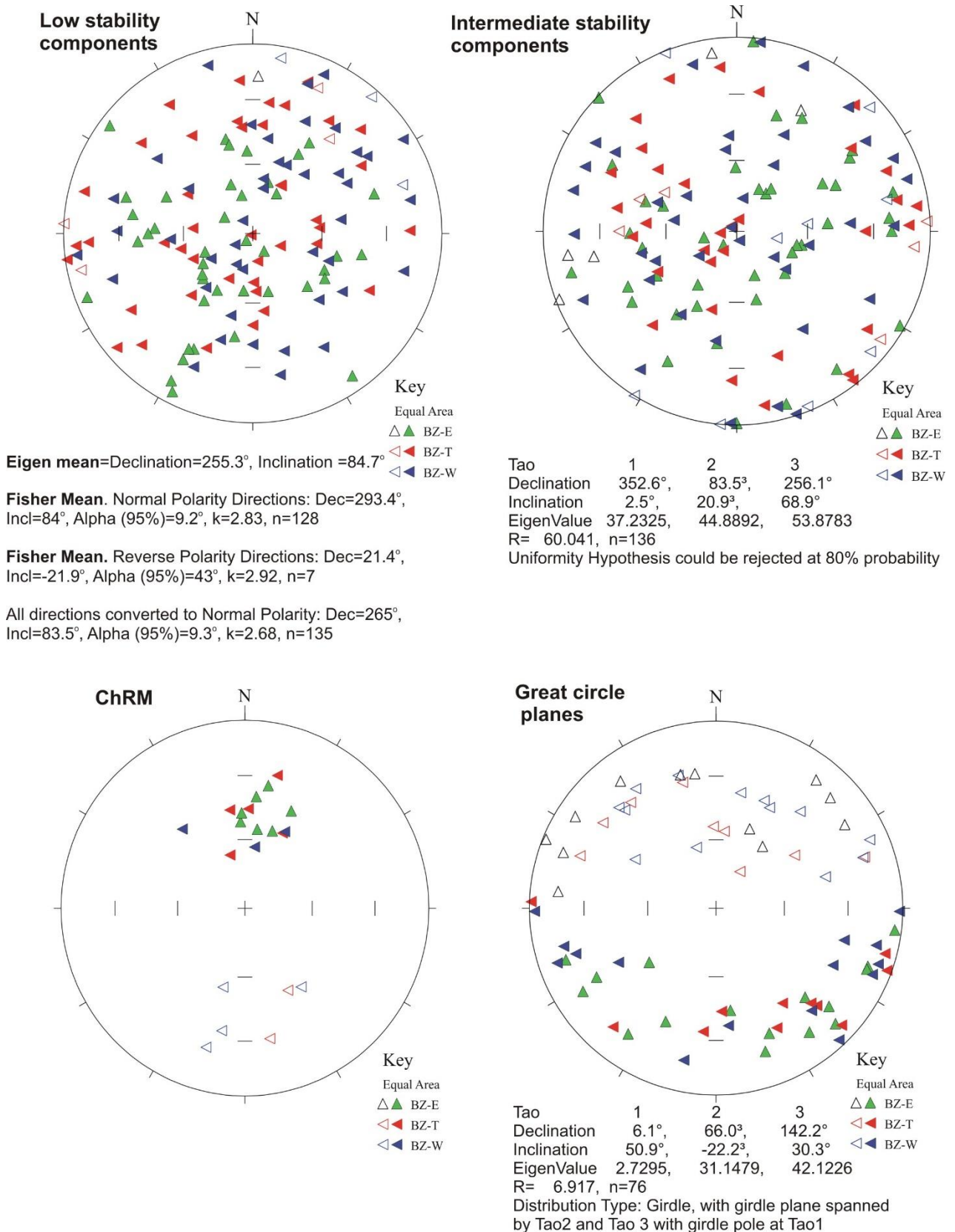


Figure 6.16 Components extracted from demagnetisation data of the BZ-E, BZ-W and BZ-T sections and their statistical evaluation. ChRM statistics can be found in Table 6.7, pg219..

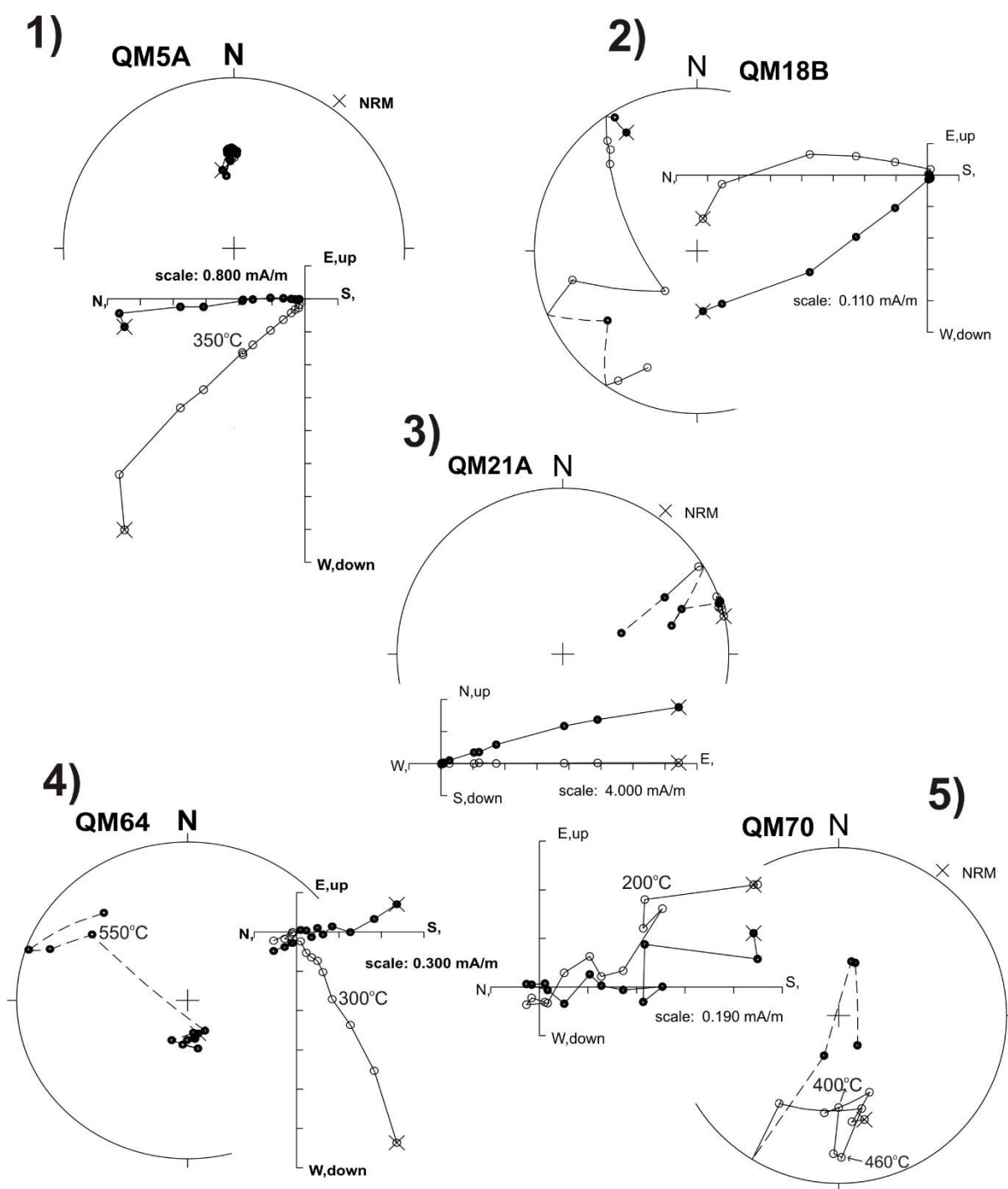


Figure 6.17 Representative demagnetisation data from the Zazur Formation. 1-3=Qarat al Mrar 1 section, 4/5=Qarat al Mrar 2 section. 1) QM5A-normal polarity (N, s1 behaviour), showing component 'A' from 100-350°C, ChRM from 375°C to the origin. 2) QM18B-reverse polarity (R,t1 behaviour), ChRM from 15-25mt.3) QM21A-?Polarity, t3 behaviour, strong component from 0-45mt, unclear polarity possibly due to the influence of lightning strikes. 4) QM64-normal polarity (N? , t3 behaviour), component 'A' from NRM to 300oC, normal polarity evident from 550°C. 5) QM70-reverse polarity (R?, s3 behaviour), component 'A' from NRM to 200°C, ChRM evident from 400-460°C, last few points likely due to a viscous component from the GM400.

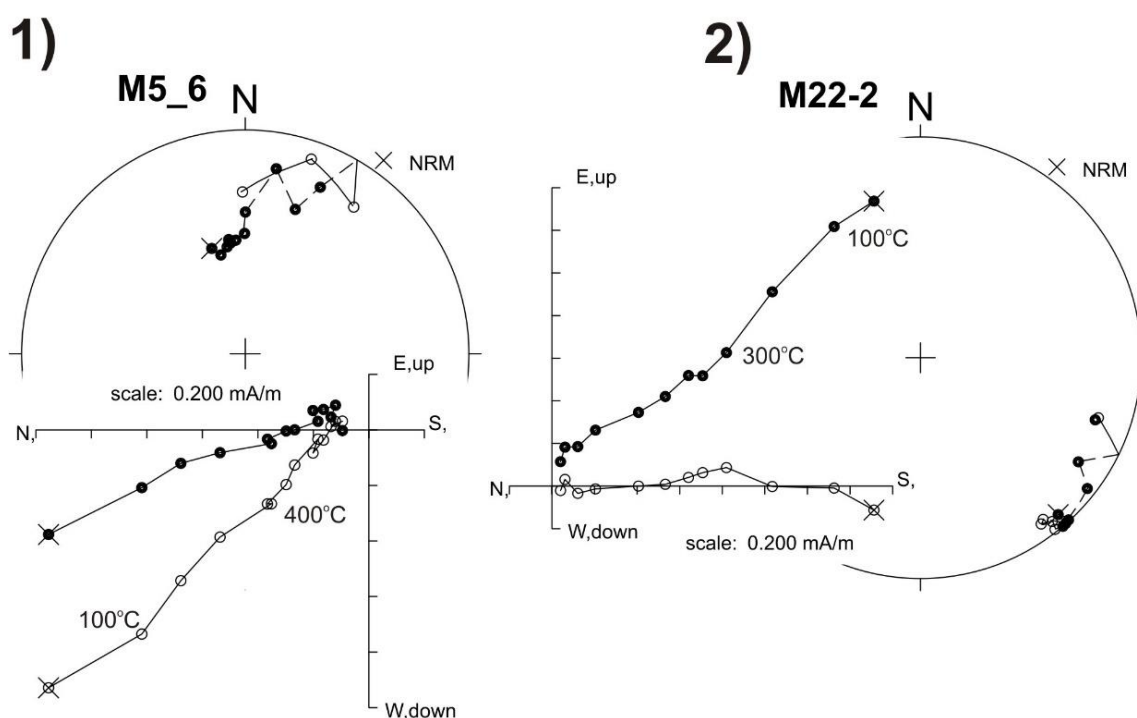


Figure 6.18 Representative demagnetisation data of the Al Wafa section from the Zazur Formation. 1) M5-6-normal polarity (N?, t1 behaviour), component 'A' from 100-400°C. 2) M22-2-reverse polarity (R?, t3 behaviour), component 'A' from 100-300°C.

	GC planes with interpreted polarity (%)	Origin intersecting GC planes (%)	S1 %/ mean α_{95} (°)/ mean excess SD (ρ)	S2 %/ mean α_{95} (°)/ mean excess SD (ρ)	S3 %/ mean α_{95} (°)/ mean excess SD (ρ)	T1 %/ mean α_{95} (°)/ mean excess SD (ρ)	T2 %/ mean α_{95} (°)/ mean excess SD (ρ)	T3 %/ mean α_{95} (°)/ mean excess SD (ρ)
ZF (QM1/2, M)	43	16	7/ 4.6/ 1.4	12/ 8.3/ 1.8	9/ 12.7/ 2.1	8/ 23.2/2.3	18/ 25.1/ 2.3	21/ 22.5/2.3
ZF (BZx3)	49	22	5/9/1.7	5/11.8/ 1.9	5/19.1/ 2	6/ 20/ 2.7	21/ 20.9/ 2.2	38/ 21.3/ 2.0

Table 6.6 Table outlining some of the key statistics of the ZF. '%' refers to the total number of specimens classified as s1-s3/t1-t3. 'mean α_{95} ' when listed under s-class refers to the mean α_{95} of the linear fits, when listed under t-class it refers to the mean α_{95} for the poles to the fitted planes. 'mean excess SD' (ρ) refers to the mean excess standard deviation parameters calculated for the different classes (for s-class-calculated from the average line ρ value in LINEFIND, for t-class calculated from the average plane ρ value in LINEFIND).

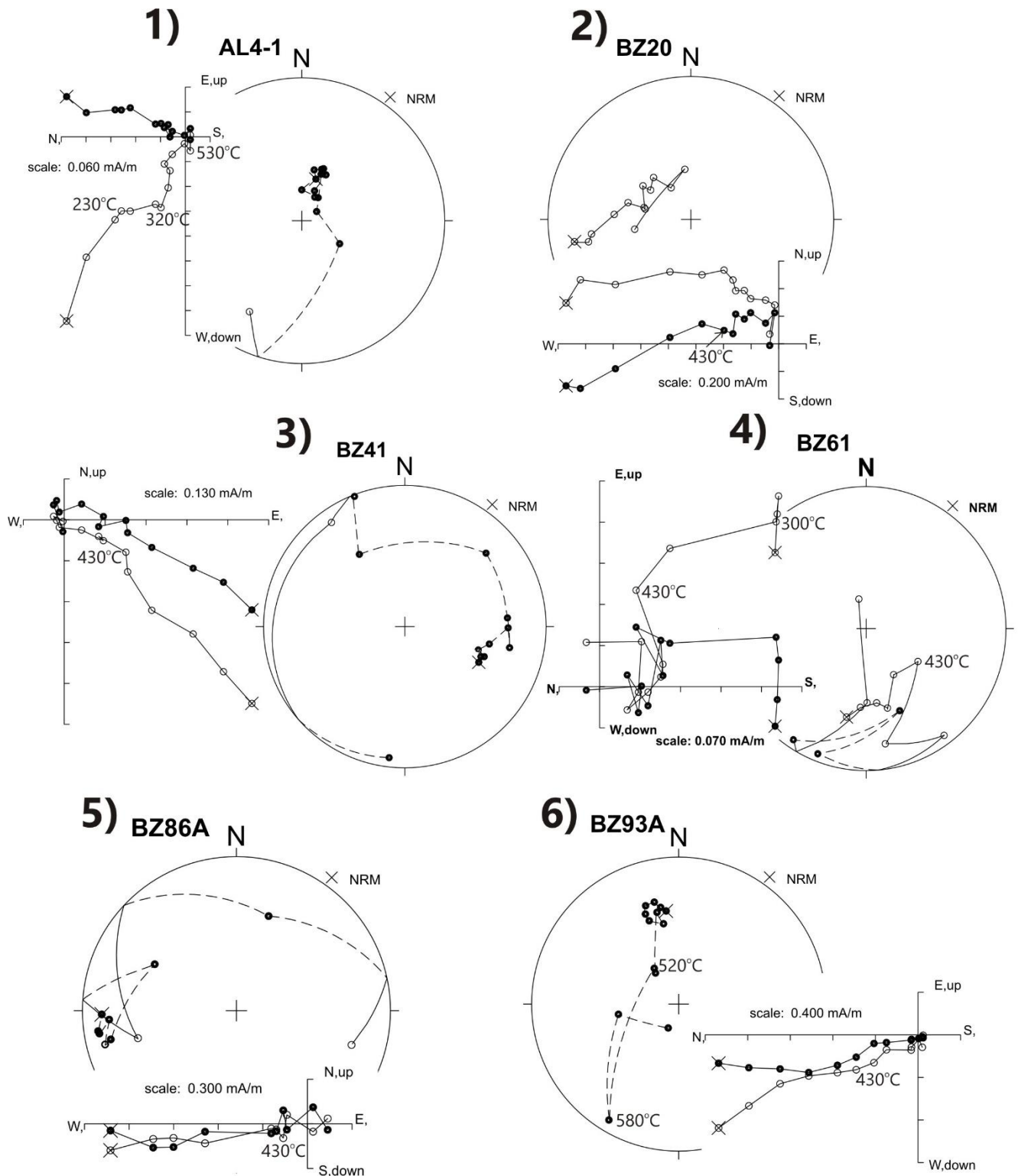
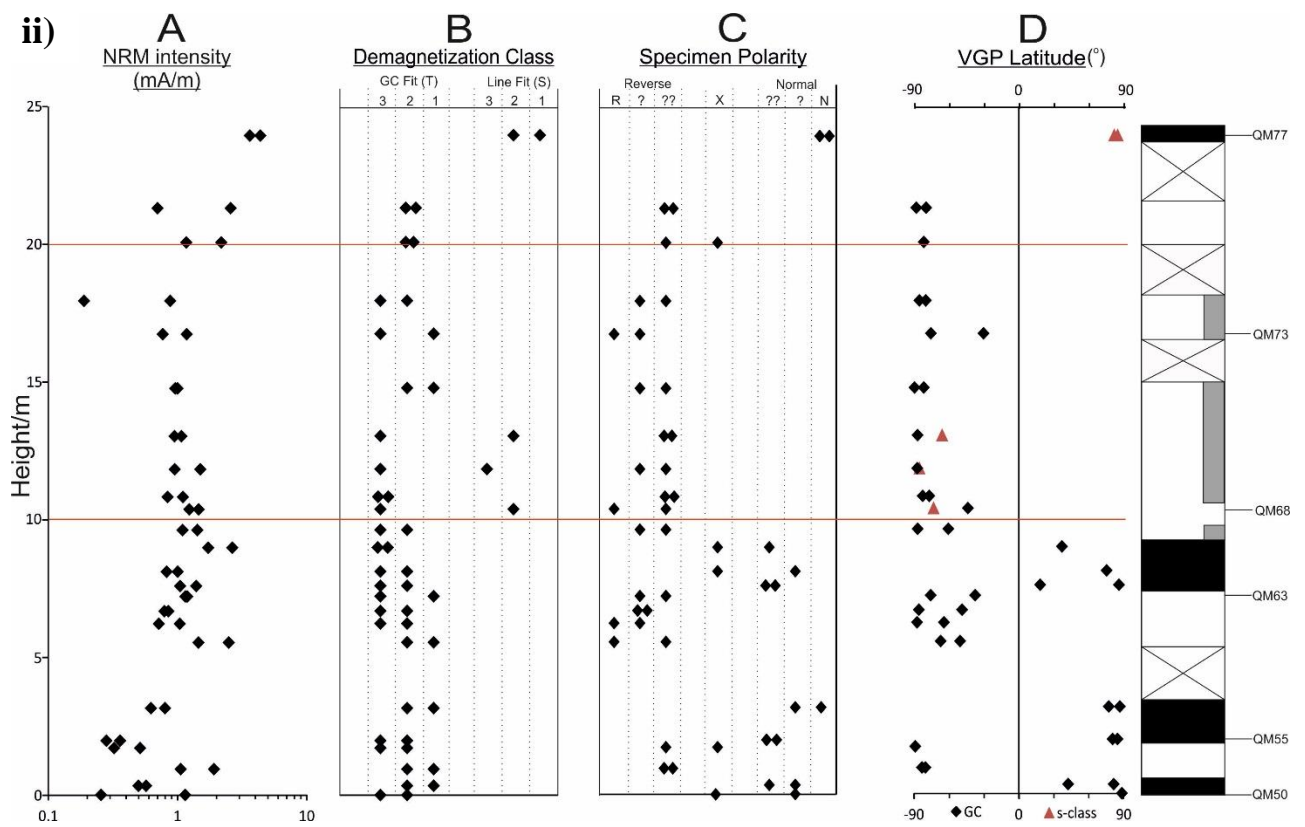
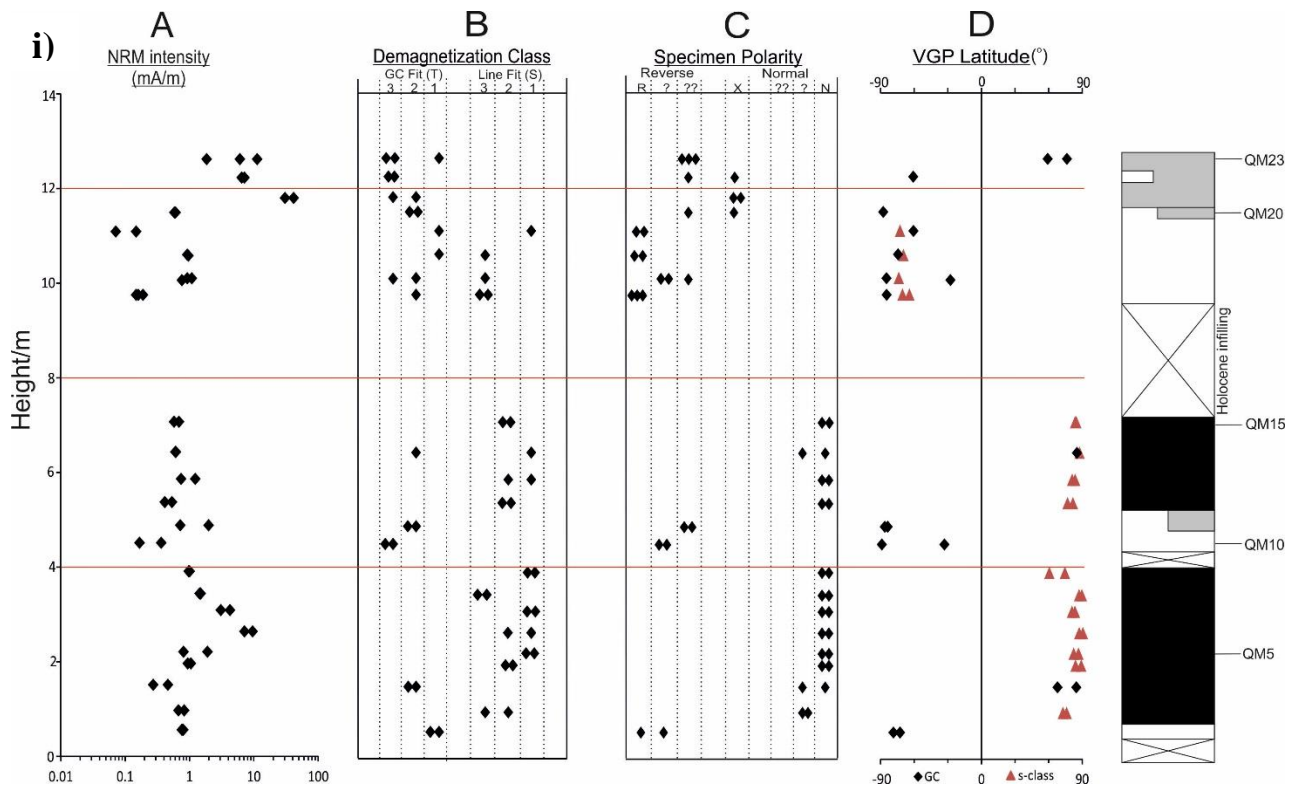
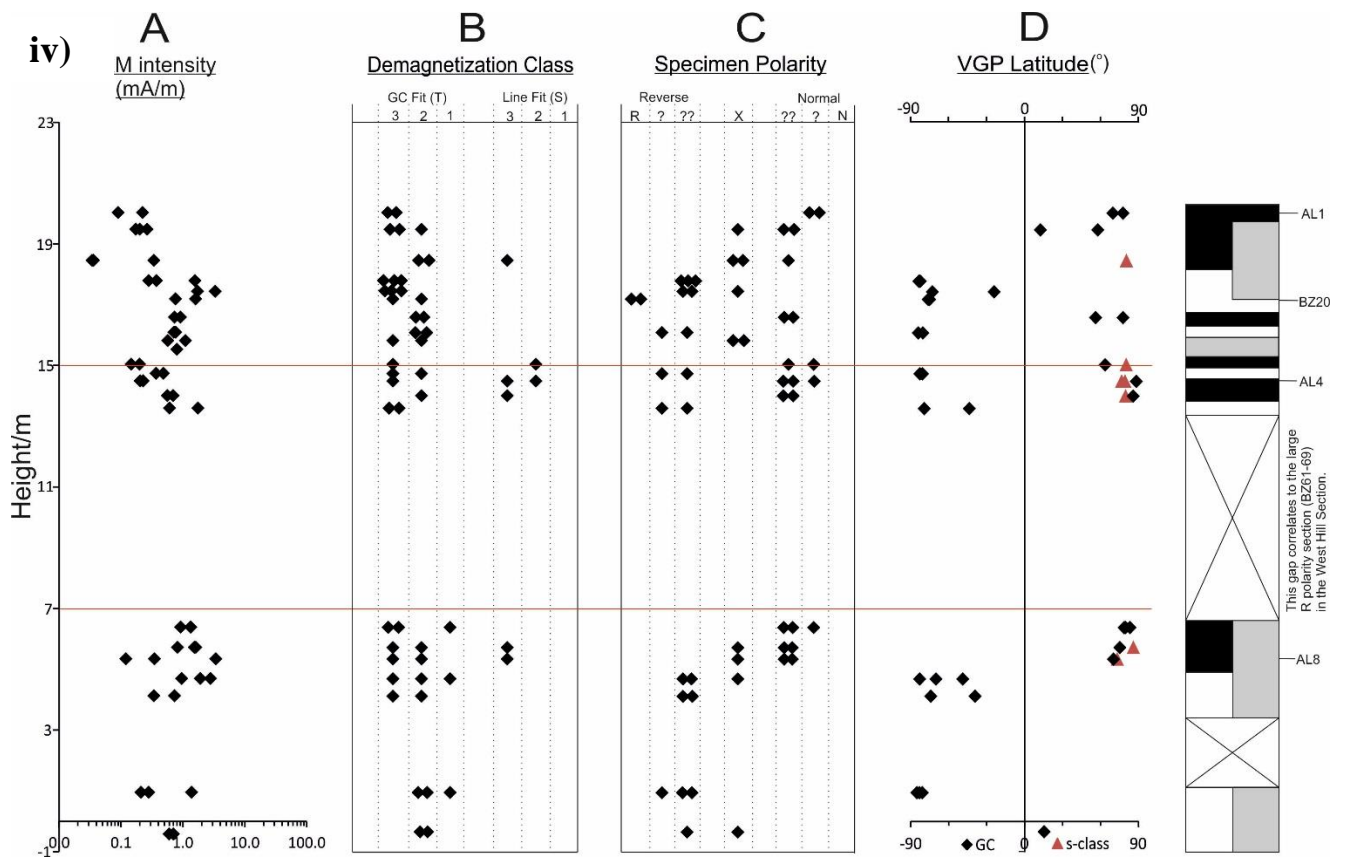
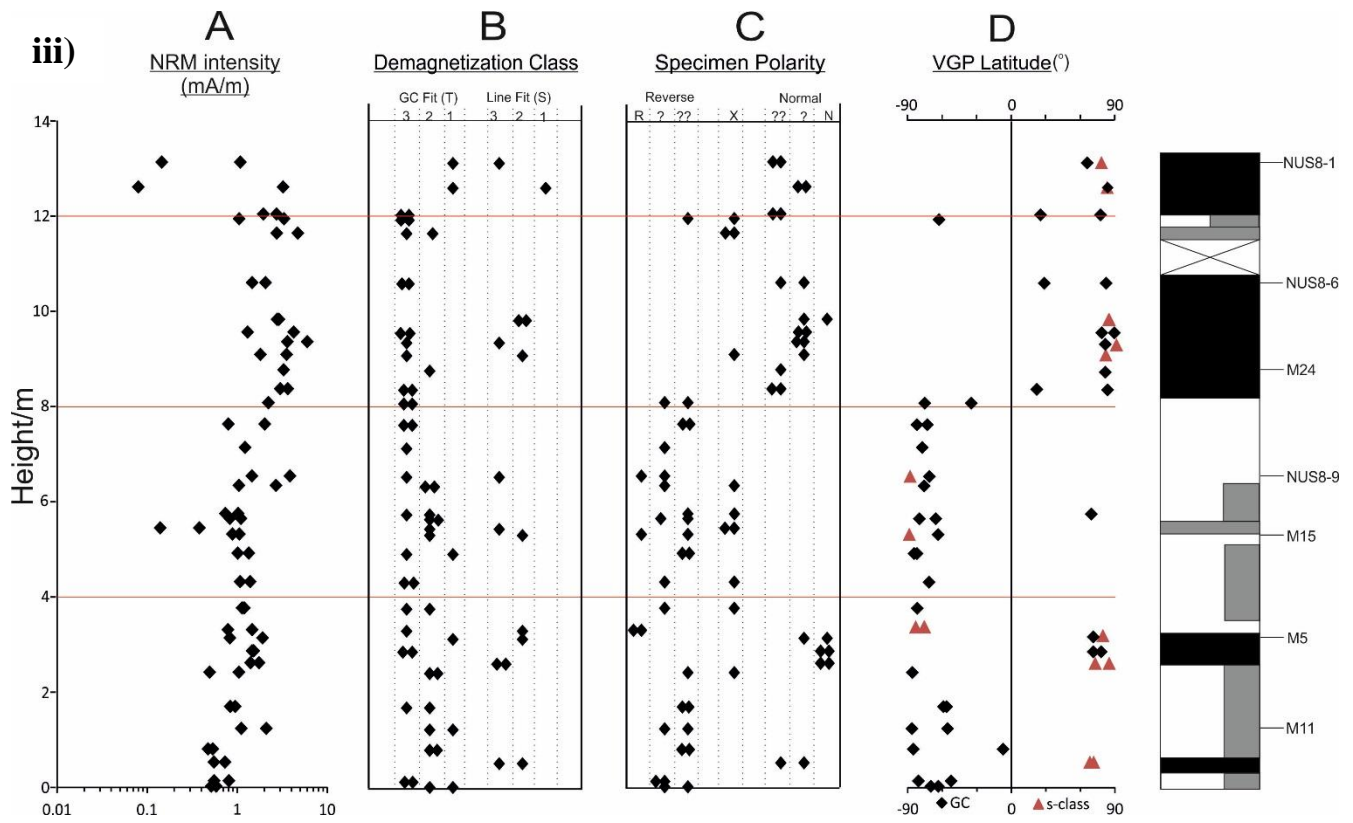


Figure 6.19 Representative demagnetisation data from the Zazur Formation. 1-2 Bir al Zallaf East section. 3-4 Bir al Zallaf West section. 5-6 Bir al Zallaf Twin Hills section. 1) AL4-1-normal polarity (N?, S2 behaviour), component 'A' from NRM to 230°C, ChRM evident from 320-530°C. 2) BZ20-reverse polarity (R, t2 behaviour), component 'A' from NRM-430°C. 3) BZ41-normal polarity (N?, t3 behaviour), component 'A' from NRM-430°C, a strong component also shown from 430-520°C. 4) BZ61-reverse polarity (R, s2 behaviour), component 'A' from NRM-300°C, ChRM evident from 300-430°C. 5) BZ86A-reverse polarity (R??, t2 behaviour), component 'A' from NRM-430°C, a GC plane fitted from 460°C to the origin. 6) BZ93A-normal polarity (N?, S2 behaviour), component 'A' from NRM-430°C, ChRM evident from 520-580°C.





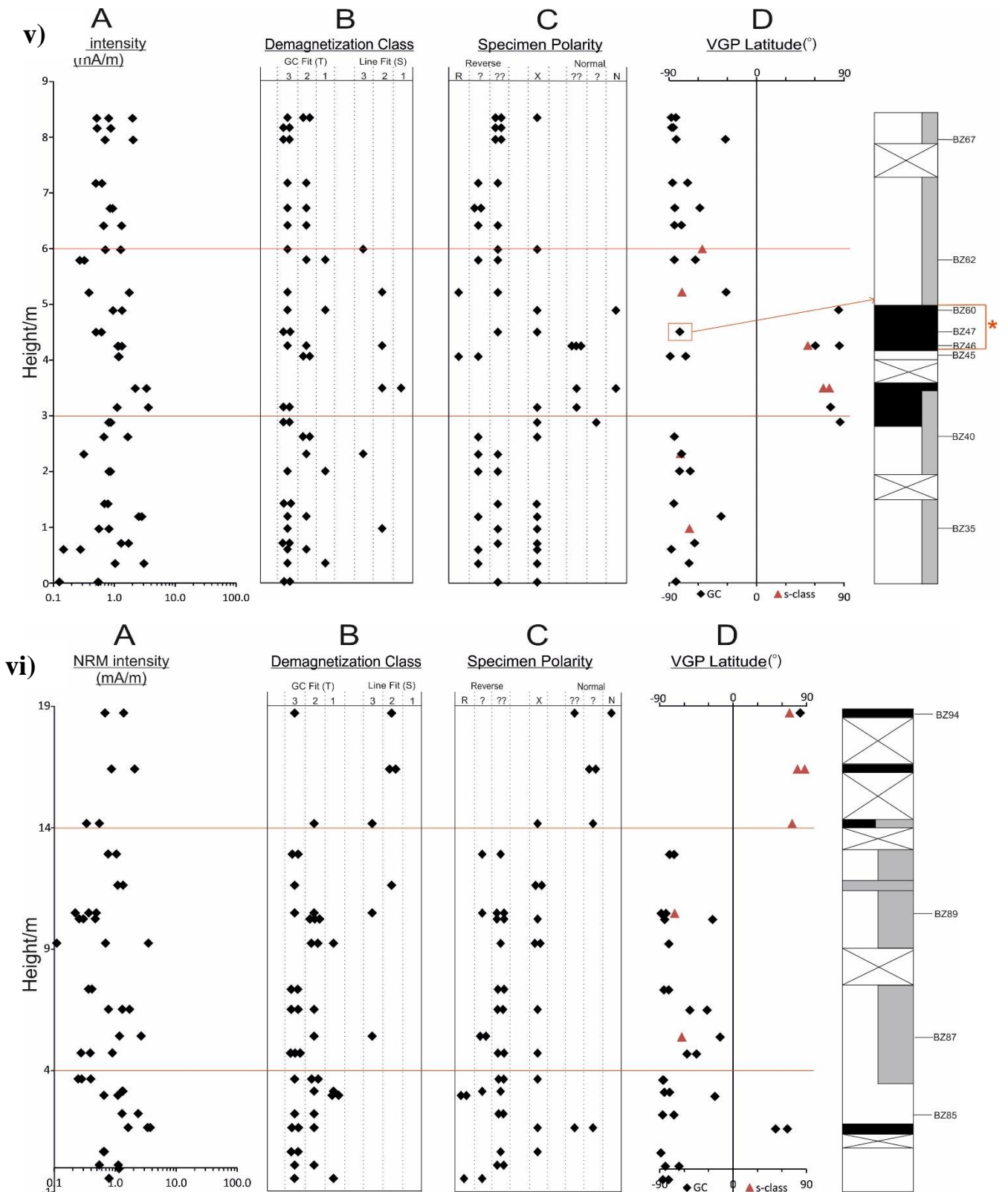


Figure 6.20 Magnetostratigraphic data summary of the i) QM1, ii) QM2, iii) M, iv) BZ-E, v) BZ-W, vi) BZ-T sections. A-Natural Remnant Magnetisation. B-Demagnetization behaviour categorised into good (s1) and poor (s3) characteristic remanent magnetisation (ChRM) line fits, great-circle (GC) fit quality range from good (t1) to poor (t3). C-Interpreted specimen polarity quality. Poor quality data in column headed X. D-The virtual geomagnetic pole (VGP) latitude, red triangles representing s-class ChRM, black diamonds t-class GC behaviour specimens. To the right is the interpreted magnetic polarity stratigraphy, white-reversed polarity, black-normal, grey-uncertain. *BZ46 is equivalent to BZ60, therefore this part of the section would have N polarity. BZ47 is equal to BZ61 and would thus be part of the overlying R polarity section.

6.2.3 Mean Directions and Palaeopoles

As in the previous chapter, the mean directions of the sections were calculated using ‘specimen based’ means. Table 6.7 A/B show the mean directions of the sections along with the VGP poles and results of the reversal tests. The BZ-W mean direction takes into account the specimens from both of the sub-sections at this site. All of the sections show a pass of the reversal test with the QM1/2 sections and the BZ-T passing particularly well with a Ra classification. The inclination values of the QM/M sections are the same (0.1° difference) with the overall mean direction of the QM1 and M sections being extremely close (declination differs by 1°). The BZ sections have steeper inclinations than the QM/M sections. All of the Zazur Formation sections, especially BZ, have steeper pole latitudes than those of the Shabirinah/Brak Formations.

VGP poles of the six sections were compared with Miocene-Pliocene palaeopoles of a similar age and location in the form of a VGP map projection (Figure 6.21). The palaeopoles of the QM1 and M sections are located near to each other as are the palaeopoles of the BZ-T and BZ-W sections. The poles of the QM2, and in particular BZ-E, are lower in latitude and more easterly compared to the other Zazur Formation sections. Similarly to the Shabirinah/Brak Formations, all the section poles are displaced to the east of the APWP yet the poles of the Zazur Formation sections are 7-8° steeper (inclination) than the Shabirinah/Brak Formations. The poles, except for QM1/M, are also located more to the east than those of the Shabirinah/Brak Formations. The confidence intervals of the palaeopoles of BZ-W, BZ-T, QM1 and M overlap with those of the 0-20Ma intervals of the APWP. The confidence cones of the QM2 section overlaps with the 30Ma interval however BZ-E does not overlap with any of the APWAP cones, possibly caused by the steep inclination of the section which is steeper than the present day value.

A)

Site	Mean Direction Dec/Inc/α_{95} (°)	NTotal	NLines	NPlanes	Reversal Test [γ_o; γ_c]	VGP Pole Lat/Long (°) (Dp/Dm) Palaeolat
Qarat al Mrar 1 (QM1)	359.7/46.3/3.6	49	26	12	Ra [2.9; 12.56]	89.5/227 (2.96/4.61) 27.62
Qarat al Mrar 2 (QM2)	6.4/46.2/3.7	48	5	26	Ra [3.2; 8.2]	84.3/105 (3.03/4.74) 27.54
Al Wafa (M)	358.7/46.3/3.8	68	15	33	Rb [6.56; 8.15]	88.8/262 (3.12/4.87) 27.62

B)

Site	Mean Direction Dec/Inc/ α_{95} ($^{\circ}$)	NTotal	NLines	NPlanes	Reversal Test [γ_0 ; γ_c]	VGP Pole Lat/Long ($^{\circ}$) (Dp/Dm) Palaeolat
Bir al Zallaf- East Hill (BZ- E)	9.6/51.1/4.6	53	7	26	Rb [8.52; 9.71]	80.7/71 (4.12/6.09) 31.78
Bir al Zallaf- West Hill (BZ-W)	3.2/50.7/4.0	56	7	28	Rb [5.77; 14.15]	85.9/58.2 (4.80/7.27) 29.91
Bir al Zallaf- Twin Hill (BZ-T)	359.4/49.2/5.4	48	7	18	Ra [2.15; 12.76]	86.4/65.1 (4.63/7.07) 29.21

Table 6.7 Directional means, reversal tests and virtual geomagnetic poles of the sections from the ZF. Note: α_{95} is the Fisher 95% cone of confidence, Ntotal= total number of specimens measured, Nlines= number specimens with s-class line fit used in the mean Fisher calculation, Nplanes= number of specimens with t-class (great circle fit) and used in the mean Fisher calculation, Ra and Rb indicate a pass of the reversal test with an observed gamma of <5 and <10 respectively, R- is a failed reversal test, γ_0 is the observed gamma, γ_c is the critical gamma. Dp/Dm is the semi-axes of the ellipse of confidence about the palaeomagnetic pole.

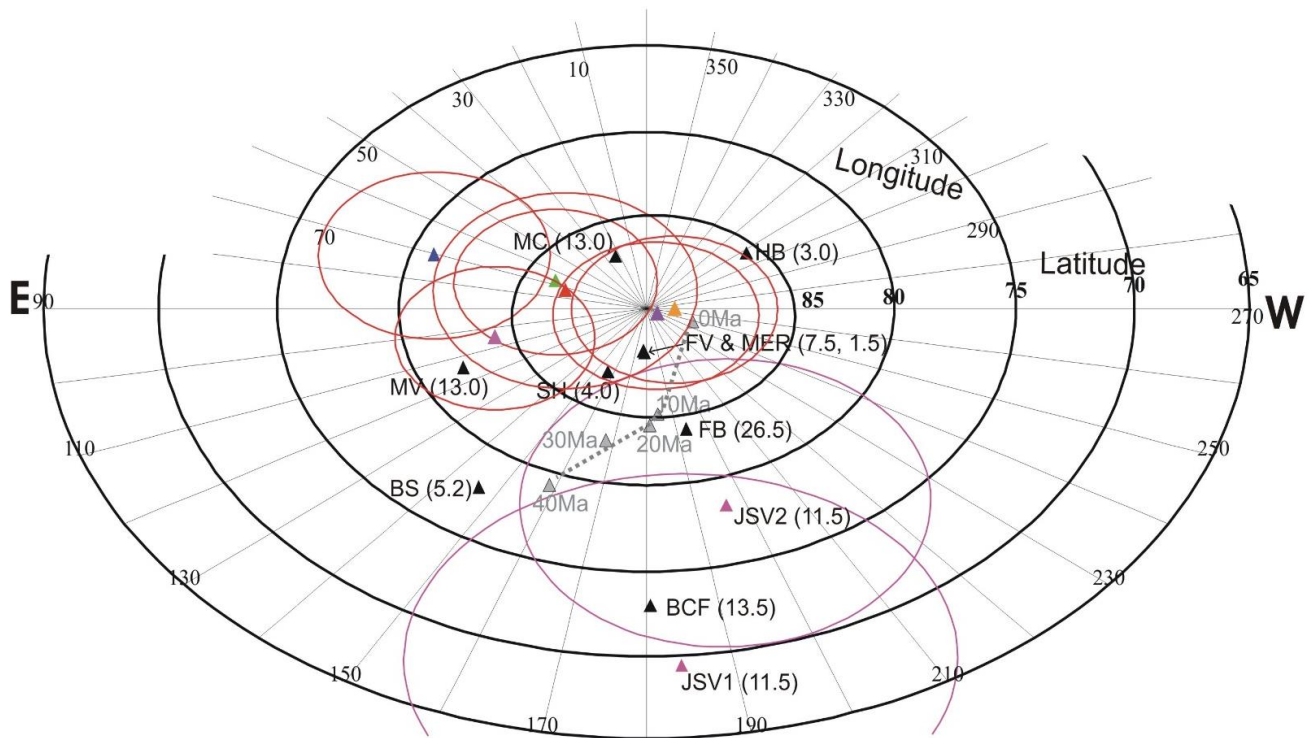


Figure 6.21 Miocene to recent North African palaeopoles, with 95% confidence cones shown for the Zazur Fm. Blue triangle-Bir al Zallaf-East, red triangle-Bir al Zallaf-Twin, Green triangle-Bir al Zallaf-West, Purple triangle-Qarat al Marar1, Orange triangle-Al Wafa, Pink triangle-Qarat al Marar2. Pink triangles (with purple confidence cones) from Jebel as Sawda (JSV1/2). Black triangles are poles (age in Ma), listed in Torsvik et al (2012). FV=Famara Volcanics, Canary Islands (CI); BS= Basalt Series II, CI; MV= Miocene Volcanics, CI; MC=Basalt Series I, CI; MERr= Main Ethiopian Rift Basalts; HB= Hadar Basin, Ethiopia; SH= South Holhol-Djibouti; BCF= Blue Clay Fm, Malta; FB=Flood Basalts, Ethiopia. Grey triangles is the Gondwana apparent polar wander path (APWP) from Torsvik et al (2012; Table 7), labelled in 10Ma increments.

6.2.4 Magnetostratigraphic Age Model

As previously described in section 5.2.4, the VGP latitude was calculated for each of the specimens from the QM1/2, M and BZ sections (Figure 6.20 i-vi D). All horizons had 2-3 specimens measured to help determine the horizon polarity, except for two horizons in the M section where the polarity was able to be determined from just one specimen (both t-class). None of the horizons had specimens of opposing polarity. For the QM1/2 and M sections, 12% of specimens failed to yield reliable data which could be used to determine the horizon polarity and 22% from the three BZ sections ('?' Figure 6.20 i-vi C). Unlike the sections of the Shabirinah/Brak Formations, four horizons (BZ90, M27, NUS8-11 and QM21) failed to yield specimens which could be reliably used to determine magnetic polarity. For BZ90 no clear polarity could be determined, whereas for M27/NUS8-11, it appears the sample had not fully demagnetised (AF not effective). The influence of lightning strikes led to the '?' pol assigned to QM21.

Section correlations and composite development

The three BZ sections, which are similar lithologically, can be correlated to one another using the base of the normal polarity unit which overlies a large reverse polarity unit of the Sifar Member in all the sections (see Figure 6.22). When trying to correlate the QM1/2 and M sections, the M section is of particular importance as it can be correlated to both of the QM sections. The QM2 and M section are correlated using the base of the distinctive, large reverse polarity unit of the Sifar Member identified in both sections. It is thought the QM1 section is the youngest in the Zazur Formation as it sits on basement. The lower part of the QM1 section correlates to the upper part of the M section based on observations in the field including reed casts seen in the QM1 section and a section close to the M site. There is some uncertainty however in exactly how to correlate these two sections. As a result, two composite options were derived. The first option (composite-A) relates the lowest normal polarity unit of the QM1 section to the upper-most normal polarity unit in the M section. The second option (composite-B) correlates the two normal polarity units of QM1 to the two upper normal polarity units of M (from ~8.4 m) as seen in Figures 6.22/6.23. It is only in composite-B that both QM sections correlate to one another. Although 200 km apart it is thought, due to the remarkably similar stratigraphy observed in the field (Drake et al., 2011), that the BZ and QM sections may link. In particular, it was hoped that the additional BZ samples collected in 2011 would allow firmer tie points to be established between the sections. The BZ sections can be correlated to the QM/M sections

based on the polarity stratigraphy of the BZ-T and BZ-E sections. In both composite options the normal polarity unit near the base of BZ-T is correlated to the normal polarity unit at the base of the Sifar Member in QM2. Differences occur however in how the BZ-E links to M/QM1 depending on the composite option (i.e. the position of QM1). In composite-A, the Bir al Zallaf Member of BZ-E is correlated to the polarity units covering both the Sifar and Bir al Zallaf Member in QM1 with the uppermost normal unit of BZ-E linked to the uppermost normal unit in QM1. In composite-B, the Bir al Zallaf Member of BZ-E only correlates to the Bir al Zallaf Member of QM1. The uppermost normal polarity unit of BZ-E is correlated to the equivalent normal unit in both the QM1 and M sections. Differences also occur in the correlations between M and BZ-E depending on the composite option (Figures 6.22/6.23).

Sixteen magnetozones were assigned to composite-A and B. The positional differences in the composites means that although there is one main magnetozones less in composite-B, an additional reverse (Za4n.1r) and normal (Za4n.2n) sub-magnetozones is present in this composite. Within both composites, sub-magnetozones Za4/5r.an and Za4/5r.ar (magnetozones number dependent on the composite) are only observed in the BZ-E section. As for the sections of the Shabirinah/Brak Formations, composites were produced using the numerical optimisation technique of Hounslow (Submitted). The polarity boundary heights were scaled to the metre scale of the BZ-E section whose data remained unscaled. For all other sections a scale change and a shift took place. As QM1 sits in basement it was thought the section may be condensed and so a stretch was also applied to QM1 in composite-B while no stretch was applied in composite-A. The overall height of composite-B is therefore ~5m greater than composite-A. A constant sedimentation rate is assumed for sections BZ-E/W, M and QM1 and so a linear rate function was applied to these sections (Hounslow, Submitted). When this rate function was also applied to BZ-T and QM2 poor model fits were produced as the sedimentation rate in these sections is variable, for example a higher sedimentation rate occurs in the palaeodune part of the QM2 section (see Figure 3.16 in section 3.2 and Figure 6.22). To help improve the model fit, a transgressive rate function was applied to both of these sections which simulates a smoothly increasing sedimentation rate upwards through the section (Hounslow, Submitted).

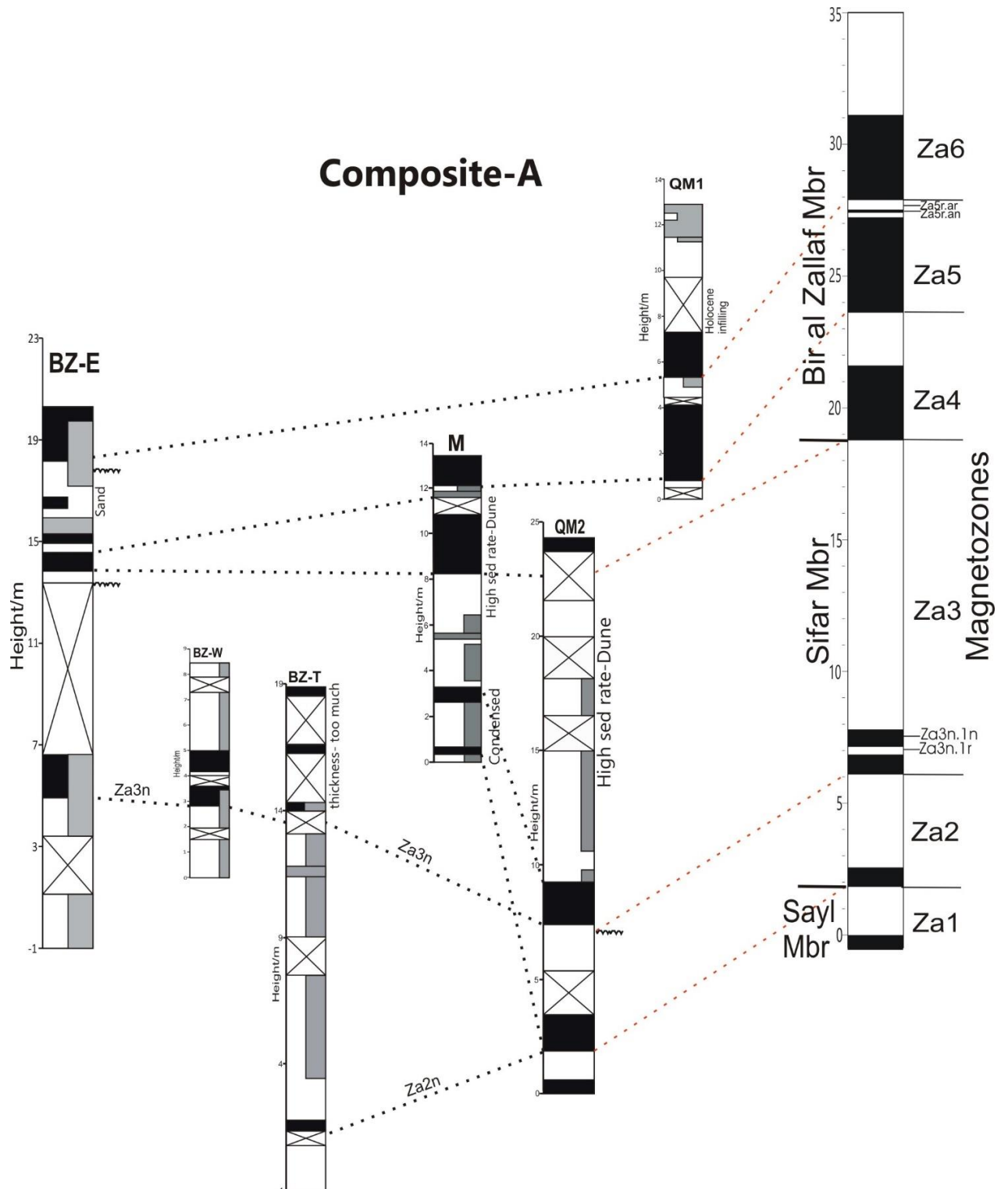


Figure 6.22. Palaeomagnetic correlations and composite-A option of the ZF sections as discussed in the text. Scale of the composite is in the metre scale of the BZ-E section. ZA codes relate to the assigned magnetozones of the composite. Note: black = normal polarity, white = reversed, grey = uncertain. For additional illustrative information please see refer back to the key in Figure 5.19.

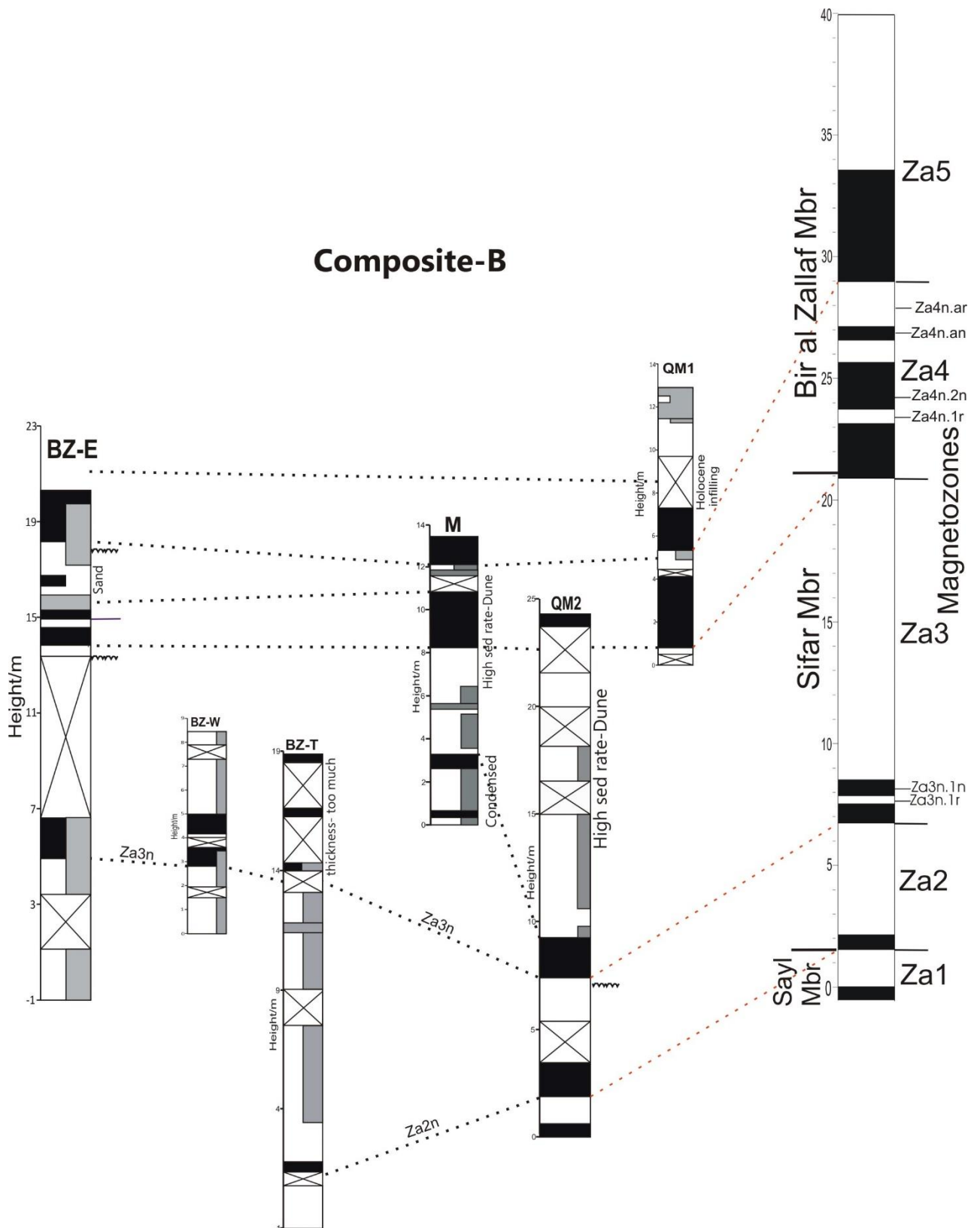


Figure 6.23 Palaeomagnetic correlations and composite-B option of the ZF sections as discussed in the text. Scale of the composite is in the metre scale of the BZ-E section. ZA codes relate to the assigned magnetozones of the composite. Note: black = normal polarity, white = reversed, grey = uncertain. For additional illustrative information please see refer back to the key in Figure 5.19.

Confirming the Palaeomagnetic Age

Sequence slotting was again employed to aid in assigning a palaeomagnetic age to the Zazur Formation composite. Both composites were run in sequence slotting using four different weighting options (see Table 13-Appendix, pg310) for each of the variables in order to see how each impacted on the model output. The best fit models generally had good Δ values but were overall quite poor with weak matrix coefficient values, especially for three (option 1, 3 & 4) of the weighting options. An advantage of sequence slotting is that it can deal with missing magnetozones, equally it can also miss out magnetozones if they do not fit well to the GPTS. It was thought that the Za4/5r.an and Za4/5r.ar magnetozones identified in the BZ-E section were confusing the sequence slotting program. Both of these magnetozones were identified in only one section from a single horizon with the specimens assigned some level of uncertainty ('?'). To see if better models were produced, the composites were run without these magnetozones.

After re-running the composites, better fit slotting solutions were produced and so it was decided that analysis should continue using data with the magnetozones removed. From the solutions, three possible models were identified. A Messinian-Zanclean model and a Tortonian-Messinian model were identified in both composites while a Tortonian model was identified in composite-A alone. The Messinian-Zanclean models were overall the best fit solutions for both composite options, often with smaller Δ values and larger matrix coefficients. Based on the statistics it was therefore decided that the Messinian-Zanclean model with option 2 weightings was the best option for both composites. This option gives a higher impact to the duration and polarity bias variables as in the preferred solution of the Shabirinah/Brak Formations.

Testing the composites places the base of both composite polarities in the very upper Tortonian (Za1r=C3Br.2r, Figure 6.24). The upper part of the composites however differ. The upper part of composite-A is placed in the Zanclean with the section top (Za6n) matched to chron C3n.2n (Nunivak) (Figure 6.25). The section top (Za5n) of composite-B is placed at the Zanclean-Piacenzian boundary to chron C2An.3n, the Gauss Chron. Composite-B therefore covers an additional 1Ma of time (Figure 22-Appendix, pg312). Although composite-B covers a time period of 3.86Ma, sequence slotting skips six chrons from the GPTS in comparison to two from composite-A. In both composites chrons C3Bn and C3Br.1r are skipped. Based on the fact that less chrons are skipped in composite-A and thus it has a higher association probability and that this composite has larger matrix

coefficient values than composite-B, the Messinian-Zanclean model using composite-A is the preferred and final solution.

Overall the composite of the Zazur Formation ranges in age from 7.454-4.493Ma. Carbonate-rich units are identified from the BZ-E and QM1 sections. All of these units are found in the early-Zanclean, more specifically the L2 unit of the BZ-E section from ~5.235-4.997Ma and the L1 unit from ~4.883-4.631Ma which also occurs at the same time as the carbonate unit of the QM1 section which is separated by Holocene infilling. An additional carbonate unit interbedded by a small siltstone unit is found in the QM1 section occurring between the L1/L2 units dating to ~4.896-4.779Ma. The sections underwent relatively detailed sampling in the field yet two chrons (C3Br.1r and C3Bn) were skipped by the slotting model. The missing chrons occur near to the composite base (above Za2n) and hence should be seen in the QM2 and BZ-T sections. There is a sampling gap of 2.38 m in the lower QM2 section above Za2n magnetozone. This gap may have missed the C3Br.1r chron which has a relatively short duration of 39kyrs however it is unlikely it has missed the longer duration (72kyrs) chron of C3Bn. The lower QM2 section also correlates to the BZ-T section which has good sample coverage in the lower part yet the chrons are still not recorded. The accumulation rates of the QM2/BZ-T sections are variable with slower rates near the base of the sections and so may not have captured these skipped chrons. As the chrons are not recorded in either of the sections which are over 200km apart it suggests there may have been a regional hiatus near the base of the Sifar Member or their relatively short duration meant that they just were not captured by the sections.

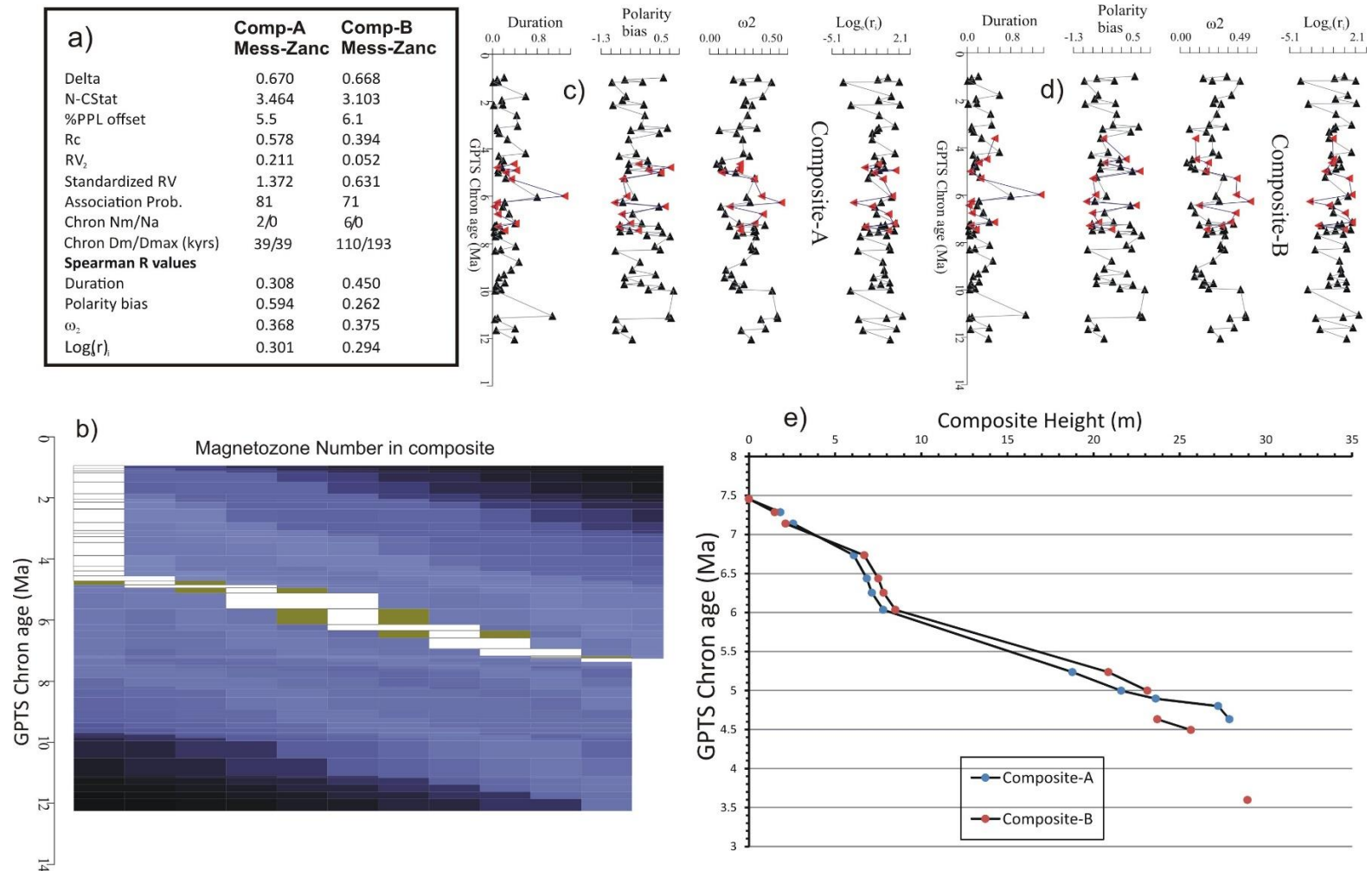


Figure 6.24 Sequence slotting model output for composites-A/B showing data for each Messinian-Zanclean correlation model. a) The statistical summary of the correlation models. b) The H-matrix, plot of Composite-A, where the brighter blue bands correspond to alternative correlation models. The Composite-A model is shown as the white boxes across the plot, with y-axis height corresponding to GPTS chron duration. The x-axis on this plot is the magnetozone number. c) and d) The input data to the slotting model, plotted against chron age for the two correlation options. e) Depth-age models for the two polarity composites A and B. The age-depth relationships for the two age models are similar for composite A and B apart from the upper part of the composite with sequence slotting placing the start of composite-B at ~1Ma younger than composite-A.

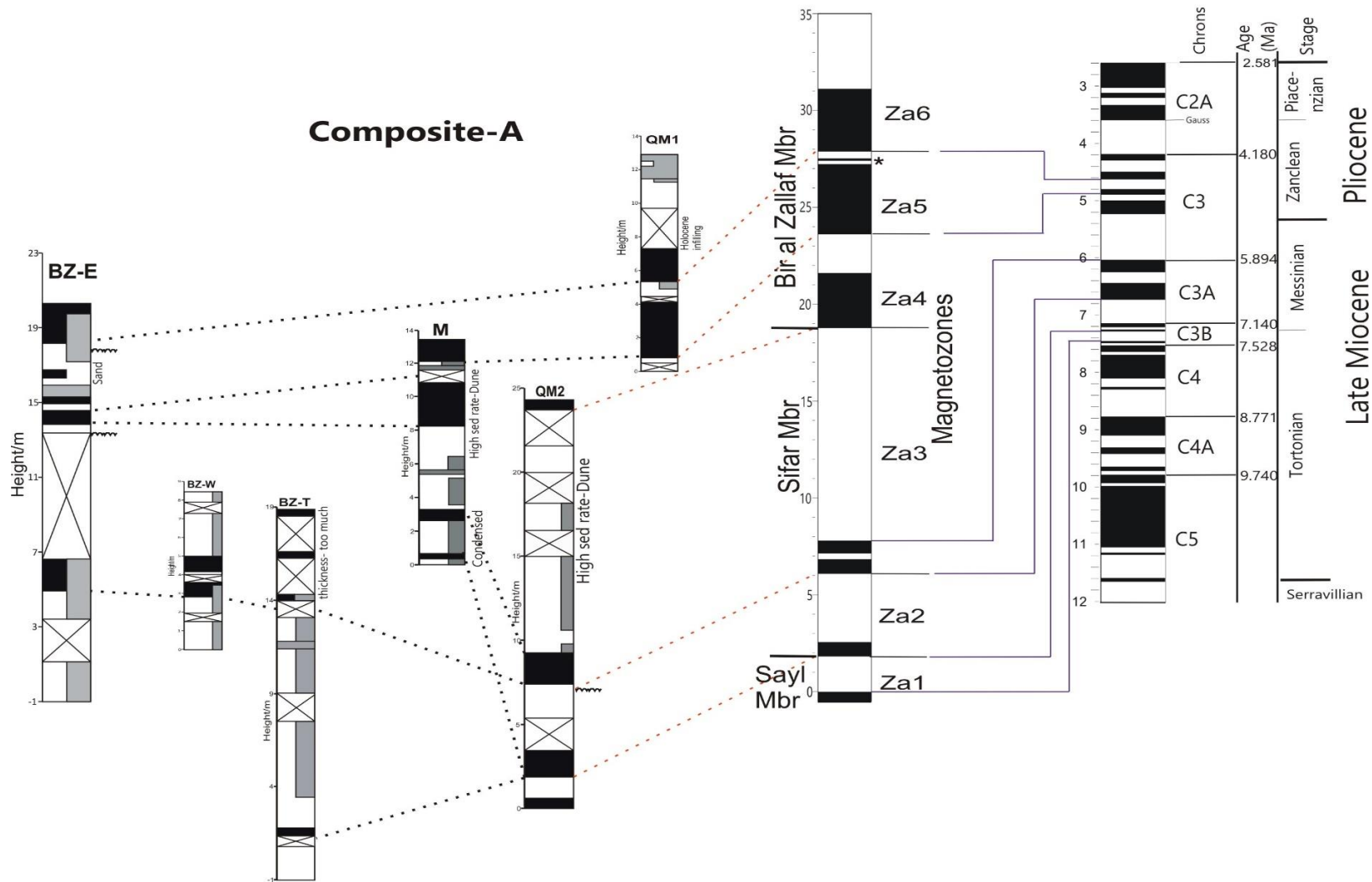


Figure 6.25 Composite-A (Messinian-Zanclean model) magnetic polarity stratigraphy with the final age model on the right. Chron correlation lines (purple) to the GPTS (Ogg, 2012) derived from sequence slotting. Note the * next to the composite represents the magnetozones (Za5r.an/Za5r.ar) not included in the sequence slotting model. Note: black = normal polarity, white = reversed, grey = uncertain. For additional illustrative information please see refer back to the key in Figure 5.19.

7 Discussion: Palaeoenvironment of the Fazzan

7.1 Interpretation of the Early Miocene (Aquitanian-Burdigalian) deposits

Based on the petrographic and geochemical data provided in section 5 the depositional environment of the formations and their associated members are proposed.

7.1.1 Shabirinah Formation (Lower Ariel section)

When interpreting the deposits of the basin it is crucial to consider not only the TS and geochemical data but also additional supporting evidence provided in the hand specimens and the section logs (refer back to section 5.1.1). The lower 25.7 m of the AP section spans ~5.8 Ma from 22.564-16.721 Ma. It contains a number of key features, in particular extensive rootletting as noted in the field log and hand samples, which suggest the deposits are palaeosols. Mottling is also ubiquitous with root traces which in modern soils results from alternating oxidising/reducing conditions due to varying degrees of soil saturation (Kraus and Aslan, 1993). The log indicates mottling to be more extensive near the base of the section while rootletting is less so. In palaeosols where rootletting is less extensive, these deposits could be classed as ‘simple palaeosols’ (Kraus and Aslan, 1993; Demko et al., 2004). Palaeosols of this nature are weakly developed and indicative of rapid deposition thus allowing little time for pedogenesis (Kraus and Aslan, 1993). This is reflected in the thin sections with many of these deposits primarily clast supported with high porosity. In the overlying deposits, rootletting is more extensive and pedogenesis better defined, as seen in Figure 7.1 below, leading to the deposits to be classed as ‘cumulative palaeosols’ (Kraus, 1999; Demko et al., 2004).



Figure 7.1 Extensive rootletting in the lower Ariel section.

These mature soils form in 'steady' environments where sediment accumulation is slow and more episodic and erosion insignificant allowing enhanced pedogenic development (Krauss, 1999; Demko et al., 2004). As in the simple palaeosols, more mature palaeosol development is reflected in TS with the increase in pore-filling cements. Kraus and Aslan (1993) note that the differences between simple and cumulative palaeosols reflects differences in deposition of their parent materials with the lower parts of many cumulative palaeosols resulting from previous development of simple palaeosols. Calcareous nodules are also present in the palaeosols often which are reflective of moderate drainage conditions (Kraus and Aslan, 1993).

Within many of the TS blackened, isotropic areas occur that are presumed to be organic. Soil forming processes, especially burial, can lead to the occurrence of dark layers (Youcef and Hamdi-Assa, 2014). Black layers which are the result of organic matter (OM) deposition often occurs in water-saturated environments and hence could be used as an indicator of a wet phase (Youcef and Hamdi-Assa, 2014). It is important to consider however that black layers can also be indicative of fires which may have occurred when vegetation became desiccated as a consequence of declining groundwater levels (Youcef and Hamdi-Assa, 2014).

The thin sections and XRF show the deposits to be dominated by quartz with Kraus (1999) stating that fluvial systems, in particular channel-margin environments (e.g. levee), are often dominated by this mineral along with feldspar and lithic fragments. Distal floodplains and also lake-margin deposits can be characterised by palaeosols (Demko et al., 2004; Pia-Pueyo et al., 2010). The sporadic presence of coarse clasts in the TS agrees with the idea of a floodplain/levee deposit with these clast sizes deposited during times of higher discharge and overbank flow. In the field, well-exposed channels were documented with channel sandstones occurring near to the top of this part of the Shabirinah Formation thus providing further support of alluvially deposited palaeosols

The relatively high Al content revealed by XRF analysis (see Table 8-appendix, pg300) is also indicative of this sediment type as Al is commonly retained by soils (Aly, 2015). Al in soils is often associated with clay formation which occurs in abundance in soils requiring warm and moist conditions as well as an effective drainage system (Ehrmann et al., 2013). Feldspar is often a major component of many igneous rocks and is susceptible to chemical alteration during weathering (Nichols, 2009, pg15). Plagioclase feldspar, which reacts with water and CO₂, produces minerals stable at low temperatures,

notably clays (Leitch et al., in press). The weathering process occurs in a series of stages converting K-feldspars to illite clay and then kaolin. Kaolin would be expected to plot at 0.00 and illite ~0.33 on the x-axis (K/Al) in Figure 5.3 (pg118). The values of the AP deposits therefore suggest incomplete weathering of illite to kaolin (Leitch et al., in press). The Fazzan contains numerous outcrops of igneous rocks which could be the source of the Al in feldspars. In particular, basement granite is documented by a number of studies such as Busrewil and Oun (1991). At the Gargaf high, Precambrian granite is penetrated by Miocene volcanics (Geyh and Thiedig, 2008). It was clear from the XRF data that deposits high in Al were also high in Nb/Nd. Nb is most abundant in alkaline igneous rocks, alkali mafic and ultramafic rocks and can also be high in alkali granite (Parker and Fleischer, 1968). The presence of these elements and their likely source may suggest some volcanic activity at the time of deposition or weathering of alkali lavas. The positive relationship of Nb and Nd with Ti, Al and Fe are also good indicators of a volcanic source (M. Norry, personal communication). The Jebal al Hasawinah, a predominantly phonolitic and basaltic volcano, was active at the time of deposition of these deposits. The Tibesti to the south was also active (Permenter and Oppenheimer, 2007). It is possible that these elements were derived fluviially or from airfall from these volcanoes. However, no basalt fragments were observed in thin section suggesting weathering and recycling of basement material is the more likely source.

7.1.2 Maharshim-Tmessah Members (Temssah section)

The three lower members of the TM section span a comparable amount of time to the deposits of the lower AP section. Analysis of the oldest member, Maharshim, shows the thin sections largely reflects what is seen in the hand specimens. As suggested by the log (Figure 5.4), the deposits of this member can be classified as marls. Marls can be formed in lakes of variable salinity and depth (Pentecost, 2005,pg 299) but are more typically found along lake margins (Murphy and Wilkinson, 1980). Lacustrine marls exhibit strong compaction and hence the degree of porosity is dependent on this (Flugel, 2010, pg 313; Pentecost, 2005,pg299). They are characterised by their primary fenestral porosity (Pentecost, 2005,pg299) as seen in the deposits here. Fenestral porosity can be formed in a number of ways either via wetting/drying of carbonate mud or degassing of decaying organic matter connected to compaction of gas bubbles (Flugel, 2010, pg 192). Pedogenic features, such as reddened glaebules and circumgranular cracks are seen

throughout the member, especially in the upper deposits. Glaebules, concretionary soil structures, are formed during pedogenesis due to concentration of soluble soil material (Platt, 1989; Klappa, 1980). Reddened glaebules most commonly contain haematite and are often found in seasonally waterlogged soils (Singh and Gilkes, 1996). Circumgranular cracks result from alternate shrinkage and expansion processes during emergent periods (Flügel, 2010, pg726). It is therefore likely the marls were deposited along the lake shoreline in a palustrine setting. The majority of quartz clasts in the deposits are rounded and thus have a likely aeolian origin, with the degree of rounding dependent on the distance travelled (Friedman, 1961).

The isotopic values also support a marginal lacustrine environment. It is assumed that carbonates are precipitated under isotopic equilibrium, implying the isotopic composition of the mineral precipitated is related to the composition of the water in which it formed (Marshall, 1992; Leng and Marshall, 2004). The three uppermost deposits of this member are isotopically similar yet the base deposit differs in its value of $\delta^{18}\text{O}/\delta^{13}\text{C}$ (Figure 5.6, pg133). Lithologically there is very little difference between the deposits and hence this cannot explain the change. The base deposit is more depleted and thus suggests wetter conditions i.e. increased lake level. Spar is also present in this deposit formed in pores which are saturated for longer periods with pore waters. The more enriched $\delta^{13}\text{C}$ value of the base deposit is likely due to photosynthesis of aquatic plants in the lake which selectively remove lighter ^{12}C thus causing enrichment. Pedogenic features are more common in the upper deposits suggesting reduced lake level, reflected in the extreme enrichment of the $\delta^{18}\text{O}$ values. In comparison the $\delta^{13}\text{C}$ undergoes a decrease, more than likely due to the increased presence of soil water which allows isotopically light CO_2 to be released during decay of terrestrial OM (Leng and Marshall, 2004). Lezine et al. (1990) attributed the decrease in $\delta^{13}\text{C}$ in the Chemchane Sebkhah, Mauritania, to this cause when a drop in lake level in the Pleistocene led to increased swamp vegetation. Poor covariance in the member also indicates the lake was hydrologically open i.e. allowing continuous through-flow of water (Talbot, 1990; Leng and Marshall, 2004).

In spite of having the form of stromatolites in the field (e.g. calcareous mounds and thick layering-see Figure 7.2), the carbonate units of the Stromatolite Member do not have the characteristic microfabric, in particular planar laminations, typical of these deposits in thin section. There are however other forms of microbialite defined by their non-laminated structure (Flügel et al., 2010, pg172). It is often difficult to categorise these deposits as

many microbial carbonates can be dominated by uniform micritic fabrics which can mask a range of possible origins (Riding, 2000). Many of the components of microbialites often form at the scale of the microbes themselves and hence complicates things further (Riding, 2000). The deposits of this member have characteristics similar to those of thrombolites, including clotted and/or peloidal micritic microfabric and fenestrations (Konishi et al., 2001; Riding, 2000). Riding (2000) notes that clotted microfabrics can be syndepositionally produced or diagenetically enhanced/created. Further evidence that these deposits are more likely to be thrombolites comes from the bioclast debris within the deposits. Stromatolites are thought to form in undisturbed and high salinity environments which excludes grazing/burrowing animals (Konishi et al., 2001; Brook et al., 2011). Thrombolites in comparison develop in less extreme saline conditions allowing the presence of fauna (Konishi et al., 2001). Fauna, including ostracods, have been found for example in cores of thrombolites from Lake Clifton, Australia (Konishi et al., 2001). It is therefore thought the deposits of this member are in fact thrombolites rather than stromatolites.

The isotope values of the deposits, in particular the carbonate, also group distinctively (refer back to Figure 5.5, pg127) when plotted and hence suggest a different origin of the carbonate. Microbial carbonate is biologically stimulated with grain trapping especially important but favourable saturation states in ambient waters are also required and rely on a combination of biotic and abiotic factors (Riding, 2000). Many isotopic studies of microbialites typically have enriched $\delta^{18}\text{O}/\delta^{13}\text{C}$, for example the stromatolites of the Etosha Pan, Namibia, have average $\delta^{18}\text{O}/\delta^{13}\text{C}$ of +4.7 and +2.1‰ respectively. The isotope values here, along with the Maharshim Member deposits, although the most enriched in $\delta^{18}\text{O}$ out of the Shabirinah Formation deposits, are depleted. Microbialites develop in shallow lacustrine environments and are often affected by evaporation causing enrichment. The depleted $\delta^{18}\text{O}$ values however indicate evaporation has had limited impact on the deposits. The low r^2 value suggests the lake was hydrologically open. Li and Ku. (1997) state that if the volume of a lake remains stable (as demonstrated by the small variation in $\delta^{18}\text{O}$ throughout the member) or undergoes small changes with few perturbations in productivity, $\delta^{13}\text{C}$ and $\delta^{18}\text{O}$ will show poor covariance resulting from effects of vapour exchange with the atmosphere. Therefore it is likely that the carbonates were precipitated in a lake with a stable lake volume experiencing slight fluctuations in the inflow composition of the water and/or vapour exchange with the atmosphere. Arenas et al. (1997) report similar $\delta^{18}\text{O}$ values of

stromatolites of Miocene age from the Ebro Basin, Spain which at times experienced increased fluvial inflow. Solari et al. (2010) states that the $\delta^{13}\text{C}$ signal in carbonates can be an effective tool to distinguish between inorganic and biologically induced precipitation with negative values characteristic of inorganic precipitation. The negative $\delta^{13}\text{C}$ of the deposits thus suggests additional input into the lake likely from isotopically light soil water and/or shallow groundwater (Leng and Marshall, 2004).



Figure 7.2 Stromatolite bed showing where deposit TM3 was sampled.

From the thin section and hand specimens (see Table 5.3, pg123) it is clear that the deposits of the Tmessah Member have been deposited under two differing depositional environments, fluvial and lacustrine/palustrine. The coarse-granule sized, clast-rich lower deposits (TM12-16) imply fluvial deposition. It was also noted in the field that the underlying mudstones of the Stromatolite Member were considerably thinner than those located to the south and west likely caused by channel erosion thus supporting the idea of a fluvial environment. Sands of fluvial deposits tend to be poorly sorted and angular (Bui et al., 1989), characteristics however which are opposite to those seen in TS. This may suggest the clasts have been transported over long distances and are the product of downstream fining or reflect the polycyclic origin of the clasts. Aeolian clasts in comparison are more rounded, moderately-to-well sorted and typically range in size from fine to coarse sand (Bui et al., 1989; McLaren, 2007). These characteristics are more

similar to those of the TM deposits possibly suggesting the channel may have cut through aeolian deposits adjacent to the channel leading to clast entrainment and deposition under fluvial conditions.

All of the pores in these deposits are occluded by large sparry pore-filling cements. Pore-filling cements are found in both the vadose and phreatic zone but are more common and characteristic of the meteoric vadose zone (McLaren; Gardner and McLaren, 1993). Porosity falls overtime with carbonate diagenesis with occluded pores therefore indicating the deposits have undergone extensive diagenesis reaching the ‘end point’ of typical diagenetic (vadose) models as shown in Figure 7.3 (McLaren and Gardner , 2004). McLaren et al. (2012) notes that the length of the wetting phase affects the rate of carbonate cement precipitation and crystal size. In wet conditions where water can remain in pores for long periods of time, coarser spar crystals develop (McLaren and Gardner, 2004; McLaren, 2007), as seen in the described deposits. Wet conditions can result from climatic influences but cemented deposits can also be found in zones of accelerated diagenesis such as near to a palaeosurface (McLaren and Gardner, 2004). The carbonate could come from a variety of sources including dissolution of bedrock and breakdown of lithoclasts (McLaren, 2007). It is therefore thought that these deposits were deposited in an incised channel with cementation taking place in the vadose zone

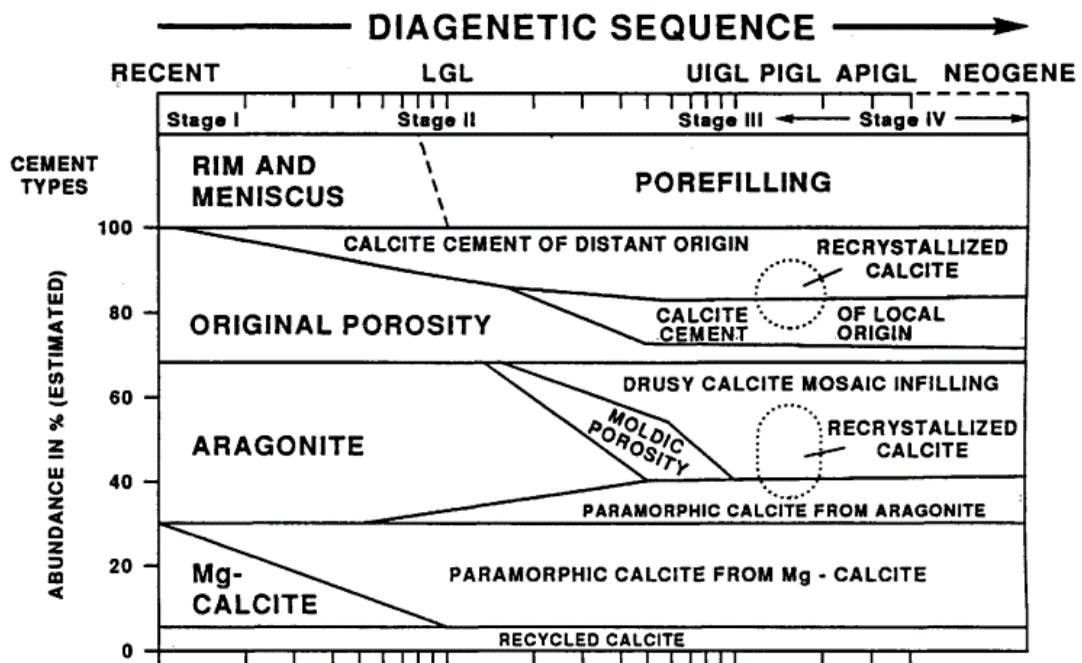


Figure 7.3. The model of progressive vadose diagenesis included cement types from Gardner and McLaren (1993).

The overlying deposits (TM18-24) in thin section, and especially in hand specimen/on the log (refer back to pg123/124), show signs of pedogenic modification. Pedogenic activity is identified as the samples are mottled, in particular with red mottles, locally argillaceous and contain rootlets and also rhizoliths (Klappa, 1980; Kraus and Aslan, 1993; Freytet and Verrecchia, 2002). Klappa (1980) identifies five types of rhizoliths. Based on the descriptions of Klappa (1980) the rhizoliths can be classed as root tubules; cemented cylinders (usually low-Mg calcite) around root moulds (Klappa, 1980). The deposits also contain carbonate. Anisopachous rim cements are clearly seen coating quartz clasts. Rim cements are generally considered to be abundant in the vadose zone with all models of vadose diagenesis agreeing that rim cements are the earliest cement types formed and are derived from an external source (McLaren, 1993; Gardner and McLaren, 1993). Secondary pore-filling cements also occur with some poorly developed. The patchy development indicates pore waters were not always present allowing full occlusion of the pores (McLaren and Gardner, 2004). This may be due to fluctuations in the water table which would also explain the presence of pedogenic features formed during lowstands allowing exposure of the deposits to subaerial conditions. These deposits may therefore be considered palustrine in origin or possibly river bank deposits experiencing increased saturation during times of high discharge and overbank flow.

The Tmessah Member in total covers ~4.6 Ma of time in the early Miocene. Despite this long time-frame, very little isotopic variation occurs in the $\delta^{18}\text{O}$ values of the deposits deposited under fluvial conditions (TM12-16). This stability suggests the drainage and precipitation feeding the river was balanced (Tucker and Wright, 1990), for example by evaporation and temperature. The $\delta^{13}\text{C}$ values on the other hand show slight enrichment of the basal and upper fluvial deposits compared to the two middle deposits. The variations are reflected in the lithology with rootlets present in the more depleted samples (see back to Figure 5.4). CO_2 production in the soils is thus likely responsible for the more isotopically depleted values. This reasoning can also be applied to the $\delta^{13}\text{C}$ values of the overlying palustrine deposits which are rootleted and show signs of pedogenesis throughout. The deposits of the palustrine deposits show poor covariance suggesting a hydrologically open system, yet the $\delta^{18}\text{O}$ values of these deposits vary. The depleted values in the basal palustrine samples are affected by increased fluvial input as noted by the channel structures in the section log. This input into the lake would have led to increased water levels and diluted surface waters (Lamb et al., 2007). The more enriched values are reflections of fluctuating and overall reduced lake levels which increases the

surface/volume ratio thus allowing evaporation to have more of an effect (Hoelzmann et al., 2001).

7.2 Interpretation of the Middle Miocene (Langhian-Serravallian) Deposits

7.2.1 Kunayr Member (Upper Tmessah/Ariel sections)

Both the upper parts of the TM and AP sections are assigned to the Kunayr Member. The member in both sections is comparable in age (TM 16.543-13.739 Ma, AP 16.721-14.07 Ma) but the TM section extends an additional ~300 ka. Petrographic evidence indicates deposits of the member from the TM section to be lacustrine in origin, however it is clear that fluctuations in the lake level have occurred. The deposits, especially in the lower half of the member, lack evidence of pedogenesis and are primarily micritic/microsparitic in texture, key features of lacustrine deposits (Freytet and Verrecchia, 2002; Verrecchia, 2007). The small crystal size suggests rapid precipitation which can be produced under strong evaporation and perhaps corresponding rapid loss of CO₂ thus indicating the cement was precipitated in a relatively shallow body of water (Watts, 1980; McLaren and Gardner, 2004). Interrupting this lacustrine phase are the texturally different deposits of TM71-72. These deposits contain fractured muddy intraclasts thought to represent a lowstand and desiccation. The presence of calcareous nodules and rootlets noted on the log support the idea of a fall in lake level allowing pedogenesis to take effect (Kraus and Aslan, 1993).

A return to lacustrine conditions follows this interruption, characterised by the predominantly micritic texture with additional lacustrine features present such as peloids (Freytet and Verrecchia, 2002). A change in texture again occurs in the upper limestones (from TM61, see Figure 5.4) with the crystal size of the cement increasing. The longer the time involved in diagenesis favours larger crystal growth suggestive of more stable conditions (Flügel, 2010, pg 95). Stability is also needed for pedogenesis to take effect (Kraus and Aslan, 1993) as noted in the section log. Fracture porosity is evident, likely caused by rootlet fracturing which may have happened at the time of deposition or post-depositionally. These features are indicative of a fall in water level and a change to a more swamp/marsh environment.

The clastic deposits of the upper part of the Kunayr Member in the AP section display characteristics similar to those observed in the underlying palaeosols, especially in hand specimen and on the section log. These include rootletting, mottling, bioturbation and reddening. The carbonate unit from the AP section can however also be described as a

lacustrine carbonate sharing similarities to the lacustrine deposits of the TM section. The deposits are also composed predominantly of micritic/microspar cements with rim cements present, characteristic of a meteoric vadose setting (McLaren, 1993). The carbonates are however more clast-rich (refer back to Figure 5.2). This suggests that carbonates of the AP section were precipitated closer to the lake margin and thus the TM section nearer to the basin centre. The quartz clasts within the AP carbonates are most likely aeolian in origin (based on their degree of rounding, size and sorting which would have been blown into the lake) (Bui et al., 1989). In regards to the source of the carbonate in both sections a number of options could be considered. Carbonates associated with lacustrine environments depend on the water chemistry along with the lake climate and geomorphological setting (Verrecchia, 2007). The carbonate could be derived from allogenic sources such as surface runoff and erosion of the shore (Verrecchia, 2007). It could also be authigenic formed inside the lake in particular during diagenesis and due to emersion/emergence (Verrecchia, 2007). High temperatures and salinities and changes in partial pressure of CO₂ can also cause authigenic precipitation (Tucker and Wright, 1990). A biogenic source cannot be ruled out yet biogenic remains are not observed in the deposits

Extreme changes in isotopic values, especially in $\delta^{18}\text{O}$ (see Table 5, pg296), occur in the deposits of the Kunayr Member in the TM section. The changes typically take place at the boundaries of the units which make up the member and thus reflect lithological changes. The poor r^2 value of the deposits of TM28-72 suggests a hydrologically open lake. Stable lake chemistry is observed in these lower two units due to a balance between inflow and outflow in the lake (Tucker and Wright, 1990, pg165). A slight enrichment in $\delta^{13}\text{C}$ and a large decrease in $\delta^{18}\text{O}$ however occurs at TM71 even though petrographically the deposits are thought to reflect a time of desiccation. The deposits of this member span ~2.8 Ma and hence climatic conditions and sources to the lake will inevitably vary. Rootlets in this unit indicate increased vegetation with plant respiration responsible for the enrichment in $\delta^{13}\text{C}$. Although reflecting a lowstand, the carbonate of TM71-72 may have been precipitated under differing climatic conditions based on the depleted $\delta^{18}\text{O}$. Amount effects are common in open lakes influenced by temperature changes with minima $\delta^{18}\text{O}$ values reflecting a cooler climate (Rozanski and Gonfiantini, 1990). It is thus possible that the deposits were deposited under both a drier and cooler climate. Alternatively the source to the lake could have changed, for example lower water temperature may be due to more influence of groundwater than precipitation.

The lower-middle unit of the TM section (TM29-35) and the carbonate unit of the AP section (AP37-42) were deposited in a closed lake revealed by the excellent covariance between $\delta^{18}\text{O}/\delta^{13}\text{C}$ in both sections. The deposition of these deposits however took place at different times during the early-middle Miocene. The closed lake phase in the TM section occurred ~16.268-15.16 Ma while the lake phase occurred earlier in the AP section at ~16.721-16.303 Ma and was much shorter in duration. Petrographic evidence suggests the TM section was located closer to the basin centre. It would thus be expected that the $\delta^{18}\text{O}$ values would be more depleted, yet the values of the deposits in both sections are comparable suggesting lake depth may not have been a major factor influencing the $\delta^{18}\text{O}$. Closed basins typically have more variable and complex lake chemistry than open lakes and are often more enriched due to the stronger effects of evaporation (Rozanski and Gonfiantini, 1990; Leng et al., 2005). These features are however not observed in the $\delta^{18}\text{O}$ values from either section possibly due to a number of factors including lower water temperatures due to increased (monsoonal) rainfall or rainfall diluting surface waters (Hoelzmann et al., 2001; Lamb et al., 2007). More variable and depleted $\delta^{18}\text{O}$ and $\delta^{13}\text{C}$ values are observed in the three upper units of the TM section reflecting fluctuating lake levels under a palustrine setting. The correlation coefficient for these deposits once again suggests an open lake was present. This return to a hydrologically open system could be caused by flooding events or due to a build-up of sediment in the lake allowing overspill.

7.2.2 Brak and the Brak Formation

The BC section ranges in age from ~14.07 to 12.174 Ma with the Brak Formations specifically dating to ~13.608-12.174 Ma. The deposits of the BC section assigned to the Shabirinah Formation have a predominantly muddy texture and suggests deposition in a low energy environment, most likely a topographic low, where bottom currents are weak (Platt, 1989; Potter et al., 2005, pg75). Clay-sized particles can settle in a range of quiet water basins but are often transported fluvially in suspension (Potter et al., 2005, pg75; Rust and Nanson, 1989). It is clear the deposits have been affected by soil processes, in particular penetration of roots, burrows, mottling and calcareous nodules. These features are typical of palaeosols (Platt, 1989; Potter et al., 2005, pg86), although their development seems relatively poor. The red colour of the deposits results from Fe-oxides being diagenetically altered in well aerated deposits (Rust and Nanson, 1989). This alteration can take place for example due to wetting/drying and also post-depositionally via oxidising pore and groundwaters (Potter et al., 2005,pg70). Well drained alluvial soils are often reddened with goethite the dominant mineral (Potter et al., 2005,pg141), as is indicated from the magnetic data of these deposits. It is therefore likely that the deposits are associated with a palustrine environment (Armenteros and Daley, 1998). Deposits of this nature are also common in distal alluvial deposits such as floodplain depressions (e.g. Freytet, 1973; Platt, 1989). The more carbonate-rich deposit of BC8 suggests increased drying allowing the upward movement of soil water and accumulation of carbonate (Potter et al., 2005,pg141).

Unlike the underlying BC deposits of the Shabirinah Formation, the depositional environment of the transitional and carbonate deposits in the Brak Formation is more difficult to interpret. In the field it was thought the deposits were calcretes based on the brecciation, however the microfabric of the deposits does not show many characteristics of these deposits such as pisoids or micrite coatings as outlined in Table 2-Appendix (pg286). The predominantly micritic/microspar cement of the transitional deposits could indicate rapid precipitation in shallow lacustrine conditions. The upper deposits contain both micrite and secondary spar, suggesting precipitation was at times less rapid and may have occurred in deeper water. Clastic material also decreases in these deposits which could be due to deposition closer to the basin centre i.e. a deeper lake. The numerous cementation and diagenetic phases especially in the upper carbonates make it extremely difficult however to determine the true origin of the deposits. In TS the deposits share many characteristics of both palustrine and lacustrine deposits including peloids, cement coatings

and brecciation (see Table 2-Appendix, pg286). It is thus likely that the deposits have experienced several oscillations in water level resulting in alternating lacustrine and palustrine conditions. Overprinting of lake-marginal carbonates occurs by the exposure of large areas of shallow lake margins during lowstands (Tandon and Andrews, 2001). Large-scale palustrine facies associations can thus include deeper water lacustrine facies, reworked lacustrine carbonates and distal alluvial deposits (Tandon and Andrews, 2001).

The spectrum of fabrics observed in thin section reflect the depositional conditions and later effects of diagenesis and possibly pedogenesis (Platt, 1989). This will thus be mirrored in the isotopic compositions which will be affected by isotopic overprinting. For example, common meteoric diagenetic processes can affect the carbonate and cause the loss of primary signatures and homogenisation of data (Alonso-Zarza et al., 2012). Due to this problem, many isotopic studies of diagenetically altered lacustrine and palustrine deposits are microdrilled to provide a more detailed analysis. Microdrilling was attempted on the carbonates but was unsuccessful due to the highly indurated nature of the samples causing material of the drill-bit to break off and contaminate the sample. Bulk samples were thus analysed meaning fully interpreting the isotopic data is difficult and often speculative.

No isotopic data of palustrine/lacustrine deposits of Miocene age from the Sahara was found in the literature. Miocene-aged palustrine deposits from other areas are however well documented and it is clear that the isotopic values of the Brak Formation are on the whole more depleted in comparison. In the Atacama, de Wet et al. (2015) reports (bulk) more enriched values as does Alonso-Zarza et al. (2012) from the Teruel Graben, NE Spain where $\delta^{18}\text{O}/\delta^{13}\text{C}$ average -6.55 and -4.60‰ respectively. The values reported by Alonso-Zarza et al. (2012) are similar to values reported from other freshwater palustrine limestones (e.g. Arenas et al., 1997). The $\delta^{13}\text{C}$ Brak Formation values are comparable to palustrine values obtained by Huerta and Armenteros (2005) from the Miocene Duero Basin, Spain ranging between -6.77 to -8.84‰. Where clastic input is reduced in the BKF deposits, good covariance indicative of a closed lake is found (refer back to Figure 5.8). Covariance in palustrine deposits is often typical of lakes in a semi-arid climate with long residence times (Huerta and Armenteros, 2005). Evaporation is often a strong control on hydrologically closed lakes resulting in low negative $\delta^{18}\text{O}/\delta^{13}\text{C}$, this however is not observed in the Brak Formation deposits. The $\delta^{18}\text{O}$ of the Brak Formation are more depleted than other Miocene palustrine deposits likely due to depleted meteoric input, increased water depths due to reduced evaporation or due to the presence of neomorphic

spar (see Figure 7.4). Diagenetic alteration will also often tend to drive values towards more negative $\delta^{18}\text{O}$ reflecting increased burial temperatures (Tandon and Andrews, 2001). The isotopic values overall likely reflect a combination of modified palustrine/lacustrine deposits but this cannot be confirmed without further investigation. In general, the extent of modification on the isotopic values depends on a) whether palustrine modification occurs associated with meteoric waters that are similar or different from the lacustrine waters b) on the degree of emergence c) on the degree of calcretisation d) on the isotopic composition of the local vegetation (Tandon and Andrews, 2001).

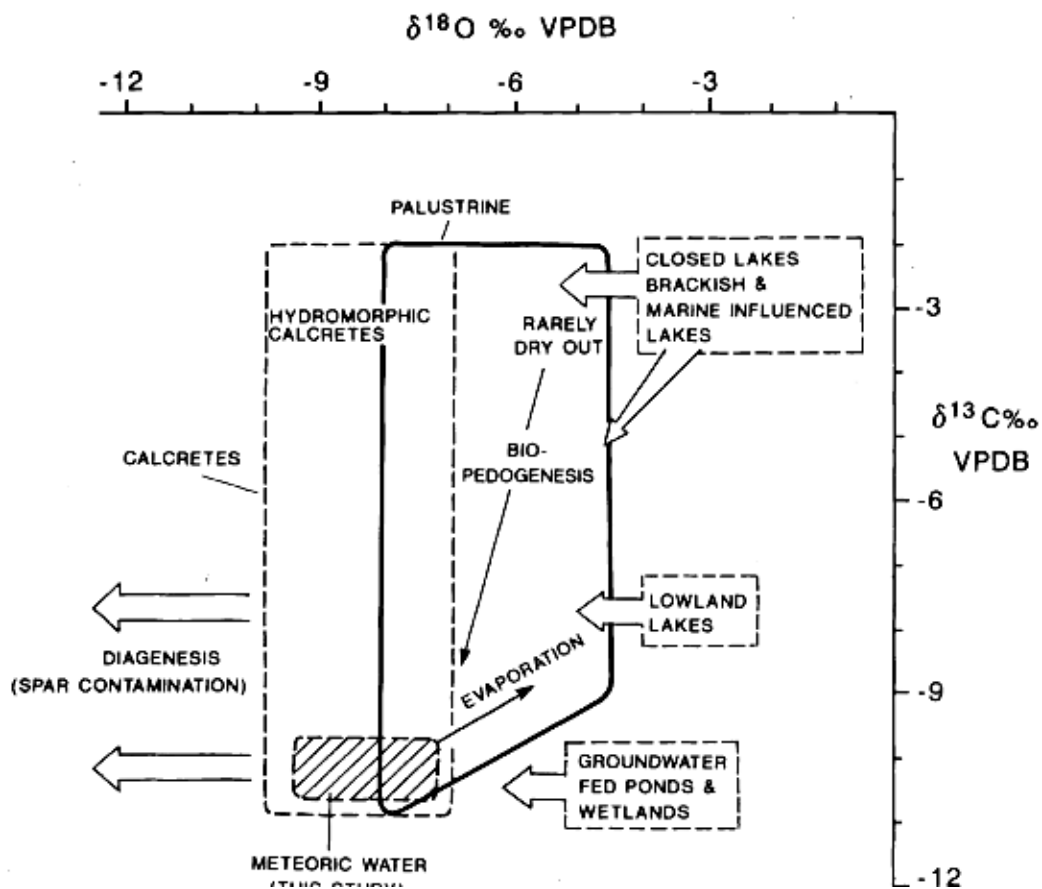


Figure 7.4 Diagram from Tandon and Andrews (2001) to illustrate the possible stable isotope variations in palustrine limestones based on Cretaceous to Tertiary calcitic data from numerous papers.

Comparisons of the Brak Formation to Previous Studies

Unlike the members discussed thus far, the deposits of the Brak Formation have been investigated by previous researchers allowing comparisons to the findings of this study. Peregí et al. (2003) documented the occurrence of the Brak Member in the western foreground of the basalt lava fields of the Al Haruj al Aswad/Abyad, some 2° to the east of the location of the BC section. When investigating the characteristics of the deposits

petrographically similarities between the deposits of Peregi et al. (2003) and those above are found. Peregi et al. (2003), who defines the deposits as lacustrine of Pleistocene age, notes the formation of several carbonate generations often surrounding quartz clasts which appear more prominently in comparison to the deposits of the Brak Formation. Three carbonate generations are noted; the first surrounding grains, the second which appears in the form of irregularly shaped micritic patches and the third which is microspar infilling space between the grains and micrite patches. Similar cementation phases occur in the Brak Formation deposits however the precise generational order cannot be correctly identified due to their complexity. Further analysis using cathodoluminescence would help to confirm the order.

The Brak Member was also interpreted as a freshwater lacustrine deposit by Geyh and Thiedig (2008). Stable isotope analysis was conducted on the Brak deposits, including two brecciated limestone samples from the same quarry where the Brak Formation was sampled. The values documented by Geyh and Thiedig (2008) are in good agreement to those of the Brak Formation with $\delta^{13}\text{C}$ averaging -7.25‰ and $\delta^{18}\text{O}$ -8.30‰ . Facies analysis of Brak deposits were also conducted by Abdullah (2010) who, unlike the previous studies, classes the deposits as calcretes. Four distinct lithological intervals up the member are defined by Abdullah (2010) yet only the upper most interval, described as a massive limestone, show similarities to the BKF deposits. Abdullah (2010) focuses on the macroscale features of these deposits, though some TS descriptions are included. These well-lithified deposits contain quartz clasts of a similar size and roundness to those from the lower Brak Formation: peloids are present as well as a micritic matrix with areas of microspar and pore spaces filled with drusy cements. Features not seen in the Brak Formation are also identified by Abdullah (2010) including pisoids with a clastic grain nucleus and gravitational cements believed to be first generation leading to the classification of a calcrete, specifically groundwater. Sampling of these deposits was from Wadi ash Shati but to the north of the Brak Formation location. It is thus possible Abdullah's (2010) deposits represent a more marginal site (e.g. development of pisoids) compared to the Brak Formation. XRD analysis conducted on the Brak Member by Abdullah (2010) revealed the deposits to contain low-Mg calcite and dolomite which makes up to 20% of the rock. To see if the deposits of the Brak Formation were also dolomitic, staining was conducted (see section 4.1.2). The slides remained unstained suggesting dolomite was not present, however dolomite is only stained purple if it is

ferroan (Zimmerle, 1995,pg44). Different staining methods and further XRD analyses would help confirm if the dolomite is non-ferroan.

7.3 Revised palaeoenvironmental understanding of the Miocene Fazzan Basin

Early Miocene

It is clear from the discussed evidence that humid intervals associated with the Al Mahruqah Group are not only found in the late Quaternary (Shati Formation) but extend into the early Miocene. Many palaeoclimatic studies of the Sahara (e.g. deMenocal et al., 2000; Casteneda et al., 2009) often discuss climatic/environmental changes based on simplistic wet/dry scenarios. It is apparent however from the range of depositional environments experienced in the Fazzan throughout the early (and middle) Miocene, as summarised in Table 7.1, that the climatic/environmental conditions are more complex and spatially variable.

Formation-Member-Section	Age (approx.)/ Ma	Deposit Type and Inferred Depositional Environment
SHF-AP section	22.564-16.721 (Aquitanian – Burdigalian)	Alluvial palaeosols, floodplain or levee setting
SHF-M Mbr-TM	22.564-21.767 (Aquitanian)	Marls, swamp/marsh. Hydrologically open lake
SHF-STR Mbr-TM	21.767-21.159 (Aquitanian)	Thrombolite, shallow lake setting. Hydrologically open lake
SHF-TM Mbr-TM	21.159-16.543 (Aquitanian – Burdigalian)	Two types and environments. Fluvial, incised channel. Palustrine, marginal lake setting. Hydrologically open lake
SHF-K Mbr-TM	16.543-13.739 (Burdigalian – Serravallian)	Lacustrine-palustrine/swamp, marginal lacustrine setting. Overall hydrologically open lake but a period of lake closure in lower-middle unit
SHF-K Mbr-AP	16.721-14.07 (Burdigalian – Langhian)	Two types and environments. Lacustrine limestone, shallow lake setting, hydrologically closed lake. Palaeosols, return to alluvial or palustrine setting
SHF-BC section	14.07-13.608 (Langhian – Serravallian)	Immature palaeosols, marsh or marginal lacustrine setting
BKF-BC section	13.608-12.174 (Serravallian)	Lacustrine/palustrine-marginal lake setting. Hydrologically closed lake

Table 7.1 Summary of the age, deposit type and depositional environments of the deposits assigned to the SHF and BKF.

Coincident with a decrease in global CO₂ levels around the Oligocene-Miocene transition (Kurschner et al., 2008) the central Saharan palaeoenvironment is assumed to have become progressively warmer and wetter during the Aquitanian (Swezey, 2009). Terrestrial evidence however is not documented at this time to allow confirmation as an end of Oligocene unconformity is documented from many basins of the central Sahara including in the north Chad and the Chotts (Swezey, 2009). This unconformity appears to be absent in the Fazzan as deposition of the lower part of the AP section, the Maharshim and Stromatolite Members and basal section of the Tmessah Member are deposited during this geological stage as summarised in Figure 7.5, and thus provide the much needed terrestrial evidence for this unknown time of the central Saharan climate history. The formations/members of the AP and TM sections are from the north-eastern and eastern fringes of the basin. Despite deposition occurring simultaneously at the AP and TM sites and hence under the same climatic regime, differences in the depositional environments occur.

Stability is observed in the AP section throughout the Aquitanian and into the Burdigalian with palaeosol development occurring in a fluvial system indicative of more humid conditions than at present. Drake et al. (2008a/b) believed many of the fluvial systems of the Fazzan to be late Miocene in age. Assuming the route of the fluvial networks is accurately documented by Drake et al. (2008a) for the late Miocene scenario, it appears the AP section lies near to the pathway of the Nashu River as seen in Figure 7.6. This may suggest that the Nashu was active at this time and is more ancient than originally thought with its initiation in the early Miocene. The AP section lies at the NE end of Wadi Kunayr, a linear topographic depression ~50 m deep and ~20 km long (Hounslow et al., 2017), could it be possible that this wadi was a tributary of the large Nashu River? To help strengthen this theory, knowledge of the palaeocurrent direction would be useful and allow greater understanding of the basin history. The anisotropy of magnetic susceptibility (AMS) is a reliable palaeoflow indicator and derives from the use of anisotropy of induced magnetisation in a low field, from measurements along at least six suitably orientated axis through a specimen (Schieber and Ellwood, 1993; Borradaile and Jackson, 2004). Applying this method to the samples studied here would thus provide a fruitful area of research. A number of studies have employed this method when conducting palaeoenvironmental reconstructions. In the Kathmandu Basin, Goddu et al. (2007) measured 250 samples from fluvial and lacustrine deposits to examine the influence of the SW Indian monsoon and tectonic activity of the Himalayas on the basin. There are also

increasing uses of the technique when studying loess and palaeosols (Bradak, 2009) as demonstrated by Lagroix and Banerjee (2002) who employed this method when studying the loess/palaeosol deposits in Alaska. Lagroix and Banerjee (2002) found however that the better candidates for AMS were palaeosol horizons which had only weak pedogenesis.

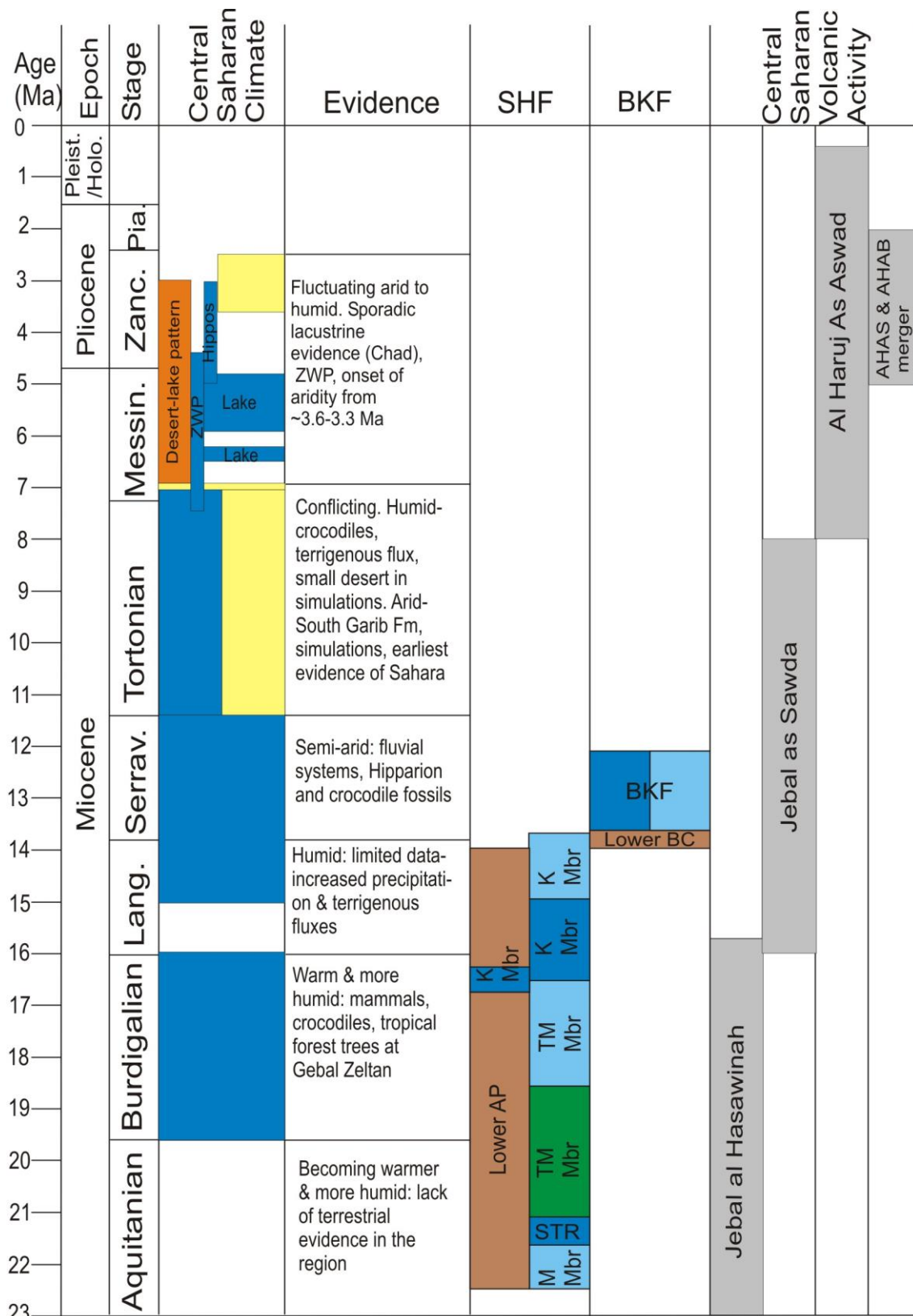


Figure 7.5 Summary of the Miocene-Pliocene palaeoenvironmental change and volcanism of the central Sahara based on the current understanding (i.e. based on the information in the literature review, section 2.1.) and the findings of this study, namely the age of the members and their depositional environment. Central Saharan Climate: Blue=humid phase, yellow=arid phase, orange=fluctuating arid/humid climate resulting in desert-lake patterns, white=no data. SHF/BKF: Dark blue=lacustrine, light blue=palustrine, green=fluvial, brown=palaeosol, white=no data. In the SHF column, the results of the AP section are to the left and the TM to the right.

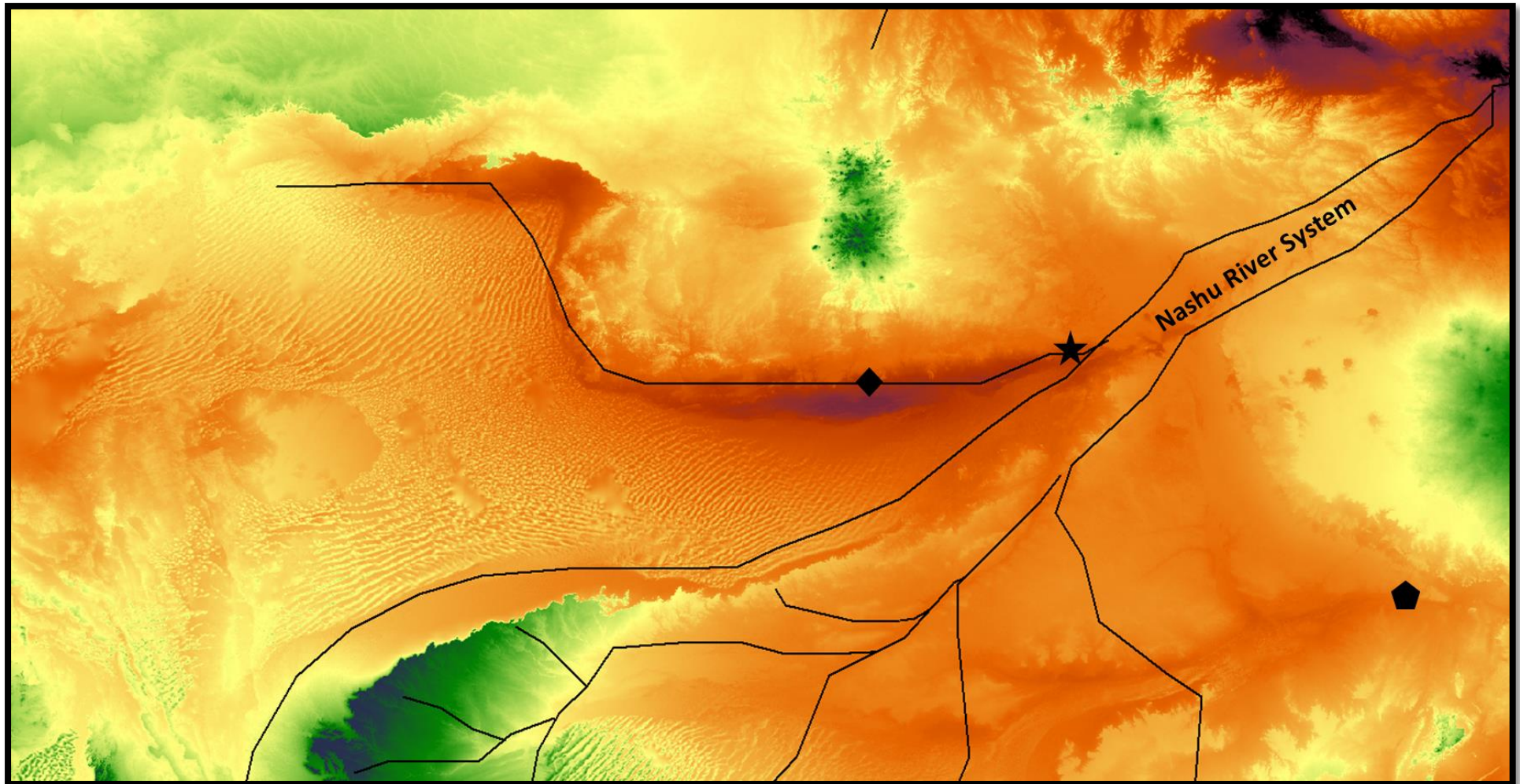


Figure 7.6 DEM of the Fazzan with the probable river systems (late Miocene) mapped by Drake et al. (2008) overlaid. Symbols of the study sites are the same as in Figure 3.1 (page 74) where the diamond = Brak, Star = Ariel and Pentagon = Tmessah.

At the same time as palaeosol development at the start of the Aquitanian in the AP section, the TM section shows deposition of the marsh/swamp deposits of the Maharshim Member. These deposits also indicate humidity in the basin was increasing at this time. The overlying Stromatolite Member documents the first lacustrine phase in the Fazzan in the middle Aquitanian. As far as the author is aware, no other lacustrine phases have been documented at this time in the wider Saharan region. It is possible that increased humidity occurred at this time to allow lake development, however no change in sediment type/depositional environment is observed in the AP section to suggest this. It is thus likely a change in the topography occurred to allow lake development. The TM site lies to the SW of the Al Haruj al Aswad. Initiation of the Al Haruj is believed to have occurred in the late Miocene-early Pliocene and thus would not have attributed to the formation of the Stromatolite Member. The understanding of the genesis of the volcanic province however is speculative, limited by few reliable ages especially as modern investigations are rare (Bardintzeff et al., 2012). Much of the dating obtained from the volcano are from samples collected in the eastern (Cvetkovic et al., 2010) and north-central (Ade-Hall et al., 1974) part of the volcano with knowledge of the timings of volcanism in the S/SW/W lacking. It is thus possible that the Al Haruj al Aswad volcanism was initiated much earlier than suggested, especially in the undated regions of the volcano, allowing formation of the Stromatolite Member. The African plate is thought to have come to rest with reference to an underlying mantle convection pattern at the beginning of the Neogene (~25-30 Ma) (Burke and Wells, 1989). Given this, the present relief shows an image of mantle convection where it begins to impact on the undersurface of the lithosphere resulting in basin and swell topography (Burke and Wells, 1989). An alternative explanation which may have allowed the development of the Stromatolite Member is that before volcanism occurred at Al Haruj al Aswad, swells in the lithosphere began in the early Miocene causing uplift in the region of Al Haruj. The lake of the Stromatolite Member was hydrologically open, suggesting uplift/volcanism was not so great so as to completely block outflow from the lake. The lacustrine phase was however widespread in the region (see Figure 7.7 and Figure 2-Appendix, pg282) with the Stromatolite Member documented to the east and north of Tmessah and is found to within 45 km south of Wadi Kunayr, It is therefore thought that the Stromatolite Member could be considered as the earliest megalake phase in the Fazzan. If this early Miocene picture of the Fazzan is correct it has implications for the timing of events, developed by Drake et al. (2008a).

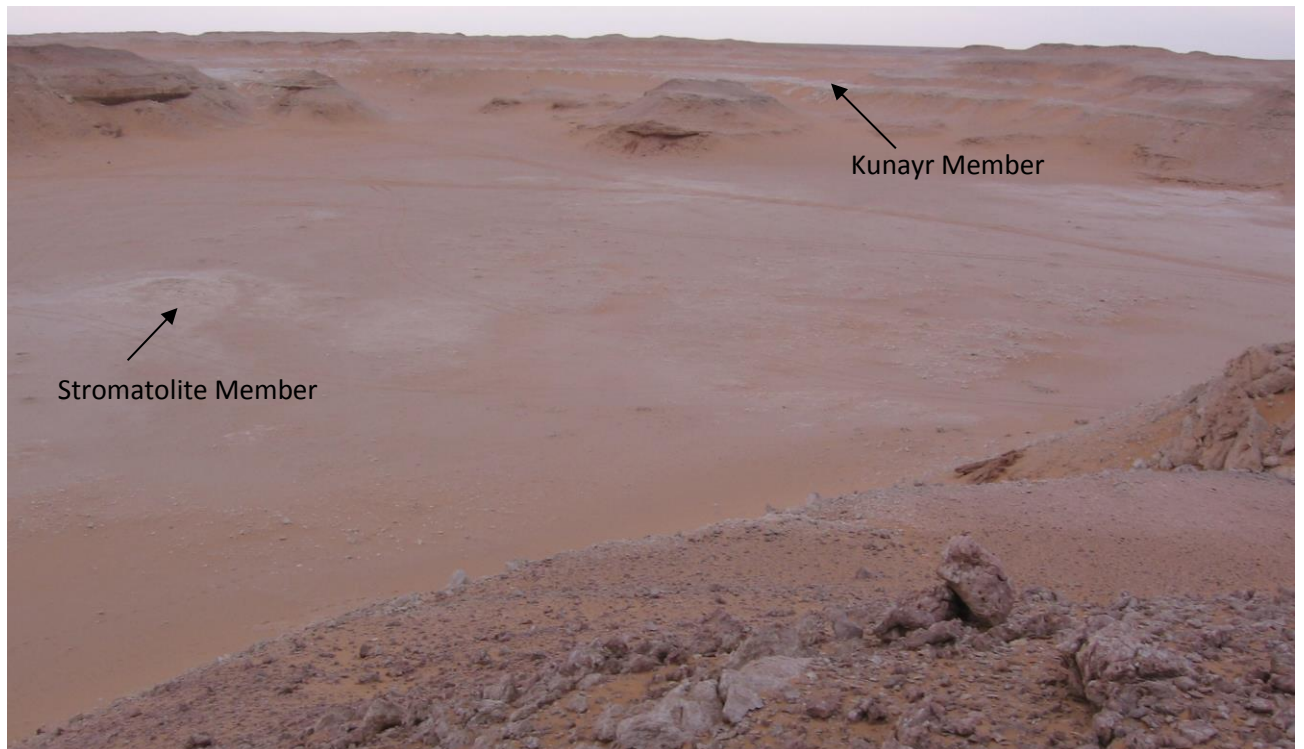


Figure 7.7 Top of the Stromatolite bed visible as white patches in the wadi bottom (and a stromatolite 'dome' - on the left). In the distance, two limestone beds of the Kunayr Member are seen. Photo taken looking NW from the hill on which the upper-most logged sandstone was sampled at the Tmessah section 26°30'48.00"N 16°29'59.77"E.

Overlying the Stromatolite Member is the Tmessah Member. The lower part is dominated by fluvial clastics which span the middle-Aquitania to early-Burdigalian. Despite the loss of the Stromatolite Member at the TM site, the thicker mudstones of the member documented to the south and west imply that the TM site was at the fluvial fringe of a larger lake. Hounslow et al. (2017) record SE cross-bedding directions in Wadi ash Shabirinah (see Figure 2-Appendix, pg286) and also clastic material supplied from the NNE. They also document evidence of proximal channels to the NE of the TM section which supplied material southwards. It is thus thought the fluvial system flowed through a low in the Palaeozoic basement north of Dur al Quassah into the Abu Tumayan Trough (refer back to Figure 2.7). In the neighbouring Sirt basin, fluvial deposits believed to be Burdigalian in age deposited in channel environments are also documented at the base of the Marada Formation (El-Hawat; 1980; Swezey, 2009). The upper part of the member dated to the mid-late Burdigalian sees the development of a hydrologically open palustrine environment at the lake margin. The presence of these deposits suggests the region was still under the influence of greater humidity, but a change in the climatic regime occurred. Deposition of these deposits coincide with the MMCO, a period of global warmth which

correspond to an increase in CO₂ to a maximum of 400-500 ppmv (Kurschner et al., 2008). Ocean water temperatures also increased (Pagani et al., 1999) which would have reduced the thermal contrast between the African continent and the ocean likely causing weakened monsoonal penetration to the region.

Middle Miocene

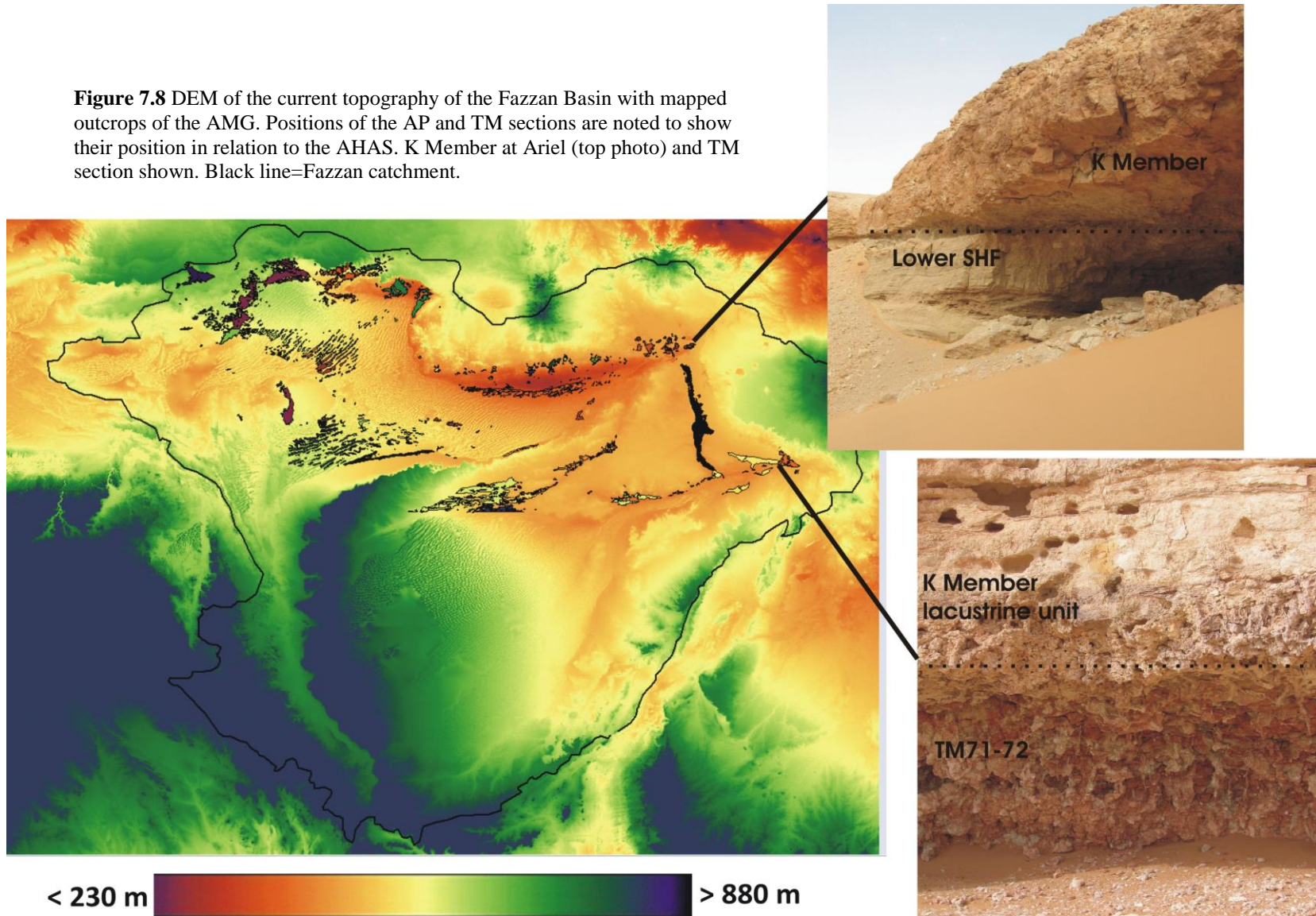
The Kunayr Member is comparable in age in both the AP and TM sections deposited in the late Burdigalian and continuing through the Langhian (Figure 7.8). The global warmth of the MMCO would have still be occurring in the early stages of this member's deposition. This is reflected in the consistent isotopic signatures of the member in the lower part of the TM section and also the AP section. Despite a peak in temperatures and likely continued reduction in the monsoon this member documents a second lacustrine phase in the eastern region of the basin. While an open lake system is in existence at the TM site, a closed lake developed at AP during the early stages of Kunayr Member deposition. This closure suggests there must have been some uplift of the lithosphere or earlier volcanic activity at the NW edge of the site of the Al Haruj al Aswad and also the SE at Jebal as Sawda. The petrography of these lake deposits indicates we are dealing with basin fringe deposits and thus the central part of the Kunayr Member palaeolake was to the S/SW of the analysed outcrops.

Even though hydrological closure occurred at the site of AP, an open lake system was still present until ~16.268 Ma at TM. A closed lake developed at TM from this time which lasted ~ 1 Ma. As for the AP site, it is likely there was another phase of upwelling/volcanism at the Al Haruj al Aswad but this time at the southern edge which blocked lake outflow. The period of lake closure at TM was also coincident with the end of the MMCO and the early transition to the MMCC (Flower and Kennet, 1994). Around the time of the MMCC open lacustrine conditions returned at TM with a change to palustrine sediment deposition. These changes could be due to sedimentation in the lake allowing outflow to be re-established or due to flooding. Contradictions in the evidence surrounding the climate history of the Sahara occur for the MMCC as commented on in section 2.1.1. The growth of the EAIS during the MMCC would have impacted on the African monsoon likely strengthening it (Zhang et al., 2014). However it appears from the return to palustrine conditions at the TM section and palaeosol development at AP that increased aridification may have occurred thus agreeing with the hypothesis of Flower and Kennet (1994) that ice development lead to an increased meridional temperature gradient

strengthening climatic boundaries resulting in increased aridification in the Sahara. Basins that lie near to latitudinal boundaries of the monsoon are also more sensitive to climate shifts (Burrough and Thomas, 2009).

A continuation of this drying trend is observed during deposition of the deposits of the Brak Formation in the Serravallian. Zhang et al. (2014) also note the climate of the Sahara was semi-arid during this time. A semi-arid climate is the main requirement for the formation of palustrine carbonates, especially when influenced by marked seasonality (Platt and Wright, 1992; Tanner, 2010). Even though an increase in aridification was occurring at this time, the Brak Formation represents the development of a lake in Wadi ash Shati, the third lacustrine phase experienced in the basin during the Miocene. In the Tindouf-Ouarzazte Basin, Morocco, lacustrine conditions are also evident at this time documented by the presence of fossil ostracods (Swezey, 2009). It is thought the Brak Formation limestones may represent the most extensive lacustrine deposits in the Fazzan as Hounslow et al. (2017) describe the deposits overstepping onto basement highs and eastern fringes of the basin, along the foot of the Sarir al Qattasah (see Figure 2.7) Palaeogene escarpment. The Brak Formation deposits are basin-margin deposits yet there is no documented evidence of the basin-centre equivalents. The extent of the deposits is likely linked to the confinement of the deposits within a closed basin. Wadi ash Shati was thought to have been formed via erosion of the Nashu/Wadi ash Shati rivers in the late Miocene (Drake et al., 2008a; Abdullah, 2010). The age of the deposits however provide further evidence that the river systems are more ancient than originally thought causing erosion of the Wadi ash Shati depression before deposition of the Brak Formation. The closed lake must have been restricted by further uplift on the eastern side of the Fazzan.

Figure 7.8 DEM of the current topography of the Fazzan Basin with mapped outcrops of the AMG. Positions of the AP and TM sections are noted to show their position in relation to the AHAS. K Member at Ariel (top photo) and TM section shown. Black line=Fazzan catchment.



7.4 Interpretation of the Late Miocene (late Tortonian-Messinian) deposits

7.4.1 Sayl Member

The Sayl Member is the oldest member of the Zazur Formation spanning ~170 ka from ~7.454-7.285 Ma. The muddy-fine grained nature of AL12 suggests deposition under low energy conditions which allowed the grains to settle in calm waters (Flügel, 2010, pg352) such as a low-energy, shallow lacustrine or pond environment. The presence of shrinkage cracks can be induced by either variations in salinity, compaction and/or temperature and are particularly common in playa lakes or lacustrine shorelines (Plummer and Gostin, 1981). Although distinctive in colour, the colour of deposits cannot be used as a reliable indicator of depositional conditions as diagenesis can have substantial effects, for example red mudstones may undergo reductive diagenesis to yield green deposits (Boggs, 2009, pg214). Patchy developed pore cements in QM2 suggests infrequent wetting leading to only partial occlusion of pores. Clasts present in mudstones are often unmodified by erosion and transport and can often reflect the original shapes of the particles (Boggs, 2009, pg197). The angularity of some of the clasts suggests limited transport and thus a more local source, however the sub-rounded clasts are suggestive of transport abrasion and hence are further travelled. Transport is likely to be aeolian based on the unimodal clast size and that active sand dune deposits tend to be sub-angular to sub-rounded (Goudie and Watson, 1981). The deposits are therefore interpreted to have been deposited in a shallow water body such as a playa lake or marsh environment where fluctuations in water level were frequent allowing the development of rootlets as documented in the section log (Figure 6.5, pg186).

7.4.2 Sifar Member

Three sites, the BZ, QM and M all contain deposits assigned to this member. Yet despite being comparable in age, distinctions can be made between the deposits of the differing sections both petrographically and isotopically.

Thin sections of the BZ sections are clearly lacustrine in origin, evident particularly by their fossil and carbonate grain content. Changes are apparent however, indicating fluctuations in the lake level. Rim cements, and especially meniscus cements, occur in deposits with patchy developed pore-filling cements. Differing amounts of pore occlusion suggests changes in the occurrence of pore waters due to fluctuations (McLaren and Gardner, 2004). Fossils (refer back to Table 6.3/Figure 6.2/6.3) are present in deposits

with increased amounts of pore-filling cements indicative of lacustrine conditions allowing pores to become saturated. The micritic cement indicates relatively high rates of evaporation and rapid precipitation in a shallow lacustrine setting, supported by the fossil evidence. Charophytes are a lacustrine biomarker living entirely submerged in fresh and brackish water (Soulie-Marsche, 2008; et al., 2010). Modern charophytes prefer warm, shallow waters with depths of <10 m and salinities <5 % (Platt, 1989). Charophytes have been documented in many Quaternary aged lakes in the Sahara including in Trou au Natron, Chad, and in Sebkha Mellala (Soulie-Marsche, 2008; et al., 2010). Geyh and Thiedig (2008) also document *Chara* when studying the BZ Member deposits. The altered and fragmented bioclast material makes it difficult to identify the species and thus further assess the lacustrine conditions. Ostracods occur in every aquatic environment in a range of settings (Martens, 1994; Ruiz et al., 2013). Abdullah (2010) also notes the poor preservation of ostracods in the BZ member but states that the ostracods are the species *Cyprideis trosta*. *Cyprideis*, which were noted by Gaven et al. (1981) in Wadi ash Shati, indicate a strongly variable physical environment with the salinity ranging to from 5-10 %. It is likely that the bioclastic material in the lake was the main source of carbonate, especially during the clearly defined lacustrine phases. Ooids are also typically associated with shallow waters which are regularly agitated by waves/currents (Flügel, 2010, pg147) suggesting there has been rolling of the clasts either at the shoreline or on the lake floor. The occurrence of forams is unexpected, especially as they are more often associated with marine environments. Gaven et al. (1981) found five species of foram in Pleistocene deposits of Wadi ash Shati with the occurrence so far inland explained by transportation of migrating birds. It is clear from the TS evidence that the deposits are of lacustrine origin deposited in a shallow lake with brackish conditions. Decreased lake levels are apparent in deposits lacking fossils and poorer developed pore cements.

Shallow lacustrine conditions are further supported by the geochemical data of these deposits. XRF analysis revealed the deposits to be high in Cl which is likely to be due to the presence of salts which have been precipitated at times of increased evaporation. MgO was also shown to be a relatively important component of some of the deposits (see Table 10-Appendix, pg303). The presence of MgO is thought to be due to dolomite. Abdullah (2010), when analysing the carbonates of the BZ member, also found dolomite to be a major component of the deposits with some composed of 80% dolomite and just 20-10% calcite. As in the BKF, when stained for dolomite however no reaction occurred. Dolomite often occurs via replacement of pre-existing calcite (Tucker and Wright, 1990,

pg372). However, in most dolomites, especially those forming at present, evaporative enrichment indicative of an arid climate is often the trigger (Tucker and Wright, 1990, pg 386). It is also possible that the dolomite may have been derived from leaching of the basic volcanic rocks in the region or from the bedrock (Tucker and Wright, 1990, pg389).

The isotopic data, in particular $\delta^{18}\text{O}$ reflects fluctuating water levels. There is good correlation between the petrographic data and $\delta^{18}\text{O}$ isotopic data with the most depleted values occurring in deposits with a high abundance of fossils such as ALA5/4. The enriched $\delta^{18}\text{O}$ reflect lowstands and increased evaporation. For example, ALA6 has a low negative $\delta^{18}\text{O}$ value and also contains a relatively increased amount of dolomite. Only moderate covariance was observed between $\delta^{18}\text{O}/\delta^{13}\text{C}$ suggesting the lake was hydrologically open. The $\delta^{13}\text{C}$ values are also the most isotopically enriched out of all the deposits analysed, including in the Shabirinah/Brak Formations, reflecting the biological activity within the lake. It is also possible that meteoric input to the lake, e.g. runoff was also more isotopically enriched. A change in the flora of the African landscape occurred at the end of the Miocene, the appearance and expansion of C4 grasses (Cerling et al., 1993; 1997). Carbonates (pedogenic) formed from C4 vegetation alone would have isotopic values of +1-3‰ (Segalen et al., 2007). The expansion of these grasses may have also had some influence on the $\delta^{13}\text{C}$ values. The values however are not as enriched as would be expected from a purely C4 influence, especially when compared to the values of the Miocene (pre C4 expansion) Shabirinah/Brak Formations which only differ by <3‰ compared to the Zazur Formation. It is possible that there was some mixing of C3/C4 plants however.

Even though the Sifar Member is assigned to the deposits from the lower QM1 and the majority of the QM2 section, differences in the timing of sediment deposition occur (refer back to Figure 6.22). In the older QM2 section dated to ~7.285-5.235 Ma more information regarding the depositional environment can be achieved when combining the limited petrographic data with the information recorded in the section log. In the lower units rootletting is less common compared to the upper units. An ostracod layer at 7.2 m indicates lacustrine conditions, likely shallow, occurred. This is further supported by the increased and better developed pore-filling cement in the TS of QM63. In the mid-upper units petrographic data is lacking but the log records a range of bedforms. The middle units record both parallel laminations and ripples. Parallel laminations are common in medium-fine grained sands (as in the deposits of this member) on surfaces with little or no relief

(Paola et al., 1989; Collinson et al., 2006, pg128). They are produced by particular flow conditions, probably related to streaks of faster and slower moving water close to the bed (Collinson et al., 2006, pg129). They are thus indicative of upper flow regime conditions with abundant sediment in suspension required (Paola et al., 1989). The current must not however be too strong to destroy the bedform. Ripples occur via movement of water over a sandbed often as unidirectional flow or oscillatory waves (Collinson et al., 2006, pg83). Ripples, like parallel laminations, are thus mostly envisaged forming in shallow water. In thin section it was observed that the clast size became more unimodal and better sorted from QM71 upwards. This is also where the bedforms change to predominantly cross-bedded (Figure 6.5, pg186). Based on the clast size, sorting and shape it is thought the cross-bedding represents a period of aeolian dune formation (Figure 7.9; Collinson et al., 2006, pg128).

From the few deposits of the QM1 section that relate to this member, the depositional environment can be inferred. The occurrence of rounded intraclasts in the deposits indicates the clasts have likely been transported to the site of deposition and incorporated into the deposit. Micritic pore-filling cements indicate rapid precipitation, possibly in shallow water, especially in the upper deposits of the member. Not all pores are occluded however in the lower deposits (QM1-3) with areas of only meniscus cements present suggesting the pores have not always been saturated with pore water. This infrequent wetting is also suggested by fenestrae which typically form due to wetting/drying of the deposit. Key features noted in the section log (pg198), but not recorded in TS, are also important to consider. Rootlets in the lower deposits suggest lower water levels allowing pedogenesis to take effect. Parallel laminations were also evident in the field. It is likely that the deposits were deposited in calm, shallow waters to allow this bedform to be preserved. The decreasing $\delta^{18}\text{O}$ isotopic values (refer back to Figure 6.11) up this member suggest increased water levels and a change from a palustrine setting to a lacustrine setting. The shell fragment in QM4 also supports an increase in lake level.



Figure 7.9 Aeolian cross-bedding in upper part of the QM2 section.

The M section spans ~2.4 Ma from 7.285-4.896 Ma yet limited petrographic changes, as demonstrated in Figure 6.7, occur over this time. Subtle differences in the amount of meniscus and pore-filling cements are the most obvious changes reflecting fluctuations in the amount of water in the intergranular porosity of the sand (Cremaschi, 2001). This is reflected in the sporadic availability of the isotopic data where depleted $\delta^{18}\text{O}$ values likely reflect times of reduced evaporation and increased precipitation and surface water in the basin. The varying $\delta^{13}\text{C}$ can be explained when comparing the values to the position on the section log. The most depleted values occur in deposits where rootletting is evident, suggesting increased vegetation growth. It is unlikely that the depleted value of M25 is 'real' based on the other $\delta^{13}\text{C}$ values obtained and hence should be discounted.

Extensive additional geochemical analyses were also conducted on the section. XRF analyses unsurprisingly revealed an abundance of Si and a relatively high amount of Zr. Zr is one of the most stable elements during chemical weathering and diagenesis (Aly, 2015). Zr is often associated with a detrital component correlating well with SiO_2 (Norry et al., 1994). Zr is typically in the form of zircon which as a heavy mineral (HM), has a density of $>2.85 \text{ g cm}^{-3}$ and thus often behaves like large quartz clasts which have typical densities of 2.65 g cm^{-3} (Nichols, 2009, pg15). HM analysis indicated the dataset to be comparable with the early Palaeozoic sandstones analysed in the Kufra Basin (Morton et al., 2012; Morton-personal communication) thus suggesting the sands in the NW edge of

the Fazzan are well-mixed and far travelled and hence recycled. This is in good agreement with the findings of the Zallaf sand sea by Muhs (2004) who found the sands to be very mineralogically mature.

In the field it was thought that the parallel laminated part of the section may indicate the presence of a large aeolian sand-sheet, while the cross-bedded section above was of unknown origin. As discussed earlier, parallel laminations can however also be indicative of shallow surface water. The cross-bedding was large (> 2 m height) but only deep flows can generate high and large aqueous dunes (Collinson et al., 2006, pg105). The petrographic data of the bedform dominated units reveal surface water was limited (poorly developed cements) and hence both the parallel laminations and cross-bedding can be considered aeolian in origin. It was hoped PSA would allow further confirmation regarding the depositional environments. PSA revealed limited variability between the two bedform dominated units, however the clast size and sorting were more typical of a fluvial environment rather than aeolian. Further analyses such as SEM may prove beneficial in helping to confirm an aeolian origin but as the deposits are so far travelled and polycyclic in nature, it is unclear how useful this approach may be.

7.5 Interpretation of the Late Miocene-Early Pliocene (Messinian-Zanclean) deposits

7.5.1 Bir al Zallaf Member

Both the upper units of the BZ-E and QM1 sections are assigned to this member (refer back to Figures 3.9/3.15). Deposition of the member began earlier at BZ-E however there is ~200 ka overlap with deposition at QM1. The L1/L2 units of the BZ-E site represent periods of lake development. The micritic cement in the deposits of these units suggests precipitation occurred rapidly and likely in a shallow lake. Fragments of bioclasts such as ostracods at the top of the L2 and base of the L1 unit provide further evidence of lacustrine conditions. The intervening clastic unit is thought to represent a lowstand. This is supported by the high open primary porosity in the deposits of this unit. It is reasoned that the drying leading to the lowstand did not occur abruptly. BZ27 represents a transition between the L2 and clastic unit displaying laminations of mud and carbonate (refer to Figure 15-Appendix, pg294) thought to represent fluctuations in the lake level. This theory is in agreement with the findings of the Bir al Zallaf Member by Geyh and Thiedig (2008) and Abdullah (2010) who interpreted the carbonates to be shallow lacustrine/playas separated by siliciclastics due to transitions between humid/arid climates.

As in the underlying Sifar Member, large changes in the $\delta^{18}\text{O}$ values occur in the deposits of this member reflecting the changing climatic conditions. Further evidence supporting the idea of deposition in a shallow, possibly playa lake, comes from the values of both $\delta^{18}\text{O}/\delta^{13}\text{C}$. The $\delta^{13}\text{C}$ are all low negative with AL2 recording an enriched value. Enrichment of $\delta^{13}\text{C}$ can be caused by lake volume decline as a result of high temperatures and subsequent evaporative enrichment (Baïoumy et al., 2010). The value could also be attributed to CO_2 exchange between the atmosphere and the lake waters, which when under equilibrium results in $\delta^{13}\text{C}$ values of 1-3‰ (Li and Ku, 1997; Leng and Marshall, 2004). The $\delta^{18}\text{O}$ values are also enriched indicative of evaporation. The L1 limestones covary and were precipitated in a hydrologically closed lake where evaporation has more influence over the $\delta^{18}\text{O}$ value. This scenario is comparable to that of Lake Qarun, Egypt studied by Baïoumy et al. (2010). Baïoumy et al. (2010) record enriched $\delta^{18}\text{O}/\delta^{13}\text{C}$ attributed to precipitation in a saline, closed lake basin and dry formational conditions with carbonate-rich mud layers corresponding to N/S shifts in the ITCZ controlling the precipitation/evaporation over North Africa. A large depleted $\delta^{18}\text{O}$ value occurs in the upper deposit of the clastic unit prior to the second lake phase. This value is likely caused by a sudden increase in surface water such as from increased/monsoonal rainfall

(Hoelzmann et al., 2001). Two isotopic values of the Bir al Zallaf Member were also recorded by Geyh and Thiedig (2008). In comparison to the majority of values from this study the $\delta^{18}\text{O}$ is more depleted averaging -5.5‰ with $\delta^{13}\text{C}$ ranging between -0.05 to -3.48‰ (Geyh and Thiedig, 2008). These results are surprising given that one of the deposits was sampled from the same outcrop as the BZ-E section. It is likely that they sampled carbonate precipitated at a time of increased/increasing lake level.

As in the BZ-E section, the Bir al Zallaf Member deposits of the QM1 section can be considered lacustrine in origin and predominantly composed of micritic/microspar cements. Unlike in the BZ-E deposits however, secondary spar also occurs infilling voids likely caused in part by rootletting. This is more prominent in the deposits above the hiatus. The larger crystal size of the spar indicates precipitation was less rapid and thus may have been precipitated in deeper water with less influence from evaporation. The isotopic values differ considerably to those of the BZ-E section. The $\delta^{13}\text{C}/\delta^{18}\text{O}$ values indicate very poor covariance and thus an open lake system. The $\delta^{18}\text{O}$ values vary very little reflecting a stable lake chemistry; a typical characteristic of open lakes (refer back TM member-section 7.1.2). The slightly more depleted values in the deposits above the hiatus is possibly due to the increased amounts of secondary spar cements formed under a different hydrological regime. As in many of the other members investigated in this study the $\delta^{13}\text{C}$ can be explained by the presence of vegetation in and surrounding the lake with most depleted $\delta^{13}\text{C}$ values occurring in deposits unaffected by rootletting.

7.6 Revised palaeoenvironmental understanding of the Late Miocene-Early

Pliocene Fazzan Basin

Approximately 4.6 Ma of time separates the Brak and Zazur Formations with an explanation for this discussed later in section 8.2. Unlike the early-mid Miocene deposits of the Fazzan, the predominantly late Miocene members of the Zazur Formation show less variation in terms of the depositional setting, all representing lake-margin environments as summarised in Table 7.2. Initiation of the Zazur Formation lies in the latest Tortonian at ~7.454 Ma with the deposition of the Sayl Member. As discussed previously in section 7.3, it appears the topography of the Fazzan basin seen today was initiated in the early Miocene and likely would have been more or less fully established by the late Miocene-Pliocene. This suggests that unlike in the Shabirinah/Brak Formations where a combination of climate and topographic changes are responsible for the varying depositional settings, in the late Miocene-Pliocene the overriding control is climatic.

Formation-Member-Section	Age (approx.)/Ma	Deposit Type and Inferred depositional environment (Petrographic analysis)
ZF-SL Mbr-QM2/BZ-E	7.454-7.285 (late Tortonian)	Palustrine siltstone/mudstone, playa lake or marsh setting
ZF-SI Mbr-BZ (all)	7.454-6.033* (late Tortonian – Messinian)	Lacustrine sandy limestones, shallow lake setting. Hydrologically open lake.
ZF-SI Mbr-QM1/2	7.285-4.896 (late Tortonian – Messinian)	QM1-palustrine to lacustrine, marginal lake setting. QM2-shallow lacustrine/palustrine to aeolian dunes, marginal lake setting
ZF-SI Mbr-M	7.285-4.896 (late Tortonian – Messinian)	Predominantly aeolian dune(?), basin fringe
ZF-BZ Mbr-BZ-E	5.235-4.631* (Zanclean)	Two lacustrine limestones separated by siliciclastic unit, shallow lake setting. Hydrologically closed.
ZF-BZ Mbr-QM1	4.848-4.493** (Zanclean)	Lacustrine limestones, marginal lake setting. Hydrologically open lake.

Table 7.2 Summary of the age, deposit type and depositional environments of the deposits assigned to the ZF. *Although the dates do not seem to be continuous between the SI Member of the BZ sections and the overlying BZ Member in the BZ-E section they in fact are. It is impossible to know the upper age of the SI member in the BZ-W section as we do not know how much of the R polarity unit is present. Likewise, the upper age of the SI Member in the BZ-E section is actually in the BZ Member so it is hard to know the cut off age for the SI Member in this section. Equally, the lower age limit of the BZ Member in the BZ-E section can only be calculated from the base of the N polarity unit as we don't know how much time the small R polarity unit at the base represents. **The boundary of the SI and BZ Mbrs in QM1 occur at approximately half way in the N pol unit therefore the lower age of the BZ Mbr was calculated from this half way point. The upper age of the BZ Member in QM1 is the age of the base of the uppermost R polarity unit (i.e. the minimum age) as it is impossible to know how much of this R polarity unit has been recorded.

The development of the palustrine Sayl Member is coincident with the onset of the ZWP as documented by Griffin (1999) and shown in Figure 7.10. Despite being originally

recorded for the Red Sea area, this wet phase appears to have affected the wider Saharan region. Terrestrial evidence of this phase occurs, for example, by the expansion of Lake Chad (Feakins and deMenocal, 2010) and can now be documented in the Fazzan. Even though increased humidity occurred at this time, repetitive arid/humid cycles affected the region resulting from the weakening/strengthening monsoon (Zhang et al., 2014). This is demonstrated by the desert-lake pattern recorded from Lake Chad (Schuster et al., 2009; Lebatard et al., 2010) and can also be identified in the deposits of the Fazzan, in particular from the deposits of the BZ sections.

The Sifar Member at the BZ site in Wadi ash Shati indicates the deposition of a shallow, brackish lake during the late Tortonian and Messinian which was punctuated by periods of reduced lake level at times of increased aridity. This member is also recorded in the west of the basin at the fringes of the Ubari sand sea in the QM2 and M sections. Deposition of these deposits takes place at the same time as those at BZ, yet the deposition at BZ commenced ~170 ka earlier. The lower QM2 section also indicates increased humidity during the early Messinian in the form of palustrine/lacustrine deposits. Humidity leading to lake development is also documented in the Chad basin during this time (Lebatard et al., 2010). It is not known however if the lake phases in the Fazzan and Chad were synchronous or if they could have become linked as they were thought to have done during the Quaternary (Drake et al., 2011), since palaeomagnetic dating does not allow absolute dating. Unlike at BZ however, where cyclical fluctuations in lake level occur, a drying trend is observed in QM2 with the upper deposits representing a period of aeolian dune building. Aeolian dunes are also recorded at the most western edge of the Ubari sand sea at M. Occasional limestone-rich deposits occur sporadically in the section, likely reflecting times of increased humidity and surface water availability. Dune building was also recorded by Schuster et al. (2006) in Chad at 7 Ma thought to represent the first appearance of the Sahara. The main dune building phases (aeolian cross-bedded units) in the Fazzan however occur later at around 6 Ma. This suggests the aridification that affected Chad was not a regional event. The dune building phases at the QM2 and M sites were substantial lasting ~765 ka and ~1.1 Ma respectively. The variance in the deposits of the member at the differing locations can be explained in part by the fluctuating climate but also due to the topography, in particular the elevation of the sites within the basin as demonstrated in Figures 7.11/7.12. The deposition of BZ in the Wadi ash Shati depression, some 175 m lower than the height of M, means that even at times of reduced humidity over

the wider region, shallow lake development can still occur, fed by drainage from the surrounding basin.

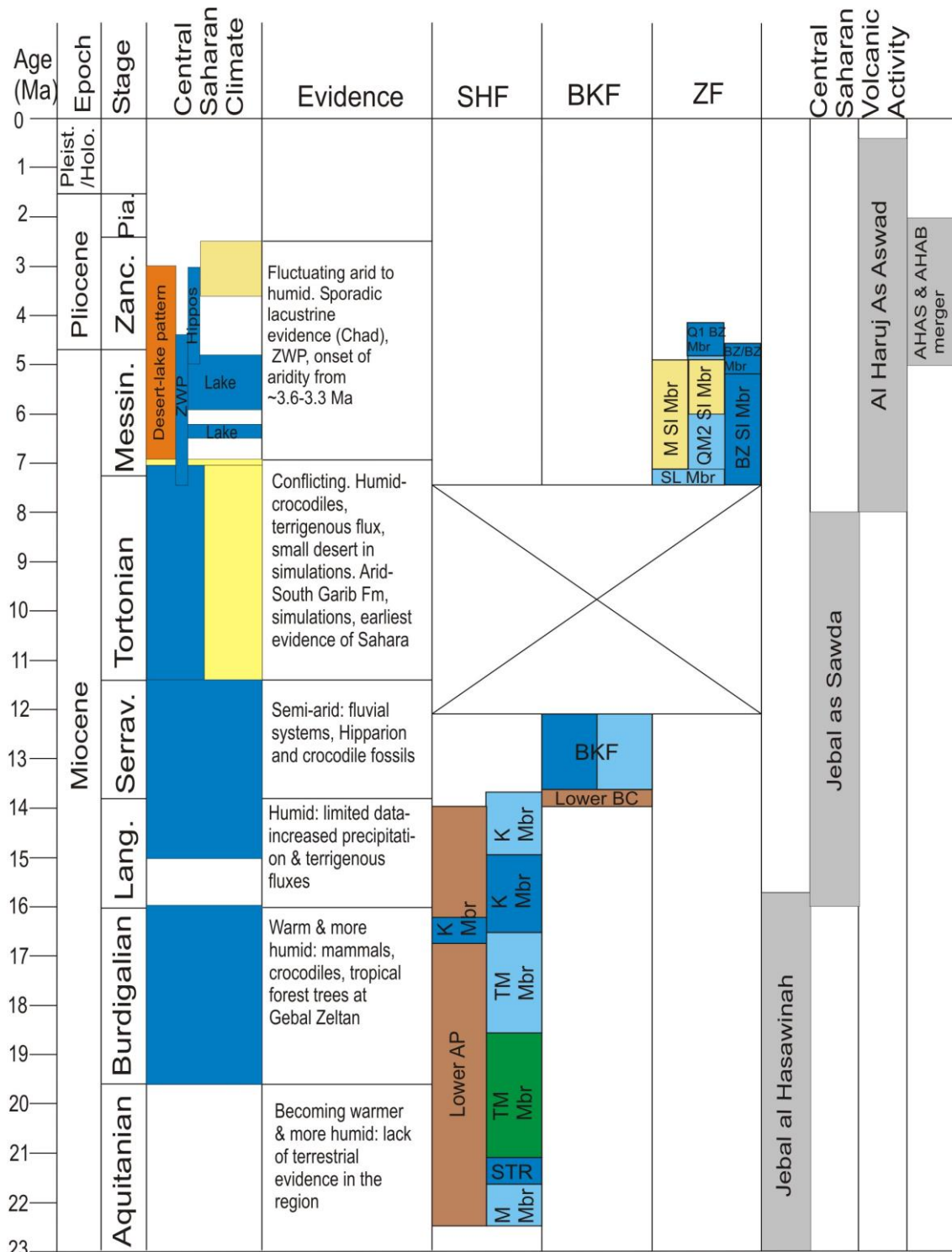


Figure 7.10 Summary of the palaeoenvironmental change and volcanism of the central Sahara throughout the Miocene-Pliocene based on the information in the literature review (section 2.1) and the findings of this study, namely the age of the members and their depositional environment. Central Saharan Climate: Blue=humid phase, yellow=arid phase, orange=fluctuating arid/humid climate resulting in desert-lake patterns, white=no data. SHF/BKF/ZF: Dark blue=lacustrine, light blue=palustrine, green=fluvial, brown=palaeosol, white=no data. In the SHF column, the results of the AP section are to the left and the TM to the right. In the ZF column, the results of the M section are to the left, QM in the middle and BZ to the right.

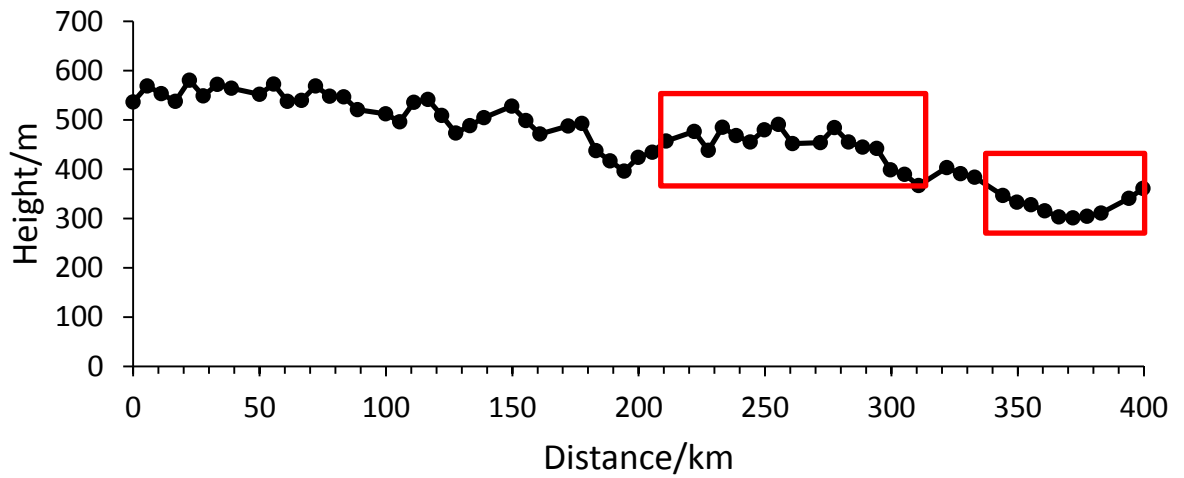
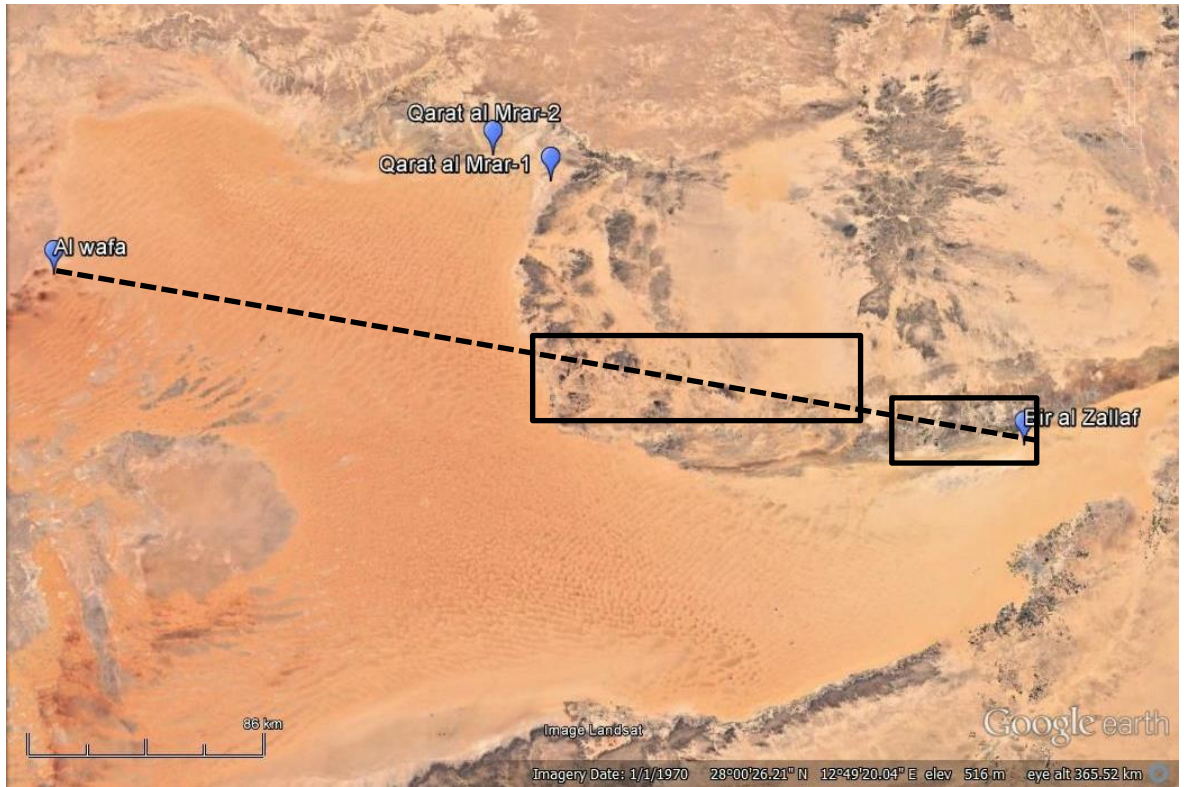


Figure 7.11 Cross-section of the basin from the M to BZ sections. The dashed line on the Google Earth image above shows the transect followed between the two sections. The larger rectangle in both the Google Earth image and the graph show the increase in elevation of the Gargaf uplift and the smaller rectangle the decrease in elevation as the transect passes through the Wadi ash Shati depression.

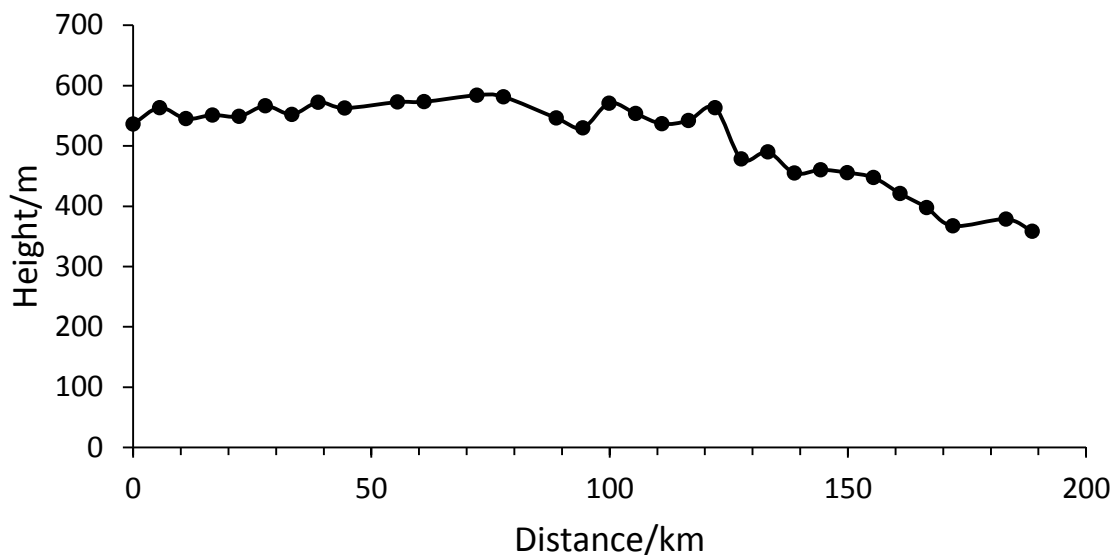
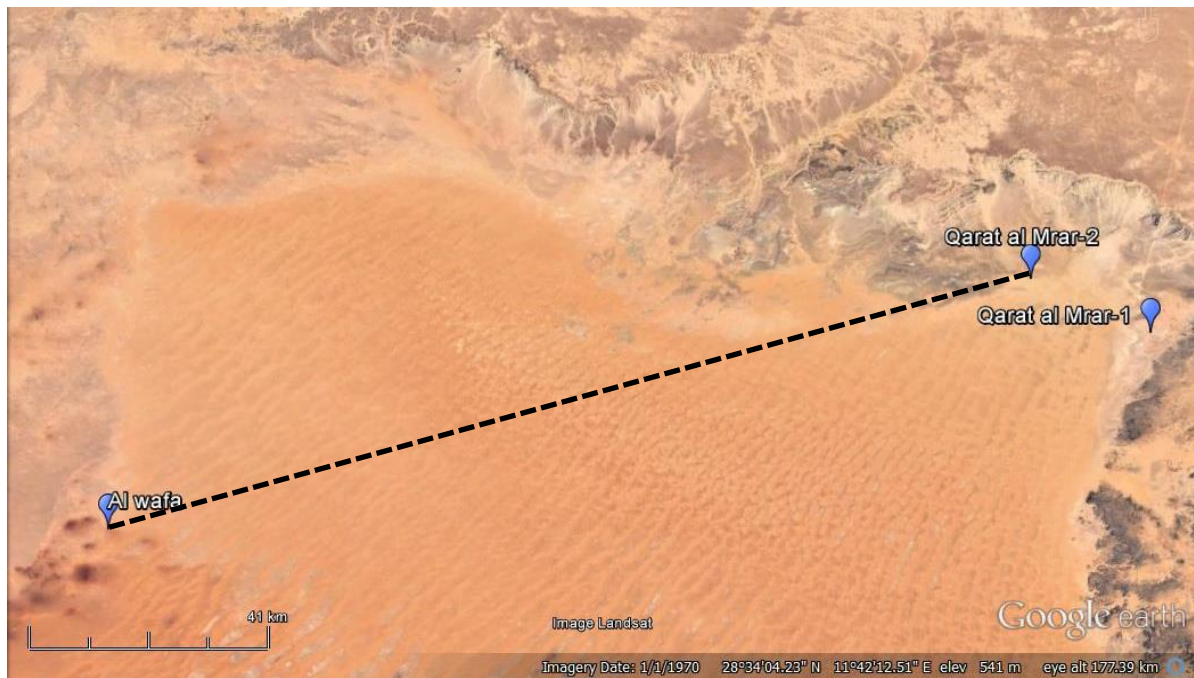


Figure 7.12 Cross-section of the basin from the M to BZ sections. The dashed line on the above Google Earth image shows the transect followed between the two sections

The upper part of the Sifar Member is recorded by the lower most deposits in the QM1 section. These deposits indicate a return to a more humid climate documented by the transition from palustrine to lacustrine deposits at the Messinian-Zanclean boundary. Lake expansion is also recorded at this time by Lebatard et al. (2010) in Lake Chad. Increasing humidity is recorded slightly earlier in Wadi ash Shati from the L2 unit of the Bir al Zallaf Member in the BZ-E section. The deposits of this member, and also those of the underlying Sifar Member, share a number of similarities to Pliocene lacustrine deposits elsewhere in the Sahara. The Garet Uedda Formation in the neighbouring Sirt Basin for

example consists of ‘continental deposits as a succession of aeolian sands with intercalations of yellow to greenish sandy clays, sometimes gypseous, and marly-sandy limestones, overlain by a grayish to whitish caliche’ (di Cesare et al., 1963). Fossil remains are rare in this formation but as in the BZ sections they comprise gastropods, forams, ostracods and oogonia of Charophytes (di Cesare et al., 1963). Further to the west in the ‘lacustrine member’ of the Ait Kandoula Formation in the Tindouf-Ouarzazate basin, Morocco, similar deposits and fossil content are also recorded in this mudstone-rich unit in addition to fossil fish and diatoms (Swezey, 2009). Lake fluctuations in response to the cyclical hydrological regime of the Sahara continued to be a feature of the Bir al Zallaf Member deposits from the BZ-E section. Unlike in the underlying Sifar Member, the Bir al Zallaf Member carbonates were precipitated under hydrological closure. The large swings in the isotopic values of these deposits are typical for closed lakes of small-medium size in comparison to large closed lakes (see Table 7.3) which generally have positive values and a subdued signal which is homogenised by the buffering of the large lake volume (Leng and Marshall, 2004).

Lake-water volume	Very small	Small-medium open lakes	Small-medium closed lakes	Large
Residence time	< 1 year (‘open lake’)	≥ 1 year	10’s years	100’s years (‘closed lake’)
Predominant forcing	S, T, δp	T, δp	P/E	P/E
$\delta^{18}\text{O}$ ranges	Often –ve values, small range of 1-2‰, possibly large range in ‰ for materials precipitated in different seasons	Often –ve values, small range of 1-2‰	-ve to +ve values, large swings (5 to >10‰)	+ve values, subdued signal homogenised by the buffering of the large lake volume

Table 7.3 Characteristics and changes in the size of hydrologically open and closed lakes based on information from Leng and Marshall (2004). $\delta^{18}\text{O}$ ranges typical for the Holocene, S=seasonality, T=temperature, δp =isotopic composition of precipitation, P/E=amount of precipitation in relation to evaporation.

Deposition of the L1 unit at BZ-E was coincident with the lower-mid lacustrine deposits of the Bir al Zallaf Member in the QM1 section documenting the increased humidity first recorded in the underlying Sifar Member. Compared to in Wadi ash Shati (BZ-E section) it appears lacustrine conditions were maintained during the deposition of QM1. This results

from the lake being hydrologically open and constantly fed by inflow, likely from the surrounding Al Hamadah al Hamra plateau, minimising the influence of evaporation. There is some overlap in the timing of deposition of the L1 unit and the QM1 deposits with the petrography of the uppermost deposit from L1 displaying similar characteristics in TS to the QM1 deposits. The question of whether a short megalake phase could have developed at this time therefore needs to be proposed. In the Ubari sand sea, over 1300 km of radar profiles have been acquired by Francke (2014) using LR-GPR. This technology can penetrate significant depths in arid deserts thus allowing us to 'see' beneath the dunes. Apparent on many radar profiles across dunes is the presence of a strong basal reflector which can be traced beneath dunes of adjacent interdunes (Francke, 2014). This reflector is believed to show an evaporate calcrete layer thought to represent palaeolake deposits (Francke, 2014). Outcrops of these deposits were also witnessed in the field along the edges of large dunes (Francke, 2014). It is thus possible that in the past a megalake did develop in the basin, however without sampling of these hidden outcrops and detailed analyses it is impossible to know when in the basin's history they were deposited. The minimal variation in isotopic data of the QM1 deposits is indicative of a small-medium sized lake and therefore it is unlikely there was megalake development at this time. A connection between the two sites cannot be completely ruled out, although it is likely a series of small-medium lakes developed at this time.

8 Discussion: Assessing the Palaeomagnetic Age

The age determinations of the AMG resulting from palaeomagnetic analyses conducted in this research project bring into question the validity of previously obtained dates, in particular via U-series dating. The palaeomagnetic results provide ages at least 4 Ma older than the oldest obtained U-series date (Geyh and Thiedig, 2008). The discussion which follows will aim to explain why such age differences occur and demonstrate chronological controls which support the dates achieved as a result of palaeomagnetic dating. It will also briefly discuss the problems encountered with the palaeomagnetic data.

8.1 Differences in age of the AMG to previous U-series dates

U-series dating is a well-established technique used to determine ages of late Quaternary carbonates as it is able to date well beyond the range of radiocarbon dating to ~500,000 years (Bischoff and Fitzpatrick, 1991; Eggins et al., 2005). This dating technique, first applied to fossil mollusc shells in the Fazzan deposits in Wadi ash Shati by Petit-Maire et al. (1980), revealed the deposits to range between 200-400 ka with peak frequency at ~135 ka in the late Pleistocene (last interglacial). Since this early work, U-series appears to have been the 'chosen method' favoured by many authors (e.g. Gaven et al., 1981; White et al., 2001; Geyh and Thiedig, 2008) who have continued palaeoclimatic investigations in the Fazzan. U-series disequilibrium methods have been successfully applied to the dating of 'clean' carbonate precipitates (e.g. speleothems, Ku and Liang, 1984). Similar successes however are more limited for many impure carbonates such as tufas and calcretes (Ku and Liang, 1984; Candy et al., 2004). Garnett et al. (2004) for example, when conducting U-series on paludal Holocene tufas from Southern England, demonstrated the results had significant detrital contamination with low initial U concentrations making high resolution dating of the tufas difficult. U-series of fossil mollusc shells are also considered notoriously unreliable often showing age estimates are subject to open system behaviour (i.e. both the loss and uptake of U, Eggins et al., 2005). McLaren and Rowe (1996) found this to be the case in fossil mollusc shells from western Mediterranean raised beach deposits. The open system behaviour observed in these shells led McLaren and Rowe (1996) to conclude that the 'unreliability of significant numbers of mollusc U-series dates means that all must be suspect in the absence of contrary evidence and that reconstruction of past geological events [...] based upon such dates are of limited

value or extremely misleading'. With this in mind, one must question the reliability of the dates obtained by Petit-Maire et al. (1980) and Gaven et al. (1981) on such deposits.

In spite of studies revealing the limitations of this dating method, U-series was employed in the most recent study of the AMG by Abdullah (2010). Abdullah (2010) conducted this dating method on deposits from the Bir al Zallaf Member and also the Brak and found similar ages to that reported by Geyh and Thiedig (2008). These dates however contradict the geological estimates which suggest a Miocene or Pliocene age (Collomb, 1962). Although it should be noted that the basis for these age estimates is not clear. As well as being out of step with the geological estimates, the high dolomite content of the BZ Member deposits reported by Abdullah (2010) led the author to question the reliability of the U-series dates. Significant questions were also raised about the dating of the BK Member (the BKF in this thesis) as these deposits were interpreted to be calcretes rather than the previously reported lacustrine carbonates (Abdullah, 2010). Abdullah (2010) puts forward two explanations for the disagreement between the dates and geological estimates. The first suggests that the ages are correct and the geological estimates are overestimated as the samples passed the quality criteria for U-series such as the correction for detrital ^{230}Th and the Osmond Ivanovich diagram to indicate closed systems. The second, and the more likely, suggestion was the U-series dates have significantly underestimated the age of the calcretes. Abdullah (2010) believes this is due to diagenetic alteration of the deposits. Establishing the processes which formed calcretes are essential to any dating of these deposits (Candy et al., 2003). Calcretes can form over 100s to 100,000s of years and hence may contain carbonate phases of a wide range of ages, especially in mature calcretes (Candy et al., 2005). During precipitation of the inorganically precipitated carbonate a certain amount of detrital material (e.g. clays) containing ^{230}Th becomes incorporated (Ku and Liang, 1984). The isochron technique, as employed by Abdullah (2010), corrects for detrital contamination however the main limitation of this technique to calcrete dating is the need to analyse sub-samples containing coeval authigenic carbonate fractions (Candy et al., 2005). As demonstrated in this study, the Brak Formation deposits contain several complex carbonate cementation phases thus complicating the extraction of coeval sub-samples. It is therefore often the norm to regard the pure authigenic component of calcrete as having a time-averaged composition integrating the different time periods and rates of carbonate accumulation (Kelly et al., 2000). As a result, the U-series date gives an apparent age which is the minimum for the commencement of significant carbonate precipitation (Kelly et al., 2000).

U-series was also conducted on 14 deposits from the Tmessah site by Hounslow et al. (2017) which included three samples from the TM section (STR Mbr) of this project. This section was chosen as it was the longest section which contained a significant amount of carbonate units. The remaining samples were from a nearby section sampled by Dr. S. McLaren. Sub-samples examined using a polarising microscope revealed most of the samples had significant amounts of silicate detritus and hence were unsuitable for dating due to the large amount of initial Th correction that would need to be applied (Hounslow et al., 2017). One of the samples was also not suitable due to the presence of several carbonate generations (Hounslow et al., 2017). In total, just six samples (three from the STR Member) were deemed relatively low in detritus for Th/U to be attempted as shown in Figure 8.1. The measured $^{230}\text{Th}/^{232}\text{Th}$ activity ratios which ranged from ~1-18 meant the samples were sufficiently contaminated to require correction (<20 problematic) (Bischoff and Fitzpatrick, 1991). When corrected however, the uncertainty on the ages became large enough to class the calculated dates as meaningless. The samples were also too homogenous yielding poor spreads of data to allow the isochron technique to be attempted. The spread of data also meant U-Pb dating could not be attempted. Detrital correction was attempted on some Th-corrected samples with the data plotting in the ‘forbidden zone’ on the Osmond Ivanovich diagram (see Figure 8.2, Hounslow et al., 2017). This data is indicative of open-system conditions.

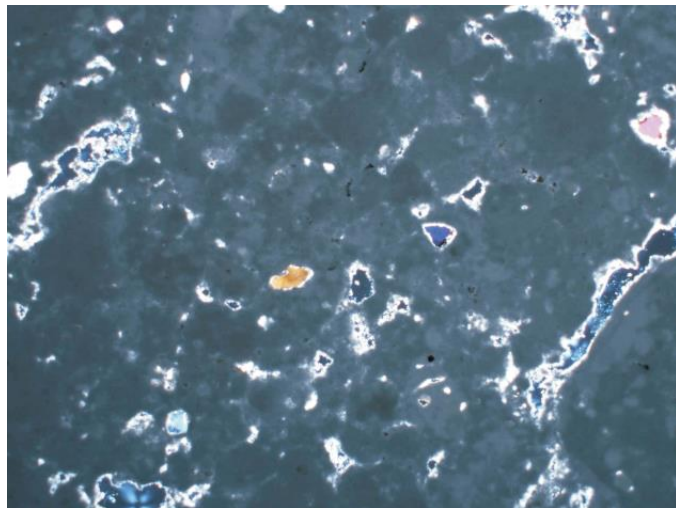


Figure 8.1 Photomicrograph of TM6 low in silicate detritus. Field fo view approximately 2.5 cm wide

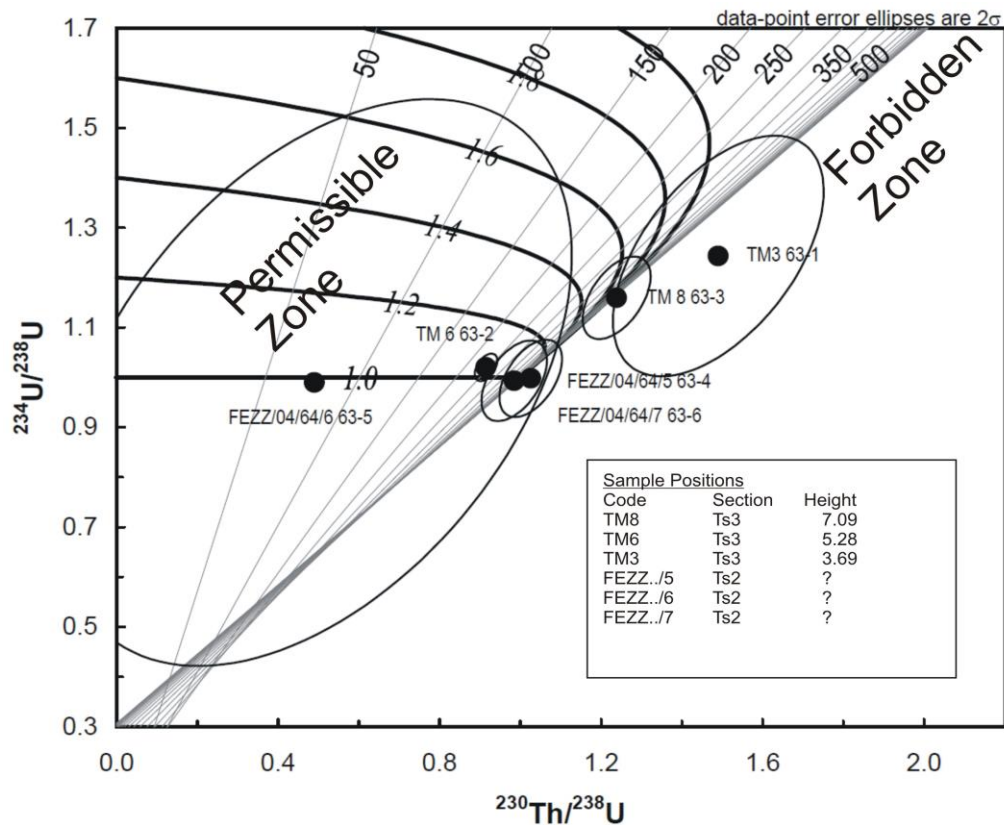


Figure 8.2 The detrital corrected $^{230}\text{Th}/^{238}\text{U}$ vs $^{234}\text{U}/^{238}\text{U}$ data. The series of sloping lines represent age contours (50 to 500 ka). Data points to the right of the 500 ka contour plot in a ‘forbidden zone’ where the observed isotope compositions cannot be generated by normal U decay to Th (Hounslow et al., 2017).

Open system behaviour, as previously mentioned, can affect the reliability of U-series ages. Accurate ages can only be produced if carbonates have experienced no migration in U or Th (Abdullah, 2010). In oxidising environments, the norm for the Fazzan, U is soluble in natural waters and is adsorbed or co-precipitated as a trace element in carbonates (Bischoff and Fitzpatrick, 1991; Garnett et al., 2004). Under changing environmental conditions U migration may occur (Porcelli and Swarzenski, 2003). Enhanced weathering in the vadose zone, for example can cause water interacting in this environment to enter groundwater (Porcelli and Swarzenski, 2003). Porcelli and Swarzenski (2003) describe how strong concentration gradients may occur along groundwater flow lines as concentrations change from initial to steady state values. It is therefore thought that surface weathering during more humid periods of the Quaternary has led to groundwater mobilisation of U and the U-series dates likely relate to this surface weathering. Hounslow et al. (2017) suggests the positive relationship between elevation and age in the U-series dates of Geyh and Thiedig (2008) may relate to groundwater modification processes with U fixed-in earlier in higher elevation sites. Evidence of Quaternary humid periods causing U mobilisation have been documented in the Egyptian

Sahara by Osmond and Dabous (2004). Other dating methods have been trialled in the Fazzan such as OSL carried out by Armitage et al. (2007). Results suggest the deposits from BZ are older than the age suggested by U-series due to the saturation of the OSL signal but exactly how much older is unclear. It is thus apparent that U-series, and potentially OSL, is not a suitable dating method for the age determination of the carbonates of the AMG due to effects of U mobilisation and diagenesis.

8.2 Chronological Controls

The large difference in age between the palaeomagnetic results and previous U-series calls for other chronological controls to be sought to help validate these new ages. Basalt fragments have been reported by Goudarzi (1970) from the basal breccias of the Brak Formation in Wadi ash Shati. Map evidence (Woller, 1984) to the north of Wadi Kunayr (see Figure 3-Appendix, pg283) also shows basalts interbedded in the boundary between the Shabirinah and Brak Formations. It is thought these basalt fragments most likely originate from the Jebal as Sawda volcano. Dating of the volcano by Ade-Hall et al. (1975) places activity at 12.3-10.5 Ma. Busrewil and Esson (1991) extended the age range to 16-8 Ma noting much of the volcanic activity, such as development of plateau lavas, occurred between 14.3 ± 1.9 and 11.1 ± 1.5 Ma. The Brak Formation must therefore be younger than these ages as suggested by the palaeomagnetic age (~ 13.608 - 12.174 Ma). In the field Hounslow et al. (2017) describe SE and E palaeocurrents in the Tmessah Member of the Shabirinah Formation. The palaeocurrent direction implies that the Shabirinah Formation predates the development of the Al Haruj as this volcano would have blocked eastwards flow into the neighbouring Sirt basin. The majority of studies (see back to section 2.2.1) of the Al Haruj al Aswad suggest development occurred ~ 5 - 0.4 Ma. Ages older than this have been reported such as by Bardintzeff et al. (2012) to 8.1 Ma. Drake et al. (2008a) report an outlier K/Ar age of 10.16 ± 1.29 Ma. Using the same dating method as Drake et al. (2008a), Cvetkovic et al. (2010) also report an anomalous date of 11.80 Ma with a small error of 0.41 Ma suggesting no analytical problem is related to this discrepancy. Taking this age into consideration, Cvetkovic et al. (2010) suggests the rock sampled is unrelated to the Pliocene/Quaternary volcanism and belongs to older Miocene events. It is likely these earlier Miocene phases of Al Haruj al Aswad growth would not have blocked the flow from the Fazzan to the Sirt. It can therefore be said with some certainty that the TM Member of the Shabirinah Formation

is older than at least 5 Ma based on the majority of Al Haruj al Aswad dates and potentially older than 11.80 Ma based on outlier ages placing this unit in the Miocene-Pliocene.

Controls on the ages of the younger Zazur Formation come from further scrutiny of the U-series ages of Geyh and Thiedig (2008). Median ages of the Brak and Bir al Zallaf Members were calculated by Hounslow et al. (2017) equalling 353 ± 31 ka and 223 ± 26 ka respectively. This gives a difference of ~ 130 ka which seems unrealistic based on the stratigraphic relationships documented by Hounslow et al. (2017). In Wadi ash Shati the Brak and Bir al Zallaf Members are separated by a major unconformity followed by ~ 90 m of deflational erosion with a later ~ 30 m of clastic deposition (Hounslow et al., 2017) now assigned to the Sayl and Sifar Members. Erosion rates of a number of desert landscapes under different (current) climatic regimes have been investigated by Fujioka and Chappell (2011) using cosmogenic nuclide methods. In the low elevation parts of the hyperarid Atacama bedrock erosion rates are 0.1-10 m/Ma (Fujioka and Chappell, 2011). The erosion rates differ in the hyperarid Namib with erosion rates of bedrock equalling 3-5 m/Ma with no difference in rate between granitic and quartzite surfaces (Fujioka and Chappell, 2011). The basin wide erosion of the Namib, which includes deposits and surface clasts, is much larger calculated at 5-16 m/Ma (Fujioka and Chappell, 2011). If the maximum erosion rate of 16 m/Ma is used to calculate the erosion rate in Wadi ash Shati, ~ 5.6 Ma of time would have been needed to allow for ~ 90 m of deflation to occur between the BK and BZ members, not 130 ka as suggested by U-series estimates. Based on the palaeomagnetic ages of this study, a difference of ~ 4.6 Ma occurs between the top of the Brak Formation and base of the Sifar Member of the BZ sections in Wadi ash Shati. This is comparable to the calculated time difference based on erosion rates, and in fact suggests erosion rates may have been slightly higher than 16 m/Ma.

The ~ 4.6 Ma of time not recorded by the AMG deposits corresponds to the Tortonian. The Tortonian was a time of contradictory climatic evidence in the Sahara with some studies (e.g. Pickford, 2000; Pound et al., 2011) favouring more humid conditions and a decrease in the size of the Sahara desert while others (e.g. Griffin, 1999; 2002; Zhang et al., 2014) favour aridification and desert expansion. Even evidence from nearby locations is opposing. Kohler et al. (2008) analysing terrigenous material in the Metochia section in the eastern Mediterranean (Greece) reveals palaeoenvironmental conditions in North Africa were arid before 8.2 Ma when conditions became more humid. This is in

conflict to the findings of Kohler et al. (2010) who find humid conditions during the Tortonian when studying the geochemical proxy records of the Monte Gibliscemi section (Sicily). A large amount of studies favouring more humid conditions are based on climatic simulations of the region with limited terrestrial evidence to validate them. Much of the terrestrial evidence for more humid conditions comes from or near to the North African margin (Mediterranean Sea), especially from Tunisia. The fluvial Beglia Formation (Tunisia) in particular appears to house much of the humid evidence (Pickford, 2000; Senut et al., 2009). Renewed uplift and extension of the Atlas Mountains into Tunisia occurred during the Tortonian (Potter and Szatmari, 2009; Swezey, 2009). The accumulation of Miocene fluvial strata is coincident with this renewal (Swezey, 2009) indicating the important influence of the Atlas on Tunisian fluvial activity. Continued uplift for example led to drainage towards the Mediterranean to become blocked causing the development of the mudstones of the Sengui formation which overlie the Beglia (Swezey, 2009). It is thus likely that the Atlas played a key role in the generation of fluvial systems of Tunisia and explains why limited evidence is not found in more central regions of the Sahara. The central Sahara, such as the Sirt basin, was also under marine influence in the Tortonian as evidenced in the Marada Formation (Barr and Walker, 1973; Amrouni and El-Hawat, 2015). The findings of this study thus agree with the idea of a Tortonian Dry Phase as described by Griffin (1999; 2002) for the Red Sea area. However, an alternative and much simpler theory may be that deposits deposited during this time have not been found or they may have been covered by the development of the large sand seas within in the Fazzan.

8.3 The use of Palaeomagnetism

Although palaeomagnetic dating is clearly a more suitable dating method applied to the carbonates of the AMG than U-series, some weaknesses in the use of this dating method should be taken into consideration. Much of the palaeomagnetic data, especially of the more carbonate rich specimens, is complicated making it at times difficult to assign a polarity without some degree of uncertainty. The carbonates of the Brak Formation are particularly complicated as their formation is complex owing to numerous cementation phases which have taken some time to form. Many of the carbonate deposits when compared to the clastics also have weak NRM intensities which can cause further difficulties in interpretation (Pillans, 2003). A contributing factor to the complexity of this

data is also likely due to the grain size of the clasts. Natural magnetic grains most often occur in trace amounts and in sub-micrometer grain sizes (Maher, 2007). When studying the separated particle size fractions of soil and loess from the Chinese Loess Plateau (CLP) the clay sized fractions were found to be six times more magnetic than the sand sized fractions (Maher, 2007). Many of the deposits in this study are rather poor in fine-grained silts/clays as show by the laser particle size results. Studies demonstrating that palaeomagnetic extractions are difficult from deposits lacking in fine grain sizes are limited but there are some recorded in the literature. The loess-palaeosol succession in the SE margin of the CLP shows part of the section analysed contained a 'pervasive remagnetisation' (Wang et al., 2005). Along with other potential causal factors such as VRM, Wang et al. (2005) report that the demagnetisation results and mineral magnetic parameters suggest the remagnetisation may depend on grain size. The authors note that all samples from the coarsest part of the section have been remagnetised while fine grain sized parts of the section have clearly defined polarities (Wang et al., 2005).

The overriding reason the rocks are so palaeomagnetically complex relates to strong secondary overprints which are superimposed at higher demagnetisation steps than usual and hence difficult to remove (Pillans, 2003). Several attempts have been made to establish the polarity stratigraphy in Tertiary sedimentary rocks and have revealed the presence of normal polarity overprints with high coercivities (Butler, 1982). These overprints are caused by a minor amount of diagenetic haematite, goethite or other ferric oxides or oxyhydroxides which form in response to oxidising groundwater or during weathering and are almost certainly the result of CRM (Butler, 1982; Cioppa et al., 1995). Weathering can be severe in the Sahara having undergone many climatic changes since the time of deposition of the deposits, especially during the Quaternary. It is also apparent that weathering (likely of magnetite) leading to the formation of haematite has occurred in these deposits as AF proved unsuccessful on many of the specimens. The normal polarity overprint can therefore be interpreted as a Brunhes-age component which confuses the extraction of the ChRM. For example, the presence of a Brunhes-age component creates a variety of intermediate components (i.e. a mix of Miocene/Pliocene and present day) which are present at mid and high demagnetisation steps.

Brunhes-age overprinting has been documented affecting the acquisition of palaeomagnetic data in a number of studies. Soils for example are especially prone to chemical weathering and CRM overprinting as in the subtropical red soil sequence of the Damei section, Bose Basin, southern China (Deng et al., 2007). Deng et al. (2007) noted

that the deposits which have undergone strong pedogenesis might be affected by a strong chemical overprint. When investigating excursions, Langereis et al. (1997) found a Brunhes overprint in the reversed interval between the Jaramillo and Brunhes. They believed this was caused by delayed NRM acquisition related to early diagenetic precipitation of magnetite through Fe-migration (Langereis et al., 1997). Overprinting has also been documented in Mesozoic carbonates/marls from the Sahara. When studying the Liassic member of the Zarzaitine Formation from the Illizi Basin (SE Algeria), Derder et al. (2001) identified two magnetisation components. The first which had relatively low blocking temperatures was considered to be a Cenozoic overprint caused by recent weathering and fluid migration (Derder et al., 2001). The second was thought to have been acquired during late diagenesis resulting in both normal/reversed polarities. The magnetisation was thought to be chemical in origin due to a lack of thermal events in the region (Derder et al., 2001). Derder et al. (2001) suggest the chemical Mesozoic event in these rocks was rubefaction with the main carrier of magnetisation formed during this event with the remanent magnetisation therefore acquired progressively during diagenesis.

Butler (1982) notes the CRM components in the NRM of Tertiary sedimentary rocks can be more difficult to detect than the equivalent component in Mesozoic or Palaeozoic rocks. The use of IRM acquisition can be useful in the detection of stratigraphic levels where CRM overprints may be significant as a result of post-depositional oxidation (Butler, 1982). Some IRM has been conducted on the deposits of the AMG (see section 7.2.1 and Hounslow et al., 2017). If palaeomagnetic work is continued on the deposits of the AMG, IRM should be conducted more thoroughly on all of the investigated sections to help detect possible overprints. Detecting potential overprints can however be challenging with it often not clear what fraction of the Fe-oxides is carrying the ChRM. This was demonstrated by Kruiver et al. (2002) who resampled part of a palustrine-alluvial section from Libilla (SE Spain) that contained a reversed overprint to investigate the behaviour of the NRM signal. They found that overprints seem to relate to lithology with them only present in gray palustrine layers (Kruiver et al., 2002). The IRM component (coercivity) analysis however revealed no clear differences between reversed overprinted magnetite samples and the samples with real NRM directions (Kruiver et al, 2002).

9 Conclusion

From this research the following conclusions can be drawn:

- This research helps to fill the gap in the climate history of the central Sahara by providing what is believed to be the most continuous, low resolution continental palaeoenvironmental record for the Miocene-Pliocene.
- Although complex due to lack of fine clast sizes and secondary overprinting, palaeomagnetic data from 307 specimens demonstrates the Shabirinah and Brak Formations contain a magnetic polarity stratigraphy which is carried by magnetite and haematite and partly by goethite. The mean directions obtained agree with the expected palaeopole positions for Africa during the Miocene to recent interval. The composite polarity stratigraphy has 10 major reverse-normal polarity magnetozone couplets. In total the composite spans ~10.4 Ma with the Shabirinah and Brak Formations spanning ~9 Ma and ~1.4 Ma respectively. Sequence slotting methods employed to quantitatively correlate the polarity stratigraphy to the GPTS reveals the composite is best matched to the early Miocene (~22.564 Ma, Aquitanian) to the late-middle Miocene (~12.174 Ma, Serravallian).
- All outcrops sampled are from the basin fringe. Three main phases of lacustrine limestones developed in the early-mid Miocene. The earliest phase, represented by the formation of an extensive thrombolitic lake, occurred in the Aquitanian. The extent of these deposits is large enough for the lake to be considered a megalake. The second and third phases occur in the Burdigalian-Langhian and the Serravallian respectively. It is thought these latter phases occurred under semi-arid conditions and developed as a result of hydrological closure. The deposits of the Serravallian lake phase were also extensive, again indicating possible megalake development.
- The early-mid Miocene deposition of the Shabirinah/Brak Formations largely suggests the major drainage networks of the Fazzan are more ancient than originally thought, initiated or established in the early Miocene. Their formation also implies topographic changes, in particular uplift on the eastern edge of the basin, possibly due to volcanism, occurred much earlier than originally thought. Uplift subsequently blocked drainage to the Gulf of Sirt resulting in basin closure and lake development. It is thus clear that the varying depositional environments of

the Fazzan in the early-mid Miocene were influenced not only by climatic changes but also topography. Ideas about the basin's geomorphological history, in particular the timings of key events, as proposed by Drake et al. (2008a) therefore needs to be re-examined in detail.

- The 319 specimens measured from the Zazur Formation demonstrate the magnetic polarity stratigraphy is carried by a combination of magnetite and haematite. The majority of the mean directions obtained agree with the expected palaeopole positions of Africa for Miocene-Pliocene to recent interval except for the BZ-E section. The composite polarity stratigraphy contains six major reverse-normal polarity magnetozone couplets which span ~3 Ma. Sequence slotting matches this composite to the late Tortonian to early Zanclean from ~7.454 to ~4.493 Ma.
- The topography of the basin was established prior to the deposition of the Zazur Formation, and hence climatic changes were the main driver of sedimentation in the basin. Deposition of the Zazur Formation deposits are coincident with the onset of the ZWP. The increased humidity at this time was unlike that experienced in the early-mid Miocene, punctuated by several periods of aridity resulting in repetitive arid-humid cycles caused by the weakening/strengthening monsoon. These cycles are reflected in the desert-lake pattern observed in the Zazur Formation deposited in the Fazzan, particularly in Wadi ash Shati. Times of greater humidity allowed lake expansion. Evidence for megalakes is limited with the basin instead likely housing a series of small-medium lakes which were predominantly shallow and slightly saline.
- As well as lake development in the late Miocene-Pliocene, phases of dune building are also recorded in the basin, especially near to the western fringe of the Ubari sand sea. These phases are not coincident with the earliest evidence of aridification of the Sahara documented in Chad, but do reveal that aridity affected the basin for substantial periods of time.
- Palaeomagnetic dating reveals the U-series (and OSL) dates previously documented are unreliable due to diagenesis and groundwater mobilisation of U, causing open system behaviour. The dating of the sections are broadly coincident with K/Ar dates of the Jebel as Sawda volcanics thought to be interbedded in the base of the

Brak Formation. The erosion rate of Wadi ash Shati between the Brak Formation and overlying Zazur Formation roughly corresponds to the difference in ages between these two formations.

9.1 Further work

It is clear from the above results/discussion that there is definite scope to take the findings of this research further. More research is needed to develop a more detailed and complete understanding of the basin history. In the author's opinion, the following work should be considered to help achieve this:

- Complete palaeomagnetic dating on the remaining QM sections that were unable to be analysed. These may help further solidify the arguments for the palaeomagnetic age of these deposits. Along with palaeomagnetic dating, IRM should be conducted on the deposits to investigate potential overprints as a result of CRM.
- Anisotropy of magnetic susceptibility (AMS) would be extremely beneficial in providing details on the palaeocurrent direction and thus the basin configuration, in particular following uplift/ volcanic activity in the region.
- Further particle size analysis and SEM work on the deposits from Al Wafa may be beneficial in helping to finalise whether the deposits are fluvial or aeolian in origin. However, as the deposits are recycled, future investigations may prove unsuccessful in deciphering this problem.
- The deposits of the Brak Formation are complex and would benefit from investigation using cathodoluminescence to confirm if the cements are due to recrystallization or complex growth histories.
- A robust technique which strips the NaSi out of the sample would need to be developed to more thoroughly investigate the deposits.
- More detailed isotopic analysis could be achieved if a method of drilling the deposits without causing contamination was found. The results would also benefit from comparison to isotopic results obtained from a site near to Tmessah by McLaren (personal communication) especially as it is known these deposits definitely do not contain NaSi. XRD analysis would also be useful to identify any dolomite within the samples.
- More detailed analysis of the XRF data and also additional XRF work on not only the clastic material, but the carbonates from all of the sections would build on the

already interesting findings. Combining this data with further magnetic susceptibility and AMS studies would be especially interesting.

Appendix

Site name included in thesis	Variants
Aqār	Aggar
Bilma	Bilmā
Brak	Brāk
Murzuq Sand Sea	Edeyen Murzuq, Murzuk Sand Sea
Ubari Sand Sea	Edeyen Ubārī, Awbari Sand Sea
Erg Uan Kasa	‘Arg Wān Kāsā
Fazzan	Fezzan
al-Ghrayf	el-Greifa
al-Ḥamāda al Hamra	al-Ḥamāda el Ḥamrā
al-Ḥarūj al-Abyad	Haurudj el-Abiad
al-Ḥarūj al-Aswad	Haurudj el-Aswad
al-Ḥatīya	el-Hatiya
Idri	Edri
Jebal al-Hasawinah	Jabal al-Ḥasāwana or Jebel el-Hassaouna
Jebal as Sawda	Jabel as Sawda, Jabal as Suida
Jarma	Jerma or Germa
al-Kufrah	al Kufra
Messak Settafat	Massāk Sattafat or Messak Sattafet
Sabhā	Sebha
Tadrart Akākūs	Akakus, Acacus
Tmessah	Tmessa, Tmassah, Tmissa
Uan Afūda	Wān Afūda
Wādī al-Aāal	Wādī el-Ajal, Wadi al Ajal
Wādī al-Ḥayāt	Wādī el-Hayat, Wadi al-Hayat
Wādī Tannezzūft	Wādī Tanzzūft
Wādī Teshuinat	Wādī Tīshūnīt

Table 1. Table to show site names mentioned in this thesis and the variants used in other sources

Literature Review

The Al Mahruqah Formation: Current Lithostratigraphic Understanding



Figure 1. Key areas highlighted where the AMG outcrops and was sampled by Hounslow et al. (2017). Imagery of these sites are in the figures below.

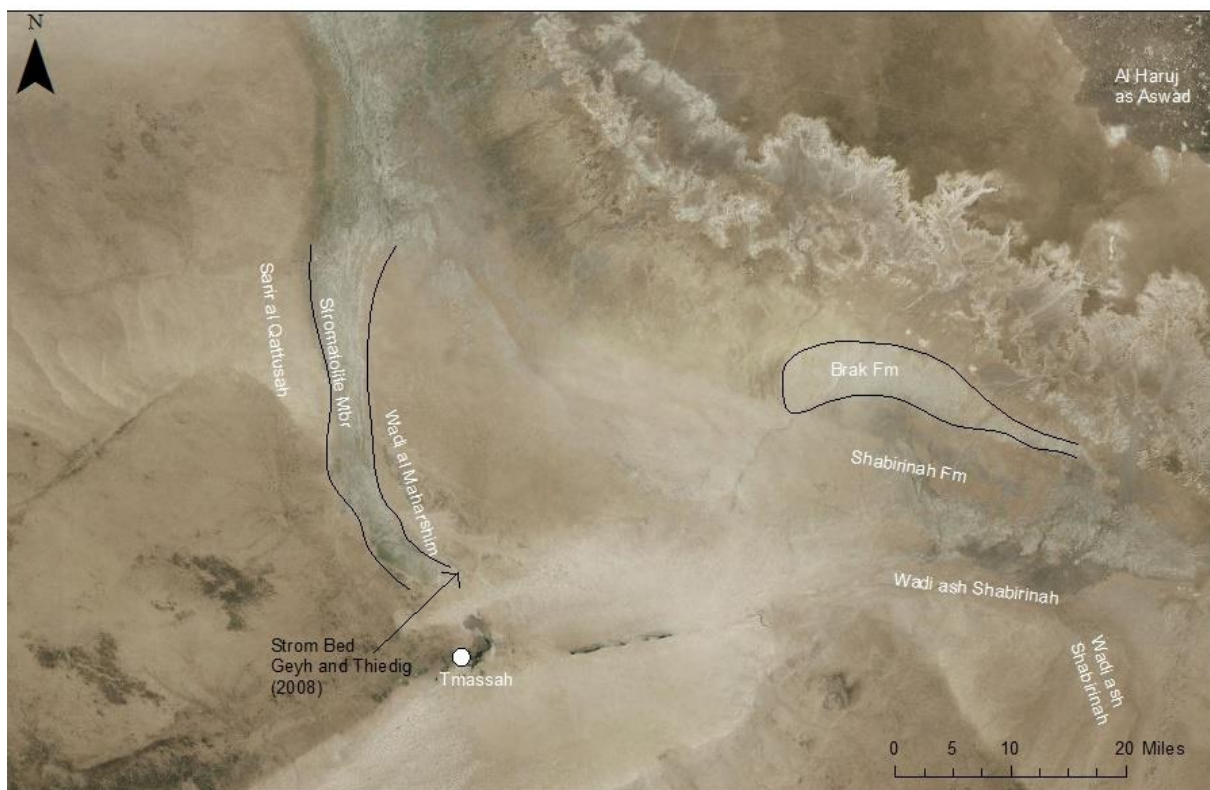


Figure 2. Box 'A' in figure 1 highlighting the route of the Wadi ash Shabirinah, the STR Mbr and the location of the TM site.



Figure 3. Box 'B' in figure 1 outlining the Washkat Zazur region, the town of Brak, Wadi Kunayr and outcrops of the SHF to the east (AP site location).



Figure 4. Box 'C' in figure 1 marking the locations of key wadis in the northern Ubari region and outcrops of the Zarzatine Formation. The location of Wadi Sifar (arrowed) is near to the location of the QM sites.

Magnetostratigraphy: numbering system of the C-sequence

The GPTS of Cande and Kent (1992; 1995) was broken down into chrons and sub-chrons based on the anomaly numbering system known as the C-sequence (Tauxe et al., 2016). Ogg (2012) discusses the use of the nomenclature well which is summarised below. A pair of polarity chrons are prefaced by the letter 'C' (for Cenozoic) before the named magnetic anomaly (Ogg, 2012). This is then suffixed with an *n* representing the younger normal polarity interval or an *r* for the older polarity interval (Ogg, 2012). A major polarity chron can be further sub-divided into sub-chrons. These are denoted by a suffix of a corresponding numbered polarity chron (Ogg, 2012) e.g. C4n.2n (the second oldest normal polarity sub-chron of the normal polarity chron of C4n). Often the name of the chrons and sub-chrons are used for the younger part of the GPTS e.g. Olduvai sub-chron (C2n) or the Jaramillo (C1r.1n) of the Matuyama chron. Cryptochrons or 'tiny wiggles' (anomalies of <30kyr) are designated with a '-' after the sub-chron in which it lies where -1 is the youngest (Tauxe et al., 2016).

	Lacustrine carbonate	Palustrine carbonate	Calcrete
Texture	Mudstones to bindstones ¹ Marl and Lacustrine Chalk ⁴	Mudstones, wackestones, intraclastic grainstones and packstones ¹	Lime mudstones, packstones or bindstones ¹
Matrix and Constituents	Micrite and Sparite ¹ Peloids-Pellets-50µm-1mm diameter ^{1,3,4} Radial ooids ¹ Oncoids ¹ Accumulations of lithoclasts and intraclasts ¹ Clots-10-20µm diameter ^{3,4} Biota-Algae, gastropods, bivalves, ostracods, charophytes, fish and amphibian remains ^{1,4} Detrital clasts e.g. quartz grains ³	Intraclasts ^{1,2} Peloids ^{1,2} Biota-Ostracods, gastropods and charophytes ¹ Clay authigenesis ⁴	Dense Micrite ¹ Clotted Micrite ¹ Micritic Peloids-0.05-0.5mm in size ¹ Micrite Coatings ¹ Pisiform accretionary bodies of micrite/microsparite ¹ Pisoids ¹
Fabric	Varved ^{3,4} Laminated ^{3,4} Homogenous ⁴ Peloidal ⁴ Brecciated ⁴ Gravelly ⁴ Bioturbated ⁴ Bioclastic ⁴ Algal/stromatolitic ⁴ Nodular ⁴	Craze, curve and skew planes ^{1,2,3,4} Nodular (subspherical or cylindrical vertical) and Brecciated ^{1,2} Mottling ^{1,2} Pseudo-Microkarst ^{1,2,4} Peloidal/Intraclastic ^{1,2} <i>Microcodium</i> ⁴	Laminar Crusts ¹ Circumgranular cracking ¹
Cement	Micritic, microsparitic, sparite ⁴ A number of cement types can occur e.g. meniscus, drusy Cement coatings also common	Fibrous and microcrystalline pendant cements ¹ Micritic or microsparitic coatings- anisopachous (in vadose cements), isopachous (in phreatic cements) ⁴ Needles of calcite ⁴	Vadose Micritic cement ¹ Blocky Calcite ¹ Meniscus Cement ¹ Microspar also common ¹
Structures	Burrows Root traces	Burrows ³ Root tubules, voids and traces ^{1,2,3} Internal sediment voids ¹	Breccia structures-in situ brecciation ¹

<p>Macro features</p>			<p>GC Well indurated¹ ≥10m thickness¹ More silica than carbonate¹</p> <p>PC Well horizoned soil profiles¹ A few metres thick¹</p>
------------------------------	--	--	---

Table 2. Table outlining the key distinguishing criteria of lacustrine, palustrine and calcrete deposits. Note: Differences between GC (groundwater calcretes) and PC (pedogenic calcretes) are noted in Table 2.3 in section 2.5.1. 1-Flugel (2010), 2-Alonso-Zarza (2003), 3-Verrecchia (2007), 4-Freytet and Verrecchia (2002).

Study Sites

Jan 2011	Qarat al Mrar-3	QM90-108	19	Section base: 28°, 24', 29.3"N 12°, 27', 53.2"E Section top: 28°, 24', 29.2"N 12°, 27', 58.0"E
Jan 2011	Qarat al Mrar-4- inside dune system	QM120-123	4	28°, 22', 51.7"N 12°, 29', 55.2"E
Jan 2011	Qarat al Mrar-5	QM130-140	11	28°, 23', 5.42"N 12°, 27', 44.97"E

Table 3. Table of the details of the additional sections sampled at the QM site. QM3 contained deposits which overlapped with the QM2 section (Drake et al., 2011).

One Specimen N	█	█	█
One Specimen R	█	█	█
One Specimen N? with S-class chrm	█	█	█
One Specimen R? with S-class chrm	█	█	█
2 or more specimens with N?	█	█	█
2 or more specimens with R?	█	█	█
2 or more specimens with N +N??	█	█	█
3 or more specimens with R +R??	█	█	█
2 or more specimens with N? +N??	█	█	█
2 or more specimens with R?+R??	█	█	█
2 or more specimens with N? +R??	█	█	█
2 or more specimens with R? +N??	█	█	█
3 or more specimens with N??	█	█	█
3 or more specimens with R??	█	█	█
One specimen with N? and t-class chrm	█	█	█
One specimen with R? and t-class chrm	█	█	█
2 specimens with N??	█	█	█
2 specimens with R??	█	█	█
One specimen N??	█	█	█
One specimen R??	█	█	█
2 specimens with main polarity and one with opposite e.g. N, N?, R?	█	█	█
2 specimens with main polarity and one with opposite e.g. R, R?, N?	█	█	█
no assigned polarity	█	█	█

Table 4. Table to show how the polarity of each horizon was defined. When the overlying horizon is of the same polarity however, the uncertainty can be reduced i.e. a half bar of grey to a bar which is just 1/3 grey.

Results: Petrography

Cause of unusual clast fracturing

Within many of the TS (e.g. the samples of the lower AP section) the larger clasts in the deposits often have an unusual pattern on the surface which looks as though the clast is fractured. This pattern is random with no specific orientation. If the clasts were fractured it would be expected that the surface would be slightly undulated and the clast would not enter extinction at once, this however is not the case. With regards to what might cause this pattern, literature searches proved unsuccessful as did seeking advice from colleagues within the Department of Geology. A technician in Geology mentioned that this cracking can occur during the process of making TSs, usually at the end when grinding down using the diamond wheel is done too quickly. This surface fracturing however is seen in TSs produced using both TS methods (section 4.1.1). It was noted that the fracturing was usually only occurring on clasts which were $\sim 250\mu\text{m}$ or more in size, in deposits that had open porosity, had been exposed to NaSi treatment and made in the Department. Based on this it is thought there may have been some adverse reaction between the NaSi and the resin used for impregnation when making the TS in the Department. This superficial fracturing is likely caused by pressure on the clast which is greatest in high porosity deposits. It may have occurred during the drying of the TS, however the true cause remains somewhat of a mystery!

Shabirinah and Brak Formations



Figure 5. Shabirinah Formation. Left: AP3-rootlets. Right: AP10- mottled, bioturbated deposit.



Figure 6. Shabirinah Formation. AP14-black, vein-like organics.



Figure 7. Maharshim Member. Hand sample of TM4 with fenestral laminoid voids.



Figure 8. Tmessah Member. Left: Reddened outer surface of TM15. Right: Cut surface of TM 15.

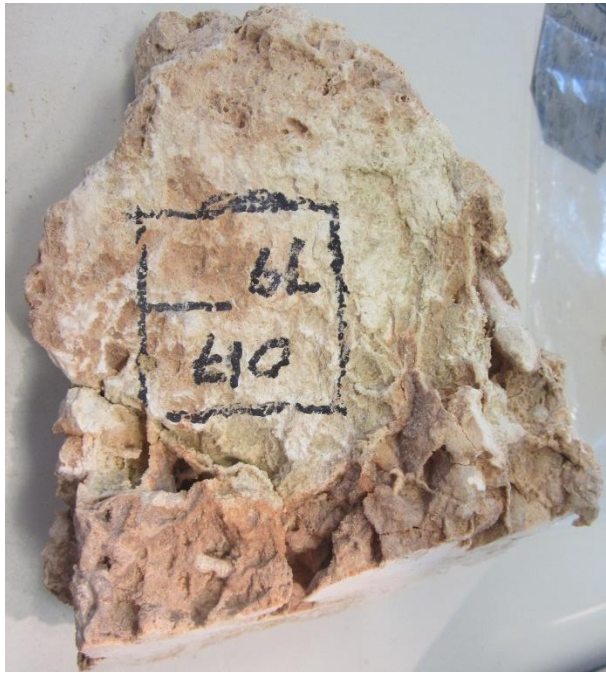


Figure 9. Tmessah Member. TM24-honey-comb texture and rhizoliths



Figure 10. Kunayr Member. AP42-fine grained white limestone.



Figure 11. Kunayr Member. AP51-mottled sandstone.



Figure 12. Kunayr Member. TM25-pitted outer surface of the sample caused by dissolution.



Figure 13. Brak Formation. Left: BC12-dense carbonate band separating more sandy intervals. Right: BC21-white lithoclasts in a carbonate matrix



Figure 14. Brak Formation. BC15-textural differences of the deposit forming areas of zoning.

Zazur Formation



Figure 15. Bir al Zallaf Member. BZ27 parallel laminated carbonate interbedded with fine-grained green muddy layers.



Figure 16. Bir al Zallaf Member. QM15-vugs partially filled with secondary cements.

Geochemical Results

Formation/Member	Section/Sample	Average $\delta^{13}\text{C}$	Average $\delta^{18}\text{O}$
BKF	Brak/BC25	-6.9	-7.9
BKF	Brak/BC24	-7.3	-8.4
BKF	Brak/BC23	-6.8	-8.0
BKF	Brak/BC22	-7.1	-8.5
BKF	Brak/BC21	-7.2	-8.4
BKF	Brak/BC20	-7.8	-8.9
BKF	Brak/BC19	-7.6	-9.1
BKF	Brak/BC17	-7.4	-8.4
BKF	Brak/BC16	-7.8	-8.8
BKF	Brak/BC15	-7.3	-8.0
BKF	Brak/BC14	-6.8	-7.9
BKF	Brak/BC13	-6.8	-7.8
BKF	Brak/BC12	-6.7	-7.7
BKF	Brak/BC11	-7.1	-6.6
SHF	Brak/BC2	-5.0	-4.0
SHF	Brak/BC1	-6.8	-6.6
SHF-K Mbr	Ariel/AP55	-4.9	-3.6
SHF-K Mbr	Ariel/AP42	-6.1	-5.4
SHF-K Mbr	Ariel/AP40	-7.1	-5.9
SHF-K Mbr	Ariel/AP39	-6.9	-5.7
SHF-K Mbr	Ariel/AP38	-6.1	-5.5
SHF-K Mbr	Ariel/AP37	-6.1	-5.3
SHF-K Mbr	Tmessah/TM69	-6.2	-5.1
SHF-K Mbr	Tmessah/TM68	-6.7	-4.9
SHF-K Mbr	Tmessah/TM67	-5.9	-9.1
SHF-K Mbr	Tmessah/TM66	-5.7	-9.2
SHF-K Mbr	Tmessah/TM65	-6.3	-10.3
SHF-K Mbr	Tmessah/TM64	-7.6	-10.8
SHF-K Mbr	Tmessah/TM63	-7.2	-10.1
SHF-K Mbr	Tmessah/TM62	-6.6	-9.5
SHF-K Mbr	Tmessah/TM61	-4.6	-5.8
SHF-K Mbr	Tmessah/TM35	-1.6	-2.2
SHF-K Mbr	Tmessah/TM 34	-6.5	-5.0
SHF-K Mbr	Tmessah/TM 60	-6.3	-5.3
SHF-K Mbr	Tmessah/TM33	-6.2	-4.5
SHF-K Mbr	Tmessah/TM32	-5.9	-5.2
SHF-K Mbr	Tmessah/TM31	-6.2	-5.4
SHF-K Mbr	Tmessah/TM30	-6.3	-5.1
SHF-K Mbr	Tmessah/TM29	-5.6	-4.9
SHF-K Mbr	Tmessah/TM72	-4.6	-9.0
SHF-K Mbr	Tmessah/TM70	-5.3	-8.6
SHF-K Mbr	Tmessah/TM71	-6.5	-9.1
SHF-K Mbr	Tmessah/TM26	-6.3	-5.4
SHF-K Mbr	Tmessah/TM27	-6.2	-5.0
SHF-K Mbr	Tmessah/TM25	-6.1	-5.5
SHF-K Mbr	Tmessah/TM28	-6.1	-5.5
SHF-TM Mbr	Tmessah/TM24	-6.6	-8.1
SHF-TM Mbr	Tmessah/TM23	-6.3	-4.5
SHF-TM Mbr	Tmessah/TM22	-6.4	-4.7

SHF-TM Mbr	Tmessah/TM21	-6.5	-5.9
SHF-TM Mbr	Tmessah/TM20	-6.1	-6.8
SHF-TM Mbr	Tmessah/TM18	-6.9	-9.4
SHF-TM Mbr	Tmessah/TM16	-4.2	-8.3
SHF-TM Mbr	Tmessah/TM17	-10.7	-3.8
SHF-TM Mbr	Tmessah/TM15	-6.7	-8.5
SHF-TM Mbr	Tmessah/TM14	-6.7	-8.8
SHF-TM Mbr	Tmessah/TM12	-4.0	-8.4
SHF-STR Mbr	Tmessah/TM9	-5.5	-2.5
SHF-STR Mbr	Tmessah/TM10	-6.0	-3.7
SHF-STR Mbr	Tmessah/TM11	-6.1	-3.7
SHF-STR Mbr	Tmessah/TM8	-6.7	-3.4
SHF-STR Mbr	Tmessah/TM7	-6.8	-3.5
SHF-STR Mbr	Tmessah/TM6	-6.8	-3.8
SHF-STR Mbr	Tmessah/TM3	-6.4	-2.9
SHF-M Mbr	Tmessah/TM2	-6.3	-3.4
SHF-M Mbr	Tmessah/TM4	-5.9	-3.9
SHF-M Mbr	Tmessah/TM1	-6.3	-4.2
SHF-M Mbr	Tmessah/TM5	-4.8	-8.8

Table 5. Average stable isotope values of the samples from the Shabirinah and Brak Formations.

Formation/Member	Section/Sample	Average $\delta^{13}\text{C}$	Average $\delta^{18}\text{O}$
ZF-BZ Mbr	Qarat al Mrar 1/QM23	-4.3	-7.6
ZF-BZ Mbr	Qarat al Mrar 1/QM22	-3.8	-7.4
ZF-BZ Mbr	Qarat al Mrar 1/QM21	-4.8	-8.4
ZF-BZ Mbr	Qarat al Mrar 1/QM20	-3.6	-7.4
ZF-BZ Mbr	Qarat al Mrar 1/QM19	-4.1	-7.6
ZF-BZ Mbr	Qarat al Mrar 1/QM18	-4.4	-7.3
ZF-BZ Mbr	Qarat al Mrar 1/QM17	-4.4	-8.4
ZF-BZ Mbr	Qarat al Mrar 1/QM16	-4.8	-8.7
ZF-BZ Mbr	Qarat al Mrar 1/QM15	-5.8	-6.6
ZF-BZ Mbr	Qarat al Mrar 1/QM14	-6.1	-6.7
ZF-BZ Mbr	Qarat al Mrar 1/QM13	-3.5	-6.4
ZF-BZ Mbr	Qarat al Mrar 1/QM12	-3.9	-7.2
ZF-BZ Mbr	Qarat al Mrar 1/QM11	-4.6	-7.5
ZF-BZ Mbr	Qarat al Mrar 1/QM10	-3.5	-7.4
ZF-BZ Mbr	Qarat al Mrar 1/QM9	-3.8	-7.7
ZF-BZ Mbr	Qarat al Mrar 1/QM7	-3.4	-7.0
ZF-BZ Mbr	Qarat al Mrar 1/QM6	-3.1	-6.8
ZF-BZ Mbr	Qarat al Mrar 1/QM5	-2.7	-7.4
ZF-BZ Mbr	Bir al Zallaf-East/AL1	-1.1	-4.4
ZF-BZ Mbr	Bir al Zallaf-East /AL2	1.0	1.7
ZF-BZ Mbr	Bir al Zallaf-East /AL3	-1.7	-8.0
ZF-BZ Mbr	Bir al Zallaf-East /AL4	-0.5	1.5
ZF-BZ Mbr	Bir al Zallaf-East /AL5	-1.2	2.6
ZF-SI Mbr	Qarat al Mrar 1/QM8	-2.9	-8.2
ZF-SI Mbr	Qarat al Mrar 1/QM4	-4.3	-7.5
ZF-SI Mbr	Qarat al Mrar 1/QM3	-4.6	-6.2
ZF-SI Mbr	Qarat al Mrar 1/QM2	-4.8	-6.0
ZF-SI Mbr	Qarat al Mrar 1/QM1	-3.8	-5.9
ZF-SI Mbr	Bir al Zallaf-East/AL6	-2.2	-6.9
ZF-SI Mbr	Bir al Zallaf-East/AL7	-2.9	-7.5

ZF-SI Mbr	Bir al Zallaf-East/AL8	-2.2	-7.8
ZF-SI Mbr	Bir al Zallaf-East/AL9	-3.3	-8.5
ZF-SI Mbr	Bir al Zallaf-East/AL10	-3.3	-9.9
ZF-SI Mbr	Bir al Zallaf-East/AL11	-1.8	0.8
ZF-SI Mbr	Bir al Zallaf-Twin/ALA1	-2.7	-8.2
ZF-SI Mbr	Bir al Zallaf-Twin/ALA2	-1.6	-8.0
ZF-SI Mbr	Bir al Zallaf-Twin/ALA3	-2.5	-0.8
ZF-SI Mbr	Bir al Zallaf-Twin/ALA4	-1.9	-7.6
ZF-SI Mbr	Bir al Zallaf-Twin/ALA5	-2.4	-8.4
ZF-SI Mbr	Bir al Zallaf-Twin/ALA6	-2.6	-0.6
ZF-SI Mbr	Al Wafa/M25	-13.7	-7.1
ZF-SI Mbr	Al Wafa/M18	-6.8	-7.7
ZF-SI Mbr	Al Wafa/M17	-2.5	-7.8
ZF-SI Mbr	Al Wafa/M14	-6.0	-9.7
ZF-SI Mbr	Al Wafa/M12	-0.9	-6.1
ZF-SI Mbr	Al Wafa/M3	-3.1	-7.0
ZF-SI Mbr	Al Wafa/M2	-2.9	-6.8

Table 6. Average stable isotope values of the samples from the Zazur Formation.

Sample	Description	V. coarse/%	Coarse/%	Medium/%	Fine/%	V.fine/%	Silts & Clays/%
M29	bimodal, poorly sorted, very coarse	33.5	26.7	20.5	10.6	3.7	5.0
M28	trimodal, poorly sorted, very coarse	42.2	32.6	18.6	6.2	0.4	0.0
M27	trimodal, poorly sorted, very coarse	36.5	30.6	21.6	7.7	1.7	1.9
M26	bimodal, poorly sorted, very coarse	42.3	32.3	16.2	5.1	2.0	2.0
M25	bimodal, poorly sorted, very coarse	49.7	32.4	11.9	3.4	1.2	1.5
M24	bimodal, poorly sorted, very coarse	51.5	29.6	10.1	4.6	1.8	2.4
M23	unimodal, moderately sorted, very coarse	46.2	31.1	16.1	4.0	1.1	1.5
M22	bimodal, poorly sorted, very coarse	51.0	30.0	11.9	3.5	1.5	2.1
M21	bimodal, moderately sorted, very coarse	42.6	30.5	16.9	6.2	1.8	2.1
M20	trimodal, poorly sorted, very coarse	38.9	32.2	20.9	5.7	1.0	1.4
M19	bimodal, poorly sorted, very coarse	39.3	33.2	20.9	4.4	0.7	1.3
M18	unimodal, poorly sorted, very coarse	34.4	25.4	18.8	11.1	5.0	5.3
M15	bimodal, poorly sorted, very coarse	34.5	28.9	21.7	8.9	2.7	3.4
M16	bimodal, poorly sorted, very coarse	41.2	31.2	19.1	5.8	1.0	1.7
M4	bimodal, poorly sorted, very coarse	43.6	32.0	16.8	5.4	0.8	1.3
M5	bimodal, poorly sorted, very coarse	41.8	31.5	18.5	6.2	0.8	1.2
M6	bimodal, poorly sorted, very coarse	44.4	28.2	15.4	7.9	2.0	2.2
M7	bimodal, moderately sorted, very coarse	48.3	31.3	14.0	4.4	0.7	1.2
M8	bimodal, moderately sorted, very coarse	45.3	32.2	15.4	5.1	0.8	1.3
M9	bimodal, poorly sorted, very coarse	38.3	30.3	18.4	8.5	2.0	2.5
M10	bimodal, poorly sorted, very coarse	35.9	30.1	21.8	8.6	1.5	2.1
M11	trimodal, moderately sorted, very coarse	42.5	34.4	17.2	4.1	0.6	1.2
M12	bimodal, poorly sorted, very coarse	37.9	32.2	23.3	4.9	0.5	1.2
SUS2-4	trimodal, moderately sorted, very coarse	47.9	34	13.2	4.9	-	-
Zibar Interdune	polymodal, poorly sorted, very coarse	46.4	28.6	15.7	8.1	1.3	-
Zibar Crest	unimodal, poorly sorted, very coarse	45.6	25.4	16.6	11.3	1.1	-
Dune Flank	bimodal, poorly sorted, very coarse	47.3	28.3	15.6	8.4	0.4	-
Dune Crest	polymodal, moderately sorted, very coarse	38.7	33.4	22.4	5.5	-	-

Table 7. Table to show the results of the laser particle size analysis of the samples from Al Wafa and the modern sample sites.

	AP3	AP8	AP10	AP27	AP29	AP31	AP44
SiO2	84.54	89.68	89.16	89.21	85.95	83.46	90.24
TiO2	0.74	0.28	0.28	0.43	0.49	0.63	0.27
Al2O3	5.18	2.29	2.34	3.44	4.41	5.26	2.31
Fe2O3	3.11	1.15	2.06	1.59	2.17	2.57	1.17
MnO	0.022	0.013	0.014	0.013	0.015	0.023	0.013
MgO	0.46	0.44	0.35	0.83	1.11	1.09	2.36
CaO	0.10	0.26	0.05	0.07	0.21	0.24	0.34
Na2O	1.92	2.37	2.89	1.85	2.49	2.42	0.09
K2O	0.338	0.208	0.146	0.339	0.527	0.777	0.231
P2O5	0.049	0.027	0.042	0.015	0.022	0.022	0.010
SO3	0.052	0.026	0.018	0.011	0.023	0.063	0.064
LOI	3.53	3.20	2.87	2.73	3.71	3.36	3.43
Total	100.02	99.95	100.24	100.53	101.11	99.92	100.52
As	10.6	1.4	3.6	<0.4	<0.4	0.7	<0.4
Ba	60.4	133.4	48.9	49.1	46.4	80.7	47.8
Ce	52.5	38.4	40.9	47.8	49.1	63.8	33.5
Co	5	4.2	7.3	4.5	5	19	3
Cr	53.3	54.7	86.2	57.2	54.3	40.6	22.3
Cs	1.7	2.3	<1.4	<1.4	2.5	1.6	<1.3
Cu	8	4.8	12.8	5.7	5.6	37.1	3.5
Ga	7.2	3	3.7	4.7	6.2	6.0	3.4
La	27.2	22.8	24.8	26.6	31.4	35.7	8.8
Mo	2.5	0.6	1.1	1.2	1.1	1.1	1.2
Nb	27.8	12.6	11.3	23.1	27.1	34.1	13.0
Nd	22.6	16.7	19.1	20.2	21.6	27.9	8.9
Ni	18.7	6.5	7.8	10.2	12.4	16.4	4.9
Pb	6.5	3.9	5	5.0	4.9	5.1	2.3
Rb	19.3	11.1	9.1	17.4	23.5	26.3	10.6
Sb	<0.8	0.9	<0.8	<0.8	<0.8	<0.8	1.1
Sc	8.4	3.6	3.6	4.5	5.5	4.4	3
Se	<0.5	<0.4	<0.5	<0.5	<0.5	<0.5	<0.4
Sn	<0.8	<0.7	2.7	<0.7	<0.7	9.1	<0.7
Sr	97.4	78.6	79.8	36.4	90.6	62.9	20.9
Th	4.9	2.4	2.4	3.2	3.9	4.4	2.3
U	1.5	1.8	1.1	1.3	1.2	0.9	0.7
V	87.5	32.2	51.7	45.7	46.1	54	56.8
W	<0.9	<0.7	<0.7	<0.7	<0.7	<0.7	<0.7
Y	13.2	9.2	11.6	9.9	12.9	17	6.8
Zn	28.3	13.1	15.6	20.4	24.3	26.4	10.5
Zr	475.7	178.2	195.4	309.4	279.6	314.6	192.4
Si/Al	16.3	39.2	38.2	25.9	19.5	15.9	39.1

MgO/Al	0.1	0.2	0.2	0.2	0.3	0.2	1
CaO/Al	0	0.1	0	0	0	0	0.1
Ba/Al	11.7	58.3	20.9	14.3	10.5	15.4	20.7
Nb/Al	5.4	5.5	4.8	6.7	6.2	6.5	5.6
Nd/Al	4.4	7.3	8.2	5.9	4.9	5.3	3.9
Sr/Al	18.8	34.3	34.2	10.6	20.6	11.9	9.1
V/Al	16.5	14.1	22.1	13.3	10.5	10.3	24.6
Zr/Al	91.9	77.8	83.7	90	63.4	59.8	83.3
(Mg+Fe)/Al	0.7	0.7	1	0.7	0.7	0.7	1.5
Mg/Mg+Fe	4.1	2.2	3.1	2.6	3.2	3.6	3.2
Al/Ti	7.0	8.2	8.2	7.9	9.1	8.3	8.7

Table 8. Raw XRF data of the Ariel samples

	M6	M14	M16	M19	M23	M28
SiO2	95.69	94.39	95.85	95.83	95.96	95.47
TiO2	0.13	0.06	0.09	0.07	0.04	0.09
Al2O3	0.90	0.73	0.91	0.73	0.49	0.85
Fe2O3	0.42	0.29	0.45	0.27	0.17	0.25
MnO	0.002	0.001	0.002	0.002	0.002	0.002
MgO	0.31	0.36	0.53	0.19	0.18	0.43
CaO	0.08	0.33	0.06	0.08	0.09	0.07
Na2O	0.58	0.47	0.59	0.95	0.88	0.92
K2O	0.306	0.213	0.250	0.176	0.101	0.178
P2O5	0.009	0.005	0.005	0.009	0.005	0.007
SO3	0.014	0.031	0.021	0.014	0.014	0.002
LOI	1.05	1.48	1.38	1.26	1.21	1.49
Total	99.49	98.37	100.14	99.58	99.15	99.77
As	1.3	0.3	0.5	2.1	0.4	1.5
Ba	57.9	50.3	53.8	43.6	27.6	51.4
Ce	21.3	12.0	11.4	10.2	9.8	18.5
Co	<1.0	1.6	2.5	<1.0	<1.0	<1.0
Cr	16.2	13.4	31.3	8.1	8.1	22.4
Cs	<1.2	<1.2	<1.3	<1.3	<1.2	<1.3
Cu	1.8	3.0	3.0	4.5	7.5	19.7
Ga	1.5	1.2	1.4	1.1	1.3	1.3
La	8.7	8.2	9.1	7.9	8.3	11.8
Mo	1.0	0.4	1.0	0.8	0.4	1.0
Nb	2.0	1.5	1.9	1.4	1.1	2.1
Nd	10.6	8.2	46.0	9.4	5.3	8.70
Ni	0.5	0.7	0.7	0.6	<0.4	<0.4
Pb	3.2	3.0	2.8	3.9	2.2	3
Rb	8.6	7.1	8.3	6.7	4.7	7.3

Sb	<0.8	<0.8	<0.8	<0.8	<0.7	0.9
Sc	1.0	1.0	1.6	<0.9	1	2.3
Se	<0.4	<0.4	<0.4	<0.4	<0.4	<0.4
Sn	<0.7	89.4	0.8	87.1	0.9	4.40
Sr	24.9	33.6	18.4	28.6	29.3	20.2
Th	1.3	0.9	0.9	0.8	0	1
U	0.5	0.4	0.7	0.5	0.4	0.1
V	15.6	8.1	19.9	41	9	13.9
W	<0.7	<0.7	<0.7	<0.7	<0.7	<0.7
Y	6.9	3.7	4.1	3.4	2.8	4.50
Zn	4.7	4.7	4.1	4.7	4.5	5.70
Zr	301	66.5	171.4	87.9	58.4	191.8
Si/Al	106.3	128.8	105.3	131.1	197.3	111.9
MgO/Al	0.3	0.5	0.6	0.3	0.4	0.50
CaO/Al	0.1	0.5	0.1	0.1	0.2	0.10
Ba/Al	64.3	68.6	59.1	59.7	56.8	60.3
Nb/Al	-	-	-	-	-	-
Nd/Al	-	-	-	-	-	-
Sr/Al	27.7	45.8	20.2	39.1	60.3	23.6
V/Al	17.3	11.1	21.9	56.1	18.5	16.2
Zr/Al	334.3	90.7	188.2	120.2	120.1	224.7
(Mg+Fe)/Al	0.8	0.9	1.1	0.6	0.7	0.8
Mg/Mg+Fe	1.4	1.3	1.4	1.3	1.2	1.2
Al/Ti	6.9	11.4	9.7	11.1	10.9	9.1

Table 9. Raw XRF data of the Al Wafa samples.

	BZ21	BZ25	BZ91	ALA6	BZ81	BZ64	BZ60	BZ46	BZ41	BZ37
SiO2	89.07	68.68	54.78	82.35	65.06	79.82	77.66	82.44	81.81	73.91
TiO2	0.09	0.28	0.05	0.16	0.12	0.08	0.07	0.12	0.12	0.17
Al2O3	0.90	2.54	0.35	0.90	0.87	0.60	0.52	0.79	0.93	1.35
Fe2O3	0.45	1.55	0.19	0.77	0.84	0.29	0.44	0.56	0.66	0.77
MnO	0.009	0.015	0.041	0.034	0.085	0.014	0.062	0.033	0.024	0.019
MgO	0.37	0.85	0.32	2.81	5.92	0.40	4.29	2.78	3.11	4.66
CaO	3.24	8.04	24.15	4.12	9.67	9.34	6.34	3.85	4.74	6.05
Na2O	1.35	4.58	0.05	0.87	0.77	0.29	0.10	1.26	0.17	1.06
K2O	0.223	0.892	0.140	0.458	0.444	0.153	0.258	0.284	0.382	0.453
P2O5	0.030	0.036	0.053	0.026	0.021	0.019	0.025	0.032	0.026	0.026
SO3	0.253	0.185	0.093	0.048	0.586	0.059	0.136	0.187	0.868	0.502
LOI	4.01	10.94	19.05	7.10	15.20	8.84	9.86	7.56	7.01	11.51
Total	99.99	98.58	99.27	99.66	99.58	99.90	99.76	99.89	99.84	100.48
As	<0.4	<0.4	1.4	<0.5	6.9	0.9	6.3	3.7	3.1	<0.4
Ba	40.2	115.8	188.1	665.1	111.6	15.2	53.3	55.1	36.7	42.7
Ce	11.3	21.0	10.1	5.8	17.5	9.9	15.7	14.4	8.9	9.9
Co	<1	3.9	2.8	<1.3	1.4	<1	1.7	4.3	1.4	<1.1
Cr	12.3	26	22.8	<0.7	24.4	7.8	15.6	22.1	13.3	4.5
Cs	<1.3	2.9	<1.5	<2	<1.4	<1.4	<1.4	<1.3	<1.4	<1.4
Cu	7.5	13.5	3.7	1.2	1.5	5.6	5.1	28.4	<0.4	1.4
Ga	1.7	2.9	1.4	0.7	1.4	2.0	1.1	1.2	0.8	1.2
La	6.2	10.5	5.9	4.6	7.5	4.0	6.7	6.4	7.2	5.1
Mo	0.9	1.6	1.6	1.7	1.6	1.5	1.6	1.2	1.3	1.2
Nb	1.8	5.4	2.1	1.2	2.6	3.1	2.2	2.3	1.5	1.5
Nd	8.4	11.2	8.9	7.6	10.2	5.5	7.9	9.8	7.0	7.5
Ni	1	5.9	<0.6	1.6	2.3	<0.5	1.5	2	1.6	1.3

Pb	2.9	5.9	4.0	4.0	5.4	2.5	4.1	3.0	3.4	3.3
Rb	6.2	24.1	4.8	10.4	9.8	7.2	7.4	8.9	9.8	10.8
Sb	0.9	<0.9	<1.0	<0.8	<0.8	<0.9	<0.8	<0.8	1.0	<0.9
Sc	2.1	3.0	9.9	2.3	3.1	1.7	2.1	1.8	2.0	2.4
Se	<0.4	<0.5	<0.6	<0.5	<0.5	<0.5	<0.5	<0.4	<0.5	0.6
Sn	1.5	3.2	<0.9	<0.7	<0.8	<0.8	<0.7	6.5	<0.7	2.9
Sr	31.1	57.3	124.1	46.5	147.6	31	56.5	44.0	64.6	50.8
Th	1.4	3.4	1.6	2.1	1.5	0.9	1.1	1.0	1.9	1.1
U	0.5	2.1	1.1	1.2	1.7	0.5	3.0	1.2	1.6	1.5
V	18.9	38.0	9.5	35.5	25.0	10.8	22.5	29.3	28.0	11.9
W	1	<0.9	<1.0	<0.8	<0.9	<0.8	<0.8	<0.8	<0.8	<0.8
Y	4	11.0	4.7	7.3	8.1	5.7	6.1	5.8	6.3	6.8
Zn	5.6	15.1	4.3	7.4	8.3	4.8	6.0	7.7	7.9	7.6
Zr	114.1	370.4	76.0	344.3	213.2	130.7	78.2	147.1	146.9	238.4
Si/Al	98.8	27.0	154.9	91.4	75.2	133.4	148.6	104.3	87.7	54.6
MgO/Al	0.4	0.3	0.9	3.1	6.8	0.7	8.2	3.5	3.3	3.4
CaO/Al	3.6	3.2	68.3	4.6	11.2	15.6	12.1	4.9	5.1	4.5
Ba/Al	44.6	45.6	1880.2	123.8	217.3	71.3	70.2	69.7	57.1	11.2
Sr/Al	34.5	22.6	350.8	51.5	170.6	51.8	108.2	55.6	69.3	37.6
V/Al	21	14.9	26.7	39.4	28.9	18	43	37.1	30	8.8
Zr/Al	126.5	145.8	214.8	382.0	246.4	218.4	149.7	186	157.5	176.1
(Mg+Fe)/Al	0.9	0.9	1.4	4.0	7.8	1.2	9	4.2	4	4
Mg/Mg+Fe	1.4	2.5	1.2	1.8	1.8	1.3	1.4	1.6	1.7	1.8
Al/Ti	10.1	9.1	7.0	7.5	5.5	8.1	8.0	6.7	7.5	7.1

Table 10. Raw XRF data of the Bir al Zallaf samples.

	BZ69	BZ61	BZ94
SiO2	82.22	69.05	64.79
TiO2	0.06	0.10	0.11
Al2O3	0.47	0.83	0.74
Fe2O3	0.38	0.72	0.43
MnO	0.047	0.003	0.008
MgO	2.09	0.78	0.53
CaO	3.01	0.16	3.80
Na2O	4.42	9.04	11.66
K2O	0.592	1.718	0.544
P2O5	0.013	0.050	0.015
SO3	0.620	2.289	0.395
LOI	3.28	7.39	6.53
Total	97.20	92.13	89.56
As	<0.4	4.4	<0.5
Ba	36.0	32.9	10.6
Ce	11.2	9.7	<4.5
Co	1.0	2.3	<0.9
Cr	38.6	19.1	11.7
Cs	<1.3	<1.2	<1.2
Cu	18.6	4.5	1.8
Ga	1.1	1.0	0.9
La	6.5	4.9	1.6
Mo	1.2	1.4	1.4
Nb	2.0	1.1	1.9
Nd	7.4	5.8	3.3
Ni	1.6	0.7	<0.6
Pb	3.0	4.4	2.2
Rb	10.8	6.5	7.6
Sb	<0.9	0.8	<1.0
Sc	1.6	<0.9	0.9
Se	0.9	<0.5	1.3
Sn	5.3	<0.8	<0.9
Sr	19.7	38.9	75.8
Th	1.3	1.0	0.6
U	1.2	2.0	1.2
V	34.0	19.8	7.9
W	<0.9	<0.8	<1.0
Y	5.5	5.0	4.1
Zn	7.7	5.7	4.7
Zr	186.6	64.3	171.8

Table 11. Raw XRF data of the BZ samples with poor totals and higher than usual Na₂O which were not reported in the main thesis.

Results: Magnetostratigraphy

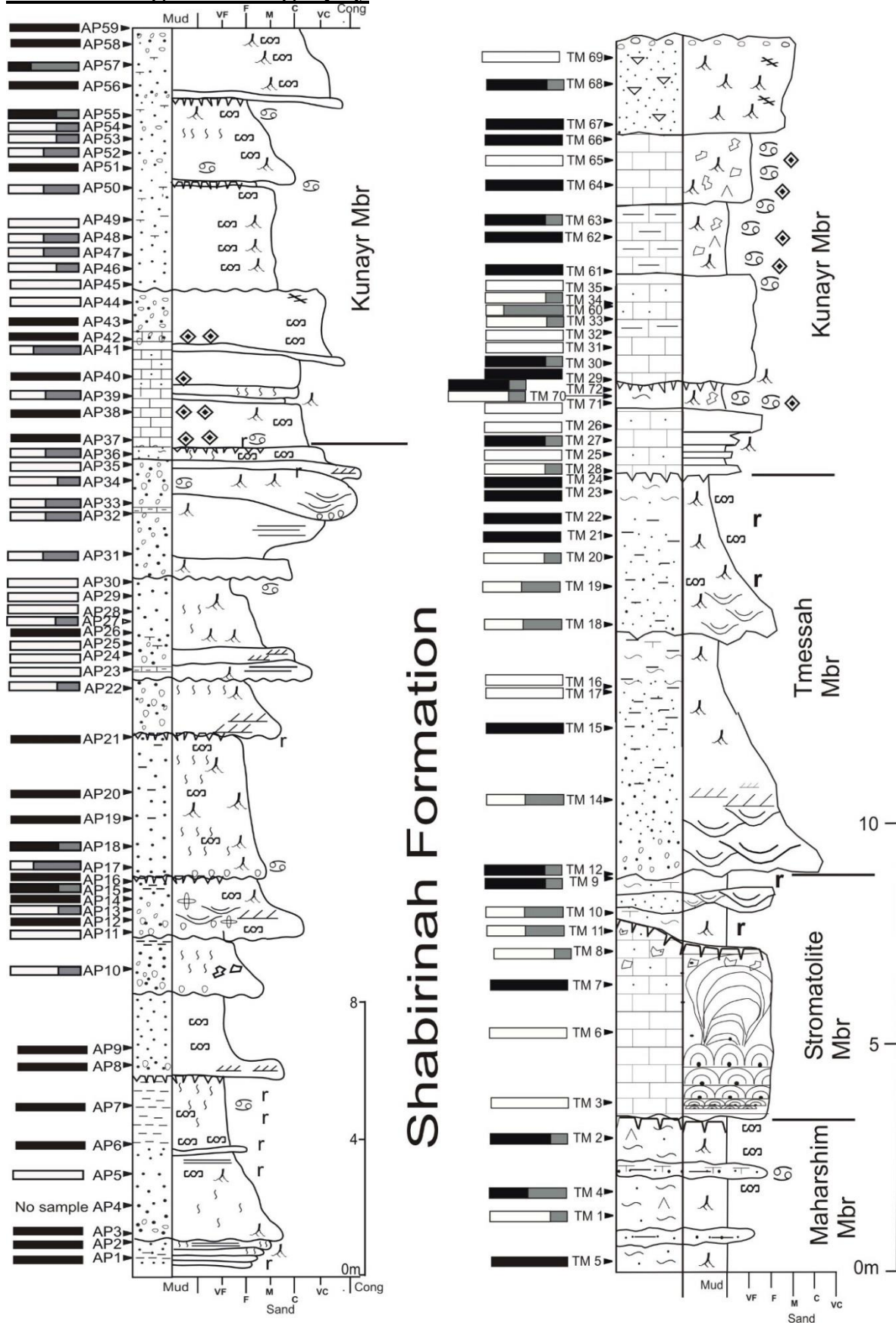


Figure 17. Section logs of AP and TM with the polarity of each horizon noted.

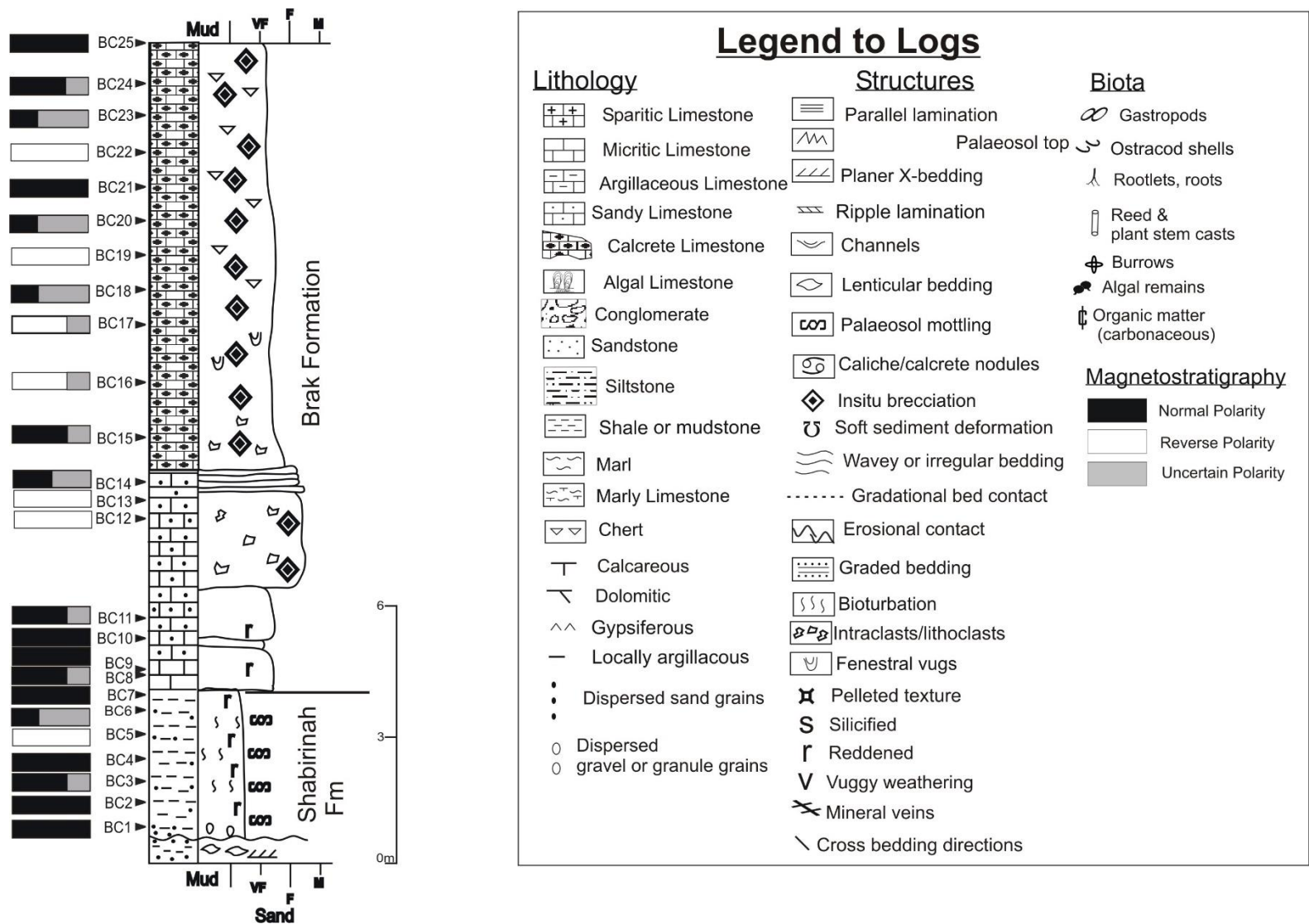


Figure 18. Section log of BC with the polarity of each horizon noted and the Key for each of the logs.

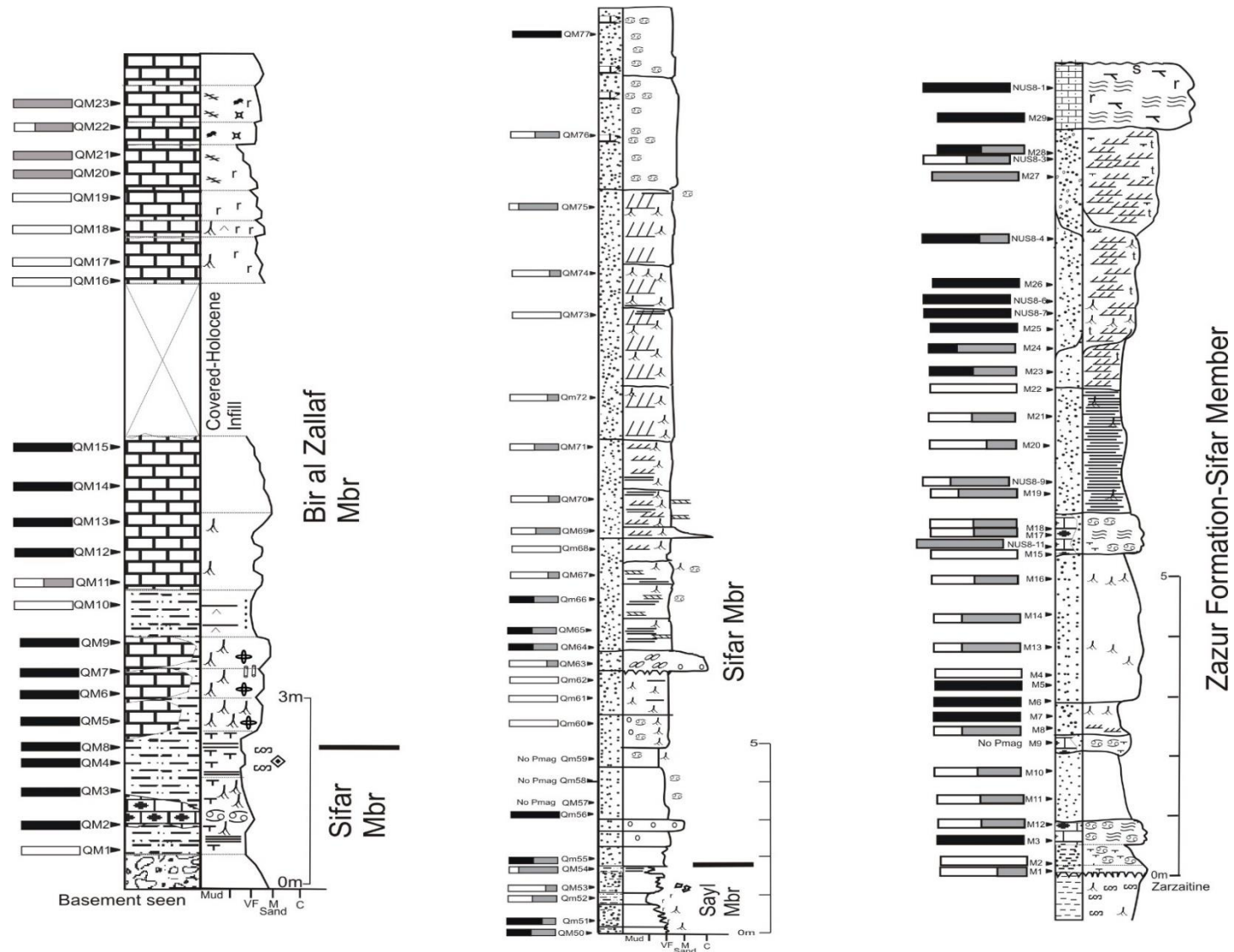


Figure 19. Logs of the QM1, QM2 and M sections with the polarity of each horizon noted.

Statistic	Description and comments
Delta (Δ)	$\Delta = (2 * \min(\text{CPL})) / (\text{APL} + \text{BPL}) - 1$, where CPL is the combined path length, or the total discordance between the start and end of the matched points (in multivariate space) when slotted together. APL is the individual path length through the GPTS chrons, and BPL is the individual path length through the matched data. The value of the CPL is controlled by the type of scaling and distance measure used, since this will control the magnitude of the discordance measured by CPL (see Thompson & Clark, 1989). The best slotting model of the many considered for each slotting run is that with the minimum CPL (hence $\min(\text{CPL})$), where the <i>min</i> indicates the search criteria. Δ is independent of the chosen distance measure and the units of measurements used, and is a measure of the ‘local-fit’ of the two sequences. If correctly scaled, Δ generally lies between zero and somewhere around 1.0; a small value of $\Delta \sim < 0.5$ indicates that Sequences A and B are interleaved or slotted together very well (Thompson & Clark, 1989; Thompson et al. 2012). Generally the Δ value expresses the goodness of fit well with datasets which have a low degree of inter-level variability (i.e. smoothly varying wiggles). In contrast, the parameterisation of the GPTS tends to give high variability between the chrons, since the chron durations have a near random distribution (Lowrie & Kent, 2004).
N-CSTAT	The normalised CSTAT. A measure of the robustness of the fit, based on a sensitivity analysis. Generally smaller N-CSTAT values are associated with better, more robust slotting. The CSTAT value is a sensitivity statistic, which is the reduction in the CPL when a particular chron in the GPTS is omitted (i.e. a test of the sensitivity of the model to missing chrons in the GPTS). i.e. each GPTS chron has a CSTAT value. The N-CSTAT value is the average CSTAT value divided by the average PPL.
%PPL offset	The PPL is the partial path length, or the discordance between adjacent points or (path length of sub-segments of the total CPL). %PPL is simply the sum of the absolute discordance between those matched chrons and magnetozones in the GPTS and matching sequence, expressed as a percentage of the CPL. Better matches should have lower %PPL in any set of slotted models.
R_c	The congruence coefficient a measure of the similarity (or association) of the two datasets. It measures the similarity of two configurations by computing a cosine between matrices of observations. R_c has a range like regression coefficients (i.e. up to +1 for positive association), but is not a regression coefficient (see Abdi, 2010). Broadbent & Elmore, (1987) provide a method to test if R_c is significantly different from zero.
RV_2	The RV coefficient is a measure of the similarity (or association) of the two datasets. It is a matrix correlation coefficient. It corresponds to a squared cosine and therefore the RV coefficient takes values between 0 and 1 (Abdi, 2010). The RV_2 coefficient is a modification of the RV coefficient (taking values -1 to +1) according to Smilde et al. (2009) and is a more robust measure of common information contained in the two datasets.
RV_{std}	This is the standardized RV coefficient of Josse et al. (2008) (and Z_{RV} statistic of Abdi 2007) which allows an approximate evaluation if the RV coefficient is significantly different from zero. Values of $RV_{\text{std}} > 1.65$ suggest the RV value reflects a significant association between the two datasets. However, the tests in Josse et al. (2008) suggest RV_{std} should be > 2 for an approximate 95% confidence value.
Association probability, P_a	This is derived from the log-transformed Z statistic in Josse et al. (2008), which is tested against a standard normal distribution. This approximation evaluates the probability ($p = 1 - P_a$) that the RV coefficient is significantly different from zero. i.e. Larger values of the association probability, P_a indicate a better match between the datasets. RV_{std} and P_a do not

	indicate the significance of the match, but only the probability of some association between the datasets.
N_m/N_a	N_m = number of chrons missing from the GPTS in the magnetostratigraphic match. N_a = number of additional magnetozone in the matched succession not present in the GPTS. These numbers should be at a minimum for a good match, but will depend on the sampling rate of the GPTS. N_a values ≥ 1 imply spurious magnetozones in the section not present in the GPTS.
D_m/D_{max}	D_m = mean duration (in kyrs) of chrons missing from the GPTS in the match. D_{max} = duration of longest chron missing from the GPTS in the match (in kyrs). These give an idea of the missing time represented in the match.
Spearman coefficients (R_s)	These are the rank correlation coefficients between the values of the two dataset of the duration, polarity bias, ω_2 and $\text{Log}_e(r_i)$ used in the sequence slotting procedure (using the correlation model given by the sequence slotting). Clearly larger values of R_s would be expected for better matches. The R_s allows a comparison of which are the stronger control variables in the matching process. In this case, for both composite models the polarity bias, and $\text{Log}_e(r_i)$ seem to be generally stronger than duration and ω_2 .
Polarity Bias parameter	For chron/magnetozone i , the polarity bias = $\sum_{j=i-1}^{j=i+1} d_j p_j / \sum_{j=i-1}^{j=i+1} d_j$, where d_j is the duration of the chron or magnetozone, and p_j is the polarity (values -1 or +1) of the chron or magnetozone. It ranges from intervals in which reverse polarity dominates (bias < -0.5) to intervals in which normal polarity dominates (bias $> +0.5$).
Shearmans spacing statistic ω_2	$\omega_2 = \frac{0.5 * \sum_{j=i-1}^{j=i+1} \text{abs}(\bar{d} - d_j)}{\sum_{j=i-1}^{j=i+1} d_j}$, where d_j is the chron or magnetozone duration, and \bar{d} is the mean duration in the interval $i-1$ to $i+1$ (see Olson et al. 2014). i.e. ω is a measure of how much the durations deviate from their average length.

Table 12. Explanation of statistics derived from sequence slotting and the parameters used in sequence slotting from Hounslow et al. (2017).

Option 1	Duration=1, Polarity Bias=1, ω_2 =1, $\text{Log}_e(r_i)$ =1, Polarity=5
Option 2	Duration=1, Polarity Bias=1, ω_2 =0.33 $\text{Log}_e(r_i)$ =0.33, Polarity=5
Option 3	Duration=0.33, Polarity Bias=0.33, ω_2 =1, $\text{Log}_e(r_i)$ =1, Polarity=5
Option 4	Duration=1, Polarity Bias=0.33, ω_2 =0.33, $\text{Log}_e(r_i)$ =1, Polarity=5

Table 13. Weighting options of the 5 variables used in sequence slotting on the ZF composites.

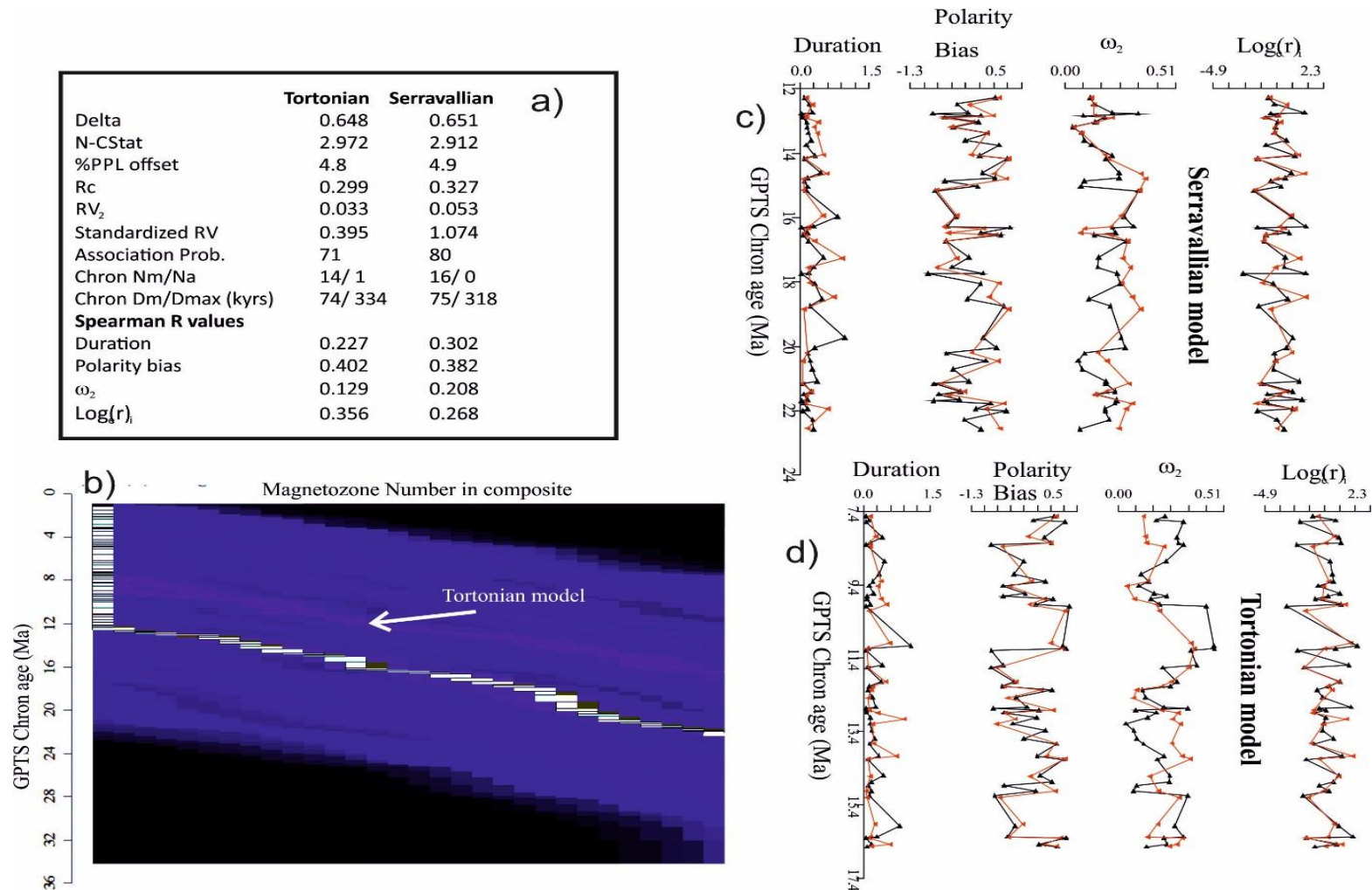


Figure 21. Composite-A (SHF/BKF) sequence slotting output. a) the statistical summary of the Tortonian and Serravallian correlation models. b) The H-matrix plot, where the brighter blue bands correspond to alternative correlation models. The mostly likely model (ending in Serravallian) is shown as the white boxes across the plot, with y-axis height corresponding to GPTS chron duration. The band corresponding to the Tortonian model is arrowed. The x-axis on this plot is the magnetozone number. c) and d) The input data to the slotting model, plotted against chron age for the two correlation options.

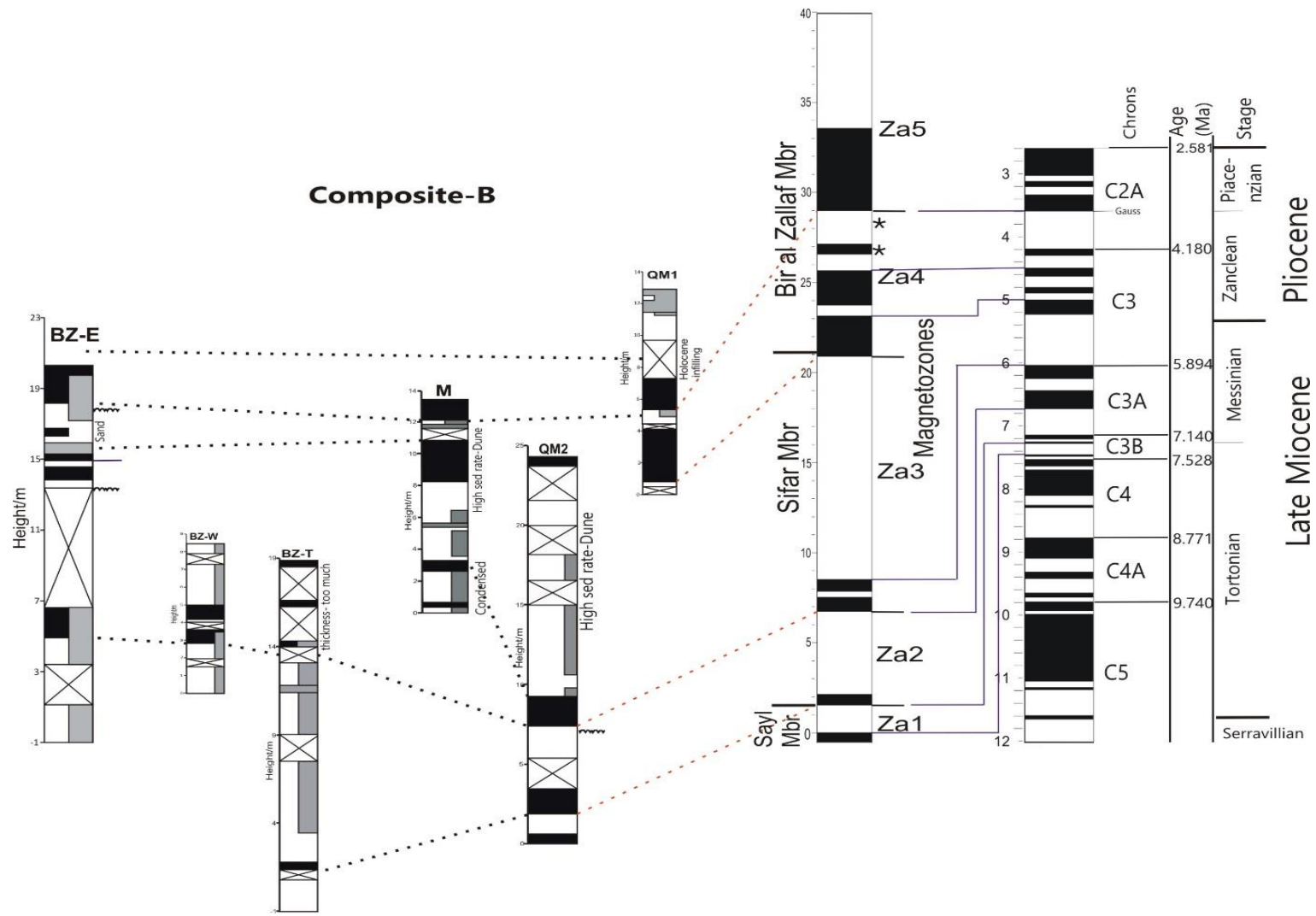


Figure 22. Composite-B (Messinian-Zanclean model) magnetic polarity stratigraphy with the final age model on the right. Chron correlation lines (purple) to the GPTS (Ogg, 2012) derived from sequence slotting. Note the * next to the composite represents the magnetozones (Za4r.an/Za4r.ar) not included in the sequence slotting model.

References

- Abdeldayem, A.L. (1996) Palaeomagnetism of some Miocene rocks, Qattara depression, Western Desert, Egypt. *Journal of African Earth Sciences*. **22**:525-533
- Abdel-Karim, A.M., Ramadan, E.M. and Embashi, M.R. (2013) Multiphase Alkaline Basalts of Central Al-Haruj Al-Abyad of Libya: Petrological and Geochemical Aspects. *Journal of Geological Research*. **2013**: 1-12
- Abdul Aziz, H., Di Stefano, A., Foresi, L.M., Hilgen, F.J., Iaccrino, S.M., Kuiper, K.F., Lirer, F., Salvatorini, G. and Turco, E. (2008) Integrated stratigraphy and $^{40}\text{Ar}/^{39}\text{Ar}$ chronology of early Middle Miocene deposits from DSDP Leg 42A, Site 372 (Western Mediterranean). *Palaeogeography, Palaeoclimatology, Palaeoecology*. **257**: 123-138
- Abdullah, M. (2010). Petrography and Facies of the Al- Mahruqah Formation in the Murzuq Basin, SW Libya. Unpublished PhD Thesis, University of Hamburg.
- Abell, P.I. and Hoelzmann, P. (2000) Holocene palaeoclimates in northwestern Sudan: stable isotope studies on molluscs. *Global and Planetary Change*. **26**:1-12
- Ade-Hall, J.M., Reynolds, P.H., Dagley, P., Musset, A.G., Hubbard, T.B., Klitzsch, E. (1974) Studies of North African Cenozoic volcanic areas: I-Haruj Assuad, Libya. *Canadian Journal of Earth Sciences*. **11**:998–1006.
- Ade-Hall, J.M., Reynolds, P.H., Dagley, P., Mussett, A.E., Hubbard, T.P. (1975) Geophysical studies of North African Cenozoic volcanic areas: II. Jebel Soda, Libya. *Canadian Journal of Earth Sciences*. **12**:1257–1263.
- Ageena, I., Macdonald, N and Morse, A.P. (2012) Variability of minimum temperature across Libya (1945-2009). *International Journal of Climatology*. **33**:641-653
- Alonso-Zarza, A.M., Calco, J.P. and Garcia del Cura, M.A. (1992) Palustrine sedimentation and associated features-grainification and pseudo-microkarst-in the Middle Miocene (Intermediate Unit) of the Madrid Basin, Spain. *Sedimentary Geology*. **76**:43-61
- Alonso-Zarza, A.M and Calvo, J.P. (2000) Palustrine sedimentation in an episodically subsiding basin: the Miocene of the northern Teruel Graben (Spain). *Palaeogeography, Palaeoclimatology, Palaeoecology*. **160**:1-21
- Alonso-Zarza, A. M. (2003). Palaeoenvironmental significance of palustrine carbonates and calcretes in the geological record. *Earth-Science Reviews*. **60**:261-298.
- Alonso-Zarza, A.M., Melendez, A., Martin-Garcia, R., Herrero, M.J. and Martin-Perez, A. (2012) Discriminating between tectonism and climate signatures in palustrine deposits: Lessons from the Miocene of the Teruel Graben, NE Spain. *Earth Science Reviews*. **113**: 141-160

- Aly, G.A.M. (2015) Mineralogical and geochemical aspects of the Miocene laterite, Sharm Lollia area, South Eastern Desert, Egypt. *Arabian Journal of Geoscience*. **8**: 10399-10418
- Amit, H., Leonhardt, R. and Wicht, J. (2010) Polarity Reversals from Palaeomagnetic Observations and Numerical Dynamo Simulations. *Space Science Reviews*. **155**: 293-335
- Amrouni, K.S. and El-Hawat, A.S. (2015) Sedimentology and Sequence Stratigraphy of the Upper Miocene Carbonate-Evaporite Sequence of the Wadi Yunis Member, Al-Khums Formation, Sirt Basin, Libya. *Gulf Coast Association of Geological Societies Transactions*. **65**: 9-19
- Anderson, N.J. and Leng, M. J. (2004) Increased aridity during the early Holocene in West Greenland inferred from stable isotopes in laminated lake-deposits. *Quaternary Science Reviews*. **23**: 841-849
- Archaeomagnetism-Bradford University. Accessed: March 2013.
<http://www.brad.ac.uk/archaeomagnetism/archaeomagnetic-dating/introduction-to-archaeomagnetism/magnetic-field/>
- Arenas, C., Cabrera, L., Ramos, E. (2007) Sedimentology of tufa facies and continental microbialites from the Palaeogene of Mallorca Island (Spain). *Sedimentary Geology*. **197**:1-27
- Arenas-Abad, C., Vazquez-Urbez, M., Pardo-Tirapu, G. and Sancho-Marcen, C. (2010) Fluvial and Associated Carbonate Deposits. *Developments in Sedimentology*. 61:133-175
- Armenteros, I. and Daley, B. (1998) Pedogenic modification and structure evolution in palustrine facies as exemplified by the Bembridge Limestone (Late Eocene) of the Isle of Wight, southern England. *Sedimentary Geology*. **119**: 275-295
- Armitage, S.J., Drake, N.A., Stokes, S., El-Hawat, A., Salem, M.J., White, K., Turner, P. and McLaren, S.J. (2007) Multiple phases of North African humidity recorded in lacustrine deposits from the Fazzan Basin, Libyan Sahara. *Quaternary Geochronology*. **2**:181–186
- Aziz, A. (2000) Stratigraphy and hydrocarbon potential of the Lower Palaeozoic succession of License NC-115, Murzuq Basin, SW Libya. In: *Geological Exploration in the Murzuq Basin* (Eds. M.A. Sola and D. Worsley). Elsevier: Amsterdam pp349-368
- Backman, J., Schneider, D.A., Rio, D. and Okada, H. (1990) Neogene low-latitude magnetostratigraphy from site 710 and revised age estimates of Miocene nanofossil datum events. *Proceedings of the Ocean Drilling Program*. **115**:271-276
- Baioumy, H., Kayanne, H., Tada, R. (2010) Record of Holocene aridification (6000-7000 BP) in Egypt (NE Africa): Authigenic carbonate minerals from laminated deposits in Lake Qarun. *Quaternary International*. **245**:170-177
- Bardintzeff, JM., Deniel, C., Guillou, H., Platevoet, B., Telouk, P. and Oun, K.M. (2012) Miocene to recent alkaline volcanism between Al Haruj and Waw and Namous (southern Libya). *International Journal of Earth Sciences*. **101**: 1047-1063

- Barr, F.T. and Walker, B.R. (1973) Late Tertiary channel system in Northern Libya and its implications on Mediterranean sea level changes. In: Ryan, W.B.F., Hsu, K.J. et al. (Eds.), *Init. Rep. DSDP 13*:1244-1251.
- Barton, C.E. and McElhinny, M.W. (1981) A 10,000 yr geomagnetic secular variation record from three Australian maars. *Geophys. J. R. astr. Soc.* **67**: 465-485
- Bellair, M.P. (1944) Sur l'âge du Calcaire de Mourzouk (Fezzan). *Compte Rendus Hebdomadaires des Seances de l'Academie des Sciences.* **219**: 490-491
- Benammi, M., Calvo, M., Prevot, M. and Jaeger, J-J. (1996) Magnetostratigraphy and palaeontology of Ait Kandoula Basin (High Atlas, Morocco) and the African-European late Miocene terrestrial fauna exchanges. *Earth and Planetary Science Letters.* **145**:15-29
- Benammi, M. and Jaeger, J-J. (2001) Magnetostratigraphy and palaeontology of the continental Middle Miocene of the Ait Kandoula Basin, Morocco. *Journal of African Earth Sciences.* **33**:335-348
- Benfield, A.C. and Wright, E.P. (1980) Post-Eocene sedimentation in the eastern Sirt Basin, Libya. In: Salem, M.J., Busrewil, M.T. (Eds.), *The Geology of Libya*, vol. 2. Academic Press, London, pp. 463–500.
- Berggren, W.A., Kent, D.V., Swisher III, C.C. and Aubry, MP. (1995) A revised Cenozoic geochronology and chronostratigraphy. *SEPM Special Publication.* **54**: 129-212
- Beyer, C. and Lundschieen, B.A. (2000) Magnetostratigraphy as a Potential Tool for Correlation in the Murzuq Basin Illustrated by an Example from the Triassic Snorre Reservoir in the Northern North Sea. In: Sola, M.A. and Worsley, D. (Eds) *Geological Exploration in Murzuq Basin*. Elsevier Science: New York. pp17-29
- Binsariti, A and Saeed, F.S. (2000) Groundwater Salinity Variations in the Cambro-Ordovician Aquifer of Eastern Jabal al Hasawnah, the Great Man-made River Project, Libya. In: *Geological Exploration in the Murzuq Basin* (Eds. M.A. Sola and D. Worsley). Elsevier: Amsterdam pp1-16
- Bischoff, J.L. and Fitzpatrick, J.A. (1991) U-series dating of impure carbonates: An isochron technique using total-sample dissolution. *Geochemica et Cosmochimica Acta.* **55**: 543-554
- Blott, S. (2010) GRADISTAT, version 8.0. Associated article-Blott, S.J. and Pye, K. (2001) GRADISTAT: a grain size distribution and statistics package for the analysis of unconsolidated deposits. *Earth Surface Processes and Landforms.* **26**: 1237-1248
- Boggs, S Jr. (2009) *Petrology of Sedimentary Rocks*. Second Edition. Cambridge University Press:UK
- Boisserie, JR., Brunet, M., Andossa, L. and Vignaud, P (2003) Hippopotamids from the Djurab Pliocene faunas, Chad, Central Africa. *Journal of African Earth Sciences.* **36**: 15-27

- Borradaile, G. (1999) Viscous remanent magnetisation of high thermal stability in limestone. In Tarling, D.H. and Turner, P. (eds) *Palaeomagnetism and Diagenesis in deposits. Geological Society London, Special Publication*. **151**:27-42
- Borradaile, G. and Jackson, M. (2004) Anisotropy of magnetic susceptibility (AMS): magnetic petrofabrics of deformed rocks. *Geological Society Special Publications*. **238**: 299-360
- Bradak, B. (2009) Application of anisotropy of magnetic susceptibility (AMS) for the determination of palaeo-wind directions and palaeoenvironment during the accumulation period of Bag Tephra, Hungary. *Quaternary International*. **198**:77-84
- Brook, G.A., Raisback, L.B. and Marais, E. (2011) Reassessment of carbonate ages by dating both carbonate and organic material from an Etosha Pan (Namibia) stromatolite: Evidence of humid phases during the last 20 ka. *Quaternary International*. **229**: 24-37
- Brooks, N., Drake, N.A., McLaren, S.J. and White, K. (2003) Studies of Geography, Geomorphology, Environment and Climate Change. In: Mattingley, (ed.) *The Archaeology of Fazzan. Vol. 1 Synthesis*. Society for Libyan Studies/Department of Antiquities, London and Tripoli, pp. 37-74
- Brooks, N., Chiapello, I., Di Lernia, S., Drake, N., Legrand, M., Moulin, C. and Prospero, J. (2005) The Climate-Environment-Society Nexus in the Sahara from Prehistoric Times to the Present Day. *The Journal of North African Studies*. **10**:253-292
- Bui, E.N., Mazzulo, J.M. and Wilding, L.P. (1989) Using quartz grain size and shape analysis to distinguish between aeolian and fluvial deposits in the Dallol Bosso of Niger (West Africa). *Earth Surface Processes and Landforms*. **14**: 157-166
- Burke, K. and Wells, G.L. (1989) Trans-Africa drainage system of the Sahara: Was it the Nile? *Geology*. **17**: 743-747
- Burrough, S.L. and Thomas, D.S.G. (2009) Geomorphological contributions to palaeolimnology on the African continent. *Geomorphology*. **103**:285-298
- Busche, D. (1980) On the Origin of the Msak Mallat and Hamadat Manghini Escarpment. In: *The Geology of Libya*, Salem, M.J. and Busrewil, M.T. (Eds). Academic Press: London. III, pg837-848
- Busrewil, M.T. and Esson, J. (1991) Chronology and Composition of the Igneous Rocks of Jabal as Sawda. In: Salem, M.J., Busrewil, M.T., Ben Ashour, A.M. (Eds.), *The Geology of Libya*, vol. 7. Elsevier, Amsterdam, pp2599-2604
- Busrewil, M.T. and Oun, K.M. (1991) Geochemistry of the Tertiary alkaline rocks of Jabal al Hasawinah, west central Libya. In: Salem, M.J., Busrewil, M.T., Ben Ashour, A.M. (Eds.), *The Geology of Libya*, vol. 7. Elsevier, Amsterdam, pp2587–2598.

- Bustillo, M.A. and Alonso-Zarza, A.M. (2007) Overlapping of pedogenesis and meteoric diagenesis in distal alluvial and shallow lacustrine deposits in the Madrid Miocene Basin, Spain. *Sedimentary Geology*. **198**: 255-271
- Butler, R.F. (1982) Magnetic Mineralogy of Continental Deposits, San Juan, New Mexico and Clark's Fork Basin, Wyoming. *Journal of Geophysical Research*. **87**: 7843-7852
- Butler, R.F. (1992) *Palaeomagnetism: Magnetic Domains to Geologic Terranes*. Blackwell Scientific Publications. Electronic Version (2004) Available from: <http://www.iag.usp.br/~agg110/moddata/GEOMAGNETISMO/butler-paleomagnetism-book.pdf>
- Butler, R.W.H., McClelland, E. and Jones, R.E. (1999) Calibrating the duration and timing of the Messinian salinity crisis in the Mediterranean: linked tectonoclimatic signals in thrust-top basins of Sicily. *Journal of the Geological Society*. **156**: 827-835
- Cande, S.C. and Kent, D.V. (1992) A New Geomagnetic Polarity Time Scale for the Late Cretaceous and Cenozoic. *Journal of Geophysical Research*. **97**: 917-951
- Cande, S.C. and Kent, D.V. (1995) Revised calibration of the geomagnetic polarity timescale for the Late Cretaceous and Cenozoic. *Journal of Geophysical Research*. **100**: 6093-6095
- Candy, I., Black, S., Sellwood, B.W. and Rowan, J.S. (2003) Calcrete profile development in Quaternary alluvial sequences, southeast Spain: Implications for using calcretes as a basis for landform chronologies. *Earth Surface Processes and Landforms*. **28**: 169-185
- Candy, I., Black, S. and Sellwood, B.W. (2004) Quantifying time scales of pedogenic calcrete formation using U-series disequilibria. *Sedimentary Geology*. **170**: 177-187
- Candy, I., Black, S. and Sellwood, B.W. (2005) U-series isochron dating of immature and mature calcretes as a basis for constructing Quaternary landform chronologies for the Sorbas basin, southeast Spain. *Quaternary Research*. **64**: 100-111
- Cane, M.A. and Molnar, P. (2001) Closing of the Indonesian seaway as a precursor to east African aridification around 3-4 million years ago. *Nature*. **411**: 157-162
- Casanova, J. and Hillaire-Marcel, C. (1993) Carbon and Oxygen Isotopes in African Lacustrine Stromatolites: Palaeohydrological Interpretations. *Geophysical Monograph*. **78**: 123-133
- Castaneda, I.S., Mulitza, S., Schefub, E., Lopes dos Santos, R.A., Sinninghe Damste, J.S. and Schouten, S. (2009) Wet phases in the Sahara/Sahel region and human migration patterns in North Africa. *Proceedings of the National Academy of Sciences*. **106**: 20,159-20,163
- Cerling, T.E. (1984) The stable isotopic composition of modern soil carbonate and its relationship to climate. *Earth and Planetary Science Letters*. **71**: 229-240

- Cerling, T.E., Wang, Y., and Quade, J. (1993) Expansion of C4 ecosystems as an indicator of global ecological change in the late Miocene. *Letters to Nature*. **361**: 344-345
- Cerling, T.E., Harris, J.M., MacFadden, B.J., Leakey, M.G., Quadel, J., Eisenmann, V. and Ehleringer, J.R. (1997) Global vegetation change through the Miocene/Pliocene boundary. *Nature*. **389**: 153-158
- Christeleit, E.C., Brandon, M.T. and Zhuang, G. (2015) Evidence for deep-water deposition of abyssal Mediterranean evaporites during the Messinian salinity crisis. *Earth and Planetary Science Letters*. **427**: 226-235
- Cioppa, M.T., Karistrom, E.T., Irving, E. and Barendregt, R.W. (1995) Palaeomagnetism of tills and associated palaeosols in southwestern Alberta and northern Montana: evidence for Late Pliocene-Early Pleistocene glaciations. *Canadian Journal of Earth Science*. **32**: 555-564
- Clark, R.M. (1985). A FORTRAN program for constrained sequence-slotting based on minimum combined path length. *Computers and Geosciences*. **11**:605–617.
Link to CPLSLOT Programme:
<http://www.lancaster.ac.uk/staff/hounslow/resources/software/cplslot.htm>
- Clement, B.M and Robinson, F. (1986) The Magnetostratigraphy of Leg 94 Deposits. In: Ruddiman, W.R., Kidd, R.B., Thomas, E. et al (Eds), Initial Results of the Deep Sea Drilling Program, 94. Pp635-950
- Clement, B.M. (2000) Assessing the fidelity of palaeomagnetic records of geomagnetic reversal. *Phil. Trans. R. Soc. Lond. A*. **358**: 1049:1064
- Colin, C., Siani, G., Liu, Z., Blamart, D., Skonieczny, C., Zhao, Y., Bory, A., Frank, N., Duchamp-Alphonse, S., Thil, F., Richter, T., Kissel, C. and Gargani, J. (2014) Late Miocene to early Pliocene climate variability off NW Africa (ODP Site 659). *Palaeogeography, Palaeoclimatology, Palaeoecology*. **401**: 81-95
- Collinson, J., Mountney, N. and Thompson, D. (2006) *Sedimentary Structures*. Terra Publishing: England
- Collomb, G.R. (1962) Étude géologique du Jebbel Fezzan et de sa bordure paleozoïque. – Notes et mémoires. *Compagnie Française des Pétroles* **1**: 5-35
- Contoux, C., Jost, A., Ramstein, G., Sepulchre, P., Krinner, G. and Schuster, M. (2013) Megalake Chad impact on climate and vegetation during the late Pliocene and the mid-Holocene. *Climate of the Past*. **9**: 1417-1430
- Coster, P., Benammi, M., Mahboubi, M., Tabuce, R., Adaci, M., Marivaux, L., Bensalah, M., Nahboubi, S., Mahboubi, A., Mebrouk, F., Maameri, C. and Jaeger, JJ. (2012) Chronology of the Eocene continental deposits of Africa: Magnetostratigraphy and biostratigraphy of the El Kohol and Glib Zegdou Formations, Algeria. *Geological Society of America*. **124**: 1590-1606

- Cox, A., Doell, R.R. and Dalrymple, G.B. (1964) Reversals of the Earth's Magnetic Field. *Science*. **144**: 1537-1543
- Cremaschi, M and Trombino, L. (1998) The palaeoclimatic significance of palaeosols in Southern Fezzan (Libyan Sahara): morphological and micromorphological aspects. *Catena*. **34**: 131-156
- Cremaschi, M. and di Lernia, S. (1999) Holocene Climatic Changes and Cultural Dynamics in the Libyan Sahara. *African Archaeological Review*. **16**:211-238
- Cremaschi, M. (2001) Holocene climatic changes in an archaeological landscape: The case study of Wadi Tanezzuft and its drainage basin (SW Fezzan, Libyan Sahara). *Libyan Studies*. **32**:3-28
- Cvetkovic, V., Toljic, M., Ammar, N.A., Rundic, L. and Trish, K.B. (2010) Petrogenesis of the eastern part of the Al Haruj basalt (Libya). *Journal of African Earth Sciences*. **58**: 37-50
- Davidson, L., Beswetherick, S., Craig, J. Eales, M., Fisher, A., Himmali, A., Jho, J., Mejrab, B. and Smart, J. (2000) The structure, stratigraphy and petroleum geology of the Murzuq Basin, southwest Libya. In: *Geological Exploration in the Murzuq Basin* (Eds. M.A. Sola and D. Worsley). Elsevier: Amsterdam pp295-320.
- Dearing, J.A., Livingstone, I.P., Bateman, M.D. and White, K. (2001) Palaeoclimate records from OIS 8.0-5.4 recorded in loess-palaeosol sequences on the Matmata Plateau, southern Tunisia, based on mineral magnetism and new luminescence dating. *Quaternary International*. **76/77**: 43-56
- Deenen, M.H.L., Langereis, C.G., van Hinsbergen, D.J.J. and Biggin, A.J. (2011) Geomagnetic secular variation and the statistics of palaeomagnetic directions. *Geophysical Journal International*. **186**: 509-520
- de Heinzelin, J. and El-Arnauti, A. (1987) The Sahabi Formation and related deposits. In: Boaz, N.T., El-Arnauti, A., Gaziry, A.W., de Heinzelin, J., Boaz, D.D. (Eds.), *Neogene Paleontology and Geology of Sahabi, Libya*. Liss,: New York. pg1-21
- Demko, T.M., Currie, B.S., Nicoll, K.A. (2004) Regional palaeoclimatic and stratigraphic implications of palaeosols and fluvial/overbank architecture in the Morrison Formation (Upper Jurassic), Western Interior, USA. *Sedimentary Geology*. **167**: 115-135
- deMenocal, P.B. (1995) Plio-Pleistocene African Climate. *Science*. **270**: 53-59
- deMenocal, P., Ortiz, J., Guilderson, T., Adkins, J., Sarnthein, M., Baker, L., and Yarusinsky, M. (2000) Abrupt onset and termination of the African Humid Period: rapid climate responses to gradual insolation forcing. *Quaternary Science Reviews*. **19**: 347-361

- Deniel, C., Vincent, P.M., Beauvilain, A. and Gourgaud, A. (2015) The Cenozoic volcanic province of Tibesti (Sahara of Chad): major units, chronology, and structural features. *Bulletin of Volcanology*. **77**: 1-21
- Deng, C., Liu, Q., Wang, W. and Liu, C. (2007) Chemical overprint on the natural remanent magnetisation of a subtropical red soil sequence in the Bose Basin, southern China. *Geophysical Research Letters*. **34**: 1-7
- Derder, M.E.M., Henry, B., Merabet, N., Bayou, B. and Amenna, M. (2001) Palaeomagnetism of the Liassic member of the Zarzaitine Formation (stable Sahran cration, Illizi basin, Algeria). *Annali di Geofisica*. **44**: 995-1010
- de Wet, C.B., Godfrey, L. and de Wet, A.P. (2015) Sedimentology and stable isotopes from a lacustrine-to-palustrine limestone deposited in an arid setting, climatic and tectonic factors: Miocene-Pliocene Opache Formation, Atacama Desert, Chile. *Palaeogeography, Palaeoclimatology, Palaeoecology*. **426**: 46-67
- di Cesare, F., Franchino, A. and Sommaruga, C. (1963) The Pliocene-Quaternary of Giarabub Erg region. *Revue de l'Institut Francais du Petrole*. **18**: 1344-1362
- Dinares-Turell, J. and Dekkers, M.J. (1999) Diagenesis and remanence acquisition in the Lower Pliocene Trubi marls at Punta di Maiata (southern Sicily): palaeomagnetic and rock magnetic observations. In: Tarling, D. H. and Turner, P. (eds) Palaeomagnetism and Diagenesis in Deposits. *Geological Society, London, Special Publications*, **151**: 53-69
- Di Stefano, C., Ferro, V. and Mirabile, S. (2010) Comparisons between grain-size analyses using laser diffraction and sedimentation methods. *Biosystems Engineering*. **106**:205-215
- Djamali, M., Soulie-Marsche, I., Esu, D., Gliozzi, E. and Okhravi, R. (2006) Palaeoenvironment of Late Quaternary lacustrine-palustrine carbonate complex: Zarand Basin, Saveh, central Iran. *Palaeogeography, Palaeoclimatology, Palaeoecology*. **237**: 315-334
- Do Couto, D., Popescu, SP., Suc, JP., Melinte-Dobrinescu, M.C., Barhoun, N., Gorini, C., Jolivet, L., Poort, J., Jouannic, G. and Auxietre, JL. (2014) Lago Mare and the Messinian Salinity Crisis: Evidence from the Alboran Sea (S. Spain). *Marine and Petroleum Geology*. **52**: 57-76
- Doell, R.R and Dalrymple, G.B. (1966) Geomagnetic Polarity Epochs: A New Polarity Event and the Age of the Brunhes-Matuyama Boundary. *Science*. **152**: 1060-1061
- Domaci, L., Roehlich, P. and Bosak, P. (1991) Neogene to Pleistocene continental deposits in Northern Fazzan and Central Sirt basin. In: M.J. Salem and M.N. Belaid (Eds). *The Geology of Libya V*. Elsevier, Amsterdam. pp1785-1801.
- Donadini, F., Korte, M. and Constable, C. (2010) Millennial Variations of the Geomagnetic Field: from Data Recovery to Field Reconstruction. *Space Science Reviews*. **155**: 219-246

- Drake, N. and Bristow, C. (2006) Shorelines in the Sahara: geomorphological evidence for an enhanced monsoon from palaeolake Megachad. *The Holocene*. **16**: 901-911
- Drake, N.A., El-Hawat, A.A., Turner, P., Armitage, S.J., Salem, M.J., White, K.H. and McLaren, S. (2008a) Palaeohydrology of the Fazzan Basin and surrounding regions: The last 7 million years. *Palaeogeography, Palaeoclimatology, Palaeoecology*. **263**:131-145
- Drake, N.A., El-Hawat, A.S. and Salem, M.J. (2008b) The Development, Decline and Demise of the As Sahabi River System over the Last Seven Million Years. *Garyounis Scientific Bulletin*, Special Issue No. 5: 95-109
- Drake, N.A., White, K., Salem, M., Armitage, S., El-Hawat, A., Francke, J., M, Hounslow, and Palmer, A. (2009) DMP VIII: Palaeohydrology and Palaeoenvironment. *Libyan Studies*. **40**: 171-178
- Drake, N.A., Blench, R.M., Armitage, S.J., Bristow, C.S. and White, K.H. (2010) Ancient watercourses and biogeography of the Sahara explain the peopling of the desert. *PNAS Early Edition*. 1-5
- Drake, N., Salem, M., Armitage, S., Francke, J., Hounslow, M., Hlal, O., White, K. and El-Hawat, A. (2011) DMP XV: Palaeohydrology and Palaeoenvironment: Initial Results and Report of 2010 and 2011 Fieldwork. *Libyan Studies*. **42**:139-149
- Drake, N., White, K., Armitage, S.J., El-Hawat, A.S., Salem, M.J. and Hounslow, M. (2012) A review of the Development and Demise of Lake Megafazzan. *Geology of Southern Libya*. **1**: 269-280
- Drake, N.A., Breeze, P. and Parker, A. (2013) Palaeoclimate in the Saharan and Arabian Deserts during the Middle Palaeolithic and the potential form hominin dispersal. *Quaternary International*. **300**: 48-61
- Dunagan, S.P. and Driese, S.G. (1999) Control of terrestrial stabilization on late Devonian palustrine carbonate deposition: Catskill Magnafacies, New York, USA. *Journal of Sedimentary Research*. **69**: 772-783
- Dupont-Nivet, G., Sier, M., Campisano, C.J., Arrowsmith, J.R., DiMaggio, E., Reed, K., Lockwood, C., Franke, C. and Husing, S. (2008) Magnetostratigraphy of the eastern Hadar Basin (Ledi-Gerau research area, Ethiopia) and implications for hominin palaeoenvironments. *Geological Society of America Special Paper*. **46**: 67-85
- Duston, N.M., Owen, R.M. and Wilkinson, B.H. (1996) Water Chemistry and Sedimentological Observations in Littlefiels Lake, Michigan: Implications for Lacustrine Marl Deposition. *Environ. Geol. Water. Sci*. **8**:229-236
- Eggins, S.M., Grun, R., McCulloch, M.T., Pike, A.W.G., Chappell, J., Kinsley, L., Mortimer, G., Shelley, M., Murray-Wallace, C.V., Spotl, C. and Taylor, L. (2005) In situ

- U-series dating by laser-ablation multi-collector ICPMS: new prospects for Quaternary geochronology. *Quaternary Science Reviews*. **24**: 2523-2538
- Ehrmann, W., Seidel, M. and Schmiedal, G. (2013) Dynamics of Late Quaternary North African humid periods documented in the clay mineral record of central Aegean Sea deposits. *Global and Planetary Change*. **107**: 186-195
- El Ebaidi., S.K. and Abdulsamad. E.O. (2005) Petrography and evaluation of some Mesozoic raw materials deposits in Murzuq Basin, SW Libya: A review and contribution. *The fourth international conference of the geology of Africa*. **2**: 255-268
- El-Hawat, A. (1980) Carbonate-Terrigenous Cyclic Sedimentation and Palaeogeography of the Marada Formation (Middle Miocene), Sirt Basin. In: Salem, M.J. and Busrewil, M.T. (eds) *The Geology of Libya*. Volume 3. London: Academic Press pp 427-448.
- El-Hawat, A. (2008) The Pre-Messinian Miocene Stratigraphy and Sedimentation in the Marada-Zaltan Area, Central Sirt Basin, Libya. *Garyounis Scientific Bulletin, Special Issue No. 5*: 21-32
- El-Shawaihdi, M.H., Muftah, A.M., Mozley, P.S. and Boaz, N.T. (2014) New age constraints for Neogene deposits of the Sahabi area, Libya (Sirt Basin) using strontium isotope ($^{87}\text{Sr}/^{86}\text{Sr}$) geochronology and calcareous nannofossils. *Journal of African Earth Sciences*. **89**: 42-49
- Feakins, S.J. and deMenocal, P. (2010) Accessed from:
http://www.ldeo.columbia.edu/~peter/site/Papers_files/Feakins.deMeniocal.Werdelin_ch4.2010.pdf
- Feakins, S.J., Levin, N.E., Liddy, H.A., Sieracki, A., Eglinton, T.I. and Bonnefille, R. (2013) Northeast African vegetation change over 12 m.y. *Geology*. **41**: 295-298
- Finlay, C.C., Dumberry, M., Chulliat, A. and M.A. Pais (2010) Short Timescale Core Dynamics: Theory and Observations. *Space Science Reviews*. **155**:177-218
- Fisher, N.I., Lewis, T., and Embleton, B.J.J. (1987) *Statistical analysis of spherical data*. Cambridge: Cambridge University Press.
- Flecker, R., Krijgsman, W., Capella, W., de Castro Martin, C., Dmitrieva, E., Mayser, J.P., Marzocchi, A., Modestou, S., Ochoa, D., Simon, D., Tulbure, M., van den Berg, B., van der Schee, M., de Lange, G., Ellam, R., Govers, R., Gutjahr, M., Hilgen, F., Kouwenhoven, T., Lofi, J., Meijer, P., Sierro, F.J., Bachiri, N., Barhoun, N., Alami, A.C., Chacon, B., Flores, J.A., Gregory, J., Howard, J., Lunt, D., Ochoa, M., Pancost, R., Vincent, S. and Yousfi, M.Z. (2015) Evolution of the late Miocene Mediterranean-Atlantic gateways and their impact on regional and global environmental change. *Earth Science Reviews*. **150**: 365-392

- Flower, B.P. and Kennett, J.P. (1994). The middle Miocene climatic transition: East Antarctic ice sheet development, deep ocean circulation and global carbon cooling. *Palaeogeography, Palaeoclimatology, Palaeoecology*. **108**: 537-555
- Flügel, E. (2010) *Microfacies of Carbonate Rocks: Analysis, Interpretation and Application*. Springer: Germany
- Francke, J. (2014) Imaging of aeolian sands with long-range ground penetrating radar. PhD Thesis: King's College London.
- Frank, U. (2007) Palaeomagnetic investigations on lake deposits from NE China: a new record of geomagnetic secular variations for the last 37ka. *Geophysical Journal International*. **169**:29-40
- Freytet, P. (1973) Petrography and palaeoenvironment of continental carbonate deposits with particular reference to the upper Cretaceous and lower Eocene of Languedoc (southern France). *Sedimentary Geology*. **10**: 25-60
- Freytet, P. and Verrecchia, E.P. (2002) Lacustrine and palustrine carbonate petrography : an overview. *Journal of Palaeolimnology*. **27**:221-237
- Friedman, G.M. (1961) Distinction between dune, beach and river sands from their textural characteristics. *Journal of Sedimentology Petrology*. **31**: 514-529
- Froehlich, K.F.O., Gonfiantini, R. and Rozanski, K. (2005) Isotopes in Lake Studies: A Historical Perspective. In Aggarwal, P.K., Gat, J.R. and Froehlich, F.O. *Isotopes in the water cycle: past, present and future of a developing science*. Springer: UK. Pp 139-150
- Fujioka, T. and Chappell, J. (2010) History of Australian aridity: Chronology in the evolution of arid landscapes. In: Bishop, P. and Pillans, B. *Australian Landscapes. Geological Society Special Publication*. **346**:121-139.
- Gammudi, A. and Keen, M.C. (1993) Ostracoda from the Miocene Marada Formation of Libya. *Journal of Micropalaeontology*. **12**: 121-139
- Gandin, A. and Capezzuoli, E. (2008) Travertine versus calcareous tufa: Distinctive petrologic features and stable isotope signatures. *Italian Journal of Quaternary Science*. **21**: 125-136
- Gardner, R. and McLaren, S. (1993) Progressive vadose diagenesis in late Quaternary aeolianite deposits? *Geological Society Special Publications*. **72**: 219-234
- Garnett, E.R., Gilmour, M.A., Rowe, P.J., Andrews, J.E. and Preece, R.C. (2004) $^{230}\text{Th}/^{234}\text{U}$ dating of Holocene tufas: possibilities and problems. *Quaternary Science Reviews*. **23**: 947-958
- Gary, A.C., Johnson, G.W., Ekart, D.D., Platon, E., and Wakefield, M.I. (2005) A method for two-well correlation using multivariate biostratigraphical data. In: Powell, A. J.,

Riding, J. B. (Eds.) Recent Developments in Applied Biostratigraphy. *The Micropalaeontological Society, Special Publications*. 205–217.

Gasse, F., Fontes, J.C., Plaziat, J.C., Carbonel, P., Kaczmarska, I., Deckker, P.D., Soulie-Marsche, I., Callot, Y. and Dupeuble, P.A. (1987) Biological remains, geochemistry and stable isotopes for the reconstruction of environmental and hydrological changes in the Holocene lakes from North Sahara. *Palaeogeography, Palaeoclimatology, Palaeoecology*. **60**:1-46

Gasse, F. (2002) Diatom-inferred salinity and carbonate oxygen isotopes in Holocene waterbodies of the western Sahara and Sahel (Africa). *Quaternary Science Reviews*. **21**:737-767

Gasse, F. (2005) Isotopic Palaeolimnology. In Aggarwal, P.K., Gat, J.R. and Froehlich, F.O. *Isotopes in the water cycle: past, present and future of a developing science*. Springer: UK. Pp353-358

Gaven, C., C. Hillaire-Marcel and Petit-Maire. N. (1981) A Pleistocene Lacustrine Episode in Southeastern Libya. *Nature*. **290**: 131-133

Geyh, M.A. and Thiedig, F. (2008) The Middle Pleistocene Al Mahruqah Formation in the Murzuq Basin, northern Sahara, Libya evidence for orbitally-forced humid episodes during the last 500,000 years. *Palaeogeography, Palaeoclimatology, Palaeoecology*. **257**:1-21

Gierlowski-Kordesch, E.H. (2010) *Lacustrine carbonates*. In: Alonso-Zarza, A.M. and Tanner, L.H. (Eds) Continental Carbonates. Developments in Sedimentology. Chapter 1: 1-101

Goddu, S.R., Appel, E., Gautam, P., Oches, E.A. and Wehland, F. (2007) The lacustrine section at Lukundol, Kathmandu basin, Nepal: Dating and magnetic fabric aspects. *Journal of Asian Earth Sciences*. **30**:73-81

Gordon, A.D., Clark, R.M. and Thompson, R. (1988) The use of constraints in sequence slotting. In: Diday (ed) Data analysis and informatics V. North- Holland Publishing: Amsterdam. Pp353-364

Goudarzi, G.H. (1970) Geology and mineral resources of Libya -a reconnaissance. U.S. Geological Survey Professional Paper. 660, 104.

Goudie, A. S. and Watson, A. (1981) The shape of desert sand dune grains. *Journal of Arid Environments*. **4**: 185-190

Gradstein, F.M., Ogg, J.G., Smith, A.G., Bleeker, W. and Lourens, L.J. (2004) A new Geologic Time Scale, with special reference to Precambrian and Neogene. *Episodes*. **27**: 83-100

Gribble, C. D. and Hall. A.J. (1992) *Optical Mineralogy*. CRC Press: USA

- Griffin, D.L. (1999) The late Miocene climate of northeastern Africa: unravelling the signals in the sedimentary succession. *Journal of the Geological Society*. **156**: 817-826
- Griffin, D.L. (2002) Aridity and humidity: two aspects of the late Miocene climate of North Africa and the Mediterranean. *Palaeogeography, Palaeoclimatology, Palaeoecology*. **182**: 65-91
- Griffin, D.L. (2006) The late Neogene Sahabi rivers of the Sahara and their climatic and environmental implications for the Chad Basin. *Journal of the Geological Society*. **163**:905–921
- Grubič, A., Dimitrijević, M., Galečić, M., Jakovljević, Z., Komarnicki, S., Protić, D., Radulović, P., Rončević, G. (1991) Stratigraphy of Western Fazzan (SW-Libya). In: Salem, M.J., Hammuda, O.S., Eliagoubi, B.A. (Eds.) *The Geology of Libya IV*. Elsevier, Amsterdam, pp1529–1624
- Gubbins, D. (1999) The distinction between geomagnetic excursions and reversals. *Geophysical Journal International*. **137**:F1-F3
- Guiraud, R., Bosworth, W., Thierry, J. and Delplanque, A. (2005) Phanerozoic geological evolution of Northern and Central Africa: An overview. *Journal of African Earth Sciences*. **43**: 83-143
- Gundobin, V.M. (1985) Geological map of Libya 1:250,000, Sheet: Qararat al Marar (NH 33-13) Explanatory Booklet. Industrial Research Centre Tripoli.
- Guo, Z., Petite-Maire, N. and Kropelin, S. (2000) Holocene non-orbital climatic events in present-day arid areas of northern Africa and China. *Global and Planetary Change*. **26**:97-103
- Haywood, A.M. and Valdes, P.J. (2006) Vegetation cover in a warmer world simulated using a dynamic global vegetation model for the Mid-Pliocene. *Palaeogeography, Palaeoclimatology, Palaeoecology*. **237**: 412-427
- Heller, F. and Tung-Sheng, L. (1982) Magnetostratigraphical dating of loess deposits in China. *Letters to Nature*. **300**: 431-433
- Heller, F., Xiuming, L., Tungsheng, L. and Tongchun, X. (1991) Magnetic susceptibility of China. *Earth and Planetary Science Letters*. **103**: 301-310
- Henry, B., Jordanova, D., Jordanova, N. and Le Goff, M. (2005) Transformations of magnetic mineralogy in rocks revealed by difference of hysteresis loops measured after stepwise heating: theory and case studies. *Geophysical Journal International*. **162**: 64-78
- Hilgen, F.J. (1991) Extension of the astronomically calibrated (polarity) time scale to the Miocene/Pliocene boundary. *Earth and Planetary Science Letters*. **107**:349-368

Hilgen, F.J., Krijgsman, W., Langeresi, C.G., Lourens, L.J., Santarelli, A. and Zachariasse, W.J. (1995) Extending the astronomical (polarity) time scale into the Miocene. *Earth and Planetary Science Letters*. **136**: 495-510

Hilgen, F.J., Bissoli, L., Iaccarino, S., Krijgsman, W., Meijer, R., Negri, A. and Villa, G. (2000) Integrated stratigraphy and astrochronology of the Messinian GSSP at Oued Akrech (Atlantic Morocco). *Earth and Planetary Science Letters*. **182**: 237-251

Hilgen, F.J., Lourens, L.J. and Van Dam, J.A. (2012) *The Neogene Period*. In: Gradstein, F. M., Ogg, J. G., Schmitz, M., Ogg, G. (Eds.), Vol.1. *The Geologic Time Scale 2012*. Elsevier, pp. 923-978.

Hinnov, L.A. and Hilgen, F.J. (2012) Cyclostratigraphy and Astrochronology. In: Gradstein, F. M., Ogg, J. G., Schmitz, M., Ogg, G. (Eds.), Vol.1. *The Geologic Time Scale 2012*. Elsevier, Pp63-83

Hoelzmann, P., Kruse, H-J. and Rottinger, F. (2000) Precipitation estimates for the eastern Saharan palaeomonsoon based on a water balance model of the West Nubian Palaeolake Basin. *Global and Planetary Change*. **26**:105–120

Hoelzmann, P., Keding, B., Berke, H., Kropelin, S. and Kruse, H.J. (2001) Environmental change and archaeology: lake evolution and human occupation in the Eastern Sahara during the Holocene. *Palaeogeography, Palaeoclimatology, Palaeoecology*. **169**:193-217

Hoelzmann, P., Schwab, A., Roberts, N., Cooper, P. and Burgess, A. (2010) Hydrological response of an east-Saharan palaeolake (NW Sudan) to early-Holocene climate. *The Holocene*. **20**:537-549

Hoffman, K.A. (1981) Palaeomagnetic excursions, aborted reversals and transitional fields. *Nature*. **294**: 67-69

Hoffman, K.A. (1992) Dipolar reversal states of the geomagnetic field and core-mantle dynamics. *Nature*. **359**: 789-794

Hogg, A.J.C., Sellier, E. and Jourdan, A.J. (1992) Cathodoluminescence of quartz cements in Brent Group sandstones, Alwyn South, UK North Sea. *Geological Society Special Publications*. **61**: 421-440

Hounslow, M.W. and McIntosh, G. (2003) Magnetostratigraphy of the Sherwood Sandstone Group (Lower and Middle Triassic), south Devon, UK: detailed correlation of the marine and non-marine Anisian. *Palaeogeography, Palaeoclimatology, Palaeoecology*. **193**: 325-348

Hounslow, M. W. (2006) PMAGTOOLS Verison 4.2a. Available from <http://geography.lancaster.ac.uk/cemp/cemp.htm>

Hounslow, M. W., Peters, C., Mork, A., Weitschat, W. and Os Vigran, J. (2008) Biomagnetostratigraphy of the Vikinghøgda Formation, Svalbard (Arctic Norway), and the geomagnetic polarity timescale for the Lower Triassic. *Geological Society of America Bulletin*. **120**:1305-1325

Hounslow, M.W., White, H.E., Drake, N.A., Salem, M., McLaren, S., El-Hawat, A., Karloukovski, V., Noble, S.R. and Hlal, O. (2017) Miocene humid intervals and establishment of drainage networks by 23 Ma in the Central Sahara, southern Libya. *Gondwana Research*. **45**: 118-137

Hounslow, M.W. (Submitted) Palaeozoic geomagnetic reversal rates following superchrons have a fast re-start mechanism

Hsu, K.J., Ryan, W.B.F. and Cita, M.B. (1973) Late Miocene Desiccation of the Mediterranean. *Nature*. **242**: 240-244

Hsu, K.H., Montadert, L., Bernoulli, D., Cita, M.B., Erickson, A., Garrison, R.E., Kidd, R.B., Melieres, F., Muller, C., Wright, R. (1977). History of the Mediterranean salinity crisis. *Nature*. **267**: 399–403.

Huerta, P and Armenteros, I. (2005) Calcrete and palustrine assemblages on a distal alluvial-floodplain: A response to local subsidence (Miocene of the Duero basin, Spain). *Sedimentary Geology*. **177**:253-270

International Geomagnetic Reference Field Model (IGRF) (2013) BGS-NERC http://www.geomag.bgs.ac.uk/data_service/models_compass/igrf_form.shtml (accessed:February 2013).

Jackson, A., Jonkers, A.R.T. and Walker, M.R. (2000) Four centuries of geomagnetic secular variation from historical records. *Phil. Trans. R. Soc. London. A*. **358**: 957-990

John, C.M., Mutti, M. and Adatte, T. (2003) Mixed carbonate-siliciclastic record on the North African margin (Malta)-coupling of weathering processes and mid Miocene climate. *GSA Bulletin*. **115**: 217-229

Josse, J., Pages, J. and Husson, F., 2008. Testing the significance of the RV Coefficient. *Computational Statistics and Data Analysis*. **53**: 82-91.

Katari, L., Tauxe, L. and King, J. (2000) A reassessment of post-depositional remanent magnetism: preliminary experiments with natural deposits. *Earth and Planetary Science Letters*. **183**: 147-160

Kelly, M., Black, S. and Rowan, J.S. (2000) A calcrete-based U/Th chronology for landform evolution in the Sorbas basin, southeast Spain. *Quaternary Science Reviews*. **19**: 995-1010

Kender, S., Peck, V.L., Jones, R.W. and Kaminski, M.A. (2009) Middle Miocene oxygen minimum zone expansion offshore West Africa: Evidence for global cooling precursor events. *Geological Society of America*. **37**: 699-702

Kent, J.T., Briden, J.C. and Mardia, K.V. (1983). Linear and planar structure in ordered multivariate data as applied to progressive demagnetisation of palaeomagnetic remanence. *Geophys. J. R. Astron. Soc.* **81**:75-87

- Kent, D.V. and Schneider, D.A. (1995) Correlation of palaeointensity variation records in the Brunhes/Matuyama polarity transition interval. *Earth and Planetary Science Letters*. **129**: 135-144
- Khalaf, F.I. (2007) Occurrences and genesis of calcrete and dolocrete in the Mio-Pleistocene fluvatile sequence in Kuwait, northeast Arabian Peninsula. *Sedimentary Geology*. **199**:129-139
- Khalaf, F.I and Gaber, A.S. (2008) Occurrence of cyclic palustrine and calcrete deposits within the lower Pliocene Hagul formation, East Cairo district, Egypt. *Journal of African Earth Sciences*. **51**: 298-312
- Kidane, T., Otofujii, Y., Brown, F.H., Takemoto, K. and Eshete, G. (2007) Two normal palaeomagnetic polarity intervals in the lower Matuyama Chron recorded in the Shungura Formation (Omo Valley, Southwest Ethiopia). *Earth and Planetary Science Letters*. **262**: 240-256
- King, J. and Peck, J. (2001) Use of Palaeomagnetism in studies of lake deposits. In Last, W.M. and Smol, J.P. (Eds) *Tracking Environmental Change Using Lake Deposits*. Volume 1: Basin Analysis, Coring and Chronological Technique. Kluwer Academic Publishers: Netherlands. Pp371-389
- Klappa, C.F. (1980) Rhizoliths in terrestrial carbonates: classification, recognition, genesis and significance. *Sedimentology*. **27**:613-629
- Klitzsch, E.H. (2000) The structural development of the Murzuq and Kufra basins- significance for oil and mineral exploration. In: *Geological Exploration in the Murzuq Basin* (Eds. M.A. Sola and D. Worsley). Elsevier: Amsterdam pp143-150.
- Kohler, C.M., Heslop, D., Krijgsman, W. and Dekkers, M.J. (2010) Late Miocene palaeoenvironmental changes in North Africa and the Mediterranean recorded by geochemical proxies (Monte Gibliscemi section, Sicily). *Palaeogeography, Palaeoclimatology, Palaeoecology*. **285**: 66-73
- Konishi, Y., Prince, J. and Knott, B. (2001) The fauna of thrombolitic microbialites, Lake Clifton, Western Australia. *Hydrobiologia*. **457**: 39-47
- Konert, M and Vandenberghe, J. (1997) Comparison of laser grain size analysis with pipette and sieve analysis: a solution for the underestimation of the clay fraction. *Sedimentology*. **44**:523-535
- Kostadinova M., Jordanova N., Jordanova D., Kovacheva M. (2004). Preliminary study on the effect of water glass impregnation on the rock-magnetic properties of baked clay. *Studia Geophysica Et Geodaetica*. **48**: 637-646
- Kraus, M.J. and Aslan, A. (1993) Eocene hydromorphic palaeosols: Significance for interpreting ancient floodplain processes. *Journal of Sedimentary Petrography*. **63**: 453-463

- Kraus, M.J. (1999) Palaeosols in clastic sedimentary rocks: their geologic application. *Earth Science Reviews*. **47**: 41-70
- Krijgsman, W., Hilgen, F.J., Langereis, C.G., Santarelli, A. and Zachariasse, W.J. (1995) Late Miocene magnetostratigraphy, biostratigraphy and cyclostratigraphy in the Mediterranean. *Earth and Planetary Science Letters*. **136**: 475-494
- Krijgsman, W., Hilgen, F.J., Raffi, I., Sierro, F.J. and Wilson, D.S. (1999) Chronology, causes and progression of the Messinian salinity crisis. *Letters to Nature*. **400**: 652-655
- Kroepelin, S. (2006). Revisiting the age of the Sahara Desert. *Science*. **312**: 1138–1139
- Kruiver, P.P., Krijgsman, W., Langereis, C.G. and Dekkers, M.J. (2002) Cyclostratigraphy and rock-magnetic investigation of the NRM signal in late Miocene palustrine-alluvial deposits of the Librilla section (SE Spain). *Journal of Geophysical Research*. **107**: 1-18
- Ku, T-L. and Liang, Z-C. (1984) The dating of impure carbonates with decay-series isotopes. *Nuclear Instruments and Methods in Physics Research*. **223**: 563-571
- Kurschner, W.M., Kvacek, Z. and Dilcher, D.L. (2008) The impact of Miocene atmospheric carbon dioxide fluctuations on climate and the evolution of terrestrial ecosystems. *PNAS*. **105**: 449-453
- Lagroix, F. and Banerjee, S.K. (2002) Palaeowind directions from the magnetic fabric of loess profiles in central Alaska. *Earth and Planetary Science Letters*. **195**: 99-112
- Lamb, A.L., Leng, M.J., Lamb, H.F. and Mohammed, M.U. (2000) A 9000-year oxygen and carbon isotope record of hydrological change in a small Ethiopian crater lake. *The Holocene*. **10**:167-177
- Lamb, H.F., Leng, M.J., Telford, R.J., Ayenew, T. and Umer, M. (2007) Oxygen and carbon isotope composition of authigenic carbonate from an Ethiopian lake: a climate record of the last 2000 years. *The Holocene*. **17**:517-526
- Langereis, C.G. (1999) Excursions in geomagnetism. *Nature*. **399**: 207-208
- Langereis, C.G., Dekkers, M.J., de Lange, G.J., Paterne, N. and van Santvoort, P.J.M. (1997) Magnetostratigraphy and astronomical calibration of the last 1.1 Myr from an eastern Mediterranean piston core and dating of short events in the Brunhes. *Geophysical Journal International*. **129**:75-94
- Langereis, C.G., Krijgsman, W., Muttoni, G. and Menning, M. (2010). Magnetostratigraphy-concepts, definitions, and applications. *Newsletter on Stratigraphy*. **43**:207-233
- Lanza, R. and Meloni, A. (2006) *The Earth's Magnetism: An Introduction for Geologists*. Springer: Germany

- Lean, C.B., Hounslow, M.W., Vine, F.J., Harwood, G.M., Elvidge, L., Fisk, K., Kendall, A.C. and Montgomery, P. (1998) Magnetostratigraphy and sedimentary evolution of the late Miocene to early Pleistocene deposits, Quseir region, Egyptian Red Sea. *Geophysical Journal International*. **133**:435-450
- Lebatard, A.E., Bourles, D.L., Braucher, R., Arnold, M., Düringer, P., Jolivet, M., Moussa, A., Deschamps, P., Roquin, C., Carcaillet, J., Schuster, M., Lihoreau, F., Likius, A., Mackaye, H.T., Vignaud, P. and Brunet, M. (2010) Application of the authigenic $^{10}\text{Be}/^{9}\text{Be}$ dating method to continental deposits: Reconstruction of the Mio-Pleistocene sedimentary sequence in the early hominid fossiliferous areas of the northern Chad Basin. *Earth and Planetary Science Letters*. **297**: 57-70
- Leitch, V., Mattingly, D., Williams, M., Norry, M.J., Wilkinson, I., Whitbread, I., Stocker, C.P. and Farman, T. (Submitted) Provenance of clay used in Garamantian ceramics from Jarma, Fazzan region (south-west Libya): a combined geochemical and nanofossil analysis. *Journal of Archaeological Science Reports*.
- Leng, M.J. and Marshall, J.D. (2004) Palaeoclimate interpretation of stable isotope data from lake sediment archives. *Quaternary Science Reviews*. **23**:811-831
- Leng, M.J., Lamb, A.L., Heaton, T.H.E., Marshall, J.D., Wolfe, B.B., Jones, M.D., Holmes, J.A. and Arrowsmith, C. (2005) Isotopes in Lake Deposits. In Leng, M.J. (ed.) *Isotopes in Palaeoenvironmental Research*. Springer: Netherlands. Pp147-184
- Leroy, S. and Dupont, L. (1994) Development of vegetation and continental aridity in northwestern Africa during the Late Pliocene: the pollen record of ODP Site 658. *Palaeogeography, Palaeoclimatology, Palaeoecology*. **109**: 295-316
- Lezine, AM., Casanova, J. and Hillaire-Michael, C. (1990) Across an early Holocene humid phase in western Sahara: Pollen and isotope stratigraphy. *Geology*. **18**:264-267
- Li, H-C. and Ku, T-L. (1997) $\delta^{13}\text{C}$ - $\delta^{18}\text{O}$ covariance as a paleohydrological indicator for closed-basin lakes. *Palaeogeography, Palaeoclimatology, Palaeoecology*. **133**:69-80
- Liddicoat, J.C. (1990) Aborted reversal of the palaeomagnetic field in the Brunhes Normal Chron in east-central California. *Geophysical Journal International*. **102**: 747-752
- Liddicoat, J.C. and Coe, R.S. (1997) Palaeomagnetic Investigation of Lake Lahontan Deposits and its Application for Dating Pluvial Events in the Northwestern Great Basin. *Quaternary Research*. **47**: 45-53
- Lisiecki, L.E. and Raymo, M.E. (2005) A Pliocene-Pleistocene stack of 57 globally distributed benthic $\delta^{18}\text{O}$ records. *Palaeoceanography*. **20**: 1-17
- Llinas Agrasar, E. (2004) Crocodile remains from the Burdigalian (lower Miocene) of Gebel Zelten (Libya). *Geodiversitas*. **26**: 309-321
- Love, J.J. (2000) Palaeomagnetic secular variation as a function of intensity. *Phil. Trans. R. Soc. Lond. A*. **358**:1191-1223

- Lovlie, R. and Leroy, S. (1995) Magnetostratigraphy of Lower Pleistocene Banyoles Palaeolake carbonate deposits from Catalonia, NE Spain: Evidence for relocation of the Cobb-Mountain sub-chron. *Quaternary Science Reviews*. **14**:473-485
- Lowe, J.J. and Walker, M.J.C. (1997) *Reconstructing Quaternary Environments*. 2nd Edition. Addison Wesley Longman Ltd: China
- Lowrie, W. (1990) Identification of ferromagnetic minerals in a rock by coercivity and unblocking temperature properties. *Geophysical Research Letters*. **17**: 159-162
- Lowrie, W. and Kent, D.V. (1983) Geomagnetic reversal frequency since the Late Cretaceous. *Earth and Planetary Science Letters*. **62**: 305-313
- Lowrie, W. and Kent, D.V. (2004) Geomagnetic Polarity Timescales and Reversal Frequency Regimes. In Timescales of the Palaeomagnetic Field, Geophysical Monograph Series 145. Pp 117-129
- Lowrie, W. and Heller, F. (1982) Magnetic Properties of Marine Limestones. *Reviews of Geophysics and Space Physics*. **20**: 171-192
- MacKenzie, W.S. and Adams, A.E. (2007) *A Colour Atlas of Rocks and Minerals in Thin Section*. Manson Publishing: UK.
- Maher, B.A. (1998) Magnetic properties of modern soils and Quaternary loessic palaeosols: palaeoclimatic implications. *Palaeogeography, Palaeoclimatology, Palaeoecology*. **137**: 25-54
- Maher, B.A., Thompson, R. and Hounslow, M.W. (1999) Introduction to Quaternary Climates, Environments and Magnetism. In Maher, B.A. & Thompson, R. (eds.), *Quaternary Climates, Environments and Magnetism*. Cambridge University Press, 1-48
- Maher, B.A. (2007) Environmental magnetism and climate change. *Contemporary Physics*. **48**: 247-274
- Maher, B.A. (2011) The magnetic properties of Quaternary aeolian dusts and deposits and their palaeoclimatic significance. *Aeolian Research*. **3**: 87-144
- Maher, B.A. and Thompson, R. (1995) Palaeorainfall Reconstructions from Pedogenic Magnetic Susceptibility Variations in the Chinese Loess and Palaeosols. *Quaternary Research*. **44**: 383-391
- Man, O. (2008) On The Identification Of Magnetostratigraphic Polarity Zones. *Stud. Geophys. Geod.* **52**:173–186.
- Man, O. (2011). The maximum likelihood dating of magnetostratigraphic sections. *Geophysical Journal International*. **185**:133-143.
- Maron, M., Rigo, M., Bertinelli, A., Katz, M.E., Godfrey, L., Zaffani, M. and Muttoni, G. (2015) Magnetostratigraphy, biostratigraphy, and chemostratigraphy of the Pignola-

- Abriola section: New constraints for the Norian-Thaetian boundary. *Geological Society of America Bulletin*. **127**: 962-974
- Marshall, J.D. (1992) Climatic and oceanographic isotopic signals from the carbonate rock record and their preservation. *Geological Magazine*. **129**:143-160.
- Martens, K. (1994) Ostracod speciation in ancient lakes: a review. *Arch. Hydrobiol. Beih. Ergebn. Limnol.* **44**: 203-222
- Márton, E., Márton, P., Heller, F. (1980) Remanent magnetization of a Pliensbachian limestone sequence at Bakonycsernye (Hungary). *Earth and Planetary Science Letters*. **48**: 218-226.
- Marzocchi, A., Flecker, R., van Baak, C.G.C., Lunt, D.J. and Krijgsman, W. (2016) Mediterranean outflow pump: An alternative mechanism for the Lago-mare and the end of the Messinian Salinity Crisis. *Geology*. **44**: 523-526
- Mattingly, D. J., Daniels, C. M., Dore, J. N., Edwards, D. and Hawthorne, J. (2003) *The Archaeology of Fazzān. Volume 1, Synthesis*. The Society for Libyan Studies/Department of Antiquities. London.
- Mattingly, D., Lahr, M., Armitage, S., Barton, H., Dore, J., Drake, N., Foley, R., Merlo, Stefania., Salem, M., Stock, J. and White, K. (2007) Desert Migrations: people, environment and culture in the Libyan Sahara. *Libyan Studies*. **38**:1-42
- McCabe, C., Van der Voo, R., Peacor, D.R., Scotese, C.R. and Freeman, R. (1983) Diagenetic magnetite carries ancient yet secondary remanence in some Palaeozoic sedimentary carbonates. *Geology*. **11**: 221-223
- McCrea, J.M. (1950). On the isotopic chemistry of carbonates and a palaeotemperature scale. *Journal of Chemistry and Physics*. **18**:849-857.
- McFadden, P. L and McElhinny, M.W. (1990) Classification of the reversal test in palaeomagnetism. *Geophys. J. Int.* **103**:725-729
- McLaren, S. J. (1993) Use of cement types in the palaeoenvironmental interpretation of coastal aeolianite sequences. From Pye, K. (ed.) *The Dynamics and Environmental Context of Aeolian Sedimentary Systems. Geological Society Special Publication*. **72**: 235-244.
- McLaren, S.J. and Rowe, P.J. (1996) The reliability of Uranium-Series mollusc dates from the Western Mediterranean Basin. *Quaternary Science Reviews*. **15**: 709-717
- McLaren, S. and Gardner, R. (2004) Late Quaternary vadose carbonate diagenesis in coastal and desert dune and beach sands: is there a palaeoclimatic signal? *Earth Surface Processes and Landforms*. **29**: 1441-1459
- McLaren, S.J., Drake, N. and White, K. (2006) Late Quaternary Environmental Changes in the Fazzan, Southern Libya: Evidence from Deposits and Duricrusts. In: Mattingly, D.

(Ed.) Environment, Climate and Resources of the Libyan Sahara. Society of Libyan Studies, London. Pp157-166

McLaren, S.J. (2007) Aeolianite. In Nash, D. J and McLaren, S. J. *Geochemical Deposits and Landscapes*. Blackwell Publishing: Singapore. Pp 144-172

McLaren, S.J., Leng, M.J., Knowles, T. and Bradley, A.V. (2012) Evidence of past environmental conditions during the evolution of a calcretised Wadi system in Southern Jordan using stable isotopes. *Palaeogeography, Palaeoclimatology, Palaeoecology*. **348-349**:1-12

McLaren, S., Wallace, M.W., Pillans, B.J., Gallagher, S.J., Miranda, J.A. and Warne, M.T. (2009) Revised stratigraphy of the Blanchetown Clay, Murray Basin: age constraints on the evolution of palaeo Lake Bungunna. *Australian Journal of Earth Sciences*. **56**: 259-270

McLaren and Wallace, M.W. (2010) Plio-Pleistocene climate change and the onset of aridity in southeastern Australia. *Global and Planetary Change*. **71**: 55-72

Merrill, R.T. and McFadden, P.L. (1994) Geomagnetic field stability: Reversal events and excursions. *Earth and Planetary Science Letters*. **121**:57-69

Micheels, A., Eronen, J. and Mosbrugger, V. (2009) The Late Miocene climate response to a modern Sahara desert. *Global and Planetary Change*. **67**: 193-204

Micheels, A., Bruch, A.A., Eronen, J., Fortelius, M., Harzhauser, M., Utescher, T. and Mosbrugger, A. (2011) Analysis of heat transport mechanisms from a Late Miocene model experiment with a fully-coupled atmosphere-ocean general circulation model. *Palaeogeography, Palaeoclimatology, Palaeoecology*. **304**: 337-350

Morton, A., Whitham, A., Howard, J., Fanning, M., Abutarruma, Y., El Dieb, M., Elkararry, F.M., Hamhooon, M., Luning, S., Phillips, R. and Thusu, B. (2012) Using heavy minerals to test the stratigraphic framework of Al Kufrah Basin. *Fourth Symposium on the Sedimentary Basins of Libya*. The Geology of Southern Libya, vol 3. (eds Salem, M.J. and Abadi, A.M.), Earth Science Society of Libya, Tripoli, pp33-76

Muhs, D.R. (2004) Mineralogical maturity in dunefields of North America, African and Australia. *Geomorphology*. **59**: 247-269

Murphy, D.H. and Wilkinson, B.H. (1980) Carbonate deposition and facies distribution in a central Michigan marl lake. *Sedimentology*. **27**: 123-135

Nash, D.J. and McLaren, S.J. (2003) Kalahari valley calcretes: their nature, origins and environmental significance. *Quaternary International*. **111**:3-22

Nash, D.J. and Smith, R.F. (2003) Properties and development of channel calcretes in a mountain catchment, Tabernas Basin, Spain. *Geomorphology*. **50**:227-250

- Nielson, K.A., Clemmensen, L.B. and Fornos, J.J. (2004) Middle Pleistocene magnetostratigraphy and susceptibility stratigraphy: data from a carbonate aeolian system, Mallorca, Western Mediterranean. *Quaternary Science Reviews*. **23**:1733-1756
- Nicolai, C. (2008) Tracing the As Sahabi channel system in the Ajdabiya Trough, Central Sirt Basin, Libya. *Garyounis Scientific Bulletin*, Special Issue No. 5: 85-94
- Nichols, G. (2009) *Sedimentology and Stratigraphy*. Second Edition. Oxford: Wiley Blackwell Publishing.
- Norry, M.J., Dunham, A.C. and Hudson, J.D. (1994) Mineralogy and geochemistry of the Peterborough Member, Oxford Clay Formation, Jurassic, UK: element fractionation during mudrock sedimentation. *Journal of the Geological Society*. **151**:195-207
- Novello, A., Lebatard, A.E., Moussa, A., Barboni, D., Sylvestre, F., Bourles, D.L., Pailles, C., Buchet, G., Decarreau, A., Düringer, P., Ghienne, F., Maley, J., Mazur, J.C., Roquin, C., Schuster, M. and Vignaud, P. (2015) Diatom, phytolith, and pollen records from a $^{10}\text{Be}/^9\text{Be}$ dated lacustrine succession in the Chad basin: Insight on the Miocene–Pliocene paleoenvironmental changes in Central Africa. *Palaeogeography, Palaeoclimatology, Palaeoecology*. **430**: 85-103
- Ochoa, D., Sierro, F.J., Lofi, J., Maillard, A., Flores, J.A. and Suarez, M. (2015) Synchronous onset of the Mediterranean evaporite precipitation: First Mediterranean offshore evidence. *Earth and Planetary Science Letters*. **427**: 112-124
- Ogg, J.G. (2012) Geomagnetic polarity timescale. In: Gradstein, F. M., Ogg, J. G., Schmitz, M., Ogg, G. (Eds.), Vol.1. *The Geologic Time Scale 2012*. Elsevier, pp. 85-114.
- Olson, P., Hinnov, L. and Driscoll, P. (2014) Non-random geomagnetic reversal times and geodynamo evolution. *Earth Planetary Science Letters*. **388**:9–17.
- Opdyke, N.D. and Channell, J.E. (1996) *Magnetic Stratigraphy*. USA: Academic Press
- Osborne, A.H., Vance, D., Rohling, E.J., Barton, N., Rogerson, M. and Fello, N. (2008) A humid corridor across the Sahara for the migration of early modern humans out of Africa 120,000 years ago. *Proceedings of the National Academy of Sciences*. **105**:16,444-16,447
- Osmond, J.K. and Dabous, A.A. (2004) Timing and intensity of groundwater movement during Egyptian Sahara pluvial periods by U-series analysis of secondary U in ores and carbonates. *Quaternary Research*. **61**: 85-94
- Otero, O., Pinton, A., Mackaye, H.T., Likius, A., Vignaud, P. and Brunet, M. (2009) Fishes and palaeogeography of the African drainage basins: Relationships between Chad and neighbouring basins throughout the Mio-Plio. *Palaeogeography, Palaeoclimatology, Palaeoecology*. **274**: 134-139
- Otero, O., Lecuyer, A., Fourel, F., Martineau, F., Mackaye, H.T., Vignaud, P. and Brunet, M. (2011) Freshwater fish $\delta^{18}\text{O}$ indicates a Messinian change of the precipitation regime in Central Africa. *Geology*. **39**: 435-438

- Pagani, M., Arthur, M.A. and Freeman, K. (1999) Miocene evolution of atmospheric carbon dioxide. *Palaeoceanography*. **14**: 273-292
- Paillou, P., Schuster, M., Tooth, S., Farr, T., Rosenqvist, A., Lopez, S. and Maleziuk, JM. (2009) Mapping of a major palaeodrainage system in eastern Libya using orbital imaging radar: The Kufrah River. *Earth and Planetary Science Letters*. **277**: 327-333
- Paillou, P., Tooth, S. and Lopez, S. (2012) The Kufrah palaeodrainage system in Libya: A past connection to the Mediterranean Sea? *Comptes Rendus Geoscience*. **344**: 406-414
- Paola, C., Wiele, S.M. and Reinhart, M.A. (1989) Upper-regime parallel lamination as the result of turbulent sediment transport and low-amplitude bedforms. *Sedimentology*. **36**: 47-59
- Pares, J.M. and Van der Voo, R. (2013) Non-antipodal directions in magnetostratigraphy: an overprint bias? *Geophysical Journal International*. **192**: 75-81
- Parizek, A., Klen, L. And Rohlich, P. (1984) Geological map of Libya 1:250,000, Sheet: Idri (NG 33-1) Explanatory Booklet. Industrial Research Centre Tripoli.
- Parker, R.L and Fleischer, M. (1968) Geochemistry of Niobium and Tantalum. *Geological Survey Professional Paper*. **612**: 1-43
- Pentecost, A. (2005) *Travertine*. Springer: Netherlands
- Peregi, Z., Less, G.Y. and Konrad, G.Y (2003) Geological map of Libya 1: 250,000, Sheet: Al Haruj al Abyad (NG 33-8) Explanatory Booklet. Geological Institute of Hungary and Industrial Research Centre, Budapest and Tripoli
- Perego, A., Zerboni, A. and Cremaschi, M. (2011) Geomorphological Map of the Messak Settafet and Mellet (Central Sahara, SW Libya). *Journal of Maps*. 464:475
- Permenter, J.L. and Oppenheimer, C. (2007) Volcanoes of the Tibesti massif (Chad, northern Africa). *Bulletin of Volcanology*. **69**: 609-626
- Petit-Maire, N., Delibrias, G., Gaven, C. (1980a). Pleistocene lakes in the Shati area, Fazzan. *Palaeoecology of Africa* **12**:289–295
- Petit-Maire, N., Casta, L., Delibria, G. and Gaven, C. (1980b) Preliminary Data on Quaternary Palaeolacustrine Deposits in the Wadi ash Shati Area, Libya. In: Salem, M.J. and Busrewil, M.T. (eds) *The Geology of Libya*. Volume 3. London: Academic Press pp797-807
- Pia-Pueyo, S., Gierlowski-Kordesch, E.H., Viseras, C. and Soria, J.M. (2010) Facies changes in the distal floodplain deposits of the Guadix Basin (Betic Cordillera, Spain): New sedimentologic data. *Geogaceta*. **48**: 43-46

- Pickford, M. (2000) Crocodiles from the Beglia Formation, Middle/Late Miocene Boundary, Tunisia, and their significance for Saharan palaeoclimatology. *Ann. Paleontol.* **86**: 59-67
- Pillans, B. (2003) Subdividing the Pleistocene using the Matuyama-Brunhes boundary (MBB): an Australasian perspective. *Quaternary Science reviews.* **22**: 1569-1577
- Pisarevsky, S.A. (1999) Studies of post-depositional remanent magnetisation and their relevance to the palaeomagnetic record. In: Tarling, D. H. and Turner, P. (eds) *Palaeomagnetism and Diagenesis in Deposits. Geological Society, London, Special Publications*, **151**: 21-26.
- Platt, N. H (1989) Lacustrine carbonates and pedogenesis: sedimentology and origin of palustrine deposits from the Early Cretaceous Rupelo Formation, W Cameros Basin, Spain. In Wright, V.P and Tucker, M.E. (1991) *Calcretes*. Blackwell Scientific Publications: Oxford. Pp 323-342
- Platt, N.H. and Wright, V.P. (1992) Palustrine carbonates at the Florida Everglades: towards an exposure index for the fresh-water environment. *Journal of Sedimentary Petrology.* **62**: 1058-1071
- Plummer, P.S. and Gostin, V.A. (1981) Shrinkage Cracks: Desiccation or Synaeresis? *Journal of Sedimentary Petrology.* **51**: 1147-1156
- Porcelli, P.W. and Swarzenski, P.W. (2003) The Behaviour of U- and Th-series Nuclides in Groundwater. *Reviews in Mineralogy and Geochemistry.* **52**: 317-361
- Potter, P.E., Maynard, J.B. and Depetris, P.J. (2005) *Mud and Mudstones*. Springer: Germany
- Potter, P.E. and Szatmari, P. (2009) Global Miocene tectonics and the modern world. *Earth Science Reviews.* **96**: 279-295
- Pound, M.J., Haywood, A.M., Salzmann, U., Riding, J.B., Lunt, D.J. and Hunter, S.J. (2011) A Tortonian (Late Miocene, 11.61-7.25) global vegetation reconstruction. *Palaeogeography, Palaeoclimatology, Palaeoecology.* **300**: 29-45
- Pound, M.J., Haywood, A.M., Salzmann, U. and Riding, J.B. (2012) Global vegetation dynamics and latitudinal temperature gradients during the Late Miocene (15.97-5.33 Ma). *Earth Science Reviews.* **112**: 1-22
- Radivojevic, M., Toljic, M., Turki, S.M., Bojic, Z., Saric, K. and Cvetkovic, V. (2015) Neogene to Quaternary basalts of the Jabal Eghei (Nuqay) area (south Libya): Two distinct volcanic events or continuous volcanism with gradual shift in magma composition? *Journal of Volcanology and Geothermal Research.* **293**: 57-74
- Riding, R. (2000) Microbial carbonates: the geological record of calcified bacterial-algal mats and biofilms. *Sedimentology.* **47**: 179-214

- Rio, D., Sprovieri, R and Thunell, R. (1991) Pliocene-lower Pleistocene chronostratigraphy: A re-evaluation of Mediterranean type sections. *Geological Society of America Bulletin*. **103**:1049-1058
- Roberts, A.P and Winklhofer, M. (2004) Why are geomagnetic excursions not always recorded in deposits? Constraints from post-depositional remanent magnetization lock-in modelling. *Earth and Planetary Science Letters*. **227**:345-359
- Rollinson, H. R. (1993) *Using geochemical data: evaluation, presentation and interpretation*. Longman Group: UK
- Rolph, T.C., Vigliotti, L. and Oldfield, F. (2004) Mineral magnetism and geomagnetic secular variation of marine and lacustrine deposits from central Italy: timing and nature of local and regional Holocene environmental change. *Quaternary Science Reviews*. **23**: 1699-1722
- Roncevic, N.S. (1984) Geological map of Libya 1:250,000, Sheet: Hasi Anjiwal (NG 32-4) Explanatory Booklet. Industrial Research Centre Tripoli.
- Rouchy, J.M. and Caruso, A. (2006) The Messinian salinity crisis in the Mediterranean basin: A reassessment of the data and an integrated scenario. *Sedimentary Geology*. **188-189**: 35-67
- Rozanski, K. and Gonfiantini, R. (1990) Isotopes in Climatological Studies. *IAEA Bulletin*. **4**: 9-15
- Ruddiman, W.F., Sarnthein, M., Backman, J., Baldauf, J.G., Curry, W., Dupont, L.M., Janecek, T., Pokras, E.M., Raymo, M.E., Stabell, B., Stein, R. and Tiedemann, R. (1989) 29. Late Miocene to Pleistocene evolution of the climate in Africa and the low-latitude Atlantic: Overview of Leg 108 Results. *Proceedings of the Ocean Drilling Program*. **108**: 463-484
- Rust, B.R. and Nanson, G.C. (1989) Bedload transport of mud as pedogenic aggregates in modern and ancient rivers. *Sedimentology*. **36**: 291-306
- Ruiz, F., Abad, M., Bodergat, A.M., Carbonnel, P., Rodriguez-Lazaro, J., Gonzalez-Regalado, M.L., Toscano, A., Garcia, E.X. and Prenda, J. (2013) Freshwater ostracods as environmental tracers. *International Journal of Environmental Science Technology*. **10**: 1115-1128
- Sagnotti, L., Roberts, A.P., Weaver, R., Verosub, K.L., Florindo, F., Pike, C.R., Clayton, T. and Wilson, G.S. (2005) Apparent magnetic polarity reversals due to remagnetisation resulting from late diagenetic growth of greigite from siderite. *Geophysical Journal International*. **160**: 89-100
- Salzmann, U., Haywood, A.M., Lunt, D.J., Valdes, P.J. and Hill, D.J. (2008) A new global biome reconstruction and data-model comparison for the Middle Pliocene. *Global Ecology and Biogeography*. **17**: 432-447

- Schleser, G.H., Helle, G., Lucke, A. and Vos, H. (1999) Isotope signals as climate proxies: the role of transfer functions in the study of terrestrial archives. *Quaternary Science Reviews*. **18**:927-943
- Schnurrenberger, D., Russell, J. and Kelts, K. (2003). Classification of lacustrine deposits based on sedimentary components. *Journal of Palaeolimnology*. **29**: 141-154
- Scholle, P.A. (1979) A Colour Illustrated Guide to Constituents, Textures, Cements and Porosities of Sandstones and Associated Rocks. *American Association of Petrology and Geology*. Memoir 28.
- Schultz, A and Soffel, H. C. (1973) Paleomagnetism of tertiary basalts from Libya. *Geophysical Journal Royal Astronomical Society*. **32**:373–380
- Schuster, M., Durringer, P., Ghienne, J-F., Vignaud, P., Mackaye, H.T., Likius, A. and Brunet, M. (2006) The Age of the Sahara Desert. *Science*. **311**:821
- Schuster, M., Durringer, P., Ghienne, J-F., Roquin, C., Sepulchre, P., Moussa, A., Lebatard, A-E., Mackaye, H.T., Likius, A., Vignaud, P. and Brunet, M. (2009) Chad Basin: Paleoenvironments of the Sahara since the Late Miocene. *Comptes Rendus Geoscience*. **341**:603–611
- Schieber, J. and Ellwood, B.B. (1993) Determination of basinwide palaeocurrent patterns in a shale sequence via AMS: A case study of the mid-Proterozoic Newland Formation, Montana. *Journal of Sedimentary Research*. **63**
- Scott, G.R. and Hotes, S.A. (1996) The reversal test: An examination of secondary directions. *Geophysical Research Letters*. **23**: 1805-1808
- Segalen, L., Lee-Thorp, J.A., Cerling, T. (2007) Timing of C4 grass expansion across the sub-Saharan Africa. *Journal of Human Evolution*. **53**: 549-559
- Seidl, K. and Rohlich, P. (1984) Geological map of Libya 1:250,000, Sheet: Sabha (NG 33-2) Explanatory Booklet. Industrial Research Centre Tripoli.
- Senut, B., Pickford, M. and Segalen, L. (2009) Neogene desertification of Africa. *C.R. Geoscience*. **341**: 591-602
- Singh, B. and Gilkes, R.J. (1996) Nature and properties of iron rich glaeboles and mottles from some south-west Australian soils. *Geoderma*. **71**: 95-120
- Smilde, A. K., Kiers, H.A.L., Bijlsma S., Rubingh C.M., van Erk, M.J. (2009) Matrix correlations for high-dimensional data: the modified RV-coefficient. *Bioinformatics* **25**: 401–405.

- Solari, M.A., Herve, F., Le Roux, J.P., Airo, A. and Sial, A.N. (2010) Palaeoclimatic significance of lacustrine microbialites: A stable isotope case study of two lakes at Torres del Paine, southern Chile. *Palaeogeography, Palaeoclimatology, Palaeoecology*. **297**: 70-82
- Soulie-Marsche, I. (2008) Charophytes, indicators for low salinity phases in North African sebkhet. *Journal of African Earth Sciences*. **51**:69-76
- Soulie-Marsche, I., Bieda, S., Lafond, R., Maley, J., M'Baitoudji, Vincent, P.M. and Hugues Faure (2010) Charophytes as bio-indicators for lake level high stand at 'Trou au Natron', Tibesti, Chad, during the Late Pleistocene. *Global and Planetary Change*. **72**:334-340
- Stokes, S. and Bray, H.E. (2005) Late Pleistocene eolian history of the Liwa region, Arabian Peninsula. *GSA Bulletin*. **117**: 1466-1480
- Stuut, J-B., Smalley, I. and O'Hara-Dhand, K. (2009) Aeolian dust in Europe: African sources and European deposits. *Quaternary International*. **198**: 234-2445
- Sun, J., Zhang, A. and Zhang, L. (2009) New evidence on the age of the Taklimakan Desert. *Geology*. **37**: 159-162
- Swezey, C. (2006) Revisiting the age of the Sahara Desert. *Science*. **312**: 1139
- Swezey, C. (2009) Cenozoic stratigraphy of the Sahara, Northern Africa. *Journal of African Earth Sciences*. **53**: 89-121
- Takatsugi, K.O. and Hyodo, M. (1995) A geomagnetic excursion during the late Matuyama Chrons, the Osaka Group, southwest Japan. *Earth and Planetary Science Letters*. **136**:511-524
- Talbot, M.R. (1990) A review of the palaeohydrological interpretation of carbon and oxygen isotopic ratios in primary lacustrine carbonates. *Chemical Geology: Isotope Geoscience section*. **80**:261-279
- Talma, A.S. and Netterberg, F. (1983) Stable isotope abundances in calcretes. In BCL Wilson (Ed.) Residual Deposits, Geological Society (London) Special Publication. 11:221-233. Blackwell: Oxford.
- Tandon, S.K. and Andrews, J.E. (2001) Lithofacies associations and stable isotopes of palustrine and calcrete carbonates: examples from an Indian Maastrichtian regolith. *Sedimentology*. **48**: 339-355
- Tanner, L.H. (2010) *Continental carbonates as indicators of palaeoclimate*. In: Alonso-Zarza, A.M. and Tanner, L.H. (Eds) Continental Carbonates. Developments in Sedimentology. Chapter 4: 179-214

- Tarling, D.H. (1983) *Palaeomagnetism: Principles and Applications in Geology, Geophysics and Archaeology*. Chapman and Hall: Great Britain
- Tarling, D.H. and Hrouda, F. (1993) *The Magnetic Anisotropy of Rocks*. Chapman and Hall: Great Britain
- Tarling, D.H. (1999) Introduction: deposits and diagenesis. In: Tarling, D. H. and Turner, P. (eds) *Palaeomagnetism and Diagenesis in Deposits. Geological Society, London, Special Publications*, **151**: 1-8.
- Tauxe, L., Banerjee, S.K., Bulter, R.F. and van der Voo, R. (2016) *Essentials of Palaeomagnetism: 4th Web Edition*.
<https://earthref.org/MagIC/books/Tauxe/Essentials/WebBook3ch15.html#x17-18400015>
- Thiedig, F.M., Oezen, D., El-Chair, M., Geyh, M.A. (2000) The absolute age of the Quaternary lacustrine limestone of the Al Mahruqah Formation — Murzuq Basin, Libya. In: Sola, M.A., Worsley, D. (Eds.), *Geological Exploration in the Murzuq Basin*. Elsevier, Amsterdam, pp. 89–116.
- Thiedig, F.M and Geyh, M.A. (2004) Zyklische lakustrine Kalke im abflusslosen Murzuq-Becken (Libyen) als Zeugnisse interglazialer Feuchtphasen in Nordafrika während der letzten 500 ka. *Beitrag zur Regionalen Geographie*. **135**: 267-288
- Thompson, R. and Clark, R.M. (1989) Sequence slotting for stratigraphic correlation between cores: theory and practice. *Journal of Palaeolimnology*. **2**: 173–184.
- Thompson, R., Clark, R.M., and Boulton, G.S. (2012) Core correlation. In: Birks, H.J.B., Lotter, A.F. Juggins, S., Smol, J.P. (Eds.): *Tracking Environmental Change Using Lake Deposits: Data Handling and Numerical Techniques. Developments in Palaeoenvironmental Research*. **5**:415–430.
- Torsvik. T.H., Van der Voo, R., Preeden, U., Niocaill, C.N., Steinberger, B., Doubrovine, P.V., van Hinsbergen, D.J.J., Domeier, M., Gaina, C., Tohver, E., Meert, J.G., McCauslan, P.J.A. and Cocks, L.R.M. (2012) Phanerozoic polar wander, palaeogeography and dynamics. *Earth-Science Reviews*. **114**:325-268
- Tucker, M.E. (1988) *Techniques in Sedimentology*. Blackwell Science: UK
- Tucker, M.E. and Wright, V.P. (1990) *Carbonate Sedimentology*. First Edition. Blackwell Scientific Publications: Oxford.
- Tucker, M.E. (2001) *Sedimentary Petrology*. Third Edition. Blackwell Science Ltd:UK
- Van Zinderen Bakker, E.M. and Mercer, J.H. (1986) Major late Cenozoic climatic events and palaeoenvironmental changes in Africa viewed in a world wide context. *Palaeogeography, Palaeoclimatology, Palaeoecology*. **56**: 217-235

- Verschuren, D. (2002) Climate reconstruction from African lake deposits. ESF–HOLIVAR workshop, Lammi Finland, April 17-20th 2002. http://www.gsf.fi/esf_holivar/verschuren.pdf
- Verrecchia, E.P. (2007) Lacustrine and palustrine geochemical deposits. In Nash, D. J and McLaren, S. J. *Geochemical Deposits and Landscapes*. Blackwell Publishing: Singapore. Pp 298-329
- Walden, J. and White, K. (1997) Investigation of the controls on dune colour in the Namib Sand Sea using mineral magnetic analyses. *Earth and Planetary Science Letters*. **152**: 187-201
- Wang, X., Lovelie, R., Yang, Z., Pei, J., Zhao, Z. and Sun, Z. (2005) Remagnetisation of Quaternary eolian deposits: A case study from SE Chinese Loess Plateau. *Geochemistry, Geophysics, Geosystems*. **6**: 1-14
- Watts, N.L. (1980) Quaternary pedogenic calcretes from the Kalahari (southern Africa): mineralogy, genesis and diagenesis. *Sedimentology*. **27**: 661-686
- White, K. McLaren, S.J., Black, S. and Parker, A. (2000) Evaporite minerals and organic horizons in sedimentary sequences in the Libyan Fezzan: Implications for palaeoenvironmental reconstruction. In: *Linking Climate Change to Land Surface Change*. Kluwer Academic Publishers: Netherlands. Pp 193-208
- White, K., Charlton, M., Drake, N., McLaren, S., Mattingly, D. and Brooks, N. (2006) Lakes of the Edeyen Awbari and the Wadi al-Hayat. In: Mattingly, D., McLaren, S., Savage, E., al-Fasatwi, Y. and Gadgood, K. (eds) *The Libyan Desert, Natural Resources and Cultural Heritage*. The Society for Libyan Studies, London: 123-130.
- White, K. and Mattingly, D.J. (2006). Ancient lakes of the Sahara. *American Scientist*. **94**:58-65
- White, K., Drake, N., Armitage, S., Salem, M.J., El-Hawat, A. And Charlton, M. (2013) Quaternary Palaeohydrology of the Fazzan Basin, SW Libya: Evidence from Satellite Remote Sensing. In Salem M.J. (eds.) *The Geology of Southern Libya*. Volume 2:281-292.
- Woller, F. and Fediuk, F. (1980) Volcanic rocks of Jabal as Sawda. In: Salem, M.J., Busrewil, M.T. (Eds.), *The Geology of Libya III*. Academic Press, London, pp1081–1093
- Woller, F. (1984) Geological Map of Libya 1: 250 000. Sheet: Al Fuqaha (NG 33-3). Explanatory Booklet. Industrial Research Center, Tripoli.
- Wright, V.P. and Tucker, M.E. (1991) *Calcretes*. Blackwell Scientific Publications: Oxford.
- Wright, V.P. and Platt, N.H. (1995) Seasonal wetland carbonate sequences and dynamic catenas: a re-appraisal of palustrine limestones. *Sedimentary Geology*. **99**: 65-71

- Wright, V.P., Alonso Zarza, A.M., Sanz, M.E. and Calvo, J.P. (1997) Diagenesis of Late Miocene micritic lacustrine carbonates, Madrid Basin, Spain. *Sedimentary Geology*. **114**:81-95
- Wright, V.P. (2007) Calcrete. In Nash, D. J and McLaren, S. J. *Geochemical Deposits and Landscapes*. Blackwell Publishing: Singapore. Pp 1-45.
- Youcef, F. and Hamdi-Assa, B. (2014) Palaeoenvironmental Reconstruction from Palaeolake Deposits in the Area of Ouargla (Northern Sahara of Algeria). *Arid Land Research and Management*. **28**: 129-146
- Zachos, J., Pagani, M., Sloan, L., Thomas, E. and Billups, K. (2001) Trends, Rhythms, and Aberrations in Global Climate 65 Ma to Present. *Science*. **292**: 686-693
- Zan, J., Fang, X., Yan, M., Zhang, W. and Lu, Y. (2015) Lithologic and rock magnetic evidence for the Mid-Miocene Climatic Optimum recorded in the sedimentary archive of the Xining Basin, NE Tibetan Plateau. *Palaeogeography, Palaeoclimatology, Palaeoecology*. **431**: 6-14
- Zhang, Z., Ramstein, G., Schuster, M., Li, C., Contoux, C and Yan, Q. (2014) Aridification of the Sahara desert caused by Tethys Sea shrinkage during the Late Miocene. *Nature Letters*. **513**: 401-418
- Zhu, R., Pan, Y. and Liu, Q. (1999) Geomagnetic excursions recorded in Chinese loess in the last 70,000 years. *Geophysical Research Letters*. **26**: 505-508
- Zimmerle, W. (1995) *Petroleum Sedimentology*. Kulwer Academic Publishers: London
- Zuppi, G.M. and Sacchi, E. (2004) Hydrogeology as a climate recorder: Sahara–Sahel (North Africa) and the Po Plain (Northern Italy). *Global and Planetary Change*. **40**:79–91